

PL-TR-96-2080
Special Reports, No. 278

**PROCEEDINGS OF THE 18TH ANNUAL
CONFERENCE ON ATMOSPHERIC
TRANSMISSION MODELS,
6-8 JUNE 1995**

Editors:

Gail P. Anderson
Richard H. Picard
James H. Chetwynd

18 April 1996

APPROVED FOR PUBLIC RELEASE; DISTRIBUTION UNLIMITED




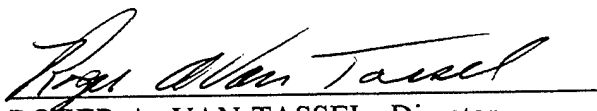
PHILLIPS LABORATORY
Directorate of Geophysics
AIR FORCE MATERIEL COMMAND
HANSCOM AFB, MA 01731-3010

19960514 046

DO NOT WRITE IN THESE SPACES

"This technical report has been reviewed and is approved for publication"


WILLIAM A.M. BLUMBERG, Chief
Simulation Branch
Optical Environment Division


ROGER A. VAN TASSEL, Director
Optical Environment Division

This document has been reviewed by the ESC Public Affairs Office (PA) and is releasable to the National Technical Information Service (NTIS).

Qualified requestors may obtain additional copies from the Defense Technical Information Center (DTIC). All others should apply to the National Technical Information Service (NTIS).

If your address has changed, or if you wish to be removed from the mailing list, or if the addressee is no longer employed by your organization, please notify PL/TSI, 29 Randolph Road, Hanscom AFB, MA 01731-3010. This will assist us in maintaining a current mailing list.

Do not return copies of this report unless contractual obligations or notices on a specific document requires that it be returned.

REPORT DOCUMENTATION PAGE

Form Approved
OMB No. 0704-0188

Public reporting burden for this collection of information is estimated to average 1 hour per response, including the time for reviewing instructions, searching existing data sources, gathering and maintaining the data needed, and completing and reviewing the collection of information. Send comments regarding this burden estimate or any other aspect of this collection of information, including suggestions for reducing this burden, to Washington Headquarters Services, Directorate for Information Operations and Reports, 1215 Jefferson Davis Highway, Suite 1204, Arlington, VA 22202-4302, and to the Office of Management and Budget, Paperwork Reduction Project (0704-0188), Washington, DC 20503.

1. AGENCY USE ONLY (Leave blank)		2. REPORT DATE 18 April 1996	3. REPORT TYPE AND DATES COVERED Scientific	
4. TITLE AND SUBTITLE PROCEEDINGS OF THE 18th ANNUAL CONFERENCE ON ATMOSPHERIC TRANSMISSION MODELS, 6-8 JUNE 1995.			5. FUNDING NUMBERS PE: 62101F PR: 3054 TA: GD WU: 01	
6. AUTHOR(S) Editors; GAIL P. ANDERSON RICHARD H. PICARD JAMES H. CHETWYND				
7. PERFORMING ORGANIZATION NAME(S) AND ADDRESS(ES) Phillips Laboratory/GPOS 29 RANDOLPH ROAD HANSCOM AFB, MA 01731-3010			8. PERFORMING ORGANIZATION REPORT NUMBER PL-TR-96-2080 SR, No. 278	
9. SPONSORING/MONITORING AGENCY NAME(S) AND ADDRESS(ES)			10. SPONSORING/MONITORING AGENCY REPORT NUMBER	
11. SUPPLEMENTARY NOTES				
12a. DISTRIBUTION/AVAILABILITY STATEMENT Approved for public release; distribution unlimited			12b. DISTRIBUTION CODE	
13. ABSTRACT (Maximum 200 words) CONTAINS THE VIEWGRAPHS AND OTHER MATERIALS FOR THE 48 PAPERS PRESENTED AT THE 18th ANNUAL REVIEW CONFERENCE ON ATMOSPHERIC TRANSMISSION MODELS HELD AT THE GEOPHYSICS DIRECTORATE, PHILLIPS LABORATORY (AFMC), HANSCOM AFB, MA ON: 6-8 JUNE 1995.				
14. SUBJECT TERMS Atmospheric transmittance codes Aerosols Atmospheric structure			15. NUMBER OF PAGES 454	
			16. PRICE CODE	
17. SECURITY CLASSIFICATION OF REPORT Unclassified		18. SECURITY CLASSIFICATION OF THIS PAGE Unclassified	19. SECURITY CLASSIFICATION OF ABSTRACT Unclassified	20. LIMITATION OF ABSTRACT SAR

TABLE OF CONTENTS

HIGH RESOLUTION SPECTROSCOPY/LBL CODES

HITRAN Atmospheric Workstation (HAWKS) L.S.Rothman, PL/Geophysics Directorate: R.R.Gamache, U.Mass Lowell: R.B.Wattson, Utah State U: A.McCann, J.Schroeder; Ontar.	1;49
Fourier Transform Absorption Spectroscopy of the Herzberg I Bands of O ₂ W.H.Parkinson, J.E.Murray, J.R. Esmond, K.Yoshino; Harvard Smithsonian Center: A.P.Thorne, R.C.M.Learner, G.Cox; Imperial College, London.	2;55
Empirical Water Vapor Continuum Models for Infrared Propagation. M.E.Thomas, Johns Hopkins/APL	3;61
Determination of the Broadening Wing Range of Absorption Lines for Line-by-line Calculation of Cross-sections. T.Yokota, Y.Matsumoto, H.Tsubaki; National Institute for Environmental Studies, Keio U. Japan.	4;
Initial Analyses of Surface Spectral Radiance Between Instrument Observations and Line-by-line Calculations. P.D.Brown, S.A.Clough; AER.: N.E.Miller, T.R.Shippert, D.D.Turner; Pacific Northwest Laboratories: R.O.Knuteson, H.E.Revercomb, W.L.Smith; U. Wisconsin.	5;84
Phillips Lab Atmospheric Radiance Code (ARC): Extensions and Recent Applications. P.P.Wintersteiner, ARCON: R.H.Picard, J.R.Winnick; PL/Geophysics Directorate.	6;72
FASCODE for the Environment (FASE) H.E.Snell, J.-L.Moncet; AER.: G.P.Anderson, J.H.Chetwynd, S.Miller, J.Wang; PL/Geophysics Directorate.	7;90
SHARC-4: Strategic High Altitude Radiance Model, a Progress Report R.D.Sharma, J.H.Brown; PL/Geophysics Directorate: J.H.Gruninger, R.Sundberg, J.Duff, S. Adler-Golden, D.Robertson; Spectral Sciences Inc.: H.Dothe, F.von Esse; Mei Technologies Inc.	8;96

MODERATE SPECTRAL RESOLUTION RADIATIVE TRANSFER CODES

FASCODE/MODTRAM/LOWTRAN: Past/Present/Future. G.P.Anderson, F.X.Kneizys, J.H.Chetwynd, J.Wang, M.L.Hoke, L.S.Rothman, L.M.Kimball, R.A.McClatchey; PL/Geophysics Directorate: E.P.Shettle, N.R.L.; S.A.Clough, W.O.Gallery, H.E.Snell; AER.: L.W.Abreu, ONTAR: J.E.A.Selby, Northrop-Grumman.	9;101
---	-------

Modular Algorithms for Radiative Transfer through Cloudy Atmospheres. P.Ricciazzi, S.Yang, W.O'Hirock, C.Gautier; ICES, U.Cal. Santa Barbara.	10;120
Second Simulation of the Satellite Signal in the Solar Spectrum (6S) An Overview. E.F.Vermote; NASA/GSFC.	11;
Recent Upgrades to MODTRAN: MODTRAN4. A.Berk, L.S.Bernstein, P.K.Acharya, D.Robertson; SSI.: G.P.Anderson, J.H.Chetwynd; PL/Geophysics Directorate.	12;125
The MOSART Code: Its Present and Future Status. W.M.Cornette, PRA: P.K.Acharya, D.C.Robertson; SSI: G.P.Anderson, PL/Geophysics Directorate.	13;144
RRTM: A Rapid Radiative Transfer Model. E.J.Mlawer, S.J.Taubman, S.A.Clough; AER.	14;150
Algorithm for Estimating Solar UV Spectral Irradiance in Atmospheric Transmittance/Radiance codes. J.Lean, NRL.	15;158
Recent Measurement Applications of OSIC UV Propagation Model. K.M.Crow, M.E.Neer; SciTec.	16;164
A Fast Multi-dimensional Atmospheric Effects Interpolator for E DIS. P.K.Acharya, D.C.Robertson; SSI: W.M.Cornette, PRA: L.Jeong, PL/Geophysics Directorate.	17;170
Simplified Expression of the Radiative Transfer Equation for Surface Temperature Estimation from LOWTRAN7. M.Moriyama, K.Mima; Nagasaki U.	18;182

AEROSOLS, LIDAR, ETC

The POAM II Experiment and Selected Measurement Results. E.P.Shettle, R.M.Bevilaqua, J.S.Hornstein, K.W.Hoppel, R.L.Lucke; NRL: J.Lumpe, S.Krigman, M.Fromm, T.L.Ainsworth, D.Debrestian; CPI: W.J.Glaccum, ARC.	19;188
The Relation Between Zenith Polarization and Optical Depth for Stratospheric Aerosols from El Chichon and Pinatubo. F.E.Volz, PL/Geophysics Directorate.	20;200
Infrared Optical Constants of Sahara Sand, Volcanic Ash, and Water Soluble Aerosols. W.G.Egan, J.Joseph; CUNY.	21;202
A Double Scatter Lidar Program to Determine Particle Size Distributions. R.Garner, Photometrics Inc.	22;210
Aerosol Size Distribution Measurements and Laser Transmission Experiments in Zurich, Switzerland. S.Kalin, A.Ohmura; Swiss Federal Inst. of Technology, Zurich.	23;218

- Non-Negative Conditioning of the Phase Function Legendre Expansion.
D.H.Tofsted, USA Research Lab. WSMR. 24;224
- Maximum Detection Range of Low Intensity Target Edges as a Function of
Variable Blur and Albedo Using Morphological and Segmentation
Image Processing Techniques. 25;230
C.A.Paiva, Naval Surface Warfare Center.
- A Bi-Static Receiver to Observe Lower Tropospheric Aerosol Properties.
T.D.Stevens, C.R.Philbrick; Penn State U./ARL Lidar Lab. 26;242
- Lidar Atmospheric Profile Sensor (LAPS): a Remote Sensing Prototype.
C.R.Philbrick, Penn State U./ARL Lidar Lab. 27;

REMOTE SENSING (PART A; H₂O)

- Airborne Visible/Infrared Imaging Spectrometer (AVIRIS).
R.O.Green, JPL: D.A.Robert, C.Gautier; U.Cal. Santa Barbara 28;248
- Modtran and Atmospheric Correction of Remote Sensing Images of
Coastal and Inland Waters. 29;
J.F.de Haan, J.M.M.Kokke; Survey Dept. Rijkswaterstaat, Delft,
The Netherlands.
- Inversion of Downwelling Spectral Radiance for Tropospheric
Profile Retrievals: Practical Aspects. 30;263
J.-M.Theriault, DREV, Quebec: J.-L.Moncet, AER.
- Temporal Phase relationships Among Atmospheric Constituents.
W.G.Egan, CUNY: A.W.Hogan, USA Cold Regions R&E Lab. 31;270

REMOTE SENSING (PART B: OTHER).

- FASCOD3 Atmospheric Modeling of an SF₆ Plume Released from a
Stationed Balloon. 32;277
J.B.Koffend, Aerospace Corp.
- Trace Constituent Spectra from CIRRIS-1A Measurements and
Concentration Profiles Retrieval. 33;281
D.K.Zhou, G.E.Bingham, A.J.Steed; Utah State U.:
G.P.Anderson, R.M.Nadile; PL/Geophysics Directorate.
- CIRRIS-1A Earthlimb Spectral Measurements, Calibration, and
Atmospheric O₃, HNO₃, CFC-12, CFC-11 Profile Retrieval. ;289
G.E.Bingham, D.K.Zhou, A.J.Steed; Utah State U.:
G.P.Anderson, D.R.Smith, J.H.Chetwynd, R.M.Nadile; PL/Geophysics
Directorate.
- Stratospheric Trace Species Measurements by Solar Occultation Fourier
Transform Spectrometry. 34;
T.Hawat, R.Tourget; Institut d'Electronique et de
Micro-Electronique du Nord (IEMN), CNRS/UMR, France: C.Camy-Peyret,
P.Jeseck; Laboratoire de Physique Molculaire et Applications,
CNRS/UPM, France. S.Payan, CEA/CESTA, France.

Non-LTE Effects on Nadir Viewing Temperature Sounding in the Stratosphere Using the CO₂ 4.3 Micron Band.

J.R.Winick, PL/Geophysics Directorate: J.-L.Moncet,
H.E.Snell, D.B.Hogan; AER.: P.P.Wintersteiner, ARCON:
J.Wang, NCAR. 35;325

Remote Sensing of Temperature in the 4.3 micrometer Band of CO₂.
H.E.Snell, J.-L.Moncet, D.B.Hogan; AER. 36;

The Use of MODTRAN to Estimate the SO₂ Content of Volcanic Plumes.
V.J.Realmuto, JPL. 37;332

Modeling Local Atmospheric Effects by MODTRAN-3 Code, and Vertical Profiles in the Area of Mt. Etna Volcano, Sicily.

S.Teggi, S.Pugnaghi; U. Modena, Italy: M.F.Buongiorno,
M.P.Bogliolo, Istituto Nazionale di Geofisica, Rome, Italy:
V.J.Realmuto, JPL. 38;340

STRUCTURE AND NON-LTE EFFECTS

Production of Vibrationally and Rotationally Excited NO in the Nighttime Terrestrial Thermosphere

R.D.Sharma, PL/Geophysics Directorate: V.A.Karchenko,
Y. Sun; Harvard Smithsonian: H.Dothe, F.von Esse; Mei Technology:
A.Dalgarno, Harvard Smithsonian. 39;345

NO(v) Densities in the Lower Thermosphere.

S.J.Lipson, W.A.M.Blumberg, R.B.Lockwood, J.R.Lowell, R.M.Nadile;
PL/Geophysics Directorate: P.S.Armstrong, J.A.Dodd; Utah State U. 40;350

Recent Advances in Gravity Wave Spectra and Implications for Radiance Structure Models.

E.M.Dewan, R.H.Picard; PL/Geophysics Directorate. 41;374

SHARC-4: Model for Atmospheric Background Radiance Structures.

J.Gruninger, J.W.Duff, R.L.Sundberg; SSI:
J.H.Brown, R.D.Sharma, W.A.M.Blumberg; PL/Geophysics Directorate. 42;385

A Fast "Stretched-Space" Method for Generating Synthetic Vertical Sheets of Non-Stationary Stochastic Atmospheric Structure for Airglow Simulation.

J.H.Brown, PL/Geophysics Directorate:
N.J.Grossbard, Boston College. 43;391

FASCODE/MODTRAN: User Access and Support

J.H.Chetwynd, G.P.Anderson; PL/Geophysics Directorate:
J.Vail, MEI Tech.: L.W.Abreu, Abreu Consulting: H.E.Snell, AER. 44;

PLEXUS Version 2.0: A Unified Knowledge-Based Approach to Atmospheric Modeling.

S.B.Downer, MRC: F.O.Clark, PL/Geophysics Directorate. 45;

PLEXUS: Geophysics Atmosphere and Weather for Synthetic Environments.
F.O.Clark, PL/Geophysics Directorate. 46;395

An Application of MODTRAN for Real-Time Infrared Scene Generation.

D.L.Quam, MTL Systems. 47;418

Land Data Base Requirements for Environmental Effects Models for
Use in Dis.

W.M.Cornette, D.C.Anding, F.C.Mertz; PRA.

48;428

ABSTRACTS

1-48

AUTHORS

438

ATTENDEES

441

THIS PAGE BLANK

PREFACE

The eighteenth DoD Tri-Service Annual Review Conference on Atmospheric Transmission Models was held at the Geophysics Directorate of the USAF Phillips Laboratory at Hanscom AFB, Bedford, Massachusetts from 6-8 June 1995.

About 200 authors and participants discussed 48 papers concerning the coupling and interaction of optical and atmospheric phenomena. The emphasis was upon high resolution for line-by-line studies and moderate resolution for other purposes. Aerosol properties, remote sensing, and lidar were other topics covered. Finally the effects of wave structure in the atmosphere and of non LTE processes were considered. The optical phenomena of interest ranged over the spectrum from the ultra-violet through the visible to the infrared.

The abstracts are grouped together at the front of the volume and the main-presentations hard-copy furnished by the authors follows. Because of the time difference involved between the writing of the abstracts and the presentations there is not always an exact correspondence between the two.

Also included are a listing of authors for the abstracts and the papers together with an attendee's list.

Gail. P. Anderson
Simulation Branch,
Optical Environment Division

ABSTRACTS

HITRAN ATMOSPHERIC WORKSTATION (HAWKS)

L.S. Rothman

GPOS, Hanscom AFB, MA 01731-3010

R.R. Gamache

U. Mass. Lowell
Lowell, MA 01854

R.B. Watson

Stewart Radiance Laboratory
Utah State University
Bedford, MA 01730

J. Schroeder and A. McCann

Ontar
9 Village Way
North Andover, MA 01845

A new edition of the HITRAN molecular spectroscopic database is being released this year. It will be included in a compilation called HAWKS (HITRAN Atmospheric Workstation). HAWKS represents more fully a "matter" database. There will be files of aerosol indices of refraction, UV line-by-line and cross-section parameters, high-temperature line-by-line parameters (HITEMP), supplemental files of gases such as ionic species and high-vibrational calculations, and more extensive IR cross-sections. In addition, there will be vastly improved software handling of the data in both Windows and UNIX platforms, all to be made available on a CD-ROM.

The presentation will discuss some of the interesting features that will be present on the compilation as well as give some interesting examples of new capabilities.

FOURIER TRANSFORM ABSORPTION SPECTROSCOPY OF THE HERZBERG I BANDS OF O₂

W.H. Parkinson, J.E. Murray, J.R. Esmond, and K. Yoshino
Harvard Smithsonian Center for Astrophysics, Cambridge, MA 02138, U.S.A.
and

A.P. Thorne, R.C.M. Learner, and G. Cox
Imperial College of Science, Technology, and Medicine, London, U.K.

Fourier transform spectroscopic measurements of the absorption bands of the Herzberg I system ($A^3\Sigma_u^+ - X^3\Sigma_g^-$) of O₂ have been made in the wavelength region 240-270 nm with resolution of 0.06 cm⁻¹. A stable, bright, line-free, background continuum and a means to limit the bandwidth of radiation are required in FTS for a good signal-to-noise ratio. We used a high pressure, Xenon lamp (Hamamatsu 300) as the background source. The bandwidth of the background radiation was limited by means of a double-prism, zero angular, and linear dispersion monochromator. For weak absorption of the Herzberg I bands, we used a White cell, in which the distance of 2.54 m between the two main mirrors was set and adjusted for 16 double passes of light, making a path length of 81.28 m. We used four different pressures of O₂ in the White cell, 60, 120, 200, and 370 Torr.

Rotational line positions are determined with an accuracy of 0.005 cm⁻¹, and rotational term values are obtained for the vibrational levels, $v = 4 - 11$. Molecular constants of these levels are also obtained. We observed and measured pressure broadening of rotational lines. Precise band oscillator strengths of the (4,0) - (11,0) bands are obtained by direct measurement, and they are significantly higher than the previous experimental values for some of the strong bands. The rotational line strengths and the branching ratios are also presented for the same bands.

This work is supported by NSF Division of Atmospheric Science grants ATM-91-16562 to Harvard College Observatory. We acknowledge the support of the UK Science and Engineering Research Council and the Paul Fund of the Royal Society for the development of UV-FTS.

EMPIRICAL WATER VAPOR CONTINUUM MODELS FOR INFRARED PROPAGATION

Michael E. Thomas*

The Johns Hopkins University/Applied Physics Laboratory
Laurel, MD 20723

*Presented by Adam Zynarski

The characterization of the water vapor continuum remains an important problem concerning infrared propagation in the atmosphere. Radiometric imaging within the atmosphere in the 8 to 12 μm and 3 to 5 μm regions, and eye safe lidar in the 2 μm and 1.6 μm window regions require accurate knowledge of the water vapor continuum.

Although the physical nature of the continuum is a complex problem, the observed frequency, pressure and temperature dependence can be represented reasonably well by simple mathematical functions consistent with far wing theories. This approach is the basis for current models used in LOWTRAN/MODTRAN and for the models listed in the SPIE/ERIM EO/IR Systems Handbook (Volume 2 Chapter 1). However, these models are based solely on a limited, but high quality, data set collected by a spectrometer and White cell. Additional information on oxygen broadening and temperature dependence is available from numerous laser measurements of the water vapor continuum.

A survey of relevant experimental data is made to determine the best available measurements of the water vapor continuum in various atmospheric window regions. Then the data are fit to an empirical model over the entire window region. A good fit is obtained for typical atmospheric conditions covering the 8 to 12 μm and 3 to 5 μm regions. No experimental data, covering atmospheric conditions, exist in the 2 μm and 1.6 μm regions. However, models can be proposed based on far wing extrapolations of the bordering vibrational water vapor bands.

DETERMINATION OF THE BROADENING WING RANGE OF ABSORPTION LINES FOR LINE-BY-LINE CALCULATION OF CROSS-SECTIONS

Tatsuya Yokota and Yukio Matsumoto
National Institute for Environmental
Studies, Japan

Hiroe Tsubaki
Faculty of Science and Technology,
Keio University, Japan

Cross section calculation for each molecular absorption line is used to estimate the amount of the absorbers in the atmosphere from satellite remote sensing data. Determination of the wing range of each absorption spectrum is essential for the precision of calculation.

If we set the range wide, the calculated spectrum is precise but it is very time consuming for computer calculation. The atmosphere radiance/transmission code FASCODE has fixed this wing range up to $\pm 25 \text{ cm}^{-1}$ in case of high pressure. We propose a new method for the determination of the wing range depending on the Lorentz and Doppler HWHM and the line strength of absorption. This method has been validated by computer simulation of line-by-line calculation for infrared ozone absorption lines.

INITIAL RESULTS OF SPECTRAL ANALYSES OF RESIDUALS BETWEEN OBSERVED DOWNWELLING RADIANCE AND MODEL CALCULATIONS

P.D. Brown and S.A. Clough

Atmospheric and Environmental Research Inc
840 Memorial Drive
Cambridge, MA 02139

R.O. Knuteson and H.E. Revercomb

Space Science and Engineering Center
University of Wisconsin-Madison
1225 West Dayton Street
Madison, WI 53706

N.E. Miller and T.R. Shippert

Pacific Northwest Laboratory
Battelle Boulevard
P.O. Box 989
Richland, WA 99352

A Quality Measurement Experiment (QME) is being conducted to analyze the spectral residuals between the downwelling longwave radiance measured by the University of Wisconsin Atmospheric Emitted Radiance Interferometer (AERI) and spectral radiance calculated by the Line By Line Radiative Transfer Model (LBLRTM), as part of the DoE Atmospheric Radiation Measurement (ARM) Program. The purpose of this study is to assess the quality of AERI measurements, LBLRTM calculations, and the definition of the radiating atmospheric column. Validations of spectral radiances have been performed over a wide range of atmospheric states from December 1993 through March 1995. Initial analyses of nominally clear sky data indicate that the present limitation on the radiative transfer validations is the current inability to specify the atmospheric state. Analyses of validations from April 1994 to the present will be shown.

FASCODE FOR THE ENVIRONMENT (FASE)

H.E. Snell and J.-L. Moncet

G.P. Anderson, J.H. Chetwynd,
S. Miller and J. Wang*

Atmospheric and Environmental
Research, Inc.
840 Memorial Dr.
Cambridge, MA 02139

GPOS, Hanscom AFB, MA 01731

* Currently at NCAR/ACD

The Optical Physics Division of the Phillips Laboratory with support from the DoE Atmospheric Radiation Measurement (ARM) Program is developing a state-of-the-art line-by-line atmospheric radiative transfer model as the successor to FASCODE. The goal of this project is to create a computationally efficient model which contains the most up-to-date physics. The new model, known as FASCODE for the Environment, or "FASE", combines the best features of FASCODE and LBLRTM, the DoE's standard radiative transfer model. FASE also contains new features such as an improved solar irradiance model, and inclusion of the Schumann-Runge bands and continuum. The code is optimized for vectorized and/or parallel processing and has been put under configuration control for easy maintenance. Additional improvements have been made to the NLTE routines and to the path geometry algorithm. Future versions will be re-structured to allow for increased flexibility and easy customization of the code for specialized applications, such as a forward model for iterative inversion algorithms. Ease-of-use will be enhanced with improved input control structures and documentation to accommodate the needs of both novice and advanced users. This paper addresses changes which have been made to FASCODE and LBLRTM to create FASE, and gives an overview of the new structure and its capabilities.

**PL ATMOSPHERIC RADIATION CODE (ARC):
EXTENSIONS AND RECENT APPLICATIONS**

P.P. Wintersteiner

**ARCON, Corp
Waltham, Ma**

R.H. Picard and J.R. Winick

GPOS, Hanscom AFB, MA 01731

We will review the present status of, and planned extensions to, the PL Atmospheric Radiation Code (ARC), the AF line-by-line code used to determine non-LTE conditions in the atmosphere and the resulting line-of-sight radiances. We will describe enhancements to the code and give examples of results that have been obtained in recent applications. We will discuss improvements that have made or will make ARC more capable of calculating radiative excitation in structured atmospheres, calculating radiance due to structured emission features and for downlooking lines of sight, interfacing with FASCODE, and being used in remote sensing applications.

SHARC-4 MODEL FOR INFRARED BACKGROUNDS

R. Sharma and J. Brown

GPOS, Hanscom AFB, MA 01731

S. Adler-Golden, J. Duff,
J. Gruninger, D. Robertson
R. Sandburg

Spectral Sciences, Inc
Burlington, MA

Strategic High Altitude Radiance Code calculates infrared radiance in the 2 - 40 μm wavelength interval and 40 - 300 km altitude range, for quiescent as well as aurorally disturbed atmospheres, and for day, night, as well as terminator regions. Current capabilities of SHARC are explained and the directions for future work are outlined.

**FASCODE/MODTRAN/LOWTRAN:
PAST/PRESENT/FUTURE**

**G.P. Anderson, J.H. Chetwynd,
M.L. Hoke, L.S. Rothman**

GPOS, Hanscom AFB, MA

E.P. Shettle

**Naval Research Laboratory
Washington, DC 20375**

S.A. Clough, H.E. Snell, W.O. Gallery

**Atmospheric and Environmental Research Inc.
Cambridge, MA**

F.X. Kneizys

Retired

L.W. Abreu

**Abreu Consulting
Chelmsford, MA**

J.E.A. Selby

**Northrop-Grumman
Aerospace Corp.
Bethpage, NY**

The historic background atmospheric radiation codes (FASCODE, MODTRAN, and LOWTRAN) of the Air Force will be described in their current configuration, including recent applications and validation. The evolutionary role of these codes as DoD and other agencies migrate to more advanced/realistic operating environments will be addressed relative to the maintenance of existing and projected "line-of-sight" capabilities. It is currently the objective of this effort to base the adoption of advancements on validation of their physics-based algorithms, reserving subsequent pragmatic parameterizations for later development. This provides the user community with a set of fiducial codes with historic foundation against which to evaluate the newer suites of algorithms.

MODULAR ALGORITHMS FOR RADIATIVE TRANSFER THROUGH CLOUDY ATMOSPHERES

Paul Ricchiazzi, Catherine Gautier, William O'Hirok and Yang Shiren

Institute for Computational Earth System Science
University of California, Santa Barbara, CA

We have developed a set of radiative transfer algorithms to model SW and LW radiation in clear and cloudy conditions. The foundation for this suite of algorithms are the numerical models that describe the details of the radiative interaction – with water and ice clouds, molecular species, and aerosols. These basic routines are incorporated into a "radiative transfer user library" composed of FORTRAN subroutines with well documented calling interfaces. The library routines are then easily available to various driver codes, each with its own approach for solving the RT equation. This separation of atmospheric microphysical properties from the methodology used to solve the RT equations allows a simple comparison of models and makes it easy to identify artifacts of the RT method. Currently we have driver codes which solve the RT equations based on the delta-Eddington, DISORT and Monte Carlo paradigms. As an illustration of the benefits of this modular approach, we will present a comparison of the reflected radiation from a horizontally non-homogeneous cloud field computed with the DISORT and Monte Carlo models.

SECOND SIMULATION OF THE SATELLITE SIGNAL IN THE SOLAR SPECTRUM (6S): AN OVERVIEW

Eric F. Vermote

Bldg 28, Room W120C
NASA/GSFC Code 923
Greenbelt, MD 20771

The remote sensing, from satellite or airborne platforms, of land or sea surface in the visible and near infrared is strongly affected by the presence of the atmosphere on the path Sun-target-Sensor. The following paper presents 6S (Second Simulation of the Satellite Signal in the Solar Spectrum), a code enabling simulation of the above problem. The 6S code is the improved version of 5S developed by the Laboratoire d'Optique Atmospherique, 10 years ago. The 6S code simulates aircraft observations taking into account target elevation, non-lambertian ground boundary conditions, and absorption spectra of new gases (CH₄, N₂O, CO). The computation accuracy regarding Rayleigh and aerosol scattering effects has been improved by the use of state-of-the-art approximations and use of the successive order of scattering method. The step used for spectral integration has been improved to 2.5 nanometers. Finally, all community approved results (e.g.: computation of Rayleigh optical depth) have been integrated in the code. The goal of this presentation is not to provide a complete description of the methods used, which are detailed in the code manual, but rather to illustrate the improvement 5S/6S by examining some typical remote sensing situations.

RECENT UPGRADES TO MODTRAN: MODTRAN 4

A. Berk, L.S. Bernstein,
P.K. Acharya, D.C. Robertson

Spectral Sciences, Inc
Burlington, MA 01803-5169

G.P. Anderson and J.H. Chetwynd

PL/GPOS
Hanscom AFB, MA 01731-3010

Two important upgrades have been incorporated into MODTRAN: (1) The MODTRAN layer cloud/rain models have been made easier to modify and more flexible, and (2) The molecular band model parameters have been recalculated using an improved algorithm. Cloud profiles have been decoupled from the aerosols, and they can now contain both liquid water droplet and ice particles. Cloud thickness, altitude, vertical extinction, column amounts, humidity and scattering phase functions can all easily be varied. The newly developed band model parameter algorithm more carefully models line overlap and location within a spectral bin; no new parameters have been introduced, but the processing of the data has been changed slightly. Comparisons to FASCODE predictions produce improved agreement. The new molecular band model parameters are calculated for an expanded temperature range (from 180 to 305 K in 25 K increments) to better model the actual temperature variations observed in the lower atmosphere.

THE MOSART CODE: ITS PRESENT AND FUTURE STATUS

William M. Cornette

Photon Research Associates, Inc
10350 No. Torrey Pines Road, Suite 300
La Jolla, California 92037

Gail P. Anderson

GPOS
Hanscom AFB, MA 01731-3010

Prabhat K. Acharya
David C. Robertson

Spectral Sciences, Inc.
99 So. Bedford St, No. 7
Burlington, MA 01803

The **MO**derate **S**pectral **A**tmospheric **R**adiance and **T**ransmittance (**MOSART**) computer code, funded by BMDO and DMSO, unifies the best features of MODTRAN and APART into a single code. These and additional features enable MOSART to be a standard tool for modeling the radiative environment for target signatures and background scenes. MOSART uses MODTRAN's band model approach to compute molecular transmittances and radiances. It has numerous built-in atmospheric species profiles and extensive terrain background and scene characteristic data bases. Additionally, MOSART provides user-friendly input modules including a graphical user interface (GUI). The initial release (Version 1.25) has been available since July 1994, with two releases with minor upgrades in December 1994 (Version 1.30) and May 1995 (Version 1.40). A brief review of MOSART will be presented, along with a summary of recent upgrades. Current and planned uses of MOSART by other simulations will be discussed, and planned and potential upgrades will be presented.

RRTM: A RAPID RADIATIVE TRANSFER MODEL

Eli J. Mlawer, Steven J. Taubman*, Shepard A. Clough

Atmospheric and Environmental Research, Inc.
840 Memorial Drive
Cambridge, MA 02139

An accurate and rapid radiative transfer model (RRTM) using the correlated-k method has been developed as part of the DOE Atmospheric Radiation Measurement (ARM) Program. The model, which uses the line-by line model LBLRTM as its foundation, calculates longwave ($10\text{--}3000\text{ cm}^{-1}$) clear sky fluxes and cooling rates for an arbitrary atmosphere. The longwave spectrum is divided into 16 bands chosen for their homogeneity of critical species. Each needed optical depth is obtained by linear interpolation from stored values obtained from LBLRTM. This linear interpolation is performed in log pressure, temperature, and a parameter representing the relative abundance of each band's critical species. This parameter is also used to determine the Planck function needed for each radiative transfer calculation.

The fluxes calculated with this model, for various atmospheres, have been compared to the results of LBLRTM flux calculations and satisfy an error criterion of 0.5% for each band. Similar cooling rate comparisons also yield favorable results.

* currently at GFDL

ALGORITHMS FOR ESTIMATING SOLAR UV SPECTRAL IRRADIANCE IN ATMOSPHERIC TRANSMITTANCE/RADIANCE CODES

Judith Lean

Naval Research Laboratory
Washington, DC 20375

Atmospheric transmittance/radiance codes such as MODTRAN and AURIC require as input the solar spectral irradiance at the top of the atmosphere. At ultraviolet wavelengths, this irradiance varies with solar activity. An algorithm is described to calculate the solar ultraviolet spectral irradiance from 120 to 300 nm for different levels of solar activity. The algorithm utilizes a solar activity proxy (such as the Mg Index or the He equivalent width) to estimate the level of solar activity and an array of variability vectors that scale the solar spectral irradiance for that activity level. Options exist for estimating the specific UV spectral irradiance on each day since 1976, or for generic solar UV spectra typical of low, moderate and high solar activity. The absolute spectral irradiances estimated by this algorithm are compared with the solar UV spectral irradiance presently utilized by LOWTRAN 7. Uncertainties in the amplitudes of the variability vectors arise from instrumental uncertainties in the UV irradiance database and will be illustrated by comparison of the UARS and SME data from which the variability vectors are derived.

RECENT MEASUREMENT APPLICATIONS OF OSIC UV PROPAGATION MODEL

Katherine M. Crow and Michael E. Neer

SciTec, Inc.
100 Wall Street
Princeton, NJ 08540

OSIC is a semi-empirical UV propagation model which incorporates the contributions of single and multiple scatter in addition to direct transmission. Both aerosol and molecular scatter and absorption are modelled. OSIC is currently being used to support both missile signature measurement as well as missile warning development. This model was developed from 1979-1984 through an extensive measurement program involving a variety of atmospheric conditions and ranges of up to 4 km. In January 1995, a calibrated UV source was measured over a 7.9 km path at WPAFB in order to test the validity of the OSIC model for long range applications. The agreement observed between the measurements and the model was quite good. In addition, the results of measurements taken by a number of different UV radiometers during JTAMS missile test at Biscarrosse, France in October 1994 and at White Sands, New Mexico in April 1995 are presented. Techniques involving the measurement of a common UV source and inter-instrument comparisons are discussed; these techniques ultimately lead to the correction of missile data for atmospheric effects.

A FAST MULTI-DIMENSIONAL ATMOSPHERIC EFFECTS INTERPOLATOR

P.K. Acharya and D.C. Robertson

Spectral Sciences, Inc.
99 S. Bedford St., Suite 7
Burlington, MA 01803-5169

W.M. Cornette

Photon Research Associates, Inc.
10350 N. Torrey Pines Road, Suite 300
La Jolla, CA 92037

L.S. Jeong

GPOS, Hanscom AFB, MA 01731-3010

An interpolation scheme using precomputed databases for quick calculations of in-band transmittances and radiances for any arbitrary line-of-sight (LOS) is presented. The need for this arises in realtime realistic wargame simulations (e.g., DIS-compliant systems). A database approach was adopted because atmospheric effects codes such as MOSART and MODTRAN are slow. In the current MOSART-based application, the user creates an off-line database by specifying the atmospheric conditions, global location, ranges of the LOS parameters, the exercise timespan, the spectral bandpass and the filter function. The database, specific to a global location, is 4-dimensional as the path radiance depends on three parameters normally used for a LOS plus the azimuth for solar scattering. During the exercise, the interpolator retrieves "nearest-time" transmittance and radiance from the database and outputs the path quantities for any LOS. In addition to target-to-sensor values, the database and the interpolator provide background-to-sensor values for contrast calculations. The database is extensible for inclusion of battlefield obscurants like munition smoke and fog.

SIMPLIFIED EXPRESSION OF THE RADIATIVE TRANSFER EQUATION FOR SURFACE TEMPERATURE ESTIMATION FROM LOWTRAN 7

Masao Moriyama and Kazuhiko Mima

Dept. Mechanical Systems Eng.,
Faculty of Eng., Nagasaki Univ.
Nagasaki, Japan

In order to estimate the surface temperature and surface emissivity via multispectral thermal IR observation data, the radiative transfer equation by LOWTRAN 7 has been simplified. The essential point of the simplification is to reduce the unknown variables which are contained in the radiative transfer equation in the thermal IR atmospheric window spectrum. For this purpose, some assumptions are adopted in the radiative transfer equation, and verified by using LOWTRAN 7. Brief descriptions of these assumptions are: 1) spectral averaging of the Planck function, 2) definition of the new unknown variable which expresses the atmospheric radiation and 3) neglect of the effect of absorbers except for water vapor. The comparison between the radiance calculated from the LOWTRAN 7 and the proposed RTE is less than 0.5 K.

THE POAM II EXPERIMENT AND SELECTED MEASUREMENT RESULTS

**E.P. Shettle, R.M. Bevilacqua,
J.S. Hornstein, K.W. Hoppel,
R.L. Lucke**

**Remote Sensing Division
NRL, Washington, DC 20375**

**J. Lumpe, S. Krigman, M. Fromm,
T.L. Ainsworth, D. Debrebian**

CPI, Fairfax, VA 20301

W.J. Glaccum

ARC, Landover, MD 20785

NRL's Polar Ozone and Aerosol Measurement (POAM II) instrument was developed to measure the distribution of atmospheric aerosols, PSC's, and several molecular species critical for understanding ozone chemistry in the polar stratosphere. It makes solar occultation measurements in nine narrow-band channels from the visible to the near TR. From the measured transmissions, it is possible to determine the profiles of atmospheric aerosols, ozone, water vapor, and nitrogen dioxide, with 1 km vertical resolution. The transmission data as function of tangent height is inverted to derive the vertical distribution of the various atmospheric constituents using a form of Rodger's optimal estimation algorithm. POAM II was launched on France's SPOT 3 satellite on 26 September 1993, which is in a 98.7 degree inclined sun-synchronous orbit at an altitude of 833 km. This results in all the POAM II measurements being in the Polar regions, making it an ideal instrument for studying the evolution of the ozone hole, related chemistry, and Polar Stratospheric Clouds, (PSC). We will discuss the POAM II instrument, the retrieval algorithm, and selected results of the measurements, including the 1994 Antarctic ozone hole, some studies of PSC's and Polar Mesospheric Clouds (PMC), and the unusually low ozone values in the Northern hemisphere this past Winter.

THE RELATION BETWEEN ZENITH POLARIZATION AND OPTICAL DEPTH FOR STRATOSPHERIC AEROSOLS FROM EL CHICHON AND PINATUBO

Frederic E. Volz

PL/GPOS
Hanscom AFB, MA 01731-3010

Low values of the degree of zenith polarization (ZP) have often been measured after major volcanic eruptions, most recently, including in the more revealing near infrared, by Steinhorst (1971, 1977) in Europe, by Coulson (1988) at Mauna Loa, and Wu and LU (1993) in Beijing. Steinhorst, and Wu and LU, used twilight scattering models to convert such sunset data into vertical profiles of aerosol. However, it appears that a more direct relationship between ZP and aerosol optical depth (OD) in the stratosphere might be obtained from the measurement at sunset of ZP for several years after an eruption. Indeed, observations in the NIR during most of the El Chichon and Pinatubo periods show that the observed range of ZP is essentially proportional to log OD. This agrees with the evaluation in terms of mixing ratios of the basic equation for polarization in hazy air.

INFRARED OPTICAL CONSTANTS OF SAHARA SAND, VOLCANIC ASH, AND WATER SOLUBLE AEROSOLS

W.G. Egan and J. Joseph

**Natural Sciences Department
York College/City University of New York
Jamaica, NY 11451**

We have adapted and improved the Volz technique for determining the absorption indices of atmospheric aerosols for use in the LOWTRAN and MODTRAN models. The new technique uses the Kubelka-Munk scattering theory to separate the scattering from the absorption in measurements with Potassium Bromide pellets containing the aerosols, resulting in absorption indices that are significantly lower in the window regions than those previously used in the models. Calibrations were achieved using lasers, and a sulfur coated integrating sphere. Also, finite wavelength effects cause a relocation of the observed absorption bands.

A DOUBLE SCATTER LIDAR PROGRAM TO DETERMINE PARTICLE SIZE DISTRIBUTIONS

Richard Garner

PhotoMetrics, Inc.
Woburn, MA 01801

We have developed a double (Mie) scatter lidar program for determining particle size distributions of media composed of spherical particles. The program, which is implemented on a PC, determines the four Stokes parameters of the doubly backscattered lidar radiation from spatially inhomogeneous media, as a function of time and as a function of field of view look angle. Size distributions are determined by comparing lidar returns from a polarization sensitive, multiple field of view lidar to a library of calculated lidar returns which is generated using a family of size distributions. The size distribution family is defined by a particular functional form (e.g., log normal) which can have one or more free parameters. Individual size distributions in the family differ according to the choice of free parameters. In this talk we describe the double scatter lidar program and the data analysis techniques used to determine size distribution. We present examples using simulated lidar data.

AEROSOL SIZE DISTRIBUTION MEASUREMENTS AND LASER TRANSMISSION EXPERIMENTS IN SWITZERLAND

Simon Kälin and Prof. Atsumu Ohmura

Swiss Federal Institute of Technology Zurich
Department of Geography
Winterthurerstr. 190
8057 Zurich
Switzerland

A field experiment at Zurich airport, Switzerland, is presented. The aim of the experiment is to get an improved knowledge about the nature and variability of aerosol size distributions in the atmospheric boundary layer and their influence on transmission and visibility. Laser transmission experiments are performed at different wavelengths in the visible and near infrared part of the spectrum. The measured values will be compared to model calculations. The intended experimental setup is discussed.

Aerosol size distribution measurements are conducted in the range of 0.1 - 7.5 μm using an optical particle counter, along with measurements of air temperature and relative humidity. The meteorological network provides additional data.

NON-NEGATIVE CONDITIONING OF THE PHASE FUNCTION LEGENDRE EXPANSION

David H. Tofsted

**U.S. Army Research Laboratory
White Sands Missile Range, NM 88002-5501**

In radiative transfer models of the atmosphere one technique commonly used is the discrete ordinates method. In this approach the scattering phase function is expanded in a Legendre series. The series coefficients are often modified using the delta-M or delta-Eddington technique to increase the accuracy of the calculation. In this paper the delta-correction method is extended to include a non-negative condition on the resulting expansion. This correction improves the ability to use predicted radiance data to produce integrated path radiance estimates. The correction involves a log-least-squares analysis of the phase function where the delta forward peak is replaced by a Gaussian phase function and the Legendre expansion coefficients are heuristically modified to ensure non-negativity. The results of this process are compared with computed phase function data and standard delta-M and delta-Eddington method results.

MAXIMUM DETECTION RANGE OF MISSILE TARGET EDGE INTENSITY

Clifford A. Paiva

**Research Branch
Countermeasures Division
Warfare Systems Department
Naval Surface Warfare Center
Dahlgren Division
Dahlgren, VA 22448-5000**

Performance of new generation precision guided munitions (PGM) and smart weapons is often unpredictable and unreliable for the global range of battlefield environments which include natural and hostile cultural (man-made) countermeasures. Field test results do not extrapolate well to the full range of operational conditions. The primary inhibitory factor for resolution of automatic target recognition (ATR) performance problems has been the inability to quantitatively characterize target discrimination algorithms which include backgrounds and countermeasures (TDB/C). This study is directed to addressing one of the more serious problems in ATR algorithm performance: efficient segmentation of imagery containing high standard deviation (clutter noise) values, generated by variable precipitation, turbulence and smoke.

A BI-STATIC RECEIVER TO OBSERVE LOWER TROPOSPHERIC AEROSOL PROPERTIES

T.D. Stevens and C.R. Philbrick

Pennsylvania State University
PSU/ARL Lidar Laboratory
University Park, PA 16802

The scattering of optical radiation in the visible, ultraviolet and infrared regions of the spectrum has a major impact on commercial air traffic and on many military systems. It has become critically important, with modern systems, that the electro-optical environment be properly characterized. We have been able to demonstrate that the rotational and vibrational Raman backscatter can be used to determine the extinction profile through optical scattering regions such as clouds. But a method is still needed to determine extinction profiles within the first several hundred meters above the Earth's surface through thin aerosol layers.

We have developed a bi-static remote receiver that utilizes a linear photodiode array to image the radiation scattered from any high power CW or pulsed laser system. By observing the angular scattering variation from a given aerosol layer, additional information contained in the scattering angle phase function can be obtained. A technique has been proposed to make measurements which can estimate particle size and distribution widths (of spherical scatterers) by placing two or more of these instruments perpendicular and parallel to the scattering plane. Polarizers are also used to measure the cross polarization and determine the amount of multiple scattering and non-sphericity of the particles in the scattering volume. The information on the particle size and distribution width along with absolute extinction measurements from Raman lidar should allow extension of the extinction and transmission calculations to a wider range of wavelengths.

LIDAR ATMOSPHERIC PROFILE SENSOR (LAPS): A REMOTE SENSING PROTOTYPE

C.R. Philbrick

**Pennsylvania State University
Applied Research Laboratory and
Department of Electrical Engineering
University Park, PA 16802**

A sensor capable of measuring profiles of the atmospheric properties has been prepared. The Lidar Atmospheric Profile Sensor (LAPS) instrument is currently undergoing testing of its automated operation and determination of its accuracy under a wide range of meteorological conditions. The instrument measures the water vapor profile based on the vibrational Raman scattering and the temperature profile based on the rotational Raman scattering. These measurements provide a realtime profile of RF refractivity. Profiles are obtained from the surface to 7 km each 5 minutes, with a vertical resolution of 75 meters. The prototype instrument has been designed to provide the realtime measurements of profiles from an instrument which includes several sub-systems to automate and monitor the operation. The instrument includes an X-band radar which detects aircraft as they approach the beam and automatically protects a 6 degree cone angle around the beam. The instrument includes self calibration, performance testing and BIT to check many functions.

In addition to the water vapor and temperature profiles, the true extinction and ozone profiles are also measured. By comparing the molecular profiles of the N_2 vibrational and rotational Raman profiles with the neutral atmosphere gradient, the extinction profile can be obtained. The day time measurements of water vapor are determined using the solar blind ultraviolet wavelengths. The ratio of the N_2 and O_2 vibrational Raman measurements on the slope of the Hartley band of ozone provides the DIAL measurement of the ozone profile in the lower atmosphere, up to 3 km. Initial results from the instrument are presented. Eventual deployment of the LAPS instrument will provide results to test and improve the optical propagation models of the atmosphere.

**COMPARISON OF MODTRAN MODELED AND AVIRIS
MEASURED WATER VAPOR ABSORPTION IN
THE SOLAR REFLECTED SPECTRUM OVER A RANGE FROM 0.5 TO 15.0
PRECIPITABLE MILLIMETERS ON THE SLOPES OF
THE 5700 METER MEXICAN VOLCANO PICO DE ORIZABA**

Robert O. Green

Jet Propulsion Laboratory
4800 Oak Grove Drive
Pasadena, CA 91109

D. A. Robert and C. Gautier

Department of Geography
University of California
Santa Barbara, CA 93106

We analyzed data collected by the Airborne Visible/infrared Imaging Spectrometer (AVIRIS) on the 28th of November 1994 over an 11 by 30 km region centered on the 5700 meter Mexican volcano, Pico de Orizaba. From the volcano summit to the adjacent low lands, water vapor ranging from 0.5 to 15.0 precipitable millimeters was observed.

The AVIRIS sensor measures upwelling spectral radiance from 400 to 2500 nm sampled contiguously at 10 nm intervals. Absolute spectral and radiometric calibration of AVIRIS is validated at the 95 percent level. Spectra are collected as images with 11 km width and up to 100 km length with 20 by 20 meter spatial sampling.

We compare the expressed water vapor absorption measured by AVIRIS to the absorption modeled by MODTRAN across the solar reflected spectrum. To allow comparison, MODTRAN was constrained to the absorption expressed in the AVIRIS data at the 940 nm band. The water vapor was then compared at bands centered at 720, 820, 1130, 1370, 1870, 2190, and 2500 nm. Overall, good agreement is shown. However, in detail, some discrepancies are noted that should provide a basis for continued improvement of the MODTRAN band and continuum water vapor absorption model.

Accurate modeling of the water absorption across the solar reflected spectrum is required for the use of MODTRAN to measure and compensate for the absorption of water vapor in the AVIRIS spectra. As an example, we present the use of MODTRAN in a nonlinear least squares fitting algorithm to simultaneously measure the absorption of water in the vapor, liquid and solid phases across the entire AVIRIS data set including the melting glaciers high on Pico de Orizaba.

MODTRAN AND ATMOSPHERIC CORRECTION OF REMOTE SENSING IMAGES OF COASTAL AND INLAND WATERS

J.F. de Haan and J.M.M. Kokke

Survey Department
Rijkswaterstaat
P.O. box 5023
2600 GA Delft
The Netherlands

The use of MODTRAN as a tool for atmospheric correction of remote sensing images of inland and coastal water is discussed. Our main aim is to evaluate the capabilities of MODTRAN3 for this purpose. Particular attention will be given to (i) the accuracy of the multiple scattering part of MODTRAN3 (i.e. the DISORT part), (ii) the derivation of atmospheric correction parameters from the standard products of MODTRAN (i.e. the path and ground radiance), and (iii) a possible extension of MODTRAN so that the water/air interface and radiative transfer in water is taken into account.

INVERSION OF DOWNWELLING EMISSION SPECTRA FOR TROPOSPHERIC PROFILE RETRIEVALS

Jean-Marc Theriault

**DREV-Defence Research Establishment Valcartier
P.O. Box 8800
Quebec, Canada, GAO 1R0**

The purpose of this presentation is to describe both theoretical and practical aspects of the inversion method (Minimum Information Type) developed to estimate tropospheric temperature and water vapor profiles from downwelling IR emission spectra recorded at one wavenumber resolution.

The method draws on the accuracy of FASCODE for forward calculations and accompanying derivatives. The development and validation of the inversion are supported by current experiments performed with the DREV interferometer (DBIS - Double Beam Interferometer Sounder). New inversion results obtained at different slant path angles (0, 30, 45, 60, 70 degrees) in mid-summer and mid-winter conditions are reported and analyzed. In particular, the impact of linearization errors, noise in measurements, spectral band selections and water vapor continuum on inversion results is discussed.

TEMPORAL PHASE RELATIONSHIPS AMONG ATMOSPHERIC CONSTITUENTS

W.G. Egan

Natural Sciences Department
York College/City University of New York
Jamaica, NY 11451

A.W. Hogan

U.S. Army Cold Regions Research
and Engineering Laboratory
Hanover, NH 03755-1290

A heretofore unrecognized temporal phase relationship between carbon dioxide, methane, ozone, aerosols, temperature, and water vapor has been found to exist at the South Pole. These temporal relationships appear to be worldwide, and have not been included in any modeling. The effects on atmospheric models will be significant.

FASCOD3 ATMOSPHERIC MODELING OF AN SF₆ PLUME RELEASED FROM A STATIONED BALLOON

J.B. Koffend

Space and Environment Technology Center
The Aerospace Corporation
El Segundo, CA 90245-4991

Assessing human exposure from and environmental impact of Titan IV launches requires the accurate prediction of the ground impact of toxic chemicals, both propellants and combustion products. As a prelude to validation experiments for these plume dispersion models, the FASCOD3 atmospheric radiance code was used in conjunction with IR camera characteristics to estimate the quality of experimental data from IR plume imaging studies of elevated tracer gas releases. We used FASCOD3 to model the radiance from SF₆ released from a blimp fixed at 2000' altitude. The narrow SF₆ feature near 950 cm⁻¹ lies in an spectral window that makes SF₆ an ideal IR imaging species for observation of plume transport in the atmosphere. These calculations coupled with noise figures for actual IR cameras lead us to conclude that experimental plume tracking data can be obtained for up to 2 km down wind. Tracking the plume to longer distances is possible using longer image integration times or larger SF₆ release rates (including "puff" releases). Such data would be extremely useful to validate current plume dispersion models, particularly if done in conjunction with real time FTIR measurements and gas sampling.

TRACE CONSTITUENTS SPECTRA IN THE 6-8.5 μm REGION FROM CIRRI-1A MEASUREMENTS AND THE CONCENTRATION PROFILES RETRIEVAL

D.K. Zhou, G.E. Bingham, A.J. Steed

Space Dynamics Laboratory
Utah State University
Logan, UT 84322

G.P. Anderson and R.M. Nadile

Geophysics Directorate
Phillips Laboratory
Hanscom AFB, MA 01731

During the STS-39 flight of April 28 - May 6, 1991, the Cryogenic Infrared Radiance Instrumentation for Shuttle (CIRRI-1A) measured spectral and spatial ("Earthlimb scan") distributions of the atmospheric infrared (IR) emissions by using a Michelson interferometer. Trace constituent (e.g., N_2O_5 , ClONO_2 , CH_4 , NO_2 , and H_2O) emissions were collected in the region of 6-8.5 μm , the spectra are analyzed to confirm the contributors of the infrared radiations. The computed spectra from AFGL FASCOD3 are used in comparison with observed spectra to identify the minor contributors to the emissions in this region. The preliminary vertical volume mixing ratio profiles of these trace gases are retrieved by an onion peel routine, using FASCOD3 as a forward model along with the NMC temperature and pressure profiles. The volume mixing ratio profiles are compared with other measurements.

STRATOSPHERIC TRACE SPECIES MEASUREMENTS BY SOLAR OCULTATION FOURIER TRANSFORM SPECTROMETRY

T. Hawat and R. Torguet

Institut d'Electronique et de Micro-Electronique
du Nord (IEMN), CNRS/UMR
9929 Dept. O.A.E. U.V.H.C, Bte 311
59304 Valenciennes, France

C. Camy-Peyret and P. Jeseck

Laboratoire de Physique
Moleculaire et Applications
(LPMA) CNRS/UPM, Bte 76
4 Place Jussieu
75252 Paris Cedex 05, France

S. Payan

Commissariat de l'Energie Atomique (CEA)
Centre d'Etudes Scientifiques et Techniques d'Aquitaine (CESTA)
33114 Le Barp, France

The Limb Profile Monitor of the Atmosphere (LPMA) is a Fourier transform infrared (FTIR) Spectrometer based on a BOMEM DA2.01 design. This Michelson interferometer operating with plane mirrors is used to retrieve stratospheric (and in some cases tropospheric) trace species concentration profiles. Spectra are recorded in absorption using the sun as a source, which allows the combination of high resolution together with high signal-to-noise-ratio. The instrument can operate under stratospheric balloons on a gondola with pointing capabilities designed by Observatoire de Geneve. With proper pointing it is possible to maintain the sun in the field of view of a heliostat whose fine tracking capabilities stabilize the solar radiation along the optical axis of the LPMA instrument. The entrance window is germanium to reject visible-UV flux.

The complete system i.e. gondola, pointing-system, FTIR, on-board processing and telemetry unit has flown several times (from Aire-sur-l'Adour in France and ESRANGE in Sweden) under a stratospheric balloon program operated by CNES. A description of the various subsystems will be given together with samples of representative ground test and in-flight measurements.

NON-LTE EFFECTS ON NADIR VIEWING TEMPERATURE SOUNDING IN THE STRATOSPHERE USING THE CO₂ 4.3 μ m BAND

J. Winick and Jinxue Wang*

GPOS, Hanscom AFB, MA

* Now at ACD NCAR

P.P. Wintersteiner

ARCON Corp.
Waltham, MA

J-L Moncet and H.E. Snell

Atmospheric and Environmental
Research, Inc.
Cambridge, MA 02139

High resolution nadir viewing instruments are being proposed for retrieval of atmospheric temperature in the stratosphere using infrared emission lines of CO₂. CO₂, especially the ν_3 bands exhibit significant non-LTE behavior in the mesosphere and lower thermosphere. We examine these effects on the nadir viewing spectral emission and their influence on the ability to accurately retrieve temperature in the stratosphere using these lines. To accomplish these ends we use the Phillips lab non-LTE radiance code (ARC) to calculate the CO₂ vibrational temperatures and investigate the sensitivity to background atmosphere (most significantly temperature profile) and other non-LTE parameters such as solar zenith angle. Using these temperatures as input to FASCOD3 in non-LTE mode, nadir spectral radiance profiles are produced and used in a non-linear retrieval algorithm based on the optimal retrieval approach of Rodgers. We investigate the feasibility of stratospheric temperature sounding in the 4.3 μ m bands of CO₂, and inquire into how well the non-LTE component of the radiance must be known in order to determine the atmospheric temperature to the required precision.

REMOTE SENSING OF TEMPERATURE IN THE 4.3 μm BAND OF CO_2

H.E. Snell, J.-L. Moncet, D.B. Hogan

Atmospheric and Environmental Research, Inc.
840 Memorial Dr.
Cambridge, MA 02139

The 4.3 μm band of CO_2 has been widely used for the remote sensing of atmospheric temperature profiles. Lines in the band head around 2330 cm^{-1} are extremely opaque, thus offering the possibility to extend the altitude range of derived temperature profiles beyond that achievable from the 15 μm band. Unfortunately many of the lines in this region are not in local thermodynamic equilibrium (LTE). Non-LTE (NLTE) effects are believed to be the cause of the excess radiances measured with the High Resolution Infrared Radiation Sounder (HIRS/2) channel at 2361 cm^{-1} . Processing of the data from this channel was problematic and it was subsequently changed in later versions of the instrument.

In this paper we present the theoretical bases for computation of NLTE radiance contributions in the 4.3 μm band and show how the NLTE lines affect optical depths and measured radiances for narrowband channels typical of a high spectral resolution sounder operating in this region. Sensitivities of the model to solar zenith angle variation and to the kinetic temperature profile assumptions are presented. Finally, a method is presented for correcting the NLTE effects which may make it possible to derive accurate temperature profiles even in the presence of the NLTE emissions.

THE USE OF MODTRAN TO ESTIMATE THE SULFUR DIOXIDE CONTENT OF VOLCANIC PLUMES

Vincent J. Realmuto

MS 183-501
Jet Propulsion Laboratory
California Institute of Technology
4800 Oak Grove Drive
Pasadena, CA 91109

The sulfur dioxide (SO_2) molecule exhibits ultraviolet, infrared, and microwave bands that are amenable to remote sensing techniques. The techniques most commonly applied to the estimation of SO_2 in volcanic plumes and clouds exploit the ultraviolet band. We have found that image data acquired with NASA's airborne Thermal Infrared Multispectral Scanner (TIMS) can also be used to map SO_2 plumes. TIMS measures ground radiance in six broad spectral channels between 8 and 12 μm . MODTRAN is used to model the radiance observed by TIMS as it views the ground through an intervening SO_2 plume. The retrieval of an SO_2 concentration from a TIMS radiance spectrum currently requires six runs of MODTRAN. We will discuss the SO_2 estimation procedure and show results obtained for the plumes of Mt. Etna (Sicily) and Kilauea (Hawaii) volcanoes. This research was conducted at the Jet Propulsion Laboratory, California Institute of Technology, under contract to the National Aeronautics and Space Administration.

MODELING LOCAL ATMOSPHERIC EFFECT BY MODTRAN-3 CODE AND VERTICAL PROFILES ACQUIRED ON MT ETNA VOLCANO, SICILY

S. Teggi and S. Pugnaghi

Osservatorio Geofisico dell'
Universita' di Modena
Modena, Italy

M.F. Buongiorno and M.P. Bogliolo

Istituto Nazionale di Geofisica
Roma, Italy

V.J. Realmuto

Jet Propulsion Laboratory
California Institute of Technology
4800 Oak Grove Drive
Pasadena, CA 91109

The atmospheric modeling with radiative transfer codes is very important when ground or atmospheric physical properties are analyzed by means of remote sensing image data acquired by sensors such as imaging spectrometers. Moreover to describe the local conditions in the low atmospheric layers, radiative transfer codes such as MODTRAN need to be adjusted with local information. In the present work several vertical profiles acquired on the Etna volcano (Sicily, Italy) were analyzed and compared to understand the local atmospheric parameter variations due to the high topographic relief, the vicinity of the sea and to the gases and water vapor clouds emitted by the volcano itself.

PRODUCTION OF VIBRATIONALLY AND ROTATIONALLY EXCITED NO IN THE NIGHTTIME TERRESTRIAL THERMOSPHERE

R.D. Sharma

PL/GPOS
Hanscom AFB, MA 01731-3010

H. Dothe

Mei Technology Co
1050 Waltham Street
Lexington, MA 02173

**V.A. Kharchenko, Y. Sun
and A. Dalgarno**

Harvard-Smithsonian Center
for Astrophysics
60 Garden Street
Cambridge, MA 02138

The rate of production of vibrationally and rotationally excited NO in the quiescent nighttime terrestrial thermosphere due to inelastic and reactive processes is calculated. The inelastic processes include the collisions of ambient NO with atomic O producing vibrationally excited, mostly $v=1$, rotationally thermalized NO. The reactive process is predominantly the reaction of ambient $N(^4S)$ with O_2 producing vibrationally and highly rotationally excited NO. Both processes, chemical and inelastic, show strong dependence on the geophysical parameters. The calculated emission is in good agreement with the rotationally thermal as well as rotationally nonthermal radiance in the fundamental vibration-rotation band of NO around $5.3 \mu m$ measured by the space shuttle experiment CIRRIS-1A. It is shown that chemically produced NO is a significant cooling mechanism at high altitudes even at night - a mechanism hitherto ignored in the calculations of the energy budget of thermosphere.

NO(v) DENSITIES IN THE LOWER THERMOSPHERE

S.J. Lipson, W.A.M. Blumberg,
R.B. Lockwood, J.R. Lowell,
R.M. Nadile

Phillips Laboratory, Hanscom AFB, MA

P.S. Armstrong and J.A. Dodd

Stewart Radiance Laboratory
Bedford, MA

Nitric oxide is a dominant infrared radiator in the 100 - 250 km region, and provides diagnostics of energy deposition, collisional energy transfer, and radiative cooling. High-resolution NO($v=1$) IR spectra from the CIRRIS 1A Space Shuttle experiment have been analyzed to obtain absolute column densities, and numerically inverted to obtain volumetric number densities from vertical sequences of spectra. The vibrational densities are comprised of rotationally thermalized and highly rotationally excited components. The first component is dominated by collisional up-pumping by O atoms, but the distribution can be extrapolated to $v=0$ to obtain an estimate of the total NO density without assuming an O atom density profile. The second component is dominated by the chemical production of NO from the reaction of fast N atoms with O₂. Therefore, the NO(v) data serve as a probe of fast N atoms, and odd-nitrogen chemistry in general.

RECENT ADVANCES IN GRAVITY WAVE SPECTRA AND IMPLICATION FOR RADIANCE STRUCTURE MODELS

E.M. Dewan and R.H. Picard

**Phillips Laboratory/ Geophysics Directorate (GPOS)
Hanscom AFB, MA 01731-3010**

Saturating and breaking gravity waves control the temporal and spatial fluctuation spectra of the middle atmosphere. Breaking waves dominate the power spectra of physical parameters, such as temperature and density, as well as those of the middle-atmospheric optical/infrared emission. Recent multi-pronged progress in gravity-wave spectra, in which PL/GP's SOAR and MAPSTAR programs have played a major role, is leading to increased understanding of middle-atmospheric structure, with resulting benefits for radiance structure models. (1) The several disparate theories of gravity-wave saturation, based on either linear instability or nonlinearity, are converging, leading to the realization that both nonlinearity and instability are important in determining the form of the power spectrum and to some measure of agreement in testable predictions. (2) Multi-instrument databases, such as those from the ALOHA-93 Campaign, are becoming available which will allow critical tests of gravity-wave spectral models to be carried out. These databases include simultaneous lidar and multi-wavelength imager data to determine vertical and horizontal structure at the same time. the physics behind leading theories of gravity-wave power spectra will be reviewed, and ways to test the theories using the new data sets will be discussed. Finally, the manner in which such spectral theories will lead to improved optical structure codes will be outlined.

THE SHARC4 MODEL FOR ATMOSPHERIC BACKGROUND RADIANCE STRUCTURES

**John Gruninger, Robert Sundberg,
James Duff**

Spectral Sciences, Inc.
99 S. Bedford St., No. 7
Burlington, MA 01803-5169

James Brown and Ramesh Sharma

GPOS, Hanscom AFB, MA 01731-3010

Infrared radiance fluctuations in the atmosphere result from fluctuations in the density of atmospheric species, individual molecular state populations, and kinetic temperatures and pressures along the sensor line of sight (LOS). A model for the prediction of atmospheric background radiance fluctuations was constructed. It predicts a two dimensional radiance spatial covariance function and power spectral density, from the underlying 3D atmospheric structures. The radiance statistics are non-stationary and are dependent on bandpass, sensor location and field of view. The goal is to understand the origin of LOS radiance fluctuations and to predict LOS radiance statistics based on local atmospheric fluctuations. The current status of the model will be reviewed.

**A FAST "STRETCHED-SPACE" METHOD FOR GENERATING
SYNTHETIC VERTICAL SHEETS OF NON-STATIONARY STOCHASTIC
ATMOSPHERIC STRUCTURE**

James H. Brown

GPOS, Hanscom AFB, MA 01731-3010

Neil J. Grossbard

Institute for Space Research
Boston College
Chestnut Hill, MA 02167

Non-stationary statistics of the earthlimb airglow presents grave difficulties in producing practical and efficient computer models. Atmospheric temperature and density fluctuations that induce spatial structure in the infrared emissions are often characterized by power spectral density functions. Since the PSD's vary with altitude, standard filtering techniques that attempt to generate synthetic scenes are nearly prohibitive in that they consume enormous computer resources. The work described herein quickly produces a large two-dimensional vertical sheet of non-stationary synthetic structure by means of a non-linear "stretched-space" transformation. We also employ an autoregressive filter to reduce the heavy computational burden.

**FASCODE/MODTRAN:
USER ACCESS AND SUPPORT**

J.H. Chetwynd, G.P. Anderson

GPOS, Hanscom AFB, MA

L.W. Abreu

Abreu Consulting, Chelmsford, MA

J. Vail

MIE Technology, Lexington, MA

H.E. Snell

AER, Inc., Cambridge, MA

Recent efforts to facilitate access to the DoD Background Radiation Codes, MODTRAN and FASCODE, will be described. These include anonymous FTP access, enhanced computer options, additional computer platforms, and general support. This last category delineates the separate spheres of getting the codes running vs. getting the correct solutions from a particular input scenario. Examples of both computer and scientific support will be demonstrated, along with answers to the most commonly asked questions.

PLEXUS VERSION 2.0: A UNIFIED KNOWLEDGE-BASED APPROACH TO ATMOSPHERIC MODELING

Susan B. Downer

Mission Research Corporation
One Tara Blvd., Suite 302
Nashua, NH 03062

Frank O. Clark

GPOB, Hanscom AFB, MA

PLEXUS Version 2.0 is now available for general use. In this version FASCODE3P has been added to the present suite of Phillips Laboratory atmospheric codes (MODTRAN, SHARC, SAG and CBSI). The inclusion of FASCODE to PLEXUS now provides users with the necessary tools to solve a diverse range of atmospheric problems such as high resolution laser applications, microwave calculations and IR scenarios. This implementation of PLEXUS couples together FASCODE and SAG, the Standard Atmospheric Generator. This allows users to run the same atmospheric profiles for both high resolution problems as well as those requiring moderate resolution solutions. This presentation will discuss PLEXUS Version 2.0 and the current development status of the PLEXUS program.

THE ATMOSPHERE AND WEATHER: PLEXUS

Frank O. Clark

GPOB, Hanscom AFB, MA 01731-3010

The Geophysics Directorate has over fifty years of expertise in field data of atmospheric phenomena, conceptual models of those data, and predictive computer models. A significant component of the Geophysics mission is to disseminate these data and models to DoD customers. PLEXUS realizes this mission by providing a single, uniform, accessible interface, both interactive and non-interactive, to a suite of Geophysics data sets and models. The combination of which provide a self consistent and validated atmosphere including weather over all spatial and spectral regimes, ultraviolet to radio frequency, including laser applications.

The expert system based dual access PLEXUS interface requires minimal input from the interactive user or calling program, with four modes of operation: hyper-fast, accurate or laser. PLEXUS code is in a portable machine independent format. The applications knowledge in PLEXUS is supplied by an expert system.

Current work includes development of WEATHERMAN which will be a PLEXUS scenario generator producing self consistent multi-spectral weather across all spectral and spatial regimes. WEATHERMAN will model time dependent frontal effects including formation & dispersal of fog, clouds, precipitation, and humidity, including time dependent cloud morphology (CSSM). PLEXUS will provide atmospheric structure through SASS. Further additions will include a low resolution terrain optical properties database for accurate down looking computations.

AN APPLICATION OF MODTRAN FOR REAL-TIME INFRARED SCENE GENERATION

David L. Quam

**MTL Systems, Inc.
3481 Dayton-Xenia Road
Dayton, OH 45432-2796**

Although MODTRAN is in wide use for calculating atmospheric transmittance and/or radiance in the infrared, visible and ultraviolet spectral regions, it is not suited for direct use in real-time simulation applications. This paper presents a table look-up method to make MODTRAN transmission and radiance data available to a real-time infrared (IR) scene generator. A description of the method is presented with respect to the IR scene generator application. An error analysis of the table linear interpolation errors is presented, along with table parameters and breakpoints. In addition, test results are presented which show the method to give very good accuracy with rather few breakpoints.

LAND DATA BASE REQUIREMENTS FOR ENVIRONMENTAL EFFECTS MODELS FOR USE IN DIS

William M. Cornette, David C. Anding, Frederic C. Mertz

Photon Research Associates, Inc.
10350 No. Torrey Pines Road, Suite 300
La Jolla, California 92037

The Environmental Effects in Distributed Interactive Simulations (E²DIS) project is integrating into a Simulation Support Environment software system, a collection of government-developed environment effects (E²) modules (e.g. MOSART) for use by simulator builders who want to incorporate E² into their simulators. Using the MOSART terrain data base as an example, this paper presents the land data base specification requirements necessary to fully support quantitative image generation systems for visible "out-the-window" views and for sensors, including data base context and level of detail. Sample terrain material temperatures calculated by the MOSART utility TERTEM will be presented. Issues, such as dealing with data base spatial resolutions (submeter to kilometer) and the necessary breadth of material types to represent real soils, vegetation, and other materials will be addressed.

HITRAN Atmospheric Workstation (HAWKS)

L.S. Rothman

Geophysics Directorate, Simulations Branch, Hanscom AFB, MA 01731-3010

R.R. Gamache

U.Mass. Lowell, Lowell, MA 01854

R.B. Wattson

Stewart Radiance Laboratory, Utah State University, Bedford, MA 01730

A. McCann and John Schroeder

Ontar, 9 Village Way, North Andover, MA 01845

Abstract

A new edition of the HITRAN molecular spectroscopic database is being released this year. It will be included in a compilation called HAWKS (HITRAN Atmospheric Workstation). HAWKS represents more fully a "matter" database. There will be files of aerosol indices of refraction, UV line-by-line and cross-section parameters, high-temperature line-by-line parameters (HITEMP), supplemental files of gases such as ionic species and high-vibrational calculations, and more extensive IR cross-sections. In addition, there will be vastly improved software handling of the data in both Windows and UNIX platforms, all to be made available on a CD-ROM.

This presentation will discuss some of the interesting features that will be present on the compilation as well as give some interesting examples of new capabilities.

1. Introduction

A comprehensive spectroscopic database of molecular parameters is required by all programs attempting to make line-by-line simulations. These simulations include both absorption and radiance calculations and generally are performed in moderately long atmospheric paths. The standard database, HITRAN, has existed for over 2 decades and is constantly being updated (expanded spectral coverage, more parameters per transition, weaker line inclusion, more species and isotopes, and enhancement to meet the needs of a wide range of applications, especially remote sensing). A companion database, in the same format as HITRAN, has now been established; this database HITEMP is designed to fulfill the requirements of hot-source gaseous emission. The applications include target or plume detection, stellar atmospheres, pollution detection, etc.

The next HITRAN release will be under the HAWKS (HITRAN Atmospheric Work Station) umbrella. This new approach comes about because of the expanded nature of the current database. It will include an updated version of the traditional HITRAN compilation of spectral parameters for atmospheric gases. However, also included will be supplemental databases, greatly expanded cross-section databases, UV (both line-by-line, and cross-sections), aerosol indices of refraction, and the aforementioned HITEMP. The "old faithful" SELECT.FOR FORTRAN source code is being superseded by DOS/WINDOWS and UNIX-based executable

code for data handling. The makeover of HITRAN, represented by HAWKS, is a significant enhancement designed to meet the changing needs of the user community. Tables 1 and 2 provide an overview of the file structure and molecular database for the next HITRAN release.

DIRECTORY	SUB-DIRECTORIES	MEGABYTES
SOFTWARE	FORTRAN programs and tables (ASCII)	~0.8
	WINDOWS-DOS	~2.5
	WINDOWS-UNIX	~2*(2.5)
HITRAN	By_Molecule	2*(101.4)
Supplemental		19.4
Cross-sections		18.0
UV	Line-by-line	1.1
	Cross-sections	2.5
Aerosols		0.2
HITEMP		236.6
MODELS	MODTRAN	~15
		Total: ~504

Table 1 File Structure of HITRAN/HAWKS [1996]

2. Improvements and enhancements to the databases

The database in the 1996 release have been significantly improved and enhanced. New molecules added to the line-by-line database include: **ClONO₂** ν_4 band of two isotopes plus one hot band, **HCOOH** in the 9 μm region, **HO₂** three fundamental bands ν_1 , ν_2 and ν_3 , and **O** (atomic oxygen).

Improvements to existing line-by-line data include: **H₂O** line positions have been corrected in the 720-1400 cm^{-1} region and new data have been added on the isotope HDO; **O₂** improved magnetic dipole transitions; **O₃** updated 2.5 μm band, updated 4.8 μm data, replaced main bands at 3.3 μm and added new hot lines at 10 μm ; **OH** improved intensities for the pure rotational lines; **CH₄** a new prediction of the CH₃D triad ν_3 , ν_5 , and ν_6 ; **CO** new and improved data at 10-480 cm^{-1} ; **HCl** improved data; **HBr** improved data; **HF** improvements in the region 41-625 cm^{-1} ; **NH₃** major updates have been added; **NO** improved positions and intensities in the 2.5-7 μm region; **HNO₃** new and improved data for ν_5 and 2 ν_9 bands; **N₂O** two pure rotational bands have been added; **NO₂** improved ν_2 , and hot ν_2 bands in the 10-17 μm region, and new results for the ν_3 band in the 6-8.6 μm region; **C₂H₂** new 3 μm data added, and upgrades to the 14 μm band; **CH₃Cl** new ν_3 data and references have been added; **ClO** new data have been added; **COF₂** the ν_4 and 2 ν_5 bands have been added; **H₂S** new data for the ν_2 region and the 2 ν_2 , ν_1 and ν_3 regions; **HOCl** updated line positions; **OCS** improved ν_1 data and additional ν_1 data for isotope 34; **SO₂** new calculations of the 2 ν_3 and 3 ν_3 bands.

A major addition to the new database are data for aerosols. These include: **H₂O** the real and imaginary indices of refraction for water at 27 C between 10 and 5000 cm⁻¹; **H₂O** the imaginary indices of refraction for water and ice in the 0.65 to 2.5 μm range; **H₂O** the real and imaginary indices of refraction of ice at -7 C for the .043 to 167 μm range, and indices of ice at -1, -5, -20, and -60 C for the 167 to 8.6e6 μm range; **H₂SO₄** the real and imaginary indices of refraction of sulfuric acid solutions at 25, 38, 50, 75, 84.5, and 95.6% H₂SO₄ by weight; **H₂SO₄** the real and imaginary indices of refraction of sulfuric acid solutions at 75 and 90% H₂SO₄ by weight, plus the standard deviations of the measurements; **H₂SO₄** theoretical equilibrium composition (weight percentage of H₂SO₄) of sulfuric acid solutions, given as a function of temperature and H₂O vapor pressure; **H₂SO₄** density (gm/cm³) values for solutions between 0 and 100% H₂SO₄ (by weight) for temperatures between 0 and 60 C; **HNO₃** the real and imaginary indices of refraction of nitric acid solutions at 68% HNO₃, by weight, plus the standard deviations of the measurements; **HNO₃** the real and imaginary indices of refraction of H₂O-ice, amorphous nitric acid solutions, and nitric acid hydrates.

Additional aerosols include: the real and imaginary indices of refraction for water, ice, sodium chloride, sea salt, water soluble aerosol, ammonium sulfate, carbonaceous aerosol, volcanic dust, sulfuric acid, meteoric dust, quartz, hematite, sand, and dust-like aerosol. The tabulations start at 0.2 μm and extend out to 40 μm (or to longer wavelengths).

Cross-sections for **CFC11**, **CFC12** and **CFC22** have been improved and have been added for **CLONO₂**. These data are now given for a range of temperatures and pressures.

High temperature (HITEMP) data for CO₂, H₂O and CO have been added and are discussed in more detail below in Section 3.

Finally, partition sum coefficients have been upgraded, partition sums are now either direct sum or formula, depending on molecule.

3. HITEMP

The high temperature datasets (HITEMP) for CO₂, H₂O and CO are a major addition and will be used in a variety of remote sensing applications ranging from exhaust gas monitoring to the investigation of stellar atmospheres. Traditionally, investigators have scaled the HITRAN database to estimate the absorption and emission spectra at elevated temperatures. Although the scaling from 296 K to higher temperatures is sufficiently accurate to estimate the line strength, etc. at the higher temperature, the additional spectral lines were missing from the simulation. This approach often leads to a significant underestimate of the source radiance.

The data were scaled to a standard reference temperature of 296K for intensity and halfwidth to make database compatible with codes such as FASCODE. The dynamic

Table 2. Statistics of Molecular Data for HITRAN96					
HITRAN/HAWKS 1996					
Band Statistics for HITRAN'96			Band Stats for Supplemental files		
1	H ₂ O	49444	3	High-vib O ₃	184724
2	CO ₂	60802	36	NO ⁺	1206
3	O ₃	275133	37	HOBr	4358
4	N ₂ O	28051 *			
5	CO	4477	Band Stats for HITEMP		
6	CH ₄	48032	1	H ₂ O	1174009
7	O ₂	6292	2	CO ₂	1032269
8	NO	15331 *	5	CO	113022
9	SO ₂	38853			
10	NO ₂	95684 *	Band Stats for UV		
11	NH ₃	11152	7	O ₂	11020
12	HNO ₃	165426			
13	OH	8676			
14	HF	107			
15	HCl	533	Cross-section Sizes		
16	HBr	576	N ₂ O -UV	143308	Bytes
17	HI	237	SO ₂ -UV	2377758	Bytes
18	ClO	7230	IR	17963586	Bytes
19	OCS	858			
20	H ₂ CO	2702	Aerosols		
21	HOCl	15565		229014	Bytes
22	N ₂	120			
23	HCN	772			
24	CH ₃ Cl	9355			
25	H ₂ O ₂	5444			
26	C ₂ H ₂	1668			
27	C ₂ H ₆	4749			
28	PH ₃	2886			
29	COF ₂	54866			
30	SF ₆	11520			
31	H ₂ S	5198			
32	HCOOH	3388			
33	HO ₂	26963			
34	O	2			
35	ClONO ₂	32199			
# lines =		994291	* = not final tally		

range has also been limited by the choice of cutoff, for example limiting the total band intensities in the driver tables. The HITEMP database spectral coverage, number of lines for each molecule and calculational method are summarized in Table 3.

The line positions and intensities of water vapor were calculated from the Direct Numerical Diagonalization method [1]. For CO₂, a table of spectroscopic constants, that is, distortion and higher order terms plus band intensities and Herman-Wallis factors was generated. However, very high weights were given to observed line positions from which lower order constants were established via a least-squares method. The final parameters were then calculated using the standard formulae [2]. Halfwidths were applied to the parameters in the same fashion as HITRAN. The CO parameters were generated with the application from solar atlas [3].

Molecules	Spectral Coverage	# of Lines	Temperature of Calculation
CO ₂	158 - 9648 cm ⁻¹ 1 - 63 μm	1,032,269 1st. three isotopes	DND ¹ @ 1000 K
H ₂ O	500 - 5000 cm ⁻¹ 2 - 20 μm	1,174,009 principal isotope	DND @ 1500 K
CO	850 -- 6418 cm ⁻¹ 1.6 - 12 μm	113,022 all significant isotopes	Solar Atlas

¹ Direct Numerical Diagonalization

Table 3 Statistics HITEMP database

Examples of using HITEMP for CO₂ and H₂O are shown below in Figures 1 and 2. The calculations were performed using PCLnWin®, the Ontar commercial version of the US Air

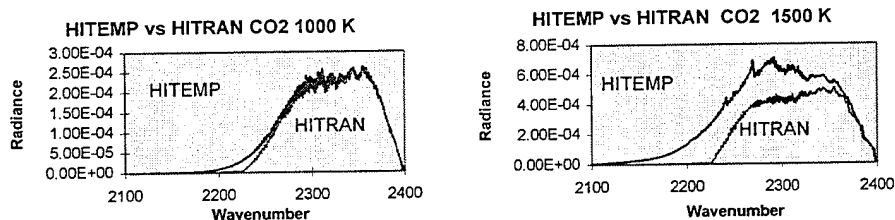


Figure 1, HITEMP Vs HITRAN for CO₂ at 1000 K and 1500 K between 2100 - 2400 cm⁻¹ (4.2 - 4.8 μm)

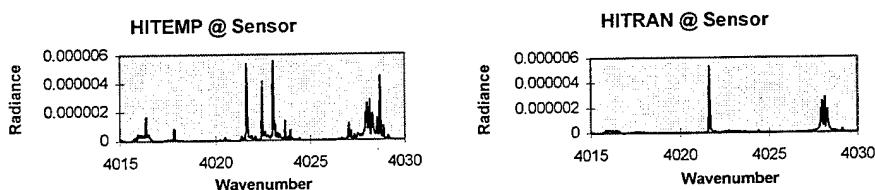


Figure 2, HITEMP Vs HITRAN for H₂O viewed over a 5 KM path at 2000 K between 4015 and 4030 cm⁻¹ (2.48 - 2.49 μm)

Force's FASCODE atmospheric transmission and radiance model. The calculations were made for a 5 meter source located 30 meters above the earth's surface at the temperature indicated in

the figures. H₂O and CO₂ concentrations were 200 and 250 PPM respectively and concentrations for the other atmospheric constituents were taken from the 1976 US Standard atmosphere.

Figure 1 shows that although there is not a significant difference for CO₂ at 1000 K, except in the wings of the band, there is a large difference across the entire band at 1500 K. Figure 2 shows the radiance received at a sensor through a 5 Km path in the H₂O band between 4015 and 4030 cm⁻¹ (2.48 - 2.49 μm) at 2000 K. The HITEMP lines (plot on the left) make a significant additional contribution over the HITRAN calculation (plot on the right) over this relatively narrow spectral region. The contribution will be quite large when integrated over a broad band.

4. SUMMARY and HITRAN/HAWKS Distribution

This paper has described the HAWKS/HITRAN database. A new version will be available in the near future which contains significant enhancement over the 1992 edition. Of particular importance is the addition of the HITEMP (High-Temperature Molecular Database) for CO₂, H₂O and CO.

The database is currently distributed on a single CD-ROM. Copies may be obtained by contacting:

Dr. L. S. Rothman

e-mail Rothman@PL.PH.AF.MIL

e-mail LRothman@CfA.Harvard.edu

or

The Ontar Corporation

Tel (USA)-508-689-9622

Fax (USA)-508-681-4585

REFERENCES

1. R.B. Wattson and L.S. Rothman, "Direct Numerical Diagonalization: Wave of the Future," *JQSRT* **48**, 763 (1992).
2. L.S. Rothman, R.L. Hawkins, R.B. Wattson, and R.R. Gamache, "Energy Levels, Intensities, and Linewidths of Atmospheric Carbon Dioxide Bands," *JQSRT* **48**, 537 (1992).
3. R. Farrenq, G. Guelachvili, A.J. Sauval, N. Grevesse, and C.B. Farmer, "Improved Dunham Coefficients for CO from Infrared Solar Lines of High Rotational Excitation," *J.Mol.Spectrosc.* **149**, 375-390 (1991); D. Goorvitch, "Infrared CO Linelist for the X¹Σ⁺ State," *Astrophys.J.Suppl.Ser.* **95**, 535-552 (1994).

FOURIER TRANSFORM ABSORPTION SPECTROSCOPY OF THE HERZBERG I BANDS OF O₂

W. H. Parkinson, J. E. Murray, J. R. Esmond, and K. Yoshino
Harvard-Smithsonian Center for Astrophysics, Cambridge, MA 02138, U.S. A.
and
A. P. Thorne, R. C. M. Learner, and G. Cox
Imperial College of Science, Technology, and Medicine, London, U.K.

INTRODUCTION

The Herzberg I system of O₂ ($A^3\Sigma_u^+ - X^3\Sigma_g^-$) was first observed in absorption and detailed assignment given by Herzberg (1932). Broida and Gaydon (1954) studied the system in emission in an oxygen afterglow and modified the earlier assignment of the upper vibrational state by one. The bands of the Herzberg I system are important contributors to the emission spectrum of the airglow and photodissociation in the Herzberg continuum is an important source of O in the stratosphere. There has been considerable and extensive interest in and publications on the system.

Our interest in making high resolution, absolute photoabsorption cross section measurements of the lines of the Herzberg I bands, followed from our earlier cross section measurements of the photodissociation continua (Yoshino 1988) associated with and contributed to by the three Herzberg band systems $A^3\Sigma_u^+ - X^3\Sigma_g^-$ (I), $C^1\Sigma_u^+ - X^3\Sigma_g^-$ (II) and $A'^3\Delta_u - X^3\Sigma_g^-$ (III); all of which are forbidden systems. Because the bands of the Herzberg I system are sharp and weak, experimental determination of the band oscillator strengths has presented difficulties. Prior to our work the only quantitative absorption measurements were those of Hasson and Nicholls (1971). Their technique used the photographic method, self-broadening at high pressure, and a resolving power of $\sim 300,000$. Recently Huestis *et al.* (1994) observed the A-X bands by the method of ring-down spectroscopy but the laser linewidth of 0.5 cm^{-1} was much larger than the room temperature Doppler width of 0.086 cm^{-1} . In the work described here, we used a Fourier transform (FT) spectrometer in combination with a White cell to obtain the Doppler limited absorption spectrum and band oscillator strengths of the $A(v) - X(0)$ bands ($v = 4-11$), with a resolution of 0.06 cm^{-1} (resolving power of 660,000) (Yoshino *et al.* 1994, 1995).

EXPERIMENTAL PROCEDURE

The FT spectrometer is located at Imperial College London. The details of the method and experimental arrangements were presented in a previous spectroscopic paper in honor of Dr. G. Herzberg FRS (Yoshino *et al.* 1994)

A high-pressure Xenon lamp (Hamamatsu 300) was used as the source to produce a continuum background over the wavelength range 240 - 280 nm. The bandwidth of the background continuum radiation was limited by means of a double-prism, zero angular and linear dispersion monochromator (Murray 1992). The need to limit the bandwidth comes from the fact that in Fourier transform spectroscopy (FTS) noise from every spectral element seen by the detector is spread uniformly through the spectrum. The signal-to-noise ratio for the background intensity was typically about 200.

To obtain the high column density of O₂ required to measure the weak photoabsorption lines of

the Herzberg I system, we used a White cell (1942) (Fig. 1). The distance of 2.54 m between the two main mirrors was set and adjusted for 16 double passes of light. The total path length in the White cell was 81.88 m.

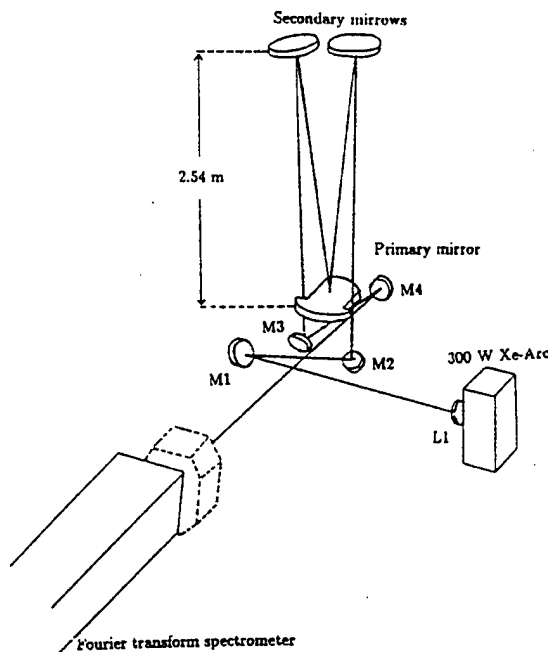


FIG. 1. Schematic diagram of the experimental arrangement

Because there were 35 mirror reflections, the reflectance coating was very critical. The mirrors were coated for almost 100% reflectance over the wavelength region 240 - 280 nm by Acton Research (525 Main Street, Acton, MA 01720).

All measurements were carried out at room temperature 295 K. We selected five different pressures of O_2 in the White cell: 60, 120, 194, 371, and 700 Torr, but at the highest pressure the background intensity in the region of the (3,0) and (4,0) bands decreased because of pressure-induced continuous absorption. Therefore we used the data for the other four pressures for the cross section measurements; the column densities were $1.88 \times 10^{22} \text{ cm}^{-2}$ at 60 Torr, $3.49 \times 10^{22} \text{ cm}^{-2}$ at 120 Torr, $5.47 \times 10^{22} \text{ cm}^{-2}$ at 194 Torr, and $1.02 \times 10^{23} \text{ cm}^{-2}$ at 371 Torr. Absorption cross sections were obtained by using Beer's law with measured optical depth and the known column density. We limited the optical depth to less than 1.5 for all measurements.

RESULTS AND DISCUSSION

The wavenumber scale of the FT spectrometer was determined to the first order by a He-Ne laser that controls the sampling of the interferogram. It is accurately linear but requires at least one reference wavenumber of absolute calibration. We observed five well separated lines at 253.7 nm from Hg isotopes as impurity lines in the spectrum. From the line positions of ^{198}Hg by Kaufman (1962) and the isotope shift relative to ^{198}Hg from Schweitzer (1963) we determined the wavenumber shift ($+ 0.028 \pm 0.003 \text{ cm}^{-1}$) in our wavenumber scale.

As an illustration of the quality of the absorption spectra, typical absorption bands of (5,0) - (8,0) are presented at the top of Fig 2; the (7,0) band is increasingly expanded to show the detail of the rotational structure.

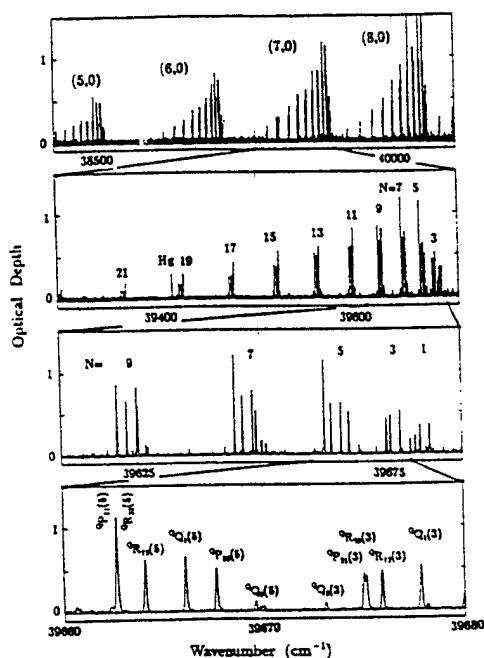


FIG. 2. Absorption bands of the $A^3\Sigma_u^+ - X^3\Sigma_g^-$ system at 121 Torr of O_2 with 81.9 m pathlengths.

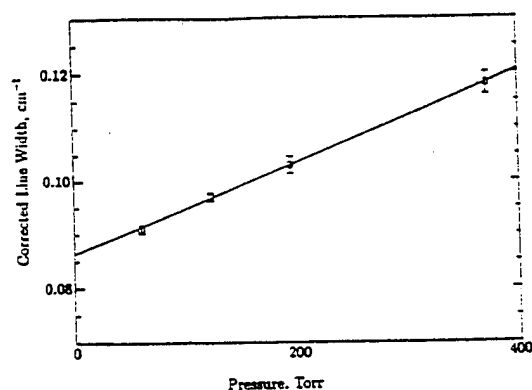


FIG. 3. Pressure broadening of rotational lines of the Herzberg I bands. The error bars are the standard deviation divided by the square root of n , the number of data points. The two runs at 120 Torr covered different wavelength regions.

The absorption lines were fitted to Voigt profiles by using the reduction routine called DECOMP (Brault 1989). This procedure provides line positions, linewidths and integrated cross sections.

Rotational line positions were obtained with an accuracy of 0.005 cm^{-1} . Rotational term values for the vibrational levels $v = 4-11$ and molecular constants for these levels were also determined (Yoshino *et al.* 1994).

To measure the observed linewidths we chose relatively strong, isolated lines from five spectra at four pressures. When corrected for the instrumental contribution, the pressure dependency of linewidths is clearly demonstrated (Fig. 3).

The linear extrapolation to zero pressure gives a linewidth of $0.086 \pm 0.002 \text{ cm}^{-1}$ which agrees well with the expected Doppler width. The slope of the graph is $(8.6 \pm 0.1 \times 10^{-5} \text{ cm}^{-1} \text{ Torr}^{-1})$ (or 0.065

$\pm 0.008 \text{ cm}^{-1} \text{ atm}^{-1}$) in agreement with air broadening measurements of O_2 in the IR region (Chance *et al.* 1991). The greater Doppler width in the UV region made it impossible to observe any variation of pressure broadening with rotational quantum number, N , unless it were significantly greater than that reported from the atmospheric bands.

The integrated cross sections of the rotational lines can be obtained by fitting the lines either with all parameters free or with the linewidths held fixed for all lines, at each pressure.

Errors in the integrated line strengths can be obtained from the noise level, which in FTS is essentially constant throughout the spectrum. Accounting for the number of points in a line profile and the 5 sets of observations, the standard deviation for a strong unblended line of integrated cross section $4 \times 10^{-24} \text{ cm}^2 \cdot \text{cm}^{-1}$ is $\pm 1.5\%$. A conservative allowance for the small random errors in pressure, temperature and path difference gives a maximum random error of $\pm 2\%$. For a weak line (integrated cross section $\sim 2.5 \times 10^{-27} \text{ cm}^2 \cdot \text{cm}^{-1}$) the spectral noise dominates all contributions and the error on a single line rises to about $\pm 8\%$. Errors on band strengths obtained by integration over all lines in the band are dominated by the errors of the strong lines and are estimated to be about 2%.

As an example of the data available for the eight bands measured, Table 1 contains the integrated cross sections of lines of the $A(6) - X(0)$ band. The cross sections are derived from the total column density of O_2 at 295 K.

Table 1. Integrated cross sections of lines of the $A(6) - X(0)$ band of O_2 in units of $10^{-26} \text{ cm}^2 \cdot \text{cm}^{-1}$.

N	Q_{Q11}	Q_{Q22}	Q_{Q33}	Q_{R12}	Q_{R23}	Q_{P21}	Q_{P32}	Q_{P12}	Q_{P23}	S_{R21}
1	115.	49.	.	62. ^a	9.	57. ^a	19.	.	.	.
3	151.	32.	20.	129.	114. ^b	111. ^b	64.	36.	10.	14.
5	189.	33.	42.	162.	157. ^c	153. ^c	116.	55.	13.	.
7	223.	32.	41.	203.	184. ^d	180. ^d	141.	25.	23.	.
9	252. ^e	25.	31.	184.	189. ^f	185. ^f	149. ^e	35.	22.	.
11	192.	22.	29.	157.	161. ^g	157. ^g	142.	30.	.	32.
13	164.	26.	24.	134.	135.	122.	126.	22.	15.	10.
15	153.	28.	21.	102.	113.	79.	107.	.	.	.
17	117.	14. ^h	.	67.	66.	67.	57.	.	.	.
19	77.	18.	.	41.	49.	47.	50.	12.	.	.
21	49.	12.	.	29.	28.	26.	23.	14. ⁱ	.	.
23	30.	.	.	16.	18.	16.	19.	.	.	.
25	18.

^aEstimated from blended lines of $Q_{R12}(1)$ and $Q_{P21}(1)$.

^bEstimated from blended lines of $Q_{R23}(3)$ and $Q_{P21}(3)$.

^cEstimated from blended lines of $Q_{R23}(5)$ and $Q_{P21}(5)$.

^dEstimated from blended lines of $Q_{R23}(7)$ and $Q_{P21}(7)$.

^eEstimated from blended lines of $Q_{Q11}(9)$ and $Q_{P32}(9)$.

^fEstimated from blended lines of $Q_{R23}(9)$ and $Q_{P21}(9)$.

^gEstimated from blended lines of $Q_{R23}(11)$ and $Q_{P21}(11)$.

^hBlended with $^aR(1)$ line of the $c(10) - X(0)$ band.

ⁱBlended with $^aQ(15)$ line of the $c(10) - X(0)$ band.

The strengths of the branches can be obtained by adding the integrated cross sections of all rotational lines in the branch. The fractions of branch strength and the average of branch strength of the (4,0)-(9,0) bands have been tabulated and used to redistribute intensities of blended lines.

Table 2. Branch strengths for the $N'' = 13$ transitions of the (10,0) band compared with model calculations. Their values are normalized to our observed values.

	Q_{11}	Q_{22}	Q_{33}	Q_{R12}	Q_{R23}	Q_{P21}	Q_{P32}	Q_{P12}	Q_{P23}	Q_{R21}
LG ^a	123.	3.	90.	347.	240.	246.	268.	71.	53.	60.
CN ^b	298.	90.	60.	243.	185.	189.	242.	121.	31.	30.
HJ ^c	328.	49.	25.	270.	275.	249.	213.	52.	24.	22.
$N'' = 13^d$	364.	66.	42.	272.	248.	265.	198.	54.	13.	.
BR ^e	348.	61.	49.	281.	257.	257.	184.	67.	14.	5.

^aLewis and Gibson [Ref. 13].

^bCann and Nicholls [Ref. 14].

^cHuestis *et al.* [Ref. 4].

^dPresent values for $N'' = 13$ transitions.

^ePresent values for total branch strengths.

In Table 2 we compare our integrated cross sections of transitions for $N'' = 13$ levels of the (10,0) band with the results of Lewis and Gibson (1990), Cann and Nicholls (1991), and Huestis *et al.* (1994). Their numbers are normalized to our observed values by the values of total cross sections. Values in the fifth row are normalized branch strength of the entire (10,0) band. Further theoretical studies should be carried out, guided by our new measurements.

Table 3 contains the integrated cross sections, the band oscillator strengths, and comparisons with other work. Considering that Hasson and Nicholls (1971) used photographic methods, the agreement with our measurements is very good. However, the recent results of cavity ring-down spectroscopy by Huestis *et al.* (1994) are significantly lower than our results, perhaps because their instrumental resolution of 0.5 cm^{-1} was much larger than the Doppler widths of O_2 lines at 295 K.

Table 3. Integrated cross sections (units of $10^{-23} \text{ cm}^2 \cdot \text{cm}^{-1}$) and absorption oscillator strengths (units of 10^{-11}) for the Herzberg I Bands of O_2

Band	Wavelength nm	Integrated Cross Sections		Band Oscillator Strengths				
		Float ^a	Fixed ^a	Present	HN ^b	H ^c -exp	H ^c -FC	Ba ^d
4,0	263.7	2.33	2.15	2.43	3.0		2.66	3.4
5,0	259.3	4.47	4.41	4.98	5.4		5.14	6.9
6,0	255.4	7.29	7.32	8.28	8.0		8.58	11.7
7,0	251.9	11.10	10.70	12.20	12.4		12.40	17.1
8,0	248.9	13.90	13.70	15.50	13.9	8.80	16.00	22.3
9,0	246.3	15.20	15.10	17.10	14.0	10.80	17.80	26.4
10,0	244.3	14.50	14.60	16.40	12.0	9.30	16.80	24.2
11,0	242.9	6.91	7.06	7.98	10.0	6.80	9.93	8.4

^aFloat and fixed refer to the computational strategy used to treat the widths of weak line (see text).

^bHN: Hasson and Nicholl [1971].

^cH: Huestis *et al.* [1994], experimental and theory.

^dBa: Bates [1989], theory.

The theoretical study of Bates (1989) presents values too high by 40%. When Huestis *et al.* (1994) calculated Franck-Condon factors, normalized to the experimental oscillator strength of the (7,0) band measured by Hasson and Nicholls which is only 2% higher than our value for the band, the normalized calculated values are only 4% higher on average than our own.

The measured band oscillator strengths of the (11,0) band is smaller than the calculated value because the (11,0) band is very close to the dissociation threshold and rotational dissociation limits

observation to $N'' \leq 15$. Other bands are observed up to $N'' = 25$.

ACKNOWLEDGMENTS

This work is supported by NSF Division of Atmospheric Sciences grant ATM-91-16562 to Harvard College. We acknowledge the support of the UK Science and Engineering Research Council and the Paul Fund of the Royal Society for the development of the UV-FT spectrometer.

REFERENCES

- Bates, D. R. 1989, *Planet. Space Sci.* **37**, 881.
- Brault, J. W. and Abrams, M. C. 1989, *Opt. Soc. Am. Tech. Dig. Ser.* **6**, 110.
- Broida, H. P. and Gaydon, A. G. 1954, *Proc. Roy. Soc. (London) A* **222**, 181.
- Cann, M. W. and Nicholls, R. W. 1991, *Can. J. Phys.* **69**, 1163.
- Chance, K. V., Traub, W. A. Jucks, K. W. and Johnson, D. G. 1991, *Int. J. Infrared and Millimeter Waves* **12**, 581.
- Hasson, V. and Nicholls, R. W. 1971, *J. Phys. B: At. Mol. Phys.* **4**, 1778.
- Herzberg, G. 1932, *Naturwissenschaften* **20**, 577.
- Huestis, D. L., Copeland, R. A., Knutsen, K., Slinger, T. G., Jongma, R. T., Boogaarts, M. G. H. and Meijer, G. 1994, *Can. J. Phys.* **72**, 1109.
- Kaufman, V. 1962, *J. Opt. Soc. Am.* **52**, 866.
- Lewis, B. R. and Gibson, S. T. 1990, *Can. J. Phys.* **68**, 231.
- Murray, J. R. 1992, Thesis, Physics Dept., Imperial College of Science, Technology and Medicine.
- Schweitzer, Jr., W. G. 1963, *J. Opt. Soc. Am.* **53**, 1055.
- White, J. U. 1942, *J. Opt. Soc. Am.* **32**, 285.
- Yoshino, K., Cheung, A. S-C., Esmond, J. R., Parkinson, W. H., Freeman, D. E., Guberman, S. L., Jenouvrier, A., Coquart, B. and Merienne, M. F. 1988, *Planet. Space Sci.* **36**, 1469.
- Yoshino, K., Murray, J. E., Esmond, J. R., Sun, Y., Parkinson, W. H., Thorne, A. P., Learner, R. C. M. and Cox, G. 1994, *Can. J. Phys.* **72**, 1101.
- Yoshino, K., Esmond, J. R., Murray, J. E., Parkinson, W. H., Thorne, A. P., Learner, R. C. M. and Cox, G. 1995, *J. Chem. Phys.* **103**, July, in press.

Empirical Water Vapor Continuum Models for Infrared Propagation

Michael E. Thomas (301-953-6000 x4414)
 The Johns Hopkins University/Applied Physics Laboratory
 Laurel, Maryland 20723

ABSTRACT

The characterization of the water vapor continuum remains an important problem concerning infrared propagation in the atmosphere. Radiometric imaging within the atmosphere in the 8 to 12 μm and 3-5 μm regions, and eye safe lidar in the 2 μm and 1.6 μm window regions require accurate knowledge of the water vapor continuum.

Although the physical nature of the continuum is a complex problem, the observed frequency, pressure and temperature dependence can be represented reasonably well by simple mathematical functions consistent with far wing theories. This approach is the basis for current models used in LOWTRAN/MODTRAN and for the models listed in the SPIE/ERIM EO/IR Systems Handbook (Volume 2 Chapter 1). However, these models are based solely on a limited, but high quality, data set collected by a spectrometer and White cell. Additional information on oxygen broadening and temperature dependence is available from numerous laser measurements of the water vapor continuum.

A survey of relevant experimental data is made to determine the best available measurements of the water vapor continuum in various atmospheric window regions. Then the data are fit to an empirical model over the entire window region. A good fit is obtained for typical atmospheric conditions covering the 8 to 12 μm and 3 to 5 μm regions. No experimental data, covering atmospheric conditions, exist in the 2 μm and 1.6 μm regions. However, models can be proposed based on far wing extrapolations of the bordering vibrational water vapor bands.

Keywords: Water vapor continuum, temperature dependence, pressure dependence, empirical model, 8-12 μm region, 3-5 μm region and oxygen dependence

1. INTRODUCTION

Current models of the water vapor continuum^{1,2} are based on a series of measurements, using a long path White cell and spectrometer combination by Burch³, and tend to ignore the wealth of information available from laboratory measurements using lasers. The main reason for this, it seems, is that the available gas lasers can't always be tuned to spectral locations with no local line contributions. However, laser lines are available with minimal local line contribution and can provide useful information on continuum absorption. Laser measurements have some advantages over long path White cell/spectrometer measurements, as well. White cell/laser measurements have at least twice the path length of spectrometer based measurements and therefore greater sensitivity. Also, photo-acoustic cells require high intensity sources to achieve high sensitivity necessary for measurements of the water vapor continuum at typical atmospheric conditions. Furthermore, all the data by Burch are taken on samples containing water vapor buffered by nitrogen. To model the atmosphere, the effects of oxygen broadening must be considered. This information is available from laser measurements.

The atmospheric infrared windows that are the best experimentally characterized concerning the water vapor continuum are the 8-12 μm and 3-5 μm regions. An extensive set of data is assembled including the spectrometer measurements by Burch from 400 to 2700 cm^{-1} , and CO_2 , CO , DF and HF laser measurements. The laser frequencies selected are continuum dominated.

A general empirical form for the continuum absorption coefficient that is commonly used to represent experimental data as a function of frequency, temperature, absorber partial pressure and foreign partial pressures of broadening gases, is given by

$$\beta_{\text{cont}}(\nu, T, p_H, \dots, p_F, p_a) = \frac{p_a}{R_{oc}T} \sum_{i=1}^{\text{imax}} [C_H(\nu, T)p_H + C_i(\nu, T)p_a] \quad (1)$$

where C_i is the self-broadening coefficient of the absorbing gas, C_H is the foreign broadening coefficient due to the i^{th} type foreign gas, $p_{a,H}$ are the absorber and foreign gas partial pressures, respectively and R_{oc} is the ideal-gas constant. These coefficients contain the frequency dependence and most of the temperature dependence. The above equation can be conveniently rewritten for $\text{imax} = 2$ to obtain

$$\beta_{\text{cont}}(\nu, T) = \frac{C_H(\nu, T)}{R_{oc}T} p_a [p_H + F(\nu, T)p_H + B(\nu, T)p_a] \quad (2)$$

where $F = C_H/C_H$ and $B = C_a/C_H$ are the dimensionless broadening coefficients. Near line center, B has a typical value of 5 for water vapor relative to nitrogen. In the real atmosphere, the effects of oxygen broadening must also be included. The dimensionless broadening coefficient F accounts for oxygen relative to nitrogen. The experimental data are presented in terms of the above formulas.

2. FAR-WING LINE SHAPE

Eq. 1 is consistent in form with a far-wing expansion of the collision broadened absorption coefficient. Based on a line shape profile by Birnbaum⁴, the far-wing extrapolation⁵ for a binary mixture is obtained to be

$$\begin{aligned} j_{\text{rw}}(\nu) = & \left(\frac{\tau_{a2}}{2\pi}\right)^{1/2} \frac{1}{\tau_{a2}} \frac{\exp\{-2\pi c|\nu - \nu_1|\tau_{a2}\}}{4\pi^2|\nu - \nu_1|^{1.5}} \exp\{2\pi c(\nu - \nu_1)\tau_a\} \\ & + \left(\frac{\tau_{b2}}{2\pi}\right)^{1/2} \frac{1}{\tau_{b2}} \frac{\exp\{-2\pi c|\nu - \nu_1|\tau_{b2}\}}{4\pi^2|\nu - \nu_1|^{1.5}} \exp\{2\pi c(\nu - \nu_1)\tau_a\} \end{aligned} \quad (3)$$

where ν_1 is the line center frequency of the i^{th} line. An exponential frequency dependence dominates in the far wing. The relaxation times τ_1 and τ_2 represent the long time (near-line-center) and short time (far-wing) behavior of the autocorrelation function. τ_a is a thermal time defined by

$$\tau_a = \frac{h}{4\pi k_B T} \quad (4)$$

(Note: for $T = 298$ K leads to $\tau_a = 1.29 \times 10^{-14}$ sec). The functional form of Eq. 3 is used to generate an empirical representation of the water vapor continuum experimental data. This suggests that the water vapor continuum is generated by far wings of the strong water vapor absorption bands that define the atmospheric windows.

3. EXPERIMENTAL DATA AND EMPIRICAL MODELS

The following subsections review the experimental data and present an empirical water vapor continuum model that represents the data. The emphasis is on the 8 to 12 μm window and the 3 to 5 μm window since these are the best experimentally characterized.

3.1 The 8- to 12- μ m window

This important atmospheric window has been studied by many investigators for three reasons. Room temperature blackbody radiation peaks within this spectral window. Thus, atmospheric heating by ground radiance depends on the vertical absorptance of the atmosphere. This is a crucial component of climate models. Also, night vision systems, which use the infrared spectrum to view thermal radiation from targets, often use the 8 to 12 μ m window. The last application, requiring knowledge of the water vapor continuum, is atmospheric remote sensing. The water vapor continuum in this spectral region is strong and can't be ignored.

Fig. 1a shows the self-broadening water vapor continuum coefficient, C_s , as a function of frequency between 7 and 22 μ m at 296 K. The experimental data come from long path White cell transmittance measurements with spectrometers³ and photoacoustic^{4,5} and White cell measurements with CO_2 ^{6,7} and diode¹⁰ lasers. The spectrometer was tuned to subwindow regions where no or minimal local line absorption contributions are made. In Fig. 1 the spectrometer data, marked with an 'x', has some local line contamination because they are strong in these near band spectral regions. The solid curve represents a fit to discrete spectrometer measurements at locations with virtually no contribution from the now weak local lines. The laser frequencies selected (indicated by '+') have minimal local line contribution. For this reason the laser data acts as an upper bound to the true continuum level. The data scatter is an indication of the success of separation of continuum from local line absorption. Thus, overall the experimental data directly represent the water vapor continuum. The self-broadening coefficient decreases exponentially as the frequency increases and then increases above 1050 cm^{-1} . The diode laser measurement by Montgomery¹⁰ and spectrometer measurements by Burch³ definitely establish the upward trend towards the ν_2 band. The same functional dependence is exhibited by the nitrogen-broadening coefficient, C_N , as shown in Fig. 1b, but the rate of change is more rapid. Thus, $B (= C_s/C_N)$ increases as the frequency increases away from the rotational band and then decrease towards the ν_2 band. Long-path White cell and photoacoustic laser measurements indicate that B can be quite large. Values ranging from 100 to 700 have been measured in the 10 μ m region with CO_2 lasers.^{6,7}

Fig. 2 illustrates a single frequency spectrometer (900 cm^{-1}) and laser measurement (952,881 cm^{-1}) as a function of the water vapor partial pressure. The total pressure is maintained at 101 kPa (1 atm) with nitrogen as the foreign broadener. Notice the nearly parabolic nature of the absorption coefficient. Based on Eq. 2, this indicates strong water vapor-water vapor interaction contributions.

The observed temperature dependence at 944.195 cm^{-1} (10.6 μ m) features a rapid decrease with increasing temperature as illustrated in Fig. 3, just as in the millimeter window region.^{7,9,11} The temperature dependence has the following functional form over a wide temperature range,⁶

$$C_s(\nu, T) = C_s(\nu, T_0) \exp(b(1/T - 1/T_0)), \quad (5)$$

where $C_s(944.195 \text{ cm}^{-1}, 296 \text{ K}) = 1.83 \times 10^{-23} \text{ cm}^2/\text{molecule-atm}$ and $b = 1680 \text{ K}$. This result at 10.59 μ m is also consistent with other measurements in the 8 to 12 μ m region. This point is made in Fig. 3 as well and extended to other spectral locations by comparing the same exponential function to temperature dependent data at 1000 cm^{-1} and 1203 cm^{-1} .^{10,12,13}

Based on experimental data and Birnbaum's line shape formula in the far wing limit, a simple formula for the nitrogen broadened water vapor continuum absorption coefficient from 400 to 1400 cm^{-1} and for typical atmospheric temperatures is obtained to be

$$\beta_{\text{cont}}(\nu, T, p_{\text{H}_2\text{O}}, p_{\text{N}_2}) = 7.34 \times 10^{-26} (p_{\text{H}_2\text{O}}/T) (C_N(\nu, T) p_{\text{N}_2} + C_s(\nu, T) p_{\text{H}_2\text{O}}) \quad [\text{km}^{-1}] \quad (6)$$

where

$$C_N(\nu, T) = [3.7 \times 10^{-23} \exp(-0.01\nu) + 5.5 \times 10^{-23} \exp(0.016\nu)] \exp(1680(1/T - 1/T_0)),$$

$$C_s(\nu, T) = [2.45 \times 10^{-23} \exp(-0.0051\nu) + 1.9 \times 10^{-23} \exp(0.0125\nu)] \exp(1680(1/T - 1/T_0))$$

p is in atmospheres, ν is in wave numbers and $T_0 = 296 \text{ K}$. The units of the broadening coefficients are $[\text{cm}^2/\text{atm molecule}]$. The dashed curves in Figs. 1-3 come from this model. The temperature dependence of the nitrogen broadening coefficient comes from a model fit to measurements by Hinderling et al.⁶. Good agreement with many different experimental data sets is obtained. Fig. 1a also compares to the CKD model¹⁴

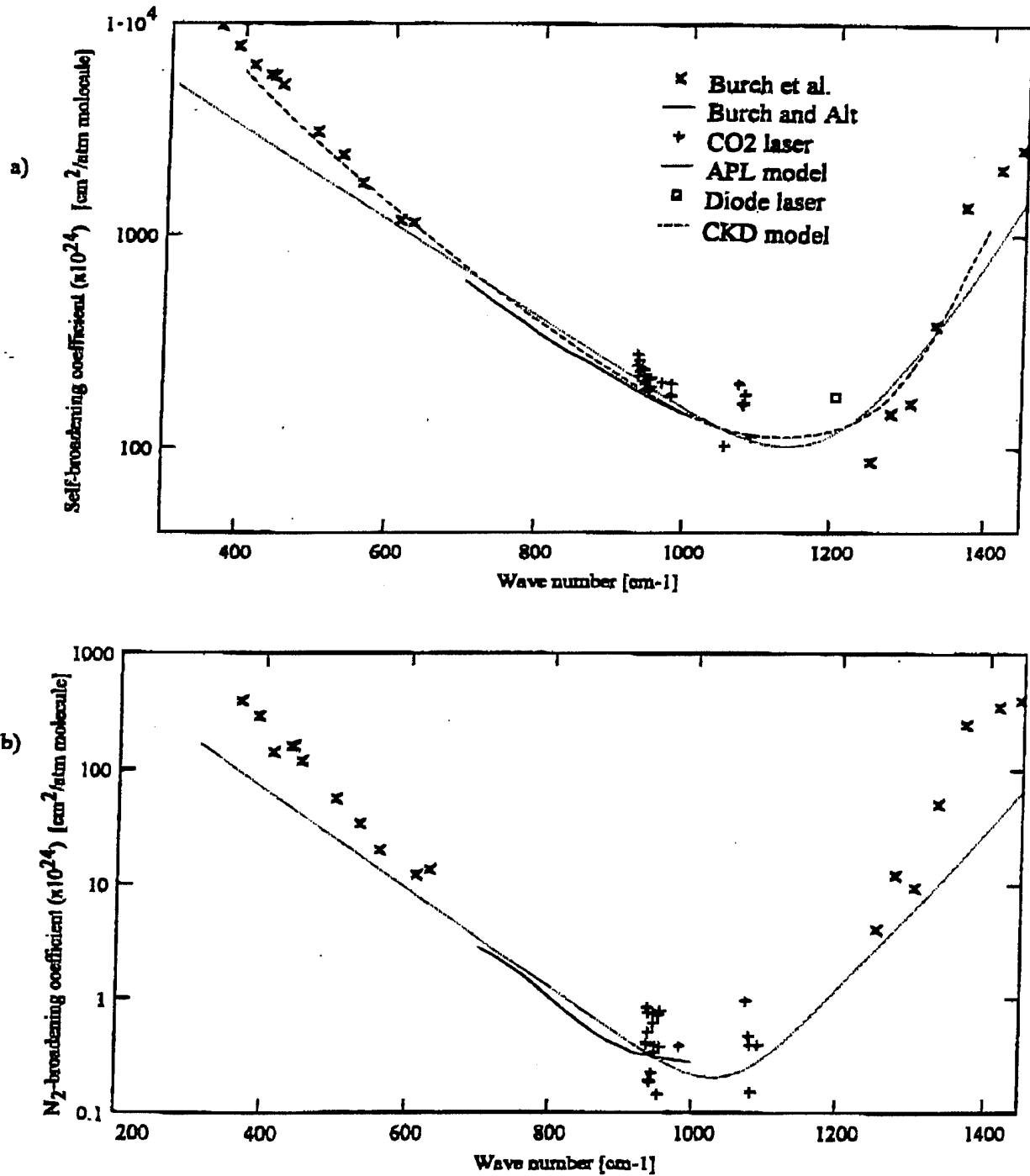


Figure 1. a.) Self-broadening coefficient [$\text{cm}^2/(\text{atm molecule})$] as a function of wave number from 300 to 1400 cm^{-1} at $T = 296 \text{ K}$. b.) Nitrogen broadening coefficient [$\text{cm}^2/(\text{atm molecule})$] as a function of wave number from 300 to 1400 cm^{-1} at 296 K. The dotted curve is a model fit to the experimental data as given by Eq. 7.16. The dashed curve is the CKD model.¹⁴ (x and solid curve - spectrometer measurements from Burch et al.³, \square - diode laser measurement¹⁰, + - CO_2 laser measurements.^{6,9})

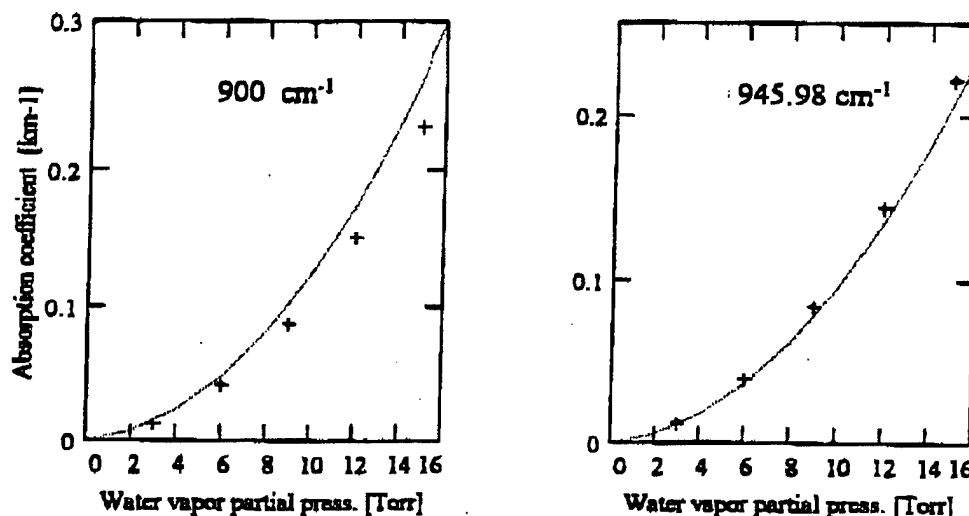


Figure 2. Water vapor partial pressure dependence of the absorption coefficient at 900 cm^{-1} and 945.98 cm^{-1} .^{2,3} Dotted curve is based on Eq. 6.

which is used in the computer codes LOWTRAN/MODTRAN and FASCODE. This model is given as a table at $T = 280\text{ K}$. The curve in Fig. 1a is scaled to $T = 296\text{ K}$ using the temperature dependence as given in Eqs. 5 and 6.

An excellent review of experimental measurements in the $10\text{-}\mu\text{m}$ region by Grant¹⁵ makes the following additional important points:

1. Oxygen does not broaden as effectively as nitrogen and must be included in a realistic model of the earth's atmosphere.
2. Understanding the local line structure is critical in determining the true continuum. Line positions are known reasonably well; however, line strength, shift and halfwidth are not known with enough accuracy. A synthetic spectrum of water vapor broadened by nitrogen from 934 to 954 cm^{-1} is compared to experimental CO_2 laser measurements in Fig. 4. The synthetic spectrum is composed of local line absorption generated using the HITRAN92 database¹⁶ and the Lorentz line shape, plus continuum absorption as given by Eq. 6. In general, good agreement is obtained when local line contributions are not important.

An experimental study of oxygen broadening has been conducted by Peterson⁹ using the photoacoustic technique and Nordstrom et al.¹⁷ using a White cell, and CO_2 laser source. An analysis is made on the CO_2 laser lines at 936.804 , 944.194 , 1048.661 and 1077.303 cm^{-1} using pure nitrogen-broadened data and pure oxygen-broadened data. An average dimensionless broadening coefficient of $F = 0.55 \pm 0.12$ for oxygen relative to nitrogen was determined for continuum absorption. Using Eq. 2, this means air has an effective broadening of 0.906 relative to nitrogen (i.e. $C_{\text{air}}(\nu, T) = 0.906 C_{\text{N}}(\nu, T)$).

3.2 The 3- to $5\text{-}\mu\text{m}$ window

The 3- to $5\text{-}\mu\text{m}$ continuum region has a different frequency dependence compared with the millimeter and 8- to $12\text{-}\mu\text{m}$ regions. Fig. 5 displays a nearly parabolic dependence with a minimum at a wave number of 2600 cm^{-1} . As shown by the spectrometer measurements of Burch and Alf³, and Burch⁷ (Fig. 5a), the self-broadening coefficient has a double exponential falloff from 2000 cm^{-1} up to 2600 cm^{-1} . Long path CO laser transmittance measurements¹⁸ near 2000 cm^{-1} verify the data by Burch. The continuum becomes relatively flat around 2600 cm^{-1} . Fig. 5a also shows long-path White cell DF laser measurements¹⁹ taken under atmospheric conditions, which indicate continuum absorption levels roughly 50% higher than those indicated by Burch and

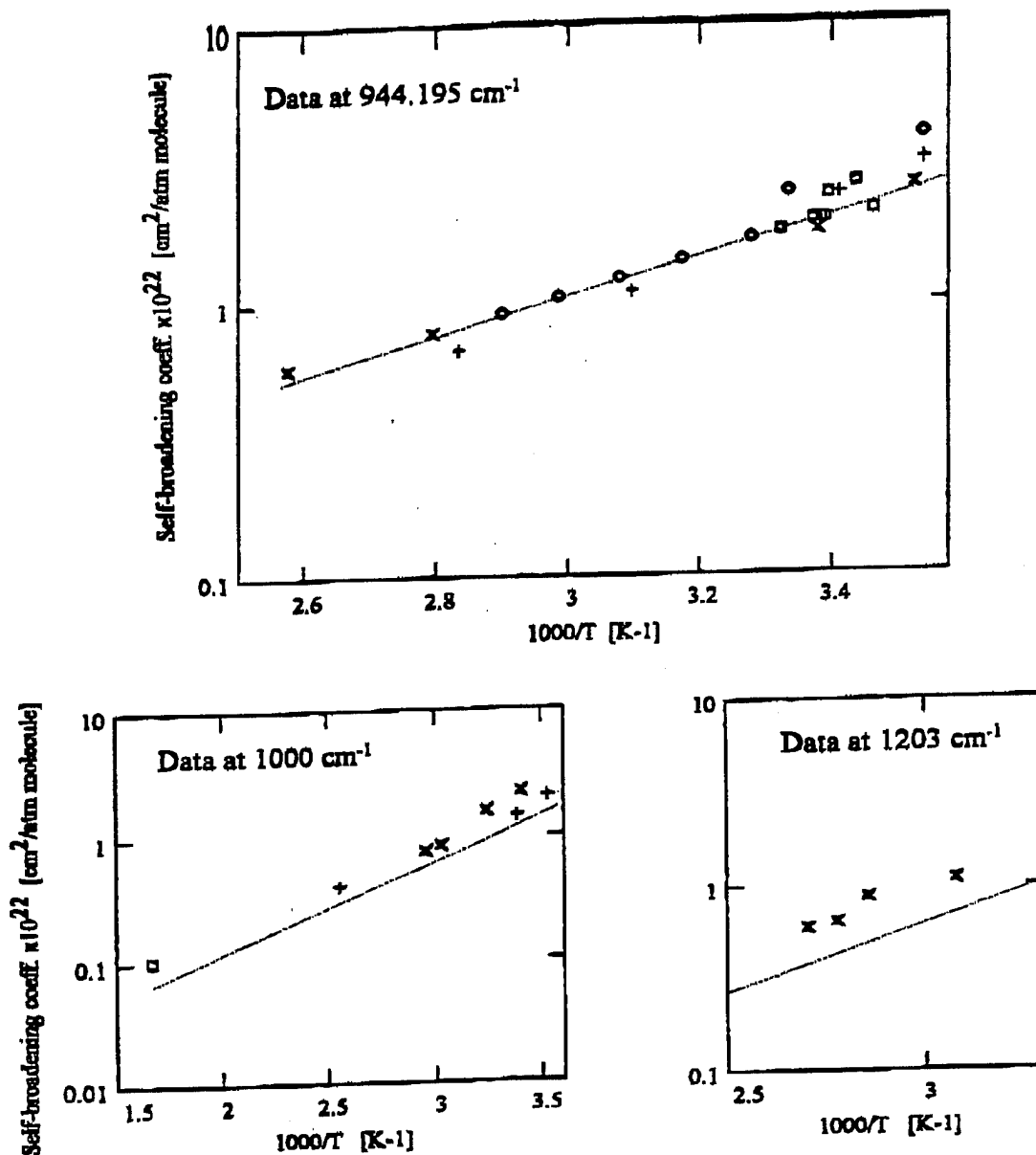


Figure 3. Temperature dependence of self-broadening coefficient in the 10 μ m region. (at 944.195 cm⁻¹ x - Burch and Alt³, \bullet - Hinderling et al.⁴, \circ - Loper et al.⁷, \square - Peterson⁹ and + - Arefev and Dianov-Klokov¹¹; at 1000 cm⁻¹ \square - Thomas¹³, + - Burch and Alt³ and x - Varanasi et al.¹²; at 1203 cm⁻¹ x - Montgomery.¹⁰)

Alt. As in the case for CO₂ laser measurements, local line absorption distorts these data and care must be used in the interpretation. The observed level of continuum absorption in the 4- μ m region is roughly an order of magnitude less than that in the 10 μ m region and thus harder to measure. The self-broadening coefficient increases as wave number approaches 3200 cm⁻¹ because the 2 ν_2 band is located there.

Long-path nitrogen-broadened CO₂, DF¹⁹, and HF²⁰ laser transmittance measurements near room temperature indicate large values for B in this continuum region, ranging from 10 to 20 at 5 μ m to approximately 50 to 60 at 4 μ m and back down to 10 at 3 μ m. This trend is represented in Fig. 5b, which shows wave number dependent C_N at room temperature. Recall that B is the ratio, C_s/C_N .

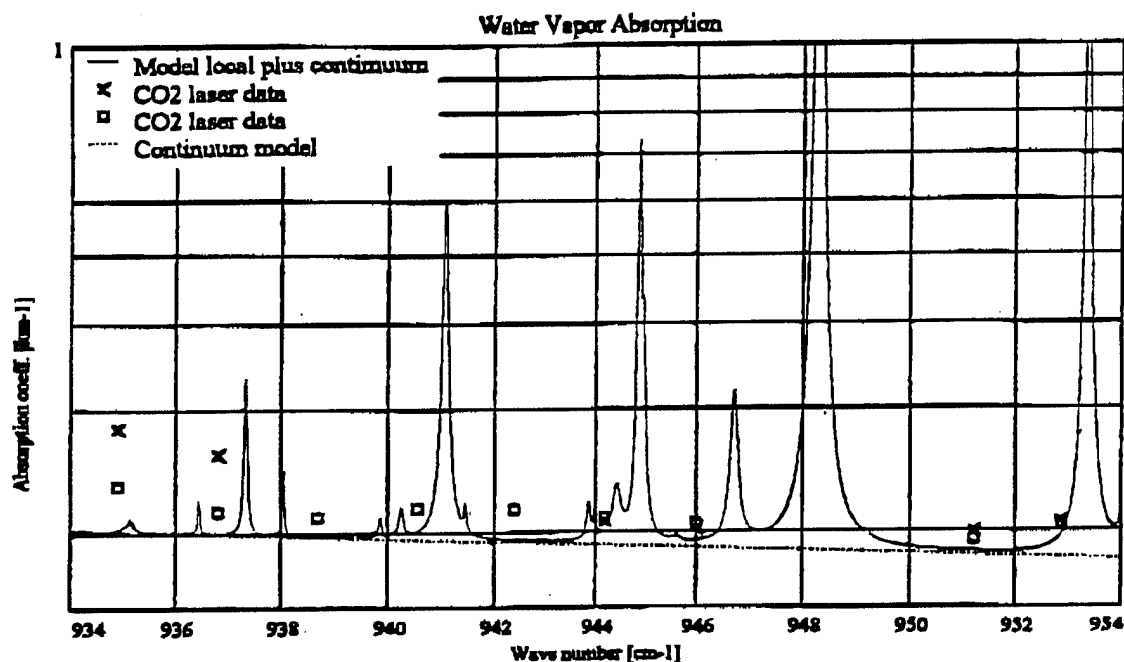


Figure 4. Total absorption coefficient (local plus continuum) computed from the HITRAN database and Eq. 6 for $p_{H_2O} = 14.3$ Torr, $p_{N_2} = 745.7$ Torr and $T = 296$ K versus wave number. The synthetic spectrum is compared to CO_2 laser measurements.⁶

A strong negative temperature dependence is again observed for the self-broadening coefficient. Fig. 6 shows the results of laboratory long-path spectrometer measurements by Burch and Al². The temperature dependence at 2400 cm^{-1} exhibits exponential fall off similar to that in the $10\text{-}\mu\text{m}$ and millimeter regions. However, the curves at 2500 and 2600 cm^{-1} show double exponential trends. The nature of the water vapor continuum in this window region is more complicated than the other windows previously discussed.

More experimental data are needed to generate a meaningful empirical model of the continuum absorption coefficient. However, an attempt at representing the existing data is given by the following empirical formula for nitrogen broadened water vapor continuum absorption coefficient valid from 1900 to 3000 cm^{-1} ,

$$\beta_{\text{cont}} = 7.34 \times 10^{-24} (p_{H_2O}/T) \{ C_1(\nu, T) p_{H_2O} + C_N(\nu, T) p_{N_2} \} \text{ [km}^{-1}] \quad (7)$$

where the broadening coefficients are given by

$$C_1(\nu, T) = [1.6 \times 10^{-11} \exp(-0.013\nu) + 7.0 \times 10^{-22} \exp(-0.002\nu)] \exp(1450\{1/T - 1/T_s\}) \\ + [1.0 \times 10^{-44} \exp(0.014\nu) + 1.5 \times 10^{-22} \exp(0.0021\nu)] \exp(6000\{1/T - 1/T_s\})$$

and

$$C_N(\nu, T) = (296/T) \{ 5.6 \times 10^{-16} \exp(-0.016\nu) + 2.5 \times 10^{-20} \exp(-0.002\nu) + \\ 2.0 \times 10^{-21} \exp(0.016\nu) + 5.4 \times 10^{-21} \exp(-0.0045\nu) \},$$

p is in atmospheres, ν is in wave numbers and $T_s = 296$ K. The units of the broadening coefficients are $[\text{cm}^2/\text{atm molecule}]$. This model is represented in Figs. 5 and 6. No studies of oxygen broadening have been conducted in this spectral region to the best of the author's knowledge.

To appreciate the importance of local line characterization as part of continuum measurements by laser techniques, Fig. 7 illustrates the total absorption coefficient (local plus continuum) as a function of wave number. The spectrum is computed using the HITRAN92 database¹⁶ and Eq. 7. The experimental data points come from White et al.²¹ and Mills.²²

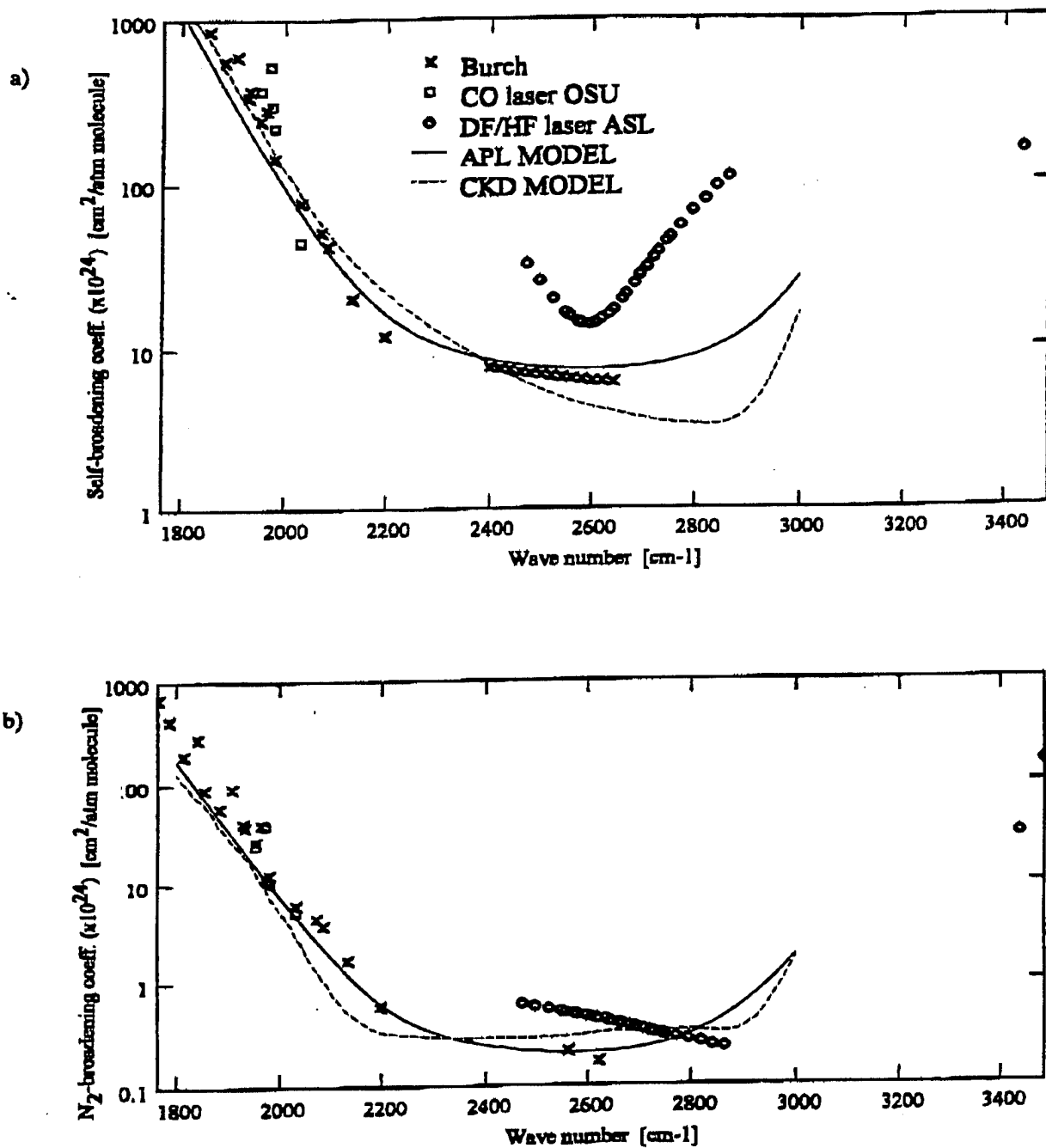


Figure 5. $4 \mu\text{m}$ water vapor continuum region at $T = 296$ K. (a) $C_s(\nu, 296)$ vs wave number and (b) $C_N(\nu, 296)$ vs wave number. The experimental data are indicated by x - Burch and Alt,³ \square - Thomas,¹⁸ o - Watkins et al.¹⁹ and Watkins et al.²⁰. The solid curve is from Eq. 7. The dashed curve is the CKD model.¹⁴

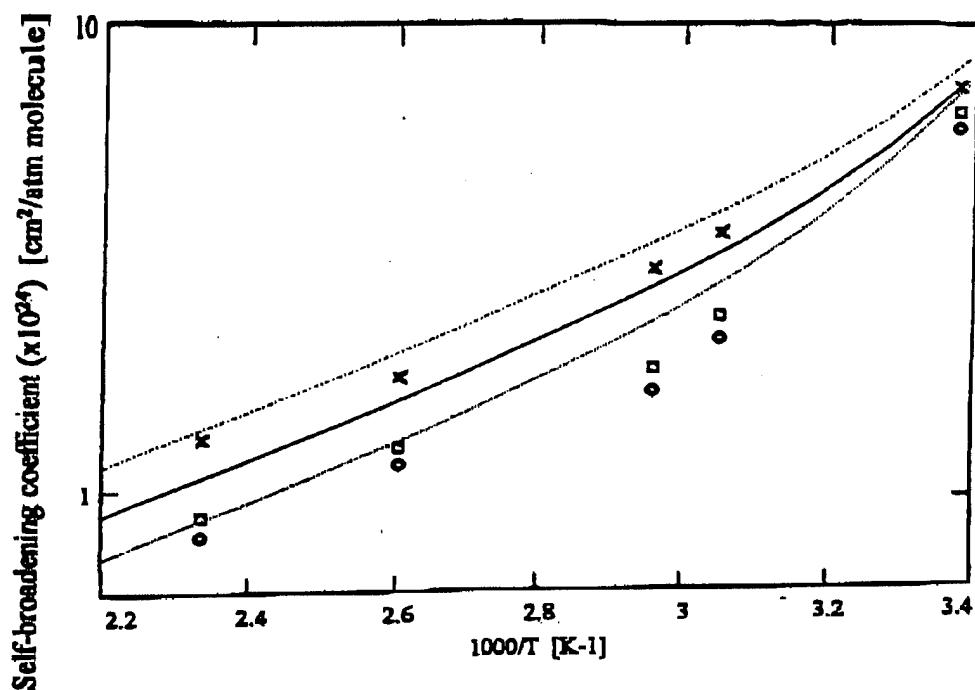


Figure 6. Plots of the water vapor self-broadening coefficients at 2400 (x and dash-dot), 2500 (\square and solid) and 2600 (\diamond and dotted) cm^{-1} versus reciprocal temperature³. The curves are generated by Eq. 7.

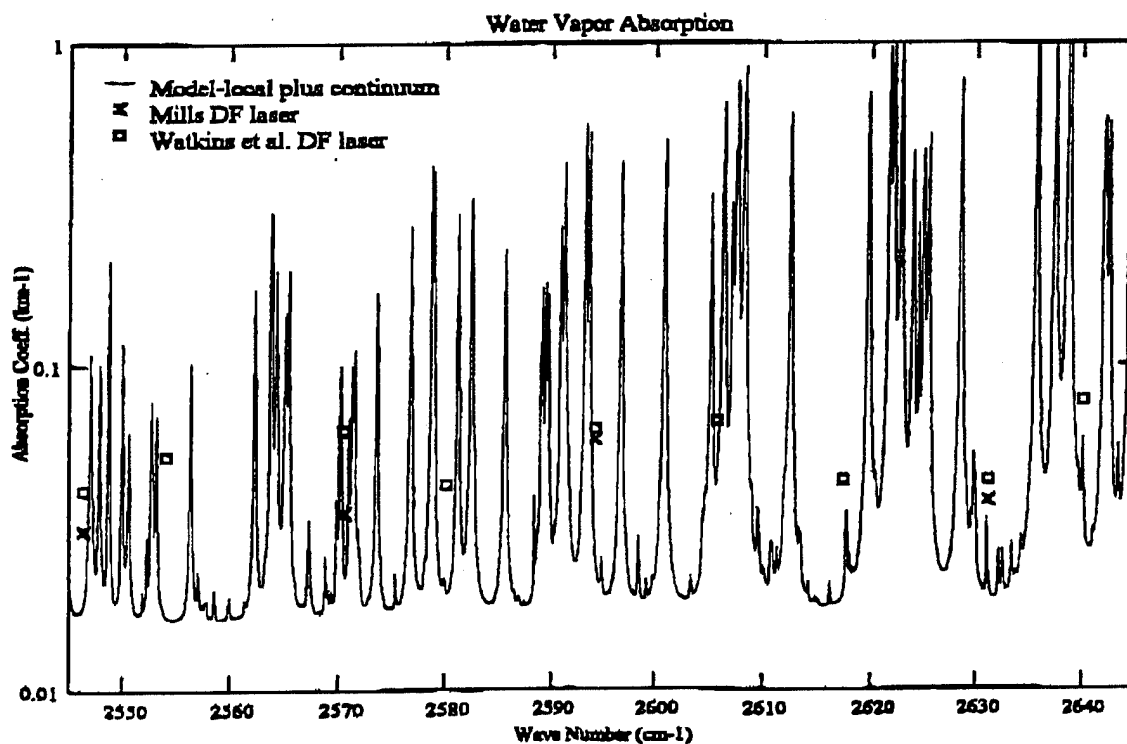


Figure 7. The absorption coefficient ($p_{\text{H}_2\text{O}} = 14.3$ Torr, $p_{\text{N}_2} = 745.7$ Torr and $T = 296$ K) as a function of wave number. The experimental data points come from DF laser measurement by White et al.²¹ and Mills.²²

3.3 Beyond 3 μm

Very little data on the water vapor continuum exist beyond 3 μm . A review is given by Thomas.¹⁵ By understanding the nature of the continuum in the well characterized spectral windows, it is hoped that crude, yet useful, models can be constructed for atmospheric windows beyond 3 μm . It is clear the strength of the strong bordering water vapor bands, that define the atmospheric windows, determines the strength of the continuum absorption. Contributions to the 10 μm region are dominated by far wings of the very strong rotational band of water vapor on the long-wavelength side of that window, whereas the 4- μm continuum absorption arises from the bordering strong vibrational bands of almost equal strength. Based on a far wing interpretation, that difference between sources explains the difference between the frequency dependence of the 10 μm continuum region and that of the 4 μm continuum region (see Figs. 1 and 5). Also, the exponential frequency dependence, as observed in the 8 to 12 μm and 3 to 5 μm windows and predicted by Eq. 3, should be expected in the shorter wavelength windows. It is interesting to note that the value of τ_0 ($2\pi\epsilon\tau_0 = 0.0024$) is used in the empirical model in the 4 μm continuum region.

4. CONCLUSIONS

An extensive set of spectrometer and laser measurements are presented and fit to an empirical water vapor continuum model for nitrogen and air broadened samples. The model is a function of wave number, absorber partial pressure, broadening partial pressure and temperature. The 8 to 12 μm and 3 to 5 μm regions are studied. The important aspect of this work is to include the many high quality laser measurements into the study of the water vapor continuum. When local line absorption can be avoided, laser measurements offer greater sensitivity to continuum absorption. Laser photoacoustic measurements will be an essential component of any experimental study of the continuum beyond 3 μm , because high sensitivity is needed. The spectrometer based measurements establish the frequency dependence of the continuum.

Good agreement is obtained between the experimental data and synthetic spectra in both window region when continuum absorption dominates. More work is needed to completely characterize the water vapor local line structure in the window regions.

5. ACKNOWLEDGEMENTS

The author wishes to recognize David Tobin of UMBC for helpful discussions throughout the course of this work.

6. REFERENCES

1. S.A. Clough, F.X. Kneizys and R. Davies, "Line Shape and Water Vapor Continuum," *Atmospheric Research* 23, pp. 229-241 (1989).
2. M.E. Thomas and D.D. Duncan, "Atmospheric Transmission," Chapter 1 Volume 2. Atmospheric Propagation of Radiation, F.G. Smith (ed.) as part of *The Infrared & Electro-Optical Systems Handbook*, J. S. Accetta and D. Shoemaker (exec. eds). SPIE/ERIM, pp. 1-156 (1993).
3. D.E. Burch and R.L. Alt, Continuum Absorption by H_2O in the 700–1200 cm^{-1} and 2400–2800 cm^{-1} Windows, AFGL-TR84-0128, Ford Aerospace and Communications Corporation, Aeronutronic Division (May 1984); D.A. Gryvnak and D.E. Burch, Infrared Absorption by CO_2 and H_2O , "Aeronutronic Publication U-6417, Air Force Geophysics Laboratories, Contract F19628-76-C-0302 (May 1978); D.E. Burch, "Absorption by H_2O in Narrow Windows Between 3000–4200 cm^{-1} ," AFGL-TR-85-0036 (1985).
4. G. Birnbaum, *J. Quant. Spectrosc. Radiat. Transfer* 21, 597 (1979).
5. C.T. Delaye and M.E. Thomas, "Atmospheric continuum absorption models," *SPIE Proceedings, Propagation Engineering: Fourth in a Series* 1487, pp. 291-298 (1991).

6. J. Hinderling, M.W. Sigrist, and F.K. Kneubuhl, "Laser photoacoustic spectroscopy of water-vapor continuum and line-absorption in the 8- to 14- μm atmospheric window," *Infrared Phys.* 27, 63 (1987).
7. G.L. Loper, M.A. O'Neill, and J.A. Gelbwachs, "Water-vapor continuum CO_2 laser absorption spectra between 27 °C and 10 °C," *Appl. Opt.* 22, 3701 (1983).
8. J.C. Peterson, M.E. Thomas, R.J. Nordstrom, E.K. Damon, and R.K. Long, "Water vapor nitrogen absorption at CO_2 laser frequencies," *Appl. Opt.* 18, 834 (1979).
9. J.C. Peterson, "A Study of Water Vapor Absorption at CO_2 Laser Frequencies Using a Differential Spectrophone and White Cell," Dissertation, The Ohio State University (June 1978).
10. G.P. Montgomery, Jr., "Temperature dependence of infrared absorption by the water vapor continuum near 1200 cm^{-1} ," *Appl. Opt.* 17, 2299 (1979).
11. V.N. Arefev and V.I. Dianov-Klovov, "Attenuation of 10.6- μm radiation by water vapor and the role of $(\text{H}_2\text{O})_2$ dimers," *Opt. Spectrosc.* 42, 488 (1977).
12. P.S. Varanasi, S. Chou, and S.S. Penner, *J. Quant. Spectrosc. Radiat. Transfer* 8, 1537 (1968), P. Varanasi and S. Chadamani, "Self- and N_2 -broadened spectra of water vapor between 7.5 and 14.5 μm ," *J. Quant. Spectrosc. Radiat. Transfer* 38, 407 (1987) and P. Varanasi, "Infrared absorption by water vapor in the atmosphere," *SPIE Proceedings Modeling of the Atmosphere*, 928 213 (1988).
13. M.E. Thomas, "Infrared and Millimeter-Wavelength Absorption in the Atmospheric Windows by Water Vapor and Nitrogen: Measurements and Models," *Infrared Physics*, 30, 161 (1990).
14. S.A. Clough, "The Water Vapor Continuum and its Role in Remote Sensing," *OSA Topical Meeting On Remote Sensing*, p 76 of Proceedings, Feb. 1995.
15. W.B. Grant, A Critical Review of Measurements of Water Vapor Absorption in the 840 to 1100 cm^{-1} Spectral Region, *Appl. Opt.* 29, pp. 451-462 (1990).
16. L.S. Rothman, R.R. Gamache, R.H. Tipping, C.P. Rinsland, M.A.H. Smith, D. Chris Benner, V. Malathy Devi, J.-M. Flaud, C. Camy-Peyret, A. Perrin, A. Goldman, S.T. Massie, L.R. Brown and R. A. Toth, "The HITRAN Molecular Database: Editions of 1991 and 1992," *J. Quant. Spectrosc. Radiat. Transfer* 48, pp. 469-507 (1992).
17. R.J. Nordstrom, M.E. Thomas, J.C. Peterson, E.K. Damon, and R.K. Long, "Effects of oxygen addition on pressure-broadened water vapor absorption in the 10- μm region," *Appl. Opt.* 17, 2724 (1978).
18. M.E. Thomas, "Tropospheric Water Vapor Absorption in the Infrared Window Regions," Dissertation, The Ohio State University (Aug. 1979).
19. W.R. Watkins, K.O. White, L.R. Bower and B.Z. Sojka, "Pressure Dependence of the Water Vapor Continuum Absorption in the 3.5 to 4.0 Micrometer Region," U.S. Army Electronics Research and Development Command, Report No. ASL-TR-0017, Sept., 1978.
20. W.R. Watkins, R.L. Spellicy, K.O. White, B.Z. Sojka, and L.R. Bower, "Water vapor absorption coefficients at HF laser wavelength (2.64 & 2.93 μm)," *Appl. Opt.* 18, 1582 (1979).
21. K.O. White, W.R. Watkins, C.W. Bruce, R.E. Meredith, and F.G. Smith, "Water vapor continuum absorption in the 3.5 to 4.0 μm region," *Appl. Opt.* 17, 2711 (1978).
22. F.S. Mills, "Absorption of Deuterium Fluoride Laser Radiation by the Atmosphere," Dissertation, The Ohio State University (Aug. 1975).

Phillips Lab Atmospheric Radiance Code (ARC): Extensions and Recent Applications

Peter P. Wintersteiner, ARCON Corporation, Waltham MA, 02154
Richard H. Picard & Jeremy R. Winick, Optical Environment Division, Phillips
Laboratory, Hanscom AFB, MA, 01731-3010

Abstract: We review the present status of, and planned extensions to, the PL Atmospheric Radiance Code (ARC), the AF line-by-line code used to determine non-LTE conditions in the atmosphere and the resulting line-of-sight radiances. We describe enhancements to the code and give examples of results that have been obtained in recent applications. We discuss improvements that have made or will make ARC more capable of calculating radiative excitation in structured atmospheres, calculating radiance due to structured emission features and for downlooking lines of sight, interfacing with FASCODE, and being used in remote sensing applications.

In this talk we discuss the current status of the Phillips Lab Atmospheric Radiance Code (ARC). We will give a brief synopsis of its capabilities and review some of the sorts of problems that it has addressed recently. At the end we will describe the directions in which we intend to move in the future.

The three authors have been involved in this work from the beginning. There have been substantial contributions from colleagues at ARCON, Bob Joseph and Armand Paboojian. We would like to acknowledge that some of the original motivation and direction was provided by Ramesh Sharma of PL, and that we have had the support of many others at PL as well.

Atmospheric Radiance Code is the name that we give to several stand-alone codes that are used, collectively, to model non-LTE behavior in the terrestrial atmosphere (Figure 1). The distinguishing feature of these codes is the use of line-by-line (LBL) methods to deal with radiative processes, in particular the radiative excitation of vibrational states by transfer from within the atmosphere (earthshine).

The principal objectives of ARC are to predict non-LTE populations, expressed as vibrational temperatures, of infrared-emitting species in the terrestrial atmosphere, and to determine the resulting line-of-sight (LOS) radiances. What this is *not* is a comprehensive non-LTE scene generator, although modules from it could be, and have been, used in comprehensive codes and scene generators. Instead, it is a research tool that is used for detailed investigations of non-LTE conditions and phenomena, and that also has served as a benchmark for faster but more approximate codes. In many ways it is a complement to SHARC, somewhat as FASCODE is a complement to MODTRAN.

The general capabilities of ARC are summarized in Figure 2. As stated earlier, the principal objectives are the vibrational temperatures and the LOS radiances. A great deal of

detailed information is available about the LBL radiative transfer—for example, a breakdown of radiative-excitation rates according to the altitude at which the contributing photons originate. Where appropriate, IR cooling-rate calculations can be performed for those radiators as well. ARC also has an auroral component known as Auroral Atmospheric Radiance Code (AARC), much of which was incorporated into SHARC a number of years ago. Last of all, a one-dimensional diurnal photochemical model, which has been developed recently by Sam Makhoul and co-workers here at PL, is used to predict O_x , HO_x , and NO_x , including the vibrational populations of OH near the mesopause.

We list a spectral range of 1.2 to 17 μm . It should be understood that the non-LTE populations are calculated only for selected molecules whose emissions fall within this range. All of these are linear molecules, although this is not an intrinsic limitation. However, the LOS radiance modules are capable of handling emissions from any molecule for which vibrational temperatures or populations can be given. We also list unlimited spectral resolution, because our calculations are all done on a completely monochromatic basis.

Figures 3 and 4 list some of the upgrades and enhancements to the ARC modules that have been developed recently. Many of them have to do with making the codes easier to use, principally by relaxing requirements on the input files and attempting to eliminate some of the more idiosyncratic features. However, there have been improvements in the science, and in some other capabilities of the codes, as well. The $CO_2(v_3)$ calculation has been improved in several ways. The auroral model also has some features that are new since its last official release. The most recent changes are in the modules that do the LOS radiance calculation, and most of these are in response to the need to more accurately simulate the variety of atmospheric observations and the instruments that acquire the data. In particular, we now have more general viewing geometry, the capability to simulate relatively large instrumental fields of view, and more detailed output including layer-by-layer contributions to the band radiance.

In addition, we have spent some time responding to the need to model the horizontal structure of the atmosphere—that is, to loosen the restriction imposed by a one-dimensional (“1-d”) atmosphere so that we can study discrete and continuously-varying structures. In particular, we have built in a capability for lines-of-sight passing through two or more discrete regions (such as might be used to represent localized emissions from auroral dosing regions, or from sprites). There also now exists the ability to vary the emission rates continuously along the lines-of-sight by interpolating the non-LTE populations (or the volume emission rates) between discrete points on the paths. This is useful for simulating, for example, low-sun or terminator conditions. In each case, the code assimilates several 1-d profiles of the emitting states’ populations and performs the calculations necessary to specify the volume emission rates at all points of all paths.

Figure 5 lists a few of the studies that we have undertaken using ARC. Without going into great detail on any of them, we will describe some of the results we have obtained.

Figure 6 compares the ARC predictions for nighttime 4.3 μm limb radiance with a CIRIS-1A spectrum, for a tangent height of about 82 km. A number of specific features

can be identified, including the CO₂ major and minor-isotope fundamentals, Q-branches of CO₂ hot bands, and both discrete lines and Q-branches of the OH 9-8 and 8-7 bands.

Figure 7 shows a daytime simulation for a tangent height of 67 km, where the solar-pumped fluorescent bands of CO₂ dominate the spectrum between 2300 and 2350 cm⁻¹. We studied the effect of including or not including excitation of N₂ vibration by O(¹D), the latter calculated by the diurnal model. We found an appreciable effect, but not quite enough to resolve small discrepancies between the model and the CIRRIS data (also shown).

We have used the ARC codes to model CO emissions, with many interesting results. We have shown that a great deal of the emission from CO at night, and a lesser fraction in the daytime, follows upon absorption of radiation from the ground or from the lowest layers of the atmosphere, and therefore strongly depends upon the state of cloud cover. To demonstrate this point, Figure 8 compares the nighttime limb band radiance for clear-sky and high-cloud conditions for the 26 and 36 isotopes of CO, the clouds having been assumed to sit at an altitude of 15 km.

Last year at this conference we presented our use of ARC as a benchmark for the radiative-excitation calculation in the widely-used modified Curtis-matrix (MCM) narrow-band model of Manuel Lopez-Puertas (Astrophysical Institute, Granada, Spain). The principal result of this comparison was to demonstrate that the narrow-band model does a good job of determining the radiance and cooling rates over a wide range of conditions. The agreement of vibrational temperatures calculated by the MCM model and ARC is shown, for a model atmosphere similar to the U.S. Standard Atmosphere, in Figure 9. Another result was to demonstrate that the principal deficiency of the MCM model, admittedly a small one, is the use of long path-average temperature and pressure for determining the absorption lineshape. To reach that conclusion, it was necessary to carefully compare the layer-by-layer contributions to the total radiative excitation, as a function of altitude. An example of such a comparison is given in Figure 10.

We have also done calculations to compare the atmospheric cooling in the presence of gravity waves with the cooling expected under ambient conditions, starting with gravity-wave models supplied by Sam Makhlof and co-workers. The results show that the instantaneous cooling is strongly affected by the presence of the waves, which cause large oscillations about the mean cooling, but also that even when the cooling is averaged over the wave's period there is a residual impact of as much as 15 K/day in the lower thermosphere. The latter point is demonstrated in Figure 11, which shows the average cooling for three simulated waves, having vertical wavelengths of approximately 8, 13, and 25 km, and compares it with the cooling to be expected in the absence of the waves.

We have modeled the IR signatures of upward-propagating lightning, or sprites, using ARC's new NLTEA module. Using vibrational populations generated by Russ Armstrong and co-workers, we find an enormous, albeit fleeting, signal at 4.3 μm. The 60-km limb spectra shown in Figure 12 were calculated for sprites located near the tangent point (#2), and approximately 360 km closer to (#1) and farther from (#3) the observer than the tangent point. In each case the lines-of-sight intersected with the sprite over a range of about 30 km, but the altitude at which the intersection took place was different for the three

cases. The effect of atmospheric attenuation can be seen by comparing #1 and #3. In all three cases there is considerable enhancement over the ambient spectrum (#4).

We looked at the efficacy of the escape function approximation (EFA) for determining the radiative excitation in IR bands, using CO₂ 4.3 μ m as an example to compare with the full LBL calculation. In daytime, when solar excitation overwhelms earthshine pumping, the EFA is not a terrible approximation, but at night it causes large underpredictions of the radiance in the mesosphere, as demonstrated in Figure 13.

These rather disparate results that we have shown are intended to give an idea of the variety of problems that we try to address with ARC. With Figures 14 and 15 we introduce a brief discussion of one of the directions in which we would like to go in the future, namely to merge ARC with other LBL codes that are better suited to deal with the lower atmosphere, like FASCODE. These figures show a portion of the 2.7 μ m region, viewing upward from the ground using emissions determined by FASCODE, with and without an IBC II aurora (NO overtone modeled by AARC). The auroral signal was propagated to the ground using transmissivity from FASCODE and is obscured over much of the range, but persists in a few "microwindows".

What we would like to do is use FASCODE to provide estimates of monochromatic upwelling radiation at the lower boundary of our models. ARC is ill-suited for calculations in the lowest part of the atmosphere, as it has no facility for calculating the effects of aerosols or line overlap. However, for the purpose of determining the radiative excitation in the stratosphere and, for some molecules, even in the mesosphere, it is necessary to consider contributions from low altitudes. FASCODE line-of-sight (LOS) radiances, calculated for suitable angles, could be used to determine these contributions. Such a calculation would be an improvement on our present procedure, which is to use a blackbody surface to estimate contributions from below the lower boundary.

We also intend to expand our efforts to simulate conditions in structured atmospheres. We are continuing work on the LOS radiance module. The downlook calculation should be improved by using FASCODE upwelling LOS radiance to replace the lower-boundary contribution. This effort will precede any attempt to use FASCODE results for improving the radiative-excitation calculation, as described above. Another improvement will be to relax the restriction that only the emission rates vary horizontally. Specifically, the capability to vary temperature and density will permit more realistic simulations of the radiative signature of gravity waves in the mesosphere. We are also going to try to modify the radiative-transfer algorithm that we use to determine earthshine pumping, in order to accommodate structured lower atmospheres.

To summarize (Figure 16), ARC is a non-LTE line-by-line model that predicts non-LTE populations, line-of-sight radiances, and radiative cooling for selected species. It is used for simulating specific experimental conditions, performing detailed investigations of non-LTE phenomena, and making benchmark comparisons with other models. We continue to upgrade the existing modules in order to use them for specific new applications, and are working on expanding ARC's capabilities to better deal with atmospheric structure.

ARC Overview

Line-by-Line (LBL) Non-LTE Model

Objectives:

- Predict non-LTE populations (vibrational temperatures) of IR-emitting species
- Predict line-of-sight (LOS) radiance for these species, for multiple paths
- Serve as a research tool

Detailed investigation of non-LTE conditions and phenomena

Radiative excitation processes

Collisional and vibrational energy transfer

Benchmarking

Modified Curtis Matrix narrow-band model

DNA/NORSE nuclear effects code

Figure 1

Summary of ARC Capabilities

- Calculation of non-LTE populations and LOS radiances
- LBL calculation of radiative excitation
 - full temperature/pressure variation of emission & absorption lineshapes
 - breakdown of radiative-excitation sources by altitude (layer)
- IR cooling-rate capability
- LBL auroral model (AARC: Auroral ARC)
- 1-d photochemical-dynamical model for O_x , HO_x , NO_x
- Spectral range: 1.2-17 microns
- Resolution: unlimited
- LOS calculation accommodates atmospheric structure

Figure 2

Code Upgrades and Enhancements

- RAD/RADC (modules for CO₂ & CO non-LTE populations)
 - Additional excitation mechanisms for N₂(v) ↔ CO₂(v₃)
 - O(¹D)
 - V-V exchange with high-lying CO₂ states
 - Less restrictive input file requirements; extensions for ease of use
- SABS (module for solar-flux absorption)
 - Less restrictive input file requirements; extensions for ease of use
- AARC (Auroral ARC):
 - Enhanced menu-driven interface
 - Easier access to climatological model input
 - More flexible viewing geometry
 - Time-dependent auroral flux (important for non-prompt emitters)
 - LOS extensions below lower boundary of dosing region
 - Excitation efficiencies calculated online

Figure 3

Code Upgrades and Enhancements (cont.)

- NLTE/NLTEA/CONV (modules for LOS radiance)
 - Viewing geometry: limb, uplook, downlook
 - Footprint calculation for limb look
 - Automatic multiple-band capability
(access multiple linefiles and population profiles)
 - Output (all for multiple paths):
 - band radiance; convolved spectral radiance; detailed (monochromatic)
 - line radiance; layer-by-layer contributions to band radiance
 - Less restrictive input file requirements; extensions for ease of use
- NLTEA (module for LOS radiance with atmospheric structure)
 - 2-d calculation; volume emission rates (VER) vary with range along LOS
 - Options for specifying "horizontal" variations:
 - 1) Multiple discrete regions (localized emissions: auroras, sprites,...)
 - 2) Continuous, obtained by interpolating VER along LOS
(VER varying over large regions: terminator, low-Sun conditions, ...)
 - Requires multiple 1-d VER profiles (e.g., vibrational temperature profiles)

Figure 4

ARC: Examples of Recent Results and Applications

- CIRRIS comparisons (4.3 μm CO_2 ; day, night)
- CO modeling
 - Significance of lower boundary (clouds/ground)
 - CIRRIS comparisons: minor-isotope signatures
- Benchmark for radiative excitation calculation
 - Validate calculation in MCM narrow-band model (Lopez-Puertas et al)
 - Small errors in heating rate due to path-average temperature & pressure
- IR cooling in the presence of gravity waves
- Sprite signatures
- Efficacy of escape-function approximation for IR radiative transfer

Figure 5

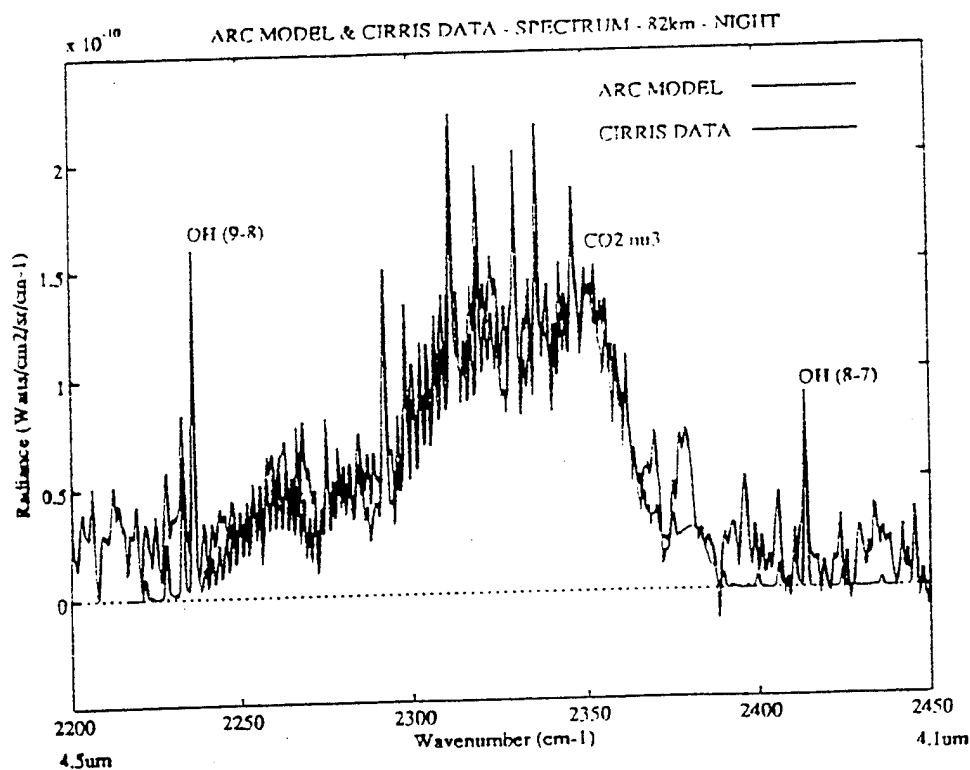


Figure 6

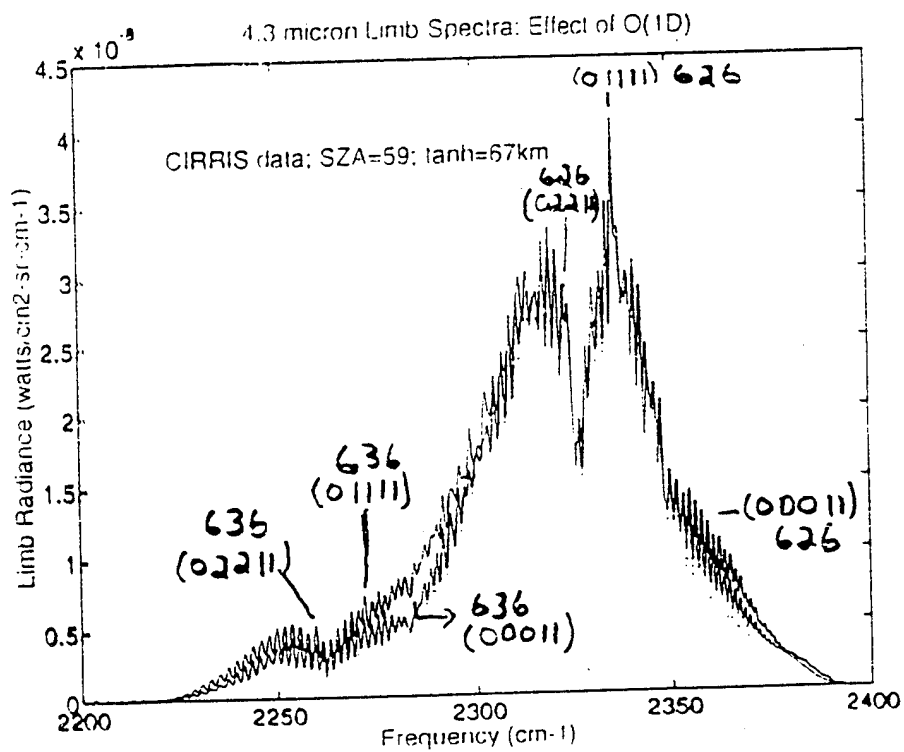


Figure 7

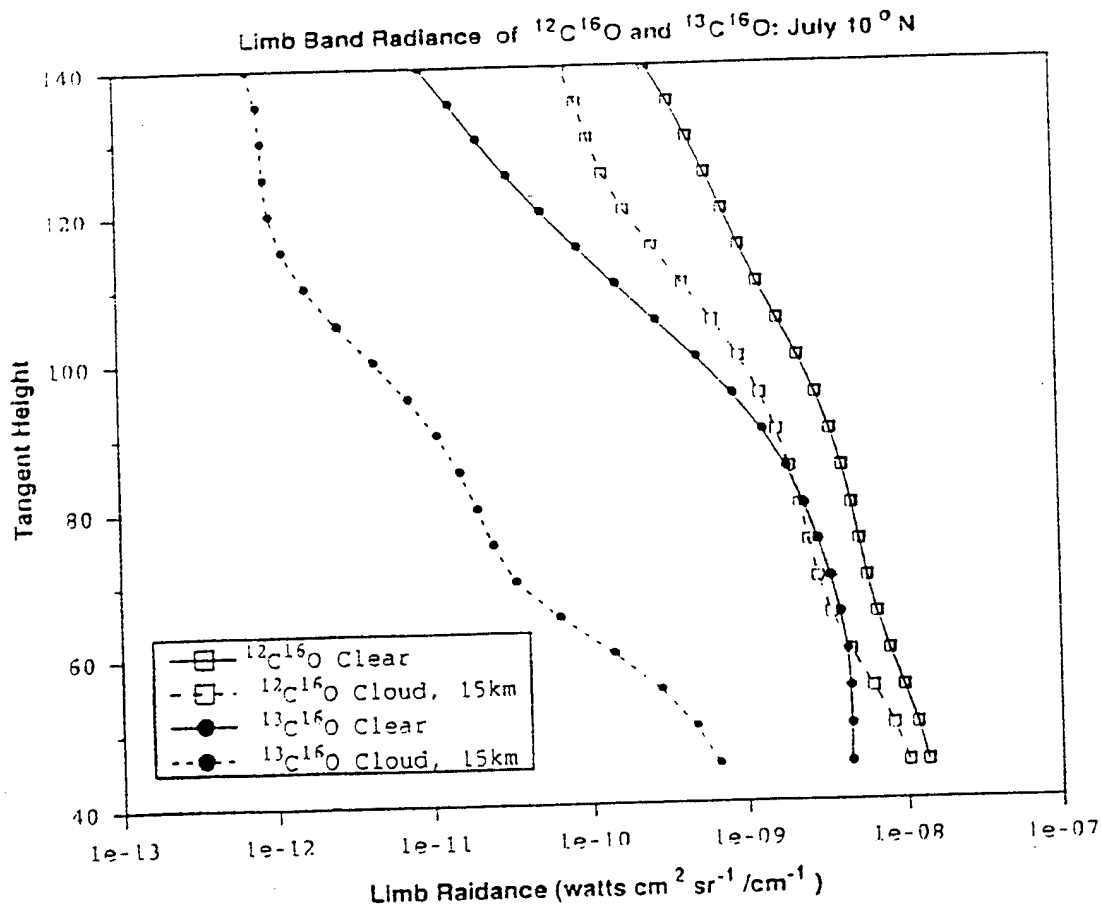


Figure 8

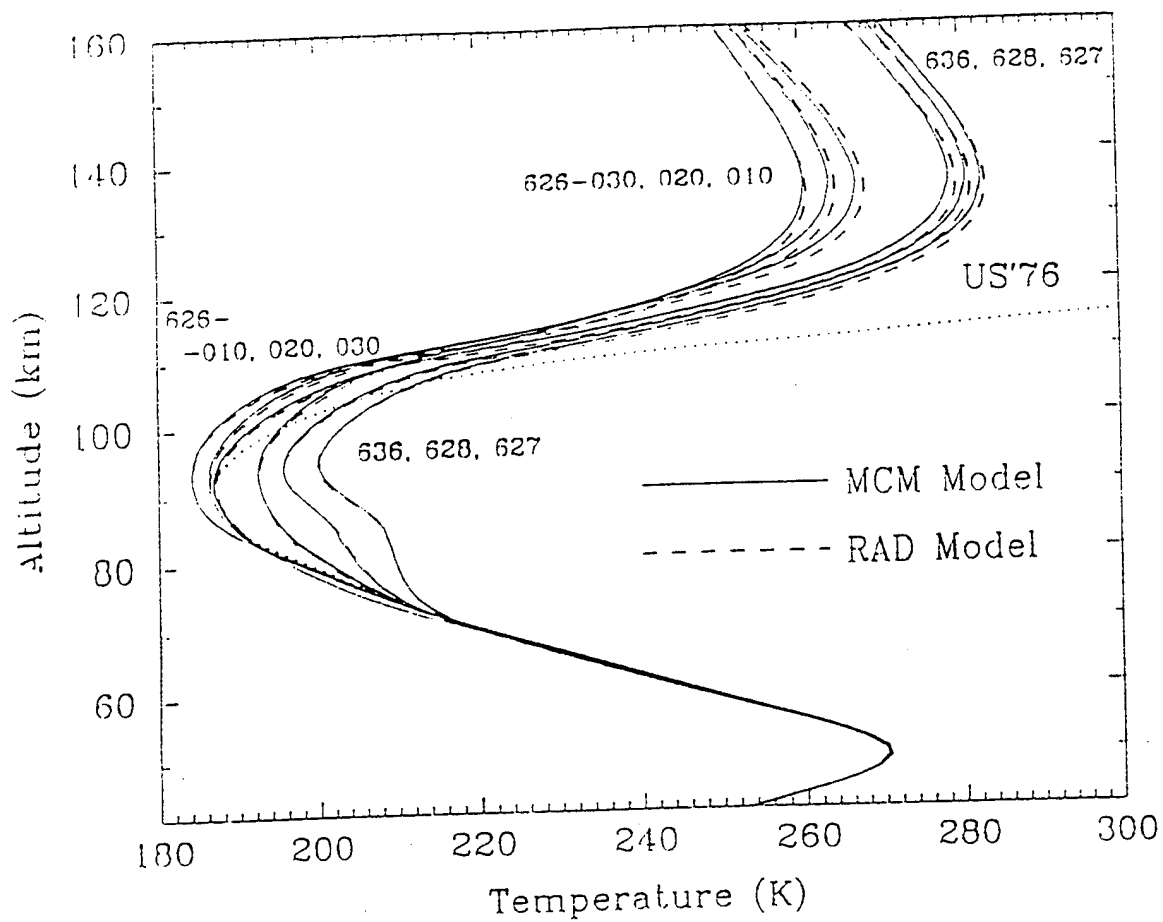


Figure 9

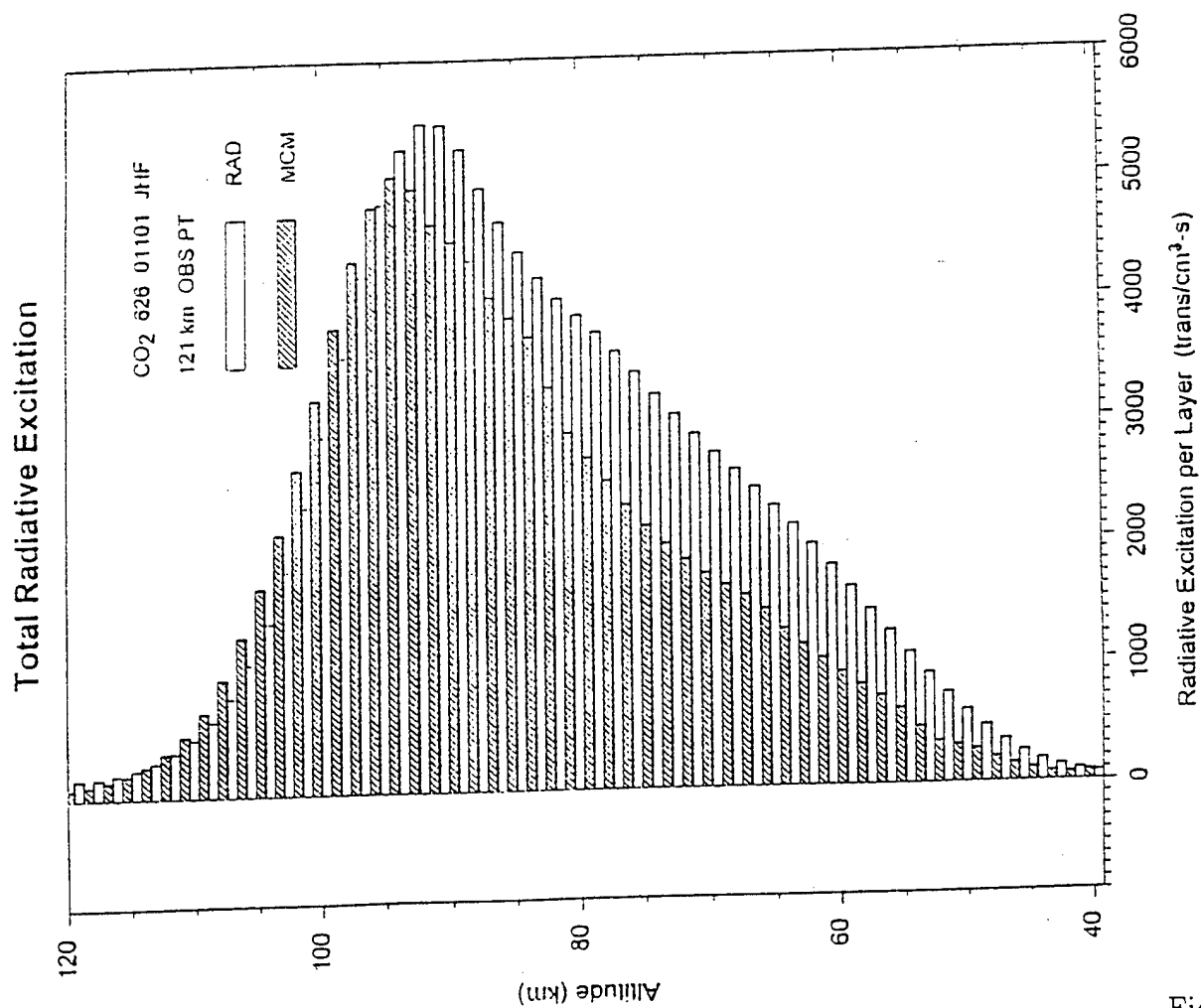


Figure 10

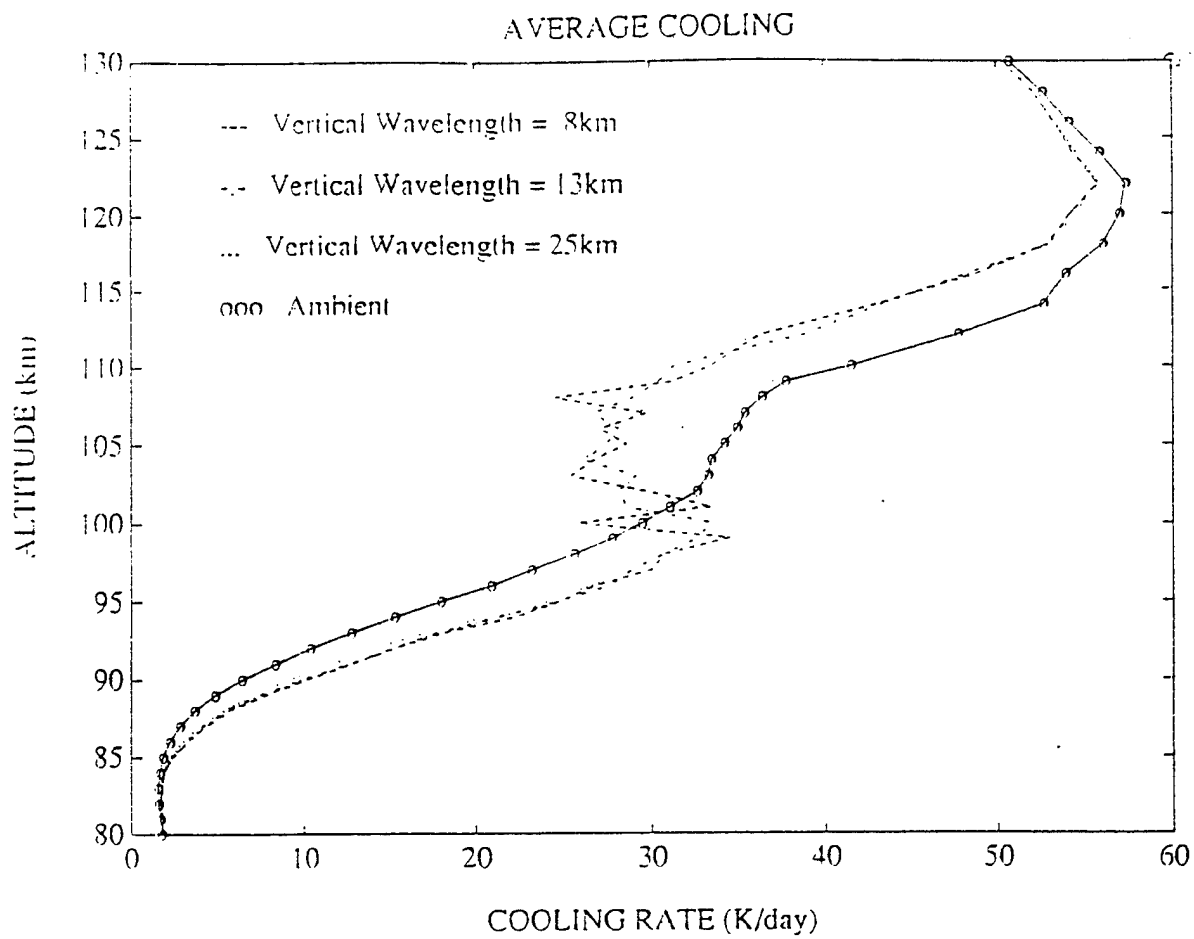


Figure 11

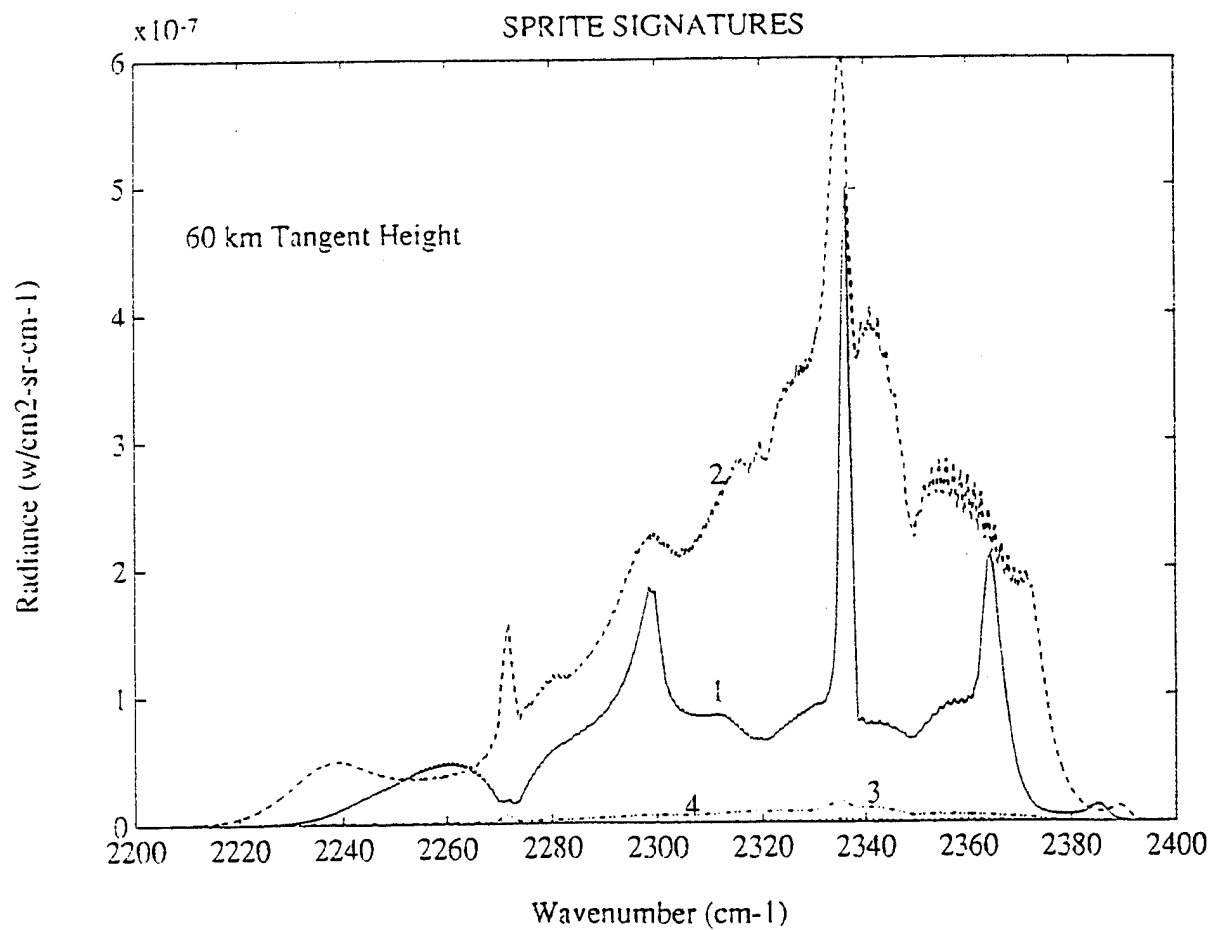


Figure 12

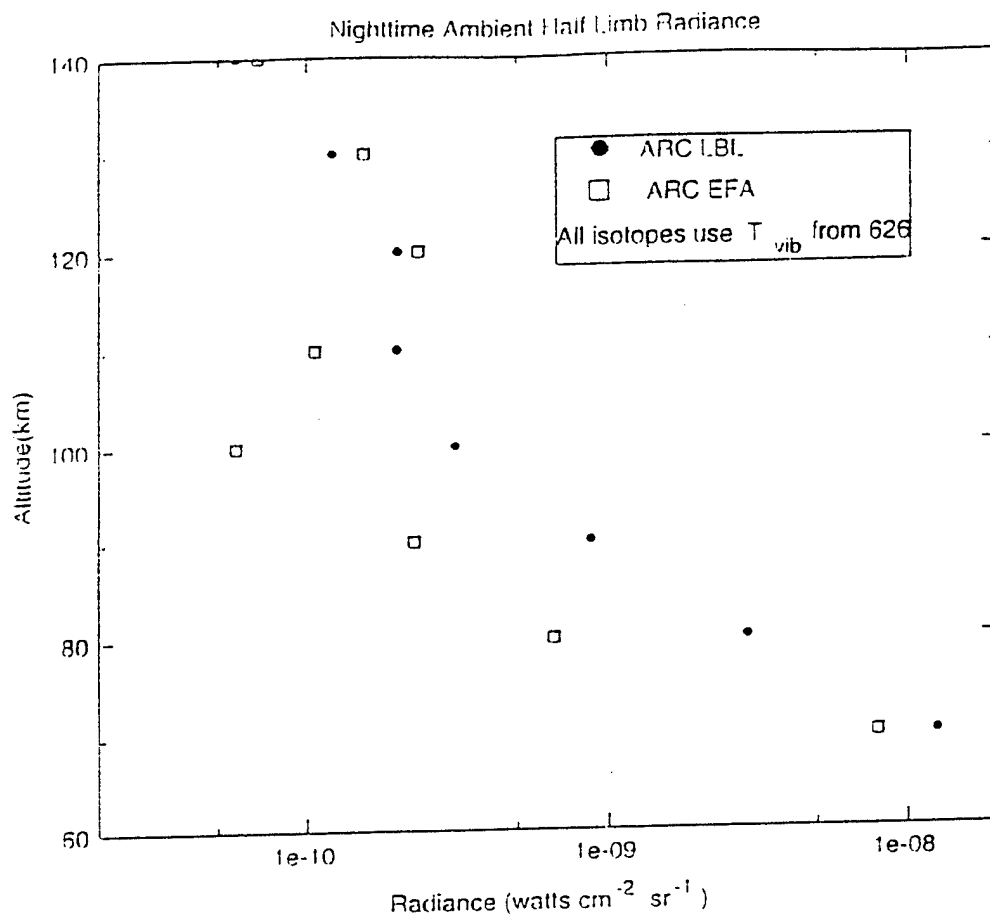


Figure 13

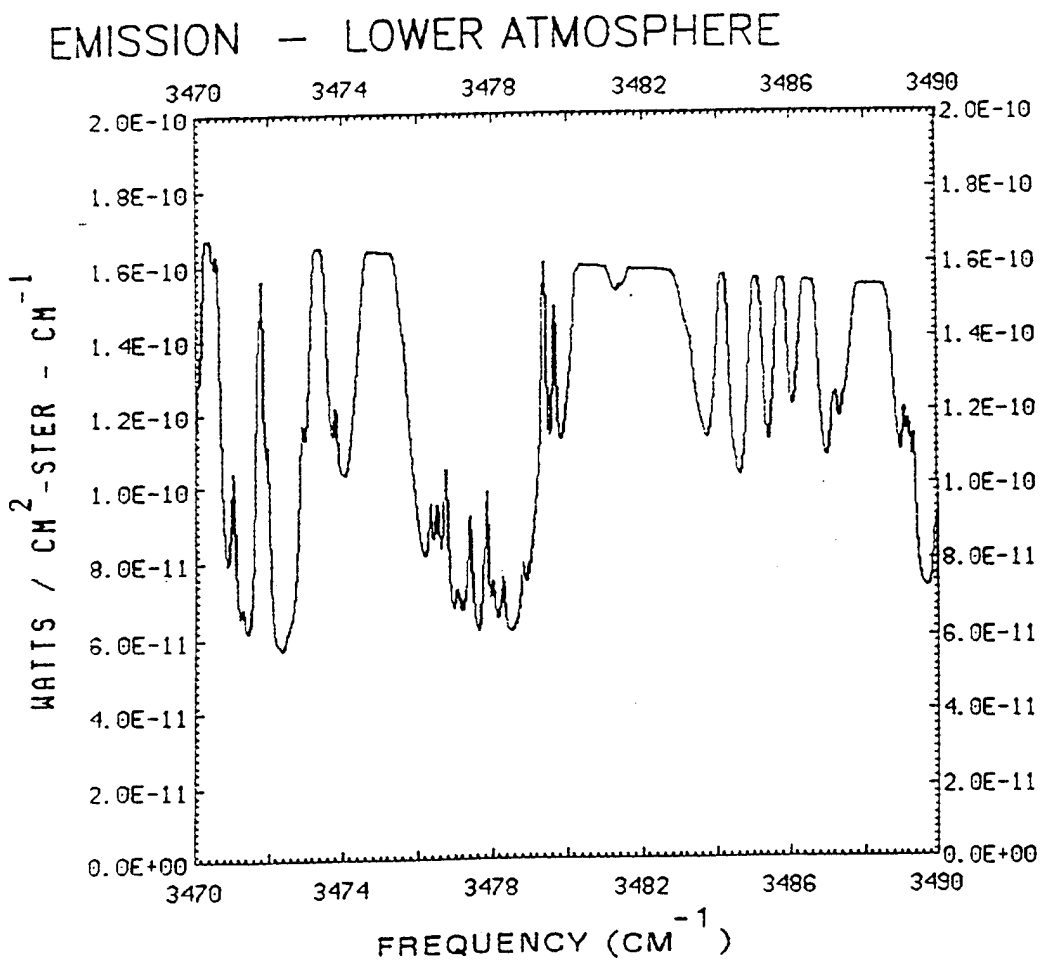


Figure 14

EMISSION — LOWER ATMOSPHERE + AURORA

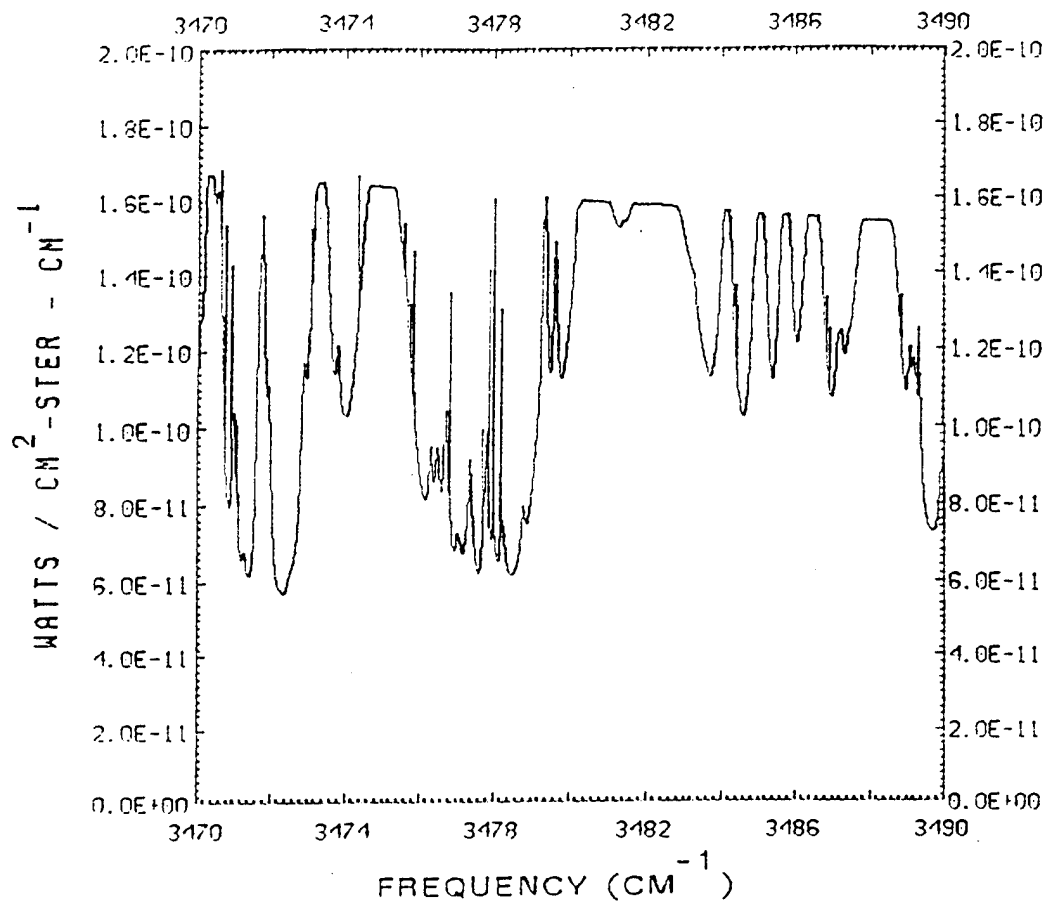


Figure 15

Future Directions

- Enhance benchmark capabilities for specific applications
- Use of monochromatic upwelling radiance (FASCODE) at lower boundary
- Extend spatial structure capabilities to non-LTE excitation calculations

Summary

ARC: Phillips Laboratory Atmospheric Radiance Code

- Non-LTE line-by-line model for the terrestrial atmosphere
- Predicts populations, line-of-sight radiances, cooling for selected IR-emitting species
- Detailed investigations of non-LTE conditions and phenomena
- Progress on calculations in structured atmospheres
- Benchmark calculations

Figure 16

INITIAL ANALYSES OF SURFACE SPECTRAL RADIANCE BETWEEN INSTRUMENT OBSERVATIONS AND LINE BY LINE CALCULATIONS

P.D. Brown and S.A. Clough
Atmospheric and Environmental Research, Inc.
Cambridge, Massachusetts

N.E. Miller, T.R. Shippert and D.D. Turner
Pacific Northwest Laboratories
Richland, Washington

R.O. Knuteson, H.E. Revercomb and W.L. Smith
University of Wisconsin
Madison, Wisconsin

1. INTRODUCTION

The evaluation and improvement of radiative transfer calculations are essential to attain improved performance of general circulation models (GCM's) for climate change applications. A Quality Measurement Experiment (QME) is being conducted to analyze the spectral residuals between the downwelling longwave radiance measured by the University of Wisconsin Atmospheric Emitted Radiance Interferometer (AERI) and spectral radiance calculated by the Line By Line Radiative Transfer Model (LBLRTM). The three critical components of this study are (1) the assessment of the quality of the high resolution AERI measurements, (2) the assessment of the ability to define the atmospheric state in the radiating column, and (3) the evaluation of the capability of the line by line model. Validations have been performed on spectral radiance data obtained from April 1994 through July 1994, through the analysis of the spectral residual differences between measured and calculated radiances. These residuals are analyzed by both spectral interval and physical process. The results are archived as a function of time, enabling the retrieval of specific data and facilitating investigations of diurnal effects, seasonal effects, and longer term trends. While the initial focus is restricted to clear sky analyses, efforts are underway to include the effects of clouds and aerosols. Plans are well formulated for the extension of the current approach to the shortwave. An overview of the concept of the QME is described by Miller et al. [1994], and a detailed description of this study is provided by Clough et al. [1994].

2. SPECTRAL RADIANCE OBSERVATIONS AND CALCULATIONS

Measurements of downwelling radiance at the surface are obtained from the AERI instrument at the Southern Great Plains (SGP) Cloud and Radiation Testbed (CART) central facility in Lamont, OK. The AERI is a zenith viewing instrument with a spectral resolution of 0.5 cm^{-1} (wavenumber value to first zero of unapodized spectrum). Radiance calculations are performed using LBLRTM [Clough et al., 1981], which includes a full water vapor continuum model [Clough et al., 1989; CKD] which has been updated to provide improved agreement with atmospheric observations [CKD_2.1]. The atmospheric column is partitioned into 54 layers, chosen to accurately model the transfer of radiation to the surface. Quality controlled radiosonde data are ingested directly into the model at all reporting levels from which the temperature and water vapor column amounts are calculated. This layering also facilitates the calculation of cooling rates, which are important for other aspects of ARM.

3. DEFINITION OF THE ATMOSPHERIC STATE

A spectral validation is currently performed for each radiosonde release, four times per day under standard conditions and eight times daily during Intensive Operating Periods (IOP). Temperature and water vapor profiles are obtained from the radiosonde observations. A constant ozone profile has been derived from a retrieval based upon an April 23, 1994 AERI spectral radiance measurement. The characterization of atmospheric state from radiosonde measurements is a major concern, not only

from the point of view of accuracy, but from the point of view of spatial and temporal displacement from the radiating column for atmospheres with variability.

4. SPECTRAL VALIDATIONS

Spectral residuals are obtained by subtracting the LBLRTM calculated results from the measured AERI spectra. The residuals are statistically analyzed using two approaches: (1) by spectral domain, similar to those from GCM bands, and (2) by physical process, as determined by assigning each spectral element to a physical process, e.g. spectral elements associated with H₂O lines. Figure 1a shows an AERI spectrum taken in June, 1994. Channel 1, spanning 550-1800 cm⁻¹, is the current region of principle emphasis due to its importance for climate related studies. Radiance in the saturated regions of CO₂ from 630-705 cm⁻¹ and of H₂O from 1350-1800 cm⁻¹ are dominated by characteristics of the Planck function associated with the atmosphere near the instrument. H₂O lines provide the dominant structure in the window regions at 800-980 cm⁻¹ and 1080-1200 cm⁻¹, and O₃ lines are dominant in the 980-1080 cm⁻¹ region. The strong effects of the underlying water vapor continuum between spectral lines is seen throughout the 800-1200 cm⁻¹ window region.

The spectral residuals for this observation, as shown in Figure 1b, are typical of those observed at the CART site within the time period of this analysis, from April 7 to July 30, 1994. Integration of the residuals over the spectral domain of Figure 1 provides a result of 1.7 W/(m² sr) in zenith radiance. An estimate of the difference in flux between the observed and model values for the atmospheric window region may be obtained by multiplying the integrated residual value by five. It should be noted that these large residuals in the window region do not exhibit spectral behavior characteristic of errors in the water vapor continuum.

The QME products include statistical results by spectral domain as well as by physical process. As shown in the expanded plot in the lower left of Figure 1a, spectral elements in the regions denoted by the sharp spikes are associated with molecular lines; spectral elements in the regions between the lines, referred to as 'transparent' regions, reflect the radiative effects of the water vapor continuum, aerosols and clouds.

An important objective of the QME is to control the quality of the data set. Problems associated with the loss of the liquid N₂ coolant in the instrument, resulting in the degradation of sensitivity in the detector, occurred during this time period. The affected spectra are characterized by a significant increase in measurement noise, and have been excluded from the analyses.

5. INITIAL ANALYSES

Figure 2 shows the equivalent brightness temperature in the channel 1 window versus the equivalent brightness temperature in the channel 2 window. The window brightness temperatures in channels 1 and 2 are determined from the average radiance across the spectral intervals 1142-1147 cm⁻¹ and 2506-2511 cm⁻¹, respectively. Circles refer to clear sky cases, while stars denote non-clear cases. This information is contained in the QME cloud product platform and is currently obtained from the cloud base heights given by the Belfort ceilometer and the NASA Micro-Pulse Lidar (MPL), as well as the total liquid water in the line of sight of the microwave radiometer (MWR). The dotted line indicates the values at which the brightness temperatures in the channel 1 and channel 2 windows are equal. The stars along this line in Figure 2 are associated with warm, opaque cloud. Cloudy cases with lower window temperatures are associated with high, cold, thin clouds. The higher brightness temperatures in the channel 2 window with a high degree of variability are caused by solar scattering from clouds and aerosols. Efforts are currently underway to assess the extent to which solar radiation may be entering the AERI light pipe directly.

Analyses of diurnal variation can be explored, as shown in Figure 3, where integrated spectral differences are analyzed as a function of time of day in Greenwich Mean Time. There is a difference of six hours between GMT and Lamont local time during daylight savings time. Only clear sky cases are plotted, distinguished by month. The columns indicate the daily radiosonde launch times, with 3 Z, 8 Z, 11 Z, and 23 Z reflecting the additional radiosonde launches during the April and July 1994 IOP's. The systematic difference from day to night on the order of 1.5 W/(m² sr) is currently unexplained.

A plot of integrated spectral residuals by physical process as a function of water vapor amounts is

shown in Figure 4. Only clear sky cases are shown and cover a wide range of precipitable water, from 0.5 to 4.0 precipitable centimeters. The dominant processes in this spectral region are those associated with absorption in the 'transparent' regions between the lines, which include the continuum, aerosols and thin cloud, and the spectral elements associated with water vapor lines and ozone lines. The sum of these differences in Figure 4 reflect 98% of the total difference in channel 1. Although a constant ozone profile is used, the differences associated with the ozone region of Figure 4c, on the order of $0.3 \text{ W}/(\text{m}^2 \text{ sr})$, are remarkably good considering the seasonal variation of O_3 . It is of interest that the differences associated with H_2O lines, as shown in Figure 4b, are not correlated with water vapor, though there is an apparent small linear correlation between the differences associated with the transparent regions with the water vapor column as shown in Figure 4a. Most importantly, the lack of a quadratic correlation between the differences associated with the transparent regions and water vapor indicates that these differences are not attributable to the water vapor continuum. A linear correlation is more consistent with the hygroscopic growth of aerosols and the consequent increase in the aerosol radiative effects.

6. CONCLUSIONS

The AERI/LBLRTM QME has been effective in assessing problems associated with the measurement of downwelling spectral radiance, the characterization of the atmosphere in the radiating column, and the line by line calculations. Issues including the loss of liquid N_2 fill in the AERI dewar and the switch from nominal mode to research mode in the processing of the radiosonde data have been identified and addressed. There are two important conclusions that can be drawn from this initial analysis of the QME products: (1) the residuals in the important channel 1 window for the clear sky are anomalously large corresponding to $\sim 10 \text{ W}/\text{m}^2$ in flux and (2) the specification of atmospheric state for the radiating column to the requisite accuracy is a difficult but tractable task.

Clear sky analyses show that the integrated radiance differences for validations of AERI measurements taken at the ARM SGP Central Facility are significantly higher than spectral validation between AERI measurement and LBLRTM calculations from Coffeyville, Kansas during the Spectral Radiance Experiment (SPECTRE) in November and

December, 1991. The integrated spectral radiance differences for SPECTRE are on the order of $0.5 \text{ W}/(\text{m}^2 \text{ sr})$ while those from ARM are $2.0 \text{ W}/(\text{m}^2 \text{ sr})$. We have established that this difference in the ARM validations is not attributable to the water vapor continuum. Radiative effects of aerosols or thin clouds may play a role, but the extinctions required appear to be too large. Another possible contributor to the residuals is the AERI calibration at low radiances as discussed by Ellingson [1995]. Inclusion in the calculation of the effects of HNO_3 and improvements in the halocarbon mixing ratios are expected to provide some reduction in the residuals but nothing approaching the required amount.

With respect to the task of adequately specifying the atmospheric state, the anticipated availability of Raman lidar and Radio Acoustic Sounding System (RASS) observations is expected to provide improvement in the water vapor and temperature profiles, respectively, particularly with respect to the spatial and temporal sampling issue. Absolute calibration of both instruments remains an important and difficult task. It is clear that more information on aerosols is essential, at an absolute minimum a value for the extinction in the visible is required.

This initial analysis strongly supports the QME as a strategy to assess our current capability to measure and model longwave radiation in the study of climate change. Before the approach can become fully effective an explanation for the ubiquitous and anomalous residuals in the window regions must be resolved. Work is underway toward the inclusion of cloud and aerosol effects in the model calculations, and in the calculation of atmospheric cooling rates from $10\text{-}3020 \text{ cm}^{-1}$ for single column model applications. In addition, analyses of validations in the microwave region between the MWR and LBLRTM are currently being implemented. Future plans include the assessment of potential improvement in atmospheric state measurement from the Radio Acoustic Sounding System (RASS) and Raman Lidar, and the extension of the analysis to solar spectra, as measured at the central facility by the University of Denver Solar Radiance Transmission Interferometer (SORTI) and the Absolute Solar Transmission Interferometer (ASTI), and to the shortwave spectral region.

7. ACKNOWLEDGEMENTS

We would like to acknowledge the significant contribution of the members of the Instantaneous Radiative Flux (IRF) Working Group with respect to this research. This research was supported by U.S. Department of Energy under Grant No. DE-FG02-90ER61064, and by the University of Wisconsin, Subgrant No. G02-77285.

8. REFERENCES

- Clough, S.A., P.D. Brown, N.E. Miller, J.C. Liljegren, T.R. and Shippert. 1994. Residual analysis of surface spectral radiances between instrument observations and line by line calculations. *Proceedings of the Fourth Atmospheric Radiation Measurement (ARM) Science Team Meeting*, pp. 101-109. CONF-940277, U.S. Department of Energy, Washington, D.C.
- Clough, S.A., F.X. Kneizys, and R.W. Davies. 1989. Line shape and the water vapor continuum. *Atmos. Res.* 23:229-241.
- Clough, S.A., M.J. Iacono, and J.-L. Moncet. 1992. Line by line calculation of atmospheric fluxes and cooling rates: Application to water vapor. *J. Geophys. Res.*, 97: 15761-15785.
- Ellingson, R.G., S. Shen. 1995. Comparisons of AERI observations with LBLRTM calculations: Magnitudes of discrepancies and possible explanations. Fifth Atmospheric Radiation Measurement (ARM) Science Team Meeting, San Diego, California.
- Miller, N.E., J.C. Liljegren, T.R. Shippert, S.A. Clough, and P.D. Brown. 1994. Quality Measurement Experiments within the Atmospheric Radiation Measurement Program. *Proceedings of the Fourth Atmospheric Radiation Measurement (ARM) Science Team Meeting*, pp. 5-9. CONF-940277, U.S. Department of Energy, Washington, D.C.
- Revercomb, H.A., F.A. Best, R.G. Dedecker, T.P. Dirkx, R.A. Herbsleb, R.O. Knuteson, J.F. Short, W.L. Smith. 1991. High spectral resolution Fourier Transform Infrared (FTIR) instruments for the Atmospheric Radiation Measurement Program: Focus on the Atmospheric Emitted Radiance Interferometer. *Proceedings of the Second Atmospheric Radiation Measurement (ARM) Science Team Meeting*, pp. 121-124. CONF-9110336, U.S. Department of Energy, Washington, D.C.

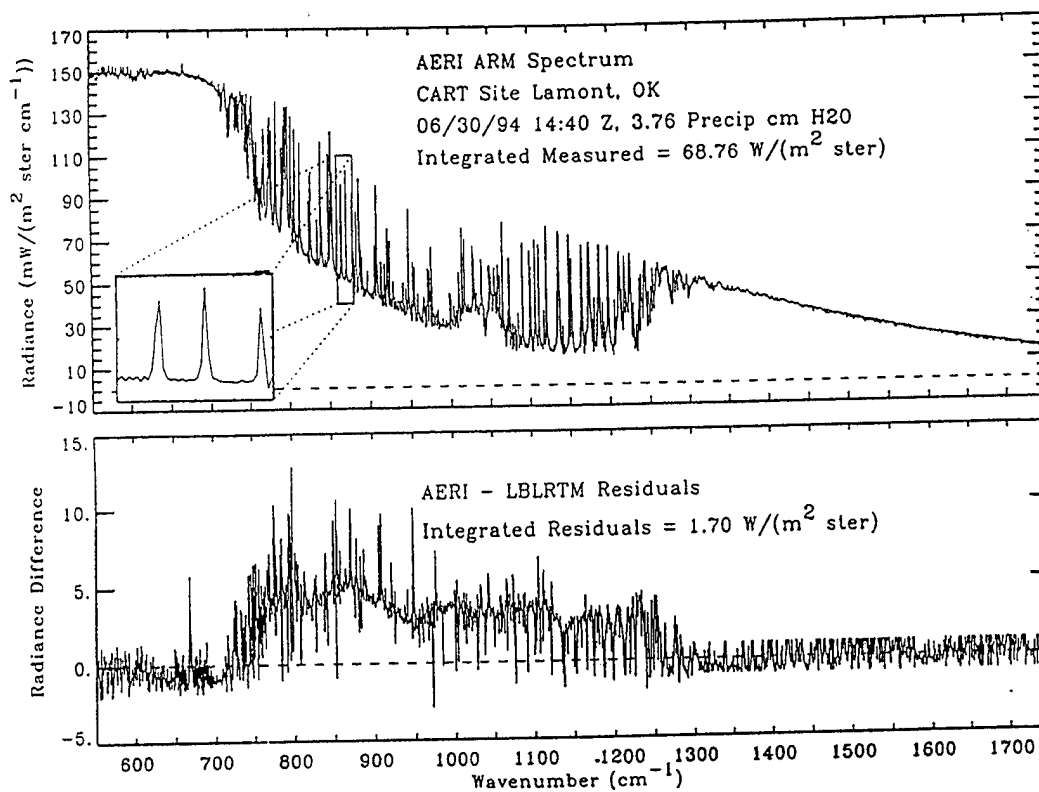


Figure 1. (a) AERI observed radiances and (b) spectral radiances between observed and LBLRTM calculated radiances.

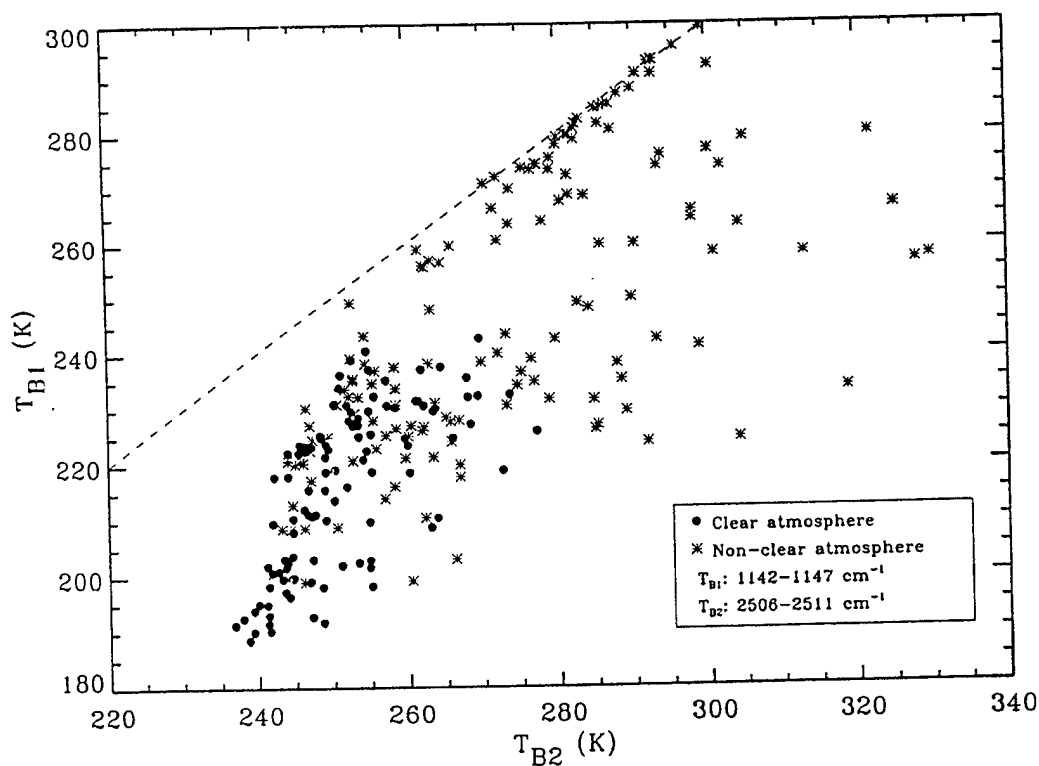


Figure 2. Channel 1 window brightness temperatures as a function of channel 2 window brightness temperatures for clear and non-clear atmospheres.

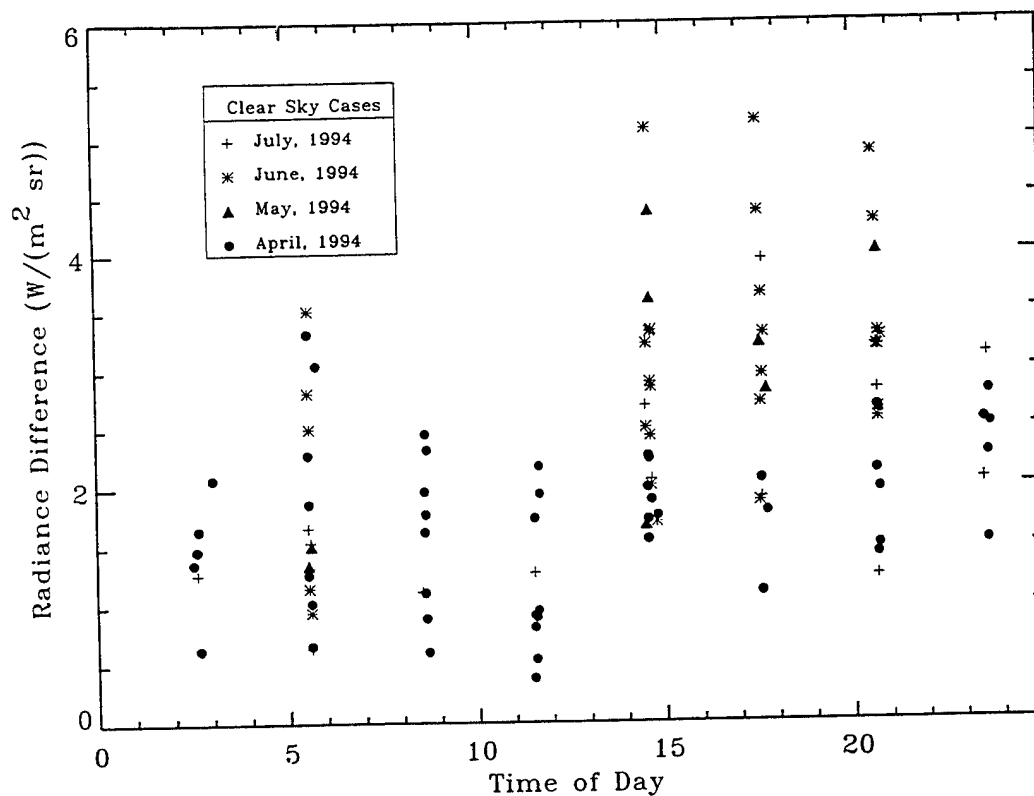


Figure 3. Channel 1 integrated radiance differences as a function of time of day.

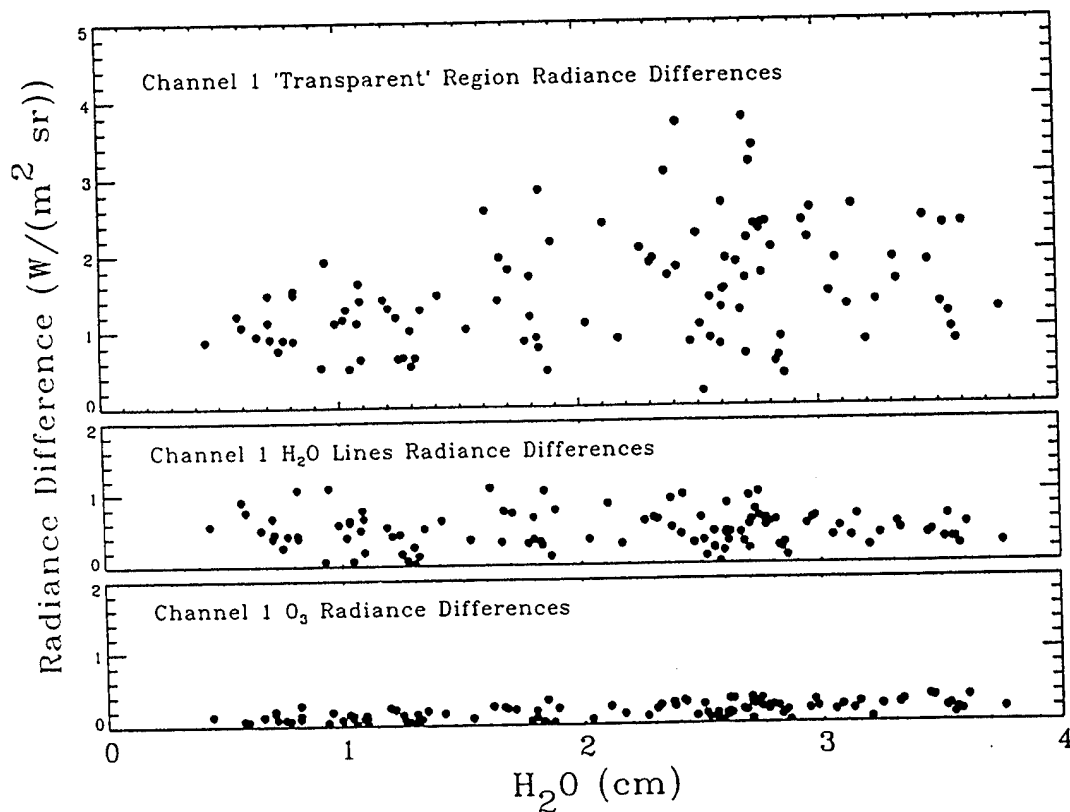


Figure 4. Integrated spectral residuals by physical process as a function of radiosonde observed water vapor amounts.

FASCODE for the Environment (FASE)

H.E. Snell and J.-L. Moncet

Atmospheric and Environmental Research, Inc.
840 Memorial Dr.
Cambridge, MA 02139
(617)-547-6207

G.P. Anderson, J.H. Chetwynd, S. Miller, and J. Wang*

Geophysics Directorate, Phillips Laboratory
Hanscom AFB, MA 01731

*now at National Center for Atmospheric Research, Boulder, CO

ABSTRACT

The Optical Physics Division of the Phillips Laboratory with support from the DoE Atmospheric Radiation Measurement (ARM) Program is developing a state-of-the-art line-by-line atmospheric radiative transfer model as the successor to FASCODE. The goal of this project is to create a computationally efficient model which contains the most up-to-date physics. The new model, known as FASCODE for the Environment, or "FASE", combines the best features of FASCODE and LBLRTM, the DoE's standard radiative transfer model. FASE also contains new features such as an improved solar irradiance model, and the Schumann-Runge bands and continuum. The code is optimized for vectorized and/or parallel processing and has been put under configuration control for easy maintenance. Additional improvements have been made to the NLTE routines and the path geometry algorithm. Future versions will be restructured to allow for increased flexibility and easy customization of the code for specialized applications, such as a forward model for iterative inversion algorithms. Ease-of-use will be enhanced with improved input control structures and documentation to accommodate the needs of novice and advanced users. This paper addresses changes which have been made to FASCODE and LBLRTM to create FASE, and gives an overview of the modular structure and its capabilities.

1.0 INTRODUCTION

The goal of the FASCODE for the Environment (FASE) program is to create an atmospheric radiance and transmittance model which is user-friendly and contains the latest atmospheric physics. The prime focus of the program is to make available to the atmospheric spectroscopy community the results of on-going work sponsored by the Department of Energy (DoE) while incorporating the results of continuing research and development at the Air Force Phillips Laboratory. In addition, advances from the wider radiative transfer community will be incorporated where appropriate within program constraints and resources.

FASE has been developed by combining features from the line-by-line radiative transfer codes of the Air Force Phillips Laboratory (FASCODE)¹ and the Department of Energy (LBLRTM)². Both of these models were derived from FASCOD3 which was based on FASCOD1B, a four-function line-by-line code developed by Clough and Kneizys³. Our basic approach to developing FASE is severalfold: (1) to modify the overall program structure of FASCODE / LBLRTM so as to improve the flexibility and maintainability of the code without significant re-coding; (2) to incorporate a number of coding improvements (also to benefit the flexibility and maintainability); (3) to improve the user interface and access to individual portions of the code; and (4) to add new modules which incorporate updated physics and improved features. These tasks have been identified as those which would be the most beneficial to

current users of the code. For those that use the code as a "blackbox" by supplying the appropriate input and examining the output, FASE will appear identical to FASCODE / LBLRTM. However, for users who wish to modify the code or incorporate it within other software, FASE will be a much easier code with which to work.

The key features of FASE are shown in Table 1. Items of scientific interest include a more accurate algorithm for the Voigt profile; updated non-local thermodynamic equilibrium (NLTE) routines; a line rejection flag to signal whether or not a particular spectral line was rejected for use in a layer⁴; the inclusion of Schumann-Runge band and continuum⁵; and the addition of a solar spectrum model⁶. Changes to the program source code include improvements to the atmospheric path geometry formulation; the ability to specify boundary emissivity and reflectivity coefficients in files (in addition to the quadratic function that is currently implemented); vectorization of routines to increase the computational speed; parameterization of dimension statements to allow for easy changes in the size of arrays, *e.g.* the maximum number of layers allowed; and the ability to configure the model for a variety of computers (which is aided by the parameter statements). Other features of FASE include the option for output that is formatted for input to multiple-scattering programs such as CHARTS⁷ or DISORT⁸; and the ability to calculate spectra over a much wider region than currently allowed by FASCODE.

Table 1: Key features of FASE.

<u>Science Improvements</u>	<u>Coding Improvements</u>
Improved Voigt Algorithm	Parameterization of Array Sizes
Updated NLTE Routines	Output in NCAR Graphics Format
Line Rejection Flag	Coded for Vectorized Computers
Schumann-Runge Bands and Continuum	Output Formatted for Multiple-Scattering Programs
Solar Spectrum Model	
Improved Hartley-Huggins and Chappuis Bands	Embedded FFT Scanning Functions
	Optional Fixed DV Output
	2020 cm ⁻¹ Spectral Region (max)
	Improvements to Geometry Algorithm
	Emissivity / Reflectivity Input Files

Because we are combining elements of FASCODE and LBLRTM and wish to make improvements to the overall structure and use of the code, there are two key issues which must be addressed: (1) what are the origins and magnitudes of numerical differences between FASCODE and LBLRTM; and (2) what coding improvements should be adopted which would maximize algorithm speed while allowing flexibility for the user community and maintainability for the code itself. While this paper addresses these issues, they are discussed elsewhere in more detail⁹.

2.0 MODEL COMPARISONS (NUMERICAL)

When combining elements of two models it is essential to understand how the models differ in terms of the underlying physics as well as in the actual numerical output. Two strategies were used to investigate differences between calculations with FASCODE and LBLRTM: (1) a comparison of model calculations with measured radiances, and (2) an examination of differences in the calculated optical depths. The results of these studies indicate that numerical differences arising from the optical depth and radiative transfer algorithms are inconsequential to the final output. However, there are significant differences due to the formulations for line coupling. Additional differences arise at microwave frequencies because of the way the two models treat the zero frequency line and the water continuum.

3.0 PROGRAM STRUCTURE

An essential point to be considered in the development of FASE is the determination of the structure of the program. In the current FASE structure (inherited from FASCODE) the optical depth and radiative

transfer calculations are performed at a spectral resolution appropriate for the local pressure conditions. This results in a complex algorithm for merging layers with different spectral resolution. Further, the various core modules for the calculation of molecular optical depth, aerosol attenuation, atmospheric path characteristics, filtering, etc., are grouped into a single executable code with a complex driver controlling the sequence of calls to the different subroutines to perform any one of numerous predefined functions (e.g. radiance in a clear atmosphere, radiance in a cloudy atmosphere, weighting functions, etc.). This structure was adopted in response to a desire to reduce the number of computations and also to accommodate the needs of users not familiar with radiative transfer. Aside from the fact that an extensive set of instructional inputs must be provided by the user in order to run the code, the current structure has a serious drawback for research applications in the sense that the code cannot be easily tailored to meet specific user needs¹⁰ or to optimize the execution time for specific applications.

One option under study to solve this issue is to split the various core modules into well documented subroutines or executable modules with clearly defined inputs and outputs. A set of simple, easily customized, standard radiative transfer routines that perform single functions would be provided, thus eliminating the need for an extensive input control file and giving the user the capability of organizing a sequence of functions to meet the requirements of a particular problem. The modules would be structured such that a novice user need only create an input file and examine the output (as with the current FASCODE), with all intermediate steps transparent to the user. However, what would be different from the current program format is that the structure of the modules would make it easy for the experienced user to rapidly implement new features or modify parameters in existing features.

As mentioned earlier, the complexity of merging layer optical depths in FASCODE / LBLRTM results from the desire to calculate layer transmittances at the local spectral resolution in order to save on the required number of exponentiations when computing the radiative transfer. However, for a non-homogeneous atmospheric path this approach requires that calculated transmittances be interpolated to the spectral resolution of the next layer. Computational savings can only be derived with this approach by merging the successive layers from bottom to top (in the direction of decreasing pressure). We believe that this approach is obsolete since, as will be shown later, performing the exponentiations is only a small fraction of the total computer time on modern computers. Furthermore for many applications such as multiple-scattering, inversions, etc., much greater gains can be obtained by merging the layers from top to bottom and bottom to top at the same time¹¹. Thus it is best not to attempt to satisfy the above merging constraint. Finally, the spectral overlap needed for performing the interpolation defeats the requirements for parallel processing.

One way to solve this problem is to build the code around a core module which computes the molecular optical depth at the same spectral resolution for each layer. The actual computation occurs at the spectral resolution appropriate for the layer but the result is then interpolated to the final spectral resolution (which corresponds to the highest resolution in the problem, usually prescribed by the geometric line-of-sight). The advantage of this technique is that the total spectral interval can be broken into sub-intervals with uniform end-points for all layers, making customization of the code easier. The size of these sub-intervals would depend on the amount of core memory available. Because of the uniform output for all layers a complete calculation can be performed in memory for each sub-interval. Further, this approach simplifies the extension to parallel processing of the sub-intervals.

The drawback of interpolating the molecular optical depths to the same resolution is that the radiative transfer must be computed at high resolution even for layers where a lower resolution would suffice for computational accuracy (the impact of this on the timing is discussed later). Nonetheless, the structure of the program is simplified and it would be very easy for the user to adapt the modules to meet the needs of specific problems. For calculations consisting of multiple runs (different atmospheres, instrument functions, viewing geometry, etc.) this structure would be more efficient and easier to use because it would eliminate the need for multiple input files and would allow the processing of different operations in parallel.

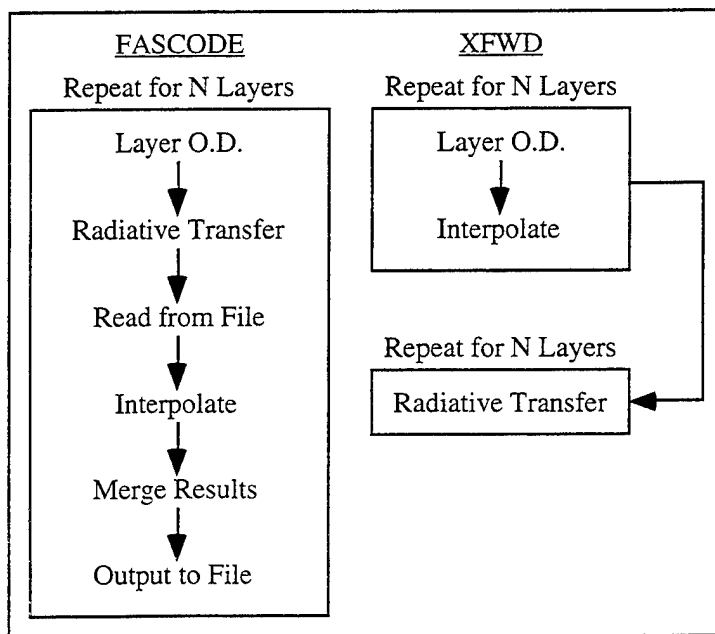
4.0 TIMING COMPARISONS

4.1 Evaluation of Proposed Program Structure

In order to determine how the proposed program structure would affect the cpu time, we conducted timing comparisons between the current version of FASE and "XFWD", a model developed from FASCOD3 with a structure similar to that under consideration for FASE. The timing tests were conducted on a "SPARCserver 1000" computer over the spectral region 1010 - 1140 cm^{-1} . The scenarios evaluated were representative of the type of calculations for which FASCODE is used; while only a single comparison is discussed in this paper, the results agree with numerous other runs of the two models.

The way in which the optical properties and radiative transfer are computed is shown in Figure 1. The two programs calculate the optical depth at a spectral resolution appropriate for the layer. XFWD then interpolates these values to the final resolution before computing the radiative transfer, while FASCODE (and LBLRTM/FASE) computes the radiative transfer, interpolates the previous layer to match the current resolution, and merges the results. The result of this merge is written to a "scratch" file. In XFWD all of the optical depth calculations are completed before the radiative transfer is done, and all calculations are carried out in core memory. Table 2 compares the computation times for XFWD and FASE.

Figure 1: Schematic of FASCODE and XFWD optical depth and radiative transfer calculations.



The timing for the optical depth calculations is similar in FASE and XFWD because the calculations were done at the same monochromatic resolution (DV) in both programs; differences in the timing occur because the calculations are interpolated to the final DV in XFWD while they are output to disk in FASE. The radiative transfer time for FASE is given both as the total time and the total time not including I/O time, illustrating that I/O time accounts for more than 15% of the total radiative transfer time. The FASE time without I/O's can be compared directly to the XFWD radiative transfer time. What is important to note is that the radiative transfer time for each layer is constant in XFWD while in FASE it increases as the DV decreases. This occurs because XFWD interpolates to the final DV within the optical depth module while FASE interpolates as part of the radiative transfer module. From these timing results we make the following conclusions:

(1) In FASE the I/Os are a limiting factor and make up more than 15% of the total radiative transfer time.

(2) While I/Os are suppressed in XFWD by making optimal use of the available core memory, the radiative transfer time in XFWD is affected by the fact that the calculations are done at high spectral resolution. Nonetheless this structure has little impact on the overall radiative transfer time compared to FASE. Further, the radiative transfer calculation represents only a small fraction of the total computation time and the impact of the proposed structure on the total execution time would be minimal.

One should also note that in XFWD the final DV is determined by the layer properties. In a case where the atmosphere is truncated at layer 2, for example, the optical depth would be interpolated to a DV appropriate for layer 2 and not the high DV of layer 15 as in the above example: the final DV is never smaller than the smallest DV in the layering scheme.

Table 2: Looking up: 0 km - 100 km. Layer 1 corresponds to 0 km while layer 15 is the top of the atmosphere. The layer DV is indicated in the table. The FASE optical depth time has been corrected to remove time differences due to increased points in the Voigt convolution. The FASE radiative transfer is given as the total time and the total not including the input/output time (*).

<u>Layer</u>	<u>Layer DV</u>	<u>Optical Depth</u>		<u>Radiative Transfer</u>		
		<u>FASE</u>	<u>XFWD</u>	<u>FASE</u>	<u>FASE*</u>	<u>XFWD</u>
1	0.00890	1.05	1.00	0.039	0.028	0.612
2	0.00593	0.96	1.08	0.060	0.053	0.595
3	0.00396	0.98	1.13	0.070	0.061	0.586
4	0.00264	1.14	1.23	0.110	0.097	0.591
5	0.00176	1.28	1.59	0.170	0.149	0.692
6	0.00088	2.44	2.90	0.330	0.293	0.661
7	0.00059	3.68	4.16	0.490	0.431	0.641
8	0.00039	5.89	6.02	0.740	0.649	0.629
9	0.00026	9.47	8.17	1.120	0.981	0.597
10	0.00026	9.42	9.15	1.090	0.900	0.554
11	0.00026	9.43	9.02	1.110	0.918	0.541
12	0.00026	9.44	9.13	1.080	0.902	0.536
13	0.00026	9.28	9.61	1.020	0.847	0.520
14	0.00026	9.27	9.84	1.050	0.875	0.513
15	0.00026	9.24	9.99	1.020	0.847	0.702
Total		82.97	84.02	9.499	7.731	8.970
		89.73%	90.35%	10.27%	8.52%	9.50%

Total FASE execution time (including radiative transfer I/O time):	92.47
Total FASE execution time (with radiative transfer I/O time removed):	90.70
Total XFWD execution time:	92.99

5.0 CONCLUSIONS

This paper discussed numerical differences between FASCODE and LBLRTM as well as the structure of the FASE software and the impact of this structure on the model timing.

No significant differences have been found between the optical depths computed using FASCODE and LBLRTM. Differences were discovered in the shape of individual spectral lines but these differences were found to cause only small differences in the total transmission and radiance. Differences in radiance in the

microwave region of the spectrum have also been identified. A better understanding of the physics is necessary before the results from one code can be accepted over the other.

Another aspect of FASE development involves the issue of how the total cpu time for a calculation will be affected by code re-structuring and the interpolation of optical depths for each layer to the final monochromatic resolution. We found that these changes to the code have a minimal effect on the overall computation time while greatly increasing the adaptability of the model to solve specific problems.

6.0 ACKNOWLEDGMENTS

AER support for this project was obtained from Phillips Laboratory (grant #F19628-93-C-0040), with partial funding from DOE/PNL ARM subcontract #218101-A-Q1 to Phillips Laboratory. Jinxue Wang was supported by the U.S. National Research Council (NRC). We thank S.A. Clough and P.D. Brown for useful discussions.

7.0 REFERENCES

- ¹Anderson, G.P., et al., History of One Family of Atmospheric Radiative Transfer Codes, The European Symposium on Satellite Remote Sensing, Conference on Passive Infrared Remote Sensing of Clouds and Atmosphere II, 26-30 September 1994, Rome, Italy.
- ²Clough, S.A., et al., Radiative Transfer Model Development in Support of the Atmospheric Radiation Measurement (ARM) Program, Proceedings of the Second ARM Science Team Meeting, DOE Conf. 9303112, Norman, OK, 1-4 March 1993.
- ³Clough, S.A. and F.X. Kneizys, Convolution Algorithm for the Lorentz Function, *Applied Optics*, 18, 2329, 1979.
- ⁴The line rejection flag is particularly useful when computing radiance derivatives with respect to temperature using a finite-difference scheme since a line could be rejected in the reference case and not after perturbing the temperature, or vice versa. In such cases large errors would be introduced unless the line was consistently rejected.
- ⁵Minschwaner, K., G.P. Anderson, L.A. Hall, and K. Yoshino, Polynomial Coefficients for Calculating O₂ Schumann-Runge Cross Sections at 0.5 cm⁻¹ Resolution, *J. Geophys. Res.*, 97, 10103-10108, 20 June 1992.
- ⁶Kurucz, R.L., The Solar Irradiance by Computation, to appear in Proc. of the 17th Annual Review Conference on Atmospheric Transmission Models, 7 June 1994, Geophysics Directorate/Phillips Laboratory, 1994.
- ⁷Moncet, J.-L., and S.A. Clough, CHARTS: Code for high resolution accelerated radiative transfer with scattering, in *IRS '92: Current Problems in Atmospheric Radiation*, Keevallik and Karner, editors, A. Deepak, pp. 493-494, 1992.
- ⁸Stamnes, K., S.C. Tsay, W.J. Wiscombe, and K. Jayaweera, Numerically Stable Algorithm for Discrete-Ordinate-Method Radiative Transfer in Multiple Scattering and Emitting Layered Media, *Appl. Opt.*, 27, 2502-2509, 1988.
- ⁹Snell, H.E., J.-L. Moncet, G.P. Anderson, J.H. Chetwynd, S. Miller, and J. Wang, FASCODE for the Environment (FASE), SPIE, 1995.
- ¹⁰Gordley, L.L., B.T. Marshall, and D.A. Chu, LINEPAK: Algorithms for Modeling Spectral Transmittance and Radiance, *JQSRT*, 52, 563-580, 1994.
- ¹¹Moncet, J.-L., and S.A. Clough, CHARTS: Code for high resolution accelerated radiative transfer with scattering, in *IRS '92: Current Problems in Atmospheric Radiation*, Keevallik and Karner, editors, A. Deepak, pp. 493-494, 1992.

SHARC - 4

Strategic High Altitude Radiance Model,
A Progress Report

R.D. Sharma, J.H. Brown
Phillips Laboratory, PL/GPOS

J.H. Gruninger, R. Sundberg, J. Duff, S.
Adler-Golden, D. Robertson
Spectral Sciences, Inc.

H. Dothe, F. von Esse
Mei Technologies, Inc.



OUTLINE

- OBJECTIVES
- SHARC OVERVIEW
- ATMOSPHERE GENERATOR
- AURORAL MODEL
- TERMINATOR MODEL
- STRUCTURE MODEL
- VALIDATION
- FUTURE PLANS
- CONCLUSIONS



STRATEGIC HIGH ALTITUDE RADIANCE CODE (SHARC)

OBJECTIVES

- COMPUTER CODE TO MODEL
HIGH-ALTITUDE STRUCTURED IR
BACKGROUNDS FROM
QUIESCENT AND AURORALLY
DISTURBED DAY, NIGHT, AND
TERMINATOR ATMOSPHERES
UNDER LTE AND NLTE
CONDITIONS



SHARC - 4 OVERVIEW

- BASIC FEATURES
 - 50 - 300 km Altitude Regime
 - 2 - 40 μm with a Resolution of 0.5 cm^{-1}
 - User-Adjustable Chemical Kinetics Mechanisms/Rates
 - Ambient Radiating Molecules: O_3 , CO , H_2O , NO , NO^+ , CH_4 , CO_2
 - Auroral Model with: NO , NO^+ , CO_2
 - Atmospheric Generator
 - Automatic LTE and NLTE Contributions
 - Day, Night, and Terminator Atmosphere

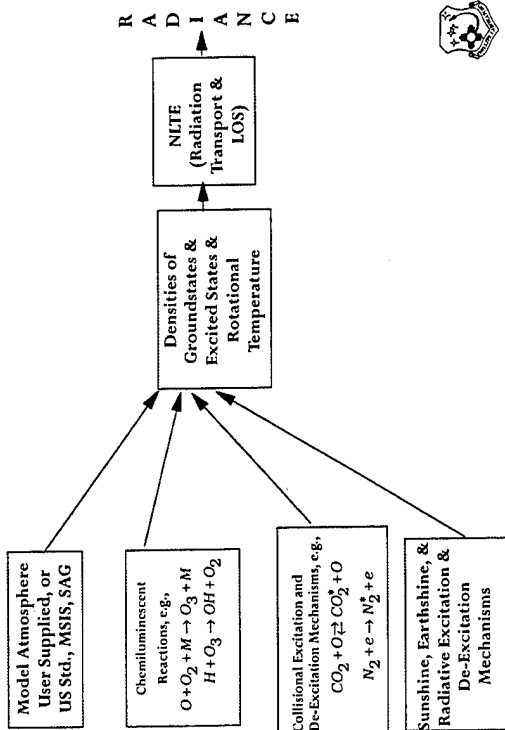


SHARC - 4 OVERVIEW (Continued)

- Stochastic Structure Model
- Arbitrary Viewing Geometries
- Multiple Output Options
- Interactive Input Module with Error Checking
- Fortran Source Code
- Workstation, Mainframe, PC Application



BACKGROUND RADIANCE COMPUTATION



SHARC/SAMM Atmospheric Generator

- Incorporates NRL Database, MSIS - 90
- Includes Empirical Terminator/Diurnal Models for O_3 , OH, NO, CO_2 , O - Uses Calculations by Rodrigo, et.al.
- 0 - 300 km Altitude Range, Arbitrary Layering
- Interactive, Menu-Driven Inputs: lat, long, day,time, F10.7, Ap; Default Options also available
- Output Formats Compatible with SHARC, SAMM, Modtran/Lowtran



Ambient Populations Module

(Chemkin/Nemesis)

- Symbolic Description of Chemical Kinetics Mechanism
 - Based on Widely Used Sandia Chemkin Code
- Example:

$$M + O + O_2 \rightarrow M + O_3 \text{ (000)}$$

$$M + O_3 \text{ (001)} \rightarrow M + O_3 \text{ (000)}$$

$$O_3 \text{ (001)} \rightarrow O_3 \text{ (000)} + h\nu$$
- Rate Equations Solved in Steady State
 - Assumes Rate Equations Depend Linearly on Vibrational Population
- Monte Carlo Calculation for First-Order Radiative Enhancements
 - Multiple Application Yields Higher Order Enhancements



SHARC Auroral Module

- Built on Phenomenology Started in AARC
 - Electron Deposition Models for Different Strength Aurorae: Class II, III, III⁺
 - Secondary Electron Distributions Result from Explicit Integration of Time/Energy-Dependent Rate Equations
 - Calculates Aurorally Enhanced Emissions for NO, NO⁺, CO₂
- Expanded Geometry Module to Insure that the LOS Intersects the Aurora as Desired
- Ambient NLTE Emissions Included in Auroral LOS Path



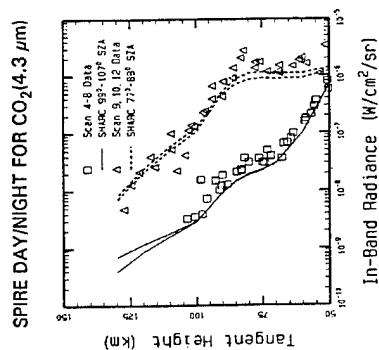
Spectral Radiance Module (SPCRAD)

- Radiation Transport Calculation Performed for Each Molecular Line
 - Uses PL Atmospheric Absorption Line Database (HITRAN)
- Rogers-Williams Approximation for the Equivalent Width (W) of a Single Line with a Voigt Lineshape
 - NASA Handbook Approximation for W_D and W_L
- Layer-Dependent Line Strengths
 - Vibrational and Rotational Temperatures
- Curtis-Godson Approximation
 - Averaging Procedure for Inhomogeneous Paths
- Line Overlap Correction for Dense Regions
- 50 - 70 Times Faster than Traditional LBL Approach



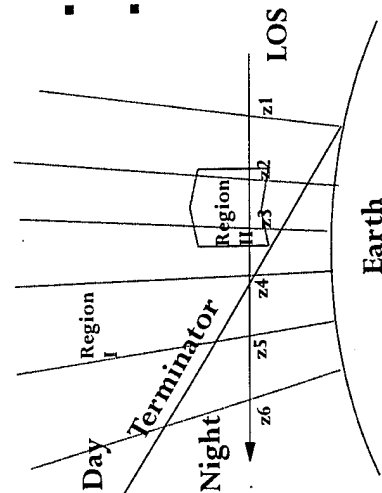
SHARC Terminator Model

- Terminator Effects Significant for Important Spectral Bands (2.7, 4.3 μm)
 - Sunshine Enhances Radiance of Day/it Atmosphere
 - Radiation from Day/it Atmosphere Enhances Radiance of Dark Atmosphere
- Terminator Model Required for Lines of Sight Crossing the Terminator
 - Required to Support Visible/IR Sensor Fusion



SHARC-4/SAMM Day-Night Terminator Model

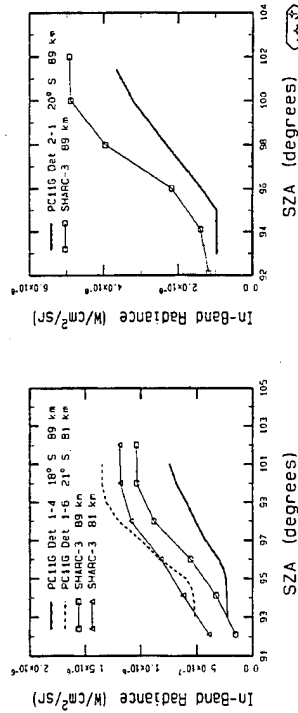
- Multiple Atmospheric Regions Along LOS Path
- Multiple Atmospheric Profiles in Each Region
- Each Atmospheric Profile Corresponds to a Specific Solar Zenith Angle



Terminator Data/Model Comparisons

SHARC - 4 Vs. CIRRIIS - 1A, Dusk Terminator

$O_3(V_3)$



The Structure Problem

- Spatial Radiance Fluctuations Depend on 3-D Atmospheric Density and Temperature Structure
- The Statistics of Atmospheric Structure are Non-Stationary
- Limited Knowledge of High Altitude Structure Statistics (Covariance, PSD, and PDF functions, Variances, Correlation Lengths)



Atmospheric Structure Approach

- Treat Limb Structure as Stochastic
- Assume Atmospheric Horizontal Structure is Isotropic and Stationary
- Assume Gaussian PDF
- Assume Wittwer-Kilb-type PSD
- Adopt Sears Estimates for Temperature Variance and Correlation Lengths
- Vertical Structure is Non-Stationary

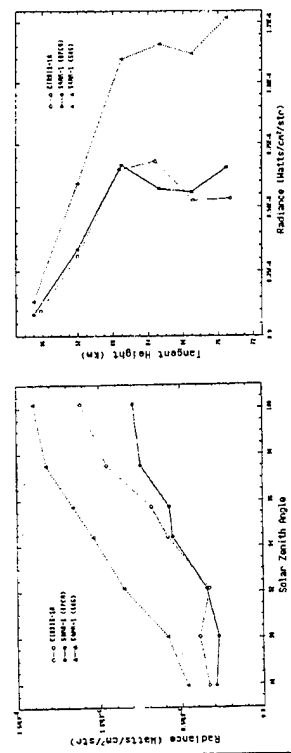


SHARC Structure Approach

- Approach 1 - Compute Radiance Covariance Functions From Specified Atmospheric Covariance Functions and SHARC Computations. Then Construct Radiance Field From Derived Covariance Functions.
- Approach 2 - Compute Path Integrated Radiance Fluctuation Amplitudes. Then Construct Structured Radiance Field From Fluctuation Amplitudes and 3-D Temperature Fluctuation Atmosphere.



Comparison of CIRRIS - 1A and SAMM O₃ Profiles Using DPCM and SAG



Tangent Height = 84 km

SAZ = 95.7 deg.



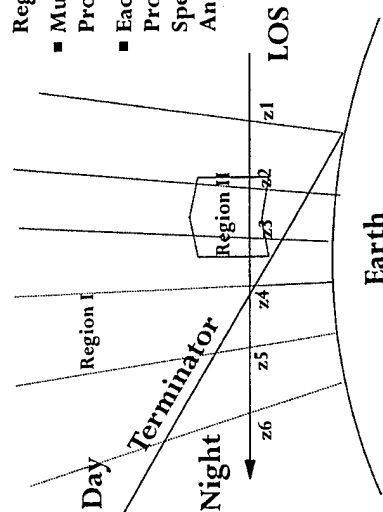
SUMMARY

- SHARC is a High-Altitude Radiance Model
 - Auroral and Quiescent Atmospheres
 - Modularized Code
 - Day, Night, Terminator Atmospheres
 - Arbitrary Paths
 - Stochastic Structure Capability
- Validated with Field Data
- Plans Call for Further Incorporation of CIRRIS -1A Results into SHARC and Distribution of Code



SHARC-4/SAMM Day-Night Terminator Model

- Multiple Atmospheric Regions Along LOS Path
- Multiple Atmospheric Profiles in Each Region
- Each Atmospheric Profile Corresponds to a Specific Solar Zenith Angle



FASCODE/MODTRAN/LOWTRAN: Past/Present/Future

G.P. Anderson, F.X. Kneizys¹, J.H. Chetwynd, J. Wang², M.L. Hoke

L.S. Rothman, L.M. Kimball³, R.A. McClatchey

PL/Geophysics Directorate, Hanscom AFB, MA 01731

E.P. Shettle, Naval Research Laboratory, Washington, D.C. 20375

S.A. Clough, W.O. Gallery, H.E. Snell, Atmospheric and Environmental Research, Cambridge, MA

L.W. Abreu, ONTAR Corp., North Andover, MA 01845

J.E.A. Selby, Northrop-Grumman Aerospace Corp., Bethpage, NY

¹ Retired; ² NRC Fellow (1994), currently at NCAR; ³ AFOSR Summer Research Fellow (Worcester Polytechnic Inst.)

ABSTRACT

Beginning in the early 1970's, the then Air Force Cambridge Research Laboratory initiated a program to develop computer-based atmospheric radiative transfer algorithms. The first attempts were translations of graphical procedures described in a 1970 report on *The Optical Properties of the Atmosphere*^{1a,b}, based on empirical transmission functions and effective absorption coefficients derived primarily from controlled laboratory transmittance measurements. The fact that spectrally-averaged atmospheric transmittance (T) does not obey the Beer-Lambert Law ($T = \exp(-\sigma \cdot \eta)$, where σ is a species absorption cross section, independent of η , the species column amount along the path) at any but the finest spectral resolution was already well known. Band models to describe this gross behavior were developed in the 1950's and 60's (see textbooks such as Goody² or Goody and Yung³). Thus began LOWTRAN, the Low Resolution Transmittance Code, first released in 1972^{4a}. This limited initial effort has now progressed to a set of codes and related algorithms (including line-of-sight spherical geometry, direct and scattered radiance and irradiance, non-local thermodynamic equilibrium, etc.) that contain thousands of coding lines, hundreds of subroutines, and improved accuracy, efficiency, and, ultimately, accessibility. This review will include LOWTRAN^{4b,c,d}, HITRAN (atlas of high-resolution molecular spectroscopic data^{5a,b,c}), FASCODE (Fast Atmospheric Signature Code^{6a,b,c,d}), and MODTRAN (Moderate Resolution Transmittance Code^{7a,b,c}), their permutations, validations, and applications, particularly as related to recent upgrades.

2.BACKGROUND

A history of the code evolution has already been compiled in a 1990 report entitled "Historical Brief of Geophysics Laboratory (GL) Atmospheric Propagation Codes for DoD Systems"⁸, authored by Ruth Liebowitz, PL/GP Historian; a small portion of this report annotates the institutional name changes under which the work was written; acronyms include AFCRC, AFCRL, AFGL, GL, and most recently, Phillips Laboratory/Geophysics Directorate or PL/GP. Because of the changing nomenclature, GeoPhysics Directorate (GP) will be given general attribution. Written from the Air Force/Department of Defense viewpoint, the report emphasizes military applications. However, of equal importance in the code evolution have been numerous applications by the general scientific community, those users who have found a reliable and mostly amenable resource. As part of this larger community, the GP codes have been rigorously tested. This international collaboration has been continuous and encouraged, blending individual contributions as simple as errata on the definition of Lambertian scattering (where, in fact, a factor of π was missing), to continual re-evaluation against measurements over the dry Israeli deserts⁹ and cold Canadian plains^{10,11}.

Accurate acknowledgment of contributions to an evolving program that is nearing its 25th Anniversary requires attributions beyond the already large authorship list. The authors are only those contributors who

participated as AFGL/GP employees during the years of code evolution. An admittedly partial search of the number of explicitly funded AF contractual contributions and their authors exceeds 35 and 100, respectively. Therefore, no particular attribution listing will be compiled other than the accompanying references.

The largest set of external contributors is even harder to appropriately acknowledge; they have, via both deliberate and inadvertent participation, provided direction and prioritization of component elements through their judicious comparisons of code calculations against both theoretical and experimental (laboratory and atmospheric) results. Such contributions have come from U.S. government agencies (Navy, Army, NASA, NOAA, DOE, NSF, NTIS, etc.) and government-funded corporations. (More specifically, the Navy and the Army have supplied entire subroutine capabilities, including the Maritime Aerosol Models and Vertical Structure Algorithms, respectively; see LOWTRAN 6 documentation^{4c}.) The government groups have been joined by the university and industrial research communities to provide a continuous stream of creative input. Additionally, without implying finality, the international scientific communities (in no particular order, Canadian, English, French, Italian, German, Norwegian, Israeli, Russian, Spanish, Japanese, Australian, Chinese) have also contributed to specific and generic applications. The depth of each collaboration often depends on the degree of overlap between existing internal and external concerns. Some of these contributions will emerge in the text and references. Those omitted are not less significant, but perhaps less well documented, often falling into the very important category of scientific interchange at the personal and collegial level: discussions at international meetings, telephone calls questioning options, topical letters offering suggestions that get implemented at some displaced time. The communities of users at all levels have proven invaluable to the open growth of this 25 year effort.

There are, of course, downsides to such open evolution. The AF radiative transfer codes, while perhaps conceptually and scientifically elegant, are not particularly user-friendly, modular, or examples of state-of-the-art programming. They can be justifiably criticized for their obliqueness and lack of documentation, both within the source codes and in their backup reports. The documentation problem is acknowledged; attempts to correct it are underway (MODTRAN/LOWTRAN Scientific Report, in press; FASCODE Scientific Report, in preparation). Additionally, there has been no singular mandate to re-approach at least this family of codes with the intent of bringing them fully into modern programming practices. There is an actual threat in such an undertaking - the historic codes have been historically validated at each step. A thorough recoding would require a parallel new validation, a difficult and time consuming task to reexamine applications over the entire spectral, spatial and platform range of the current capabilities. From the research point of view, however, the codes were and continue to be scientifically evolutionary. The choice has almost always been to continue to advance the scientific content rather than to revisit the antiquated programming techniques. However, as much as possible, all new coding and much of the old is now structured according to accepted standards.

At the same time, other agencies have undertaken development of new approaches to both line-by-line (LBL) and band model (BM) algorithms; see GENLN2¹² and LINEPAK¹³ for comparison to FASCODE, or 6S¹⁴, GOMETRAN¹⁵ and APART¹⁶ for comparisons to LOWTRAN/MODTRAN capabilities. Both APART and GOMETRAN directly incorporate portions of LOWTRAN/MODTRAN so are not strictly independent algorithms. As another example, LBLRTM^{17a}, a Department of Energy-funded, FASCODE-derivative, line-by-line code has been restructured with the view of maintaining the expediency of the FASCODE line shape algorithm, while providing new insight and efficiency into optimized radiance, scattering and weighting function capabilities. The very existence of the AF family of codes is strengthened by these new additions, through the process of validation and authentication. In this vein, continual participation in international intercomparisons of algorithms, particularly as sponsored by the World Meteorological Organizations efforts (ITRA^{18a,b}, ICRCCM¹⁹) to assure consistency and confidence, has been undertaken.

Ultimately, this history of the AF codes cannot be literal. Rather it will include: (1) the DoD mandate, a restatement of the need to pursue accurate and accessible atmospheric radiative transfer algorithms for both the military and scientific communities; (2) a brief description of the relevant radiative transfer physics, based on molecular spectroscopy in thermodynamic equilibrium; and, finally, (3) a more expansive description/contrast of the current AF codes and their relevance to remote sensing and energy deposition applications. The future development of the codes will depend to a large extent on external funding sources. This is a relatively new approach, in contrast to the historic funding driven almost solely by the AF. Some discussion of the impact of these directions will also be addressed.

3. DoD MANDATE

Understanding the atmospheric system and its perturbations (both natural and as modified by the expanding demands of industry, agriculture, housing, transportation, etc.) is inherently important to man's successful functioning within his complex environment. The total atmospheric system consists of radiative, chemical, dynamical and geomagnetic interactions controlled by the boundary conditions of the sun at the outer extreme and the ocean-land masses at the inner extreme, that totality embedded within the solar/earth magnetic fields. The separations imposed upon this system by the scientific and/or military disciplines are always arbitrary. The boundary layer, lower, middle and upper atmosphere, ionosphere, magnetosphere, solar wind, and solar atmosphere comprise one logical set of divisions; this same subset can be recast as surface, troposphere, stratosphere, mesosphere, thermosphere and exosphere. However, these are only subsets that are crossed by others, each constrained by its own selected definitions (e.g. spectral, photochemical, dynamic and/or geomagnetic limitations).

Because of both personal and calculational constraints, individual atmospheric studies have inevitably narrowed their focus. That narrowed focus is continued here, targeting only the radiative properties of the natural (unperturbed) atmosphere for the electro-optical (E/O) spectrum between the ultraviolet and microwave wavelengths. The altitude regime has also been limited to regions dominated by the spectroscopy of molecular transitions. Thus, the thermosphere where atomic and ionic species begin to contribute has been largely ignored; GP and other groups have developed radiative transfer algorithms for this region (SHARC²⁰, ARC²¹, etc). [In fact, there is no logical upper altitude limit for FASCODE except for the necessary specifications of the appropriate atmospheric properties; however, the FASCODE line shape and layering algorithms, developed for the lower atmosphere, impose a time-penalty that restricts its usefulness, except for occasional validation tests; see subsequent discussion.] Neutral molecular species, plus clouds and other particulates contributing within this envelope are addressed by representative physical and mathematical algorithms. Not all available or necessary options are realistically modeled, but some provision is usually made, even if primitive. For instance, of particular current concern is the lack of proper cloud treatments for high spatial resolution images (e.g. as measured by AVIRIS, the NASA/JPL Airborne Visible Infrared Imaging Spectrometer²²) which must isolate cumulus towers underlying light cirrus against water and snow backgrounds.

Other agencies have undertaken the complex, computer intensive tasks of merging the radiative, chemical, and dynamical (and geomagnetic when appropriate) exchanges of the fuller, more authentic atmospheric envelope through massive four-dimensional (including temporal) modeling; see papers by Garcia and Solomon²³, Roble and Dickenson²⁴, and the Community Climate Model authors²⁵ for just one set of contributions by NCAR and NOAA. However, these new capabilities continue to require piece-wise validation as well as optimization, assuring the future of the more narrowly focussed radiative transfer codes.

Having now limited the scope of the AF codes to the E/O spectrum for altitudes below ~ 100 km, the actual modeling of radiative transfer properties of the atmosphere and/or the design of observing systems to operate within its envelope depends on one of two points of view: (1) is the atmosphere an obscurant to be

mathematically eliminated from the field of view or (2) is the atmosphere the holder of the desired signature, providing unique information of its instantaneous state? The latter view is that adopted by the passive remote sensing community: characterization of the atmosphere is contained in its spectroscopic signature. The first view is traditionally the priority of the surveillance community, separating a target or background from the intervening atmospheric contributions. However, what is conventionally a military preoccupation has also been an historic part of modern atmospheric studies (e.g. Earth Radiation Budget Experiment²⁶, cloud imaging from GOES observations²⁷, etc.). This aspect is emerging anew as the capabilities of high spatial/spectral resolution nadir imaging²² permit separation of surface albedo components (agricultural, geologic, sea surface, and pollutant), related to both local and climatic system understanding.

The important distinction between the two primary points of view (atmosphere as contaminant or signature) controls whether instruments are designed to operate in naturally occurring windows (spectral ranges with low atmospheric opacity) or within strong (and hopefully spectrally isolated) molecular band systems, providing maximum information on the profile and variability of the examined species. The AF codes provide tools for both types of implementation. A simple procedure for E/O design would include: (a) selection of the basic problem - atmosphere as signature or contaminant; (b) selection of species, viewing platform, necessary geometric considerations, and electro-optical system characteristics to be employed; (c) selection of forward modeling algorithm for instrument simulation (line-by-line or band model), based on ease of use and confidence in achieving required accuracy; and (d) selection and/or design of data analyses schemes and their implementation. The last of these issues rests on the prior information content estimates and, to a large extent, is now mathematically constrained by the studies of Rodgers and colleagues^{28,29,30}. That work, of course, has its own rich history of contributions, beginning in the late 50's and early 60's with Kaplan, King, Dütsch, Twomey, Mateer, Davé, etc. Remaining questions concerning the tradeoffs among spectral, spatial, and vertical resolution balanced against required instrumental and algorithmic accuracy are the dominant questions for the scientific community as embodied in each particular investigation and, ultimately, the successful interfacing and fusion of those separate investigations.

Recognition of the scope of these issues led the US Department of Defense to pursue generic development of radiative transfer algorithms in the early 1970's, subsequently appointing the AF with oversight of the atmospheric component in 1978. The program has been continuing since, all to the purpose of solving the atmospheric radiative transfer equations as accurately and efficiently as possible. The outgrowth of the program is, at its simplest, a family of three codes: LOWTRAN and MODTRAN (both band models) and FASCODE (a true, highly optimized line-by-line algorithm). This family is being expanded under a variety of scientific and architectural umbrellas, all of which have the intent of facilitating correct usage. Serious attempts to optimize timing have yet to be undertaken, although both MODTRAN (especially when employing multiple scattering over large solar-impacted spectral intervals) and FASCODE (for almost any reasonable spectral interval) would certainly benefit from such research.

4. RADIATIVE TRANSFER

4.1 THERMODYNAMIC EQUILIBRIUM: A closed system, in which no thermal or radiant energy is entering or leaving the system will be in thermodynamic equilibrium. Collisional and radiative detailed balance will be in effect and the rate of excitation of lower state energy levels by radiative processes is exactly balanced by an equivalent radiative deexcitation of upper state energy levels by either spontaneous or stimulated emission. Likewise, collisional excitation events will balance collisional deexcitation events. The system will be characterized by a unique temperature with the population of the energy levels described by a Boltzmann distribution and the radiation field by the Planck distribution. This description is a special case of a more general case of a statistical steady state, in which the aggregate of the excitation processes balances the aggregate of the de-excitation processes³¹.

The atmosphere, however, is not a closed system and, therefore, on a large scale, not necessarily in thermodynamic equilibrium. On a smaller scale, particularly in the lower atmosphere, collisions occur frequently enough to maintain a local thermodynamic equilibrium (LTE). That is, over sufficiently narrow thermal regimes (where the temperature and pressure are considered constant by some average definition; e.g. Curtis-Godson), the population of excited states may be described by Boltzmann statistics appropriate for the local ambient temperature (θ_{amb}). It follows that the Planck function will describe the radiation field. However, even when collisions are not frequent, collisional detailed balance may still be maintained, independent of the radiation processes, if the molecules do not travel far between collisions. At the same time radiative detailed balance may fail. Then radiated photons may travel large distances relative to the corresponding mean free path of particle collisions. LTE will not apply to the radiation field and the distribution of populations will not necessarily be governed by the ambient temperature. The population might be described by a Boltzmann distribution employing a non-LTE equivalent temperature (θ_{nle}), specific to each vibrational transition, rather than the molecule as a whole. LBL codes (such as FASCODE) are typically written with separate parallel paths, for LTE processes controlled by θ_{amb} , and non-LTE processes which calculate the fractional contributions from θ_{nle} transition populations, both as a function of altitude. For altitudes below 50 km, most species transitions are in LTE, permitting the elimination of the time-consuming non-LTE algorithm for many calculations. [Note that there is no equivalent non-LTE capability for the AF band models in their current formulation, thus setting an upper limit to suitable line-of-sight altitude configurations. This issue is being addressed programmatically, with the expectation of the release of a pragmatic surface-to-space non-LTE band model in the near future.]

Given the above description of detailed balance for LTE conditions within an atmospheric layer, what then is the source of the spectral line structure observed in typical electro-optical measurements (transmittance, radiance, irradiance)? The features, of course, reflect the discrete energy level transitions between molecular energy states, including rotational, vibrational and electronic transitions. If detailed balance and LTE are wholly maintained within the total system, no structure should be observed. The presence of structure indicates the gas sample is perturbed from LTE. There is an apparent inconsistency in defining LTE as a prerequisite for populating the local energy levels and then measuring signatures that indicate that the system is out of equilibrium. To study the spectral line structure requires that radiant energy enter or leave the gas sample volume, consequently disturbing the energy level population distribution from equilibrium. For example, this perturbation is typically achieved in the laboratory by providing a radiating source at one end of the cell and observing the induced absorption or emission at the other. Similarly, in the stratified atmosphere, the radiative properties of any layer will influence its neighbors, both far and near, depending on transparency and relative temperature differences. Couple in the sun and the radiating surface and the tools for remote sensing are at hand. The thermodynamic properties of each local layer serve as a source or sink along a line-of-sight for the observing system, or, taking a more global perspective, each layer serves as a source or sink for energy deposition and exchange processes, leading to heating/cooling rate calculations and photolysis studies.

4.2 BASIC LINE-BY-LINE EQUATIONS: A set of primitive radiative transfer equations are listed in Table 1. The definition of the absorption cross section (κ_{ν}) is the critical parameter that differentiates a line-by-line "exact" radiative transfer code from the more rapid band models. Historically, as previously noted, the LOWTRAN band model was the first AF-developed transmittance algorithm. However, it is FASCODE that contains the critically precise calculations of absorption (optical depth) per layer, required for exercising the Beer-Lambert law. The mathematics necessary to determine the appropriate absorption/emission rests with the conversion of individual spectroscopic parameters^{5b,c} related to molecular transitions (rotational, vibrational, and electronic), the magnitude of those transitions being governed by lower state populations and the probability of a transition occurring between paired upper and lower states, plus the statistically appropriate line shape factor. The simplest absorption coefficient definition can then be written:

$$\kappa_\nu = S \cdot f((\nu-\nu_0), \alpha)$$

where S is the line strength, $f((\nu-\nu_0), \alpha)$ is the line shape factor, as described below, ν_0 is the central frequency of the transition, and α the halfwidth of the appropriate line shape formulation. The fundamental energy level difference between emitting (or absorbing) states defines the central frequency of that transition. The temperature dependence of line strengths is calculated in terms of the appropriate Boltzmann distribution function:

$$S = S_0 \left(\frac{Q}{Q_0} \right) \exp \left[-\frac{hcE}{k} \left(\frac{\theta_0 - \theta}{\theta_0 \theta} \right) \right]$$

where h is Planck's constant; c is the vacuum speed of light; k is Boltzmann's constant, S_0 is the line intensity (from HITRAN or some other source) at the reference temperature, θ_0 ; and E is the energy of the lower state of the transition. The remaining term, Q/Q_0 , is the ratio of partition function to the reference value, governing the distribution of states for the appropriate temperature and molecular species. Fuller definitions for the spectroscopic quantities can be found in any of the HITRAN references.

4.3 LINE SHAPE: A spectral line centered at ν_0 , is the convolution of a normalized line shape with the transition strength. Briefly, there are three basic line broadening mechanisms, each of which causes the transition to be statistically displaced from the expected line center. If the molecule is influenced by its neighbors through collisions, it will perturb the energy level spacing. This is Lorentz or pressure broadening, intuitively a function of pressure because the proximity between neighbors and collisions increases with increasing density. The second line broadening mechanism is dependent upon both frequency and temperature, governed by the Doppler motion (velocity) of the molecule at the time of transition, again impacting the apparent energy level spacing. The velocity, of course, is dependent upon the temperature. The combination of Lorentz and Doppler broadening leads to the Voigt line shape which adequately describes most transitions in the atmosphere. Exceptions to the simple Voigt line shape are accommodated by multiplicative χ correction factors, particularly for H_2O^{32} and CO_2 . FASCODE and MODTRAN both presume full Voigt line shapes, modified by appropriate χ 's, over the entire altitude range, while LOWTRAN is limited to the Lorentz pressure-dominated line shape regime, below approximately 40 km. For a description of the altitude and frequency dependence of the line shapes, refer to FASCOD1B^{6c}. A related line shape issue, of general importance, is line-coupling, arising from a dense overlap of lines from the same species which act in concert to apparently narrow the expected Voigt line shape; to maintain detailed balance and line shape normalization, the narrowing actually asymmetrically shifts transitions from the wings towards the line centers^{33,34}. This behavior is exhibited by both CO_2 in the Q-branches of the 15 μm band and O_2 in the microwave, plus other species with closely spaced transitions. FASCODE and other LBL codes provide pragmatic accommodation for line coupling (CO_2 and O_2 only) as it has a measurable impact on nadir remote sensing by altering the apparent weighting function maxima for tropospheric sounding channels.

The third line broadening mechanism is natural broadening arising from the uncertainty principle. This is typically very narrow and usually plays no role in atmospheric radiation calculations. However two cases do arise. For predissociated lines, such as the Schumann-Runge system of molecular oxygen, the natural halfwidth is determined by intersecting potential wells, independent of pressure, but highly dependent on temperature through the Boltzmann populations. The other is not really line shape theory, but the impact of the magnetic field on magnetic dipoles, leading to fine Zeeman splitting, again exhibited in molecular oxygen and observable in the microwave region.

TABLE 1: DEFINITIONS

- a. κ_i = absorption cross section, related to molecular properties,
pressure (p), temperature (θ), species (i) for a single layer (ℓ)
- b. η_i = column amount of absorbing (i'th) species = $\int n_i ds$
- c. ds = path increment; n_i = volumn density
- d. τ_i = optical depth = $\kappa_i \eta_i$
- e. T_i = transmittance = $\exp (-\tau_i)$
- f. T_{mol} = total molecular transmittance = $\Pi T_i = T_1 \cdot T_2 \cdot T_3 \cdot T_4 \dots$
- g. T_T = total transmittance = $\Pi_{\ell} T_{mol,\ell} T_{continua,\ell} T_{scat,\ell} T_{aerosol,\ell}$
- h. $B(\theta)$ = Planck Function for temperature θ
- i. $\pi \mathcal{F}$ = Solar (Lunar) Source Function
- j. \mathcal{E} = Non-LTE Source Term
- k. W = Weighting Function = (dT_T/ds)

OPERATIVE EQUATION:

$\ell.$ \mathfrak{R} = Thermal Radiance = $\int B(\theta) dT_T = \int B(\theta) (dT_T/ds) ds$

AND FOR A SINGLE LAYER:

m. $\mathfrak{R} = \int B(\theta) dT_T = B(\theta) [1-T_T]$

Finally, combining thermal, solar, and non-LTE sources with multiple scattering, one can replace the Planck source function with a more general source function:

n. $B(\theta) \Rightarrow J(\tau, \zeta)$

o. $J(\tau, \zeta)$ = general source function dependent on optical depth (τ) and viewing geometry (ζ = zenith & azimuth cosines)

$$= (\omega_o/4\pi) \pi \mathcal{F} T(\zeta) \varphi \quad \begin{array}{l} \text{[SOLAR]} \\ \text{[THERMAL]} \\ \text{[N-LTE]} \\ \text{[MUL.SCAT.]} \end{array} + [1-\omega_o] B(\theta) + \mathcal{E} + J_{MS}$$

where:

- p. ω_o = single scattering albedo = $\tau_s / (\tau_s + \tau_a)$
- q. $T(\zeta)$ = transmittance from top of atmosphere to layer
- r. φ = scattering phase function
- s. J_{MS} = m.s. for both solar and thermal terms (complicated)
and other terms are as previously defined!!

It is important, given the basic equations of radiative transfer, listed in Table 1, to note that FASCODE attempts to solve for layer optical depth (Table 1:d) exactly, that is, to better than 1%. Total transmittance (Table 1:g) is the product of the layer molecular transmittances, with the additional product terms of transmittance effects due to scattering (by both molecules (Rayleigh) and aerosols (e.g. Mie)) and appropriate continua, these being either layer or full path quantities. It is in this sense that FASCODE also provides an "exact" treatment of the transmission calculation.

4.4 BAND MODEL EQUATIONS: The comparable treatment necessary to calculate transmittance using the MODTRAN band model is quite different, relying as it does upon the product of full-path, species-specific transmittances. A band model fundamentally calculates "full-path" quantities rather than layer quantities. By definition, then, it cannot obey the Beer-Lambert law. Differences from the transmittance equations in Table 1 begin with the column amounts. MODTRAN requires a total column amount weighted by pressure or density, not the individual layer amounts. This weighting (Curtis-Godson^{7a} or a variant) couples with the spectroscopic band model parameters (n/d and S/d , defined as the average number of lines in the interval and the average strength^{7a}, respectively, plus associated continua to describe the extended line shape beyond the 1 cm^{-1} bin interval), to yield the path transmittance by species. The total transmittance is then the product of the full-path individual species transmittances, along with transmittances associated with scattering attenuation and the continua. The MODTRAN radiance algorithms are directly related to equations ℓ , m , and o in Table 1, similar to the FASCODE implementation.

5. BASIC CODE DESCRIPTIONS

5.1 COMMON ELEMENTS: Briefly, all three codes share a set of common elements, facilitating intercomparisons and coding modularity. These shared elements are meant to include everything except the detailed treatment of the molecular spectroscopy, the singular component which each code approaches uniquely. Thus, default profiles for molecular species, aerosols, and clouds are shared, as are the viewing geometry, basic instrument scanning and filter functions, plus particulate and molecular continua, the latter usually in the form of cross-sections. The basic viewing geometries for standard platforms (surface, aircraft, balloon, satellite) and observational requirements include full spherical refraction³⁵. The default molecular profiles, while dating to 1986 values³⁶, can be changed to user-specification. Note, particularly, that the CO_2 mixing ratios remain at 330 ppmv, rather than a more current estimate of 355-360 ppmv; the older value still serves as an internationally accepted fiducial, but can be simply changed with final release of the 1995 versions of FASCODE and MODTRAN. The traditional continua include ultraviolet and visible cross sections for O_2 (Herzberg)^{37a} and O_3 ^{37b} (Hartley, Huggins, and Chappuis), IR pressure-induced cross sections for O_2 and N_2 ^{38a,b}, plus CO_2 and H_2O continua. The last two differ from the former in that they are essentially the sum of contributions from the far wings of individual molecular lines^{32,39} rather than true continua arising from photodissociation or collisionally forced homonuclear processes^{38b}. Nonetheless, the far wing continua have been deliberately designed for flexible incorporation into all the codes. In particular, the H_2O continua, both self and foreign, have been adopted from the recommendations of S.A. Clough (private communication, funded by the DOE/ARM Program). Figure 1 shows the magnitudes of the changes for the spectral range from 0 to 3000 cm^{-1} . The spectral properties of aerosols and hydrometeors (including fogs and rain) are also shared, primarily as developed and described by Shettle and colleagues⁴⁰. [As noted previously, external specific contributions have been supplied by the Army and the Navy.] In a companion paper in this volume (Berk, et al., 1995), the newest attributes of MODTRAN4 are described and include a simplification of the I/O for flexible/realistic cloud scenarios.

While the common elements are not identically incorporated, every attempt is made to maintain parallelism. Current exceptions arise primarily from programmatic leaps, usually governed by specific funding initiatives. Examples include the newly corrected geometry⁴¹ for near horizontal paths, now fully operational

in MODTRAN (and embedded LOWTRAN), but only now being integrated into FASE (FASCODE for the Environment; see below⁴⁸), and new MODTRAN UV temperature-dependent cross sections for SO₂⁴² and NO₂⁴³, which may or may not be appropriate for FASCODE. Improved temperature-dependent O₂ Schumann-Runge⁴⁴ and O₃ Chappuis cross-sections⁴⁵, plus a higher resolution solar irradiance^{46,47a,b} (Figure 2, after R.F. Cahalan, private communication) are being provided to FASCODE, as part of a joint DoD/DOE initiative to develop a more accessible validated LBL code for both agencies, FASE⁴⁸. Also, while all three codes calculate thermal radiance with scattering, the mathematical algorithms are slightly different. This is particularly apparent in spectral regions of high opacity. The FASCODE algorithms employ recommended⁴⁹ linear-in-tau approximations appropriate for LBL calculations. Currently MODTRAN emulates this approach with a modified version^{50,51}; however, an improved band model algorithm is being developed by Bernstein and colleagues^{52a,b}. An even newer difference in algorithm implementation centers on the treatment of multiple scattering. Historically each code has had slightly different two stream approximations^{53a,b}; the LOWTRAN and MODTRAN algorithms differed only in spectral resolution and LOWTRAN's need to implement a "k-distribution" function⁵⁴ to accommodate differences in band model opacity over the 20 cm⁻¹ intervals. FASCODE, given its high spectral sampling, uses a simpler monochromatic two-stream "flux adding" method, redeveloped by Isaacs^{53a}. With MODTRAN3, the multi-stream capabilities of the DISORT (Discrete Ordinate Method)^{55a,b} now allow user definition of the number of streams, providing increased accuracy (approaching 20-40% for some solar cases) with a correspondingly larger increase in operating time. While implementing the addition of DISORT to MODTRAN, a failure mode for layer derivative quantities was uncovered; this error, while not having immediate impact on typical line-of-sight calculations, initiated the development of a "correlated-k" distribution for the 1 cm⁻¹ MODTRAN intervals, comparable to the LOWTRAN7 formulation. This is an ongoing effort, being funded by SERDP, the Strategic Environmental Research and Development Program.

5.2 MOLECULAR SPECTROSCOPY IMPLEMENTATION: The final and most significant component of the codes is also the one containing the major kernel of divergence among them. Each code relies upon a catalog of fundamental molecular constants, as contained in the HITRAN databases^{5b,c} and each code employs this information differently. Correct handling of the detailed spectroscopy to convert these constants to transmittance and radiance is, of course, critical for an accurate radiative transfer code. The original LOWTRAN^{4a}, predating the HITRAN-like cataloging, initially incorporated empirical transmission functions and effective absorption coefficients at 20 cm⁻¹ resolution. Each version of LOWTRAN was subsequently improved in both number of species and efficiency in calculation until, in 1986, the LOWTRAN 7 band model⁵⁶ was introduced. Its band model does directly interface with HITRAN86^{5b}, employing a least squares fitting to LBL transmittance calculations for a variety of optical depths. MODTRAN employs a two-parameter band model at 2 cm⁻¹ resolution^{7a}, capable of more accurately following the temperature and pressure dependence of molecular transitions (energy level populations and Voigt line shapes). Both LOWTRAN and MODTRAN also calculate direct and scattered solar/lunar contributions⁵⁷. Finally, FASCODE is a full line-by-line Beer-Lambert algorithm, permitting the "exact" calculation of individual, overlapping molecular lines at the highest spectral resolution necessary to capture the collective behavior of any arbitrary set of HITRAN cataloged transitions. FASCODE spectral accuracy, like that of other LBL codes, is essential for assessing the capabilities of any physically-based remote sensing system and/or parameterized band model. HITRAN95 will be the basis for MODTRAN3 in its final revision. Again, the companion paper by Berk, et al. 1995, on MODTRAN4 shows the impact of changes in the HITRAN database.

Because LOWTRAN originated the AF family of codes, it deserves more than a passing mention. However, in spite of its historic importance, it is essential that the scientific community acknowledge its limitations and adopt more current and accurate algorithms. This is often a difficult message since historic reference has often been lost and the results are frequently quite satisfactory. The initial LOWTRAN accuracy and ease of use enabled the non-spectroscopist to perform adequate atmospheric calculations with confidence.

The approach changed, beginning with LOWTRAN7, which adopted the more systematic band model described above. Even with the improvements of LOWTRAN 7, calculations for paths for which the original LOWTRAN BM had been "tuned" occasionally deteriorated⁵⁸. In general, however, LOWTRAN 7 has enjoyed an even larger audience and success, in part because of its transfer to the private sector (ONTAR Corp.) for commercial distribution for personal computer (PC) access⁵⁹, and, in part, because of its unique improvements, including thermal and solar two-stream multiple scattering, extended ultraviolet cross sections, etc. The combined LOWTRAN distribution (government-provided mainframe and workstation plus ONTAR'S PC version) exceeds 1300 designated recipients.

But now LOWTRAN 7 has been displaced by its progeny - MODTRAN - with a current combined (AF and ONTAR) distribution to over 1000 users. The basic advantages of MODTRAN center on the improved spectral resolution and compatibility with HITRAN in its most recent issue ('92 and '95 for MODTRAN2 and 3, respectively). The most important generic message, however, is that in most cases, all LOWTRAN versions should be replaced by MODTRAN. A discussion of MODTRAN3's validation relative to FASCODE appears in Wang and Anderson^{45b}. Because MODTRAN3 is now undergoing external release in mid-1995 (along with its ONTAR PC version), its advantages are restated here. The primary changes from older versions include: (1) a new solar irradiance, at 1 cm⁻¹ resolution (first suggested by B.-C. Gao⁴⁶ and developed by R. Kurucz^{47a,b}); (2) an alternate multiple scattering algorithm based on DISORT^{55a,b}; (3) parameter statement control over the total number of atmospheric layers, facilitating user control over the degree of accuracy in replicating atmospheric structure⁶⁰; (4) new IR and UV temperature dependent cross sections⁶¹ and (5) improved band model and radiance algorithms, developed and validated against LBL calculations^{52b}. Subsequent modifications will be made to MODTRAN as they become available. For instance, a new measurement-based solar irradiance (from Shuttle measurements from the 1992 ATLAS campaign, expected in 1995) will be provided, along with the existing options.

6. MODTRAN3 APPLICATIONS

Coupled with all previous descriptions of MODTRAN capabilities, MODTRAN3 calculations are demonstrating a breadth of unique applications. In a series of papers, led by the work of J.-M. Thériault^{7b,62a,b}, preliminary use of MODTRAN for analysis of moderate resolution interferometer data has been established. These papers did not advocate using MODTRAN alone as the forward radiance algorithm, but, rather, showed that MODTRAN could be employed to obtain the large derivative matrices used in physical inversion algorithms. Because these matrix elements are calculated from determining the sensitivity of small single layer perturbations of each detectable species upon the full path radiance (by subtraction of comparably large numbers; see equations in Thériault et al., 1993⁶²), the near equivalence of the individual matrix elements to those derived analytically from LBL codes was unexpected. This set of studies did not recommend that the iterative least squares minimization test of forward calculation vs. measurement employ MODTRAN. That recommendation can only be made after careful analyses of the impact of spectral resolution (and its accuracy) on vertical resolution and instrument signal to noise and other error sources. Such studies are currently being undertaken.

A direct outgrowth of the sensitivity of the matrix elements was the suggestion that the MODTRAN layer-specific optical properties (effective optical depth and transmittance/radiance differentials; that is, those quantities derived from differences and ratios of adjacent full path BM calculations) were essentially equivalent to the LBL direct layer calculations. Given the near linearity of this sensitivity, MODTRAN became a candidate for flux-divergence and energy deposition calculations. As mentioned previously, the WMO InterComparison of Radiation Codes used in Climate Models (ICRCCM) had already established the basis for evaluation of LBL codes, so MODTRAN was tested against these evaluations. Initial work by L. Kimball⁶³, L. Bernstein^{52b}, and colleagues^{7b,c} has now confirmed that with appropriate modifications (an improved radiance

algorithm, implemented in MODTRAN3, and introduction of the mathematics to reduce spherical geometry to the "flat earth" approximation of ICRCCM), the IR spectrally integrated (0-3000 cm^{-1}) cooling rates for H_2O , CO_2 , and O_3 fall within the range of the LBL codes participating in the initial studies.

Two specific examples of a newer ICRCCM comparison (R. Ellingson, private communication) for MODTRAN3 and FASCODE are provided in Figures 3a/b; the measurements are from the AERI¹⁶, a well-calibrated, surface-based interferometer developed by the Univ. of Wisconsin. The results and residuals have been degraded to 10 cm^{-1} resolution and subsequently compared to the ICRCCM standard radiative transfer model: LBLRTM¹⁷. Table 2 shows the statistical level of agreement for all cases, while Case 4 was plotted here because it was a completely blind test. This case also exhibits a strong local temperature inversion near the surface, denoted by the concave structure in the center of the very strong 15 μm band of CO_2 (600-700 cm^{-1}). The statistics in Table 2 demonstrate that FASCODE and LBLRTM are relatively indistinguishable, although the DOE-funded effort has made much progress in both computational efficiency and upgraded spectral sampling (resulting in improvements to $\leq 0.5\%$ ^{17b}). This agreement is not unreasonable in that both codes have a common lineage. The important aspect is that these two line-by-line codes (and the next generation, FASE) share the best agreement with the ICRCCM measurement set, approximately 2-3% mean difference and 4-6% rms difference (with values beyond 2500 cm^{-1} dropped because of extremely low S/N). The comparable statistics for MODTRAN are approximately twice as large, 5-10% mean and 6-12% rms. The difference in the statistical errors between MODTRAN and the line-by-line codes can also be seen in any direct comparison of their calculations, whether in transmittance or radiance; MODTRAN residuals are usually within a few percent of exact calculations, and every attempt is being made to reduce this magnitude; again see the companion paper, Berk et al., 1995).

Table 2: ICRCCM Statistics

F A S C O D E, M O D T R A N								
CODE	Case1/50.862 $\text{W m}^{-2} \text{st}^{-1}$				Case2/38.111 $\text{W m}^{-2} \text{st}^{-1}$			
	diff	mean	rms	LBL	diff	mean	rms	LBL
LBLRTM (R)	-.274	-.112	1.23	0	-.09	-.036	0.51	0
FASCODE (R)	-.141	-.058	1.24	.18	.003	.001	0.49	.15
(%) LBL*		0.00	5.47	0		1.06	4.24	0
(%) FAS*		0.50	5.65	1.8		2.09	4.96	3.5
MODTRAN (R)	.378	.154	1.48	.79	.452	.184	.741	.665
(%) MOD2*		2.51	8.19	4.7		5.37	10.6	8.6
(%) MOD+		1.67	7.57	4.8		4.16	9.84	8.5
(%) MOD3		2.06	7.98	5.2		5.17	11.4	9.8
CODE	Case3/31.466 $\text{W m}^{-2} \text{st}^{-1}$				Case4/37.144 $\text{W m}^{-2} \text{st}^{-1}$			
	diff	mean	rms	LBL	diff	mean	rms	LBL
LBLRTM (R)	-.574	-.234	.616	0	-.838	-.342	.831	0
FASCODE (R)	-.533	-.218	.587	.115	-.736	-.300	.805	.147
(%) LBL*		-2.90	4.94	0		-2.80	4.05	0
(%) FAS*		-2.39	3.79	3.2		-2.01	2.78	2.9
MODTRAN (R)	-.227	-.093	.664	.498	-.366	-.149	.822	.640
(%) MOD2*		.73	7.43	8.7		0.40	6.24	7.4
(%) MOD+		-0.62	7.12	8.8		-0.63	6.27	7.3
(%) MOD3		0.59	7.67	10.1		-0.08	6.60	8.2

LBLRTM is the DOE Standard Reference Line-by-Line Code, related to FASCODE; see discussion

* indicates % statistics truncated at 2500 cm^{-1}

+, 3 indicates MOD3 (%) with m.s., and MOD3 w/o m.s. statistics, both truncated at 2500 cm^{-1}

R indicates units of $\text{W m}^{-2} \text{st}^{-1}$

Another recent example of validation of both FASCODE and MODTRAN also employs a Univ. of Wisconsin measurement set derived from their airborne instrument: HIS^{18b}. Figure 4 shows just a small spectral range (2000-2700 cm^{-1}) of a measurement taken from the NASA ER-2 over the Eastern Pacific. This spectral band has been chosen because it demonstrates the overlap in the thermal and solar Planck functions. The residual between measurement and FASCODE longward of 2400 cm^{-1} is due to reflected solar contributions. Putting in a minimum surface albedo of 0.05 and employing the MODTRAN solar capability reduces this residual between measurement and model almost completely. The virtue of having a single model with full thermal and solar radiation fields is quite apparent.

Given this success and general agreement with the LBL spectral cooling rate distributions for H_2O calculated by Clough et al.⁶⁴, a more general energy deposition study has been undertaken⁶⁵. Again, the "flat earth" assumption has been maintained but otherwise a preliminary version of MODTRAN3 (missing only the new solar irradiance and the DISORT algorithm) was used for all calculations. The code was run from 0 to 50,000 cm^{-1} in two modes: (1) radiance with single scattering (which includes both thermal and solar sources), and (2) direct solar irradiance. Figure 5 provides a typical pair of up- and down-welling radiances for the full path at 15 km, as might be measured from an aircraft flying at the tropical tropopause. The direct solar contribution is omitted and the assumed surface albedo is 0.1. Similar radiance calculations were done for 4 quadrature angles at each of 60 layer boundaries to approximate the 2π fluxes while the approximations for daily averaged solar insolation were based upon a single solar incidence angle weighted for day of year (120) and latitude (tropical, 15N)⁶⁶. The combined results for both direct solar heating and thermal heating/cooling can be seen in Figure 6, at a degraded spectral resolution of 50 cm^{-1} . Note that the calculations were first done at 1 cm^{-1} intervals, providing much more spectral detail than actually shown. Dashed contours and negative values (mK/day/cm^{-1}) denote heating while solid contours (and positive values) denote cooling. Obviously many (over 300) MODTRAN calculations were required to yield the energy budget in Figure 6, representing only one very complex application of the AF codes. An actual energy budget as determined from measurement, would also be the end result of complex sets of integrated data and spectral syntheses, no single instrument being able to provide the spectrally appropriate up- and down-welling contributions over the entire spectral range. Of course, this preliminary demonstration can only begin to provide estimates of sensitivities, even when validating data are available.

7. DISCUSSION/CONCLUSIONS

Figure 6 required producing two different energy budgets, one related directly to the solar Planck function ($\sim 5500^\circ\text{K}$) as a source, the other generated primarily from the Planck function associated with the tropical surface (300°K) and the accompanying temperature profile with $\theta_{\text{amb}} < 300^\circ\text{K}$. Most of the cooling, then, takes place in the 0 - 3000 cm^{-1} range, encompassing the thermal Planck function, and is due to the presence of the CO_2 15 μm (centered at 666 cm^{-1}) and O_3 9.6 μm (near 1040 cm^{-1}) bands. The combination of maximum cooling occurs at the stratopause where the spectrally integrated CO_2 and O_3 cooling between 0 and 3000 cm^{-1} amounts to about 13 $^\circ\text{K/day}$, 10 $^\circ\text{K}$ from CO_2 and 3 $^\circ\text{K}$ from O_3 . The tropospheric radiative cooling over the same spectral range derives primarily from H_2O bands, yielding an integrated 3-4 $^\circ\text{K/day}$. All of these values agree well with those found in the ICRCCM-related studies^{19,49,52b,64}. The maximum cooling (loss of energy within the layer) for the clear sky can be expected to occur where the temperature is high and the opacity low, the configuration at the stratopause. The mesopause heating values are only coarse estimates of the appropriate radiative forcing in that MODTRAN3 does not include important non-LTE effects. The heating at the tropopause, on the other hand, is a relatively realistic representation, matching the ICRCCM values very well in spite of incorporating only single scattering. (The multiple scattering fluxes may tend to cancel in a "clear-sky" layer where only the pressure gradient would impose a hemispheric difference.)

The prior discussion has centered on the thermal radiation and its relative cooling and heating. Additional discussion could be provided on the role of green house gases (HNO_3 , CFC-11 and -12, O_3 , and CO_2) in the spectral range between 500 and 3000 cm^{-1} , readily apparent in Figure 6. Preliminary comparisons again show excellent agreement with CFC forcing as calculated by Briegleb⁶⁷, but further discussion requires higher spectral resolution than that presented here.

Switching to the calculations of direct and scattered solar irradiance as a heating source, one must look primarily at the frequencies between 3000 and 50,000 cm^{-1} , encompassing the maximum in the solar Planck function. Ozone predominates as the heating agent, particularly in the UV between 30,000 and 50,000 cm^{-1} , the site of the weak Huggins and strong Hartley bands. Both lead to dissociation of O_3 , with subsequent direct heating of approximately 12-13°K/day, maximizing at the stratopause, again in agreement with the ICRCCM-related studies. These values effectively balance the IR cooling at the same altitudes. The much weaker O_3 Chappuis bands (.45-.7 μm or 14,000-22,000 cm^{-1}) contributes a significantly smaller but discernible heating in the middle stratosphere.

The tropospheric solar heating sources for the clear sky are due primarily to the water vapor bands, systematically observable between the near IR (3500 cm^{-1}) through the visible (18,000 cm^{-1}). This tropospheric heat source is not sufficient to balance the thermal cooling, at least for this set of calculations. Such radiative imbalance is one driving mechanism for atmospheric dynamics and overturning. However, part of the imbalance could be due to the approximation of the solar day integral. According to Cogley and Borucki⁶⁸ the technique of choosing the mean solar angle and multiplying by a daily weighting factor can lead to relatively large errors. This error could also arise because of the assumption of single scattering for solar irradiance, rather than the more realistic (20% or greater) contributions of multiple scattering. The multiple scattering capability, when implemented, will provide a more correct estimate, but will also impose major time penalties not warranted for this "proof-of-concept" study.

Separating and/or isolating the regions of optimum heating and cooling as a function of both altitude and frequency provides the research community with an important tool for recognizing the potential impact of any natural or artificial contaminant. Similar studies can be done for clouds and aerosol loading (for instance, tropical cirrus and the Pinatubo eruption, respectively). However, before such isolated studies can be extended to the global environment, MODTRAN3 must become highly optimized and vectorized, including the proposed "k-distribution" algorithm. Even this very rapid band model (running full path, full frequency transmittance and radiance calculations in tens of seconds) is inordinately slow when forced to undertake the many runs necessary for flux divergence energy budgets. Microwave and laser applications, along with higher spectral resolution interferometer data (for instance, HIS and AERI^{18b}) will continue to require the capabilities of LBL codes, as will the initial assessments of physical remote sensing algorithms currently being developed.

ACKNOWLEDGEMENT: This work was partially supported by the Strategic Environmental Research and Development Program (SERDP) and the 1994 AFOSR Summer Research Fellow Program. This paper is derived from G.P. Anderson, et al., 1995, as first published in *Passive Infrared Remote Sensing of Clouds and the Atmosphere II*, David K. Lynch, Editor, Proc. SPIE 2309, 170-183, 1994. The contributions of Julia Vail to the production of this manuscript are greatly appreciated.

8. REFERENCES

- 1a. McClatchey, R.A., R.W. Fenn, J.E.A. Selby, F.E. Volz, and J.S. Garing, *Optical Properties of the Atmosphere*, AFCRL-70-0527, (AD A715270), 1970.
- 1b. McClatchey, R.A., R.W. Fenn, J.E.A. Selby, F.E. Volz, and J.S. Garing, *Optical Properties of the Atmosphere (3rd Edition)*, AFCRL-72-0497, (AD A753075), 1972.
2. Goody, R.M., *Atmospheric Radiation, I: Theoretical Basis*, Clarendon Press, Oxford, England, 1964.
3. Goody, R.M. and Y.L. Yung, *Atmospheric Radiation: Theoretical Basis (Second Edition)*, Oxford University Press, New York, N.Y., 1989.
- 4a. Selby, J.E.A. and R.A. McClatchey, *Atmospheric Transmittance from 0.25 to 28.5 μm : Computer Code LOWTRAN 2*, AFCRL-TR-72-0745, AD 76371, 1972.
- 4b. Kneizys, F.X., E.P. Shettle, W.O. Gallery, J.H. Chetwynd, L.W. Abreu, J.E.A. Selby, R.W. Fenn, R.A. McClatchey, *Atmospheric Transmittance/Radiance: Computer Code LOWTRAN 5*, AFGL-TR-80-0067, (NTIS AD A088215), 1980.
- 4c. Kneizys, F.X., E.P. Shettle, W.O. Gallery, J.H. Chetwynd, L.W. Abreu, J.E.A. Selby, S.A. Clough, R.W. Fenn, *Atmospheric Transmittance/Radiance: Computer Code LOWTRAN 6*, AFGL-TR-83-0187, (NTIS AD A137796), 1983.
- 4d. Kneizys, F.X., E.P. Shettle, L.W. Abreu, J.H. Chetwynd, G.P. Anderson, W.O. Gallery, J.E.A. Selby, S.A. Clough, *Users Guide to LOWTRAN 7*, AFGL-TR-88-0177, (NTIS AD A206773), 1988.
- 5a. McClatchey, R.A., W.S. Benedict, S.A. Clough, D.E. Burch, R.F. Calfee, K. Fox, L.S. Rothman, J.S. Garing, *AFCRL Atmospheric Absorption Line Parameters Compilation*, AFCRL-TR-0096, 1973.
- 5b. Rothman, L.S., et al., The HITRAN Database: 1986 Edition, *Appl. Opt.*, 26, 4058-4097, 1987.
- 5c. Rothman, L.S., et al., The HITRAN Molecular Database: Editions of 1991 and 1992, *J. Quant. Spectrosc. Radiat. Transfer*, 48, 469-507, 1992.
- 6a. Smith, H.J.P., D.J. Dube, M.E. Gardner, S.A. Clough, F.X. Kneizys, L.S. Rothman, *FASCODE- Fast Atmospheric Signature Code (Spectral Transmittance and Radiance)*, AFGL-TR-78-0081, 1978.
- 6b. Clough, S.A. and F.X. Kneizys, Convolution Algorithm for the Lorentz Function, *Appl. Opt.*, 18, 2329, 1979.
- 6c. Clough, S.A., F.X. Kneizys, L.S. Rothman, W.O. Gallery, *Atmospheric Spectral Transmittance and Radiance: FASCODE 1B*, *Proc. of SPIE*, 277, *Atm. Transm.*, 1981.
- 6d. Chetwynd, J.G., J. Wang, G.P. Anderson, *FASCODE: An Update and Applications in Atmospheric Remote Sensing*, *Proc. of SPIE*, 2266, *Optical Spectroscopic Techniques for Atmospheric Research*, 1994.
- 7a. Berk, A., L.S. Bernstein, D.C. Robertson, *MODTRAN: A Moderate Resolution Model for LOWTRAN 7*, GL-TR-89-0122, 1989.
- 7b. Anderson, G.P., J.H. Chetwynd, J.-M. Thériault, P.K. Acharya, A. Berk, D.C. Robertson, F.X. Kneizys, M.L. Hoke, L.W. Abreu, E.P. Shettle, *MODTRAN2: Suitability for Remote Sensing*, *Proc. of SPIE*, xxxx, *Remote Sensing*, 1993.
- 7c. Anderson, G.P., J.H. Chetwynd, F.X. Kneizys, L.A. Hall, L.M. Kimball, L. Bernstein, P. Acharya, A. Berk, D.C. Robertson, E.P. Shettle, L.W. Abreu, K. Minschwaner, J.A. Conant, *MODTRAN3: Suitability as a Flux-Divergence Code*, *Proc. of the 4th ARM Science Team Meeting, Charleston, S.C.*, 1994.
8. Liebowitz, R.P., *Historical Brief: GL Atmospheric Propagation Codes for DoD Systems (Revised Edition)*, Phillips Laboratory/Geophysics Directorate, 35 pages, 1990.
9. Devir, A.D., A. Ben-Shalom, S.G. Lipson, U.P. Oppenheim, E. Ribak, *Atmospheric Transmittance Measurements: Comparison with LOWTRAN 6*, Report RAA/99-85, Technion-Israel Institute of Technology, Haifa 32000, Israel, 1988.
10. J.-M. Thériault, P.L. Roney, S. St.-Germain, H.E. Revercomb, R.O. Knuteson, W.L. Smith, Analysis of the FASCODE Model and its H₂O Continuum Based on Long-Path Atmospheric Transmission Measurements in the 4.5-11.5 μm Region, *Appl. Opt.*, 33, 232-233, 1994.
11. Roney, P.L., F. Reid, J.-M. Thériault, Transmission Window near 2400 cm^{-1} : An Experimental and Modeling Study, *Appl. Opt.*, 30, 1995-2004, 1991.
12. Edwards, D.P., *GENLN2: A General Line-by-Line Atmospheric Transmittance and Radiance Model*, NCAR Technical Note, NCAR/TN-367+STR, Boulder, CO, 1992.
13. Gordley, L.L., B.T. Marshall, D.A. Chu, LINEPAK: Algorithms for Modeling Spectral Transmittance and Radiance, *J. Quant. Spectrosc. Radiat. Transfer*, in press, 1994.
14. Vermote, E., D. Tanre, J.L. Deuze, M. Herman, and J.J. Morcrette, *Second Simulation of the Satellite Signal in the Solar Spectrum (6S): User Guide*, 183 pages, 1994.
15. Burrows, J., D. Diebel, H. Frank, K. Muirhead, R. Munroe, B. Kerridge, D. Pemberton, U. Platt, *A Study of Methods for Retrieval of Atmospheric Constituents*, Final Report, ESA 9687/91/NL/BI, July 1994.
16. Cornette, W.M., *Atmospheric Propagation and Radiative Transfer (APART) Computer Code*, Vol. I: Installation Reference Manual, PRA-R-024-90; Vol. II: Users Reference Manual, PRA-R-062-90; Vol. III: Technical Reference Manual, PRA-R-077-90; Vol. IV: Software reference Manual, PRA-R-075-90, Photon Research Assoc., Inc. 1990.
- 17a. Clough, S.A., Radiative Transfer Model Development in Support of the Atmospheric Radiation Measurement Program, *Proceedings of the 3rd Atmospheric Radiation Measurement (ARM) Science Team Meeting*, CONF-9303112, Norman, OK, 1993.
- 17b. Clough, S.A., P.D. Brown, N.E. Miller, J.C. Liljegren, T.R. Shippert, Residual Analysis of surface Spectral Radiances Between Instrument Observations and Line-by-Line Calculations, *Proceedings of the 4th Atmospheric Radiation Measurement (ARM) Science Team Meeting*, CONF-940277, Charleston, SC, 1994.
- 18a. Chédin, A., H. Fischer, K. Kunzi, D. Spankuch, N.A. Scott, *Report on the Intercomparison of Transmittance and Radiance Algorithms (ITRA)*, pub. IRC Working Group on Remote Sensing: Direct Problems, Campaign and Workshop, Univ. of Maryland, 1988.
- 18b. Knuteson, R.O., H.E. Revercomb, W.L. Smith, Forward Model Comparisons with the High-resolution Interferometer Sounder (HIS), *Optical Remote Sensing of the Atmosphere, 1993 Technical Digest*, 5, 1993.

19. Ellingson, R.G. and Y. Fouquart, The Intercomparison of Radiation Codes in Climate Models: An Overview, *J. Geophys. Res.*, **96**, 8925-8927, 1991.
20. Sharma, R.D., A.J. Ratkowski, R.L. Sundberg, J.W. Duff, L.S. Bernstein, P.K. Acharya, J.H. Gruninger, D.C. Robertson, R.J. Healy, *Description of SHARC, The Strategic High-Altitude Radiance Code*, GL-TR-89-0229, (NTIS AD A 213806), 1989.
21. López-Puertas, M., P.P. Wintersteiner, R.H. Picard, J.R. Winick, and R.D. Sharma, Comparison of Line-by-Line and Curtis Matrix Calculations for the Vibrational Temperatures and Radiative Cooling of the CO₂ 15 μ m Bands in the Middle and Upper Atmosphere, *J. Quant. Spectrosc. Radiat. Transfer*, to appear in Sep., 1994.
22. Green, R.O., J.E. Conel, C.J. Bruegge, J.S. Margolis, V. Carrere, G. Vane, G. Hoover, In-flight Calibration and Validation of the Spectral and Radiometric Characteristics of the Airborne Visible/Infrared Imaging Spectrometer (AVIRIS), *Remote Sensing of the Environment*, 1992.
23. Garcia, R.R. and S. Solomon, A New Numerical Model of the Middle Atmosphere, 2, Ozone and Related Species, *J. Geophys. Res.*, **99**, 12,937-12,952, 1994.
24. Roble, R.G. and R.E. Dickinson, How Will Changes in Carbon dioxide and Methane Modify the Mean Structure of the Mesosphere of the Mesosphere and Thermosphere, *Geophys. Res. Lett.*, **16**, 1441, 1989.
25. Williamson, D.L., J.T. Kiehl, V. Ramanathan, R.E. Dickinson, J.J. Hack, *Description of the NCAR of the NCAR Community Climate Model (CCM1)*, Tech. Note NCAR/TN-285+SRT, 112 pp., Natl. Cent. for Atmos. Res., Boulder, CO., 1987.
26. Barkstrom, B.R., The Earth Radiation Budget Experiment (ERBE), *Bull. Amer. Meteor. Soc.*, **65**, 1170-1185, 1984.
27. Menzel, W.P. and J.F.W. Purdom, Introducing GOES-I: The First of a New Generation of Geostationary Operational Environmental Satellites, *Bull. Amer. Meteor. Soc.*, **75**, 757-781, 1994.
28. Rodgers, C.D., Retrieval of Atmospheric Temperature and Composition from Remote Measurements of Thermal Radiation, *Rev. Geophys. Spac. Phys.*, **14**, 609-624, 1976.
29. Rodgers, C.D., Characterization and Error Analysis of Profiles Retrieved from Remote Sounding Measurements, *J. Geophys. Res.*, **95**, 5587-5595, 1990.
30. Marks, C.J. and C.D. Rodgers, A Retrieval Method for Atmospheric Composition from Limb Emission Measurements, *J. Geophys. Res.*, **98**, 14,939-14,953, 1993.
31. Cannon, C.J., *The Transfer of Spectral Line Radiation*, Cambridge University Press, 1985.
32. Ma, Q. and R.H. Tipping, A Far Wing Line Shape Theory and Its Application to the Water Continuum Absorption in the Infrared Region: I, *J. Chem. Phys.*, **95**, 6290, 1991.
33. Strow, L.L. and B.M. Gentry, Rotational Collisional Narrowing in an Infrared CO₂ Q Branch Studies with a Tunable Diode Laser, *J. Chem. Phys.*, **84**, 1149, 1986.
34. Liebe, J., P.W. Rosenkranz, G.A. Hufford, Atmospheric 60 GHz Oxygen Spectrum: New Laboratory Measurements and Line Parameters, *J. Quant. Spectrosc. Radiat. Transfer*, **48**, 1992.
35. Gallery, W.O., F.X. Kneizys, S.A. Clough, *Air Mass Computer Program for Atmospheric Transmittance/Radiance Calculations: FSCATM*, AFGL-TR-83-0065, (NTIS AD A 132108), 1983.
36. Anderson, G.P., S.A. Clough, F.X. Kneizys, J.H. Chetwynd, E.P. Shettle, *AFGL Atmospheric Constituent Profiles (0-120 km)*, AFGL-TR-86-0110, (NTIS AD A175173), 1986.
- 37a. Yoshino, K., A.S.-C. Cheung, J.R. Esmond, W.H. Parkinson, D.E. Freeman, S.L. Guberman, A. Jenouvrier, B. Coquart, M.F. Merienne, Improved Absorption Cross Sections of Oxygen in the Wavelength Region 205-240nm of the Herzberg Continuum, *Planet. Space Sci.*, **36**, 1469-1475, 1988.
- 37b. Anderson, G.P., F.X. Kneizys, E.P. Shettle, L.W. Abreu, J.H. Chetwynd, R.E. Huffman, and L.A. Hall, UV Spectral Simulations Using LOWTRAN 7, in *Atmospheric Propagation in the UV, Visible, IR and MM-Wave Region and Related Systems Aspects*, AGARD-CP-454, 1990.
- 38a. Gordley, L. (private communication; code written by E. Thompson, 1984)
- 38b. Herzberg, G., *Spectra of Diatomic Molecules*, VanNostrand Reinhold Company, pg.51, 1950.
39. Clough, S.A., F.X. Kneizys, R.W. Davies, Line Shape and the Water Vapor Continuum, *Atmos. Res.*, **23**, 229-241, 1989.
40. E.P. Shettle, Models of Aerosols, Clouds, and Precipitation for Atmospheric Propagation Studies, in *Atmospheric Propagation in the UV, Visible, IR and MM-Wave Region and Related Systems Aspects*, AGARD-CP-454, 1990.
41. P.K. Acharya, D.C. Robertson, A. Berk, *Upgraded Line-of-Sight Geometry Package and Band Model Parameters for MODTRAN*, PL-TR-93-2127, 1993.
42. Lane, L., S.L. Manatt, R. Cageao, Private Communication in Advance of Publication.
43. Schneider, W., G.K. Moortgat, G.S. Tyndall, J.P. Burrows, Absorption Cross-sections on NO₂ in the UV and Visible Region (200-700 nm) at 298K, *J. Photochem. Photobiol., A: Chemistry*, **40**, 195-217, 1987.
44. Minschwaner, K., G.P. Anderson, L.A. Hall, and K. Yoshino, Polynomial Coefficients for Calculating O₂ Schumann-Runge Cross Sections at 0.5 cm⁻¹ Resolution, *J. Geophys. Res.*, **97**, 10103-10108, 1992.
45. Shettle, E.P. and S.M. Anderson, Ozone Cross-Sections for the Chappuis and Wulf Absorption Bands, to be submitted to *GRL*, 1994.
- 45b. Wang, J. and G.P. Anderson, Validation of FASCOD3 and MODTRAN3: Comparison of Model Calculations with Interferometer Observations from SPECTRE and ITRA, in *Passive Infrared Remote Sensing of Clouds and the Atmosphere II*, David K. Lynch, Editor, Proc. SPIE 2309, 170-183, 1994.
46. Gao, B.-C., The Presence of Terrestrial Atmospheric Gas Absorption Bands in Standard Extraterrestrial Solar Irradiance Curves in the Near-IR Spectral Region, Submitted to *Appl. Opt.*, 1993.
- 47a. Kurucz, R.L., The Solar Irradiance by Computation, to appear in Proc. of the 17th Annual Review Conference on Atmospheric Transmission Models, 7 June 1994, Geophysics Directorate/Phillips Laboratory, 1994.
- 47b. Kurucz, R.L., Atomic and Molecular Data for Opacity Calculations; "Finding" the "Missing" Solar Ultraviolet Opacity; remaining Line Opacity Problems for the Solar Spectrum, all in *Revista Mexicana de Astronomia y Astrofisica*, **23**, 1992.

48. Anderson, G.P., J. Wang, S. Miller, H.E. Snell, J.-L. Moncet, W.O. Gallery, *FASCODE for the Environment (FASE): Comparisons between FASCODE and LBLRTM*, DOE Report on FASE, 1994.
49. Ridgway, W.L., Harshvardhan, A. Arking, Computation of Atmospheric Cooling Rates by Exact and Approximate Method, Appendix: Cooling Rate Sensitivity to Layering and Vertical Integration Method, *J. Geophys. Res.*, 96, 8969-8984, 1991.
50. Cornette, W.M., Robust Algorithm for Correcting the Layer Problem in LOWTRAN, *Appl. Opt.*, 31, 5767-5769, 1992.
51. Minschwaner, K., G.P. Anderson, L.A. Hall, R.J. Thomas, D. Rusch, A. Berk, J. Conant, Scattered Ultraviolet Radiation in the Upper Stratosphere, II: Modeling and Analysis, submitted to *J. Geophys. Res.*, 1994.
- 52a. Bernstein, L.S., A Treatment of the Layer Temperature-Gradient Problem in Band Model Emission Codes, accepted for publication in *Appl. Opt.*, 1994.
- 52b. Bernstein, L.S., A. Berk, P.K. Acharya, D.C. Robertson, G.P. Anderson, J.H. Chetwynd, L.M. Kimball, Very Narrow Band Model Calculations of Atmospheric Fluxes and Cooling Rates Using the MODTRAN Code, submitted to *J. Geophys. Res.*, 1994.
- 53a. Isaacs, R.G., W.-C. Wang, R.D. Worsham, S. Goldenberg, Multiple Scattering Treatment for Use in the LOWTRAN and FASCODE Models, AFGL-TR-86-0073, (NTIS AD A173990), 1986.
- 53b. Isaacs, R.G., W.-C. Wang, R.D. Worsham, S. Goldenberg, Multiple Scattering LOWTRAN and FASCODE Models, *Appl. Opt.*, 26, 1272-1281, 1987.
54. Wiscombe, W.J. and J.W. Evans, Exponential-Sum Fitting of Radiative Transmission Functions, *J. Comput. Phys.*, 24, 416-444, 1977.
- 55a. Stamnes, K., S.-C. Tsay, W.J. Wiscombe, K. Jayaweera, Numerically Stable Algorithm for Discrete-Ordinate-Method Radiative Transfer in Multiple Scattering and Emitting Layered Media, *Appl. Opt.*, 27, 2502-2509, 1988.
- 55b. Stamnes, K., S.C. Tsay, M. Yeh, *Upgrade of FASCODE and MODTRAN to Full Solar Capability Including Multiple Scattering and Spherical Geometry*, Draft Final Report to PL/Geophysics Directorate, 1994.
56. Pierluissi, J.H. and Maragoudakis, C.E., *Molecular Transmission Band Models for LOWTRAN*, AFGL-TR-86-0272, (NTIS AD A180655), 1986.
57. Ridgway, W.L., R.A. Moose, A.C. Cogley, *Single and Multiple Scattered Solar Radiation*, AFGL-TR-82-0299, (NTIS AD A126323), 1982.
58. Kneizys, F.X., G.P. Anderson, E.P. Shettle, L.W. Abreu, J.H. Chetwynd, J.E.A. Selby, W.O. Gallery, S.A. Clough, LOWTRAN 7: Status, Review, and Impact for Short-to-Long Wavelength Infrared Applications, in *Atmospheric Propagation in the UV, Visible, IR, and MM-wave Region and Related Systems Aspects*, AGARD-CP-454, 1990.
59. Schroeder, J., S. Harvey, *ONTAR Products for the Environment*, Bull. 5086899622, North Andover, MA., 1994.
60. Conant, J., *AURIC-M: Atmospheric Ultraviolet Radiance Integrated Code as an Extension of MODTRAN*, Aerodyne Final Report, in preparation, 1994.
61. Acharya, P.K., Private Communication, 1994.
- 62a. Thériault, J.-M., G.P. Anderson, J.H. Chetwynd, Y. Qu, E. Murphy, V. Turner, M. Cloutier, A. Smith, Retrieval of Tropospheric Profiles from IR Emission Spectra: Investigations with the Double Beam Interferometer Sounder (DBIS), *Optical Remote Sensing of the Atmosphere, 1993 Technical Digest*, 5, 78, 1993.
- 62b. Thériault, J.-M., J.-L. Moncet, G.P. Anderson, J.H. Chetwynd, Remote Sensing of Tropospheric Profiles from Ground-Based IR Spectra, to be published in *Proc. of 1993-OSO Annual Meeting*, Toronto, 1994.
63. Kimball, L.M., Calculation of Atmospheric Cooling Rates Using MODTRAN2, *USAF Summer Research Project 1993 Final Reports*, 8, pp 1.1-1.14, AFOSR, Washington, D.C., 1993.
64. Clough, S.A., M.J. Iacono, J.-L. Moncet, Line-by-Line Calculations of Atmospheric Fluxes and Cooling Rates: Applications to Water Vapor, *J. Geophys. Res.*, 97, 15761, 1992.
65. Kimball, L.M., Investigation of Atmospheric Heating and Cooling Balance Using MODTRAN3, *AFOSR Summer Faculty Report*, in press, 1994.
66. Manabe, S. and F. Moller, On the Radiative Equilibrium and Heat Balance of the Atmosphere, *Monthly Weather Review*, 89, 12, 503-530, 1961.
67. Briegleb, E.P., Longwave Band Model for Thermal Radiation in Climate Studies, *J. Geophys. Res.*, 97, 11475-11485, 1992.
68. Cogley, A.C. and W.J. Borucki, Exponential Approximation for Daily Average Solar Heating or Photolysis, *J. Atmos. Sci.*, 33, 1347-1356, 1976.

WATER VAPOR CONTINUUM MODEL COMPARISON

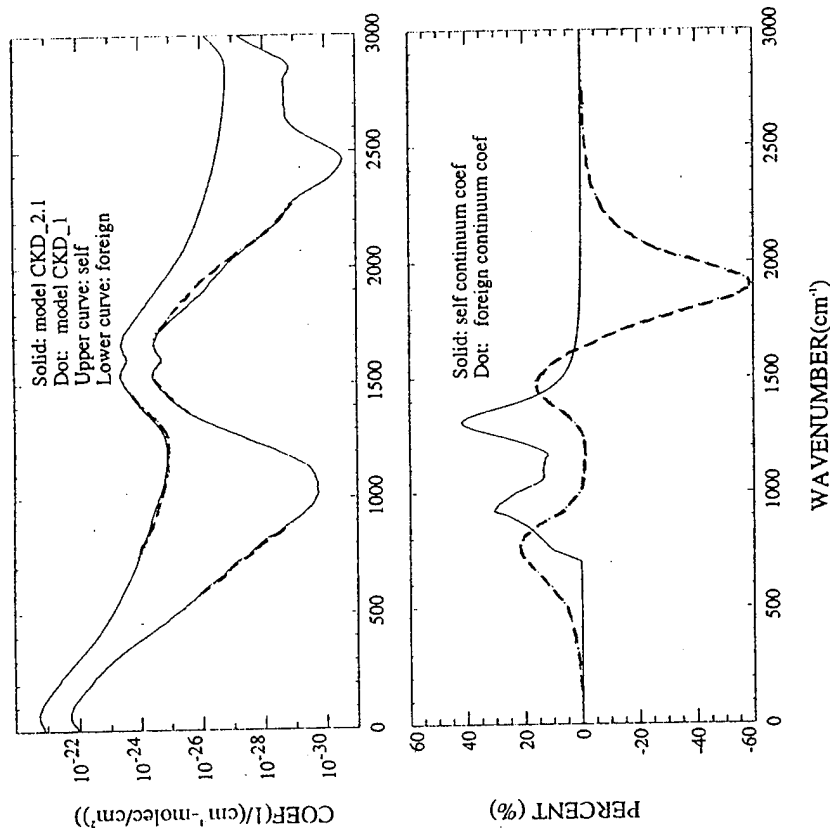


Figure 1: Changes made in the H₂O continuum, based on the recommendations of S.A. Clough (private communication), developed under the DOE/ARM Program; see text.

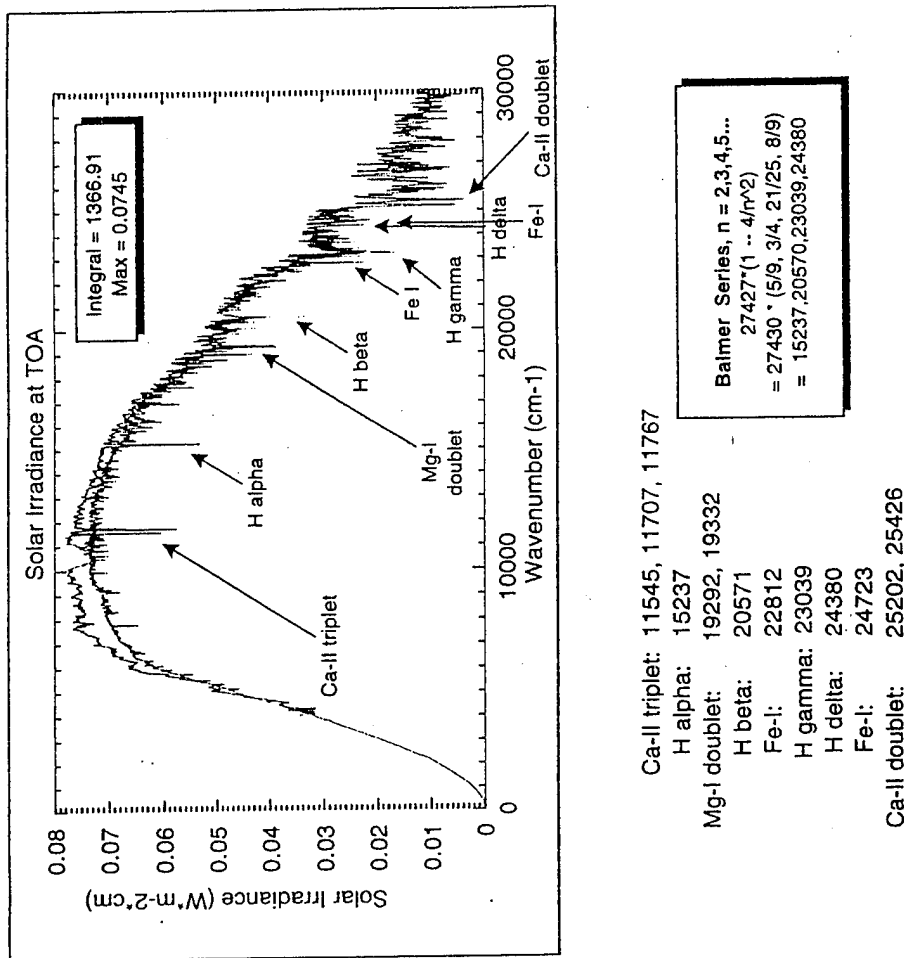


Figure 2: New solar irradiance, after Kurucz^{7a,b}, the upper curve is the original LOWTRAN 7 irradiance. Figure supplied by R. Cahalan, NASA.

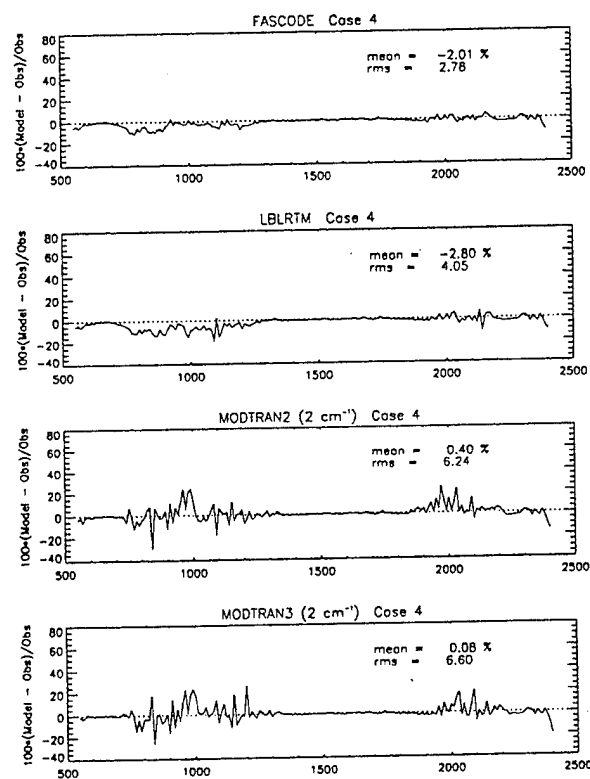
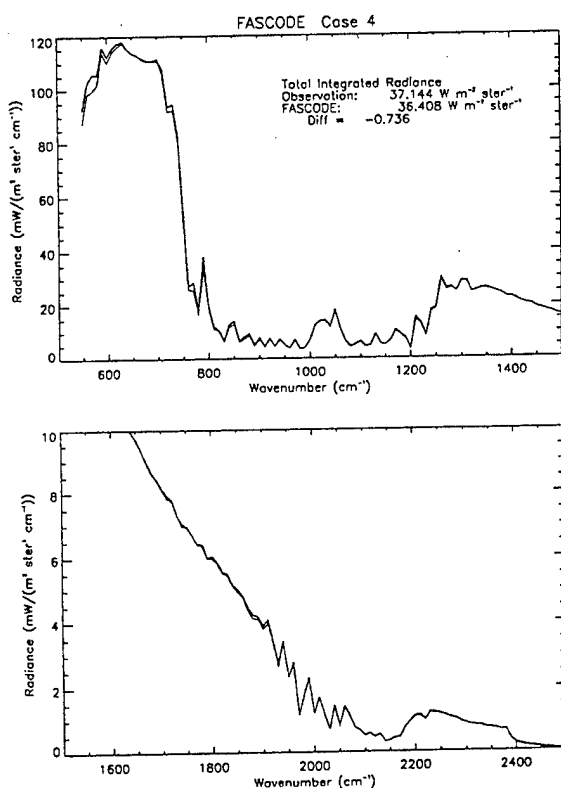


Figure 3: Preliminary ICRCCM radiance comparison for CASE 4 (AERI up-looking measurement and FASCODE simulation, both at 10 cm^{-1} resolution), broken into two spectral segments to show full range; data as provided by R. Ellingson, Univ. of Maryland. The percent residuals appear on the left, for FASCODE, LBLRTM (the adopted standard, as developed for ARM; see text), MODTRAN2, and MODTRAN3. See Table 2 for full statistical comparisons.

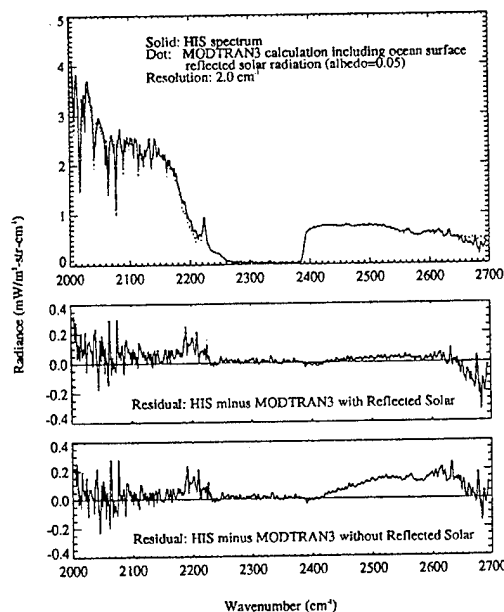
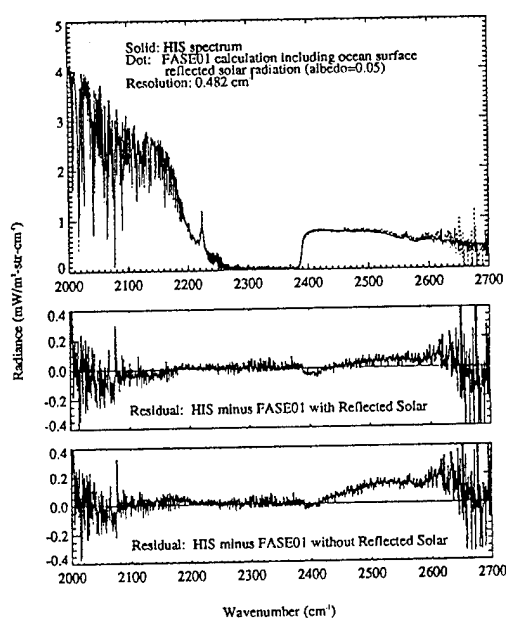


Figure 4: Preliminary ITRA94 radiance comparison (HIS nadir measurement from 20 km and FASCODE/right, MODTRAN3/left simulations); data as supplied by Noelle Scott, CNRS. FASCODE resolution has been matched to the instrument, while the MODTRAN comparison necessitated degrading the data to MODTRAN resolution (2 cm^{-1}). The residuals are in the lower plots. Note that the addition of a surface albedo and solar scattering reduces the residual between 2400 and 2600 cm^{-1} to approximately zero. FASCODE currently has no solar capability.

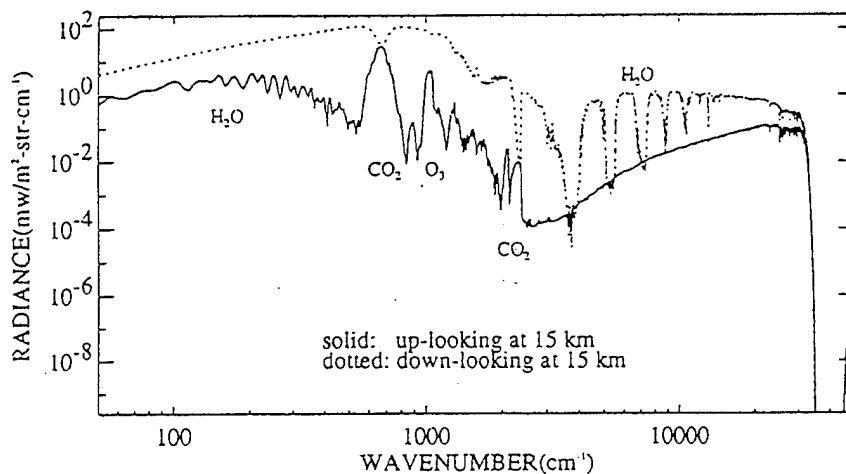


Figure 5: Up- and downwelling direct and single scattered radiances for both the thermal and solar regimes. The direct solar contribution is not included. The surface albedo is 0.1. The two strong CO₂ bands at 15 and 4.3 μm are optically thick and, therefore, both the up and down views converge to a radiance commensurate with θ_{amb} at 15 km. The visible H₂O bands are seen in primarily in absorption of the reflected solar irradiance. See text for further discussion.

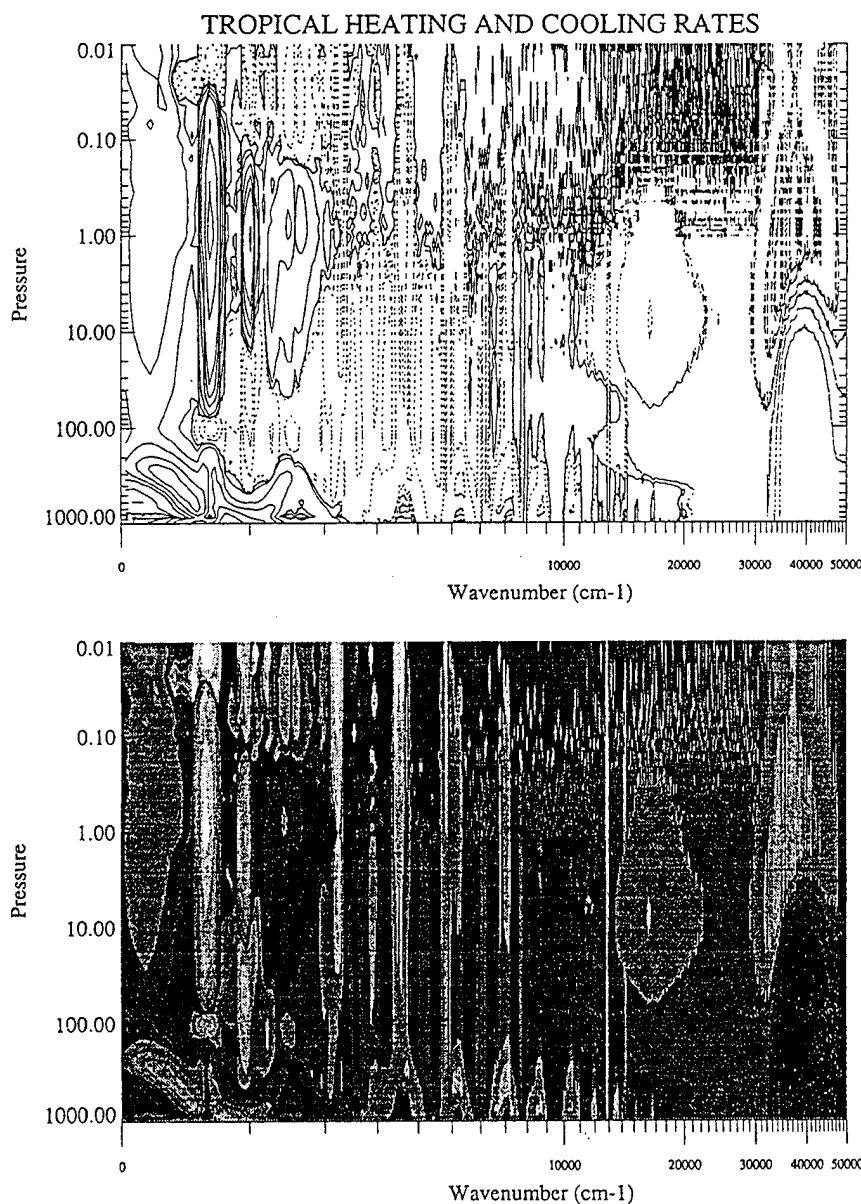


Figure 6: The upper and lower figures both represent the total radiant energy budget for the tropical atmosphere at equinox. Units are $^{\circ}\text{mK}/\text{day}/\text{cm}^{-1}$. Solid contours indicate cooling; dashed contours indicate heating. The magnitudes of the contours are indicated by the accompanying grey scale. Values above 0.1 mb (~ 60 km) may be ignored; see text.

Modular Algorithms for Radiative Transfer through Cloudy Atmospheres

Paul Ricchiazzi
Shiren Yang
William O'Hirok
Catherine Gautier

Institute for Computational Earth System Science (ICESS)
University of California
Santa Barbara, CA 93106

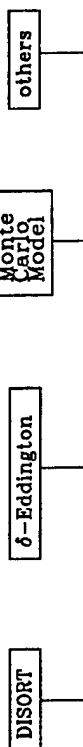
18th Annual Conference on Atmospheric Transmission Models
SCIENCE CENTER
Phillips Laboratory
Geophysics Directorate

8-8 June 1995

OVERVIEW

1. Modularity of Radiative Transfer Code
2. User Interface
3. Applications
4. Comparison of Model Results to SPECTRE
5. Energy budget calculations
6. Future Work

Modular Algorithms for Radiative Transfer



Library functions

atms.f
cloudpar.f
filter.f
solirr.f
suralb.f
tauaero.f
taugas.f

Modular Algorithms for Radiative Transfer library functions

atms standard atmospheric models (midlat summer, etc....)
(density, temperature, pressure, trace species, etc....)
cloudpar Cloud radiative properties from Mie scattering theory:
scattering coefficient, single scattering albedo and asymmetry
factor. Uses a table of entries for a range of cloud droplet
radii between 2 and 128 um
filter Standard satellite filter functions: AVHRR 1,2,3,4,5
GOES, METEOSAT...
solirr solar spectral irradiance. Two versions: a low resolution model
from 65 and a more highly resolved model from LOWTRAN 7
suralb surface spectral reflectivity for wavelength range 0.25 - 4.0 um
of several standard surface types (sand, ocean, veg, snow)
based on the 6s model
tauaero LOWTRAN 7 aerosol models both for boundary layer aerosols
(E.g., urban, maritime, rural) and for stratospheric aerosols
(E.g., volcanic, background)
taugas gaseous absorption model from LOWTRAN 7. Also provides
k-distribution parameters to enable RT in cloudy conditions.

k-Distribution Implementation

$$T(x, \mu) = A_1 \exp(-\alpha \tau_1) + A_2 \exp(-\alpha \tau_2) + A_3 \exp(-\alpha \tau_3)$$

LOWTRAN7 provides a simple three term k-distribution model which has the unusual feature of allowing weighting factors for each exponential term to vary as a function of altitude ($A_i(z)$).

This added flexibility is used within LOWTRAN to optimize the fits for cases in which the dominant absorber is different at different levels in the atmosphere. In the DISORT implementation the k-distribution weighting factors must remain fixed throughout the atmosphere. This is accomplished by fixing the weighting factors to the values that best represent the transmission curve of the dominant absorber.

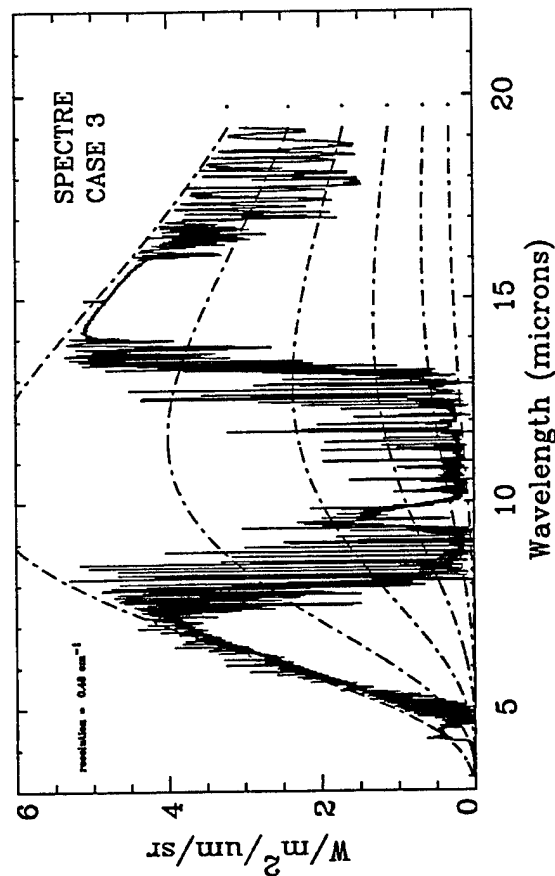
Slant Path Correction --- Because the LOWTRAN k-distribution fits carry only three terms, the quality of fits may not adequately model the transmission function for all possible values of the solar zenith angle. This can present a problem when computing the surface radiation through a thin cloud layer. In this case the radiation at the surface may be dominated by the direct beam transmission. To improve the RT predictions for this case we modify the k-fit transmission function using the "a" coefficient, above, so that it matches the results obtained by the LOWTRAN double exponential fit model. I.e., we require that $T(x, \mu) = T_{DE}(x, \mu)$. This fixes the value of coefficient "a."

Applications

1. Effects of Cloud Geometry on 3-D Radiation Field
2. Broadband Downwelling Longwave Surface Radiation Validation Studies
3. Analysis of Solar Radiation Absorption in the Presence of Cloud
4. Mapping the High Latitude UVB Surface Radiation Budget in the Presence of Cloud

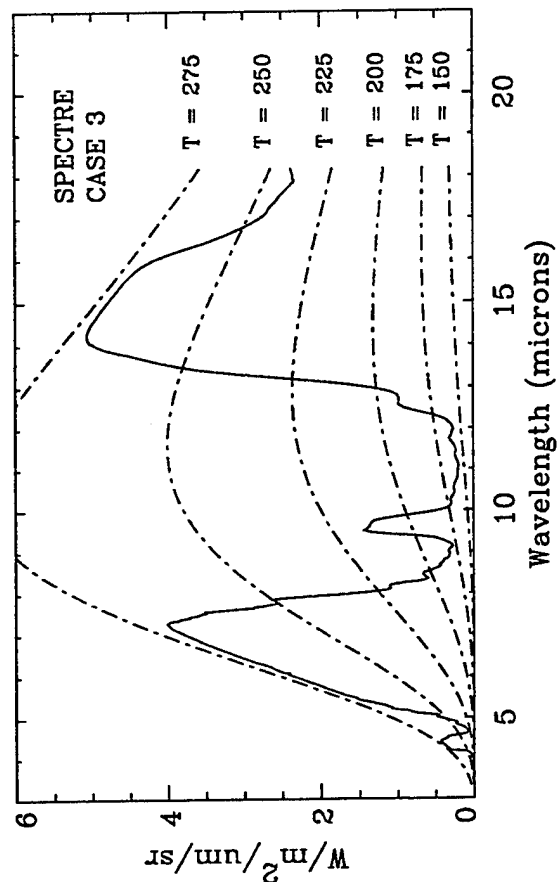
Downwelling Radiance

---observed---



Downwelling Radiance

--- DISORT ---



UCSB/ESRG HY Model (DISORT)

Case

View

Help

Status: Case: 941104-203606 (DONE)

Date/Time

Current Time

Local Noon

Day Of Year

110

GMT (Hours)

17.50

Location

Use Current Location

Lat: 36.64

Lon: -97.40

UAV Altitude (km)

10.0

Solar Geometry:

Zenith = 28.6 degs

Azimuth = 148.7 degs

Cloud Base (km) --- Tau / Re

20		10	
19		09	
18		08	
17		07	
16		06	
15		05	
14		04	
13		03	
12		02	
11		01	

Tau = 100 / Re = 32 um

Set Cloud Parameters

Calculate Cloud Effects

Instrument Characteristics

Select Instrument

Broadband Solar

Atmospheric Characteristics

Select Profile

sgp.940420.172900 (

Integrated Water Vapor (g/cm2)

2.5

Instrument

Select Instrument

Broadband IR (4.5-10.0 um)

Broadband IR (10.0-20.0 um)

01 - METEO

02 - GOES (EAST)

03 - GOES (WEST)

04 - AVHRR1 (NOAA8)

05 - AVHRR2 (NOAA8)

06 - AVHRR1 (NOAA9)

07 - AVHRR2 (NOAA9)

08 - AVHRR1 (NOAA10)

OK

Apply

Cancel

Profile

Standard Models

1-TROPICAL (4.1 g/cm2)

2-MID-LATITUDE SUMMER (2.9 g/cm2)

3-MID-LATITUDE WINTER (0.9 g/cm2)

4-SUB-ARCTIC SUMMER (2.1 g/cm2)

5-SUB-ARCTIC WINTER (0.4 g/cm2)

6-J862 (1.4 g/cm2)

----- Sondes -----

sgp.940423.143000 (2.9 g/cm2)

sgp.940423.112800 (2.6 g/cm2)

sgp.940423.083000 (2.6 g/cm2)

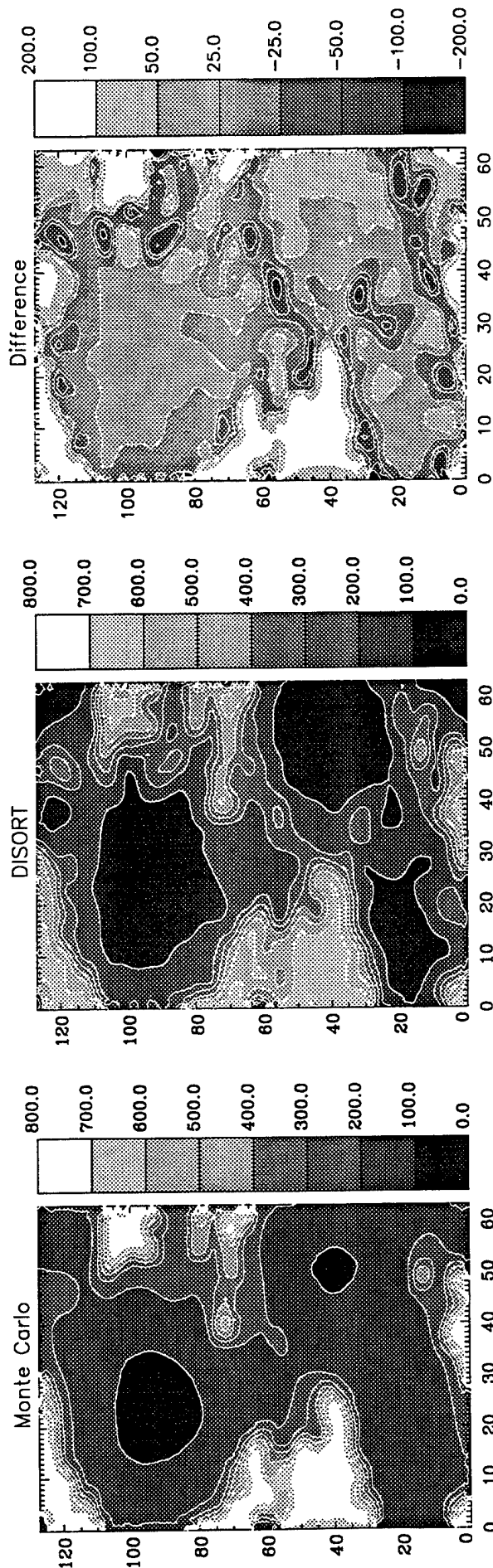
sgp.940423.023000 (2.7 g/cm2)

OK

Apply

Cancel

Shortwave surface absorption, with and without horizontal transport



This is an overhead view of a horizontally variable cloud field, generated by a 2-D multifractal cascade model. The first two frames show the downwelling surface flux (Wm^{-2}) computed by Monte Carlo (with horizontal transport) and the DISORT model (no horizontal transport), respectively, while the third frame shows their difference. As one would expect, compared to DISORT, the Monte Carlo model tends to smooth the scene's horizontal structure. Horizontal transport also increases the overall downward transport to the surface by an average of 33.6 Wm^{-2} . This result may have bearing

on the current controversy concerning the so called anomalous absorption of clouds. One of the strengths of the our modular RT code is that it is simple to verify that the differences we observe between the 1-D and 3-D RT methodologies is really due to the method of solving the RT equation and not due to spurious differences in the specification of the atmospheric microphysics. It would be difficult to make this separation if the Monte Carlo and DISORT codes did not share the same set of microphysical models.

Future Work

1. Modularize the MODTRAN transmission subroutines
2. Expand functionality of graphical user interface
3. Improve RT modules

REFERENCE LIST

- o Paul Ricchiazzi
paul@icess.ucsb.edu
- o Catherine Gautier
gautier@icess.ucsb.edu
- o Starting in August 1995, the DISORT (with fancy GUI) version of our radiative transfer model will be available on the World Wide Web at:
<http://top.mrcsb.com/stm/pub>

RECENT UPGRADES TO MODTRAN: MODTRAN4

by

A. Berk, L.S. Bernstein, P.K. Acharya and D.C. Robertson
Spectral Sciences, Inc., Burlington, MA

G.P. Anderson and J.H. Chetwynd
Geophysics Directorate, Phillips Laboratory, Hanscom AFB, MA

Presented At

18th Annual Review Conference
on Atmospheric Radiation Models

6 JUNE 1995

OUTLINE

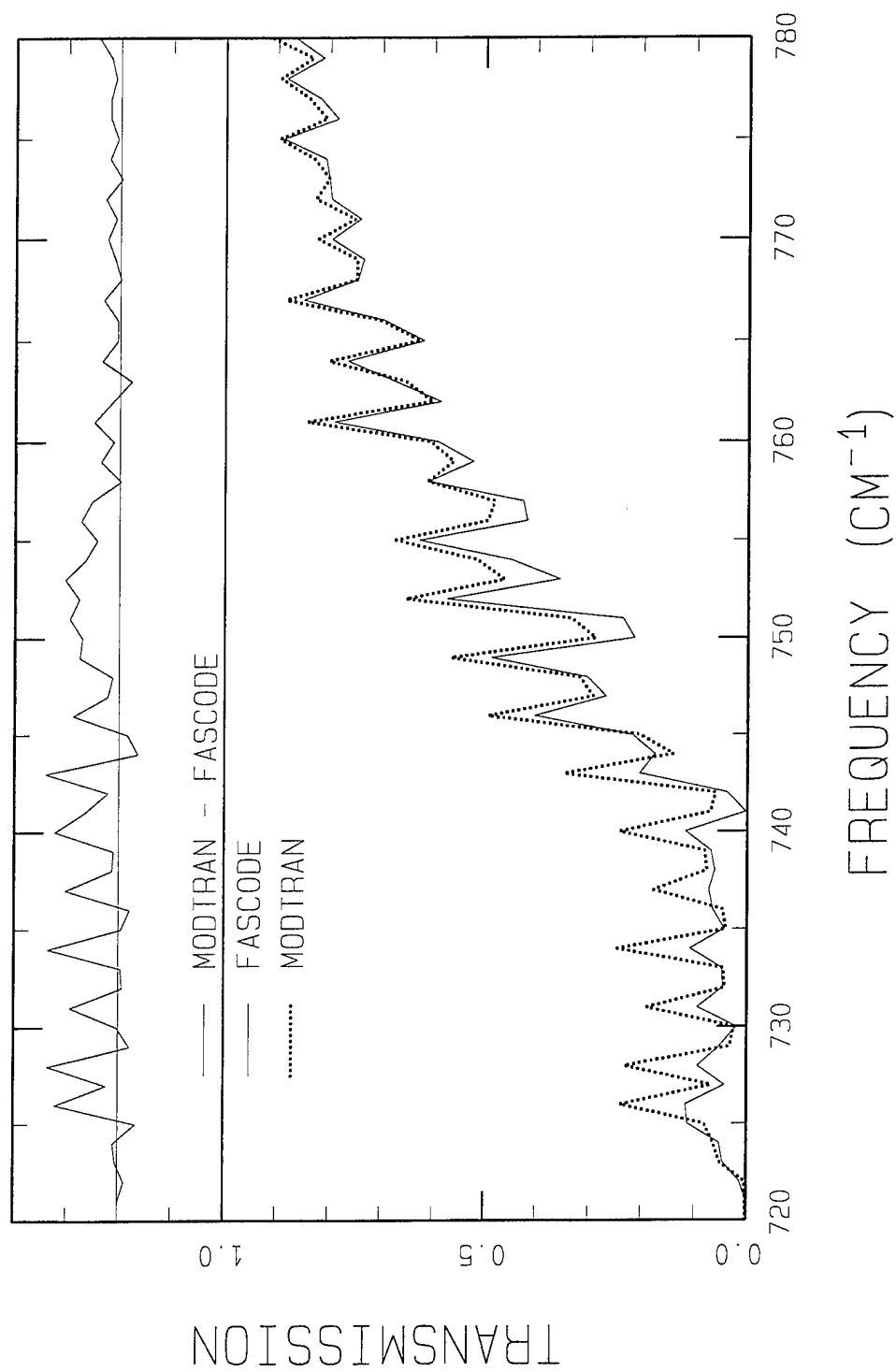
- BAND MODEL UPGRADES
 - IMPROVE LINE OVERLAP MODEL
 - UPGRADE LINE CENTERING
 - CORRECT N₂ CONTINUUM
 - CREATE A HITRAN95 TAPE
- CLOUD MODEL UPGRADES
 - SENSITIVITY ANALYSIS
- SUMMARY

BAND MODEL UPGRADES

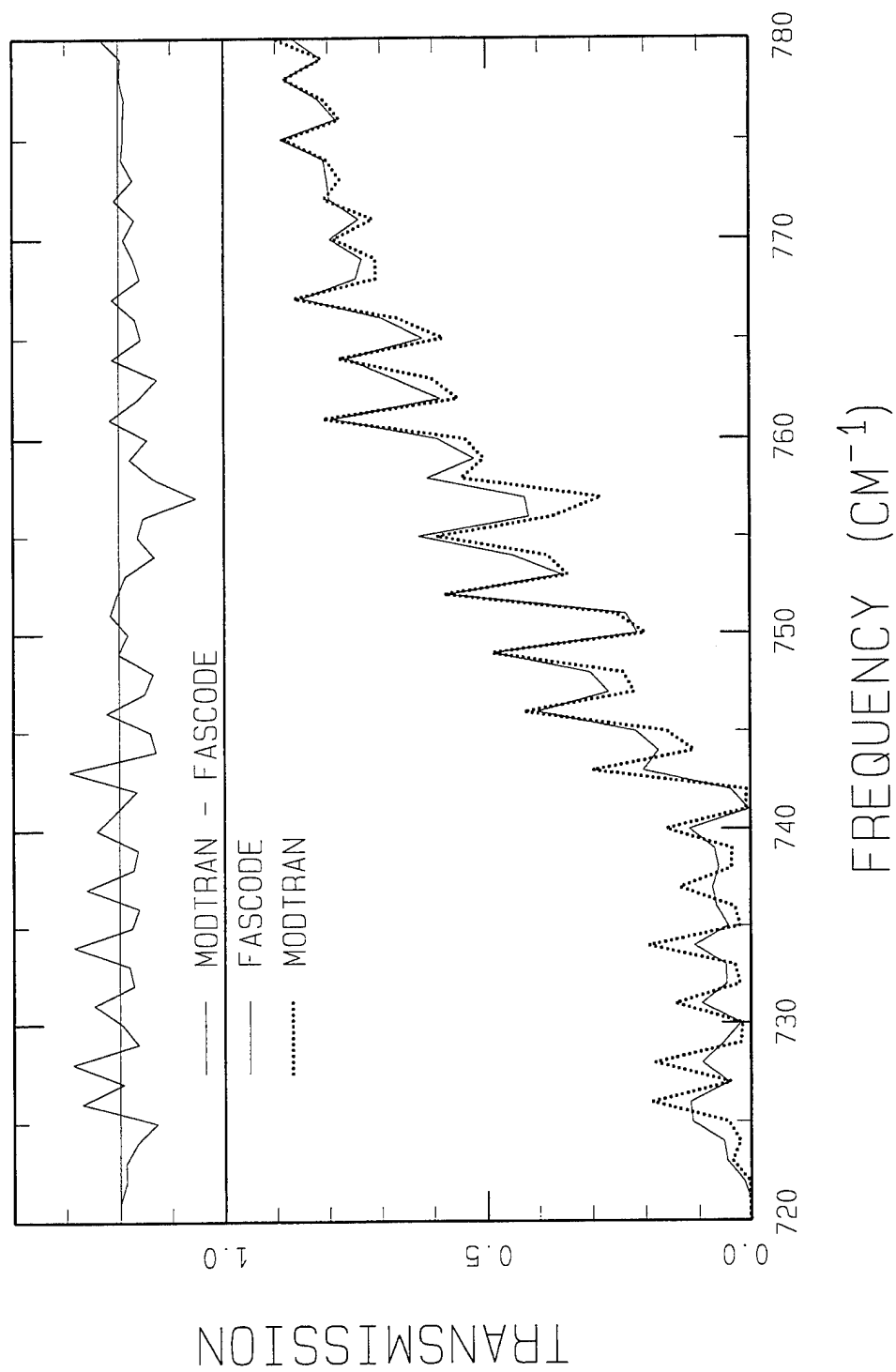
- 15 μm CO_2 BAND USED FOR TEMPERATURE RETRIEVAL
 - ACCURACY IS CRITICAL
 - MODTRAN2 UNDERPREDICTS ABSORPTION IN WINGS
- ADJUSTMENTS TO BAND MODEL
 - LINE SPACING PARAMETER IS TOO LOW ($\Delta = .0325$)^{*}
 - SWITCH TO TRADITIONAL LINE SPACING PARAMETER BASED ON \sqrt{S} WEIGHTING ($\Delta = .0251$)^{*}
 - COALESCE LINES WITHIN 0.01 cm^{-1} SUB-INTERVALS ($\Delta = .0241$)^{*}
 - ADJUST LOCATION OF EQUIVALENT WIDTH LINE ($\Delta = .0206$)^{*}

^{*} Δ IS THE AVERAGE TRANSMITTANCE ERROR BETWEEN
500 AND 3000 cm^{-1} FOR A 500 KM CONSTANT
PRESSURE/TEMPERATURE PATH AT 15 KM ALTITUDE

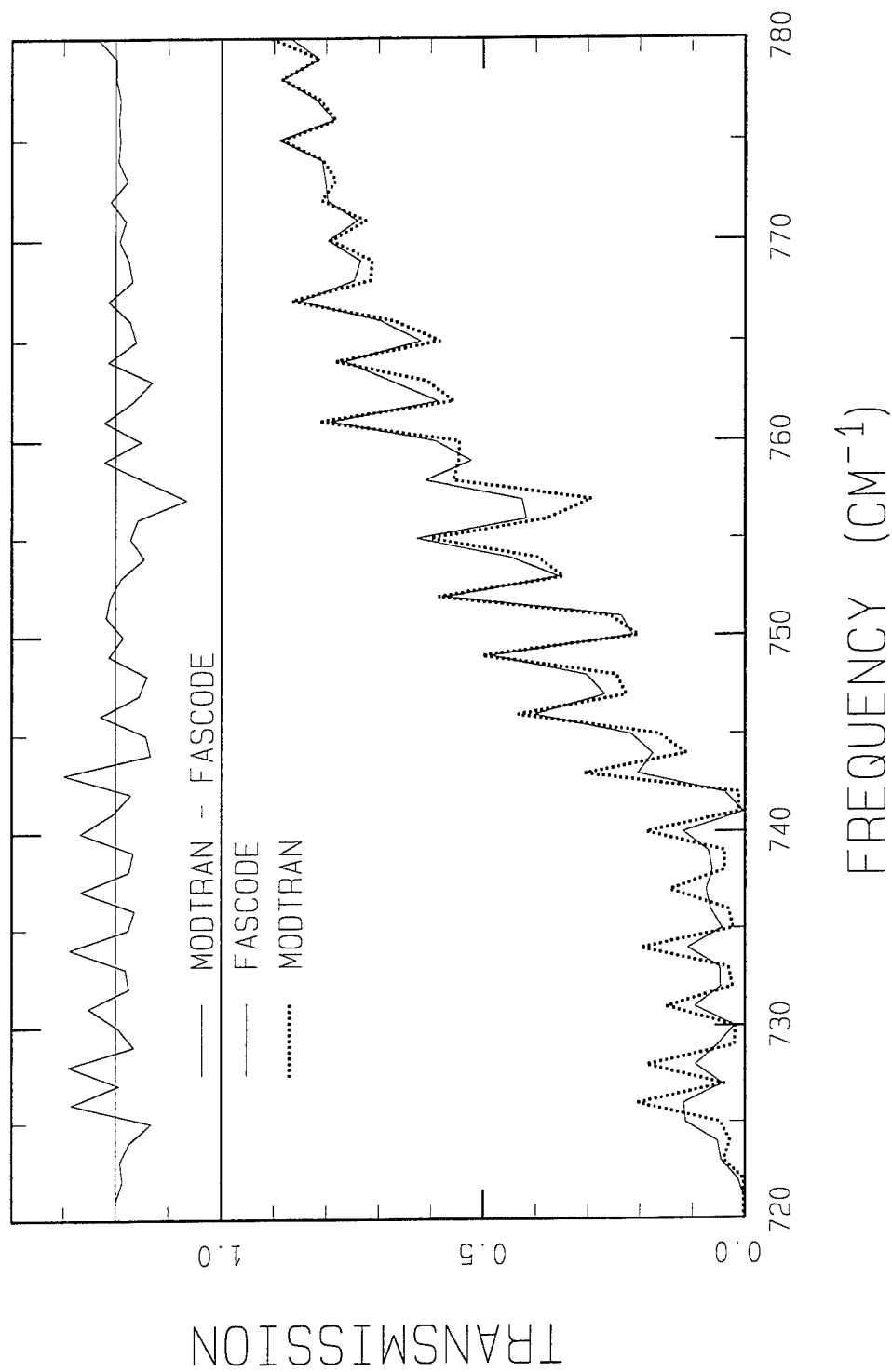
MODTRAN2 PREDICTION



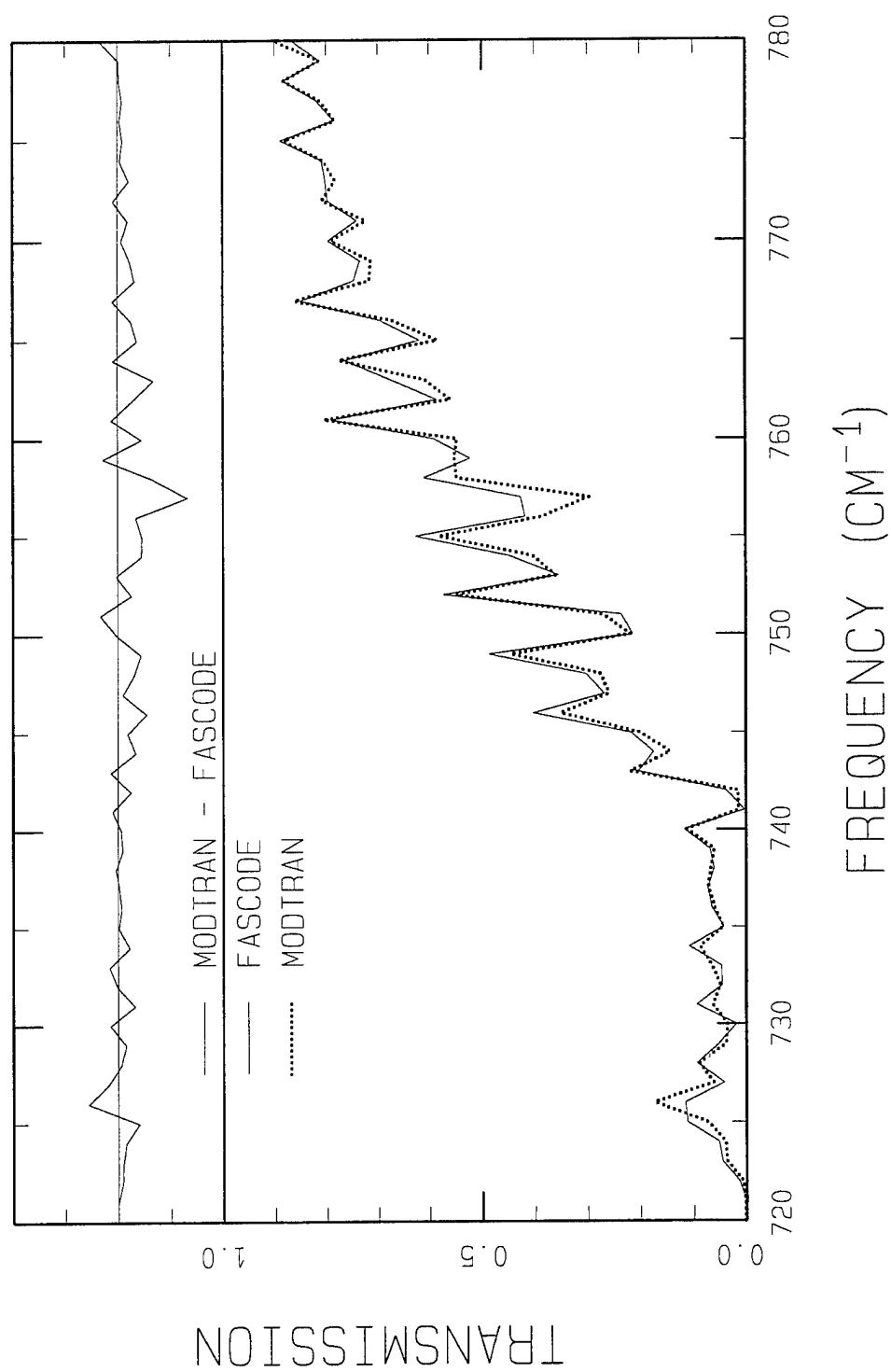
TRADITIONAL LINE SPACING PARAMETER



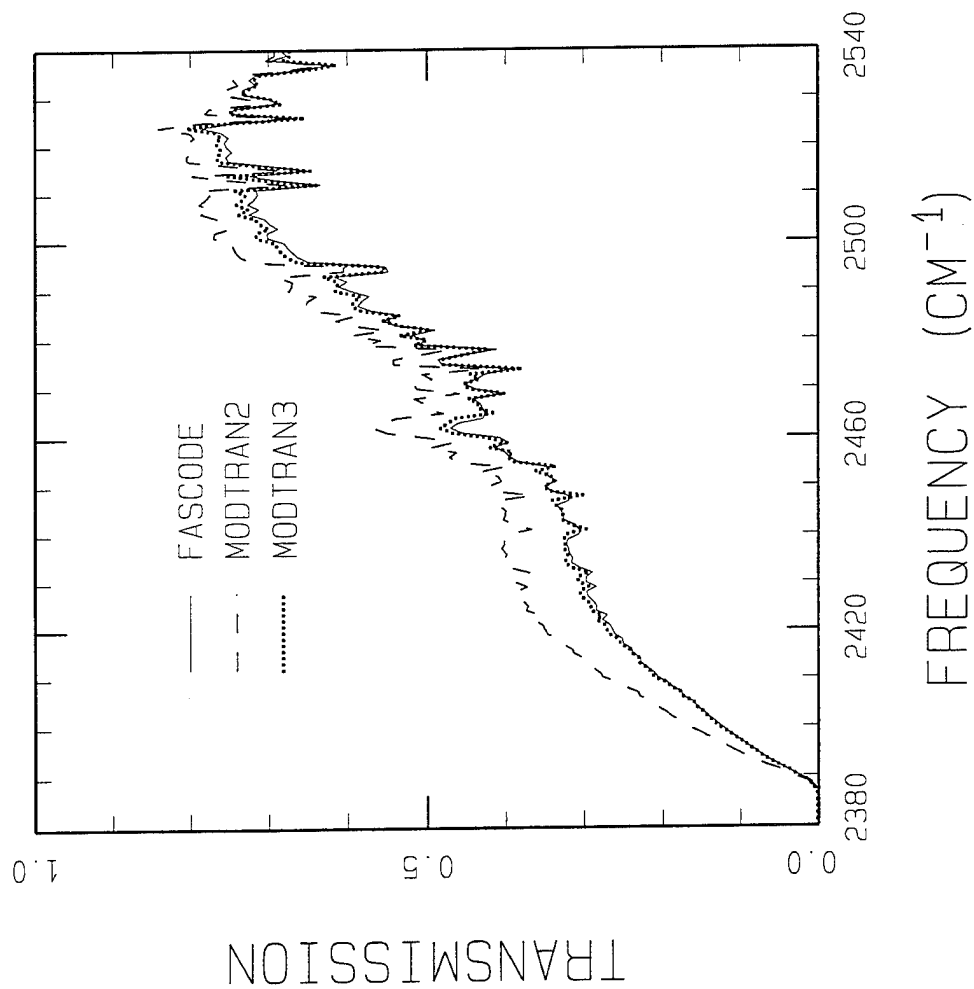
LINE OVERLAP CORRECTION



LINE CENTERING AND OVERLAP CORRECTION



N2 CONTINUUM

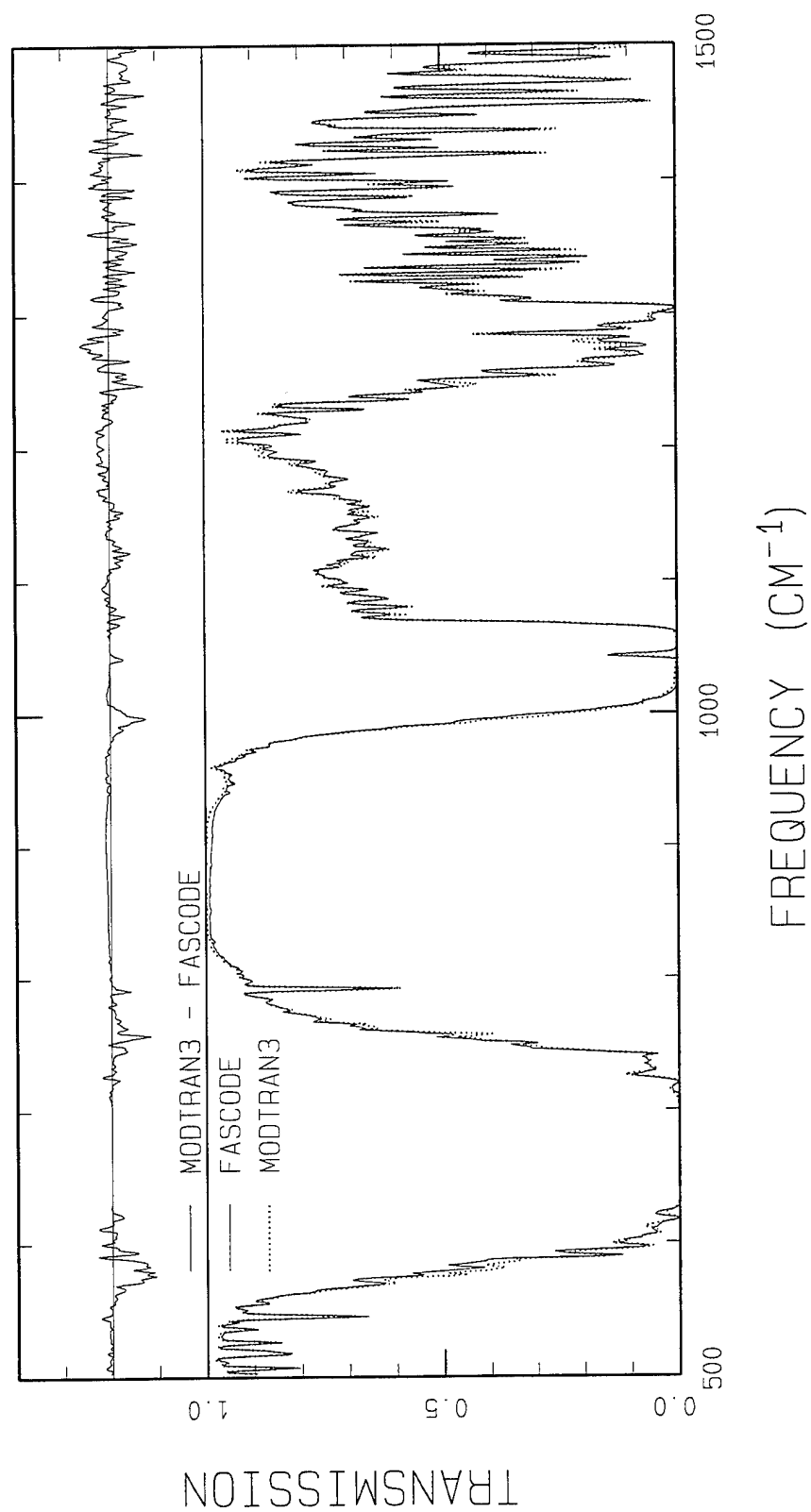


MODTRAN2 USES AN OLD
N₂ CONTINUUM BAND
MODEL.

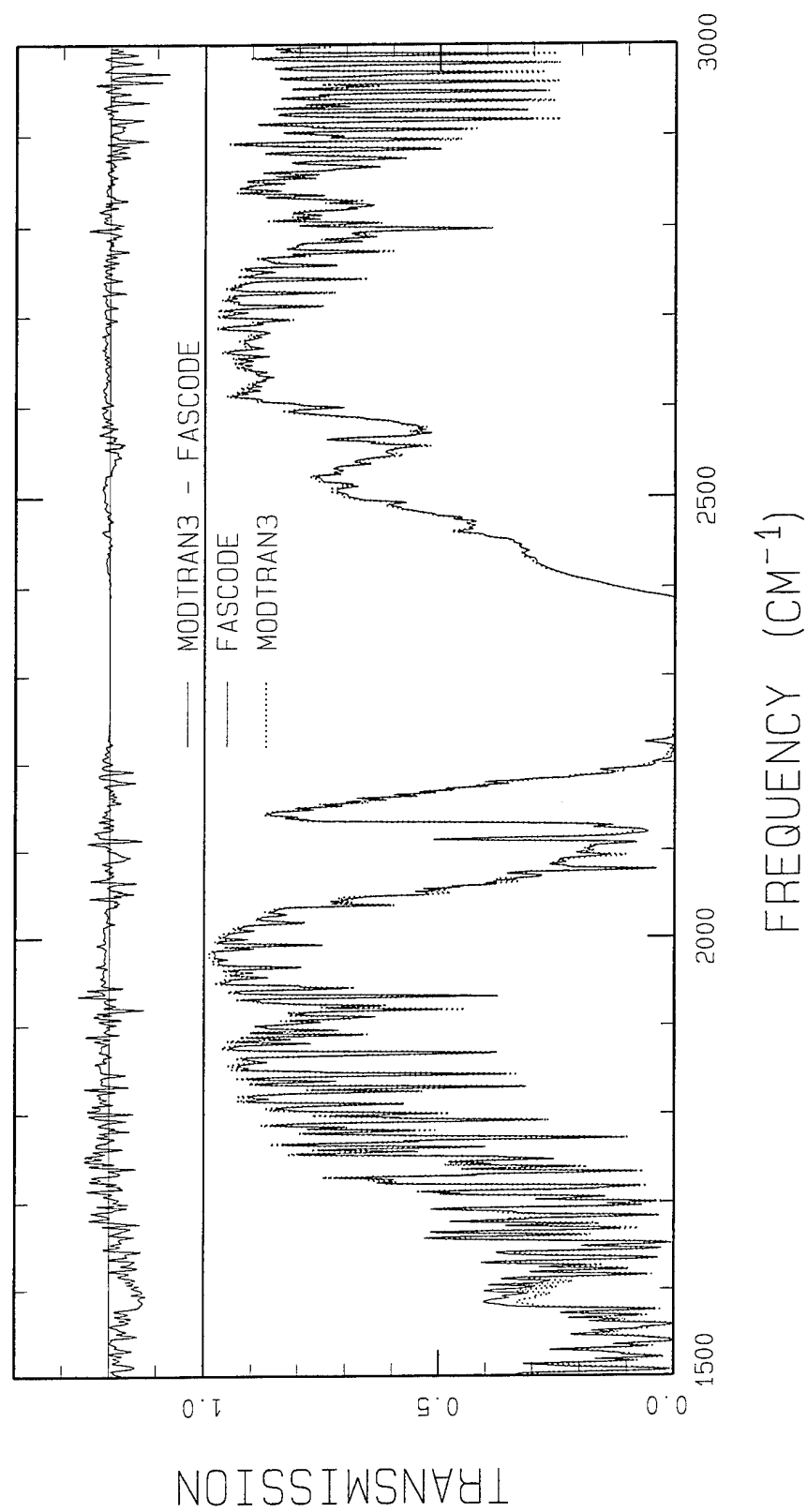
FASCODE USES A MORE
ACCURATE N₂ CONTINUUM
MODEL WHICH SCALES
WITH DENSITY SQUARED.

THE MODEL IN FASCODE
HAS BEEN INTEGRATED
INTO MODTRAN3.

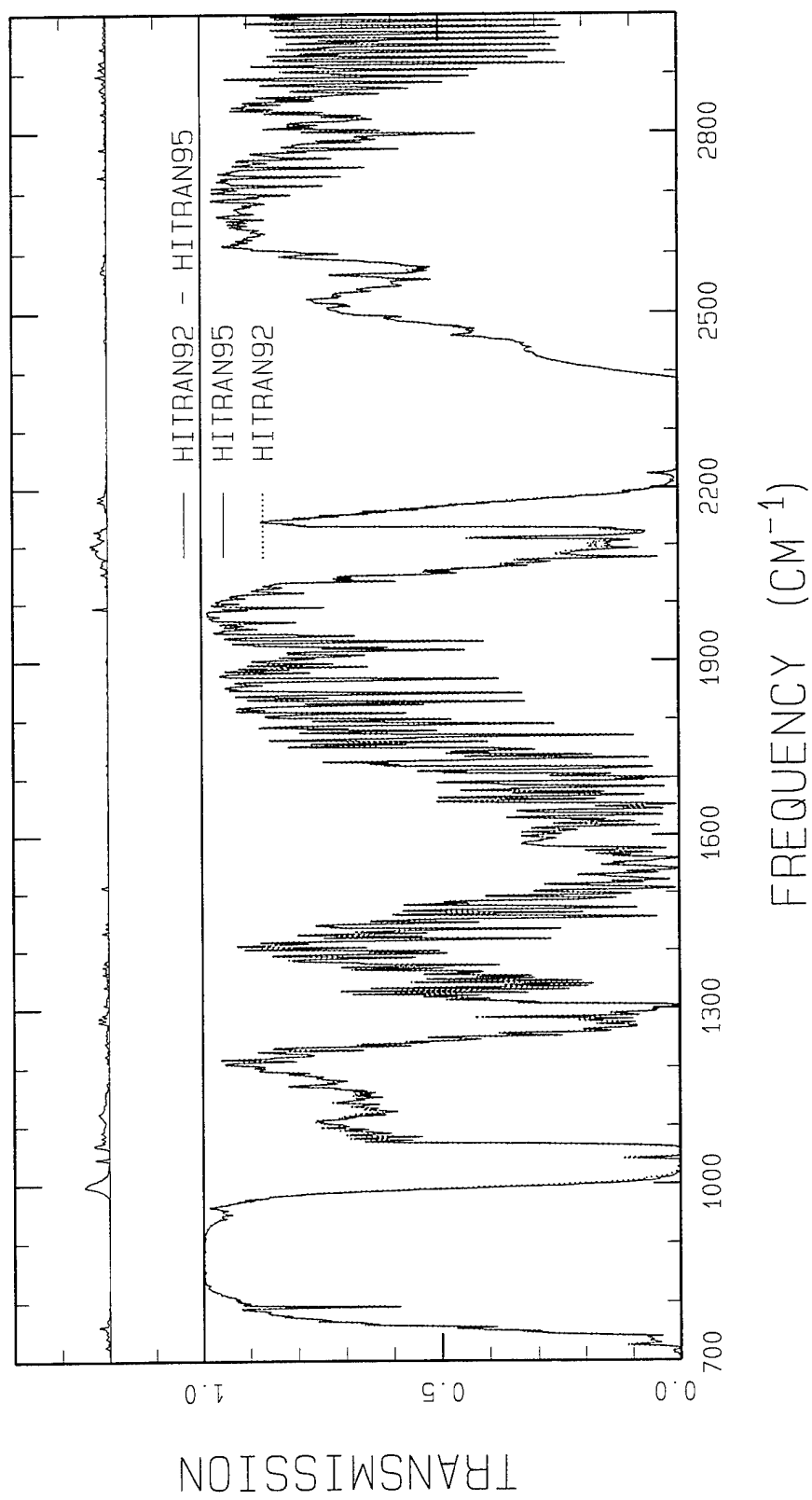
LATEST BENCHMARK (2 CM⁻¹ TRIANGULAR SLIT)



LATEST BENCHMARK (2 CM⁻¹ TRIANGULAR SLIT)



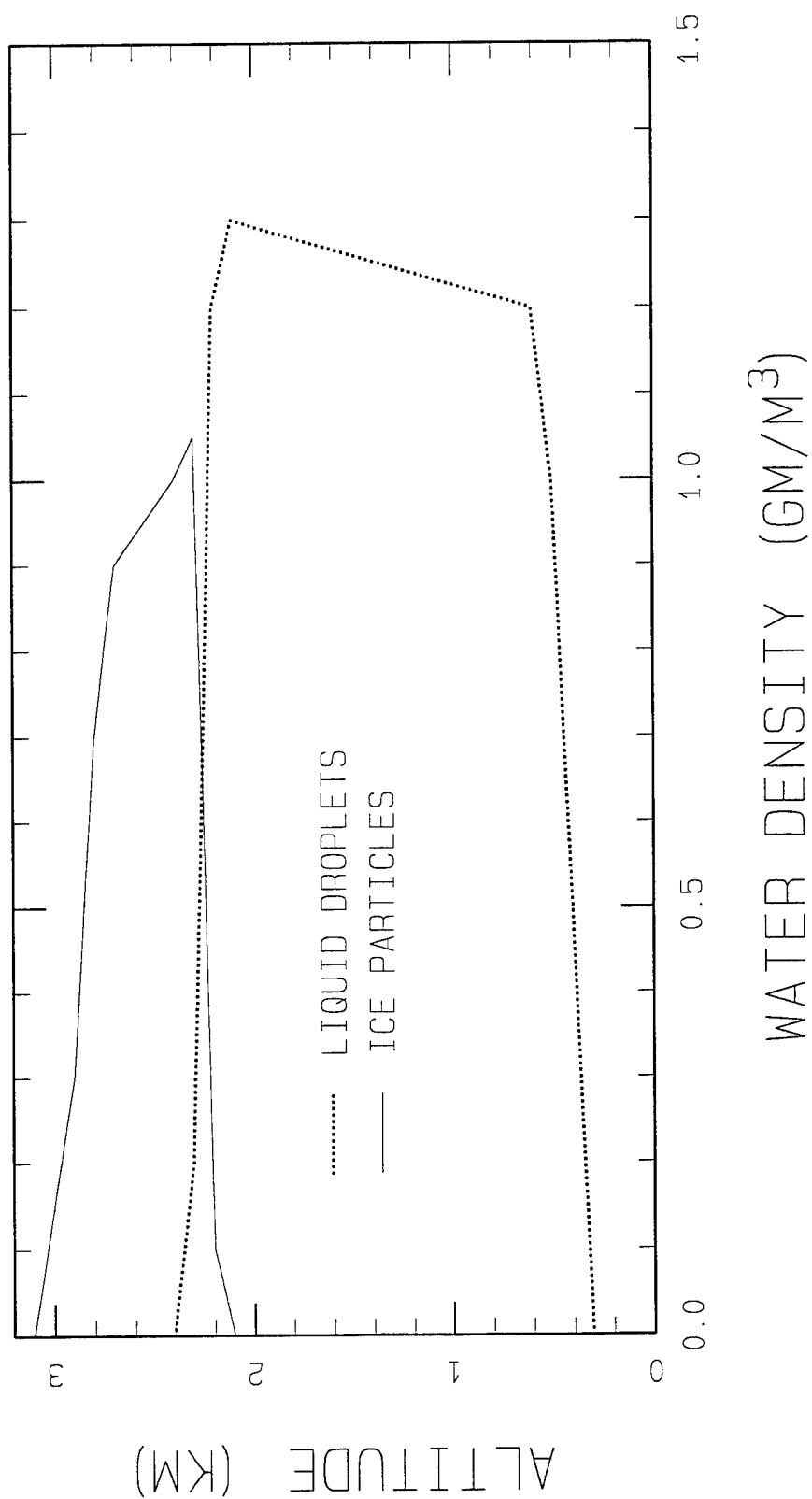
UPGRADE TO HITRAN95 (2 CM⁻¹ TRIANGULAR SLIT)



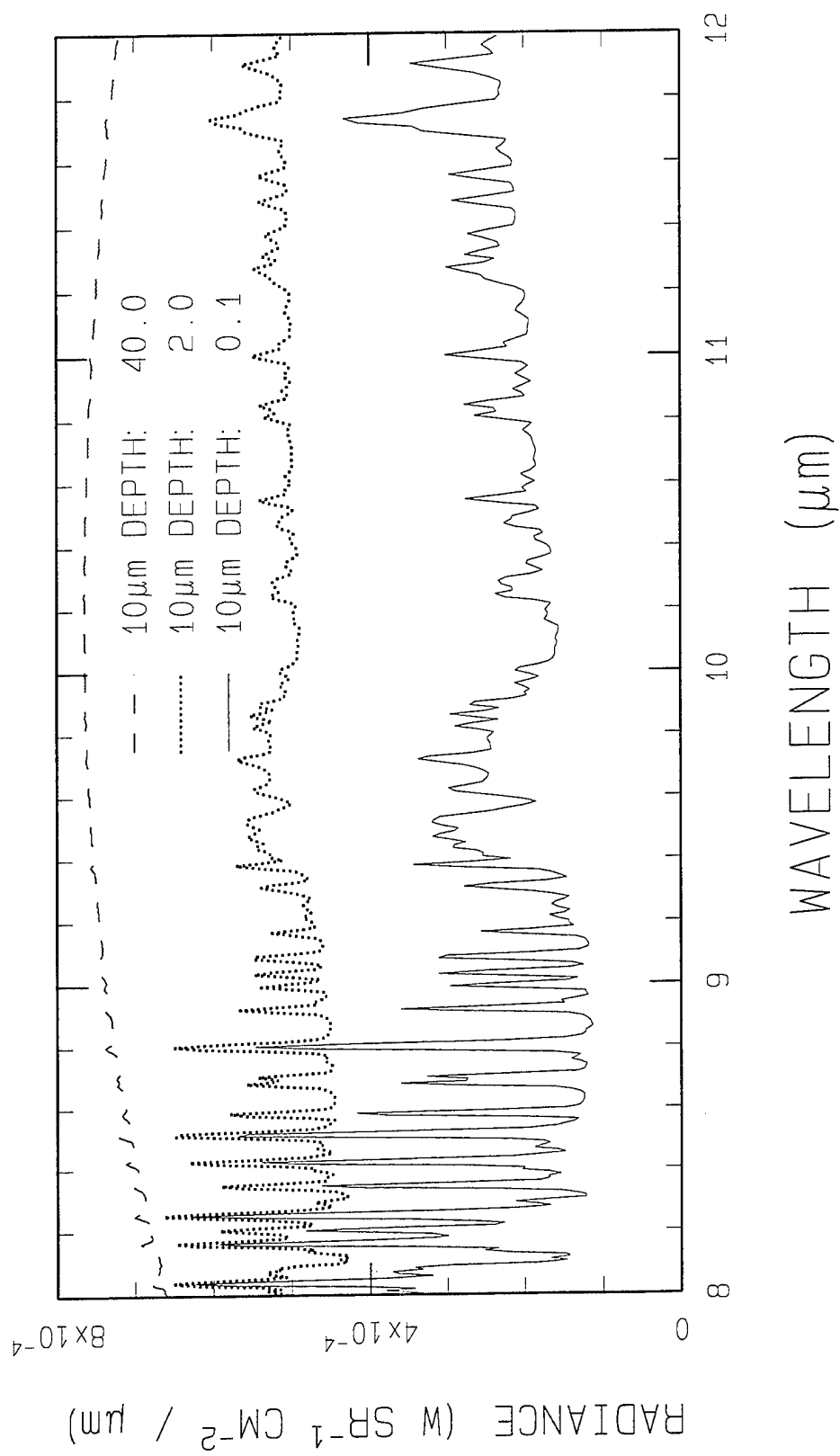
MODTRAN4 CLOUD/RAIN MODEL UPGRADES

- ADJUSTABLE CLOUD PARAMETERS
 - THICKNESS
 - VERTICAL EXTINCTION
 - HUMIDITY
 - BASE ALTITUDE
 - COLUMN AMOUNTS
 - ASYMMETRY FACTORS
- DECOUPLING OF CLOUDS FROM AEROSOLS
- COMBINED WATER DROPLET AND ICE PARTICLE CLOUDS
- USER-DEFINED CLOUD AND RAIN PROFILES
- USER-DEFINED SPECTRAL PROPERTIES
- TABULATED PROFILE AND SPECTRAL OUTPUTS

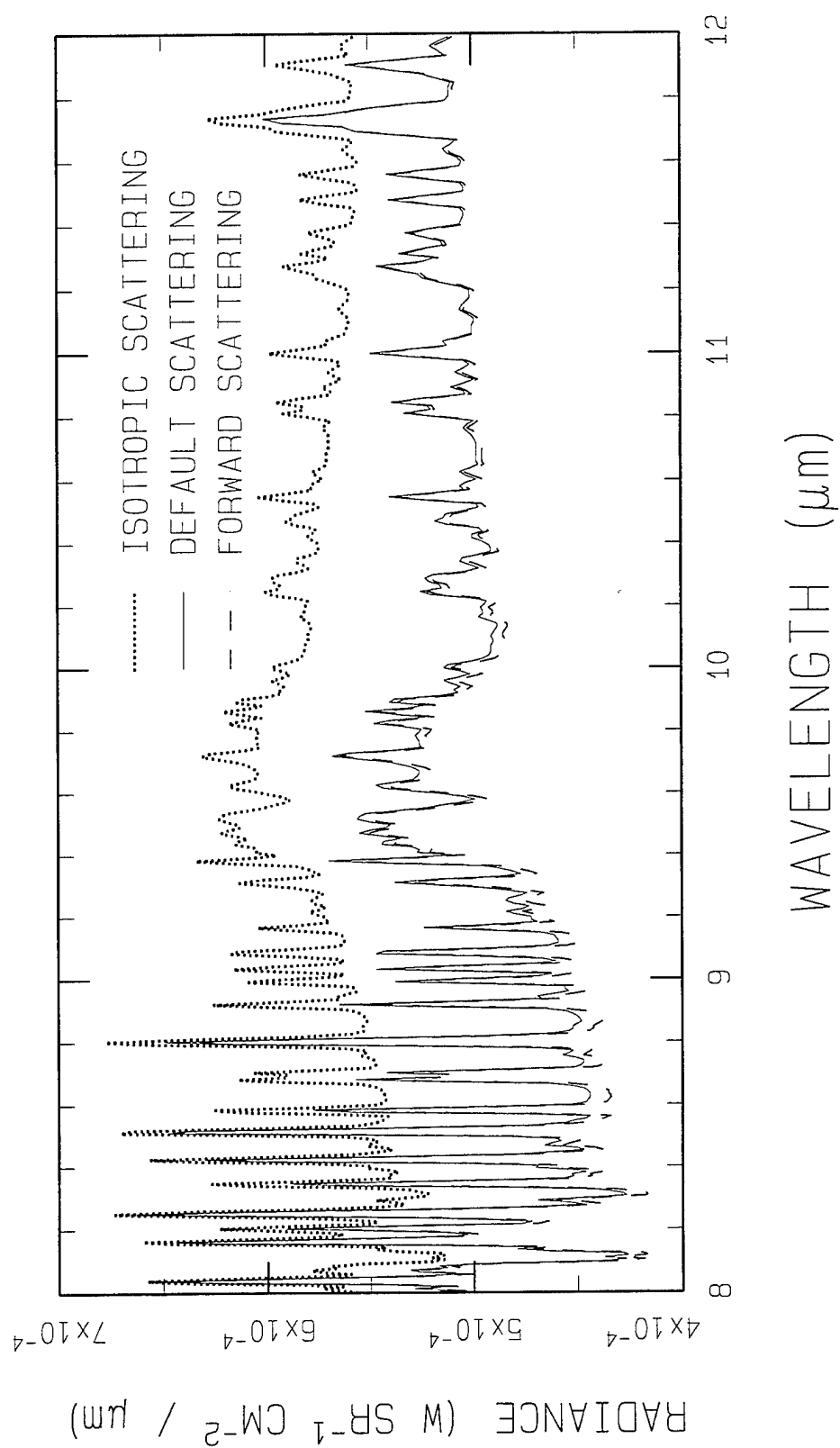
SAMPLE CLOUD PROFILE



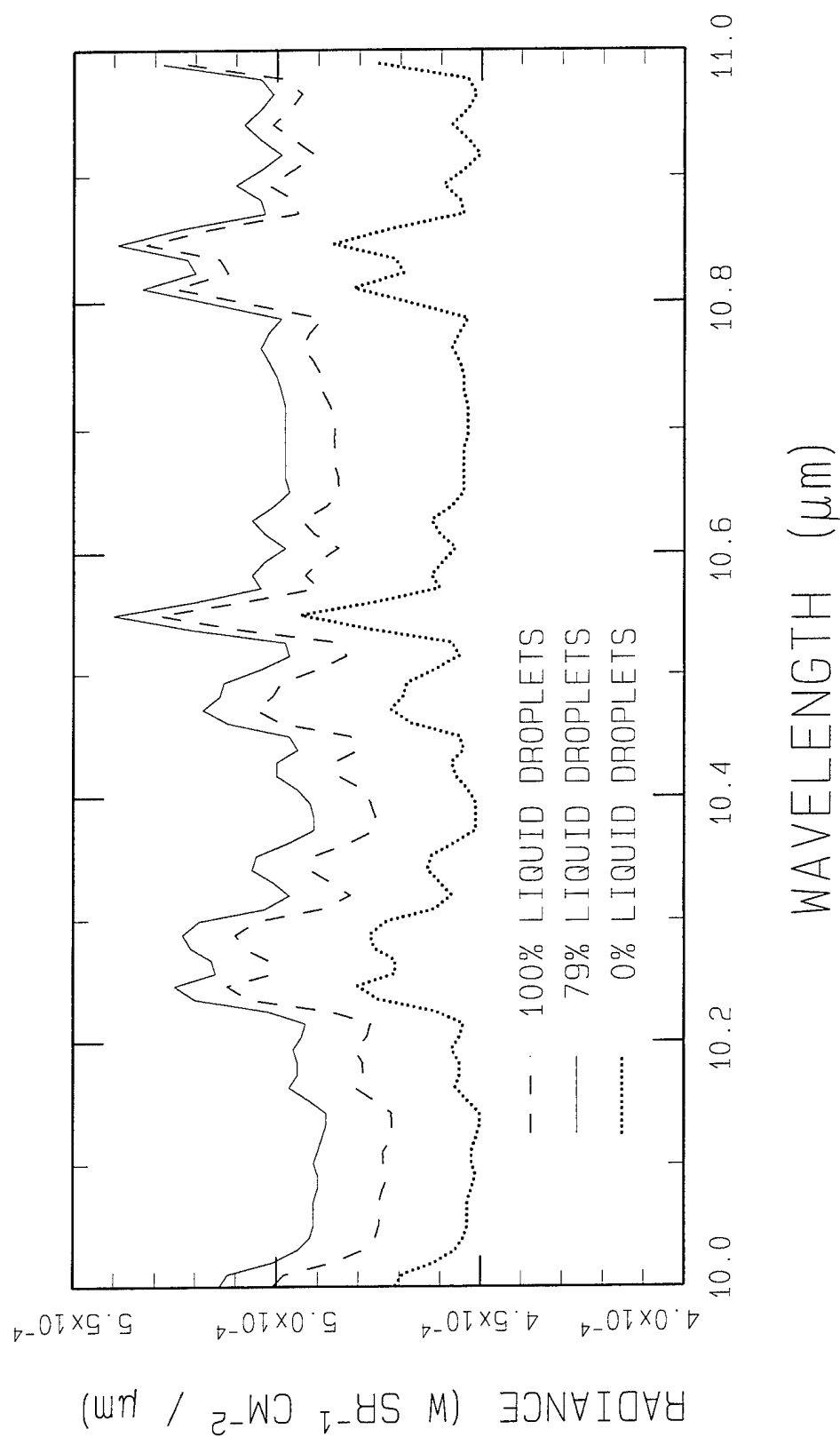
VARYING CLOUD DEPTH (ZENITH FROM GROUND)



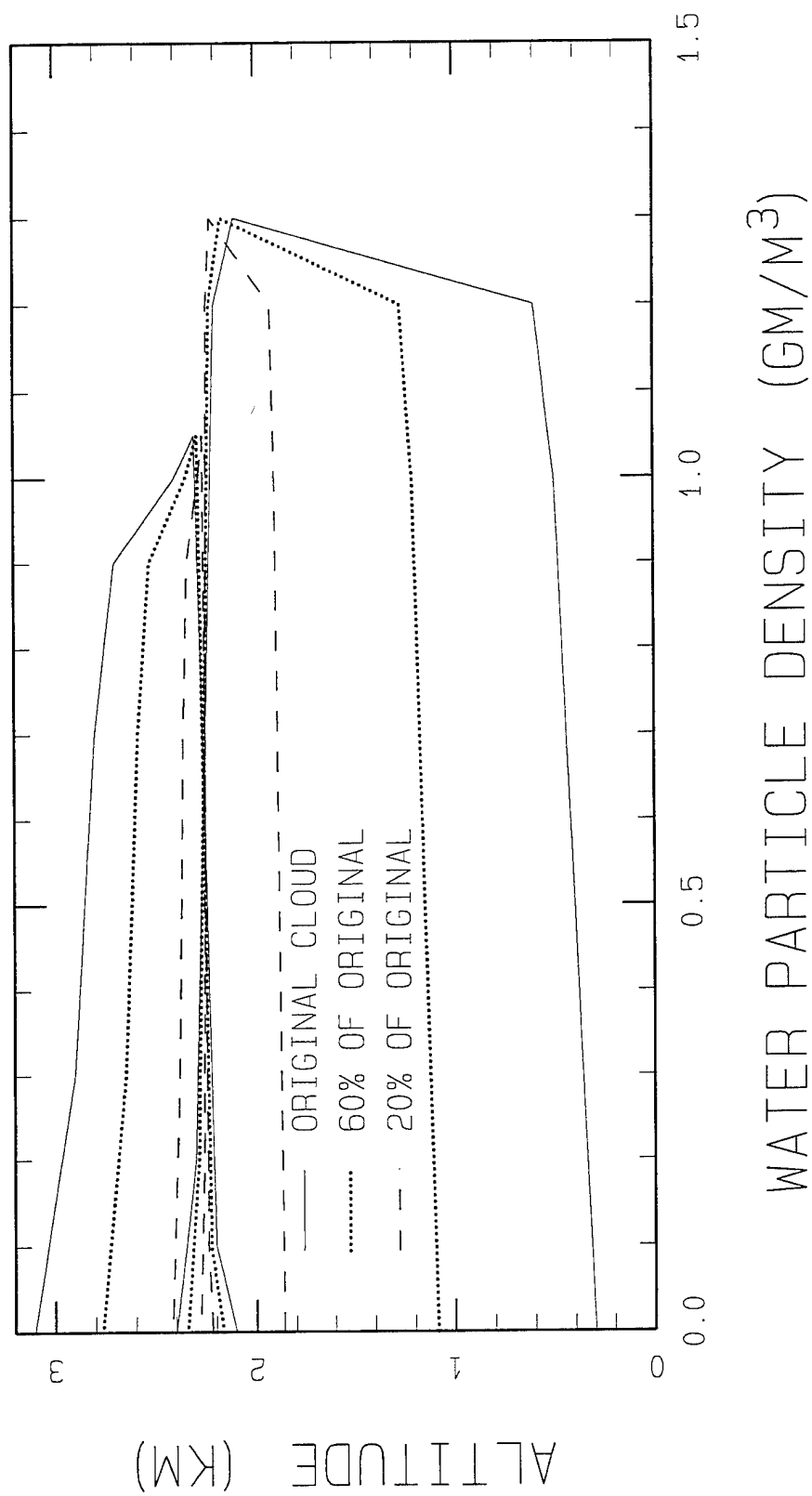
VARYING CLOUD SCATTERING PHASE FUNCTION



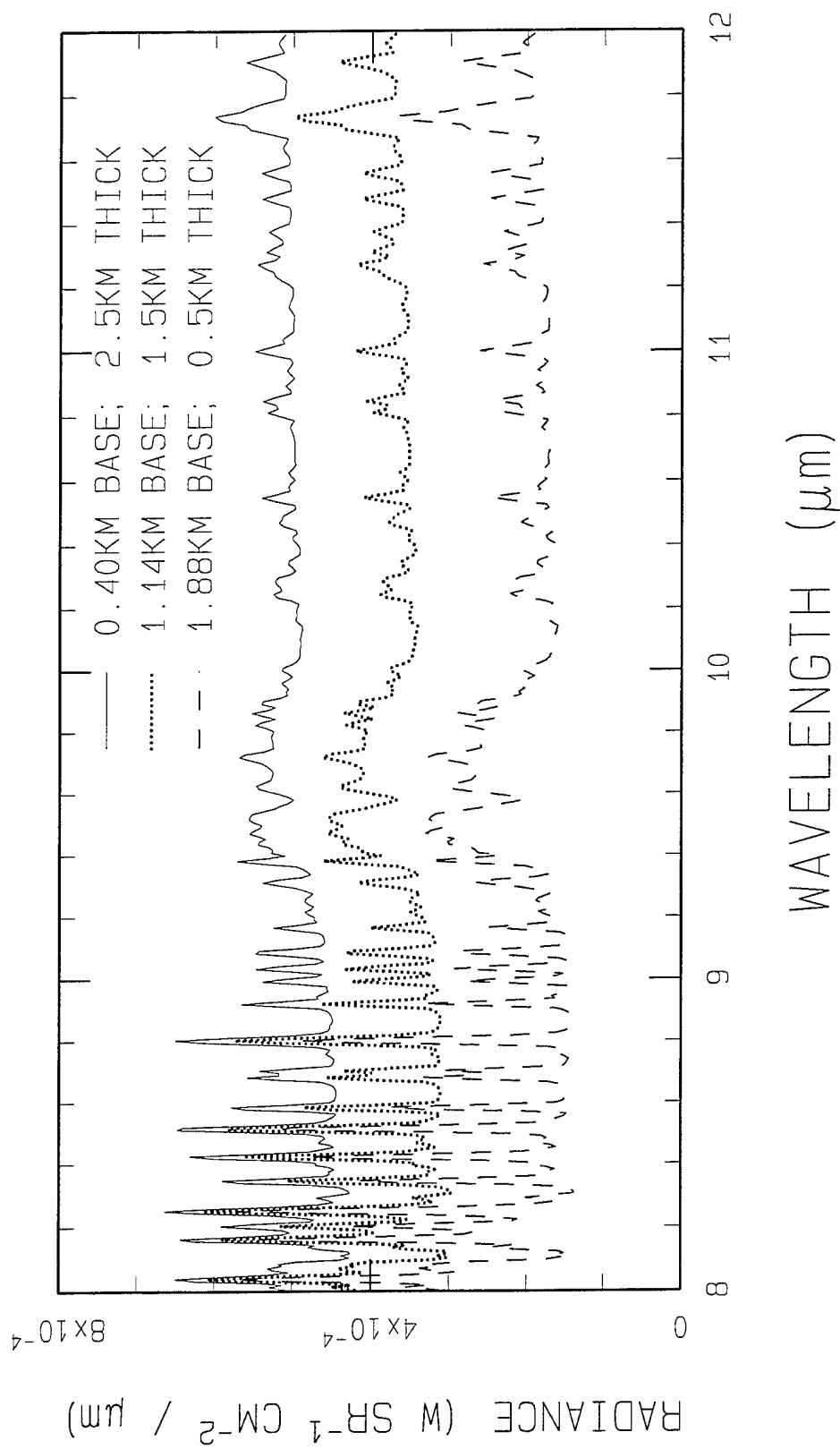
VARYING WATER DROPLET TO ICE PARTICLE RATIO



COMPRESSING CLOUD PROFILE



VARYING CLOUD THICKNESS AND BASE



SUMMARY / STATUS

- RECENT UPGRADES TO MODTRAN BAND MODELS ELIMINATE DISCREPANCIES BETWEEN FASCODE AND MODTRAN FOR THE N₂ CONTINUUM AND REDUCE OVERALL RESIDUALS BETWEEN THE TWO CODES BY MORE THAN A THIRD.
- SMALL INCREASES IN 4.8 AND 9.6 μm O₃ BAND ABSORPTION RESULT FROM UPGRADE TO HITRAN95 BAND MODEL PARAMETERS.
- THE MODTRAN LAYER CLOUD/RAIN MODELS NOW PERMIT THE USER TO EASILY VARY KEY PARAMETERS LIKE ALTITUDE, THICKNESS AND OPTICAL DEPTH. ICE PARTICLE AND WATER DROPLET CLOUDS CAN BE MERGED, AND THEIR PROFILES AND SPECTRAL PROPERTIES VARIED.

The MOSART Code: Its Present and Future Status

by

Dr. William M. Cornette
Photon Research Associates, Inc.
10350 No. Torrey Pines Road, Suite 300, La Jolla, California 92037
wmc@photon.com

Dr. Prabhat K. Acharya
Dr. David R. Robertson
Spectral Sciences, Inc.
99 So. Bedford Street, No. 7, Burlington, Massachusetts 01803
prab@spectral.com
dave@spectral.com

Gail P. Anderson
Geophysics Directorate
Phillips Laboratory (PL/GPOS), Hanscom AFB, Massachusetts 01731
ganderson@plh.af.mil

ABSTRACT

The **MO**derate Spectral Atmospheric Radiance and Transmittance (MOSART) computer code, funded by BMDO and DMSO, unifies the best features of MODTRAN and APART into a single code. These and additional features enable MOSART to be a standard tool for modeling the radiative environment for target signatures and background scenes. MOSART uses MODTRAN's band model approach to compute molecular transmittances and radiances. It has numerous built-in atmospheric species profiles and extensive terrain background and scene characteristic data bases. Additionally, MOSART provides user-friendly input modules including a graphical user interface (GUI). The initial release (Version 1.25) has been available since July 1994, with two releases with minor upgrades in December 1994 (Version 1.30) and May 1995 (Version 1.40). A brief review of MOSART will be presented, along with a summary of recent upgrades. Current and planned uses of MOSART by other simulations will be discussed, and planned and potential upgrades will be presented.

1.0 The MOSART Code

The **MO**derate Spectral Atmospheric Radiance and Transmittance (MOSART) computer code, funded by BMDO and DMSO, unifies the best features of MODTRAN and APART into a single code. These and other additional features enable MOSART to be a standard tool for modeling the radiative environment for target signatures and background scenes. As such, MOSART was selected to provide E²DIS with the natural radiative environment.

1.1 Upgrades for MOSART

The MOSART transmittance and radiance code combines the best features of

MODTRAN 3 and APART 7. In addition to retaining all their features and capabilities, MOSART also represents numerous improvements upon MODTRAN and APART. Below is a summary of new features (new to either MODTRAN or APART) and upgrades in MOSART.

1.1.1 General Improvements and Features

- o Upgraded numerical algorithms for faster speed and better accuracy.
- o Utility to assist in the determination of machine-dependent parameters.
- o Portable code, written in ANSI X3.9-1978 FORTRAN (FORTRAN 77).
- o Versatile line-of-sight (los) specification and robust los computation.
- o Multiple azimuth los computations to reduce computational overhead.
- o Simultaneous computation of background and target path-radiances and transmittances also to reduce overhead.
- o Ability to use MODTRAN's combined band model tape or individual molecular band model parameters.

1.1.2 Input and Output

- o Improved input scheme
 - Interactive, menu driven utility program to create input files (a GUI version is also available).
 - User-friendly input file (descriptive words, mnemonic and case-insensitive character inputs, list-directed numerical inputs).
 - Capability to translate MODTRAN input files into MOSART input files.
- o Output files corresponding to TAPE7 and TAPE8 of MODTRAN.
- o Binary output files for various utilities and other codes.

1.1.3 Radiative Transfer

- o Upgrade to the exponential sum fit for multiple scatter.
- o Addition of scattering (both aerosol and molecular) to sky-noise calculations.
- o Sensor aperture correction to scintillation calculations.
- o New phase function, based on the work of Cornette and Shanks.

1.1.4 Terrain Materials

- o Upgrades to the terrain material thermal properties database.
- o Upgrades to the models for water density; latent heat of water; specific heat of water and ice; thermal conductivity of water, ice, and snow.
- o Upgrades to scene definition to allow water and snow amounts to modify local terrain scene.
- o Improved algorithm for estimating index of refraction from reflectance.
- o A directional emissivity model for terrain.
- o A bidirectional reflectivity model for terrain.
- o Incorporation of Beaufort scale for wave height as a function of wind speed.
- o A sea surface temperature model and database.
- o A sea water reflectivity model.

1.1.5 Atmospheric Models

- o Upgrade of interpolation of model atmosphere parameters from 1D to 2D, with

- o capability to increase to 3D.
- o Upgrade of relative humidity to the Goff-Gratch algorithm.
- o A temperature dependent stratospheric aerosol model.
- o A temperature dependent cirrus cloud model.
- o Capability to index the default boundary layer aerosol to terrain scene type.
- o Capability to estimate visibility based upon aerosol type and relative humidity.
- o Temporal variations in molecular concentrations.
- o Addition of aerosols to broad-band heat transfer calculations.

1.2 Recent Upgrades for Version 1.40

In preparing the release of Version 1.40, a number of upgrades were included, as presented below.

1.2.1 Terrain Data Base Upgrades

To provide appropriate interfaces with other phenomenology codes used by E²DIS (e.g., CLDSIM, GENESSIS), MOSART was modified to produce a data base of atmospheric radiance and transmittance parameters that could be accessed by a fast interpolator. Also, to assist in the terrain scene generation, data bases for supporting the prediction of terrain material temperatures were upgraded and augmented. The algorithms for predicting these temperatures were compared against available data and modified as appropriate. Additional terrain materials were added to the MOSART data base:

MODTRAN Ocean
 GENESSIS Water Ocean
 MODTRAN Snow Cover (Fresh)
 GENESSIS Fresh Snow (50 micron radius)
 GENESSIS Old Snow (1000 micron radius)
 MODTRAN Cloud Deck (diffuse only)
 Still Air
 Dry grass (Dry meadow fescue grass)
 MODTRAN Grass
 MODTRAN Dead Grass
 MODTRAN Burnt Grass
 Lawn grass (Apple leaves to simulate irrigated crops)
 MODTRAN Forest
 MODTRAN Farm
 MODTRAN Maple Leaf
 Beach sand (Beach sand; silica sand and silt loam)
 Limestone-Silt-Sand
 Limestone-Silt
 Salt-Silt
 Silt-Sand
 Limestone Rock (Solid limestone rock)
 Sandstone Rock (Red)
 Varnished Sand
 Varnished Sandstone (Desert varnish)
 Dry Silt Playa
 Wet Silt Playa
 Dry Silt-Salt Flats
 Wet Silt-Salt Flats
 MODTRAN Desert

These additional terrain materials will assist the E²DIS scene generator in selecting appropriate material classifications within a given scene. A new global ecosystem/scene index/water content data base at higher spatial resolution was incorporated into the model for scene construction. Also, several statistical scenes were added to the MOSART data base:

Iraq and Syria
North Korea
Kern River, California
Global

Iran
Pakistan
USA (North America)

1.2.2 MODTRAN 3 Compatibility

Also, to insure that MOSART includes the most current models, the following upgrades were incorporated from the soon-to-be-released MODTRAN 3:

New Band model

- Goody addition
- Modified algorithm
- New band parameters

New Clough H₂O continuum

N₂ pressure induced continuum

New CO₂ continuum

New UV cross-sections for SO₂, NO₂, O₃

Heavy molecule IR cross sections (CFC's, CCl₄, N₂O₅)

New solar irradiance

Variable surface emissivity-reflectivity

Heavy molecule amounts in user-defined atmosphere

2.0 MOSART UTILITIES

In addition to the main MOSART code, a number of utilities have been developed to assist the user in interpreting or modifying the output of MOSART. These utilities include:

2.1 Installation Utilities

FPTEST: Performs floating point numeric checks and determines system-specific parameters to assist in the installation of MOSART

INSTDB: Installs the various MOSART data bases

2.2 Formatting and display utilities

ASCBIN: Converts binary files to ASCII text files (and vice versa) and creates spectral tables of various parameters

CRFILE: Creates various MOSART input files in an interactive manner; converts MODTRAN input files into MOSART input files

MIB: MOSART Input Builder is a Graphical User Interface (GUI) for creating MOSART input files and submitting jobs;

it requires X-Windows and MOTIF

PLTGEN Creates spectral plots of a number of spectral parameters;
it requires the NCAR plotting package

2.3 Phenomenology utilities

BBTEMP: Converts radiance to equivalent blackbody temperature

FACET: Calculates source, apparent, and contrast signatures
associated with flat, cylindrical, and spherical surfaces

MRFLTR: Integrates MOSART output over user-specified sensor
response functions

SCNGEN: Creates a statistical two-dimensional scene representation

TERTEM: Calculates the terrain material temperatures as a function
of the time of day, altitude, and surface orientation for
a library of terrain materials

VISUAL: Converts radiance in the visible spectral region
(0.35-0.80 micron) to luminance and determines the color
content of the luminance

4.0 CONCLUSION

With the release of Version 1.40, all current efforts have been completed. However,
a number of potential upgrades are being considered, including:

4.1 Cloud Modeling Upgrades

- o Diffuse transmission through clouds
- o Broken cloud fields (multi-layered)

4.2 Atmospheric Characterization

- o Interface with weather/climatology data bases
- o 3-dimensional representation
- o Allow insertion of user-defined elements (e.g., clouds, smoke)
- o Include global humidity data bases

4.3 Terrain Characterization

- o Higher spectral resolution terrain material reflectivity
- o Interface with Defense Mapping Agency/Terrain Modeling Project Office
Materials
- o Improved snow cover, sea ice, and sea temperature data bases
- o Include soil moisture data base

4.4 Radiative Transfer

- o Add the DISORT routines from MODTRAN 3 to MOSART

- o Refine new exponential sum fit algorithm
- o Improved solution to equation of radiative transfer
- o Add microwave/millimeter wave capability
- o Add polarization

4.5 User-interface

- o Allow multiple, overlapping sensor response curves
- o Provide a geometry visualizer with GUI

5.0 REFERENCES

Cornette, W.M., D.C. Robertson, and G.P. Anderson, The Moderate Spectral Atmospheric Radiance and Transmittance (MOSART) Program. Proc. Workshop on Atmospheric Correction of Landsat Imagery. (1993) pp 70-74. Also presented at the Annual Review Conference on Atmospheric Transmission Modeling, Geophysics Directorate (1993)

Cornette, W.M., The MOSART Global Climatological and Terrain Data Bases. Presented at the Annual Review Conference on Atmospheric Transmission Modeling, Geophysics Directorate (1993). Also presented at the Aerial Targeting Environment Meeting (1993).

Cornette, W.M., Update on the Moderate Spectral Atmospheric Radiance and Transmittance (MOSART) Code. Presented at the Annual Review Conference on Atmospheric Transmission Modeling, Geophysics Directorate (1994)

Cornette, W.M., P.K. Acharya, and G.P. Anderson, Using the MOSART Code for Atmospheric Correction. Invited Paper. 1994 International Geoscience and Remote Sensing Symposium Proceedings. pp 215-219 (1994)

Cornette, W.M. and P.K. Acharya, Moderate Spectral Atmospheric Radiance and Transmittance (MOSART) Code. Vol. I: Installation Reference Manual, PRA R-067-93; Vol. II: User's Reference Manual, PRA-054-94; Vol. III: Technical Reference Manual, PRA R-090-93; Vol. IV: Software Reference Manual, R-069-93. (1994)

RRTM: A Rapid Radiative Transfer Model

Eli J. Mlawer, Steven J. Taubman*, Shepard A. Clough
Atmospheric and Environmental Research, Inc.,
Cambridge, Massachusetts

Introduction

A rapid radiative transfer model (RRTM) for the calculation of longwave clear sky fluxes and cooling rates has been developed. The model, which uses the correlated-k method, is both accurate and computationally fast. The foundation for RRTM is the LBLRTM line-by-line radiative transfer model from which the relevant k-distributions are obtained. LBLRTM, which has been extensively validated against spectral observations (e.g., HIS, AERI (Brown et al. 1995)), is used to validate the flux and cooling rate results from RRTM. Validations of RRTM's results have been performed for the tropical, midlatitude summer, and midlatitude winter atmospheres, as well as for the four ICRCCM (InterComparison of Radiation Codes used in Climate Models (Ellingson and Fouquart, 1991)) cases from the SPECTRE experiment. Details of some of these validations are presented below. RRTM has the identical atmospheric input module as LBLRTM, facilitating intercomparisons with LBLRTM and application of the model at the ARM CART sites.

Optical depths

RRTM divides the longwave spectral region into 16 bands chosen for their homogeneity of contributing species and radiative transfer properties. A list of these bands and their respective key species is presented in Table 1. The selection of the spectral regions is facilitated by consideration of the Plates of spectral cooling rate as a function of log pressure provided by Clough and Iacono (1995).

In RRTM, all the optical depths in a given spectral band are represented by a small set of characteristic values that are used to perform the radiative transfer. The procedure that determines these characteristic values begins with the creation of a k-distribution, which involves the assignment to each absorption coefficient $k(\nu)$ a value g ($0 \leq g \leq 1$) that represents the fraction of the absorption coefficients in the band smaller than $k(\nu)$. This procedure arranges the k-values in ascending order and defines a mapping $\nu \rightarrow g$ that provides an important perspective in the development of the model (West et al. 1990). The

* currently at GFDL

function $k(g)$ is then divided into a small number of intervals each having a limited range of $k(g)$ values and a representative value $k(g_i)$ is obtained for each interval. Since the equations used to calculate radiances have no explicit dependence on wavenumber, $k(g_i)$ can be used to estimate the radiance for the entire interval. The resulting radiances, weighted by the sizes of their respective intervals, can then be summed to yield the total radiance for the spectral band. This method for calculating radiances for inhomogeneous atmospheres is referred to as the correlated- k method.

Each spectral band in RRTM is broken into 16 intervals with half-gauss quadrature spacing modified such that 7 intervals lie between $g = 0.98$ and $g = 1.0$. This modified quadrature spacing is done to better represent the high values of $k(g)$ associated with the centers of the spectral lines. For RRTM we have chosen to calculate each $k(g_i)$ by averaging the $k(g)$ values in each interval so as to include the contribution from every k -value in the interval. The full set of k -values comes from LBLRTM, which uses the water vapor continuum model CKD_2.1 (Clough et al. 1989) and the 1992 HITRAN line parameter database (Rothman et al. 1992).

For an arbitrary atmosphere, $k(g_i)$ values are obtained by linear interpolating in log pressure and temperature stored values of $k(g_i)$. In bands with more than one key contributing species, an additional interpolation is performed in a parameter, η , that represents the relative (strength-weighted) abundance of the two most critical species, which greatly affects the mapping $\nu \rightarrow g$. This parameter, called the binary species parameter, is defined as

$$\eta \equiv \frac{S_1 W_1}{S_1 W_1 + S_2 W_2} ,$$

where S_i is the integrated line strength of species i over the spectral band and W_i is the layer column amount of that species. For these overlap bands, values of $k(g_i)$ are stored for reference atmospheres with values of η equal to $0, \frac{1}{8}, \frac{2}{8}, \dots, 1$ for a given pressure and temperature in the lower atmosphere and for values of η equal to $0, \frac{1}{4}, \frac{1}{2}, \frac{3}{4}$, and 1 in the upper atmosphere. For certain bands the species considered most critical are changed with altitude regime. (See Table 1.) In all bands, reference $k(g_i)$ values are stored for 59 pressure levels from 1050 - 0.01 mb, with a fixed ratio of ~ 1.2 between successive pressure values. At each reference pressure level, $k(g_i)$ values are stored at 5 temperatures $T_{\text{ref}}, T_{\text{ref}} \pm 15\text{K}, T_{\text{ref}} \pm 30\text{K}$, where T_{ref} is obtained from the midlatitude summer temperature profile. The $k(g_i)$ values that are the result of this interpolation procedure include the spectral line contributions from the major species and the water vapor foreign continuum.

The contribution of the water vapor self-continuum to the optical depth is included by a separate procedure due to its quadratic dependence on water vapor abundance. First, the mapping $\nu \rightarrow g$ for all absorbers in each band is determined for two midlatitude summer atmospheric layers at 296 K and 260 K. The two mappings are then applied to the self-continuum absorption coefficients in the band at the respective temperatures. This procedure yields, at each temperature, a set of average self-continuum absorption coefficients $k_s(g_i)$, which are used to obtain the values of $k_s(g_i)$ at any temperature by appropriately interpolating. Finally, the contribution of the self-continuum to the optical depth is computed by multiplying $k_s(g_i)$ by a scaling factor that is quadratic in water vapor density.

Radiative transfer algorithm

RRTM performs a separate radiative transfer through the specified altitude range for each interval in each band. This, in effect, treats each interval, which "represents" a large number of frequencies in the band, in the same manner as a single spectral point is treated in a line-by-line model. As does LBLRTM, RRTM makes use of the "linear in τ " approximation for vertically inhomogeneous atmospheres and uses a Pade approximation to calculate an effective Planck function for each layer (applicable for any τ in the layer) by creating an appropriately weighted combination of the Planck function at the layer boundary temperature and the Planck function at the mean layer temperature (Clough et al. 1992). However, for a model using the correlated-k method it is non-trivial to determine the appropriate (layer and level) Planck functions for any interval in a band since the Planck functions evaluated at all frequencies that are associated with that interval must be taken into account. Moreover, the mapping $\nu \rightarrow g$ can vary dramatically with atmospheric properties, especially the abundance of the band's key species, thereby limiting the accuracy of approximating the Planck function for the interval by the value of the Planck function at a single "dominant" frequency. This issue is addressed in RRTM by a two-part procedure. First, the integrated Planck energy for a band is a function only of temperature and is easily calculated and stored. The fraction of this energy that is due to the frequencies associated with an interval, defined by

$$f_g \equiv \frac{B_g W_g}{\frac{1}{\nu_2 - \nu_1} \int_{\nu_1}^{\nu_2} B_\nu(T) d\nu}$$

where B_g is the average Planck function of the frequencies in the interval, W_g is the weight for the interval, and ν_1 and ν_2 are the frequency boundaries of the band, depends primarily on the mapping $\nu \rightarrow g$, which, in turn, is mainly dependent on the abundance of the band's

key species. Therefore, for bands with one key species, f_g is considered constant. For bands with two key species, f_g is treated as a function of η and is computed by linear interpolation from stored f_g values calculated for reference values of η . All calculations performed to generate reference f_g values for a band are done at a pressure level appropriate for that band and use a midlatitude summer atmospheric profile. At execution time, RRTM computes the Planck function for an interval by multiplying the calculated f_g by the integrated Planck function for the band. The use of this procedure to calculate the Planck function assures that the total Planck energy is correct at every level in each band. The radiances calculated by the methods described above are then integrated (which is approximated by a first-moment Gaussian quadrature) over a hemisphere to yield fluxes.

Timing

Results of preliminary timing tests for RRTM indicate that computing the fluxes and cooling rates for a 51-layer atmosphere, which includes the performance of 256 (16 intervals · 16 bands) upward and downward radiative transfer calculations and, therefore, the computation of 256 optical depths per layer, takes 0.05 s on a SPARCserver 1000. This compares favorably to other rapid radiative transfer models. A further indication of the computational efficiency of the model is that these radiative transfer operations in RRTM take 1.8 times the amount of time needed to perform 51·16·16 exponentials. Further evaluation of RRTM's timing is in progress.

Validations

The results of flux and cooling rate calculations performed by RRTM have been compared to those done by LBLRTM for the midlatitude summer, midlatitude winter, and tropical atmospheres. Figures 1-4 show the results of these validations for the midlatitude summer atmosphere for the spectral range 10-980 cm^{-1} . The RRTM and LBLRTM upward flux calculations at all altitudes differ by no more than 0.25 W/m^2 (Figure 2). For downward fluxes, errors of a few percent for the entire spectral range are typical in the upper atmosphere, with an error at the tropopause of 0.4 W/m^2 . The errors in downward flux in the lower atmosphere are smaller, including an error in surface downward flux of 0.1 W/m^2 . The errors in the heating rate calculations (Figure 4) also are smaller near the surface, with typical errors in the 1000-100 mb range of less than 0.05 K/day. Errors in cooling rates between 1.0 and 0.1 mb can be as high as 0.5 K/day. Similar results to these have been found for the midlatitude winter and tropical atmospheres. In addition, very satisfactory results

are obtained relative to both LBLRTM and observations for the calculation of downward surface radiance for the four SPECTRE atmospheres used in ICRCCM.

Summary

RRTM currently provides an accurate and rapid method for computing longwave fluxes and cooling rates for an arbitrary clear atmosphere. RRTM, due to its use of linear interpolation to determine all necessary physical quantities, does not suffer from discreteness problems, enabling the model to accommodate microlayering.

The next phase in the development of RRTM will involve the extension of the algorithm to include the shortwave region of the spectrum and will allow the calculation of fluxes and cooling rates for both clear and cloudy skies.

Acknowledgments

The authors would like to thank Luke Chen for providing the code used to create the k-distributions. The authors also wish to acknowledge the contributions of Robert Bergstrom, Patrick Brown, Ronald Farren, Richard Goody, and Michael Iacono. This research was supported by the Department of Energy (DE-FG02-90ER61064).

References

Bergstrom, R., private communication.

Brown, P.D., S.A. Clough, N.E. Miller, T.R. Shippert, D.D. Turner, R.O. Knuteson, H.E. Revercomb and W.L. Smith, Initial analyses of surface spectral radiance between instrument observations and line by line calculations. Fifth Atmospheric Radiation Measurement (ARM) Science Team Meeting, San Diego, California.

Clough, S.A., F.X. Kneizys, and R.W. Davies, Line shape and the water vapor continuum, *Atmos. Res.*, **23**, 229-241, 1989.

Clough, S.A., M.J. Iacono, and J.-L. Moncet, Line-by-line calculations of atmospheric fluxes and cooling rates: application to water vapor, *J. Geophys. Res.*, **97**, 15761-15785, 1992.

Clough, S.A. and M.J. Iacono, Line-by-line calculation of atmospheric fluxes and cooling rates: 2. Application to carbon dioxide, ozone, methane, nitrous oxide and the halocarbons. *J. Geophys. Res.*, in press.

Ellingson, R.G. and Y. Fouquart, The intercomparison of radiation codes in climate models: an overview, *J. Geophys. Res.*, **96**, 8925-8927, 1991.

Fu, Q., and K.N. Liou, On the correlated k-distribution method for radiative transfer in nonhomogeneous atmospheres, *J. Atmos. Sci.*, **49**, 2139-2156, 1992.

Lacis, A.A. and V. Oinas, A description of the correlated k-distribution method for modeling nongray gaseous absorption, thermal emission, and multiple scattering in vertically inhomogeneous atmospheres, *J. Geophys. Res.*, **96**, 9027-9074, 1991.

Rothman, L.S., R.R. Gamache, R.H. Tipping, C.P. Rinsland, M.A.H. Smith, D. C. Benner, V. Malathy Devi, J.-M. Flaud, C. Camy-Peret, A. Perrin, A. Goldman, S.T. Massie, L.R. Brown, and R.A. Toth. HITRAN molecular database: Edition '92. *J. Quant Spectrosc. Radiat. Transfer*, **48**, 469-507, 1992.

Toon, O.B., C.P. McKay, T.P. Ackerman, and K. Santhanam, Rapid calculation of radiative heating rates and photodissociation rates in inhomogeneous multiple scattering atmospheres, *J. Geophys. Res.*, **94**, 16287-16301, 1989.

West, R., D. Crisp, and L. Chen, Mapping transformations for broadband atmospheric radiation calculations, *J. Quant. Spectrosc. Radiat. Transfer*, **43**, 191-199, 1990.

RRTM Bands

Wavenumber Range (cm ⁻¹)	Key Species in RRTM	
	1050 - 96 mb	96 - 0.01 mb
10 - 250	H ₂ O	H ₂ O
250 - 500	H ₂ O	H ₂ O
500 - 630	H ₂ O, CO ₂	H ₂ O, CO ₂
630 - 700	H ₂ O, CO ₂	CO ₂ , O ₃
700 - 820	H ₂ O, CO ₂	CO ₂ , O ₃
820 - 980	H ₂ O	—
980 - 1080	H ₂ O, O ₃	O ₃
1080 - 1180	H ₂ O	O ₃
1180 - 1390	H ₂ O, CH ₄	CH ₄
1390 - 1480	H ₂ O	H ₂ O
1480 - 1800	H ₂ O	H ₂ O
1800 - 2080	H ₂ O, CO ₂	—
2080 - 2250	H ₂ O, N ₂ O	—
2250 - 2380	CO ₂	CO ₂
2380 - 2600	N ₂ O, CO ₂	—
2600 - 3000	H ₂ O, CH ₄	—

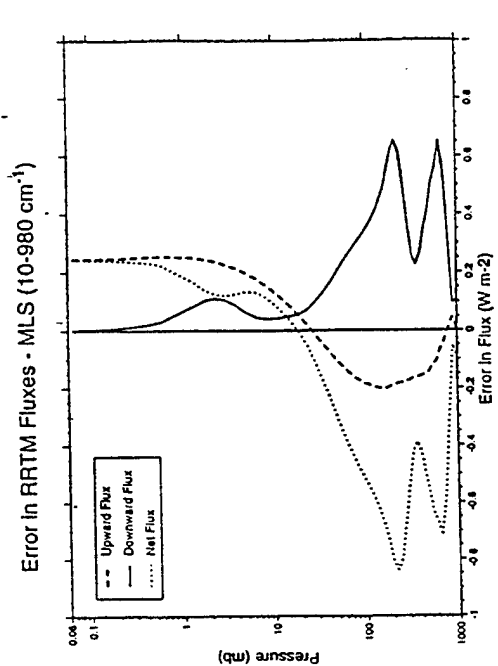


Fig. 1. Fluxes as a function of log pressure from the LBLRTM line by line model and from the RRTM rapid radiative transfer model.

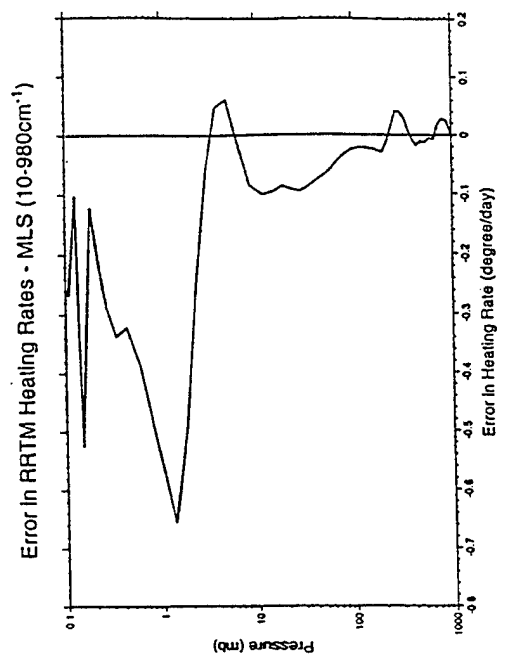


Fig. 2. Difference between RRTM and LBLRTM heating rates as a function of pressure.

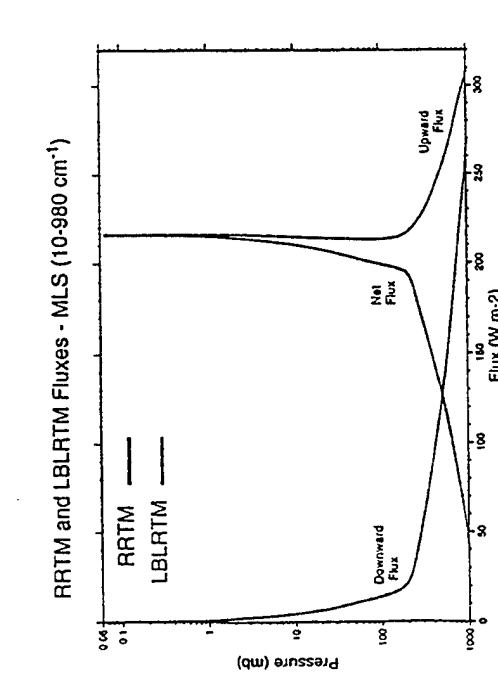


Fig. 3. Heating rates as a function of log pressure from the LBLRTM line by line model and from the RRTM rapid radiative transfer model.

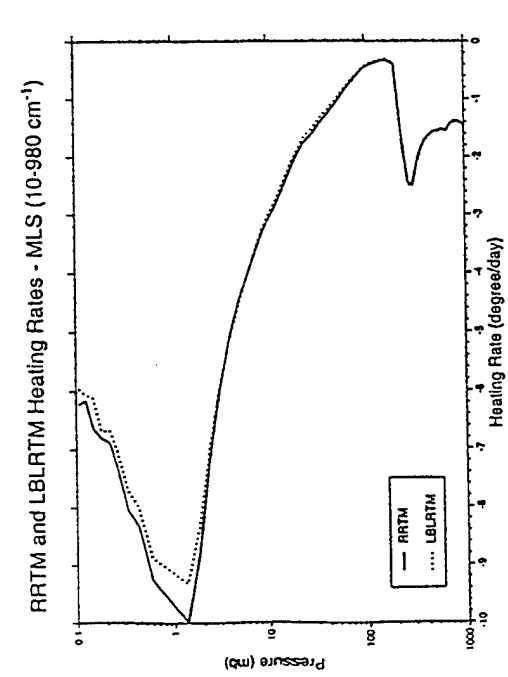


Fig. 4. Difference between RRTM and LBLRTM heating rates as a function of pressure.

Algorithm for estimating solar UV spectral irradiance in atmospheric transmittance/radiance codes

Judith Lean

E.O. Hulburt Center for Space Research
Naval Research Laboratory, Washington, DC 20375

ABSTRACT

MODTRAN and AURIC atmospheric transmittance/radiance codes require as input the solar spectral irradiance at the top of the Earth's atmosphere. At ultraviolet wavelengths, this irradiance varies with solar activity. An algorithm is developed to calculate the solar ultraviolet spectral irradiance from 120 to 300 nm for different levels of solar activity. The algorithm utilizes a chromospheric proxy (either the Mg II 280 nm core-to-wing ratio or the He I 1083 nm equivalent width) to estimate the level of solar activity and an array of variability vectors to linearly scale the solar spectral irradiance according to the specified activity. The absolute spectral irradiances estimated by this algorithm are based on measurements by the UARS/SOLSTICE in early 1992, near maximum activity level in solar cycle 22. Uncertainties in the amplitudes of the variability vectors arise from instrumental uncertainties in the UV irradiance database and are illustrated by comparison of the SME and UARS irradiance data from which the variability vectors are derived.

INTRODUCTION

Solar spectral irradiance at the top of the Earth's atmosphere is the initiating energy for a wide variety of atmospheric transmittance and radiance processes. The present version of MODTRAN, like Lowtran 7, utilizes one solar spectrum from 0.2 to 100 μ for all levels of solar activity [Kneizys *et al.*, 1988]. However, the actual solar spectrum varies continuously as a result of solar activity modulation by the 11-year Schwabe cycle and the Sun's 27-day rotation on its axis. Fig. 1 shows the solar spectral irradiance and estimated Schwabe cycle variability. Variations are of the order of a few tenths percent at visible and infrared wavelengths, while the solar ultraviolet (UV) spectral irradiance varies considerably more. From the maximum to the minimum of the Schwabe cycle the 200 nm irradiance decreases by about 7%. Solar cycle changes in the HI Lyman α line at 121.6 nm are larger still, in the range 50 to 80% (see, for example, review by Lean [1991]).

Solar spectrum variations at different wavelengths impact the Earth's environment in many ways, depending on where the radiation is deposited in the terrestrial system [National Research Council, 1994]. As shown in Fig. 1, the solar spectrum that reaches the Earth's surface differs from that incident on top of the Earth's atmosphere because atmospheric constituents selectively absorb various spectral regions. In particular, oxygen, nitrogen and ozone absorb essentially all the Sun's UV radiation at wavelengths shortward of 300 nm. Deposited in the Earth's atmosphere, this UV radiation is the primary energy that drives much of the atmosphere's dynamical, chemical and radiative processes. By

dissociating diatomic oxygen, solar UV radiation in the region 170 to 240 nm produces the atmospheric ozone layer. Longer wavelength UV radiation from 240 to 300 nm subsequently dissociates ozone, an absorption process which prevents this biologically damaging radiation from reaching the biosphere. Because solar UV radiation impacts both the production and destruction mechanisms of ozone, changes in solar activity cause related changes in ozone levels and temperature [Hood *et al.*, 1993] which affect atmospheric transmittance and radiance.

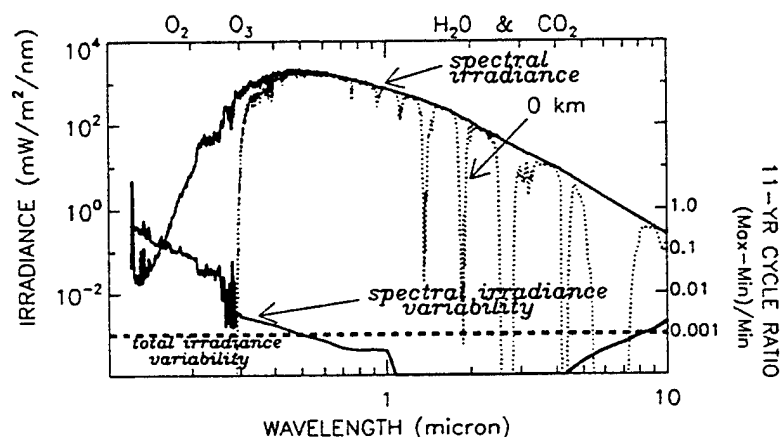


Fig. 1. Shown are the solar spectral irradiance (solid line, left ordinate) and its estimated variability (right ordinate) during the 11-year Schwabe cycle. Also shown (dotted line) is the spectrum incident at the Earth's surface (0 km), after specific spectral regions have been absorbed by various atmospheric constituents such as O_2 , O_3 , H_2O and CO_2 . The thick dashed line is the amplitude of the recent Schwabe cycle modulation of solar total (spectrally integrated) irradiance.

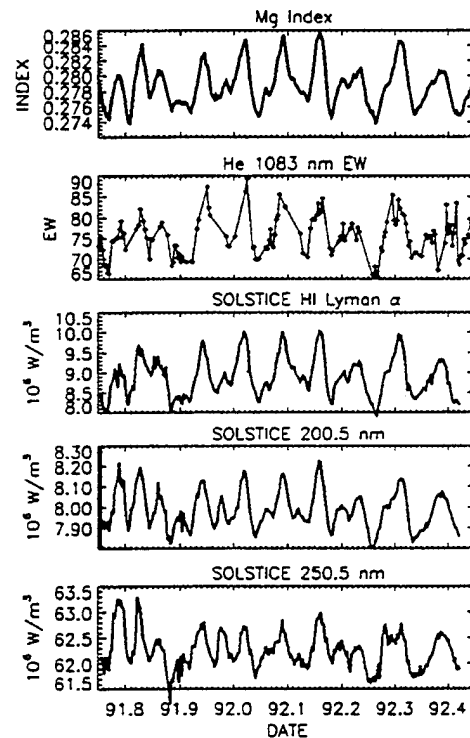
SOLAR UV IRRADIANCE VARIABILITY

Although the entire solar UV spectrum changes continuously in response to solar activity, the true amplitude of the changes have proven difficult to establish observationally. Space-based solar UV radiation monitors frequently suffer significant responsivity degradation as a result of exposure to high energy solar radiation. Knowledge of Schwabe cycle variability requires adequate specification of the instrument changes over time scales of many years. This information has not been available until recently, following the launch of solar monitoring instruments on the Upper Atmosphere Research Satellite (UARS) in September, 1991.

Because of the limited solar UV spectral irradiance database coupled with the difficulty of separating long term solar irradiance variability and instrumental responsivity changes, one approach for determining solar variability amplitudes utilizes measurements of the 27-day irradiance rotational modulation. These variations are a substantial fraction of the Schwabe cycle variations but occur over much shorter time scales, so that instrumental effects can be minimized. Studies of solar rotational

modulation of the UV irradiances indicate that variations at different UV wavelengths are tightly correlated with each other [Donnelly, 1988] and that this mutual variability tracks certain solar activity indices, in particular the ground-based He I 1083 nm equivalent width (EW) [Harvey and Livingston, 1994] and the space-based core-to-wing ratio (CWR) of emission in the Mg II Fraunhofer line at 280 nm [DeLand and Cebula, 1993]. Both the Mg CWR and the He EW are indicators of solar activity in the Sun's chromosphere. Fig. 2 illustrates the high correspondence between rotational modulation of these chromospheric indices and of the solar UV irradiances at three selected wavelengths measured by the Solar Stellar Irradiance Comparison Experiment (SOLSTICE) on UARS [Rottman *et al.*, 1993; London *et al.*, 1993].

Fig. 2. Compared are modulation by the Sun's 27-day rotation on its axis during 1991 and 1992 of two solar activity proxies with the UV irradiances at three wavelengths. In the upper two panels are the Mg II CWR and the He I 1083 nm EW and in the bottom three panels are the UV irradiances measured by the SOLSTICE instrument onboard UARS at HI Lyman α (121.6 nm), 200.5 nm and 250.5 nm.



VARIABILITY ALGORITHM

An algorithm to estimate solar UV irradiance is developed from linear parameterizations of either the Mg CWR or the He EW with the UV irradiances on a 1 nm grid from 120 to 300 nm (following Lean *et al.*, 1992). The parameterizations are determined using data such as those in Fig. 2 from which long term trends have been removed by subtracting a running mean time series. Fig. 3 illustrates this approach for the detrended SOLSTICE UV irradiance at 200.5 nm and the Mg CWR time series produced by L. Puga [private communication, 1994]. Subtracting the entire long term trend removes long term solar variations from both the proxy data and the irradiances as well as potential instrumental effects in the UV irradiance signals. The linear relationships are thus established only for the 27-day rotational modulation effects. The UV irradiance $F(\lambda, t)$ at wavelength λ and time t is then calculated from the actual (not detrended) proxy data $P(t)$ according to $F(\lambda, t) = a + b \times P(t)$ where a and b are the linear regression coefficients established using the detrended rotational modulation data.

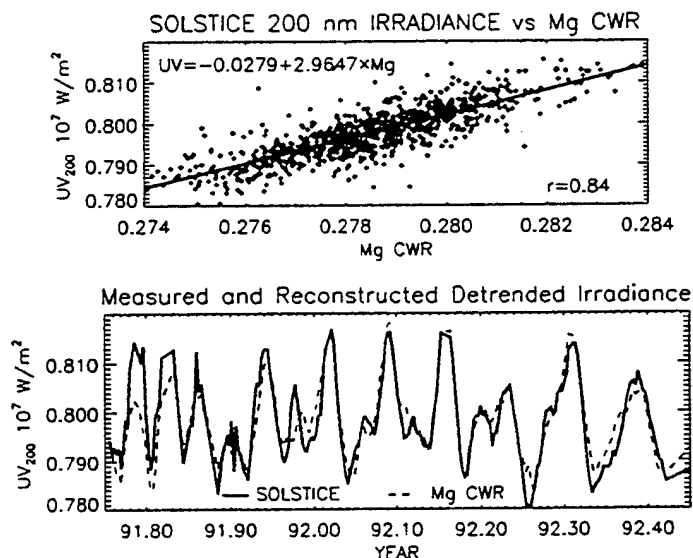


Fig. 3. Shown in the upper panel is a scatter plot of the SOLSTICE UV irradiance at 200.5 nm and the Mg II CWR, using the detrended data in Fig. 2. The regression coefficients derived from linear correlation of the two time series yields an algorithm to calculate the 200.5 m irradiance using the Mg CRW. In the lower panel, this algorithm (dashed line) is compared with the detrended irradiances (solid line).

The He EW and Mg CWR data are available for more than a decade (Fig. 4). Assuming that the high correlations exhibited by the UV irradiances and the chromospheric proxies extend linearly to the longer time scale of the Schwabe cycle, the algorithm uses the rotational modulation regressions and the long term proxy data to infer solar UV irradiance spectra since 1976. Fig. 5 compares solar cycle irradiance variability estimated by this algorithm with the longer term changes actually measured by SOLSTICE. The figure shows the ratio of an average solar spectrum near activity maximum in cycle 22 (29 Dec 91 to 5 Mar 92) to an average spectrum at a low level of solar activity (27 May 94 to 30 May 94); this ratio is essentially an estimate of Schwabe cycle variability amplitudes. Observations by the Solar Mesosphere Explorer [Rottman, 1988] in solar cycle 21 are shown for comparison.

SUMMARY

An algorithm is developed to estimate the solar UV spectral irradiance from 120 to 300 nm (on a 1 nm grid) based on the value of either the Mg CWR or the He EW solar activity proxy. This algorithm provides long term UV irradiance variability amplitudes that are generally consistent with available direct measurements at wavelengths from 170 to 300 nm. At the HI Lyman α line (121.6 nm) the algorithm produces long term variability consistent with the SME observations in solar cycle 21 but somewhat less than the SOLSTICE measurements in cycle 22. Whether the differences between SME and SOLSTICE reflect real differences in the behavior of the shorter wavelength UV irradiances for the two different solar cycles [Chandra *et al.*, 1995] or are the result of unaccounted for instrumental effects in SOLSTICE is still under investigation [see, for example, Tobiska *et al.*, 1995].

Acknowledgements. The He EW data are produced cooperatively by NSF/NOAO, NOAA/SEL and NASA/GSFC. L. Puga of NOAA kindly provided the Mg CWR ratios. G. Rottman is the PI of the UARS/SOLSTICE. This work was supported in part by the UARS Guest Investigator Program (NASA S4135 2F) and by the Strategic Environmental Research and Development Program.

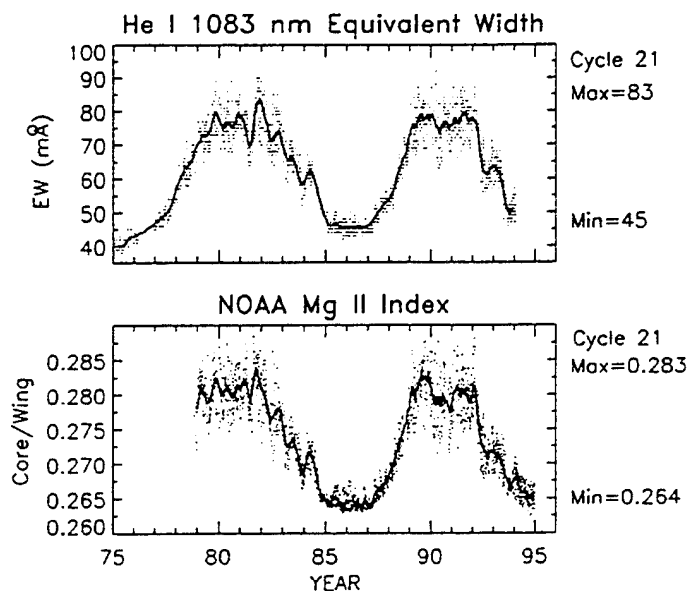
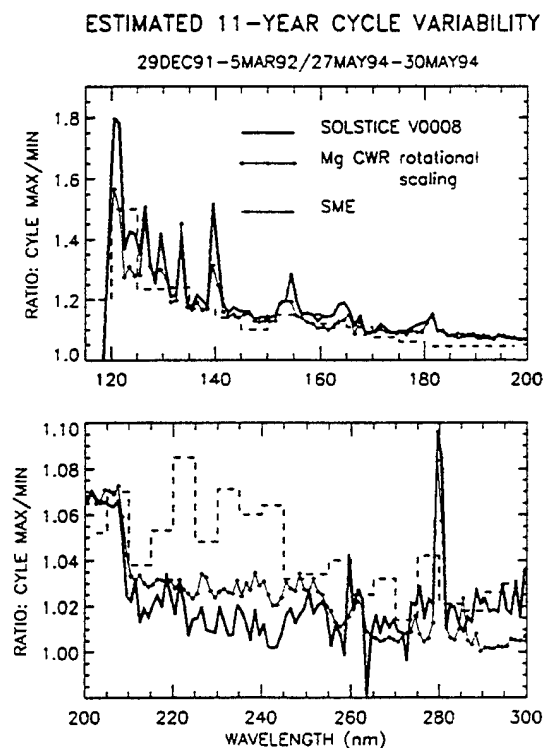


Fig. 4. Long term solar activity according to two chromospheric indicators. Shown in the upper panel is the He I 1083 nm EW and in the lower panel is the Mg II CWR.

Fig. 5. Estimates of the 11-year Schwabe cycle variations of the solar UV spectrum derived by the rotational modulation scaling algorithm (thin line with small diamonds) are compared with SOLSTICE observations in cycle 22 (solid line) and SME observations in cycle 21 (dashed line).



REFERENCES

- Chandra, S., J.L. Lean, O.R. White, D.K. Prinz, G.J. Rottman, and G.E. Brueckner, Solar UV irradiance variability during the declining phase of solar cycle 22, *Geophys. Res. Lett.*, submitted, 1995.
- DeLand, M.T., and R.P. Cebula, The composite Mg II solar activity index for solar cycles 21 and 22, *J. Geophys. Res.*, 98, 12809-12823, 1993.
- Donnelly, R.F., Uniformity in solar UV flux variations important to the stratosphere, *Annales Geophys.*, 6, 417-424, 1988.
- Harvey, J.W., and W.C. Livingston, Variability of the solar He I 10830 A triplet, Pp. 59-64 in *International Astronomical Union Symposium 154: Infrared Solar Physics*, D.M. Rabin, J.T. Jefferies, and C. Lindsey (eds.), 1994.
- Hood, L.L., J.L. Jirikowic, and J.P. McCormack, Quasi-decadal variability of the stratosphere: Influence of long-term solar ultraviolet variations, *J. Atmos. Sci.*, 50, 3941-3958, 1993.
- Kneizys, F.X., E.P. Shettle, L.W. Abreu, J.H. Chetwynd, G.P. Anderson, W.O. Gallery, J.E.A. Selby, and S.A. Clough, *Users guide to LOWTRAN 7*, AFGL-TR-88-0177, Environmental Research Papers, No. 1010, Air Force Geophysics Laboratory, 1988.
- Lean, J., Variations in the Sun's Radiative Output, *Rev. Geophys.*, 29, 505-535, 1991.
- Lean, J., M. VanHoosier, G. Brueckner, D. Prinz, L. Floyd, and K. Edlow, SUSIM/UARS observations of the 120 to 300 nm flux variations during the maximum of the solar cycle: inferences for the 11-year cycle, *Geophys. Res. Lett.*, 19, 2203-2206, 1992.
- London, J., G. Rottman, T. Woods, and F. Wu, Time variations of solar UV irradiance measured by the SOLSTICE (UARS) instrument, *Geophys. Res. Lett.*, 20, 1315-1318, 1993.
- National Research Council, Board on Global Change, *Solar Influences on Global Change*, National Academy Press, 1994.
- Rottman, G.J., Observations of solar UV and EUV variability, *Adv. Space Res.*, 8, (7)53-(7)66, 1988.
- Rottman, G.J., T.N. Woods, and T.P. Sparr, Solar-Stellar Irradiance Comparison Experiment, 1, Instrument Design and Operation, *J. Geophys. Res.*, 98, 10667-10677, 1993.
- Tobiska, W.K., W.R. Pryor and J.M. Ajello, Comparison of full-disk and line-center Lyman-alpha during solar cycles 21 and 22, *Supplement to Eos*, Transactions, American Geophysical Union 1995 Spring Meeting, S240, 1995.

Recent Measurement Applications of OSIC UV Propagation Model

Dr. Katherine M. Crow
Dr. Michael E. Neer
SciTec, Inc.
100 Wall Street
Princeton, NJ 08540

1. Introduction

This paper describes the results of recent work using the OSIC UV propagation model. The OSIC model is a semi-empirical multiple scatter model which was developed through an extensive measurement program which took place from 1979-1984. In recent years, renewed focus on the UV wavelengths has revived interest in the OSIC model. It has been adopted by the Advanced Tactical Infrared Countermeasure (ATIRCM) program for use in the Advanced Tactical Missile Detector (ATMD) system development, and has been accepted for use in the Air Force AEM*AT (AVLAB Electro-Optical Model for Aerial Targeting) model. It is being used in the Joint Tactical Missile Signatures (JTAMS) program to extract source signatures from measured missile data. In addition, it will be evaluated for inclusion in the NEOTAM model of NATO RSG-18, and is being provided to this group by the U.S. government.

This paper will focus on work done recently using the OSIC model. Measurements were made to test the validity of the model for longer ranges than those used during its development period; the results of this analysis will be discussed. In addition, the model has been used to characterize atmospheric conditions during several recent missile tests. These techniques will be described and the results of such characterizations will be presented.

The model requires a description of the source radiant intensity, as a function of wavelength, aspect angle, and time. The relative orientations of the source and the sensor are needed. Sensor characteristics must be provided, in terms of wavelength response and sensor responsivity as a function of field of view. Atmospheric conditions must be described: pressure, temperature, ozone concentration, and aerosol scatter and absorption coefficients as a function of wavelength, and the normalized single scatter phase function are all model inputs. Vertical gradients of these atmospheric conditions are also required.

The model computes the irradiance measured by the modeled sensor, in terms of a direct component as well as a scattered component contributed by annular cones in the field of view. The scattered component contains contributions from both single and multiple scatter, computed using the semi-empirical relationship established through measurements made during the model development period. Depending upon atmospheric conditions as well as path length, this off-axis contribution may be quite significant for a wide field of view sensor. A full description of the model, as well as a user's manual for the associated code, is available in references 1-3.

2. Model Validation Measurements

The measurements made during the model development phase were all for ranges of under 4 km. Recently, interest has arisen in UV propagation for paths of 7-9 km. In order to support the use of the model at these ranges, a model validation measurement was performed at Wright-Patterson Air Force Base (WPAFB) in January 1995, through the sponsorship of the AMWS (ATMD) SPO.

The measurements involved placing a calibrated 500 Watt Mercury Xenon lamp, the UV source, on the ground at a site with a 7.9 km clear line-of-sight to the tower of Building 620, a 13-story building at WPAFB. An ozone analyzer and aerosol particle counters were also situated at this ground site in order to characterize atmospheric conditions at the time of the measurement. Temperature, pressure, and relative humidity were also measured for use in the subsequent analysis. A variable field of view, photon-counting UV radiometer was used on the roof of Building 620 to make the actual measurements.

Two types of measurements were made, as illustrated in Figure 1. The first is called the direct transmission and forward scatter, or "collapsing field of view" experiment. With a wide field of view, both the directly transmitted and near-forward scattered radiation from the lamp is measured. As the field of view is decreased, the near-forward scatter is gradually eliminated. In the limit, i.e. with an infinitesimally small field of view pointed directly at the lamp, only the directly transmitted radiation would remain. This process is illustrated by the diagrams at the top of Figure 1. The second experiment is known as the off-axis scatter experiment and is depicted in the diagrams at the bottom of Figure 1. These measurements are taken with the radiometer pointed at increasing elevation angles above the source and characterize off-axis aerosol and molecular scatter.

The data for the direct transmission and forward scatter experiment are presented in Figures 2 and 3. These figures display the data in context of the problem as a whole. Figure 2 shows the measured data and the corresponding predictions in addition to predictions made for ozone concentrations

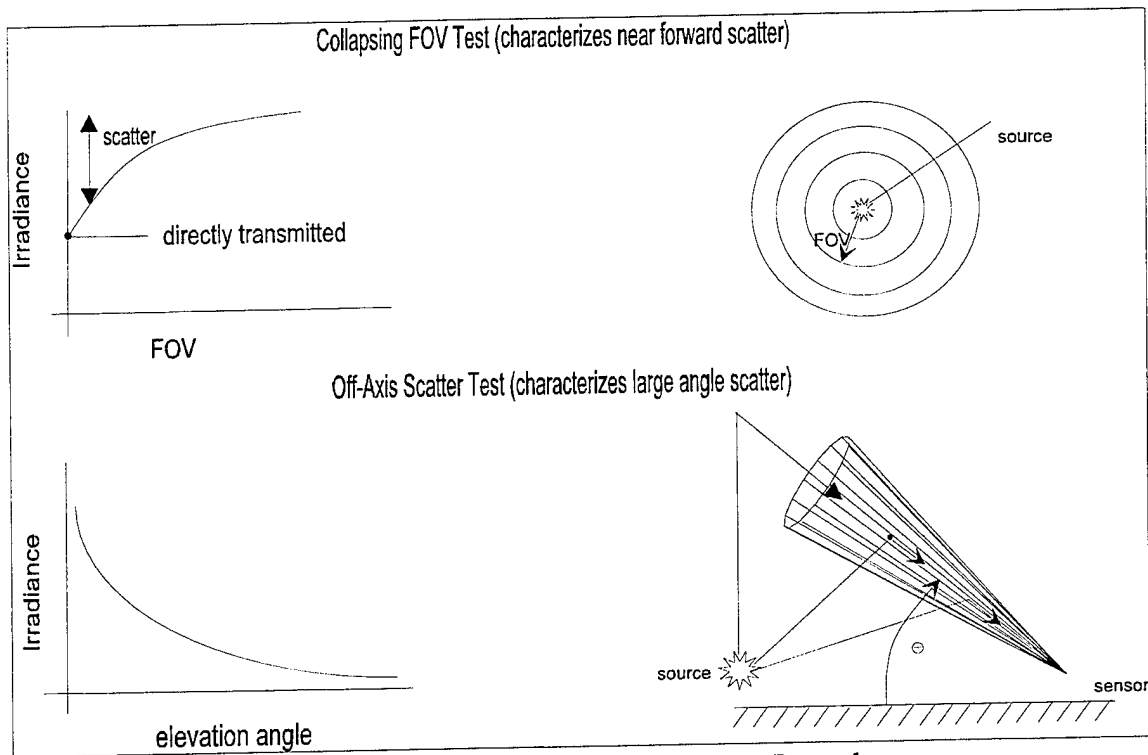


Figure 1. UV Propagation Measurement Procedures

varying from 0 to 40 ppb. It is observed that when compared to variations arising from slight changes in the ozone level, the measurements correspond quite well to the predictions made for the measured ozone level of 15 ppb. Similarly, Figure 3 shows the measured data and the corresponding predictions in addition to predictions made for visibilities varying from 8 to 32 km.

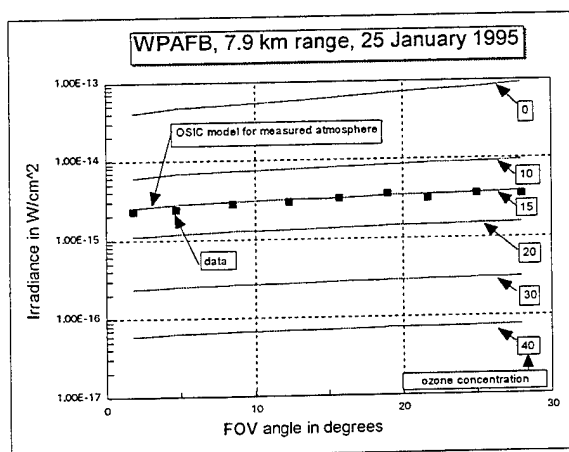


Figure 2. Impact of Ozone Concentration on UV Irradiance

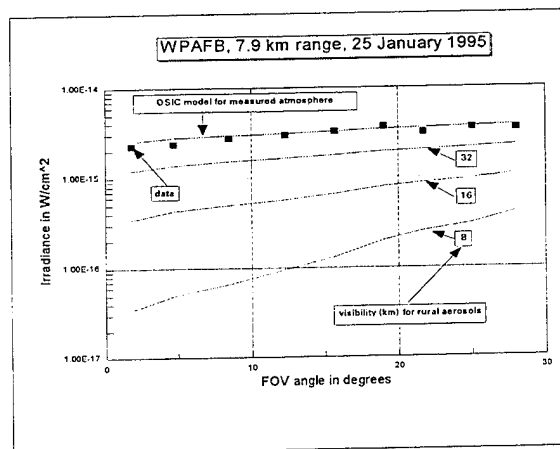


Figure 3. Impact of Aerosols on UV Irradiance

Due to the difficulty in gaining enough signal from the lamp over the long transmission path, as well as to highly variable background UV radiation experienced during the measurements, the data from the off-axis scatter experiment had unacceptable signal-to-noise. OSIC predictions for the measured atmospheric conditions confirmed the lack of adequate signal for the off-axis scatter test.

It is concluded that the measurements taken agreed quite well with the model predictions; however, more measurements should be taken under a variety of atmospheric conditions before the model is considered to be thoroughly validated for longer ranges.

3. Characterization of Atmospherics during Missile Tests

During missile testing, if one wants to be able to arrive at source signatures, or to extrapolate the measurements to different atmospheric conditions, it is important to accurately characterize the atmospheric conditions prevailing at the time of the measurements. Ozone analyzers and aerosol particle counters, along with standard meteorological measurements, are typically used for this purpose. However, these measurements are generally only made at a single point in space; such measurements will be referred to as point measurements. The missile irradiance, on the other hand, travels over a potentially non-uniform path of significant length before it arrives at the UV radiometer. Thus it is better to characterize the path-integrated atmospheric conditions over this path, rather than using a single data point to represent the entire path. In the course of work on the JTAMS program, measurement and analysis techniques have been developed in order to arrive at such path-integrated atmospheric conditions. In this section, these techniques are outlined and some results are presented.

Before the missile test, a measurement of a calibrated UV source (the common source) is made by all UV instruments on site. During these common source measurements, a UV transmissometer is used to perform the direct transmission and forward scatter and the off-axis scatter measurements discussed above. The results of these measurements are then used to establish path-integrated absorption and scatter characteristics. Since the scatter effects recorded by the two separate experiments are intertwined with the effects of ozone absorption, both along the direct path as well as along the paths of single and multiple scatter, arriving at these path-integrated properties is necessarily an iterative process. Further description of these techniques is available in reference 4.

Sample results of this process are shown in Figure 4, which shows the effects of progressively improving atmospheric corrections on common source measurements. The data shown are from the common source measurements taken on the JTAMS free flight ATGM test in March-April 1994 in Huntsville, Alabama. Similar analyses have been performed on the common source measurements

July 18, 1995 taken on the JTAMS static stand and sled tests in October 1994 in Biscarosse, France, and on the JTAMS free flight test in April 1995 at White Sands, New Mexico. For these measurements, all the UV instruments were looking at the same common source, which was systematically pointed at each instrument; therefore, they all should ideally report the same source radiant intensity. The dashed line across all the plots at an accuracy factor of 1 represents this ideal condition. The leftmost plot in both figures is for the measurements uncorrected for atmospherics. Note that the instruments reporting accuracy factors closest to one are the instruments at the closest ranges to the common source (and therefore experiencing less atmospheric attenuation than those at longer ranges). The center plot in both figures shows the data corrected for atmospherics using the point measurements of ozone and aerosols; the rightmost plot shows the data corrected using the path-integrated ozone and aerosols computed from the UV propagation experiments as described above. The successive improvement in the data (clustering about the dashed line) from left to right illustrates the utility of the technique of applying path-integrated atmospheric correction. The bars on the plots represent the estimated errors in the reported quantities.

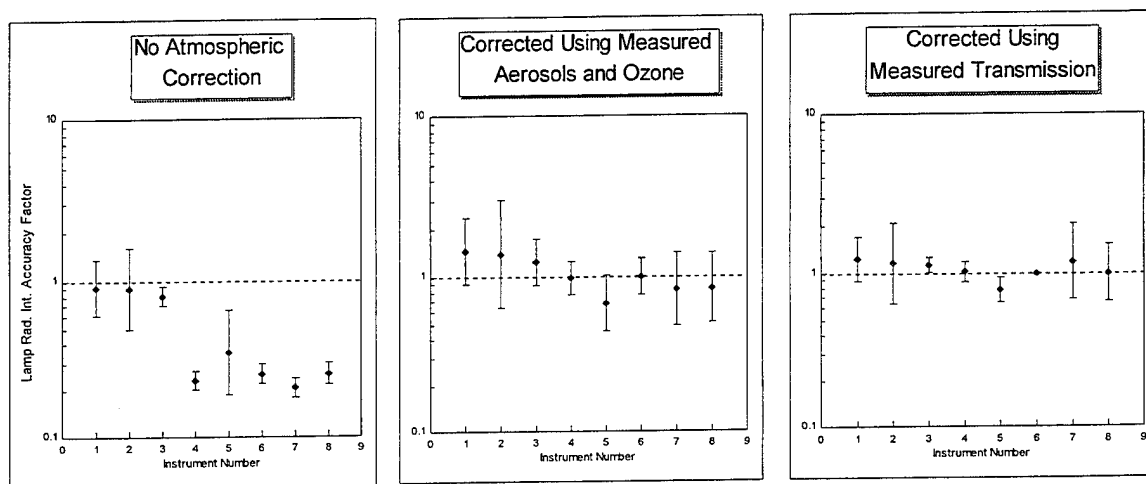


Figure 4. Role of UV Atmospheric in Error Reduction for Common Source Measurements

4. Conclusions

The OSIC model is proving to be a useful tool for analysis and prediction in the UV. The 8 km measurement taken at WPAFB provides optimism as to the model's applicability for longer ranges, and is a good starting point for future validation efforts. The use of the OSIC model in the analysis of UV data from JTAMS tests has proven to be quite beneficial in terms of improving the inter-instrument consistency of measured data.

5. References

1. J. M. Schlupf, B. J. Morgan and M. E. Neer, The Missile Warning Receiver Code, Volume I., Model Description and Validation, SciTec Report No. TR-82-004, March 1982.
2. J. M. Schlupf, B. J. Morgan and M. E. Neer, The Missile Warning Receiver Code, Volume II., Documentation of Atmospheric Optical Properties, SciTec Report No. TR-82-004, March 1982.
3. J. M. Schlupf, B. J. Morgan and M. E. Neer, The Missile Warning Receiver Code, Volume III., User's Manual, SciTec Report No. TR-82-004, March 1982.
4. JTAMS Tactical Missile Signatures Handbook, Chapter 8, under development by JTAMS Joint Test Force, Lackland AFB, TX, P.O.C. Greg McGill, telephone (210) 671-1911.

A FAST MULTI-DIMENSIONAL ATMOSPHERIC EFFECTS INTERPOLATOR FOR E²DIS

P. K. ACHARYA & D. C. ROBERTSON
Spectral Sciences, Incorporated, Burlington, MA

W.M. CORNETTE
Photon Research Associates, La Jolla, CA

L. JEONG
Phillips Laboratory/GPOS, Hanscom AFB, MA

Presented at
**THE 18TH ANNUAL REVIEW CONFERENCE ON
ATMOSPHERIC TRANSMISSION MODELS (6-8 JUNE, 1995)**

E²DIS OVERVIEW

- DIS - DISTRIBUTED INTERACTIVE SIMULATION
 - REALTIME WAR GAMING
 - DISTRIBUTED (INDEPENDENT) PLAYERS/NODES
- E²DIS - ENVIRONMENTAL EFFECTS IN DIS
 - KEY OBJECTIVE IS TO ACCOUNT FOR THE ENVIRONMENT IN WARGAME SIMULATIONS
 - NATURAL RADIATIVE ENVIRONMENT IS CHARACTERIZED BY T, P, MOLECULAR SPECIES, RAIN, CLOUD, AEROSOLS, SUN
 - MANMADE BATTLEFIELD EFFECTS INCLUDE TARGET OBSCURANTS, SMOKE, DUST, PLUME
- MOSART IS USED IN E²DIS TO MODEL ENVIRONMENTAL EFFECTS

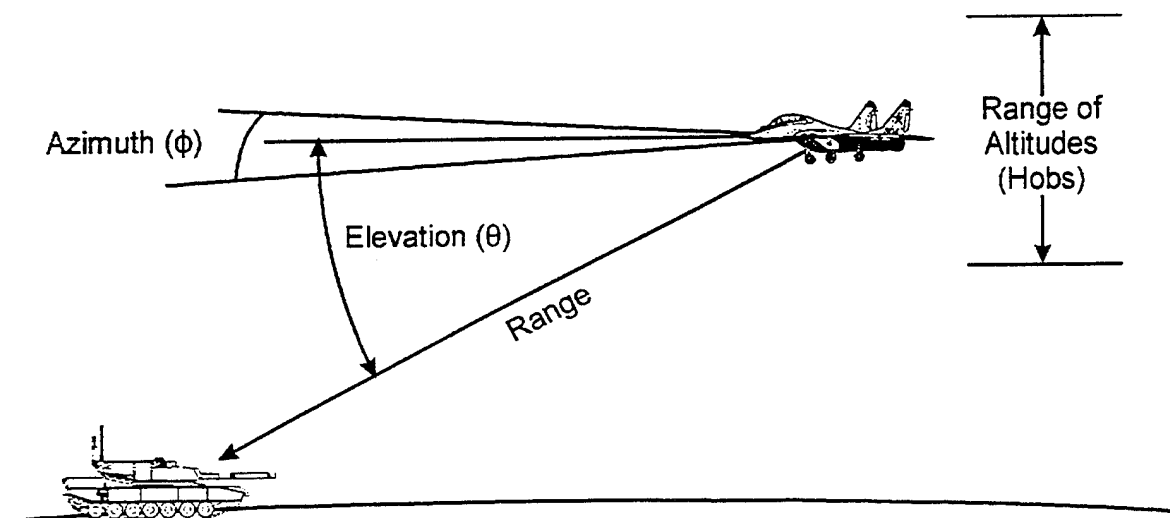
MOSART OVERVIEW

- MODERATE SPECTRAL ATMOSPHERIC RADIANCE AND TRANSMITTANCE CODE
- NEW PL/GPOS PHYSICS-BASED CODE BUILT UPON MODTRAN & APART
 - ALTITUDE REGION: 0-60 km
 - SPECTRAL RANGE: 0-50,000 cm^{-1} (0.2 μM - MM WAVELENGTHS)
 - SPECTRAL RESOLUTION: 2 cm^{-1}
 - 24 ATMOSPHERIC, 50 AEROSOL & 24 CLOUD/RAIN/SNOW/FOG PROFILES
 - USER-DEFINED PROFILES
 - EXTENSIVE GLOBAL DATABASES: CLIMATOLOGIES, TERRAIN TYPES, SURFACE ELEVATION & THERMAL PROPERTIES
- SPONSORED BY BMDO FOR SYNTHETIC SCENE GENERATION MODEL (SSGM)
 - INTERFACE WITH CLOUD MULTIPLE SCATTERING CODE (CLDSIM)
 - INTERFACE WITH GROUND IR SCENE MODEL (GENESSIS)
- VARIOUS OUTPUT FILES FOR SIGNATURES & SCENARIO MODELING
 - INTERFACE WITH TARGET SIGNATURE CODES (E.G., EXPIRT, SPIRITS)
 - DIURNAL BROAD-BASED HEAT TRANSFER PARAMETERS (TERTEM)
 - SPECTRAL AND ALTITUDE PROFILES OF TRANSMITTANCE AND RADIANCE

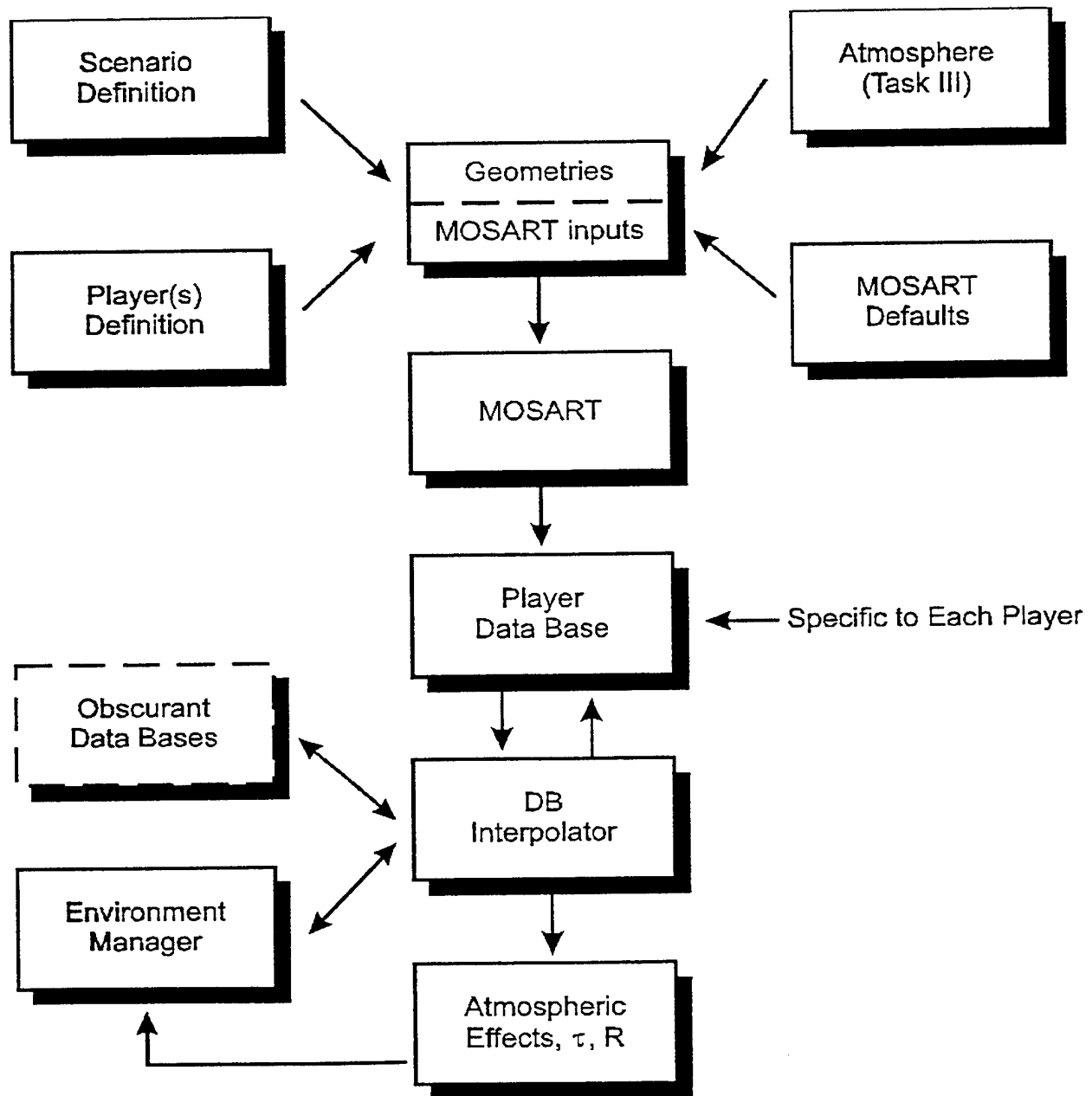
DATABASE APPROACH FOR REALTIME ATMOSPHERIC CALCULATIONS

- E²DIS REQUIRES REALTIME UPDATES FOR
ATMOSPHERIC EFFECTS
 - CHANGING ATMOSPHERIC CONDITIONS
 - MULTIPLE, MOBILE SENSORS AND TARGETS
 - VARIOUS LOOK DIRECTIONS
- PHYSICS-BASED CODES ARE JUST NOT FAST ENOUGH
- MUST HAVE TRADE-OFF BETWEEN ADEQUATE FIDELITY AND
SPEED
- APPROACH: CREATE SENSOR-SPECIFIC DATABASES
OFFLINE AND INTERPOLATE OVER THEM IN REALTIME
 - RANGE OF PARAMETERS ARE CHOSEN TO ENCOMPASS SIMULATION
 - SUFFICIENT ACCURACY FOR SYSTEMS APPLICATIONS

LINE-OF-SIGHT PARAMETERS



MOSART DATABASE GENERATOR AND INTERPOLATOR



DATABASE GENERATOR

- GENERATED OFF-LINE FOR EACH SENSOR
 - SPANS ALLOWED OPERATIONAL RANGE IN TIME AND SPACE
- REQUIRED SIMULATION-SPECIFIC INTERVALS OF STANDARD LOS PARAMETERS
 - SENSOR ALTITUDE
 - LINE-OF-SIGHT RANGE
 - ELEVATION ANGLE
 - SOLAR AZIMUTH ANGLE
- SENSOR INPUTS PLUS A DEFAULT MOSART INPUT FILE ARE USED TO GENERATE DATABASES
- CALCULATED MOSART LOS QUANTITIES
 - IN-BAND PATH TRANSMITTANCES
 - IN-BAND PATH RADIANCES (WITH SOLAR SCATTERING)

DATABASE STRUCTURE

- SENSOR ID, TIME AND DATE FORM PART OF FILE NAME
- CONTENTS:
 - TIME AND DATE
 - BANDPASS
 - LOS VARIABLES (INTERPOLATING VARIABLES):
 1. SENSOR POSITIONS : HOB1, HOB2, ... (TOTAL OF NH VALUES)
 2. ELEVATION ANGLES: THETA1, THETA2, ... (NT VALUES)
 3. SOLAR AZIMUTHS : PHI1, PHI2, ... (NP VALUES)
 4. LOS RANGES : RANGE1, RANGE2, ... (NR VALUES)
 - PATH QUANTITIES FOR EACH LOS:
 1. SENSOR-TO-TARGET PATH RADIANCE AND TRANSMITTANCE
 2. EARTH/SPACE BACKGROUND-TO-SENSOR TRANS AND RAD
- DATABASE FILE IS DIRECT-ACCESS

DATABASE INTERPOLATOR

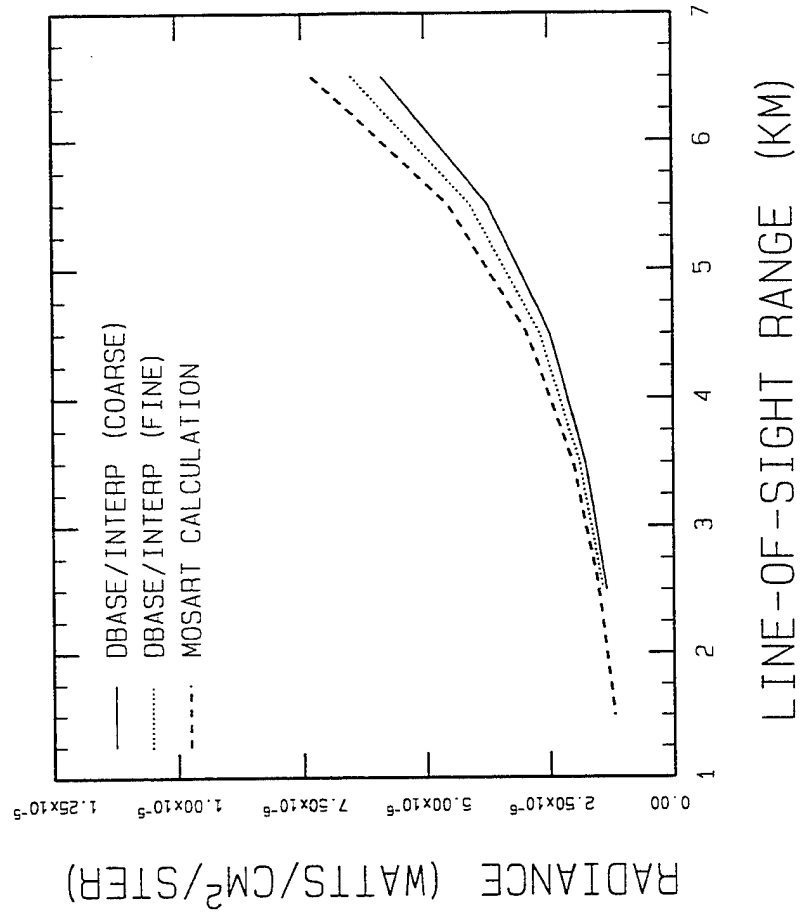
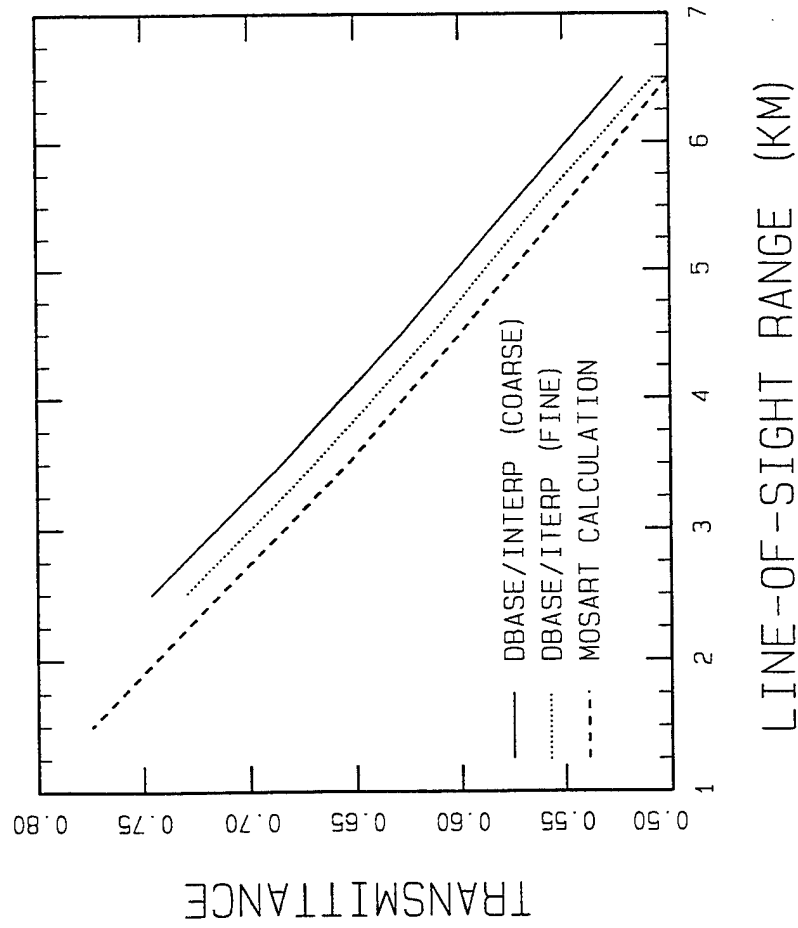
- QUERIES FOR SENSOR ID, DESIRED TIME AND INPUT LOS PARAMETERS (HOBS, THETA, PHI, RANGE)
- USES NEAREST-TIME DATABASE
- OUTPUTS NEEDED LOS TRANSMITTANCES AND RADIANCES
- MULTI-VARIABLE LINEAR INTERPOLATOR
- READS ONLY REQUIRED VALUES FROM DIRECT-ACCESS DATABASE
 - SAVINGS IN COMPUTER MEMORY AS THE QUANTITIES ARE NOT STORED IN ARRAYS
 - FASTER ACCESS TIME THAN SEQUENTIAL AND FORMATTED FILES
 - NO PENALTY IN EXECUTION TIME WITH DATABASE SIZE INCREASE
 - ACCURACY INCREASES WITH DECREASING GRID SPACINGS OF LOS PARAMETERS

ILLUSTRATIVE CALCULATIONS

BANDPASS=2.5-5.0 μ M, HOBS=9.5 KM, THETA=-85°, PHI=175°

FINE GRID : Δ HOBS= Δ RANGE=0.5 KM, Δ THETA= Δ PHI=5°

COARSE GRID: Δ HOBS= Δ RANGE=1 KM, Δ THETA= Δ PHI=10°



OBSCURANT EFFECTS

- USE OPTICAL DEPTH

- IN-BAND BEER'S LAW FOR TRANSMITTANCE

$$\tau = \exp(-X)$$

- OPTICAL DEPTHS BECOME ADDITIVE

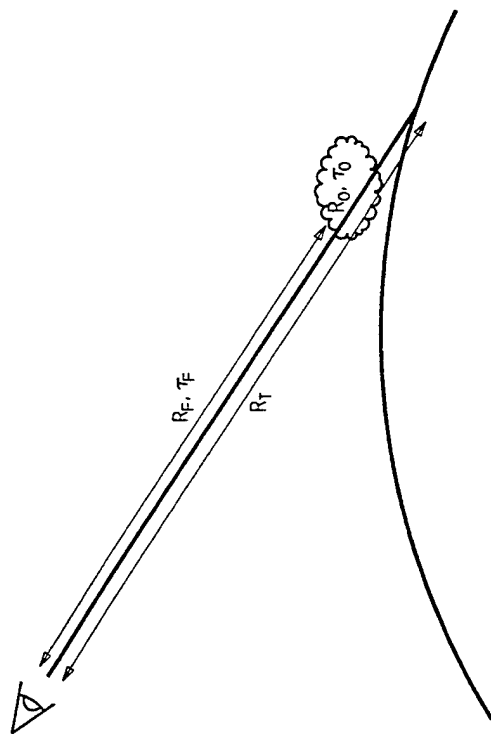
$$X = \sum_i X_i$$

- MOLECULAR SOURCES (LIKE PLUMES) ARE NOT AS WELL DESCRIBED, MAY REQUIRE ALGORITHM UPGRADES

- EXPONENTIAL SUM FIT
- ANALYTIC MODEL

INTEGRATING OBSCURANT RADIANCES

- MUST DISTINGUISH BETWEEN FOREGROUND AND BACKGROUND RADIANCES



$$\begin{aligned}
 R &= (R_T - R_F)\tau_O && \text{(BEHIND OBSCURANT)} \\
 &+ R_O \tau_F && \text{(OBSCURANT)} \\
 &+ R_F && \text{(FRONT OF OBSCURANT)}
 \end{aligned}$$

Simplified Expression of the Radiative Transfer Equation for Surface Temperature Estimation from LOWTRAN 7

Masao Moriyama, Kazuhiko Mima

Dept. Mechanical Systems Eng., Faculty of Eng., Nagasaki Univ.
1 - 14 bunkyo-machi Nagasaki 852 Japan.

Abstract : An attempt is made to simplify the radiative transfer equation of the atmospheric window spectrum for the estimation of the surface temperature and surface emissivity. For the simplification, some assumptions are adopted and the unknown variables are reduced. The comparison between the radiance reaching the satellite computed from LOWTRAN 7 and the proposed radiative transfer equation shows the good correspondence.

1 Introduction

The thermal IR remote sensing is widely used for the earth environment monitoring such as surface temperature estimation, atmospheric condition estimation and so on. For the surface temperature estimation, especially for the sea surface temperature estimation, the multiple regression analysis between the observed values and the surface temperature is commonly used [1]. But since the high correlation between the observed values, it is not expected to achieve the high accuracy estimation with the multiple regression method for the upcoming multiple channel sensor. Also for the surface emissivity estimation, the multiple regression analysis is not powerful as in the case of the temperature estimation because the radiative transfer process is hard to be expressed by the regression formula.

To make the physical based estimation method of the surface temperature and emissivity, the attempt is made to simplify the radiative transfer equation. The physical based estimation method is to solve the simplified radiative transfer equation by means of the inversion method [2], [3]. In other word, the equation is used for the forward model of the estimation method. It is necessary to define the accuracy and simple (the number of the unknown variables are small) forward model for the inversion estimation. For the simplification, some assumptions are adopted to reduce the number of unknown variables. To verify the simplification, radiance reaching the satellite computed from LOWTRAN 7 and the proposed simplified radiative transfer equation are compared.

2 Radiative transfer equation

In the case of clear sky, negligible solar radiation and scattering effect, the radiance: I_ν reaching the satellite at the wavenumber: ν is expressed into the following equation [4].

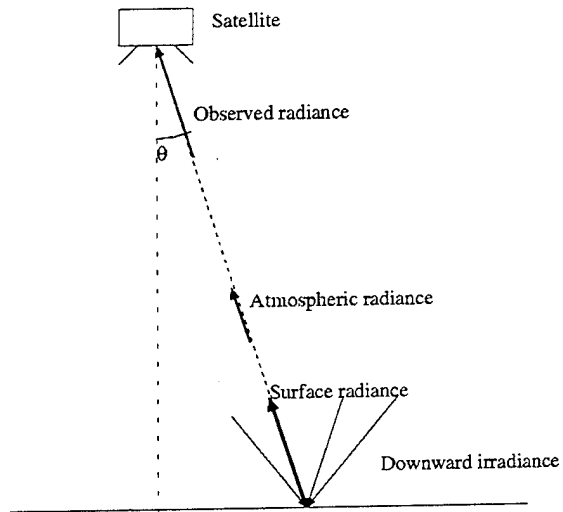


Figure 1: Schematic of the radiative transfer process

$$\begin{aligned}
 I_\nu = & \epsilon_\nu B_\nu[T_s] \tau_\nu(0, Z, \theta) \\
 & + \int_0^Z B_\nu[T(z)] \frac{\partial \tau_\nu(z, Z, \theta)}{\partial z} dz \\
 & + \tau_\nu(0, Z, \theta) \frac{1 - \epsilon_\nu}{\pi} F_\nu,
 \end{aligned} \tag{1}$$

$$F_\nu = \int_0^{2\pi} \int_0^{\pi/2} \int_0^Z B_\nu[T(z)] \frac{\partial \tau_\nu(0, z, \vartheta)}{\partial z} \cos \vartheta \sin \vartheta dz d\vartheta d\phi \quad (2)$$

where ε_ν , $B_\nu[T]$, $\tau_\nu(z_1, z_2, \theta)$, F_ν , T_S and $T(z)$ are the spectral surface emissivity, Planck function, transmittance from altitude z_1 to z_2 at the observation zenith angle θ , downward atmospheric irradiance at the surface at the wavenumber ν , surface temperature and air temperature at the altitude z , respectively.

This equation contains the huge number of the unknown variables such as vertical profiles of the absorber and air temperature, also it has to be computed that the weighted average of the spectral radiance (line by line computation) for the analysis of the satellite detected radiance and this becomes large computation amount.

3 Simplification

For the inversion solution of the radiative transfer equation, it has to define the accurate and simple radiative transfer equation. To simplify the radiative transfer equation, the following assumptions are adopted.

3.1 Spectral integration of the spectral values

The line-by-line computation consume the huge amount of computation time, so in this research the spectral values such as surface emissivity, Planck function, transmittance and downward irradiance are spectrally integrated with the sensor response function: $\varphi(\nu)$.

$$B_i(T) = \int_0^\infty \varphi_i(\nu) B_\nu(T) d\nu \quad (3)$$

$$\tau_i(z_1, z_2, \theta) = \int_0^\infty \varphi_i(\nu) \tau_\nu(z_1, z_2, \theta) d\nu \quad (4)$$

$$\varepsilon_i = \int_0^\infty \varphi_i(\nu) \varepsilon_\nu d\nu \quad (5)$$

$$F_i = \int_0^\infty \varphi_i(\nu) F_\nu d\nu \quad (6)$$

$$\int_0^\infty \varphi_i(\nu) d\nu = 1$$

where the subscript i means the spectral channel. And the channel-wise radiative transfer equation is assumed to be expressed as follows.

$$\begin{aligned} I_i &= \varepsilon_i B_i[T_S] \tau_i(0, Z, \theta) \\ &+ \int_0^Z B_i[T(z)] \frac{\partial \tau_i(z, Z, \theta)}{\partial z} dz \\ &+ \tau_i(0, Z, \theta) \frac{1 - \varepsilon_i}{\pi} F_i \end{aligned} \quad (7)$$

3.2 Simplification of the atmospheric radiation

To compute the atmospheric radiation term, it is necessary to know the atmospheric profile, in other word, it is the unknown variables and its number is so large. To reduce the unknown variables, the integration term is simplified as follows after the mean value theorem,

$$\begin{aligned} &\int_0^Z B_i[T(z)] \frac{\partial \tau_i(z, Z, \theta)}{\partial z} dz \\ &= [1 - \tau_i(0, Z', \theta)] \frac{1}{Z'} \int_0^{Z'} B_i[T(z)] dz \end{aligned} \quad (8)$$

where Z' means the altitude which satisfy the above equation. The transmittance $\tau_i(0, Z', \theta)$ is assumed to be equal to the total transmittance $\tau_i(0, Z, \theta)$ and the new unknown variables: I_{ai} is defined as follows

$$I_{ai} = \frac{1}{Z'} \int_0^{Z'} B_i[T(z)] dz \quad (9)$$

The new variable is named **representative atmospheric radiation**. Moreover, the representative atmospheric radiation (RAR) is essentially related to the air temperature, so the RAR at the each spectral channel (i -th. channel) is assumed to be expressed by only the that of the certain channel (k -th. channel).

$$I_{ai} = f_i(I_{ak}) \quad (10)$$

3.3 Simplification of the downward irradiance

After the same procedure of the simplification of the atmospheric radiation, the downward irradiance at the surface can be simplified as follows,

$$F_i = \int_0^{2\pi} \int_0^{\pi/2} [1 - \tau_i(0, z, \vartheta)] I_{ai}^d \cos \vartheta \sin \vartheta d\vartheta d\phi \quad (11)$$

where I_{ai}^d means simplified downward atmospheric radiance, and I_{ai}^d is assumed to be the same as the representative atmospheric radiation. And the solid angle integration is assumed to be the coefficient multiplication to the normal component of the downward radiance.

$$F_i = \alpha_i [1 - \tau_i(0, Z, 0)] f_i(I_{ak}) \quad (12)$$

3.4 Approximation of the transmittance computation

Since at the IR atmospheric window spectrum the water vapor is dominative for the transmittance, the total transmittance can be the function of only

the water vapor amount, however in this case, transmittance is the spectrally integrated one and the other absorber (aerosol etc) effect is still remained, so the optical thickness: ξ_i is assumed to be the following function,

$$\xi_i = C_0 + C_1 u + C_2 u^2 \quad (13)$$

where u and C 's are precipitable water and regression coefficients. The total transmittance: $\tau_i(\theta)$ can be computed as follows.

$$\tau_i(\theta) = \tau_i(0, Z, \theta) = \exp(-\xi_i / \cos \theta) \quad (14)$$

3.5 Simplified radiative transfer equation

After the above assumptions, the simplified radiative transfer equation is defined.

$$\begin{aligned} I_i &= \varepsilon_i \tau_i(\theta) B_i[T_S] \\ &+ [1 - \tau_i(\theta)] f_i(I_{ak}) \\ &+ (1 - \varepsilon_i) \tau_i(\theta) \frac{\alpha_i [1 - \tau_i(0)] f_i(I_{ak})}{\pi} \end{aligned} \quad (15)$$

In this equation, there are 4 unknown variables, surface temperature: T_S , surface emissivity: ε_i , precipitable water: u and the representative atmospheric radiation at the certain channel: I_{ak} . So the surface temperature can be estimated in the case of blackbody surface (ex. sea surface) with 3 channel sensor [5], and for the non-blackbody case surface temperature and emissivity can be estimated by using the channel-wise emissivity approximation (polynomial approximation) and the area based atmospheric correction [2], [3].

4 Verification

To verify the above equation, the numerical simulation are made. As the target sensor, ASTER/TIR on-board EOS-am1 which will be launched 1998 is selected. ASTER/TIR has 5 spectral channel in IR atmospheric window spectrum and it is designed for the temperature/emissivity monitoring. For the regression coefficients definition and the verification, the observed radiance, total transmittance, atmospheric radiation and downward irradiance at the surface are computed by LOWTRAN 7 [6] under the following simulation condition.

Sensor : ASTER/TIR chs. 10, 11, 12, 13, 14

Fundamental Model : Tropic, Midlatitude summer/winter, Subarctic summer/winter, 1976 US standard

Surface temperature : $\pm 0, \pm 3, \pm 6$ [K]

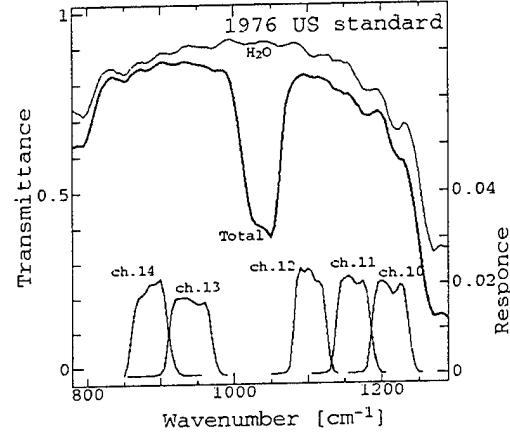


Figure 2: Response function of ASTER/TIR and the total transmittance

Relative humidity : $\times 1.0, \times 1.1, \times 1.2, \times 0.9, \times 0.8$ (0-10 km)

Air temperature : $\pm 0, \pm 3$ [K] (0-10 km)

Observation angle : 0, 10 [deg.]

Aerosol : rural (surface visibility 23km)

Emissivity : 0.8, 0.9, 1.0

Other : Values in LOWTRAN 7

4.1 Transmittance (Optical thickness)

For the total transmittance computation, the regression coefficients of optical thickness definition formula is defined, the values are tabled and illustrated as follows.

Table 1: Regression coef. of the optical thickness definition

ch.	C2	C1	C0	RMS
10	.3850E-02	.1803E+00	.1712E+00	.1116E-02
11	.6626E-02	.1018E+00	.1317E+00	.7872E-03
12	.8366E-02	.6262E-01	.1020E+00	.6713E-03
13	.1558E-01	.5841E-01	.4479E-01	.1117E-02
14	.2033E-01	.7150E-01	.2683E-01	.1498E-02

u: [cm]

Each result shows the good correspondence.

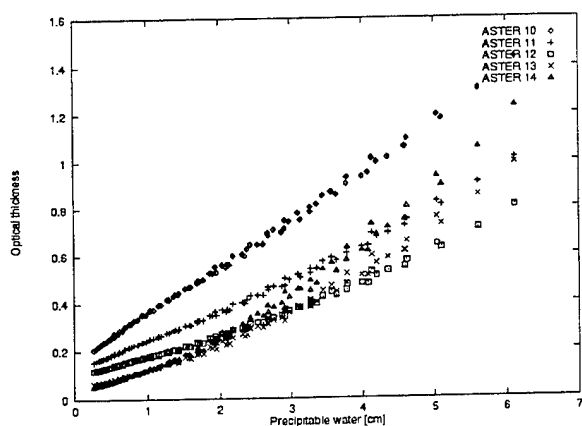


Figure 3: The Comparison between the precipitable water and optical thickness

4.2 Channel dependence of the representative atmospheric radiation

In this case, the representative atmospheric radiation is assumed to be the function of that of 13th. channel and the channel dependence can be expressed by second order polynomial.

$$I_{ai} = B_2 I_{a13}^2 + B_1 I_{a13} + B_0 \quad (16)$$

the result shows as follows.

Table 2: Regression coef. of the channel dependence of the representative atmospheric radiation.

ch.	B2	B1	B0	RMS
10	.2203E+05	.2522E+00	.2966E-06	3.268E-08
11	.2045E+05	.3742E+00	.1291E-06	2.223E-08
12	.2338E+05	.4519E+00	.1042E-06	2.963E-08
13	.0000E+00	.1000E+01	.0000E+00	0.000E+00
14	-.9209E+04	.1180E+01	.6408E-07	2.359E-08

I_a : [W/cm²/sr]

4.3 Conversion factor from the representative atmospheric radiation to the downward irradiance

The conversion factor from the representative atmospheric radiation to the downward irradiance is computed from above two variables. The result tabled as follows.

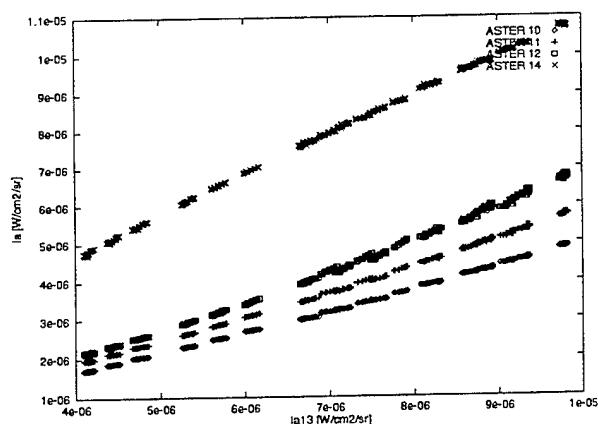


Figure 4: The comparison between the representative atmospheric radiation of 13-th. channel and the others

Table 3: Conversion factor

ch.	ai
10	1.499
11	1.456
12	1.435
13	1.230
14	1.242

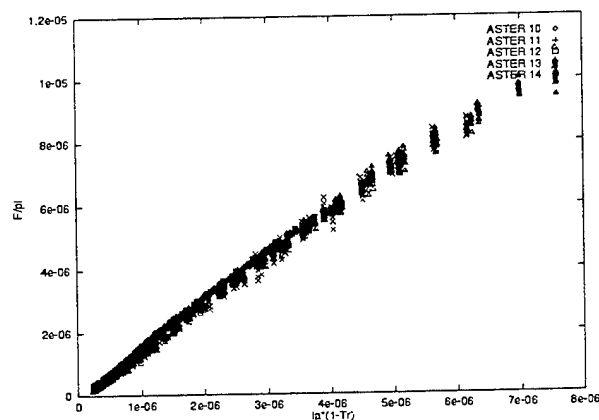


Figure 5: The comparison between upward atmospheric radiance at the top of the atmosphere and the downward irradiance at the surface

4.4 Observed brightness temperature

After the above coefficients, the comparison between the observed brightness temperature computed from LOWTRAN 7 and the proposed simplified radiative transfer equation are made. The RMS

Table 4: Comparison between the brightness temperature computed from LOWTRAN 7 and the proposed equation

ch.	RMS [K]
10	0.1520
11	0.1587
12	0.1949
13	0.6421
14	0.3145

difference at ch. 13 is worse, this is because the conversion factor is not appropriate. In this channel the downward irradiance has to be expressed in the more precise model.

5 Conclusion

These results lead the following conclusion. To simplify the radiative transfer equation in IR window spectrum by means of the adoption of some assumption are almost successful. For more precise and useful equation, there are some problems which has to be clarified as follows,

- Aerosol effect.
- Precise downward irradiance model

As the example of the difficulty of the aerosol effect consideration, The comparison between the optical thickness of the 12-th. channel and the precipitable water under the hazy/clear condition of the maritime and rural aerosol model is shown as follows. Under the hazy maritime aerosol condition, the optical thickness cannot be expressed by only the precipitable water. To define more precise model, aerosol effect has to be considered in transmittance, representative atmospheric radiation and the downward irradiance at the surface but the number of the unknown variable related to the aerosol effect is desired to be small.

Also as the example of the difficulty of the downward irradiance modelling, the comparison between the upward atmospheric radiance at the top of the atmosphere and the downward irradiance at the surface of 13-th. channels is shown. The comparison shows the slightly dispersion but it becomes the

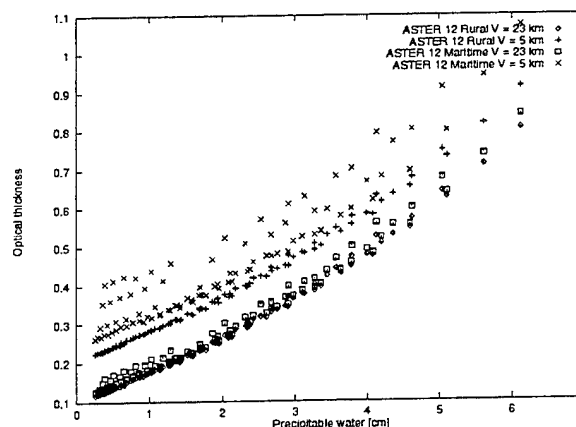


Figure 6: The comparison between the precipitable water and the optical thickness of 12-th. channel under the hazy/clear condition of maritime and rural aerosol models.

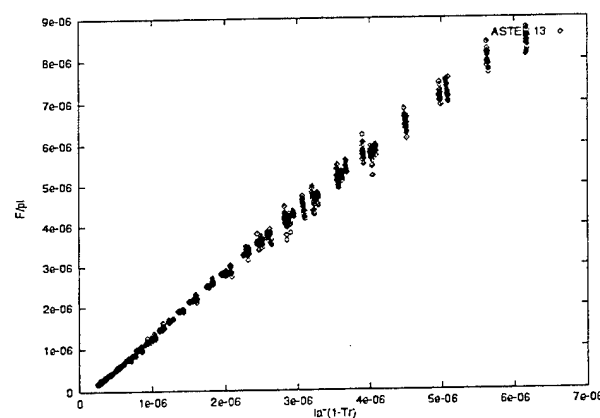


Figure 7: The comparison between the atmospheric radiance at the top of the atmosphere and the downward irradiance at the surface of 13-th. channel.

main cause of the observed brightness temperature error. The new unknown variables which show the downward irradiance at the surface is desired to be defined and the channel dependence of the unknown variable has to be considered to reduce the number of unknown variables. Also the constraints of the atmospheric unknown variables, optical thickness, representative atmospheric radiation has to be considered to avoid the convergence to the undesirable solution at the inversion estimation.

References

- [1] McMillin, L. M., and D. S. Crosby, Theory and Validation of the multiple-window sea surface temperature technique, *J. Geophys. Res.*, 89, 3655-3661, 1984.
- [2] M. Matsumoto-Moriyama and K. Arai, Some ideas for iterative estimation of atmospheric condition, surface temperature and emissivity, *Proc. IGRASS93*, Vol. 3, pp. 1291-1293, Tokyo Japan, 1993.
- [3] M. Matsumoto-Moriyama and K. Arai, An inversion for emissivity-temperature separation with ASTER data, *Adv. Space Res.*, Vol. 14, No. 3, pp. 67-70, 1994.
- [4] Chandrasekher, S., *Radiative transfer*, pp. 393, Dover Pub. Co., 1960.
- [5] M. Moriyama, M. Mima, K. Arai, Comparison of the sea surface temperature estimation methods, *Adv. Space Res.*, Vol. 16, No. 10, pp. 123-126, 1995.
- [6] Kneizys, F. X., et al, USERS' GUIDE FOR LOWTRAN 7, AFGL-TR-1988, 137pp., 1988.

The POAM II Experiment and Selected Measurement Results

E.P.Shettle, R.M.Bevilacqua, J.S.Hornstein, K.W.Hoppel, R.L.Lucke
(Remote Sensing Division, NRL, Washington, DC 20375-5351)

J.Lumpe, S.Krigman, M.Fromm, T.L.Ainsworth, and D.Debrestian
(CPI, Fairfax, VA 220301)

W.J.Glaccum
(ARC, Landover, MD, 20785)

Abstract

The Polar Ozone and Aerosol Measurement (POAM II) instrument has been collecting data on the vertical distribution of ozone and other species in the polar stratosphere, since its launch on the SPOT 3 satellite, early in autumn 1993. POAM II makes solar occultation measurements at nine wavelengths from 353 to 1059 nm, allowing it to retrieve ozone, aerosols, water vapor, and nitrogen dioxide with a about a 1 km vertical resolution. The POAM instrument will be briefly described along with a presentation of selected results from the first two of years of POAM measurements.

Introduction

NRL's Polar Ozone and Aerosol Measurement (POAM II) instrument was developed to measure the distribution of atmospheric, ozone, aerosols, PSC's, and several molecular species critical for understanding ozone chemistry in the polar stratosphere using solar occultation techniques. From the measured transmissions in the 9 visible & near IR channels, it is possible to determine the profiles of atmospheric aerosols, ozone, water vapor, and nitrogen dioxide, with 1 km vertical resolution. POAM II was launched on France's SPOT 3 satellite on 26 September 1993, which is in a 98.7° inclined sun-synchronous orbit at an altitude of 833 km. This results in all the POAM II measurements being in the Polar regions, making it an ideal instrument for studying the evolution of the ozone hole, related chemistry, and Polar Stratospheric Clouds, (PSC). In this paper we will discuss the POAM II instrument, the retrieval algorithm, and selected results of the measurements, including the 1994 Antarctic ozone hole, some studies of PSC's and Polar Mesospheric Clouds (PMC). POAM II has been collecting data for over a year and a half to date. Some preliminary ozone measurements and validation have published [Bevilacqua et al., 1995 and Randall et al., 1995], or will be published shortly, [Shettle et al., 1996]. Some early results on PSCs have been presented by Fromm et al. [1994 & 1995]. Preliminary results on POAM II observations of PMCs have been given by Debrestian et al. [1995] and Olivero et al. [1995].

POAM II Instrument

The Polar Ozone & Aerosol Measurement [POAM II] instrument uses the solar occultation technique similar to the SAM [McCormick et al., 1979] and SAGE instruments, [Mauldin et al., 1985]. Water vapor, O₂, and NO₂ are measured using a differential on/off technique. Ozone is measured at 600 nm, near the peak of the Chappius band. Aerosol extinction is measured at five wavelengths: the three "off" channels, and at 353 nm and 1059 nm. The field of view is limited by a long, narrow slit in the focal plane of the lens which subtends an angle of approximately 0.01° in elevation by 1.5° in azimuth. Light that enters the slit then passes through an interference filter before falling on a

photodiode detector. For the 833-km altitude of the SPOT 3 satellite, the 0.01° height of the slit combines with the spherical aberration of the lens to give an instantaneous vertical resolution of about 0.7 km at the Earth's limb.

In operation, during each of the fourteen orbital sunrises and sunsets which occur daily, the instrument tracks the Sun from a tangent altitude of about 150 km down to about 5 km (in clear sky: the Sun tracker threshold is about 3-5% of the signal strength of the unattenuated Sun, I_0). During orbital sunrise, at tangent altitudes above about 100 km, a solar scan is initiated in which the elevation tracking is disabled (tracking in azimuth continues), and the instrument slews ahead of the Sun and remains fixed in position. The Sun drifts through the instrument field of view providing the solar scan. This allows measurement of the unattenuated solar signal at all positions on the solar disk. This data is necessary in order to properly calculate transmissions because the Sun sensor points to the center of brightness (not the geometric center) of the Sun. Under normal aerosol loading conditions, below 25 to 30 km the center of brightness and the geometric center of the Sun begin to diverge, primarily because of differential extinction, with maximum displacements of about 0.15° . In addition, the solar scans provide a measure of the misalignment in the pointing of the nine science channels, which can be deduced by examining the differences in the times of the peak signals in the various channels. A complete discussion of the POAM II instrument is found in Glaccum et al. [1996].

Vertical profiles of the atmospheric species are operationally retrieved via a three-step process consisting of first calculating the total optical depth for each science channel, by dividing the measured signal by the appropriate signal level of I_0 . The total optical depths are then separated into their individual components (aerosols, molecular scattering, ozone, etc) using an optimal estimation retrieval algorithm [Rodgers, 1976 & 1990, and Marks & Rodgers, 1993] at each altitude. Finally, the individual-component optical depths as a function of tangent altitude are inverted to yield the vertical profiles of the absorbing species or aerosol extinction. The details of the retrieval algorithm have presented by Krigman et al., [1994] will be described in a future publication.

Antarctic Ozone Hole

Figure 1 shows the daily average ozone profiles measured by POAM II for each of three days covering 8 September 1994 through 1 October 1994. The marked decrease in ozone below 25 km, over this three week period is obvious. The formation of the ozone hole appears to progress downward from 25 km over time. Over three-quarters of the ozone near the peak concentrations, [18 to 19 km] was lost over this time period.

The dissipation of the ozone hole is illustrated by figure 2, which shows the gradual increase of the daily mean ozone profile, for our days, over the period from mid October through mid December. This ozone increase is due to combination of an actual change in the ozone profile, and a change in where POAM II is making its measurements relative to the polar vortex. This will be addressed further in the discussion section below.

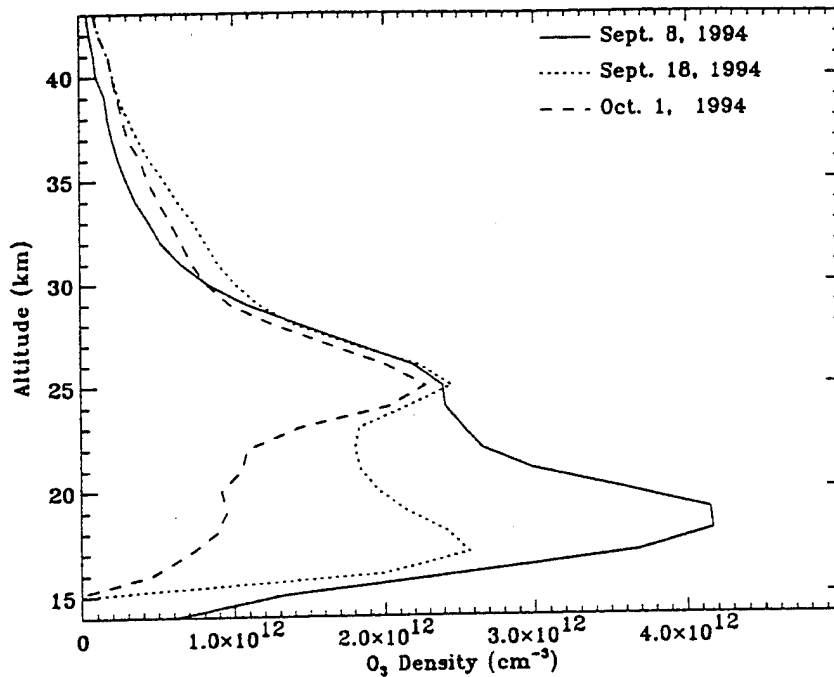


Figure 1. Individual daily zonal average ozone profile obtained by POAM II for 3 days covering the development of the 1994 ozone hole. While the latitude of the POAM measurements varied over this period, all the POAM observations during this period, were completely inside the Polar vortex.

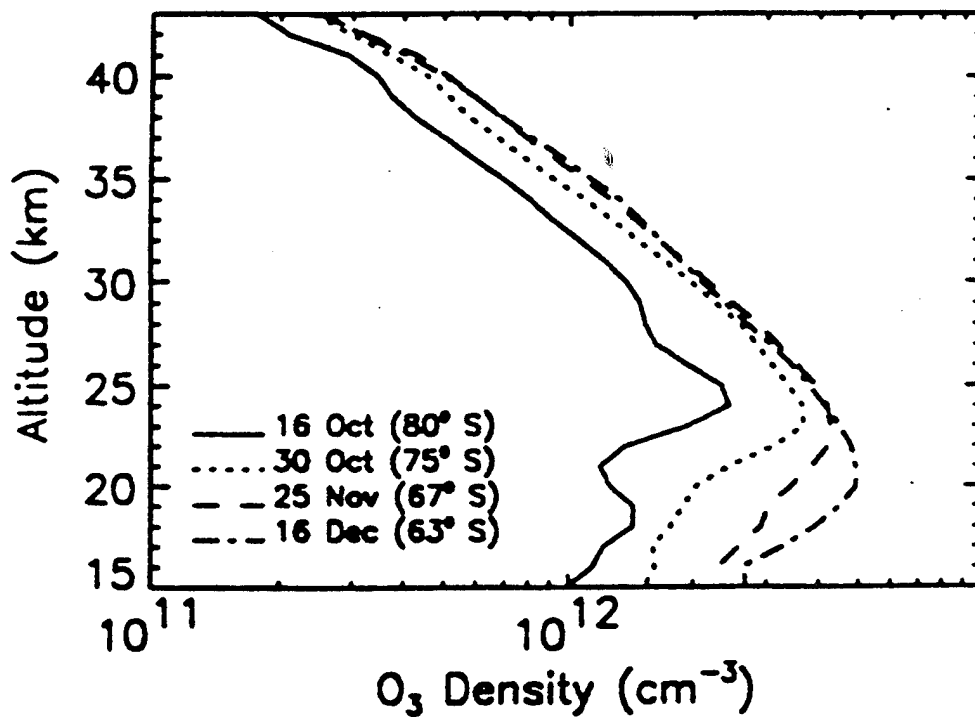


Figure 2. Zonally averaged ozone profiles obtained by POAM II during the dissipation of the 1993 Antarctic ozone hole at four selected dates.

Figure 3 shows the daily mean ozone concentration at 18 km separately for all POAM II measurements inside and outside the polar vortex for each day for May 1994 through early December 1994. There are three periods apparent; the first covering May through the end of August, where the ozone concentration is stable and there is little difference between air inside and outside the polar vortex. The second period is the rapid decline of the ozone within the polar vortex during September. During the third period from mid October through early December, the ozone concentrations inside the polar vortex has very low values compared with outside the vortex, which is about the same as during the May through August period.

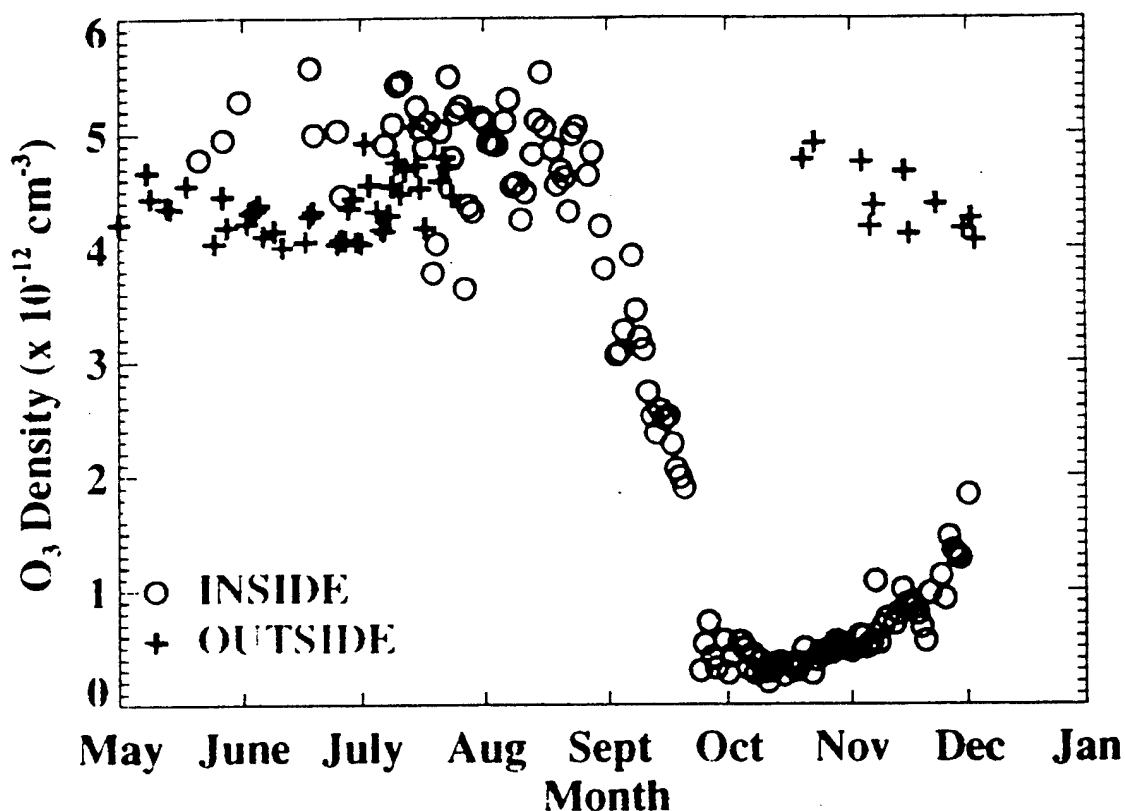


Figure 3. The daily average 18 km ozone concentration, for all measurements inside the polar vortex and for all measurements outside the polar vortex each day, June through early December 1994. The rapid depletion of ozone during September is clearly seen. After the ozone reduction within the polar vortex, the ozone outside of the vortex remains elevated.

During the third period there is a gradual increase in the ozone concentration within the polar vortex, and a decrease outside the vortex, as the vortex weakens. During August through mid October all the POAM II measurements are inside the vortex due to the position of the vortex and the latitudes at which POAM II is observing. At the end of July, the POAM observations are at 70°S moving towards the South Pole, reaching 88°S on 20 September, before starting to moving away from the pole reaching 80°S in mid October.

The marked difference between the ozone inside and outside the polar vortex demonstrates the strong containment properties of the vortex. That this strong containment occurs over the full altitude

range of the ozone hole, is seen in Figure 4 which compares the mean concentrations of ozone inside and outside the vortex averaged over the 16 October to 20 December 1993 period. While the difference is greatest below 25 km where the values inside the vortex are less than half those outside, inside the vortex is less than half outside up through 40 km.

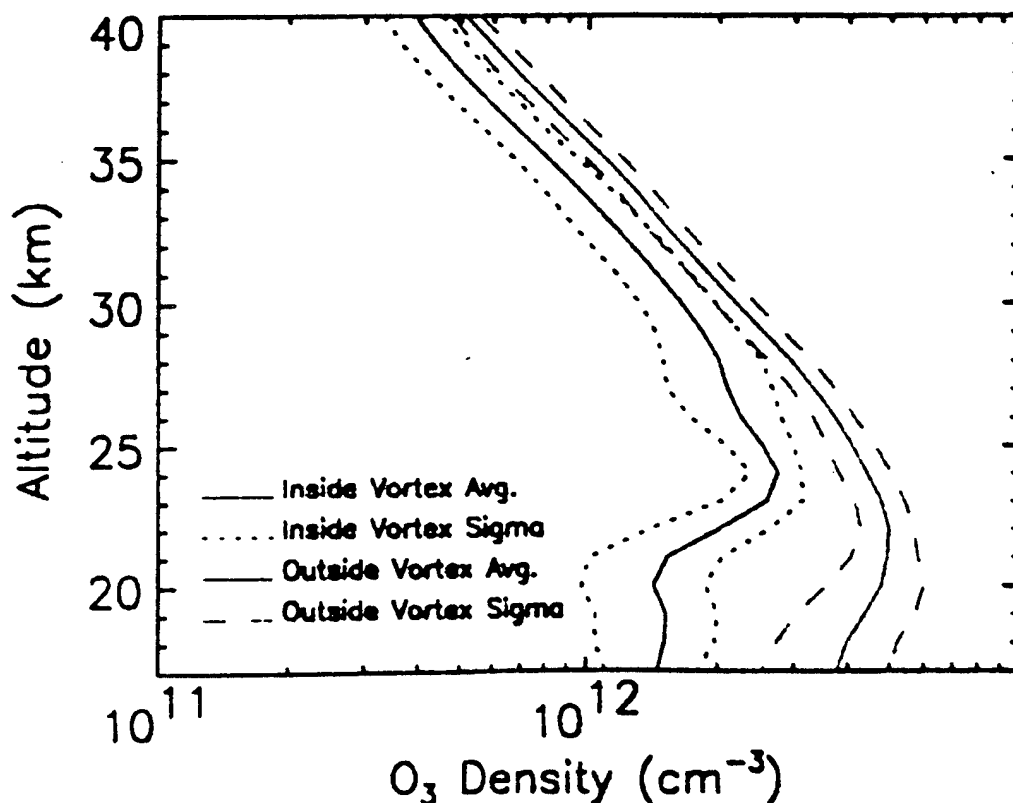


Figure 4. Average [± 1 standard deviation] ozone profiles [16 October to 20 December 1993] inside and outside the polar vortex showing typical contrast between profiles in these two categories.

Discussion of Antarctic Ozone Hole

The Antarctic ozone hole was first reported by Farman et al. [1985] and by Stolarski et al. [1986]. The primary explanation for the development of the Antarctic ozone hole, is the destruction of ozone through a catalytic cycle with atomic chlorine, which has been released by photo-dissociation of Cl_2O_2 and Cl_2 produced by heterogeneous chemical reactions on the surface of polar stratospheric clouds [PSCs], [Solomon et al., 1986; Molina et al., 1987; and Solomon, 1990]. That this ozone loss, seen particularly in Figures 1 and 3, is observed to occur primarily below 25 km is consistent with the POAM II observations of PSCs primarily below 25 km, [Fromm et al. 1994; and Shettle et al., 1995]. The apparent downward motion of the ozone depletion, [in Figure 1] is consistent with more sunlight being available at higher altitudes first, as the solar illumination returns to the South polar region with the approach of the September equinox. We find that the bulk of the depletion occurred during the month of September, with ozone destruction rates exceeding 2% per day. The POAM II measurements clearly demonstrate the strong containment properties of the polar vortex, which permits the necessary chemical processing to take place in the isolated polar air inside the polar vortex, during the polar winter.

Polar Stratospheric Clouds

PSCs were first observed by the SAM II [Stratospheric Aerosol Measurement] sensor, [McCormick et al., 1982]. They are observed to occur in the polar stratosphere primarily at temperatures below 195 K, [Poole & Pitts, 1994]. The PSCs are generally grouped into 2 classes: type 1, $\text{HNO}_3\text{-H}_2\text{O}$ clouds which form several degrees above the ice water frost point, and type 2, H_2O ice clouds which form below the frost point [typically about 188 K]. Some evidence also suggests PSCs may take the form of ternary solution droplets, [Dye et al., 1995]. These conditions primarily occur during the polar winters, especially in the Antarctic. The Polar Ozone and Aerosol Measurement (POAM II) instrument is uniquely equipped and positioned to provide coverage of PSCs. Its 98.7° sun synchronous orbit results in its observations all being from 63° S to 88° S and 55° N to 72° N .

To screen the POAM II measurements for PSCs, we use an approach similar to that of Poole & Pitts [1994]. The 1059 nm aerosol extinction profiles were first screened for those cases when the minimum NMC [National Meteorological Center] temperature analysis was below 200 K, at the location of the POAM observations. PSCs were considered to be present when one of two conditions were satisfied: (i) the aerosol extinction at 1059 nm was more than 4 standard deviations above the mean value, [using 3 or 5 standard deviations did not significantly alter the resulting frequency distribution]; or (ii) the atmospheric transmission along the POAM line-of-sight was reduced to the value at which the POAM sun-tracker lost lock on the sun, at an altitude at least 3 km above the maximum altitude at which this normally occurred.

Figure 5 shows all the POAM II Southern hemisphere observations during the period from 1 May 1994 to 9 November 1994, with pluses, +, denoting observations for which no PSCs were detected, and closed circles, •, indicating observations of a PSC. It can be seen that the POAM II measurements cover essentially all of the Antarctic continent over this period.

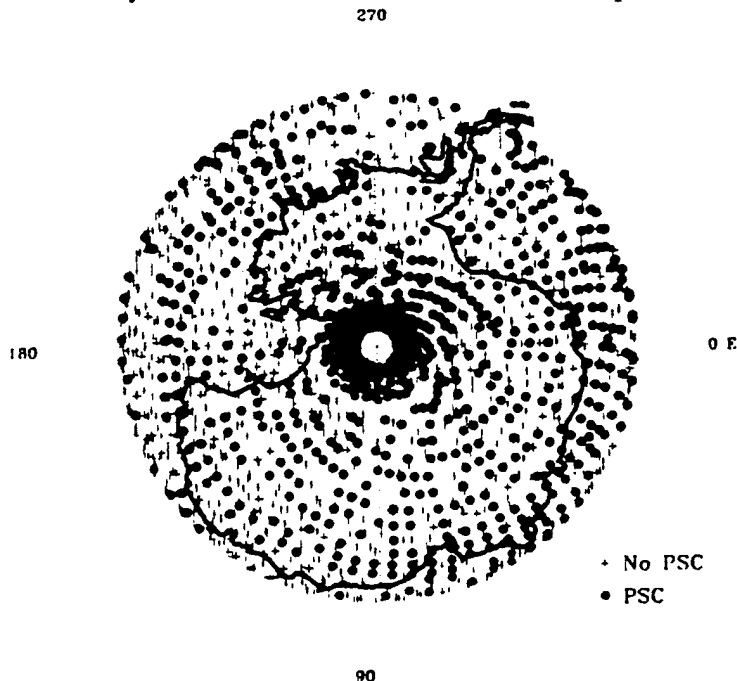


Figure 5. All the POAM II measurements in the Southern hemisphere during the 1994 Antarctic PSC season, with pluses, +, denoting observations for which no PSCs were detected, and closed circles, •, indicating observations of a PSC.

A pronounced longitudinal dependence of the PSC frequency of occurrence can be seen, with significantly more POAM II observations for which no PSC was detected, longitudes centered around 180°, and PSCs detected for a much higher fraction of the measurements centered around the prime meridian [0°].

Figure 6 shows the monthly frequency of occurrence for PSCs during the May to November 1994 season in the Antarctic, (left side of figure). This is similar to that reported by Poole & Pitts [1994] for the 1979 to 1991 period based on the SAM II observations, although the POAM II observations indicate a somewhat higher frequency of occurrence. The righthand side of figure 6 shows the corresponding POAM data in the Arctic for the 1994-95 season.

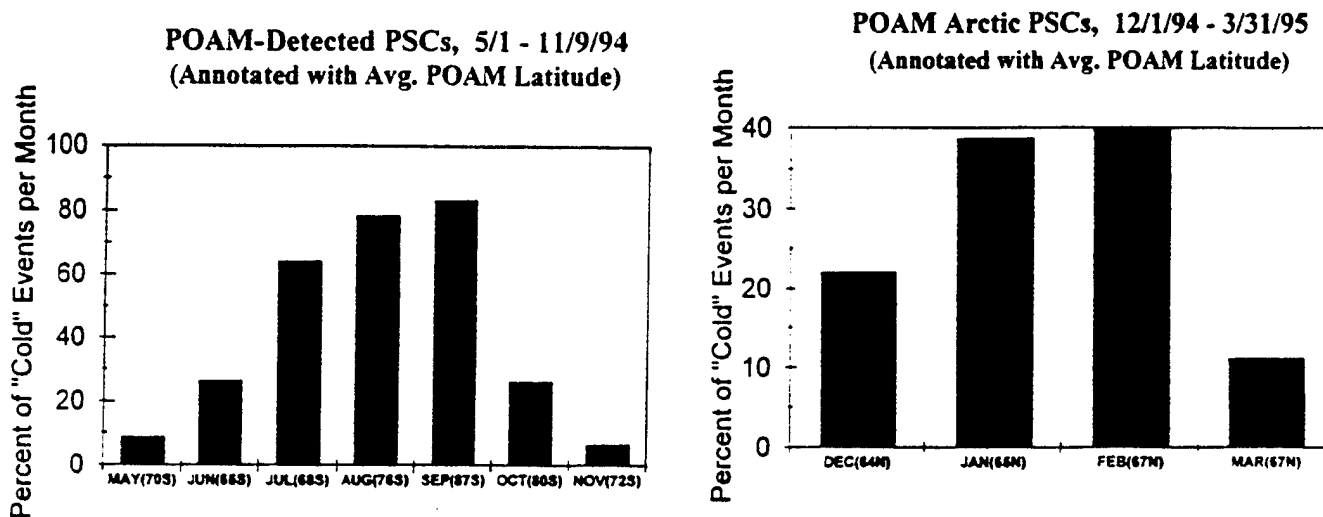


Figure 6. *Left side* - The monthly frequency of occurrence for PSCs for the May to November 1994 season in the Antarctic. *Right side* - The monthly frequency of occurrence for PSCs for the December 1994 to March 1995 season in the Arctic.

Polar Mesospheric Clouds

The characteristics of PMCs, have been reviewed by Thomas [1989] and by Gadsen & Schröder, [1989]. They are believed to be small ice particles formed at or below the summer mesopause (near an altitude of 80 to 90 km), where the temperatures can go below 140 K, at latitudes poleward of about 55°. They are generally observed during an about twelve week period centered two weeks after the summer solstice, [Olivero & Thomas, 1986 and Thomas & Olivero, 1989]. Satellite observations of PMCs have been reported from scattered light observed by OGO 6 [Donahue et al., 1972] and by the Solar Mesospheric Explorer (SME) satellite, [Olivero & Thomas, 1986 and Thomas & Olivero, 1989]. They have also been observed from the ground during twilight. The historical surface observation are reviewed by Gadsen & Schröder, [1989].

For the detection and analysis of the PMCs in the POAM II data, the full retrieval algorithm, as discussed above, was not used. Rather we started with the total optical thickness as a function of tangent altitude, [for the POAM II line-of-sight to the sun], since the full retrievals were normally only performed up to 50 or 60 km. To detect the PMCs channels 2 and 3 [442 and 448 nm] were used, since they had the best signal to noise given the wavelength dependence of extinction due to PMCs. All data for altitudes from 70 to 95 km were screened. First the molecular Rayleigh scattering

background was subtracted from the from the line-of-sight, or slant path optical depth, to determine the residual optical depth, as shown in Figure 7. For these altitude range, the extinction due to molecular absorption or background aerosols normally is negligible, for those channels. A PSC was detected when the residual signal was more than 3 standard deviations above 0.0 in both channels at the same altitude. This gave a detection threshold of 0.0005 in the slant path optical depth.

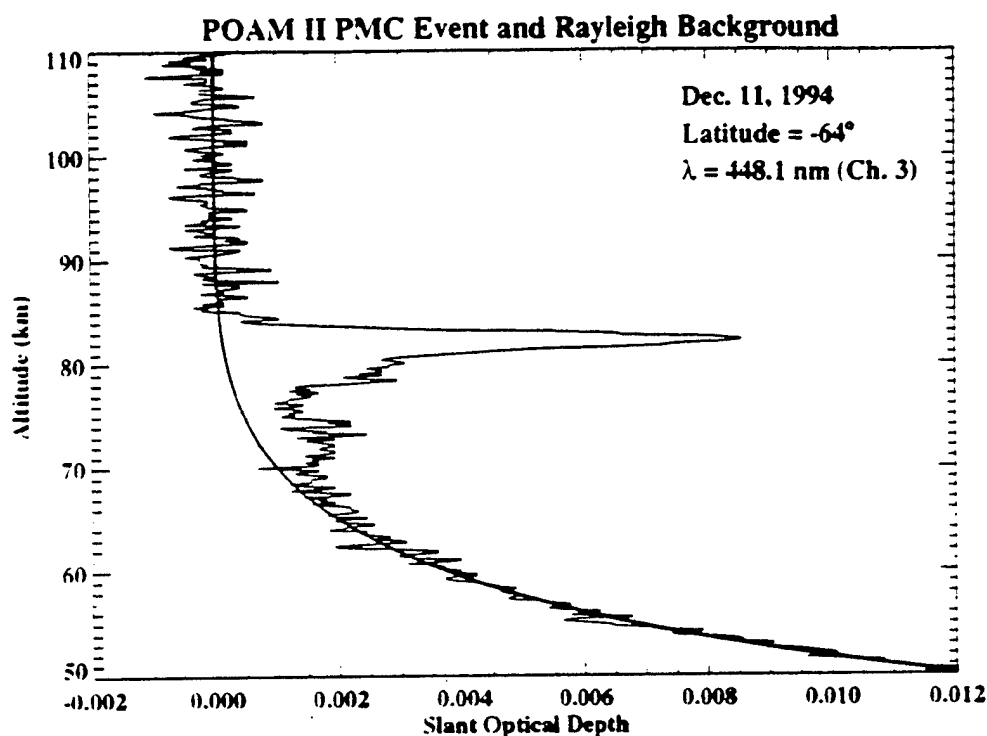


Figure 7. The measured POAM II line-of-sight optical depth for the strongest PMC event, (jagged light line), with the molecular Rayleigh scattering background superimposed, (smooth heavy line).

To determine the cloud top altitude, the altitude of its base, and the cloud extinction coefficient, the expected optical thickness based on a simple cloud model was fit to the residual slant optical depth as function of altitude. This model assumed the cloud extinction coefficient was constant throughout the cloud, and that the cloud was horizontally homogeneous for the full horizontal extent of a given POAM measurement, which is several hundred kilometers, within the PMC. The results of such a fit are shown in Figure 8. The results of this fit shows that in this case the actual PMC was a reasonable match to the simple cloud model. Not all cases matched this simplistic model as well, exhibiting behavior expected for multi-layered clouds or clouds with finite horizontal extent.

POAM II has observed PMCs at altitudes between 80 and 90 km, during approximately three month periods centered near the summer solstice in each hemisphere. The geometry of the solar occultation measurements with a long near horizontal line-of-sight through the earth's atmospheric limb, make it sensitive to the small extinction coefficients of the PMCs. It is believed that the POAM II measurements, represent the first reported observations of PMCs directly by extinction; all the early measurements being by scattered sunlight. It should be recognized that seasonal variation of the latitude of the POAM II observations limits its utility for extensive study of PMCs. The period around the Summer solstice, is when the POAM II measurements are furthest from the Poles. This is especially a limitation in the Northern hemisphere, where the POAM II observations during the PMC

season are generally between 55°N and 60°N, which are near the lowest latitudes reported by Thomas & Olivero [1989] based on the SME data.

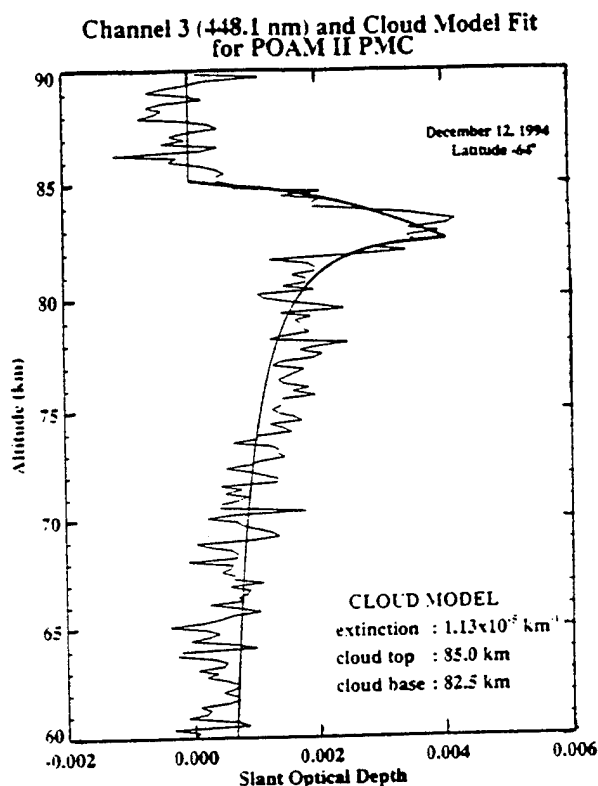


Figure 8. Comparison of PMC model calculation (smooth heavy line), with residual optical depth measured by POAM II after the Rayleigh scattering has been subtracted, (jagged light line).

The strongest PMC observed by POAM II to date, had a slant optical depth of 0.01 (for a wavelength of 442 nm), with the weakest PMC being limited by their signal-to-noise to an optical depth of 0.0005 along their tangent line of sight. These correspond to the brightest of the SME observation, which cover 2.5 orders of magnitude or twice the brightness range of the POAM II observations. The POAM observations exhibited a strong wavelength dependence, usually only detecting the cloud layers at their shortest wavelengths (353 to 600 nm). The wavelength dependence of the PMC slant optical depth for the nine strongest PMCs, which gave a measurable signal for all the POAM channels, indicated a particle size of 20 to 70 nm, with all cases smaller than 100 nm. This is consistent with the small particle sizes inferred from the SME data with a mean radius of 43 ± 16 nm [Rusch et al., 1991].

References

Bevilacqua, R.M., K.Hoppel, J.Hornstein, R.Lucke, E.Shettle, T.Ainsworth, D.Debrestian, M.Fromm, J.Lumpe, S.Krigman, W.Glaccum, J.Olivero, R.T.Clancy, D.Rusch, C.Randall, F.Daladier, C.Daniel, E.Chassefière, C.Brogniez, & J.Lenoble, "First results from POAM II: The Dissipation of the 1993 Antarctic Ozone Hole", *Geophys. Res. Letters*, **21**, 909-912, (1995).

Bevilacqua, R.M., E.P. Shettle, J.S. Hornstein, W.J. Glaccum, J.D. Lumpe, S.S.Krigman, P.R.Schwartz, and D.T.Chen "Polar Stratospheric Studies with the Polar Ozone and Aerosol Measurement Experiment (POAM II)", pg 174-176 in the *Proceedings of the Eighth American Meteorological Society Conference on Atmospheric Radiation*, (1994).

Debrestian, D., E.P.Shettle, J.Lumpe, R.Bevilacqua, J.Hornstein, W.Glaccum, & J.Olivero, "POAM II Observations of Polar Mesospheric Clouds: Preliminary Analysis", presented at the Spring 1995 AGU Meeting, Baltimore, MD, 30 May - 2 June 1995.

Donahue, T.M., B. Guenther, & J.E. Blamont, "Noctilucent Clouds in Daytime: Circumpolar Particulate Layers Near the Summer Mesopause", *J. Atmos. Sci.*, **30**, 515-517, (1972).

Dye, J.E., D.Baumgardner, K.Drdla, B.W.Gandrud, K.Barr, D.W.Fahey, A.Tabazadeh, & M.Loewenstein, "In-situ Observations of Polar Stratospheric Clouds in the Southern Hemisphere during ASHOE and Comparisons with Previous Observations", Presented at the International Conference on Ozone in the Lower Stratosphere, 15-19 May 1995, Halkidiki, Greece, (1995).

Farman, J.C., B.G.Gardiner, & J.D.Shanklin, "Large losses of total ozone in Antarctica reveal seasonal ClO_x/NO_x interaction", *Nature*, **315**, 207-210, (1985).

Fromm, M.D., E.P.Shettle, R.M. Bevilacqua, A. Wilkins, J. Lumpe, and S. Krigman, "PSC's in the 1994 Antarctic Autumn/Winter: Observations From POAM II", Presented at the Fall 1994 AGU Meeting, 5-9 December, 1994, San Francisco, CA, (1994).

Fromm, M.D., E.P.Shettle, R.M.Bevilacqua, J.S.Hornstein, K.W.Hoppel, A.Wilkins, J.Lumpe, S.S.Krigman, "Observations of PSC's from POAM II", Presented at the International Conference on Ozone in the Lower Stratosphere, 15-19 May 1995, Halkidiki, Greece, (1995).

Fromm, M.D., E.P.Shettle, R.M.Bevilacqua, J.Lumpe, & J.Hornstein, "PSCs in the 1994/95 Arctic Fall/Winter: Observations from POAM II", presented at the Spring 1995 AGU Meeting, Baltimore, MD, 30 May - 2 June 1995.

Gadsen, M., & W.Schröder, *Noctilucent Clouds*, Springer-Verlag, (1989).

Glaccum, W., R.Lucke, R.M.Bevilacqua, E.P.Shettle, J.S.Hornstein, D.T.Chen, J.D.Lumpe, S.S.Krigman, D.J.Debrestian, M.D.Fromm, F.Daladier, E.Chassefière, C.Daniel, C.E.Randall, D.W.Rusch, J.J.Olivero, C.Brogniez, J.Lenoble, R.Kremer, "The Polar Ozone and Aerosol Measurement (POAM II) Instrument", To be published in *J. Geophys. Res.*, **101**, (1996).

Krigman, S.S., J.D.Lumpe, R.M.Bevilacqua, and E.P.Shettle, "POAM II Retrieval Algorithms", Presented at the Fall 1994 AGU Meeting, 5-9 December, 1994, San Francisco, CA, (1994).

Marks, C.J. and C.D.Rodgers, "A Retrieval Method for Atmospheric Composition From Limb Emission Measurements", *J. Geophys. Res.*, **98**, 14,939-14,953, (1993).

Mauldin III, L.E., N.H.Zaun, M.P.McCormick, J.H.Guy, & W.R.Vaughn, "Stratospheric Aerosol and Gas Experiment II instrument: a functional description", *Opt. Engineering*, **24**, 307-312, (1985).

McCormick, M.P., P. Hamill, T.J. Pepin, W.P. Chu, T.J. Swissler, and L.R. McMaster, Satellite studies of the stratospheric aerosol, *Bull. Amer. Meteor. Soc.*, **60**, 1038-1046, (1979).

McCormick, M.P., H.M.Steele, P.Hamill, W.p.Chu, & T.J.Swissler, "Polar Stratospheric Cloud Sightings by SAM II", *J. Atmos. Sci.*, **39**, 1387-1397, (1982).

Molina, M.J., T.-L.Tso, L.T.Molina, & F.C.-Y.Wang, "Antarctic Stratospheric Chemistry of Chlorine Nitrate, Hydrogen Chloride, and Ice: Release of Active Chlorine", *Science*, **238**, 1253-1257, (1987).

Olivero, J.J., D.Debrestian, E.P.Shettle, J.S.Hornstein, R.M.Bevilacqua, J.Lumpe, & W.Glaccum, "Polar Mesospheric Clouds Seen in Solar Occultation by POAM II: Preliminary Analysis", presented at the IUGG XXI General Assembly, Boulder, CO, 2-14 July 1995.

Olivero, J.J. and G.E.Thomas, "Climatology of Polar Mesospheric Clouds", *J. Atmos. Sci.*, **43**, 1263-1274, (1984).

Poole, L.R. & M.C.Pitts, "Polar Stratospheric Cloud Climatology based on Stratospheric Aerosol Measurement II observations from 1978 to 1989", *J. Geophys. Res.*, **99**, 13083-13089, (1994).

Randall, C.E., D.W.Rusch, R.T. Clancy, R.M.Bevilacqua, E.Shettle, J.H.Hornstein, J.Lumpe, S.S.Krigman, M.Fromm, D.Debrestian, & J.J.Olivero, "Preliminary Results from POAM II: Stratospheric Ozone Densities at Northern Latitudes", *Geophys. Res. Letters*, **21**, 2733-2736, (1995).

Rodgers, C.D., "Retrieval of atmospheric temperature and composition from remote measurements of thermal radiation", *Rev. Geophys. Space Phys.*, **14**, 609-624, (1976).

Rodgers, C.D., "Characterization and error analysis of profiles retrieved from remote sounding measurements", *J. Geophys. Res.*, **95**, 5587-5595, (1990).

Rusch, D.W., G.E.Thomas, & E.J.Jensen, "Particle Size Distributions in Polar Mesospheric Clouds Derived from Solar Mesospheric Explorer Measurements", *J. Geophys. Res.*, **96**, 12,933-12,939, (1991).

Shettle, E.P., R.M.Bevilacqua, J.S.Hornstein, W.J.Glaccum, D.Debrestian, M.Fromm, S.Krigman, J.Lumpe, J.L.Bertaux, E.Chassefière, F.Dalaudier, C.Daniel, C.Brogniez, J.Lenoble, P.Pruvost, J.Olivero, C.Randall, & D.Rusch, "POAM II: Early Results and Comparisons with the COSPAR International Reference Atmosphere Models", to be published in *Adv. Space Res.*, **18**, (1996).

Shettle, E.P., R.M.Bevilacqua, T.L.Ainsworth, J.Lumpe, K.W.Hoppel, S.S.Krigman, M.D.Fromm, & J.S.Hornstein, "Measurements of Antarctic Ozone by POAM II", page 306-312, in *Atmospheric Sensing and Modeling II*, Proceedings of SPIE Conference No. 2582, ed. by R.Santer., (1995)

Shettle, E.P., M.D.Fromm, D.Debrestian, J.S.Hornstein, K.W.Hoppel, J.Lumpe, W.J.Glaccum, J.Olivero, R.M.Bevilacqua, & S.S.Krigman, "Observations of Clouds in the Polar Stratosphere and Polar Mesosphere from POAM II", page 138-145, in *Passive Infrared Remote Sensing of Clouds and the Atmosphere III*, Proceedings of SPIE Conference No. 2578, ed. by D. Lynch & E.P.Shettle, 1995.

Solomon, S., R.R.Garcia, F.S.Rowland, & D.J.Wuebbles, "On the depletion of Antarctic ozone", *Nature*, **321**, 755-758, (1986).

Solomon, S., "Progress towards a quantitative understanding of Antarctic ozone depletion", *Nature*, **347**, 347-354, (1990).

Stolarski, R.S., A.J.Krueger, M.R.Schoeberl, R.D.McPeters, P.A.Newman, & J.C.Alpert, "Nimbus 7 satellite measurements of the springtime Antarctic ozone decrease", *Nature*, **322**, 808-811, (1986).

Thomas, G.E., "Mesopause clouds and the Physics of the Mesopause Region", *Rev. Geophys.*, **29**, 553, (1989).

Thomas, G.E. and J.J.Olivero, "Climatology of Polar Mesospheric Clouds, 2. Further Analysis of Solar Mesospheric Explorer Data", *J. Geophys. Res.*, **94**, 14,673-14,702, (1989).

THE RELATION BETWEEN ZENITH POLARIZATION AND OPTICAL DEPTH FOR STRATOSPHERIC AEROSOLS FROM EL CHICHON AND PINATUBO

Frederic E. Volz

PL/GPOS

Hanscom AFB, MA 01731-3010

Low values of the degree of zenith polarization (ZP) have often been measured after major volcanic eruptions, most recently, including in the more revealing near infrared, by Steinhorst (1971, 1977) in Europe, by Coulson (1988) at Mauna Loa, and Wu and LU (1993) in Beijing. Steinhorst, and Wu and LU, used twilight scattering models to convert such sunset data into vertical profiles of aerosol. However, it appears that a more direct relationship between ZP and aerosol optical depth (OD) in the stratosphere might be obtained from the measurement at sunset of ZP for several years after an eruption. Indeed, observations in the NIR during most of the El Chichon and Pinatubo periods show that the observed range of ZP is essentially proportional to log OD. This agrees with the evaluation in terms of mixing ratios of the basic equation for polarization in hazy air.

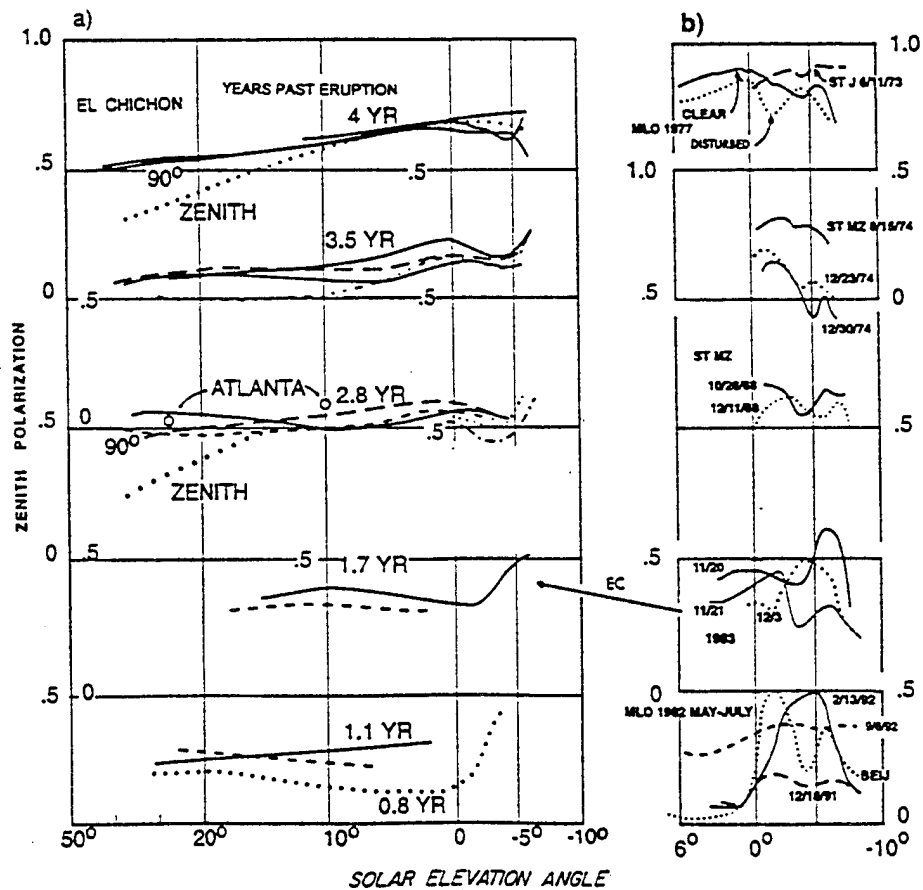


Figure 1. Selected profiles in NIR of degree of polarization at 90° from the sun (that is in the zenith for solar elevations < 15°). Note scale change at 20° elevation. a) from Bedford/Lexington after the El Chichon eruption; b) data from the more recent literature (Coulson, Steinhorst, Wu and Lu, for wavelengths of 0.7 or 0.8 μm).

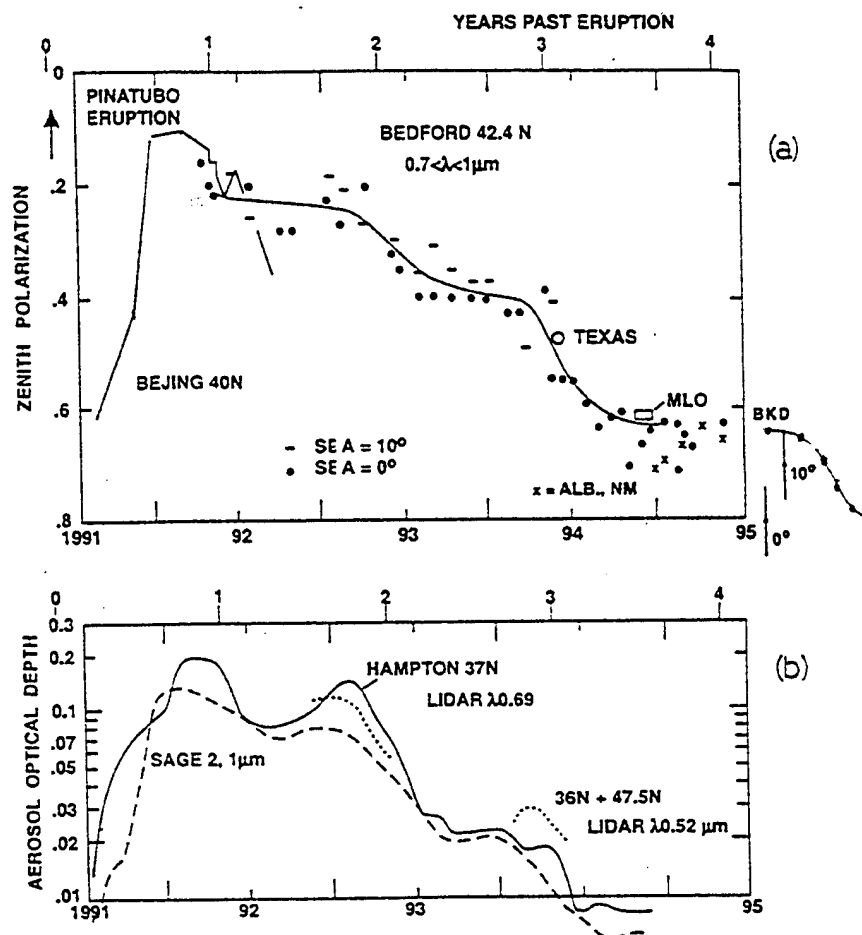


Figure 2. a) Average trend of ZP in the Pinatubo period, including data by Wu and Lu from Beijing and, for 1995, by J. Roadcap from Albuquerque, NM; b) Trend of aerosol optical depth (OD) from lidar at Hampton, VA and segments of combined lidar data from 36N and 47.5N by Jaeger et al (1995), and SAGE II.

ZP increases downwards, that is depolarization increases upwards.

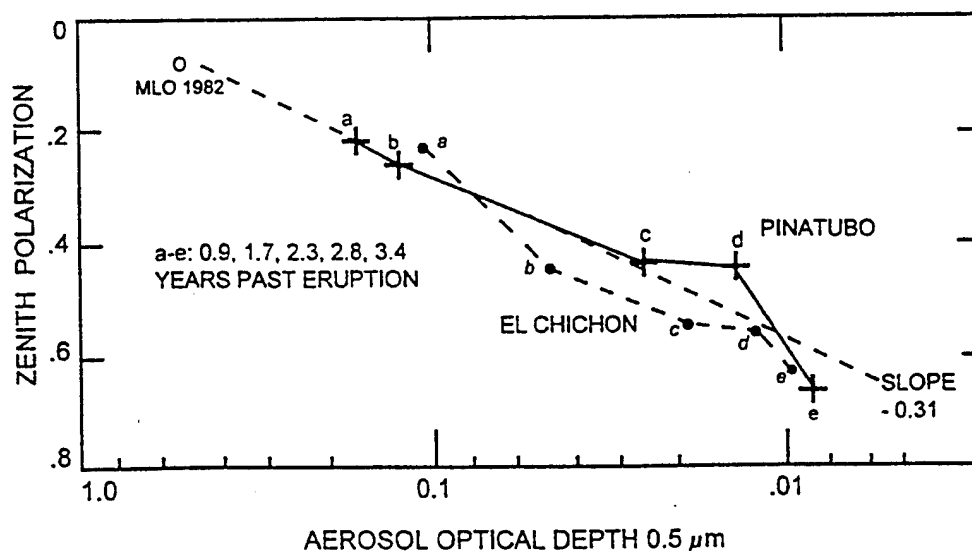


Figure 3. The relation between ZP and log OD for El Chichon and Pinatubo periods.

OD of data points c to e should be increased by a factor of about two.

**Infrared Optical Constants of Sahara Sand, Volcanic Ash, and
Water Soluble Aerosols**

W. G. Egan and J. Jr. Joseph, Natural Sciences Department,
York College/City University of New York
Jamaica, NY 11451

E-Mail: EGAN@YCVAX.YORK.CUNY.EDU

ABSTRACT

We have adapted and improved the Volz technique for determining the absorption indices of atmospheric aerosols for use in the LOWTRAN and MODTRAN models. The new technique uses the Kubelka-Munk scattering theory to separate the scattering from the absorption in measurements with potassium bromide pellets containing the aerosols, resulting in absorption indices that are significantly lower in the window regions than those previously used in the models. Calibrations were achieved using lasers, and a sulfur coated integrating sphere. Also, finite wavelength effects cause a relocation of the observed absorption bands.

INTRODUCTION

An essential component in the LOWTRAN and MODTRAN infrared atmospheric models is the optical properties of aerosols. The original determinations of the infrared optical constants of Sahara sand, volcanic ash and water soluble aerosols were from compressed samples and powders of the samples in potassium bromide pellets (Ref.1). In potassium bromide pellets, there is significant

scattering among the particles which causes an apparent increase in the absorption. This can result in a measured absorption that is one to two orders of magnitude greater than the true absorption.

In this paper we will trace the development of various techniques for separating the scattering from the absorption in potassium bromide pellets leading to accurate values of the infrared absorption index of some representative aerosols. There are at present seven scattering models that include absorption (Table 1, from Ref. 2). In this paper we will consider the simplest Two Flux Model [Kubelka-Munk (K-M) Theory], which requires the least computing time.

The two variables of scattering and absorption in potassium bromide pellets which thus require two measurements to separate them uniquely. The theoretical models generally require the measurement of total diffuse transmission and absorption by the pellet sample. This is best accomplished using an integrating sphere, although point-by-point equivalent measurements can be made. Visual range integrating spheres are readily available for use in the range from 0.185 μm to 2.8 μm wavelength, with a magnesium oxide coating. One such is the Gier-Dunkle system. We have used this system to determine the total diffuse transmission and reflection of various mineral and aerosol samples in the range 0.185-2.8 μm wavelength. However the question arises as to the accuracy of the technique in determining the absorption indices of the (scattering) powders contained in the potassium bromide pellets.

To check the validity of measurements, a standard Corning

CS1-64 colored glass with known visual to near infrared absorption indices as a function of wavelength was used for calibration. The diffuse transmission and reflection of powdered and sintered samples was measured; pellets were made containing glass powders uniformly distributed and also with the glass powder forming a layer on the surface of the pellet (Ref. 2). Scattering analyses were made using the Kubelka-Munk Theory and the Modified Kubelka-Munk (M-K-M) Theory; The most accurate results were obtained using the layered samples and the M-K-M model. Typical results for a Sahara sand are shown in Fig. 1 for the absorption portion of the absorption index of refraction; also shown is the refractive portion in the wavelength region from 0.185-1.105 μm region. The refractive portion was determined using a Brewster angle measurement as described in Ref. 2.

However, for infrared measurements, an integrating sphere system was required that would operate in the range 0.8 to 20 μm spectral region. There have been gold coated integrating spheres used for total transmission and reflection measurements on samples, and a check of the validity of gold as a diffuse coating for an integrating sphere was in order. Whether the gold was shiny, dull, sintered, or sand blasted, point-by-point measurements of the gold surfaces showed that they were not diffuse, with a low hemispherical reflectance. In the literature, a paper appeared describing flowers of sulfur as a diffuse standard (Refs. 3 and 4). This appeared to be a good coating for the 0.8-20 μm spectral region. The question then arose as to the obtaining of an integrating sphere with detectors in the long wavelength infrared

region.

An integrating sphere system was constructed that could be checked for accuracy in the UV-Visible-near IR spectral region, and then adapt it to the longer wavelength IR by constructing a duplicate system with a sulfur coating. There are many integrating sphere systems described in the literature, and the main point in the design is that the first scatter from the sample not be seen by the detector in reflection, nor the direct incident beam in transmission. Thus, an integrating sphere system was constructed as shown in Fig. 2 (Ref.2), which allowed the use of photomultipliers in the UV-Visible-Near IR regions, and, for the duplicate system, indium antimonide in the near IR, and arsenic doped silicon in the far IR. Since the latter detectors have to be cryogenically cooled, the reduced sensitivity produced by the external location had to be tolerated. A detector immersed in the sphere would have been better. Another problem arose, source strengths proved to be inadequate for reasonable measuring times. To obviate this problem, lasers were used: a HeNe for 1.159 and 3.159 μm and a Carbon Dioxide for 9.2 and 10.6 μm . The accuracy of the UV-Visible-Near IR system (with a barium sulfate coating) was compared to the Gier-Dunkle and found to yield closely comparable results, thus validating the extension to the sulfur coated integrating sphere. We further compared samples at 1.139 μm in both the barium sulfate and sulfur coated integrating sphere systems using the HeNe laser, with results in close agreement. Then we used the diffuse transmission and reflection measurements to calibrate measurements of transmission and reflection from a Perkin-Elmer Model 283B

infrared recording spectrophotometer in the spectral region 2.5-50 μm spectral region (similar to the Volz technique:Ref. 1). Data was analyzed using the K-M theory, and the results for a Sahara sand are shown in Fig. 3, in a comparison with the results of Volz.

It is seen that the separation of the scattering component produces an absorptive portion of the index of refraction that is one to two orders of magnitude less on the Sahara sand sample than of Volz (Ref.1). The results are similar for water soluble aerosols and volcanic soil (Figs.3 and 4). The spectral resolution is limited by the long time constant used in the spectrophotometer for reasonable scan times. It appears that scattering has not been completely eliminated, and further analyses would be desirable using the M-K-M scattering theory.

There are also differences between the Volz measurements of the refractive indices of the samples as evidenced by Figs, 6a and 6b; they could possibly be caused by sample differences, finite wavelength effects, or differences in measurement techniques. However, the silicate bands are evident in the volcanic ash and Sahara sand samples.

REFERENCES

1. F. E. Volz, "Infrared Optical Constants of Ammonium Sulfate, Sahara Dust, Volcanic Pumice, and Flyash", *Applied Optics*, 12, 564-568 (1973).
2. W. G. Egan and T. W. Hilgeman, "Optical Properties of Inhomogeneous Materials", Academic Press, New York, 235pp, (1979).

3. J. T. Agnew and R. B. McQuistan, "Experiments Concerning Infrared Diffuse Reflectance Standards in the Range 0.8-20.0 Microns", J. Optical Society of America, 43, 999-1007, (1953).
4. M. Kronstein, R. J. Kraushaar, and R. E. Deacle, "Sulfur as a Standard of Reflectance in the Infrared", J. Optical Society of America, 53, 458-465 (1963).

TABLE 1

SCATTERING MODELS THAT INCLUDE ABSORPTION

1. Two Flux Model [Kubelka-Munk (K-M) Theory
2. Two Flux Model with Surface Scattering (M-K-M)
3. Six Flux Model
4. Modified Dispersion Model
5. Mie Scattering
6. Radiative Transfer
7. Multiple Scattering Model

Doubling

Successive Orders of Scattering

Invariant Embedding

The Monte-Carlo Method

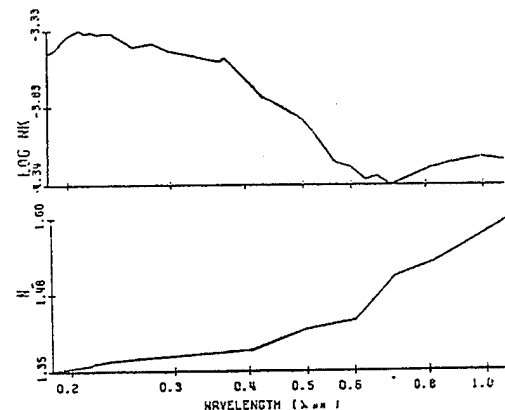
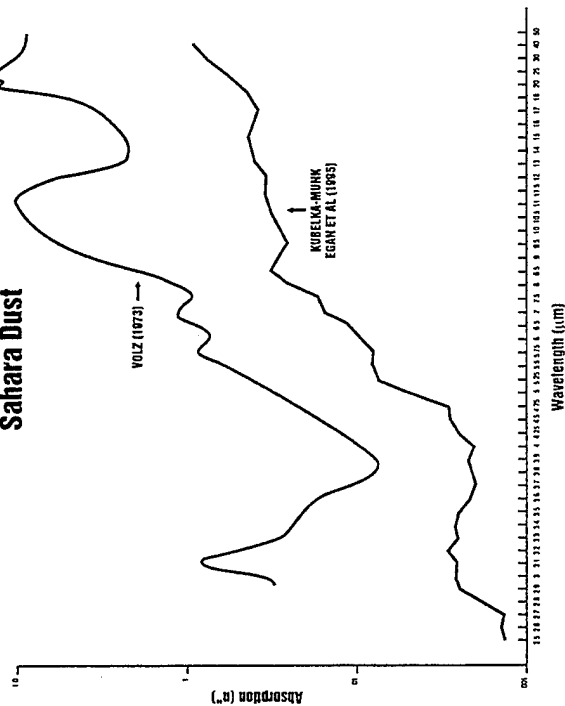


Fig. 1 Sahara Sand # 3: Amokon Dune Sand from Tenere Desert East from Air

Absorption vs. Wavelength Sahara Dust

Fig. 3



Absorption vs. Wavelength Volcanic Dust

Fig. 5

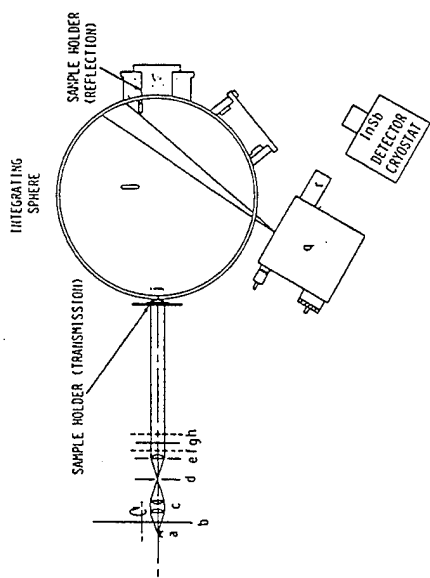
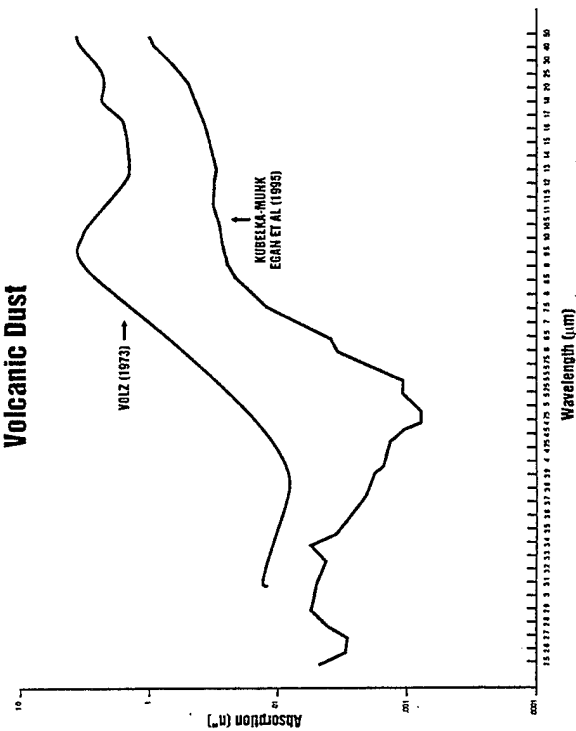


FIG. 2 Layout of optical system for integrating sphere. [From Egan and Hilgeman (1975a).]

Absorption vs. Wavelength Aerosol Water Solubles

Fig. 4

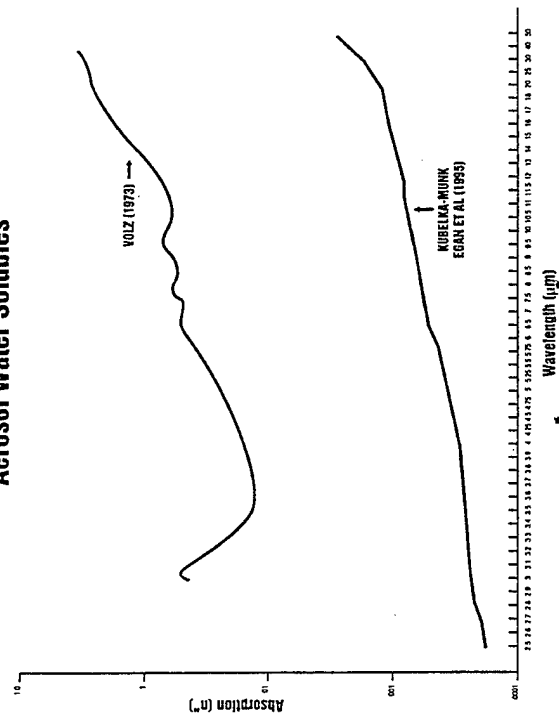


Fig. 6a
Egan et al, 1995

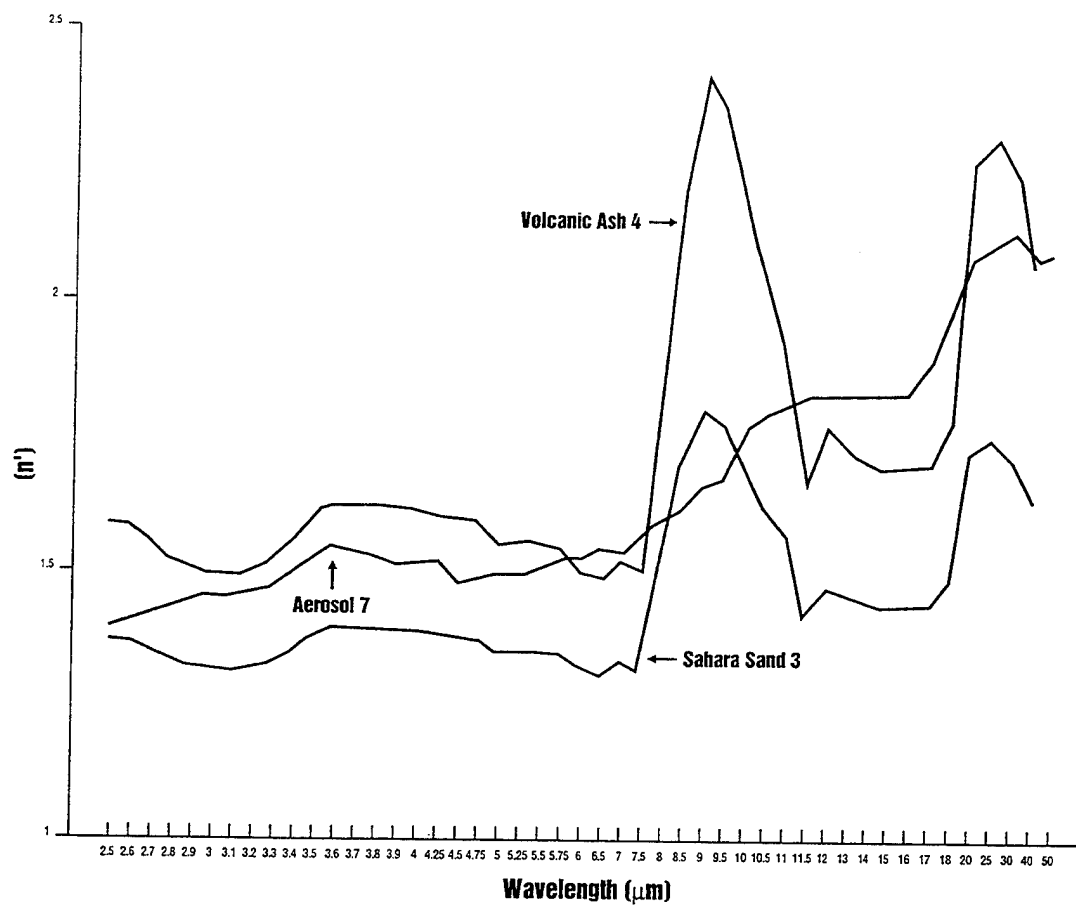
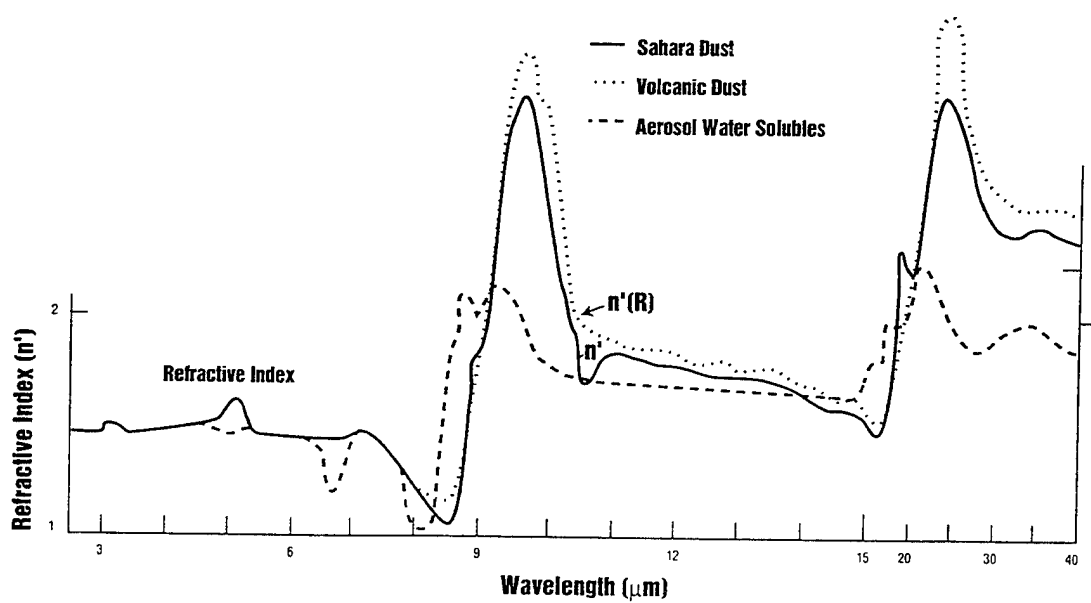


Fig. 6b
Volz 1973



A double scatter lidar program to determine particle size distributions

Richard Garner, PhotoMetrics, Inc., 4 Arrow Dr., Woburn, MA 01801

We have developed a double scatter lidar program for determining particle size distributions of media composed of spherical particles. The program, which is implemented on a DOS-based computer, determines the four Stokes parameters of the doubly backscattered lidar radiation from spatially inhomogeneous media, as a function of time and as a function of field-of-view look angle. Size distributions are determined by comparing lidar returns from a polarization sensitive, multiple field-of-view lidar to a library of calculated lidar returns which is generated using a family of size distributions. In this report we describe the double scatter model, the technique for determining size distributions, and show some examples using simulated lidar data.

1 Description of double scatter lidar model

The Stokes vector of the doubly scattered lidar radiation is determined, at each designated instant of time, by considering all radiation which has traveled the same path length from transmitter to receiver while making two successive single scatters. Each single scatter is considered a Mie scatter from a collection of particles characterized by a size distribution. The size distribution shape is assumed constant but its normalization (i.e., particle density and, therefore, extinction coefficient) is allowed to vary with distance into the medium.

Figure 1 shows the geometry of double scattering. At $t = 0$ a laser pulse is emitted from the origin of the "laboratory" coordinate system (displayed) along the z axis. Two scattering locations are shown, the first at \mathbf{R}_1 and the second at $\mathbf{R} = \mathbf{R}_1 + \mathbf{R}_2$. The scattering angles are θ_1 and θ_2 , respectively. Both scatters have the same scattering plane, oriented at an angle ϕ with respect to the x ("parallel") axis. To ease the computational burden the first scatter is constrained to lie on the z axis. The second scatter must lie within the receiver's field-of-view.

The instantaneous (differential) Stokes vector representing the double scattered radiation which returns to the receiver at time $t = (R_1 + R_2 + R)/c$ due to the two specific scatters depicted in Fig. 1 is

$$d\mathbf{P}_r(t) = \frac{A_r(\theta) \cos \theta}{16\pi^2 R^2 R_2^2} \alpha(\mathbf{R}_1) \alpha(\mathbf{R}) e^{-\tau} \left[\tilde{\mathbf{L}}(-\phi) \tilde{\mathbf{P}}(\theta_2) \tilde{\mathbf{P}}(\theta_1) \tilde{\mathbf{L}}(-\phi) \mathbf{P}_o \right] dR_1 dV_2 \quad (1)$$

where

$$dV_2 = R_2^2 dR_2 d\theta_1 d\phi \sin \theta_1 \quad (2)$$

or

$$dV_2 = R^2 dR d\theta d\phi \sin \theta, \quad (3)$$

and α is the total extinction coefficient (scattering plus absorption), τ is the total optical path length from laser to receiver, $\tilde{\mathbf{L}}$ is a 4×4 rotation matrix which is only a function of ϕ (the first $\tilde{\mathbf{L}}$ rotates the laser Stokes vector from the laboratory reference frame to the scattering plane and the second $\tilde{\mathbf{L}}$ rotates the double scattered radiation back to the laboratory reference frame), $\tilde{\mathbf{P}}$ is the 4×4 phase matrix (equal to the scattering matrix with $\alpha/4\pi$ factored out), $A_r(\theta)$ is the receiver response function, assumed to be a function of polar angle of incidence and normalized to aperture area, and \mathbf{P}_o is the instantaneous incident Stokes vector (with units of power). The quantity $d\mathbf{P}_r(t)$ has units of power.

The differential dV_2 can be written in terms of the variables (R_2, θ_1, ϕ) (Eq. 2) or (R, θ, ϕ) (Eq. 3). The form that is used depends on how the integration of Eq. 2 is performed which, in turn, depends on how the double scatter model is implemented. There are two implementations, which we refer to as the 3D model and 1D model. The 3D model is applicable to all double scatter situations, while the 1D model is an approximation applicable to situations in which θ is small and the field-of-view does not contain zenith. Both models are described respectively in the two following subsections.

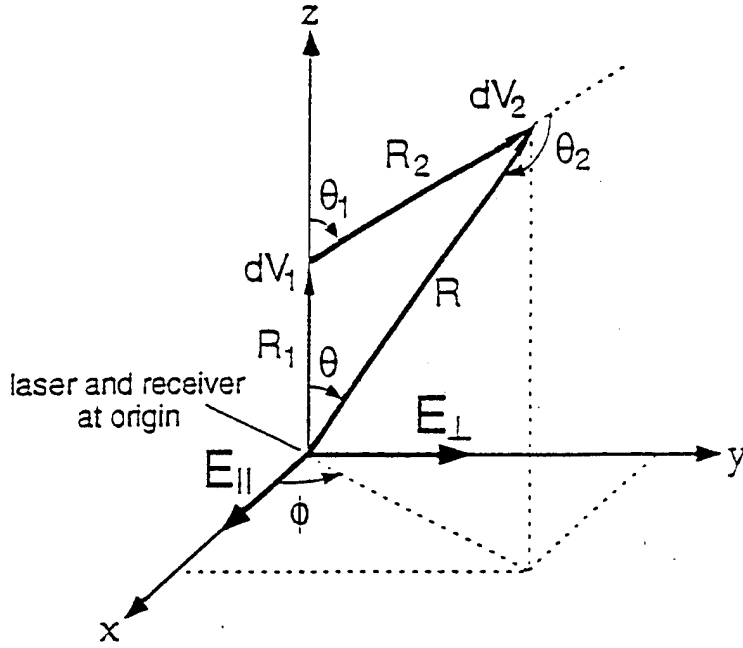


Figure 1: Geometry of double scattering.

1.1 Full (3D) model

With the 3D model the detected double scattered radiation is calculated for any annular, pie-shaped, or circular field of view. The Stokes vector $P_r(t)$ at time t is the integral of Eq. 1, together with Eq. 2, over R_1 , θ_1 , R_2 , and ϕ , subject to the conditions that the total path length is constant, the two scattering volumes are within the scattering medium, and the second scatter is within the receiver field-of-view. The integral in ϕ can be performed analytically. The remaining three integrals are performed numerically.

The variable set containing (R_2, θ_1) (Eq. 2) is chosen over the set containing (R, θ) (Eq. 3) in order to avoid a nonintegrable singularity when the field-of-view includes zenith. Note that Eq. 1 together with Eq. 3 has the factor R_2^2 in the denominator. When the field-of-view contains zenith R_2 will equal zero during the integration. By using Eq. 1 together with Eq. 2, which has R^2 in the denominator instead, the singularity is moved to the origin (i.e., the integrand is zero when $R = 0$) and is never encountered as long as the scattering medium does not extend to zero range.

The total instantaneous double scattered Stokes vector at time t is

$$P_r(t) = \int_{z_0}^{ct/2} dR_1 \int_{\theta_{1l}(R_1)}^{\theta_{1h}(R_1)} \sin \theta_1 d\theta_1 \int_{R_{2l}(R_1, \theta_1)}^{R_{2h}(R_1, \theta_1)} dR_2 \frac{A_r \cos \theta \alpha(R_1) \alpha(R)}{16\pi^2 R^2} e^{-r} \times M \quad (4)$$

where z_0 is the lower bound of the scattering medium and

$$M = \int_{\phi_l}^{\phi_h} \bar{L}(-\phi) \bar{P}(\theta_2) \bar{P}(\theta_1) \bar{L}(-\phi) P_o \quad (5)$$

The ϕ integral is performed analytically. The expression for M for arbitrary values of ϕ_l and ϕ_h is very long and therefore not presented here. When the limits are $\phi_l = 0$ and $\phi_h = 2\pi$ (i.e., annular field-of-view), Eq. 5 becomes

$$M = \begin{bmatrix} \frac{\pi}{4}(A_1 A_2 + B_1 B_2)(3P_{||o} + P_{\perp o}) - \frac{\pi}{2}(C_1 C_2 - D_1 D_2)(P_{||o} - P_{\perp o}) \\ \frac{\pi}{4}(A_1 A_2 + B_1 B_2)(P_{||o} + 3P_{\perp o}) + \frac{\pi}{2}(C_1 C_2 - D_1 D_2)(P_{||o} - P_{\perp o}) \\ \pi U_o [(C_1 C_2 - D_1 D_2) - \frac{1}{2}(A_1 A_2 + B_1 B_2)] \\ 2\pi V_o (C_1 C_2 - D_1 D_2) \end{bmatrix} \quad (6)$$

where $(P_{||o}, P_{\perp o}, U_o, V_o)$ is the Stokes vector of the incident laser radiation. The quantities A, B, C , and D are the four nonzero components of the Mie scattering phase matrix which, in the representation of the above Stokes vector, is written as

$$\begin{bmatrix} A & 0 & 0 & 0 \\ 0 & B & 0 & 0 \\ 0 & 0 & C & D \\ 0 & 0 & -D & C \end{bmatrix}. \quad (7)$$

The subscripts 1 and 2 indicate evaluation at the scattering angle at volumes dV_1 and dV_2 respectively. Note that when the laser radiation is linearly polarized (e.g., $P_o = P_{||o}, 0, 0, 0$) then the Stokes vector of the double scattered radiation has only two nonzero components ($P_{||}$ and P_{\perp}). This indicates that the received radiation is depolarized and its polarized portion is in the same direction as the laser radiation. This is expected from symmetry considerations.

1.2 Small θ , off zenith (1D) model

The 1D model is used to calculate double scatter returns when the field-of-view has a small polar angle (θ) spread and does not contain zenith. Since zenith is not included then the singularity at $R_2 = 0$ (Eq. 1 with dV_2 from Eq. 3) is not encountered. Therefore, dV_2 from Eq. 3 is used in the integration of Eq. 1 since it has more natural coordinates than dV_2 from Eq. 2.

Since the polar angle θ has a small range of values we can make the approximations $d\theta \rightarrow \Delta\theta$, $dR \rightarrow \Delta R$, and $\theta \rightarrow \theta_o$. Here, $\Delta\theta$, a constant, is equal to the detector full angle field of view, ΔR , a function of R_1 , is equal to the total range of R values for a particular value of R_1 and for $\theta = \theta_o$,* and θ_o , a constant, is equal to the central polar angle value of the field-of-view.

With these approximations the total instantaneous double scattered Stokes vector is

$$P_r(t) = \frac{A_r}{16\pi^2} \cos \theta_o \sin \theta_o \Delta\theta \int_{x_o}^{ct/2} dR_1 \Delta R \frac{\alpha(R_1)\alpha(R_2)}{R_2^2} e^{-\tau} \times M \quad (8)$$

where M is given by Eq. 6.

We have demonstrated that the 1D implementation agrees well with the 3D implementation as long as the polar angle range is not too large. And, even when the polar angle range is large, the two implementations converge toward agreement as single scatter range (time) increases.

Figure 2 shows results of the 1D and 3D implementations run for the same conditions. Shown are the instantaneous double and single scattered powers, normalized to 10^{12} times the incident peak laser power, versus single scatter range ($ct/2$). Both the double scattered parallel and perpendicularly polarized components are presented. The incident Stokes vector is $(1, 0, 0, 0)$. The field-of-view is defined by

$$\begin{aligned} 0.2 \text{ mrad} < \theta < 5.0 \text{ mrad} \\ 0^\circ < \phi < 22.5^\circ \end{aligned}$$

The extinction coefficient is a constant 0.35 km^{-1} . The particle size distribution is the following log normal

$$g(r) = \frac{1}{\sqrt{2\pi r \ln(\sigma)}} \exp \left[\frac{-\ln^2(r/\bar{r})}{2 \ln^2(\sigma)} \right], \quad (9)$$

where $\bar{r} = 0.1 \text{ } \mu\text{m}$ and $\sigma = 1.6$. Note that the parallel components of the 1D and 3D implementations are slightly different for the first two hundred meters but they converge as range increases. For this situation zenith is very close to being contained within the field-of-view.

* ΔR is the distance between the boundary ellipses along the line $\theta = \theta_o$. The boundary ellipses are the boundaries of the region defined by the locus of all second scatter locations for constant t and R_1 .

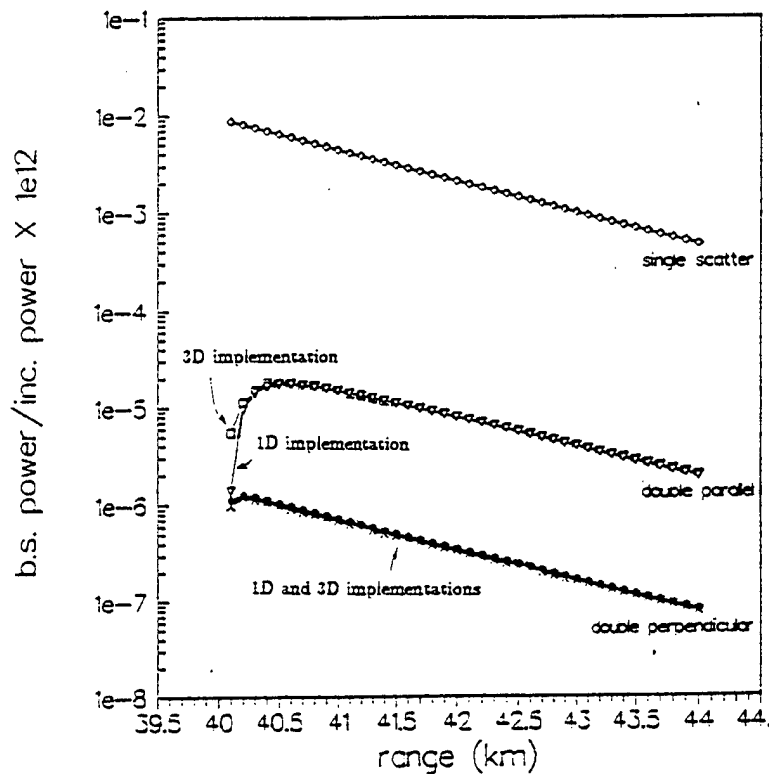


Figure 2: Results of the 1D and 3D implementations run for the same conditions and parameters (see text).

2 Determining size distribution

Size distribution is determined by comparing lidar data to double scatter calculations in which the size distribution has an assumed functional form with one or more free parameters. The size distribution functional forms that we have considered include

$$\begin{array}{ll}
 \text{log normal:} & \frac{1}{(2\pi)^{1/2} \ln(\sigma)} \exp \left[\frac{-\ln^2(r/\bar{r})}{2 \ln^2(\sigma)} \right], & \bar{p} = (\bar{r}, \sigma) \\
 \text{modified gamma:} & \frac{a^{a+1}}{a! r_m} \left(\frac{r}{r_m} \right)^a \exp \left(-\frac{ar}{r_m} \right), & \bar{p} = (r_m, a) \\
 \text{delta function:} & \delta(r) & \bar{p} = (r) \\
 \text{sum of deltas:} & \sum_i A_i \delta(r_i), & \bar{p} = (A_1, A_2, \dots) \quad (r_i \text{ fixed parameters})
 \end{array}$$

The vector \bar{p} denotes the list of free parameters which are varied in order to find the best match between data and calculations.

The log normal distribution is useful for modeling certain types of man-made dust clouds. The modified gamma distribution is useful for modeling cumulus clouds. The delta function is useful for determining the average or peak size when the true size distribution is relatively narrow. The sum of delta functions can be used when the true size distribution functional form is unknown.

Ideally, the lidar should be polarization sensitive, should have several off-axis detectors which sense only multiple scattered radiation, and an on-axis detector which senses mostly single scattered radiation. The off-axis, parallel polarized lidar data is better suited to comparison with double scatter calculation results. The reason for this is that parallel polarized return is more sensitive to azimuthal angle (ϕ) and particle size variations.

The double scattered, perpendicularly polarized return has a four-leaf clover pattern, with maxima at $\pi/4, 3\pi/4, 5\pi/4,$ and $7\pi/4$, and zeros at $0, \pi/2, \pi,$ and $3\pi/2$, independent of particle size. The

perpendicularly polarized return is useful for understanding experimental conditions (e.g., possible cross talk between polarization channels and depolarization due to the presence of aspherically shaped particles).

The on-axis lidar data is used to determine the extinction profile that is needed for the double scatter calculations. For this, single scatter assumptions are used. After determining size distribution one may then re-calculate the extinction coefficient using the size distribution information in order to ascertain a multiple scatter corrected extinction profile. The on-axis lidar data can also provide a baseline depolarization level if the scattering medium contains aspherically shaped particles.

To determine size distribution we construct a figure-of-merit function which has a minimum for the "best" choice of size distribution. The function, of course, is not unique. We use the following least squares-like function:

$$\chi^2(\vec{p}) = \sum_{r,d} \left[\frac{M_{r,d} - C_{r,d}(\vec{p})}{M_{r,d}} \right]^2 \quad (10)$$

where $M_{r,d}$ and $C_{r,d}(\vec{p})$ are, respectively, the measured and calculated lidar returns corresponding to range r and detector d . The calculated returns are a function of \vec{p} , the size distribution free parameters.

3 Examples using simulated lidar data

3.1 Test size distribution: delta function

A single delta function can be used to predict particle size if the scattering medium's true size distribution is relatively narrow. This is revealed by the plots in Fig. 3. For each plot simulated lidar data was generated with the double scatter lidar program using a unique log normal size distribution. The two parameters of the log normal distributions are designated on the graphs. For the final plot the size distribution is the sum of two log normals. χ^2 was then calculated for several different test size distributions of the form $\delta(x)$, where $x = 2\pi r/\lambda$ is the size parameter. The curves depicting χ^2 versus x for each simulation are shown. For comparison, the simulated size distributions are shown in each graph as well.

The graphs clearly show that χ^2 has a minimum for size parameter corresponding to the maximum of the simulation's log normal size distribution. For the situation in which the simulation is the sum of two log normals, χ^2 has two minima corresponding to the two maxima of the two log normals. For all the graphs in Fig. 3 the σ parameter of each log normal is 1.05, producing relatively narrow size distributions. Additional calculations, which we do not show, indicate similar results for σ values as high as 1.3. For σ values greater than 1.3 the χ^2 function does not have a conclusive minimum.

3.2 Test size distribution: log normal

Figure 4 shows the situation in which both the simulated and test size distributions are log normals. Each plot in the figure corresponds to the same simulated data set, but with different amounts of white noise added before calculation of χ^2 . The simulated log normal size distribution functions have free parameters $\bar{x} = 2.05$ and $\sigma = 1.15$. Each graph shows χ^2 versus \bar{x} of the test size distribution, for different values of the test size distribution σ . The amount of added white noise and the minimum signal to noise ratio of the data considered for the χ^2 calculation are designated on the graphs.

The graphs show a clear minimum for the values of \bar{x} and σ which are closest to those of the simulated data. As more white noise is added to the simulated data the minima persist, although they become less well-defined. A conclusion from these plots, as well as others which we do not show, is that a clear minimum is discernible as long as data points with signal to noise less than three are discarded.

4 Conclusions

We have studied the size distribution extraction technique for many situations, in addition to the ones described above, using simulated lidar data. We make the following conclusions based on these studies.

- Size distribution can be determined unambiguously if there are some particles with diameters on the order of, or larger than (but not much larger than), the wavelength. Thus, if a size distribution peaks at a diameter much smaller than the wavelength, but has a significant spread so that its tail extends into a regime of diameters on the order of a wavelength, then the size distribution can be determined by this technique. The reason for this is that the double scatter lidar returns for particle diameters small or very large compared to a wavelength only vary in magnitude while the functional dependence varies negligibly.
- If the real (simulated) size distribution is narrow enough (e.g., $\sigma < 1.3$ for a log normal "true" size distribution) then it is sufficient to consider test size distributions which are mono-size (i.e., delta function).
- Size distribution can be determined if only those data points with signal to noise ratio greater than three are used.
- If the real size distribution is log normal then utilizing a modified gamma test size distribution will give a minimum χ^2 at a parameter space location for which the modified gamma resembles the log normal. This works for size distributions which are not too wide because, for such conditions, the modified gamma functional form deviates too much from the log normal functional form.
- It is best to have at least two pixels which are located in the focal plane at 90° with respect to each other. The double scattered parallel polarized lidar return is a sensitive function of the field-of-view azimuth angle. Two pixels located at 90° are best able to exploit this sensitivity. Additional pixels are helpful as far as making the χ^2 minimum more well-defined. However, if signal to noise is adequate then the additional complexity of more pixels may offset any advantages.
- The sizes of the pixels is dictated by signal to noise considerations. The behavior of χ^2 is affected by pixel sizes only insofar as it is affected by inadequate signal to noise ratio.
- One only needs to consider the range of the return over which the double scatter returns from the different pixels differ significantly from each other. This usually occurs over the first 0.2-0.5 optical path length.

We have utilized real lidar data from cumulus clouds for comparison with double scatter calculations. The results were presented at the 16th Annual Conference on Atmospheric Transmissions (1993). For those studies lidar data was acquired with a polarization sensitive, single field-of-view lidar (one on-axis detector for two polarization channels). Single scatter extinction was derived from the lidar data and used with the double scatter lidar program. The size distribution was assumed to have a modified gamma functional form. Agreement between the calculated and measured returns was good for a particular choice of the free parameters.

Acknowledgements

This work was supported by the U.S. Air Force, Defense Nuclear Agency, and Strategic Defense Initiative Office under contracts F19628-91-C-0009, DNA001-92-C-0078, and SDIO84-92-C-0008, respectively. We thank Douglas Youmans of W.J. Schafer Associates, Inc. for his help and support.

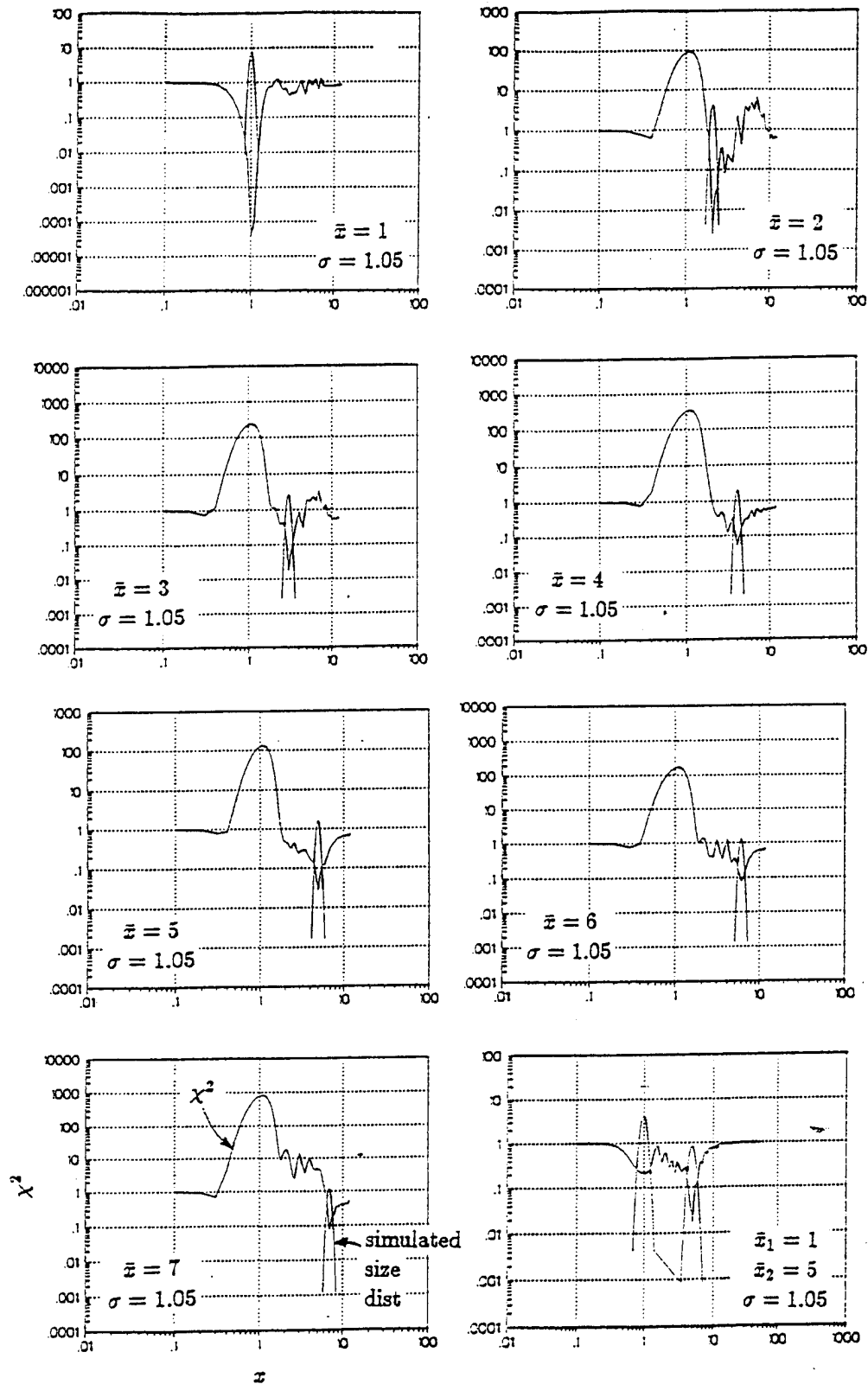


Figure 3: χ^2 versus z for several different simulated lidar data sets. Simulated size distributions are log normal and test size distributions are delta functions with one free parameter, z .

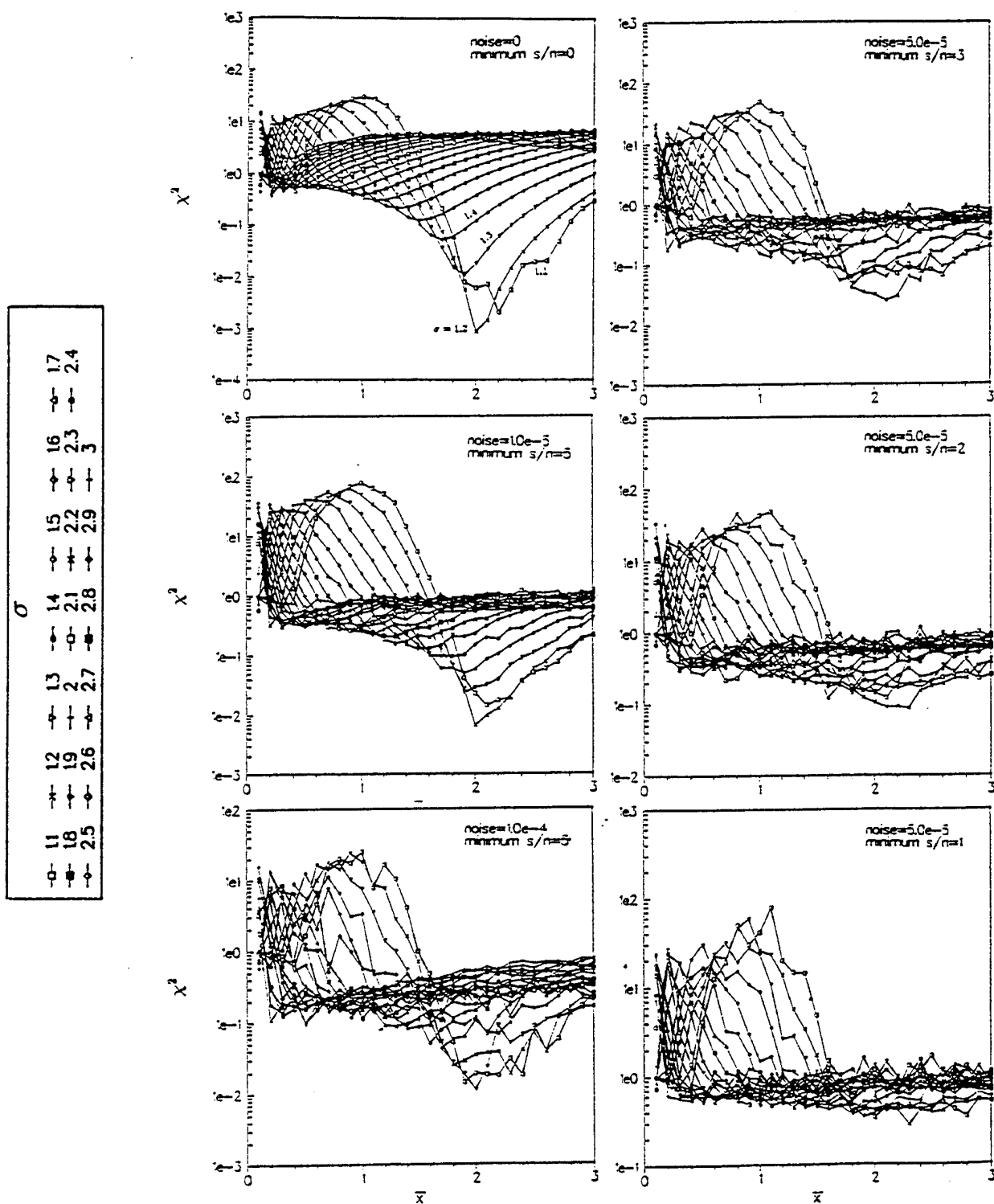


Figure 4: χ^2 versus \bar{z} for different σ values of a log normal test size distribution. The simulated size distribution is log normal ($\bar{z} = 2.05$, $\sigma = 1.15$). Each plot corresponds to different amount of added white noise and a different minimum s/n threshold (data points below minimum s/n are not considered).

Aerosol Size Distribution Measurements and Laser - Transmission Experiments in Zurich, Switzerland

Simon Kälin and Atsumu Ohmura

1. Introduction

The Department of Geography at the Swiss Federal Institute of Technology Zurich is engaged in global climatology. Research topics are the prediction of possible future climate changes, the energy balance at the surface, radiation measurements and instrument development, foundation of an international data center for surface based radiation data, radiative transfer processes and the role of turbulence within the boundary layer. The different subjects include field measurements as well as computer modeling tasks.

Chemical and physical properties of aerosol particles are still an ongoing issue. Much discussed is for example the role of sulfate aerosols from natural and anthropogenic sources. The radiative effects of sulfate aerosol particles and greenhouse gases are opposite in sign and comparable in magnitude. Due to the inhomogeneous distribution of aerosols, the radiative effects may cancel each other locally as has been demonstrated in numerical experiments (Kiehl a. Briegleb, 1993). In order to predict future radiative changes reliably, it is not sufficient to calculate the order of magnitude for the radiative effects, but the detailed processes involved have to be studied.

The aim of the field experiment described in the following section is to obtain an improved knowledge about the nature and variability of aerosol size distributions in the atmospheric boundary layer and its influence on the atmospheric transmission and visibility under various meteorological conditions.

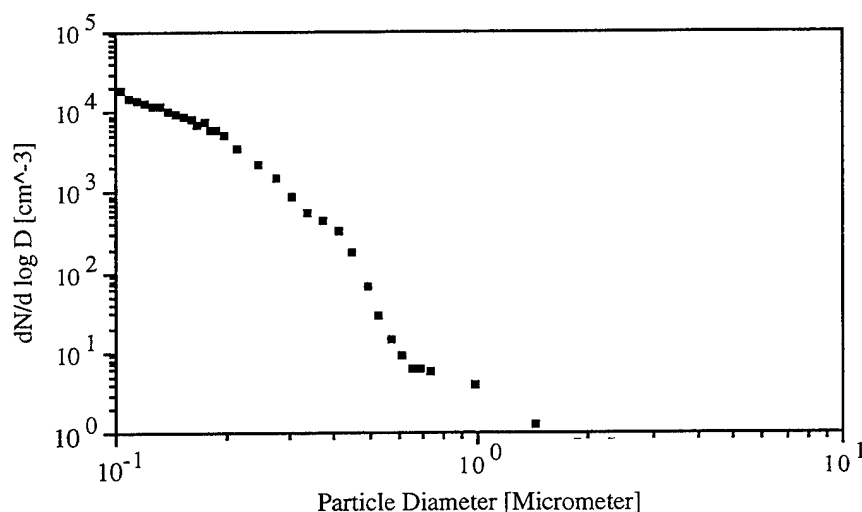
2. Measurements of Aerosol Size Distributions at Oberglatt

Size distribution measurements are currently carried out at Oberglatt, Switzerland. The instrument used is a Laser Aerosol Spectrometer (Model LAS-X-CRT, Particle Measuring Systems Inc., Boulder, Colorado), allowing measurements in the size ranges of 0.1 - 0.2, 0.2 - 0.75 and 0.75 - 7.5 μm . Each range provides 15 channels for the particle classification. In its automatic mode, the three size ranges are measured sequentially, using a time interval of 300 seconds. Based on the assumption that there are no fundamental changes in the size distribution on a time scale of 15 minutes, measurements of the three ranges can be combined to give a size distribution in the range of 0.1 - 7.5 μm . An example is presented in Fig. 1.

3. Meteorological Database

The uptake of water and the subsequent growth of aerosol particles is a well known behaviour of most ambient aerosol particles. Hygroscopic particles begin to grow at about 75% relative humidity. Precipitation scavenging is an important sink for aerosol particles. These two examples demonstrate a need to collect additional data in order to interpret the aerosol measurements. At the same site, the temperature and relative humidity is therefore measured. Additional elements such as pressure, wind speed, wind direction, precipitation, cloud base, cloud type, insolation and visibility are observed at a site nearby from the Swiss Meteorological Institute.

Fig. 1. Size Distribution measured at Oberglatt, May 6th 1995, 2.55 - 3.10 MET. Size Range: 0.1 - 7.5 μm , $N = 4286 \text{ cm}^{-3}$.

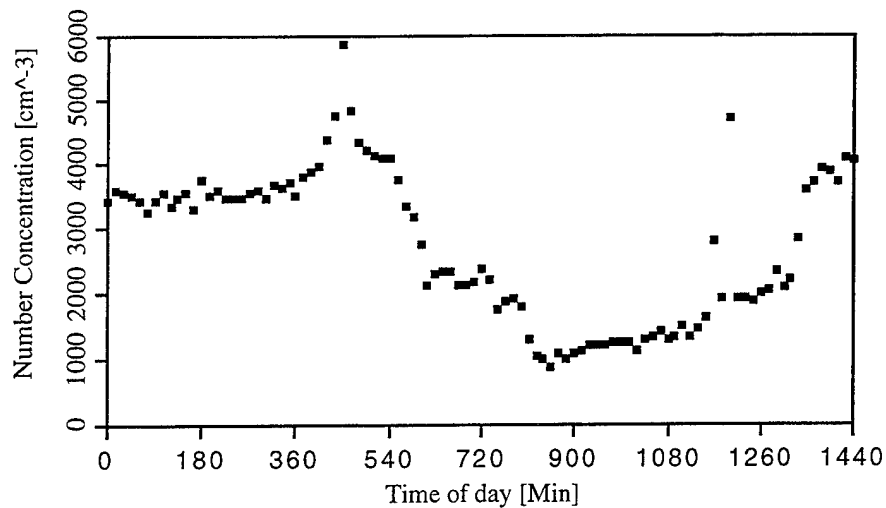


4. Diurnal Variability of the Aerosol Concentration

Aerosol number concentration in the size range 0.1 - 0.2 μm shows a strong variation with time during the day considered, see Fig. 2. High values can be observed in the morning and during the night, low values during the day and in the evening. Pronounced peaks occur at 7.30 am, 5866 cm^{-3} , and at 8 pm, 4721 cm^{-3} .

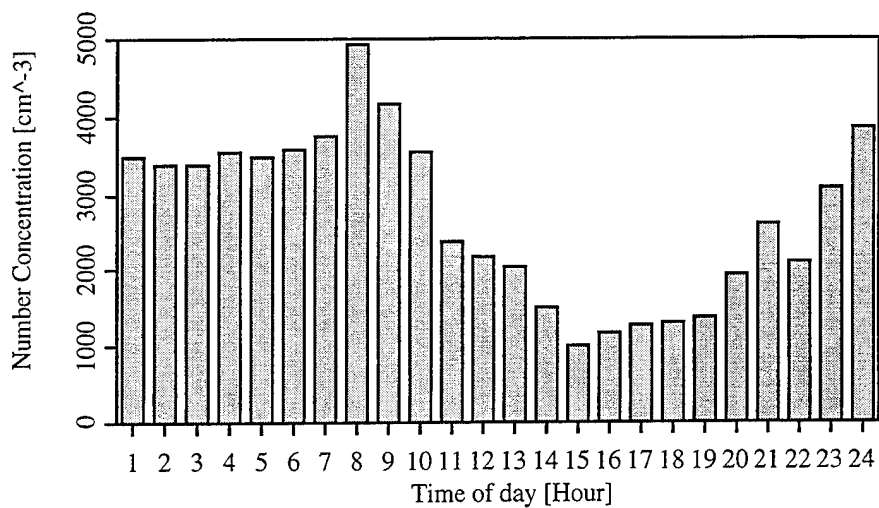
Fig. 3 shows hourly mean values of the number concentration, calculated from the four measurements available per hour.

Fig. 2. Aerosol concentration in the size range 0.1-0.2 μm , measured at Oberglatt May 6th 1995.



Maximal mean values of 4948 cm^{-3} and 4182 cm^{-3} result from 7 to 9 am. The lowest value of 993 cm^{-3} is observed from 2 to 3 pm.

Fig. 3. Hourly mean values of aerosol number concentration for the size range 0.1 - 0.2 μm , measured at Oberglatt May 6th 1995.

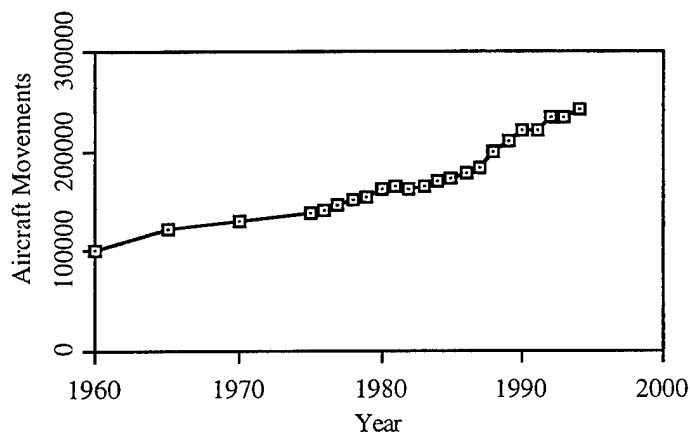


To explain the observed behaviour, three main factors have to be considered. First, the strengths of local sources and sinks have to be described as a function of time. Second, the boundary layer dynamics has to be considered. Third, transport terms have to be taken into account. In absence of precipitation scavenging on May 6th, the variation of the source strength as well as transport processes of the aerosol have to be used to explain the number concentration observed. During the day, convective mixing takes place within the boundary layer and tends to decrease the concentration of aerosol particles.

5. The Airport as a Source of Particles

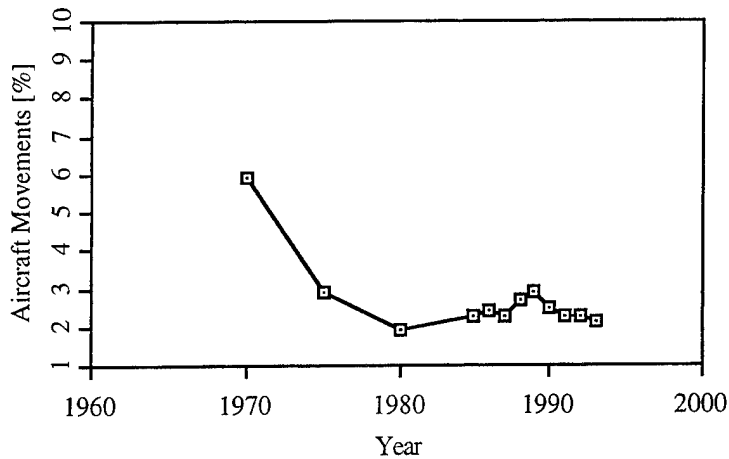
Jet engines of leaving and incoming aircrafts are the dominant source of aerosol particles at the site of observation. Data about the production of particles in the different types of aircraft engines (George *et al.*, 1972) are usually given per LTO (Landing - Take Off cycle). Based on the airport statistics (Airport Authority Flughafen Zürich, 1993) an estimate of the total annual matter emitted as particles during the LTOs can be calculated. For the year 1993, values for the airport Zurich - Kloten amount to about 111 t for the Boeing 747 and to about 320.9 t for the DC-9. These two types of aircrafts are responsible for 33.4 % of all 1993 aircraft movements. The total number of aircraft movements at the airport Zurich - Kloten has increased steadily since 1960, see Fig. 4. From 1965 to 1994, the number of aircraft movements has more than doubled from 120988 to 242498.

Fig. 4. Number of aircraft movements at the airport Zurich - Kloten since 1960.



Aircraft movements between 10 pm and 6 am are defined to be nighttime movements. Only a small fraction of all aircraft movements falls within this category, see Fig. 5.

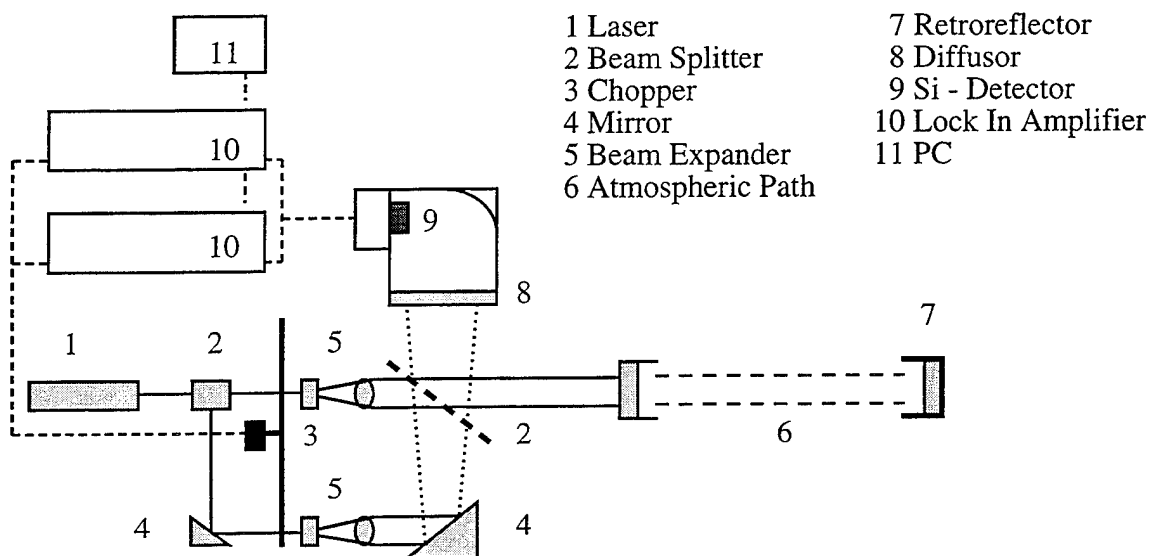
Fig. 5. Aircraft movements between 10 pm and 6 am at the airport Zurich - Kloten, in percent of all aircraft movements. Statistics started 1970.



6. Laser Transmissometer

To allow measurements of the spectral atmospheric transmission, a Laser Transmissometer is currently developed. The instrument discussed is shown in Fig. 6. Lock - In technology used in a two beam configuration will allow measurements of small differences in the transmission. The influence of atmospheric turbulence on the beam propagation will have to be considered carefully.

Fig. 6. Laser Transmissometer, schematically.



7. Outlook

Analysis of the aerosol measurements will be continued in order to achieve a sound statistical basis for the particle size distributions as well as for the concentrations. Errors of the OPC will be considered carefully. Correlation analysis including different meteorological datasets will be executed. Using a numerical model for the boundary layer dynamics should allow for a discussion of observed variations in the aerosol particle concentrations with time.

Along with the development of a transmissometer, numerical experiments to perform sensitivity studies will be done using a high resolution radiation transfer code.

8. Acknowledgments

Financial support of this work provided by the Swiss Defense Technology and Procurement Agency is gratefully acknowledged.

9. References

Airport Authority Flughafen Zürich (1993): *Statistik 93*. Flughafendirektion Zürich, 104 p.

George, R.E., Nevitt, J.S. and Verssen, J.A.(1972): Jet Aircraft Operations: Impact On The Air Environment. *J. Air Pollution Control Association*, **22**, 507 - 515.

Kiehl, J.T. and Briegleb, B.P.(1993): The Relative Roles of Sulfate Aerosols and Greenhouse Gases in Climate Forcing. *Science*, **260**, 311 - 314.

NON-NEGATIVE CONDITIONING OF THE PHASE FUNCTION LEGENDRE EXPANSION

David H. Tofsted
U.S. Army Research Laboratory
White Sands Missile Range, NM 88002-5501

Abstract

In radiative transfer models of the atmosphere one technique commonly used is the discrete ordinates method. In this approach the scattering phase function is expanded in a Legendre series. The series coefficients are often modified using the delta-M or delta-Eddington technique to increase the accuracy of the calculation. In this paper the delta-correction method is extended to include a non-negative condition on the resulting expansion. This correction improves the ability to use predicted radiance data to produce integrated path radiance estimates. The correction involves a log-least-squares analysis of the phase function where the delta forward peak is replaced by a Gaussian phase function and the Legendre expansion coefficients are heuristically modified to ensure non-negativity. The results of this process are compared with computed phase function data and standard delta-M and delta-Eddington method results.

1. Introduction

The discrete-ordinates approach to solving the radiative transfer equation is a valuable tool to studying scattering in three-dimensionally varying media (Carlson and Lathrop, 1968; Lewis and Miller, 1985). This technique normally involves establishing a level symmetric quadrature and expanding the scattering phase function in a series of Legendre terms (Lewis and Miller, 1985). Often for greater accuracy the Legendre expansion is modified according to the delta correction (Joseph et al., 1976; Wiscombe, 1977; McKellar and Box, 1981). In previous applications normally only expansions to the first Legendre term were considered. No consideration was given to ensuring that the phase function remained positive at all scattering angles. Yet Fiveland (1984) used the discrete ordinates method he limited the asymmetry parameter g to the range 0 to $1/3$, thereby ensuring non-negativity. This factor holds increased importance when the computed radiance fields are used to evaluate integrated path radiances in arbitrary look directions. In such cases negative phase function values can produce non-physical negative path radiances. This paper describes specific methods developed to avoid these negative conditions.

In the traditional delta correction approach, the phase function is modeled as an expansion in a small number of Legendre terms augmented by a delta forward peak. Various heuristic arguments have been suggested for the means of setting the forward scattering fraction f . Joseph et al. (1976) used $f = g^2$. Liou (1992) proposes using a constant f for a given scattering order. McKellar and Box (1981) recommended various functions of the Legendre coefficients. Wiscombe used the $L + 1$ st Legendre coefficient in an expansion of L Legendre terms, such that, following the correction, the expansion is valid for one extra term. The net assumption of the delta approximation is to treat the energy in the forward

scatter peak as though it remained unscattered. Removing the energy scattered in the peak requires a modification of the extinction coefficient for energy conservation (McKellar and Box, 1977).

For illustrative purposes a sample phase function was used which simulates an advection fog with a modified gamma particle size distribution (Shettle and Fenn, 1979) and a characteristic particle radius of 10 μm (with additional parameters $\alpha = 1$ and $\gamma = 6$).

2. Least Squares Derivation

The traditional delta correction method can be shown to be related to the results of a least squares analysis of the Legendre estimated phase function to the actual phase function. The actual phase function is represented by $P(\mu)$, where $\mu = \cos(\theta)$, θ is the scattering angle. The phase function is assumed azimuthally independent (aerosol droplets of random orientation). $P(\mu)$ is normalized according to

$$\int_0^{2\pi} d\phi \int_0^\pi P[\cos(\theta)] \sin(\theta) d\theta = 2\pi \int_{-1}^1 P(\mu) d\mu = 1. \quad (1)$$

This phase function can be expanded in an infinite Legendre series as,

$$P(\mu) = \sum_{\ell=0}^{\infty} \alpha_\ell X_\ell P_\ell(\mu), \quad X_\ell = 2\pi \int_{-1}^1 P(\mu) P_\ell(\mu) d\mu, \quad \alpha_\ell = \frac{2\ell+1}{4\pi} \quad (2)$$

where $P_\ell(\mu)$ is the Legendre polynomial of order ℓ . However, when using a delta correction (Joseph et al., 1976; Wiscombe, 1977), the phase function is approximated by

$$P_E(\mu) = f \frac{\delta(\mu-1)}{2\pi} + (1-f) \sum_{\ell=0}^L \alpha_\ell c_\ell P_\ell(\mu). \quad (3)$$

Here the δ is divided by 2π after van de Hulst (1980), which assumes the full peak falls within the integral bounds.

In evaluating the appropriate weights for f and c_ℓ using least squares, the δ forward peak is approximated by a gaussian form

$$\delta(\mu-1)/2\pi \approx \frac{N(\sigma)}{2\pi\sigma^2} \exp(-\theta^2/2\sigma^2), \quad N^{-1}(\sigma) = \sigma^{-2} \int_0^\pi \exp(-\theta^2/2\sigma^2) \sin(\theta) d\theta, \quad (4)$$

where $N(\sigma)$ ensures proper normalization.

Using this definition for the δ , a least squares integral over the angular domain can be minimized by setting its derivative with respect to the individual variables to zero, where we use

$$I_\ell(\sigma) = \int_0^{\pi/\sigma} \exp(-u^2/2) P_\ell[\cos(\sigma u)] \{\sin(\sigma u)/\sigma\} du,$$

$$I_P(\sigma) = \int_0^{\pi/\sigma} \exp(-u^2/2) P[\cos(\sigma u)] \{\sin(\sigma u)/\sigma\} du, \quad (5)$$

$$I_\delta(\sigma) = \frac{1}{2\pi\sigma^2} \int_0^{\pi/\sigma} \exp(-u^2) \{\sin(\sigma u)/\sigma\} du.$$

For derivatives taken with respect to the c_ℓ 's one obtains

$$c_\ell = \frac{X_\ell - f N(\sigma) I_\ell(\sigma)}{1 - f}. \quad (6)$$

Substituting the expression for c_ℓ in the least squares integral and taking the partial with respect to f yields,

$$f N(\sigma) = S_n(\sigma)/S_d(\sigma) = \left[I_P(\sigma) - \sum_{\ell=0}^L \alpha_\ell X_\ell I_\ell(\sigma) \right] / \left[I_\delta(\sigma) - \sum_{\ell=0}^L \alpha_\ell I_\ell^2(\sigma) \right]. \quad (7)$$

This new form is again introduced into the least square integral equation, obtaining,

$$\Delta^2 = C_0 - K_0 - S_n^2(\sigma)/S_d(\sigma), \quad K_0 = \sum_{\ell=0}^L \alpha_\ell X_\ell^2, \quad (8)$$

where K_0 is a constant with respect to the phase function parameters, and Δ^2 is the least squares integral.

This leaves a function of σ which can be optimized. Note that we require $S_n(0) = P(1) - \sum \alpha_\ell X_\ell > 0$ or no forward peak is predicted. If this condition is not met f is set to zero and $c_\ell = X_\ell$. For phase functions which pass this criterion, σ can be determined, then f , and finally the c_ℓ 's. Thus, the optimization of the estimated phase function is reduced to a search over the domain of σ .

Like the conventional technique, this approach will yields results for all orders L , but the result is optimized, depending on the number of expansion terms.

3. Non-Negative Conditioning

Following the method described in the previous section the test phase function was processed at various wavelengths across the visible and infrared bands. For each wavelength, σ , f , and the c_ℓ 's were determined using eqs. (8), (7), and (6), respectively. However, as seen in figure 1, there is a problem with the least squares results: Because the real phase function is often small at large scattering angles the least squares approach leads to negative phase function predictions over a significant solid angle. Of course, as more terms are carried in the Legendre expansion this problem is eventually eliminated. However, at intermediate length expansions, the situation may become very complex with numerous zero crossings. Also, adding terms increases computational costs in the discrete ordinates method. In avoiding these negative predictions several stages of correction are possible.

As a first step, consider a three-term Legendre expansion ($L=2$). This level of expansion is compatible with an 8-stream discrete ordinates scattering method (Lewis and Miller, 1984). The Legendre expansion for this case equals

$$\Sigma_{L=2}(\mu) = (4\pi)^{-1} [1 + 3c_1\mu + 5c_2(3\mu^2 - 1)/2]. \quad (9)$$

Solving for zero, one finds intercepts of

$$\mu_{0\pm} = -\frac{c_1}{5c_2} \pm \left(\frac{1}{3} + \frac{c_1^2}{25c_2^2} - \frac{2}{15c_2} \right)^{1/2}. \quad (10)$$

In order to avoid any zeros one must have $3c_1^2 + (5c_2 - 1)^2 \leq 1$. Taking this result a step further the c_ℓ 's were replaced with the heuristic model

$$c'_\ell = (X_\ell - f)/[e^\ell(1 - f)]. \quad (11)$$

This model is equivalent to the least squares c_ℓ values when $e = 1$. Then, using $e = 1$ as a nominal value, valid f 's are found in the range $|f - \bar{f}| \leq \Delta f$, where,

$$\bar{f} = \frac{3X_1 + 20X_2 - 5}{18}, \quad \Delta f = \frac{[25 + 15X_1(8X_2 - 3X_1 - 2) - 10X_2(5X_2 + 2)]^{1/2}}{18}. \quad (12)$$

This equation was used in an analysis of the sample fog phase function data. Figure 2 shows a plot of the valid range for f as a function of wavelength from the visible band through the infrared. Note that for a critical interval in the 8-12 μm infrared band, Δf is complex at $e = 1$. That is, no choice for f alone can avoid the negative phase function conditions. For this case a minimum e , greater than 1, can be determined analytically:

$$e_{\min} = \left[\frac{5(X_1 - X_2)^2}{(X_1 - X_2)^2 + (X_1 - 1)^2 + \frac{2}{3}(X_2 - 1)^2} \right]^{1/2}. \quad (13)$$

For this choice of e , $\Delta f = 0$, and

$$\bar{f}_e = [3e^2X_1 + (25 - 5e^2)X_2 - 5e^2] / [25 - 7e^2]. \quad (14)$$

Note that due to the form of the \bar{f}_e equation, the maximum value of e is $5/\sqrt{7}$. Otherwise the denominator becomes negative.

For Legendre expansions of $L > 2$ there is no direct solution for e and f . Also, the discussion leading to eqs. (11) through (14) has ignored optimization issues. Returning, then, to this issue, a heuristic optimization approach has been developed which uses eq. (11) for the c_ℓ , and treats f and e as the free parameters to be optimized. In this approach a search is made within the space of f and e for a minimum log square error, defined by

$$\Delta_{\log}^2 = 2\pi \int_{-1}^1 d\mu \{ \log_{10}[P(\mu)] - \mathcal{H}[P_E(\mu)] \}^2, \quad (15)$$

$$\mathcal{H}(x) = \begin{cases} \log_{10}(x), & x > 10^{-4} \\ -4 + 10^6(x - 10^{-4}), & x \leq 10^{-4}. \end{cases} \quad (16)$$

where a heuristic function $\mathcal{H}(x)$ avoids problems due to negative estimated phase function values. Because f and e are now the free parameters, σ must be derived computationally using a modified form of eq. (7):

$$f = \frac{1}{N(\sigma)} \frac{S'_n(\sigma)}{S'_d(\sigma)} = \frac{1}{N(\sigma)} \frac{I_P(\sigma) - \sum_{\ell=0}^L \beta_{\ell} X_{\ell} I_{\ell}(\sigma)}{I_{\delta}(\sigma) - \sum_{\ell=0}^L \beta_{\ell} I_{\ell}^2(\sigma)}, \quad \beta_{\ell} = \alpha_{\ell} \frac{(2e^{\ell} - 1)}{e^{2\ell}}. \quad (17)$$

Under this approach $f = G(\sigma)$, so $\sigma = G^{-1}(f)$ is the inverse of equation (17), where a standard least squares approach is used to determine σ and the log least squares is used to determine f and e . This approach is reasonable since negative phase function effects should not be encountered in the forward peak region. In figure 3 typical results of the variations of the optimal value for e , and the resulting sum of squares are shown as functions of f for the $0.35 \mu\text{m}$ fog phase function. In other cases studied, the minimum e also coincided with the minimum least squares. In figure 4 the optimal f and e parameters shown in figure 3 ($f = 0.58$, $e = 1.075$) are used in creating an $L = 4$ expansion phase function. This result is compared with the actual phase function and an $L = 2$ expansion choice of f within the valid range for non-negative phase functions based on eq. (12). As seen, the $L = 4$ expansion captures the forward hemisphere behavior better than the $L = 2$ expansion.

4. Conclusions

From figure 2 it is clear that a simple rule of thumb for determining the forward scattering fraction can easily lead to negative phase functions evaluations at some angles. Under certain circumstances any choice of f yields some negative values. The method developed here results in a much more robust means of obtaining an optimal approximate phase function including the forward scattering correction, while simultaneously avoiding the problems inherent with negative phase function predictions. In treating scattering problems, once an order of expansion has been decided upon for a simulation, the phase function properties can be preprocessed to derive appropriate f , σ , and e values. Thus runtime efficiency can be maintained by offline processing.

References

- Carlson, B.G., and K.D. Lathrop, 1968: *Transport Theory - The Method of Discrete-Ordinates in Computing Methods in Reactor Physics*, Greenspan, Kelber, and Okrent, eds., Gordon and Breach, New York.
- Fiveland, W.A., 1984: Discrete-Ordinates Solutions of the Radiative Transport Equation for Rectangular Enclosures, *ASME-J. of Heat Transfer*, 106:699-706.
- Joseph, J.H., W.J. Wiscombe, and J.A. Weinman, 1976: The delta-Eddington Approximation for Radiative Flux Transfer, *J. Atmos. Sci.*, 33:2452-2459.

Lewis, E.E., and W.F. Miller, 1984: *Computational Methods of Neutron Transport*, J. Wiley and Sons, New York.

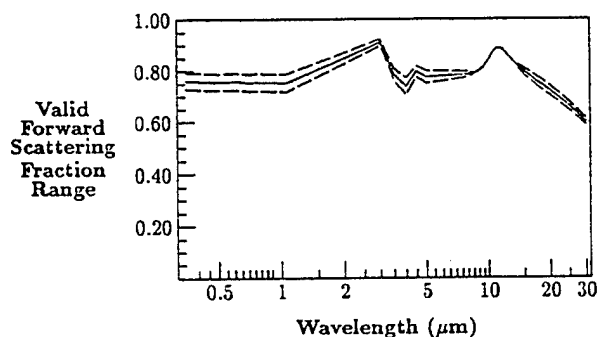
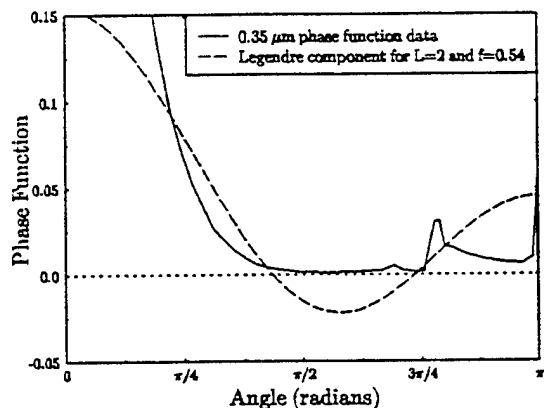
Liou, K.N., 1992: *Radiation and Cloud Processes in the Atmosphere*, Oxford University Press, New York, p. 127.

McKellar, B.H.J., and M.A. Box, 1981: The Scaling Group of the Radiative Transfer Equation, *J. Atmos. Sci.*, 38:1063-1068.

Shettle, E.P., and R.W. Fenn, 1979: *Models for the Aerosols of the Lower Atmosphere and the Effects of Humidity Variations on Their Optical Properties*, AFGL-TR-79-0214, Air Force Geophysics Laboratory, Hanscom Air Force Base, MA 01731.

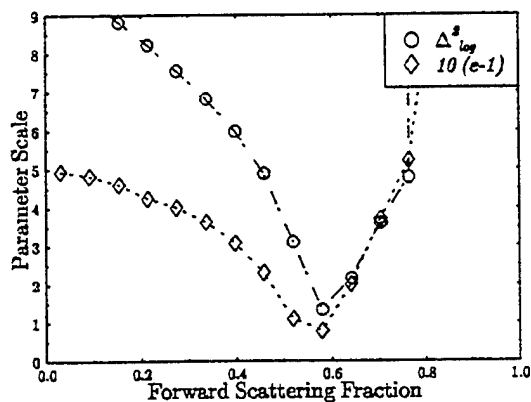
van de Hulst, H.C., 1980: *Multiple Light Scattering: Tables, Formulas, and Applications, Volume II*, Academic Press, New York.

Wiscombe, W.J., 1977: The delta-M Method. Rapid yet Accurate Radiative Flux Calculations for Strongly Asymmetric Phase Functions, *J. Atmos. Sci.*, 34:1408-1422.

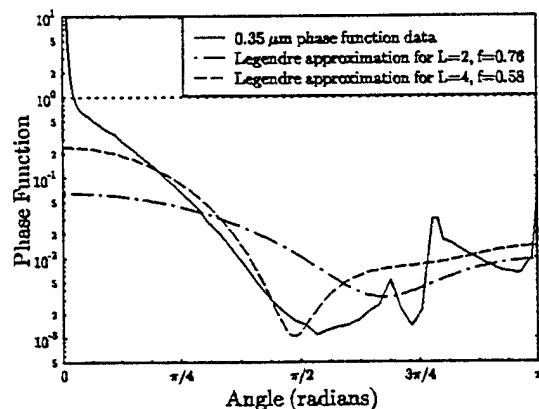


1. Least-squares delta-adjusted Legendre phase function compared to tabulated phase function data. The least squares phase function is negative between $\pi/2$ and $3\pi/4$.

2. Evaluated range of f values (maximum, minimum, and mean) yielding non-negative phase function. No valid f values exist in range about $10 \mu\text{m}$, where Δf is imaginary.



3. Log-least-squares behavior as a function of f .



4. Comparison of Legendre $L = 2$ and $L = 4$ expansions and Mie calculations.

Maximum Detection Range Of Low Intensity Target Edges
As A Function Of Variable Blurr and Albedo
Using Morphological And Segmentation Image Processing Techniques

Clifford A. Paiva

Research Branch,
Countermeasures Division,
Warfare Systems Department
Naval Surface Warfare Center
Dahlgren Division
Dahlgren, VA 22448-5000

ABSTRACT

The surveillance and detection of targets in occlusion and concealment (i.e. decoys, camouflage) is a subject which has gained intense attention over the last few years. The ability to deep-hide targets via use of occlusion and obscuration techniques (including use of terrain) has proved the most challenging for intelligence and automatic target detection, classification, and identification ATDC/I communities. In this regard sensor and weapon platform fusion techniques alleviate the occlusion and obscuration problems, although the primary challenge of obtaining high quality segmented edges, while efficiently rejecting clutter (including obscurants), remains intact. Fusion of millimeter and infrared imagery for clutter rejection and target extraction currently requires comprehensive statistical and pattern referencing algorithms. Therefore the ability of geometric pattern referencing algorithms to successfully correlate a candidate target set to a stored training set is a direct function of the efficiency of the edge segmentation routines incorporated in the ATDC/I suite.

One of the primary inhibitory factors for resolution of automatic target recognition (ATDC/I) performance problems has been the inability to quantitatively characterize low signal-to-noise (SNR) target detection and classification algorithms, especially those which are challenged by high spatial frequency backgrounds and sensor degradative factors.¹ The preceding work² addressed obtaining classification statistics and geometric pattern referencing characteristics with the target mean intensity distribution commensurate with the background intensities. The current effort maintains a similar approach; however, the ratio of target-to-background intensity is significantly *reduced* and the point spread function (PSF) is *increased*. This is accomplished by convolution of gaussian and random filter masks (low pass filtering). The resultant imagery is then morphologically (erosion-dilation) processed and segmented. Albedo variation is achieved by increasing the obscurant's ratio of differential scattering cross section-to-total cross section and the incorporation of intense blurr. The objective is to establish 50 percent of the edgels (target edge pixels) on the target at maximum sensor-to-target range in the presence of high spatial background frequencies, including significant blurr, in the presence of obscurants. The findings are that the target set need not be of a higher intensity than the surrounding imagery, as required in many matched filter operations³; the target need only possess a higher blurr intensity *gradient* than the background clutter and obscurants. Aerosol obscurant intensities may be significantly reduced or even removed by this type of morphological image processing. Finally the morphological network is applied to post-launch midair blurred Synthetic Scene Generator Model (SSGM) targets. This is intended to demonstrate the effectiveness of image processing in missile target edge extraction and segmentation, directed to Theater Missile Defense (TMD) applications.

2.0 APPROACH

Two precipitation rates (75 and 5 mm/hr) through a turbulent and saturated atmosphere (with obscurants) were selected for a perturbation analysis from which available target edge intensities and first and second order discrimination statistics were obtained. Since transmission through atmospheric turbulence at long path lengths cannot be assumed constant across the bandpass, the Low Resolution Atmospheric Transmission Model LOWTRAN 7 was used in this study.⁴ Precipitation was also modelled with LOWTRAN implementing the initial Law-Parsons⁵ and Marshall-Palmer approaches.⁶ (Both precipitation models incorporate Mie scattering effects.)^{7,8} Further the general effects of rain on long wave infrared radiation may also be extrapolated to the millimeter wave absorption and scattering regime.^{9,10}

The use of LOWTRAN increases the accuracy of the albedo variations which include 50% and 100% increase from nominal. In this intense scattering environment the intensities of the targets (truck and tank) are typically a factor of five less than that of the large differentially scattering smoke. This allows an assessment of the effectiveness of target edge extraction via morphological image processing techniques. The final edge intensities were obtained and the associated statistics, including the t-test¹¹ sufficient statistic, were then available for automatic target recognition (ATR) geometric pattern referencing mapping correlation routines. Finally maximum detection range (in terms of edgels) as a function of variable precipitation rates and albedo is summarized. The engagement scenario specifics are:

Engagement Scenario Parameters

Sensor-to-Target Range:	1600 m
Sensor Closing Velocity:	322 m/s
Frame Per Second:	30 fps
Meters Per Frame:	11.067 m/f
Sensor PSF:	.12 mrad
Sensor f-Number:	1.93
Cross Wind Velocity:	6 m/s
Turbulence:	1.e-14 m ^{-2/3}
Mass Extinction Coefficient:	1.25 m ² /g

Blurring of the image has been accomplished via 5x5, 10x10 and 20x20 random filter masks. These masks have been processed by FFT multiplication and IFFT of the input imagery.

Image processing techniques for this analysis include erosion-dilation and open-close operations, as well as region-growing image segmentation computed with the Advanced Visual Systems (AVS) image processing environment. The scenario includes smoke grenades generating obscurants which moves 6 m/s normal to the line-of-sight (LOS) path the of sensor-to-target. The target and background imagery is non-synthetic and has been made available from the US Army Tank Automotive Command (TACOM), Keweenaw Research Center. Sensor-to-target range commences at 1600 meters (maximum) and closes to 700 meters (minimum) at Mach 1. Pixels on target edge (edgels) are, as a function of sensor-to-target range, partially obscured. Extracted edges are then counted and plotted versus range, precipitation rate and variations in albedo. Discrimination potential is assessed via t-test approach.

3.0 BATTLEFIELD OBSCURANT EFFECTS

3.1 Albedo of Obscurants

The obscurant cloud is treated as a single particle reflecting body from which the ratio of differential scattering cross section-to-total cross section (albedo) varies. Assuming the magnetic inductive capacity within the smoke is negligible, the the cumulative electric inductive capacity within the volume is¹²

$$\Sigma \epsilon_r(\mathbf{r}) = \sum \left[\frac{\epsilon(\mathbf{r})}{\epsilon_1} \right] = \sum [\epsilon_r'(\mathbf{r}) + i\epsilon_r''(\mathbf{r})] \quad (1)$$

where $\epsilon_1(\mathbf{r})$ and $\epsilon_r(\mathbf{r})$ are the electric inductive capacities within the obscurant and ambient atmosphere respectively. $\epsilon_r'(\mathbf{r})$ may be considered the diffracted and reflected portions of the radiation. The absorption and internally generated emission is represented by $i\epsilon_r''(\mathbf{r})$.

If the dielectric obscurant body occupies the volume V which is surrounded by a medium (precipitative atmosphere) whose dielectric constant is ϵ_0 , then from Maxwell's equations for static fields¹³

$$\begin{aligned}\nabla \times \mathbf{E} &= -\frac{\partial}{\partial t}[(\mathbf{H}\mu_2)] \\ \nabla \times \mathbf{H} &= \frac{\partial}{\partial t}[(\mathbf{E}\epsilon_2)] + \sigma \mathbf{E} + \frac{\partial}{\partial t}[\mathbf{P}_E] + \nabla \times \mathbf{P}_M\end{aligned}\quad (2)$$

at

$$\mathbf{E} = -\nabla \phi - \frac{\partial \mathbf{A}}{\partial t} = -\nabla \phi - 0 \quad (3)$$

where the electric field intensity is temporally dependent. μ_2 is the magnetic inductive capacity and $\nabla \phi$ is the gradient of the electric field strength. If the electric and magnetic inductive capacities are considered constant (although both are at least temperature dependent)¹⁴; and if the electric and magnetic polarization susceptibilities (\mathbf{P}_E and \mathbf{P}_M) are considered negligible, then $\nabla \times \mathbf{H}$ within the obscurant cloud becomes

$$\nabla \times \mathbf{H} = \frac{\partial}{\partial t}[(\mathbf{E}\epsilon_2)] + \sigma \mathbf{E} \quad (4)$$

$$\mathbf{J} = \begin{cases} -i\omega\epsilon[\epsilon_1(\mathbf{r}) - 1]\mathbf{E}_{(inside)} \\ 0_{(outside)} \end{cases} \quad (5)$$

where the electric field intensity is assumed temporally invariant. The term \mathbf{J} is equivalent to $\sigma \mathbf{E}$ (the vector current density) and may be considered as an equivalent current albedo *source* (through $\frac{\partial \rho}{\partial t} = \nabla \cdot \mathbf{J}$, where ρ is the obscurant cloud's cumulative charge density) which generates the scattered wave from the cloud. Note that in (4) the current density outside the obscurant cloud is assumed zero. A primary formula for infrared scattering from obscurant materials is¹⁵

$$\text{Reflection} = 1 - 4.22(10)^{-4} \sqrt{\frac{\nu k_m k_e}{\sigma}} \quad (6)$$

where ν is the incident frequency and $\frac{k_m k_e}{\sigma}$ is the ratio of the product of specific magnetic and electric inductive capacities ratios to particle conductivity. It is assumed in this paper that the specific magnetic inductive capacity ratio k_m of the smoke particles is unity. Therefore the reflection coefficient is

$$\begin{aligned}\text{Reflection} &= 1 - 4.22(10)^{-4} \sqrt{\frac{\nu k_e}{\sigma}} \\ \therefore @ \lim_{\sigma \rightarrow 0} \left\{ 1 - 4.22(10)^{-4} \sqrt{\frac{\nu k_e}{\sigma}} \right\} &= \infty\end{aligned} \quad (7)$$

and the albedo (reflection) is, for the purpose of modeling, assumed infinite.

Figure 1 indicates the general concept of a particle approaching magnetic and electric non-conductivity. In this physical regime all of the incident radiation is scattered. Although this is not physically correct since all particles are to some degree electrically and magnetically conductive, this approach is necessary in the prediction in order to increase the reflectivity of the obscurant cloud. This in turn reduces the signal-to-noise ratio (SNR) of the target to its background.

Radiation scattering amplitude, which is a function of the product of the particle distribution density and the incident intensity, is considered in the next section. It will further be shown that the intensity does not affect the morphological routines (dilation, erosion, etc.) since intensity gradients are the primary contributors for effective obscurant removal from imagery.

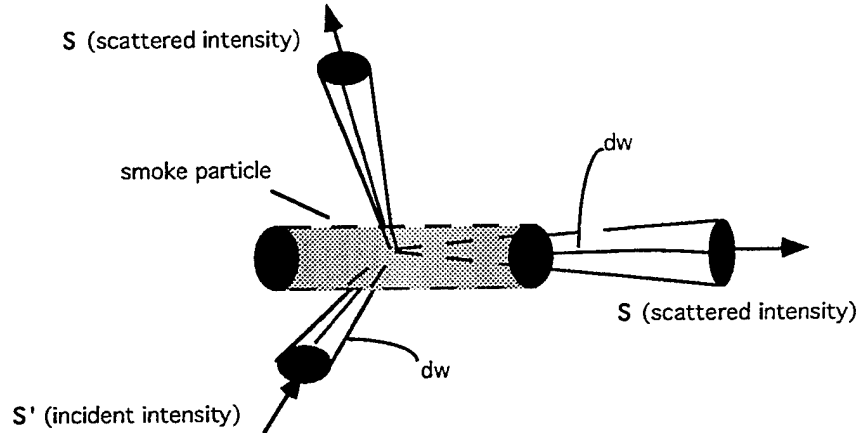


Figure 1. Scattering of specific intensity incident upon the volume ds from the direction s' into the direction s . (From Ishimaru)

3.2 Scattering Amplitude

To characterize the portion of the specific intensity of scattered external source radiation from the obscurant cloud, consider a wave incident in the direction s on a single smoke particle. The incident flux density through an angle ω is given by $S_i = I(r, s_i) d\omega^{16}$ into the cloud. The power flux density of the wave scattered by a system of particles in the direction s' at a distance R from the particle is then given by $\Sigma S_r = \Sigma \left\{ [f(s, s')]^2 / R^2 \right\} S_i$, where $f(s, s')$ is the scattering *amplitude*. The scattered specific intensity scattered in all directions is

$$\int_{4\pi} \rho ds [f(s, s')]^2 I(r, s') d\omega' \quad (8)$$

from which the albedo of the cloud becomes

$$\frac{1}{4\pi} \int_{4\pi} p(s, s') d\omega = W_0 = \frac{\sigma_s}{\sigma_t} \quad (9)$$

where $p(s, s')$ is the differential scattering cross-section (phase function) of the cloud.

4.0 BEER-BOURGUER TRANSMISSION FOR TARGET EXTRACTION ASSESSMENT

4.1 Beer-Bourguier Over-Prediction of Extinction and Applications to Morphologically Processed Imagery

Smoke does not have constant spectral mass extinction coefficients a few seconds after detonation. This is primarily due to the $(H_2O)_{\text{vapor}}$ density variations and atmospheric water vapor absorption rates of the diffusing smoke phosphates. When spectral mass extinction coefficients are not constant, estimates of target transmittance as a function of concentration length, using band averaged extinction coefficients, may be significantly in error. Over-prediction of obscurant attenuation is obviously undesirable from the standpoint of countermeasures simulation, since if applied to the field, the enemy may "see" you when you think that he doesn't!¹⁷ However in the context of assessing ATR algorithm robustness, over-prediction of attenuation is desirable, since a target detection and classification algorithm may be evaluated in representative battlefield environments.

Consider the mean transmission from an external source through the obscurant to be

$$\tau(\text{mean}) = \int_{\lambda_1}^{\lambda_2} \exp(-\alpha \text{CL}) d\lambda \quad (10)$$

where we assume a simple flat mass spectral extinction across the bandpass and through the concentration length (CL) of the obscurant, which then yields

$$\tau(\text{mean}) = \exp(-\alpha \text{CL}) \quad (11)$$

Equation 11 is the Beer-Bourguier Transmission Law which may result in overprediction of transmission when $\lambda_2 = \lambda_1$.

The over-prediction of attenuation will, in combination with edge operators (Sobel, Marr-Hildreth, etc.), determine the effectiveness of morphological operations on effectual removal of diffuse obscurants. Diffuse smokes are susceptible to open-close and edge ATR processes as Plates A through T demonstrate. The synthetic smoke generated for these plates incorporate the Combat Obscuration Model for Battlefield Induced Contaminants (COMBIC) architecture. The target and background imagery is taken in the LWIR by a Keewenaw Research Center (KRC) TMI FLIR.

5.0 IMAGE PROCESSING EFFECTS AND EDGE EXTRACTION

5.1 Edge Generation and Extraction

The primary method for determination of pixels-on-edge (edgels) and assessing of the associated statistics for correlation mapping routines include, within the Advanced Visual Systems (AVS) image processing environment:

- contrast input TTIM non-synthetic (real) target/background imagery
- erosion/dilation
- image subtraction
- Marr-Hildreth (zero-crossing) second order edge detection
- segmentation (region growing)

AVS erosion and dilation, open-close routines filter inner and outer edge protrusions (generated from clutter noise) from the image, as well as eliminate background spurious spatial frequencies.¹⁸ This tends to smooth both inner and outer edged target geometries. The structuring elements (four 5x5 mask crosses) define the amount of erosion and dilation performed on each image. The *open* operation performs an erosion-dilation routine on a single frame and stores the scene. The *close* operation does the reverse. Image subtraction of open-close operations generate minimum high and low spatial frequencies. The final differenced image is then forwarded to a second order edge operator, Marr-Hildreth.¹⁹ (In effect this operator looks for first and second order peaks in severe, spatially cluttered scenes.) Although no single edge operator was successful in determining edges possessing narrow, wide, horizontal and vertical characteristics simultaneously, the Marr-Hildreth routine performed effectively as it determined sharp gradients in first derivatives of intensities and zero-crossings (edge peaks) in the second derivatives.²⁰

The final image is a morphologically processed, segmented, high SNR scene. The target need not be of a higher intensity than the surrounding imagery, as required in many matched filter operations; **the target need only possess a higher intensity gradient than the background clutter and obscurants.** Smoke and obscurant intensities may be significantly reduced, or even removed, by this type of morphological image processing.

5.2 Morphology and Segmentation

Each plate set (Plates A through T) contains the final segmented scene which has been region-grown around the selected target pixel. High and low thresholds were set on high and low pixels of the target region-of-interest (ROI). Plate A is the sensor degradative effects imagery generated by the US Tank and Automotive Command Tactical Thermal Imaging Model (TACOM/TTIM) including pointspread, precipitation turbulence, and noise functions.

Initially the opened (erosion→dilation) scenes were stored. Next the closed scenes (dilation→erosion) were stored. The difference was then taken, contrasted and edged with a second order (Marr-Hildreth) operator. Plates B and D are single line grayscale histograms taken horizontally through the ROI and indicate the dramatic effects of erosion and dilation. Note that in Plate B the truck intensity is well below the intensity of the obscurant representing a very low signal-to-noise ratio. However in Plate C most of the obscurant is removed on the peripheral diffused edges of the smoke via the open-close operation. (Also the Marr-Hildreth operator does reveal remnant edges of the obscurant which may be beneficial in confirming the presence of a target, if one were not previously detected.) The region-grown segmented scene is presented in Plate E. Thresholds and seeding were manually selected from Plate C imagery. This identical procedure would, for an ATR, be automatically performed based upon correlation of the target edge geometry to geometrical pattern referencing information resident within the weapon system sensor suite.

Plates F through J reflect the same procedure differing only in the addition of three-dimensional rendering of the TTIM contrast imagery and the morphological processed scenes. In particular one may clearly observe (Plate G and Q) how the truck and tank targets are relatively "buried" within the ambient background intensities in both Plate G and Q the high albedo obscurants completely dominate the imagery. Nevertheless the smoke is effectively removed and the target intensity successfully revealed in Plates I and S. Plates E and T demonstrate the results of region-grown segmentation of the ROI, the thresholds of which were selected from histogram analysis of morphologically processed imagery.

Plates V.a-V.b display some future applications of target extraction in low signal-to-noise environments. In particular they show input imagery from the Naval Research Laboratory (NRL) Synthetic Scene Generator Model (SSGM)/Generic Scene Generator System (GENESIS). Similar techniques for tactical target detection via image processing is applied to theater missile defense (TMD) for boosting and re-entry ATDC/I. Although the terrain imagery is in the LWIR (8-12 um) and consequently intense, nevertheless with appropriate morphological suppression the target is successfully edged and segmented.

Plate U shows the general AVS network which has been formulated for this study. The key sections of the network include contrast, image differencing, segmentation, and image analysis.

5.3 Image Statistics For Correlation Mappers

The edgel count for the 100 percent increase in albedo (at 75 mm/hr precipitation) increases significantly (factor of two) when system sensor-to-target range decreases from 1200 meters. Also the t-test values, which has been investigated by Schachter¹¹, have been plotted (Figure 2) with reference to standard deviation and sensor-to-target range. This sufficient statistic which is used in false alarm assessments

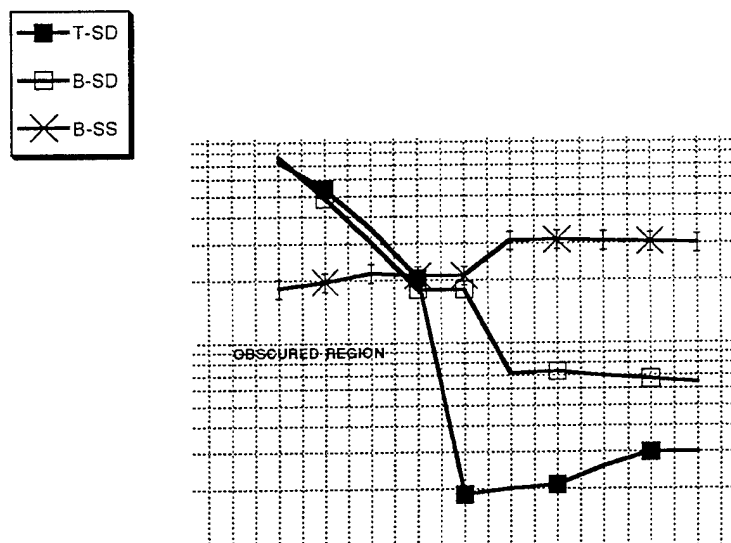


Figure 2

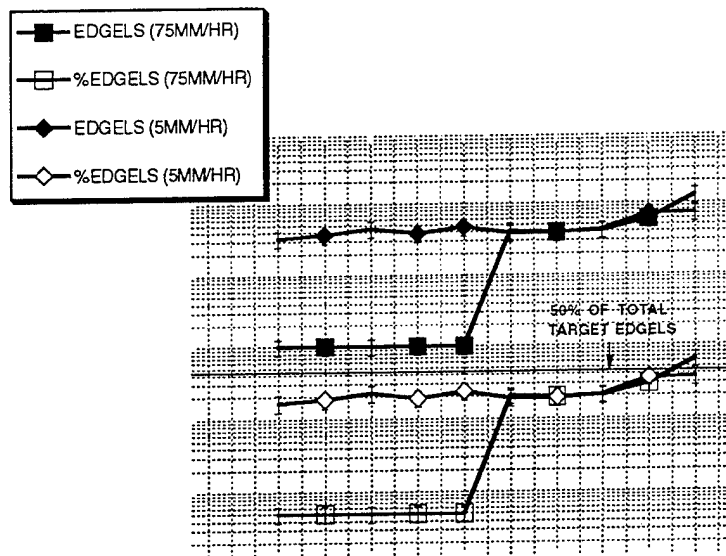


Figure 3

remains approximately stable, especially under ranges of 1000 meters. The standard deviation is of course very high in the intensely obscured region (>1200 meters range-to-target).

Figure 3 compares the actual edgel count as a function of 75 mm/hr and 5 mm/hr precipitation rates. Also plotted is the percent of edgels available from morphological processing to total edgels which would be available in a non-obscured, zero sensor-to-target range. Many ATR algorithm suites require 50% available target edges for geometrical pattern referencing, therefore in this context ATRs may begin processing at ranges, within this scenario, at less than 1000 meters sensor-to-target. Note that for both 75 mm/hr and 5 mm/hr precipitation rates, the 50% of the target edgels become available for classification at approximately the 800 meters sensor-to-target range. **This indicates that if morphological image processing techniques are used in heavy precipitative and obscured environments, low intensity targets may be detected and classification may nevertheless be feasible, depending upon range-to-target, precipitation rates and obscuration diffusion and mobility.**

6.0 SUMMARY

The results indicate that the number of edgels vary as a function of changes in four independent variables: (1) range; (2) precipitation rate; (3) albedo; and (4) sensor range-to-target. For the scenarios analyzed, the target intensity was less than the smoke intensity. This is due to the high target intensity *gradients* and low smoke *gradients*. The final subtracted, edged and segmented scene successfully revealed only the low intensity targets within ranges less than 1000 meters. Smoke and obscurants were effectively filtered from the imagery as the sensor headed toward the target. The actual count of edgels versus precipitation rates and albedo indicate strong dependence of obscurant cloud position relative to target position (occlusion), precipitation rate and range.

7.0 CONCLUSIONS

This analysis generated some insight as to maximum detection ranges which may be expected in severely stressed environments and very low signal-to-noise ratios. Particularly that:

- gaussian distribution of the COMBIC generated smoke provides even sharper gradients than would be expected from non-gaussian smoke diffusion; therefore non-gaussian obscurant distributions would be removed even more effectively than gaussian generated puffs.

- 50% target edgels are available for statistical and geometric correlation pattern referencing at less than 800 m for both 75 mm/hr and 5 mm/hr precipitation rates, assuming the rate of movement of obscurant across the line-of-sight
- when implementing these morphological processing techniques maximum detection ranges were approximately 1000 meters
- flat spectral mass extinction coefficients for smoke phosphates in saturated precipitative environments should be used to stress ATR algorithms against high intensity gaussian gradients

8.0 FUTURE EFFORTS

These morphological techniques are being tested against theater missile defense related imagery for missile target extraction which include backgrounds with high spatial frequencies. The Synthetic Scene Generator Model (SSGM) is being used to provide LANDSAT imagery on Defense Mapping Agency (DMA) digitized elevation data. Also a variety of background clouds (CLOUDSIM, Photon Research Associates) and and nuclear disturbed atmospheres, provided by the Defense Nuclear Agency (DNA), will be assessed. Low altitude exhaust plume imagery is provided by the Air Force Standard Infrared Radiation Model (SIRRM). The high altitude plumes will be generated by the Composite High Altitude Radiation Model (CHARM), Air Force Phillips Laboratory, Rocket Propulsion Directorate. These models CLOUDSIM, SIRRM, CHARM and NORSE have been selected from the SSGM architecture. The areas addressed will include:

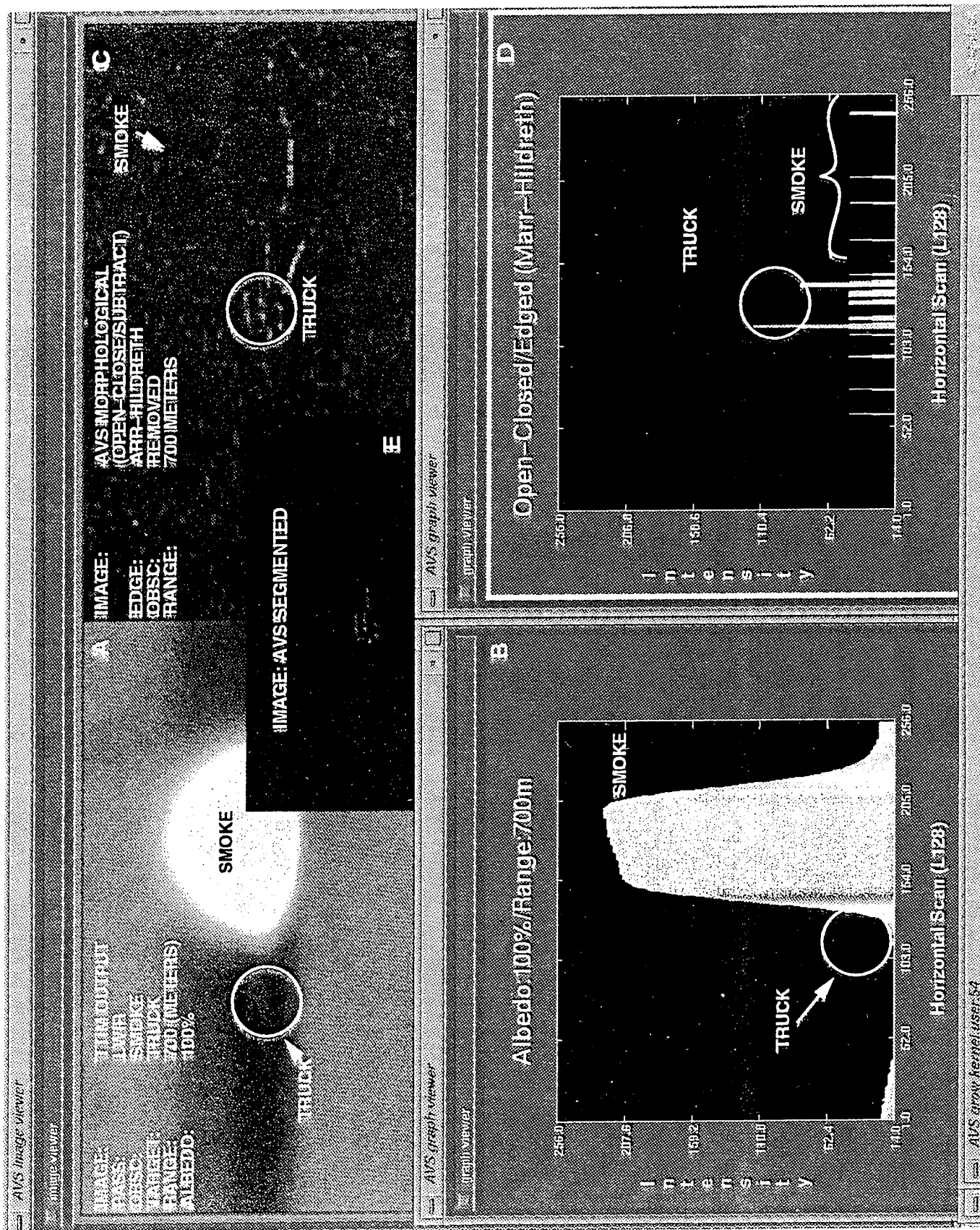
- identify missile plumes of launch vehicles at large sensor-to-target ranges (>100 km)
- discriminate missile plume emissions from ambients (background/foreground) clutter
- detect and classify aerosol and vapor trails
- predict countermeasure techniques via alteration of plume radiation as a function of rocket combustion instabilities, propellant alteration, after-burning recombinations, and angle-of-attack variations

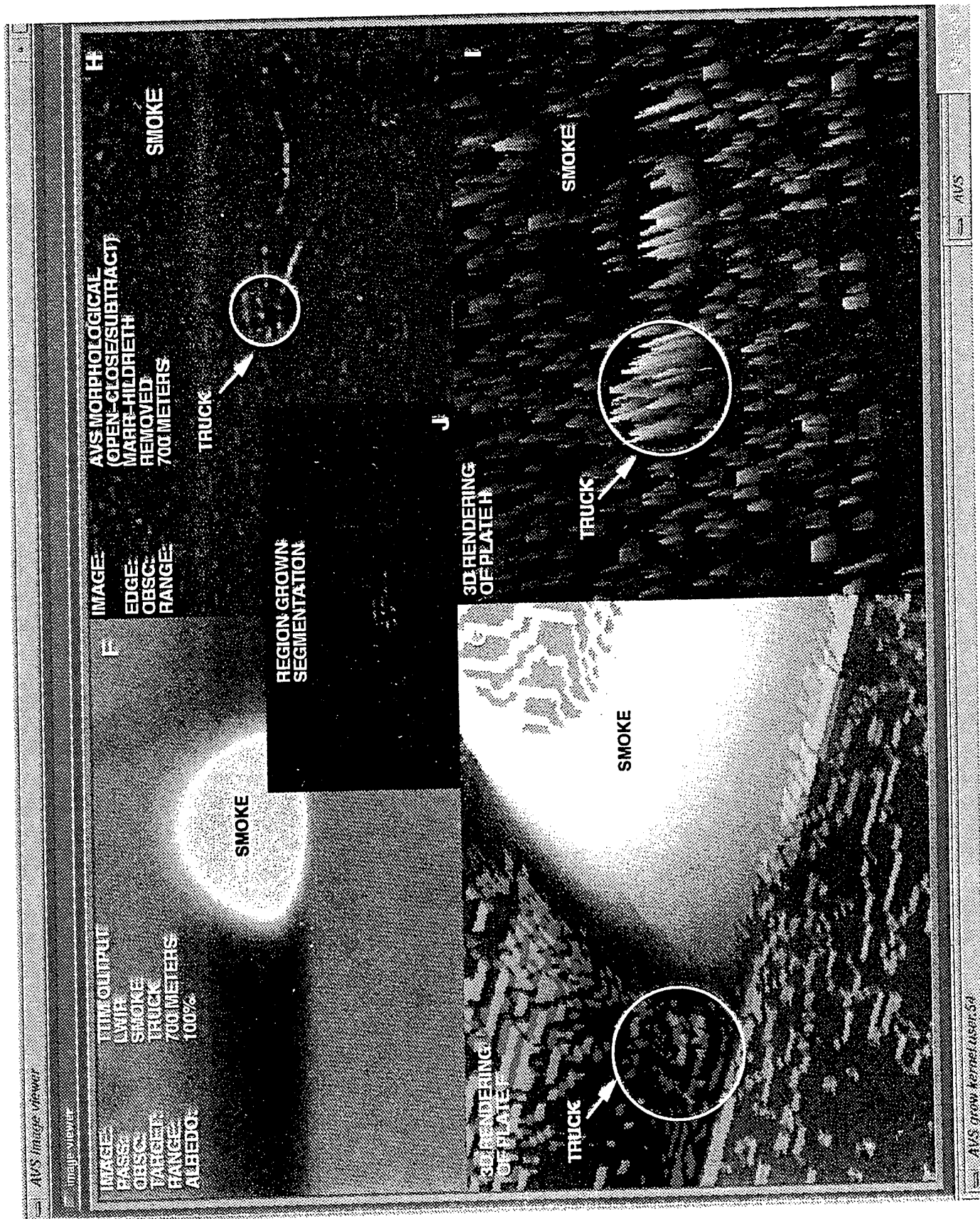
9.0 ACKNOWLEDGEMENTS

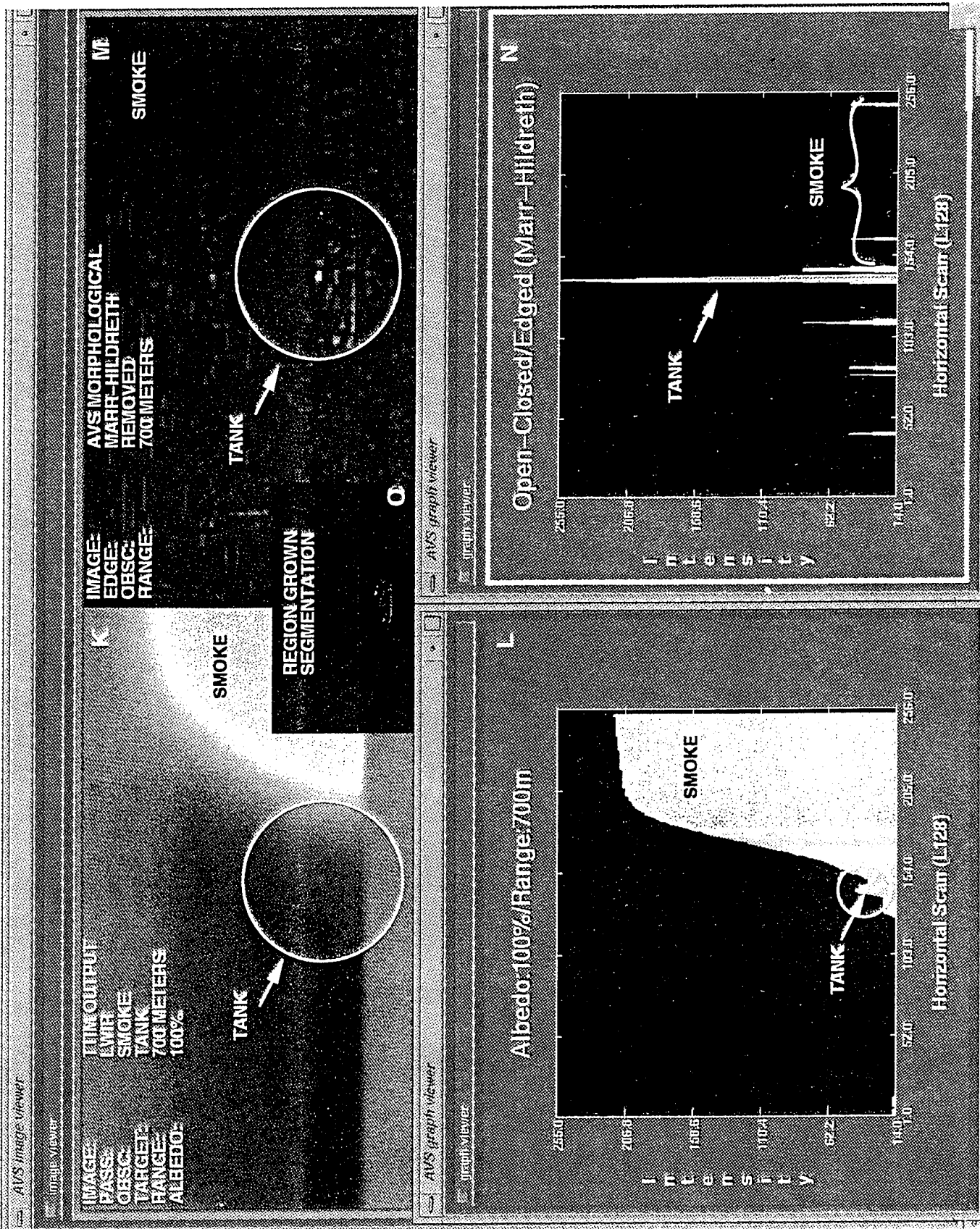
The initial developments of this work (radiative scattering) commenced at Air Force Phillips Laboratory, Rocket Propulsion Directorate (AFPL/RPD), Edward Air Force Base, and extended to the present facility (Naval Surface Warfare Center, Dahlgren Division). In particular some very interesting insight with respect to infrared spectra and imaging has been provided by Dr. David Stanford (AFPL/RPD) and Dr. Phillip Bushong (NSWC, Dahlgren Division), respectively. Mr. Art Blankenship, Research Branch Head, NSWCDD, has been invaluable in scrutinizing this paper for technical consistency. Also Dave Toftsted of the Battlefield Environment Directorate, Army Research Lab (ARL/BED), has contributed valuable information with respect to atmospheric turbulence effects on longwave infrared imagery. Finally Mr. Art Curtis has been particularly helpful in his management of the Silicon Graphics complex without which these findings could not have been generated.

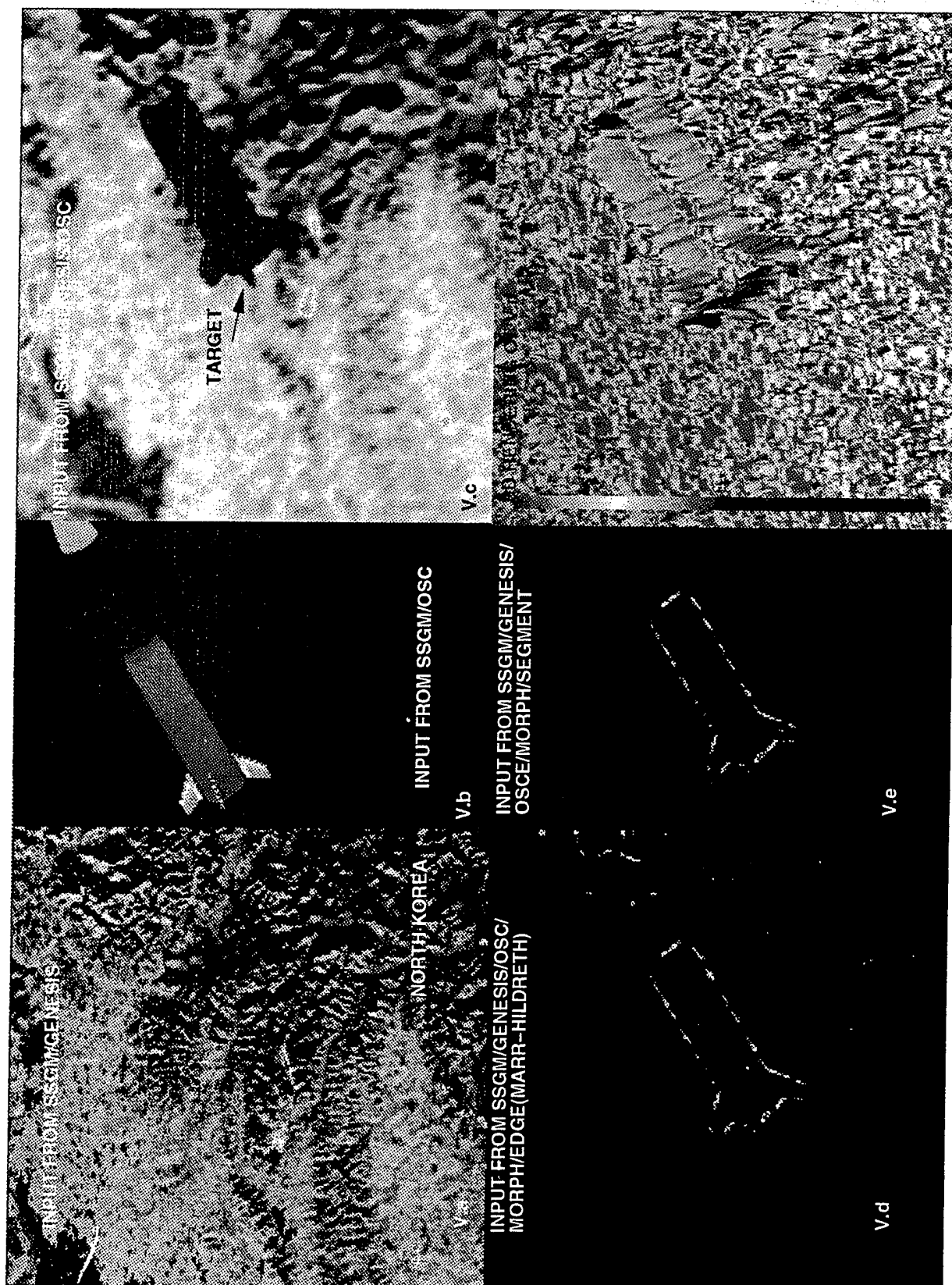
10.0 REFERENCES AND ENDNOTES

1. Welsh, J.P.; "Smart Weapons Operational Enhancement" SWOE) *Fact Sheet*, Army Cold Regions Research and Engineering Laboratory (CRRE), pp2-3, (1994) .
2. Paiva, C., "Maximum Detection Range Of Target Edge Intensity As A Function of Variable Precipitation" Proceedings Of The Fifth Annual Modeling and Validation Conference; U.S. Army Tank-Automotive Command Research, Development & Engineering Center, (1994)
3. Skolnik, M. I., Introduction To Radar Systems; McGraw-Hill Book Company, Chapter 9, pp 409 - 410, (1962).
4. Drakes, J.A.; Hiers III, R.S.; Reed, R.A.; "Doppler Shift Effects on Infrared Band Models", *Journal of Thermophysics*, Vol. 6, No. 1; pp 45-47, (1990) . The blue and red wings of the LWIR transmission spectrum can become critical over significant propagation path lengths. This is the reason for the generation of low (LOWTRAN), medium (MODTRAN) and high (HITRAN) resolution atmospheric transmission codes which do not assume Beer-Lambertian transmission.









A BISTATIC LIDAR RECEIVER TO OBSERVE LOWER TROPOSPHERIC AEROSOL PROPERTIES

T. D. Stevens and C. R. Philbrick
(tds102@psu.edu, crp3@psu.edu)

The Pennsylvania State University
PSU/ARL Lidar Laboratory
University Park, PA 16802

Abstract

The scattering of optical radiation in the visible, ultraviolet and infrared regions of the spectrum has a major impact on commercial air traffic and on many military systems. It has become critically important, with modern systems, that the electro-optical environment be properly characterized. We have been able to demonstrate that the rotational and vibrational Raman backscatter can be used to determine the extinction profile through optical scattering regions such as clouds. But a method is still needed to determine extinction profiles within the first several hundred meters above the Earth's surface through aerosol layers.

We have developed a bistatic remote receiver that utilizes a linear photodiode array to image the radiation scattered from any high power CW or pulsed laser system. By observing the angular scattering variation from a given aerosol layer, additional information contained in the scattering angle phase function can be obtained. A technique has been developed to estimate particle size and distribution widths (of spherical scatterers) by placing two or more of these instruments perpendicular and parallel to the scattering plane. Polarizers are also used to measure the cross polarization to determine the amount of multiple scattering and nonsphericity of the particles in the scattering volume. The information on the particle size and distribution width along with absolute extinction measurements from Raman lidar should allow extension of the extinction and transmission calculations to a wider range of wavelengths.

Background

The challenge is to remotely measure the extinction and transmission through regions of the atmosphere without having to assume any relationship between backscatter and extinction. Lidar techniques show the best promise for describing the local electro-optical environment. However, most of the past applications of lidar have failed to provide satisfactory results because the techniques used have generally focused on measurements of the backscattered radiation at the laser fundamental wavelength. The extinction can be related to the backscattered energy by the equation $\beta(r) = C(r)\alpha(r)^k$, where $\beta(r)$ is the backscattered intensity, $\alpha(r)$ is the extinction and $C(r)$ and k are frequently assumed constant. But $C(r)$ is a function of range and k is different for each scatterer, so given only the backscatter intensity $\beta(r)$, the extinction $\alpha(r)$ can not be reliably obtained. This presents a problem for techniques relying on the inversion of a single-ended lidar return to obtain range dependent atmospheric

extinction coefficients. This technique will only be useful for regions of the atmosphere with uniform scatterers and small extinction coefficients, like those found in stratospheric aerosols [1,2]. A more reliable method using lidar to measure atmospheric extinction has been developed independently by M. R. Paulson, 1987 and G. J. Kunz, 1987. This lidar inversion algorithm uses a double ended lidar technique where the relationship between the backscatter and extinction coefficients is eliminated by comparing the backscatter signal returned from a volume common to each lidar located at opposite ends of the propagation path. The double ended lidar technique is presented to show that the β/α ratio in general is not constant with range and that the technique of inverting a single ended lidar return (Klett inversion) can produce inaccurate extinctions. Figure 1 shows plots of extinction calculated from both single-ended [$C(r)$ assumed constant] and double-ended lidar backscattered returns (Richter and Hughes, 1991).

Instrumentation

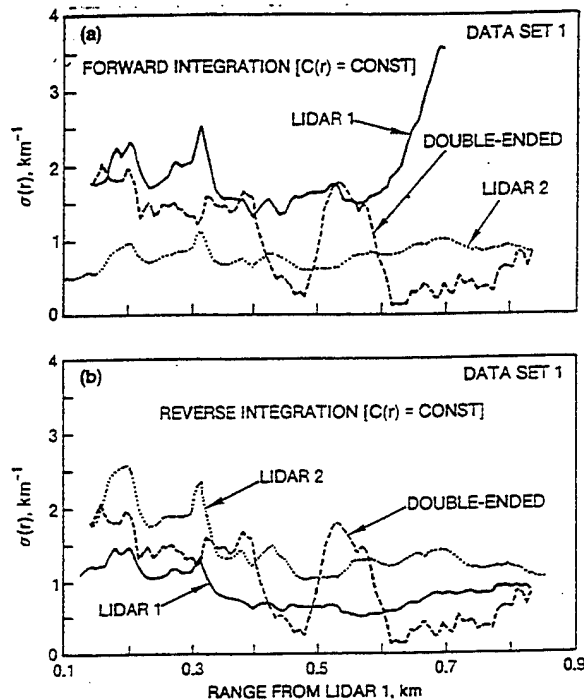


Figure 1. Comparison of extinction coefficients versus range calculated using forward and reverse integration on a single-ended lidar return and using the double-ended lidar technique. (from Richter and Hughes, 1991) [5]

These data sets show very clearly how unreliable standard inversion techniques are at obtaining extinction from a single backscattered lidar return. However, if the values of $C(r)$ are known as a function of range and allowed to vary, standard single-ended lidar returns could be inverted to reliably obtain extinction coefficients. More information is needed about the scatterers so that $C(r)$ can be calculated for each range bin. The ratio of the 532 nm to the 355 nm backscatter for a two-color lidar return is theoretically proportional to $C(r)$. But this has yet to be used in an inversion algorithm to accurately and uniquely calculate extinction (Rau, 1994). The double-ended lidar technique is a proven method for measuring the extinction along a path, but it is not a practical solution for instantaneous measurements above altitudes of a few meters and for locations where instruments can not be located at each of the end points. The scattering properties are much too complicated for the simplistic single-ended backscattered inversion approach and much more information is needed to characterize the processes.

The only way to collect scattered radiation at angles other than 180° from a lidar system is to set up a bistatic receiver located some distance from the laser. We have developed a unique bistatic receiver that can remain fixed with respect to the laser (e.g. it does not have to scan up and down the laser beam). The scattering volume's height is derived from the location of the laser's image on a photodiode array. This type of receiver is small, about the twice the size of a regular SLR camera, making it ideal as a permanent fixture at many locations. This type of receiver is also independent of the laser/lidar system and requires no electrical connection to the laser source. Multiple receivers could be set up on ships and at airports to continually monitor atmospheric aerosol variability.

The bistatic receiver collects an image of the radiation scattered from the first few kilometers of the atmospheric path to help determine atmospheric particle size distributions. The instrument is a straight forward use of a linear photodiode array detector in the image plane of a standard 35 mm SLR camera. The receiver is a hand held unit composed of three parts, a Ricoh XR-10m SLR camera, a digital control and data storage box, and a power source (either a 6 v battery, or an extension cord). This receiver is essentially a very sensitive, high resolution digital camera. The camera images the laser light onto an EG&G monolithic linear photodiode array. The array has 1024 photodiode elements with a $25 \mu\text{m}$ center-to-center spacing. Each element has a 100:1 aspect ratio of $25 \mu\text{m} \times 2.5 \text{ mm}$ making it easy to image the laser beam onto the array. The data collection process starts with a remote start switch. The embedded micro-computer reads the input and starts a series of events defined by the data acquisition and control program. The scattered laser light is filtered by a 10 nm bandwidth, 532 nm filter and focused onto the photodiode array by a 50 mm lens. First, the array is cleared and then the shutter is opened for about ten seconds (200 laser shots). The data is digitized with a 12 bit, 100 kHz digitizer and transferred directly to RAM. A background sample is then digitized with the shutter closed and also stored directly to RAM. The background is subtracted from the signal and saved to a PCMCIA solid state memory. One data sample requires about 55 seconds, and 1000 samples can be saved to one PCMCIA card. At the end of the night, the data can then be saved to a standard 3.5" floppy disk.

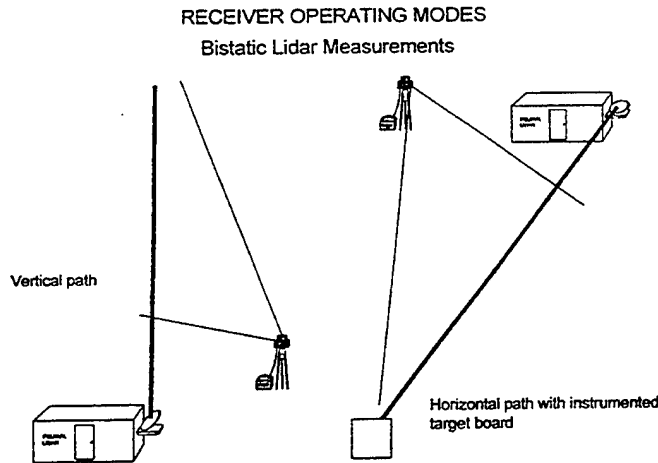


Figure 2. The lidar and bi-static receiver will be operated both vertically and horizontally. By operating a receiver with a linear array off-axis from the laser beam, phase information can be collected about the scatterers.

Figure 2 shows the two modes of operation for the lidar and bistatic receiver. All measurements thus far have been obtained with the laser pointed vertical. The horizontal mode of operation is also important so that ground based measurements can be compared with the lidar data. In this mode of operation an instrumented target board can be used to directly measure the total extinction between it and the laser source. The data inversion process is more difficult in the vertical mode of operation because the end point of the laser is not well defined. The camera is positioned so that the infinity point of the laser is imaged onto the last few pixels of the array. The last pixel with a signal is assigned a value of infinity for its altitude, and the inversion is processed downward. Because of the geometry, the last pixel has a range of about 8 km to infinity, and the first pixel has a range size of about 1 cm. This means that an error in assignment of the end point could cause large errors at high altitudes, but relatively small errors within the first kilometer. Figure 3 shows a plot of altitude versus angle for the vertical mode and with the receiver positioned 18 m from the laser. This plot shows the range of scattering angles that would be observed from a 60 m thick layer between 40 and 100 m. Lidars normally measure only the backscattered radiation at 180 degrees. The bistatic receiver will be able to observe scattered radiation at angles between 155 and 170 degrees with this geometry. It will be shown later that there is valuable information contained in this small range of angles. The optimal position of the receiver will be slightly different depending on the

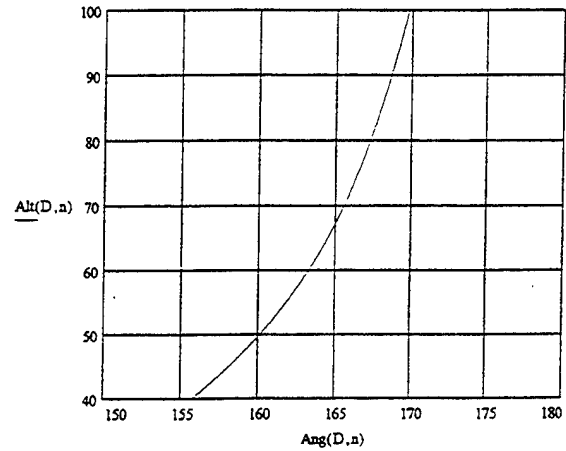


Figure 3. Plot of altitude versus angle for a receiver located 18 m from the laser transmitter. This plot shows the maximum range of angles that can be observed with the laser pointed vertical. Altitude is in meters.

height of the aerosol layer. But the maximum range of observed angles will always be 15 degrees. For the same aerosol layer between 40 and 100 m, the spatial resolution is less than 0.6 m, and is as small as 0.17 m at 40 m altitude. The height resolution for this type of instrument is very small because it is dependant not on electronic timing, but on geometry.

Initial Results

Figure 4 is a plot of unprocessed data from the photodiode array. The ordinate is digitized voltage minus background and the abscissa is the pixel number out of 1024. This data was collected

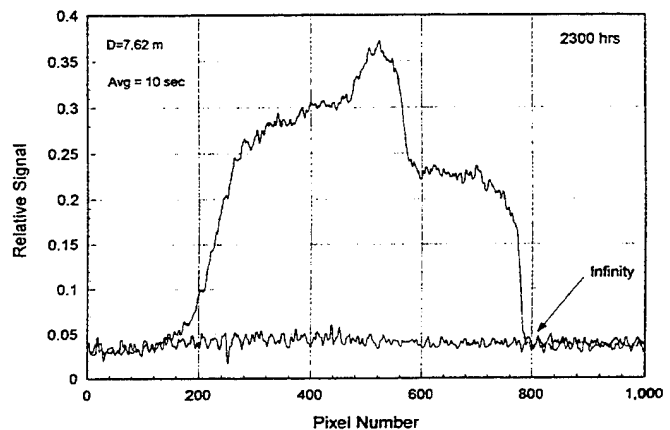


Figure 4. Raw data collected at Penn State with a bistatic receiver, using a linear photodiode array on March 14, 1995.

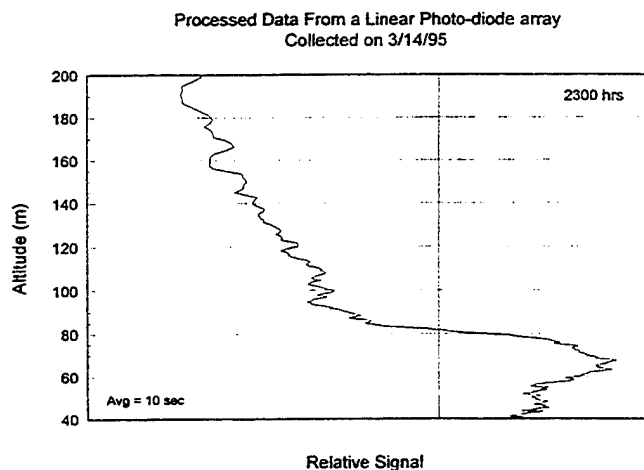


Figure 5. First measurements from a bistatic receiver collected on March 14, 1995. The integration time was 10 seconds. The spatial resolution through the layer is less than 0.4 m.

using the LAPS (Lidar Atmospheric Profile Sensor) laser on March 14, 1995 in State College, PA. The data were averaged for 10 seconds (300 laser pulses), and the receiver was located 7.62 m from the laser. There were no clouds that night so the last pixel with signal was assigned an altitude of infinity for data processing. The data must be processed to provide a profile of relative signal versus altitude. As the altitude increases the scattering volume also increases, due to the geometry of a bistatic receiver intersecting the laser. Therefore, the relative signal must be corrected for the size of the volume being measured. A (R^2) correction must also be applied due to the increasing distance between the scatterers and the receiver.

Figure 5 shows a plot of the data from Figure 4 with these corrections applied. It can now be seen that the aerosol layer is between about 60 and 80 m. To obtain the maximum angle range for a layer at this height, the receiver should have been placed 18 m not 7 m from the laser. The height resolution in the layer is between 0.2 and 0.4 m. Aerosol profiles with this resolution and this close to the ground are very difficult to obtain with any other instrument. Monostatic lidars are not able to reliably measure aerosol scattering closer than about 1500 m from the surface because their telescopes are generally far field instruments. Many more data sets like these will be collected to verify the operation of the instrument and to determine the best method for obtaining particle size and distribution.

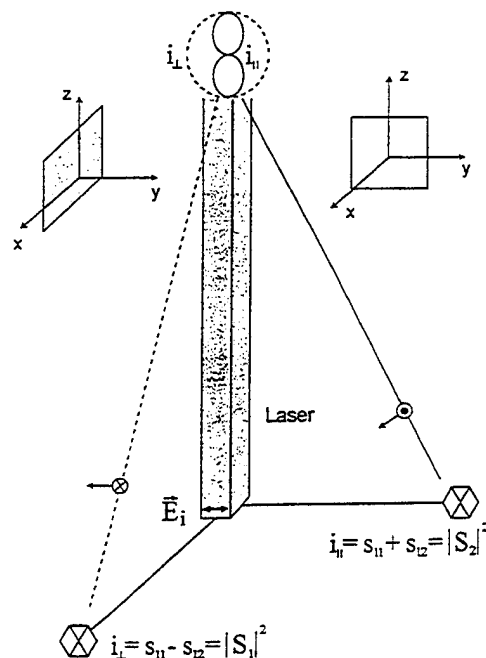


Figure 6. Geometry for a bistatic lidar setup to show which components of the electric field will be measured at each location.

Data Analysis

Figure 6 shows the geometry for a bistatic lidar setup to illustrate which scattering matrix elements must be calculated to model and predict the results of the bistatic receiver. The laser beam propagates vertically into the atmosphere with its electric field polarized in the y-z plane. We would observe the scattered radiation from two separate locations, one perpendicular to the scattering plane and one parallel to the scattering plane. At the top of Figure 6 the radiation pattern for a dipole radiator is drawn to show which components of the electric field are observed at each measurement location. For the perpendicular component no variation is seen, but for the parallel component the standard variation of a dipole radiator is measured. Of course this is the simplest case, the radiation pattern for most scatterers is much more complicated as will be shown later. The ratio of these two components would then provide unique information about the size and distribution of the scatterers.

A simple and limited model has been developed to determine if this technique is feasible. This model uses a fortran subroutine from Bohren and Huffman, 1983 called "bhmie" to calculate the scattering matrix elements S_1 and S_2 . A single mode

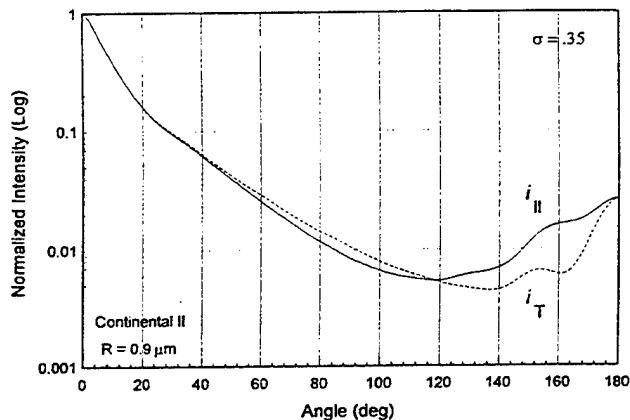


Figure 7. The two components of scattered radiation according to Mie theory calculated for a single log-normal size distribution.

log-normal distribution is used to calculate the scattering between angles of 140 and 180 degrees. This simplifies the calculation because the relative number densities between the three modes of a trimodal distribution can not be ignored. For example, a few large diameter scatterers could dominate the effects of many smaller diameter scatterers. In other words, the largest mode with only 1000 scatterers could cause much more extinction than 1×10^6 scatterers in the smallest mode.

Figure 7 is a plot of the parallel and perpendicular scattering components between 0 degrees (forward scatter) and 180 degrees (backscatter) for the scattering geometry in Figure 6. A single log-normal distribution was used with a standard deviation of 0.35 and a mean radius of $0.9 \mu\text{m}$, typical values for "Continental type II" aerosols. The distribution of sizes smooths all the fine structure out of the curves. However, a sizable difference in the scattering intensity still remains between 120 and 180 degrees. Figure 8 shows the ratio of the parallel to the perpendicular component of scattered radiation. The bistatic lidar will be able to observe angles between 155 and 170 degrees. Different standard deviations were plotted to estimate how much variation would result in the measured ratio. It should be noted that the ratio peaks between 2.5 and 3.5 for a scatterer of radius $0.9 \mu\text{m}$.

A few assumptions must be made before any inversion algorithm can determine size distributions from these bistatic measurements. The scatterers must be assumed to be spherical, if they are not spheres this measurement technique could determine how non-spherical they are. A polarizer is placed on

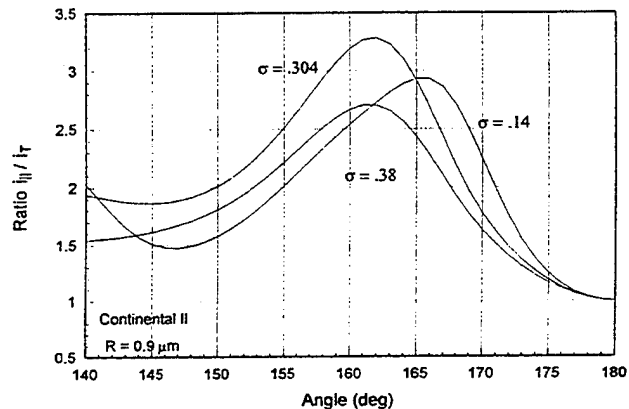


Figure 8. Ratio of the two electric field components plotted in Figure 7. Three different size distribution widths were chosen to see how much the ratio would vary.

the receiver to look for electric field components perpendicular to the one being transmitted. If there is a large return from the "cross polarized" component it can be assumed that either there is strong multiple scattering or the particles are not spheres. The index of refraction for the inversion will be estimated from the geography and meteorological conditions (e.g. is the data collected at sea). In order to measure a range of angles from an aerosol layer without moving the instrument to many different locations, it will be assumed that the layer consists of a uniform particle distribution. Using the above assumptions, a method will be used to invert or fit the returns from the two components to a model to obtain particle size and distribution for the scattering layer.

Acknowledgements

Special appreciation for the support of this work goes to Dr. Juergen Richter of NCCOSC NraD. The efforts of D.B. Lysak, P.A.T. Haris, Y.-C. Rau, S. Rajan, M. O'Brien, and G. Evanisko have contributed much to the success of the LAMP project.

References

1. T. D. Stevens, S. Maruvada, T. J. Kane, and C. R. Philbrick, "Lidar Observations of Mt. Pinatubo Aerosols: Effects on the Global Radiation Budget," in *Optical Remote Sensing of the Atmosphere Technical Digest*, 1993 (Optical Society of America, Washington, D.C.), Vol. 5, pp. 313-316, 1993.
2. C. R. Philbrick, D. B. Lysak and Y.-C. Rau, "Lidar measurements of aerosol scattering in the troposphere and stratosphere," *Proceedings of the IEEE Topical Symposium on Combined Optical-Microwave Earth and Atmosphere Sensing*, 107-110, 1993.
3. M. R. Paulson, "Evaluation of a dual-lidar method for measuring aerosol extinction," *Naval Ocean Systems Center*, TD-1075 (1987).
4. G. J. Kunz, "Bipath method as a way to measure the spatial backscatter and extinction coefficients with lidar," *Appl. Opt.* 26, 794-795, 1987.
5. J. H. Richter, and H. G. Hughes, "Marine atmospheric effects on electro-optical systems performance," *Opt. Engr*, Vol. 30, 1991.
6. Y.-C. Rau, "Multi-wavelength Raman-Rayleigh lidar for atmospheric remote sensing," PhD dissertation, Penn State University, 1994.
7. K. Parameswaran, K. O. Rose, and B. V. Krishna Murthy, "Aerosol characteristics from bistatic lidar observations," *J. Geophys. Res.*, Vol. 89, 2541-2552, 1984.
8. P. Ernest Raj and P. C. S. Devara, "Some results of lidar aerosol measurements and their relationship with meteorological parameters," *Atm. Environment*. Vol. 23, 831-838, 1989.
9. C. F. Bohren, and D. R. Huffman, *Absorption and Scattering of Light by Small Particles*, John Wiley & Sons, 1983.

AIRBORNE VISIBLE/INFRARED IMAGING SPECTROMETER (AVIRIS)

PROGRAM OVERVIEW

Robert O. Green

Jet Propulsion Laboratory

23 and 24 January 1995

rog@gomez.jpl.nasa.gov

AVIRIS OBJECTIVE

Quantitative characterization of the Earth's terrestrial surface and atmosphere from calibrated spectra acquired as images.

APPROACH

Measure the contiguous upwelling radiance spectrum from 400 to 2500 nm

Use the resolved molecular spectral absorptions and particle scattering signatures to:

- Detect and identify the surface and atmospheric constituents present
- Assess and measure the expressed constituent concentrations
- Assign proportions to constituents in mixed spatial elements
- Delineate spatial distribution of the constituents
- Monitor changes in constituents through periodic data acquisitions

AVIRIS SCIENCE/APPLICATION DISCIPLINES

SURFACE AND ATMOSPHERE MOLECULAR ABSORPTIONS

Ecology and vegetation: chlorophyll, leaf water, cellulose, lignin, nitrogen compounds, pigments, etc.

Oceanography and limnology: phytoplankton chlorophyll, dissolved organic compounds, suspended sediments, planktonic organisms, marine plants, corals, bathymetry, etc.

Soils and geology: clay minerals, iron minerals, carbonates, sulfates, mineral grainsize ,etc.

Snow and ice hydrology: ice absorption, water absorption, ice particle scattering, impurity absorption, etc.

Atmosphere: water vapor, aerosols, water clouds, ice clouds, smoke, oxygen, carbon dioxide, ozone, methane, etc.

Other: lava temperature, biomass fires, etc.

Calibration: atmosphere, satellites, aircraft systems

DATA CHARACTERISTICS

SPECTRAL

Wavelength range
Sampling
Spectral response (fwhm)
Calibration

400 to 2500 nm
<10 nm
10 nm nominal
1 nm

RADIOMETRIC

Radiometric range
Sampling
Absolute calibration
Intra flight calibration
Noise

0 to maximum lambertian radiance
~ 1 dn noise rms
≤ 95 %
≤ 98 %
Exceeding nedl/snr requirement

GEOMETRIC

Field of view
Instantaneous FOV
Calibration
Flight line length

30 degrees (11 km)
1.0 mrad (20 m)
≤ 0.1 mrad
800 km

AVIRIS OPERATIONAL CHARACTERISTICS

SENSOR

Imager type	Whiskbroom scanner (12 hz)
Dispersion	Four grating spectrometers (a,b,c,d)
Detection	224 detectors (32,64,64,64) Si and InSb
Digitization	12 bits
Data rate	20.4 mbits/second
Spectrum rate	7300 spectra/second
Data capacity	>10 gigabytes (>8,000 km ²)
Launches	~30 per year

DATA FACILITY

Performance monitoring	48 hours from acquisition
Archiving	One week from acquisition
Quicklook distribution	One week from acquisition
Calibration	Two weeks from request
Quality monitoring	Prior to distribution
Distribution	Two weeks from request
Engineering analysis	As required

PLATFORM

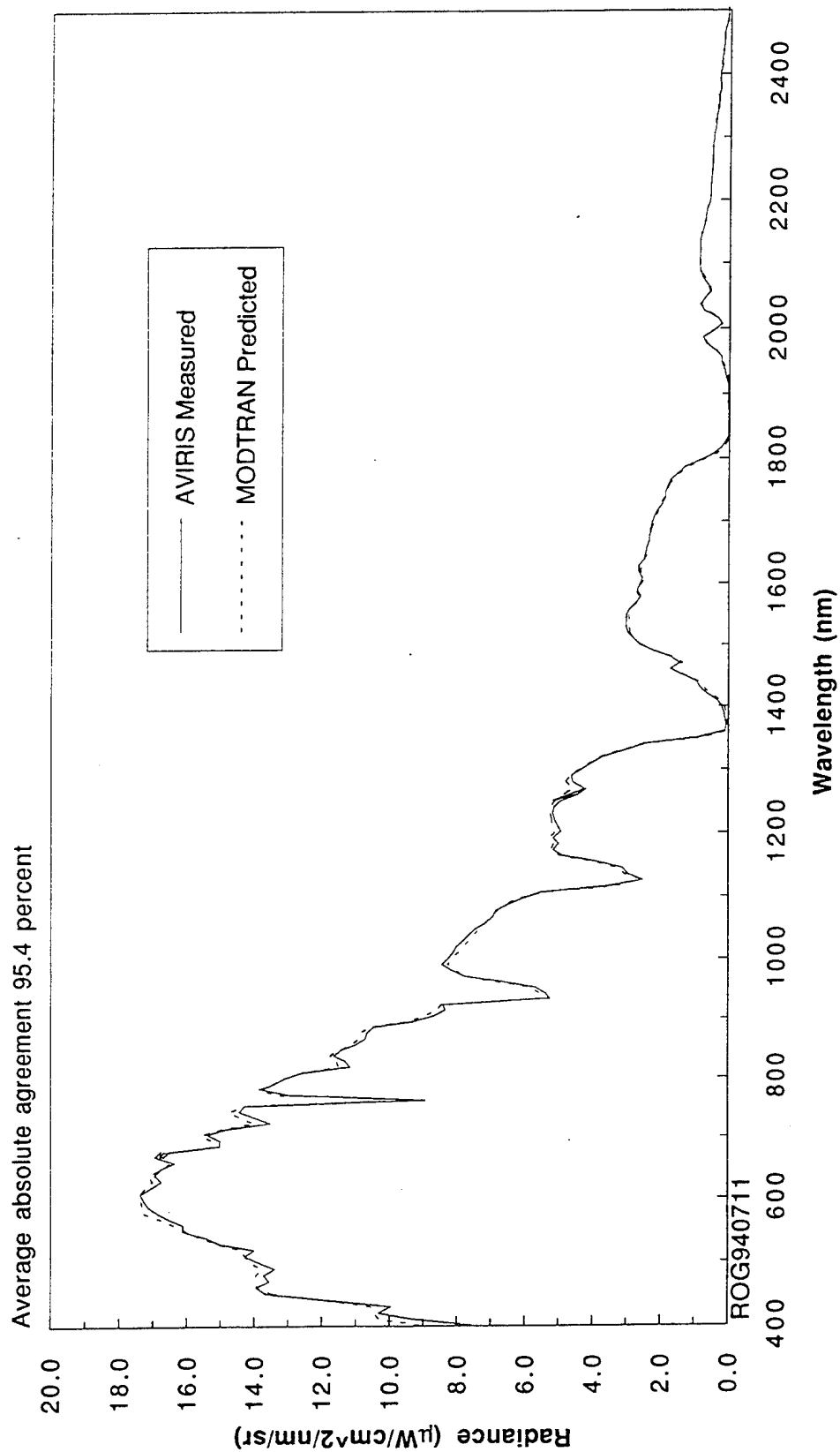
Aircraft	NASA ER-2
Altitude	20 km
Velocity	734 km/h
Range	<= 2100km
Flight duration	<=6.5 hours
Launch sites	Domestic & foreign

AVIRIS CALIBRATION REQUIREMENT

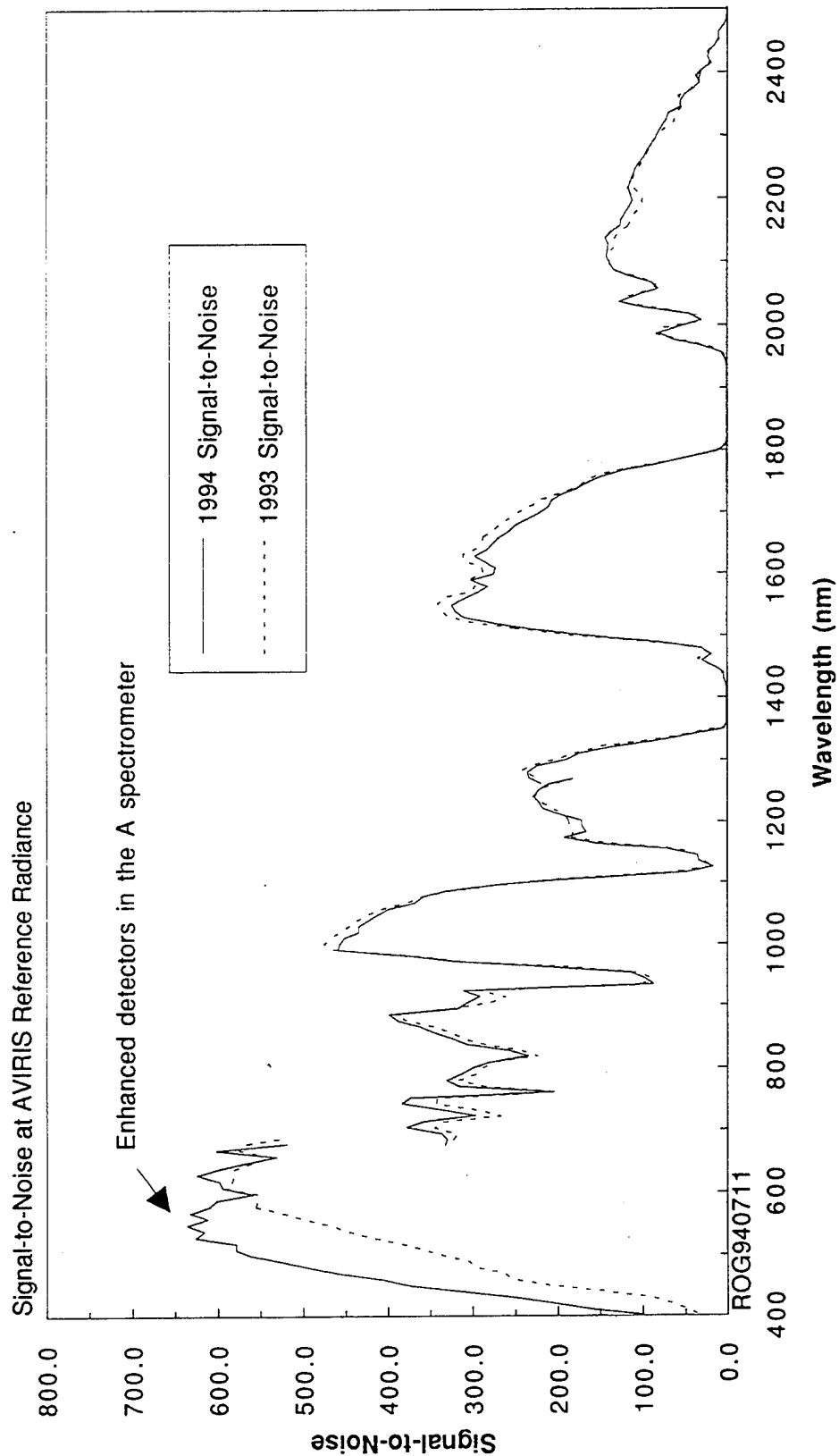
Imaging spectrometry data must be spectrally, radiometrically and geometrically calibrated in order to:

- Derive physical parameters from measured radiance
- Compare data acquired from different regions and from different times
- Compare and analyze imaging spectrometry data with data acquired by other instruments
- Compare and analyze data with results from computer models

AVIRIS Calibration Experiment: Lunar Lake, NV, 5 April 1994



AVIRIS Calibration Experiment: Lunar Lake, NV, 5 April 1994



AVIRIS 1994 ACCOMPLISHMENTS

The 1994 AVIRIS sensor maintenance was completed on schedule for the NASA BOREAS experiment.

The signal-to-noise between 400 and 600 nm was doubled, during AVIRIS sensor maintenance.

A very successful AVIRIS workshop was held in Washington D.C.

Inflight calibration was shown to be at the 95% level during 1994.

The seventh and eighth successful underflights of the Japanese JERS-1 satellite were completed in support of the NASDA/NASA JERS-1 Onorbit Calibration Experiment.

AVIRIS adopted a plan for level funding in FY95 using JPL policy of zero raises in 1995.

AVIRIS quicklook images were placed on-line through the internet for all 1992, 1993 & 1994 data.

AVIRIS was launched 50 times on the ER-2 in 1994 with no malfunctions.

More deployments were supported and more data were collected than in any previous year.

AVIRIS 1994 OPERATION PERFORMANCE

Metric	Nominal	1992	1993	1994
Months of Operations	6	8	7	8
Months for Maintenance	6	4	5	4
Major Deployments	4	4	4	6
ER-2 Launches	30	34	38	50
Investigator sites flown	150	172	211	372
Scenes Acquired	1000	1143	1384	2581
Square kilometers	100,000	114,300	138,400	258,100
Scenes Delivered and in Queue	1000	1120	1412	2000*
Gigabytes processed	280	317	391	641*
On-line quick looks provided	1000	---	---	1872**

*projected

**Since 1 January 1995

AVIRIS 1995 ACTIVITIES

The AVIRIS data facility server and software are being upgraded to increase responsiveness to investigators.

Four new focal planes will be installed **doubling the signal-to-noise** and include both simultaneous detector-read-out and 12 bit digitization.

The end-of-line dark signal will be summed to eliminate introduction of noise during calibration.

The onboard calibrator will be actively stabilized with Si detector.

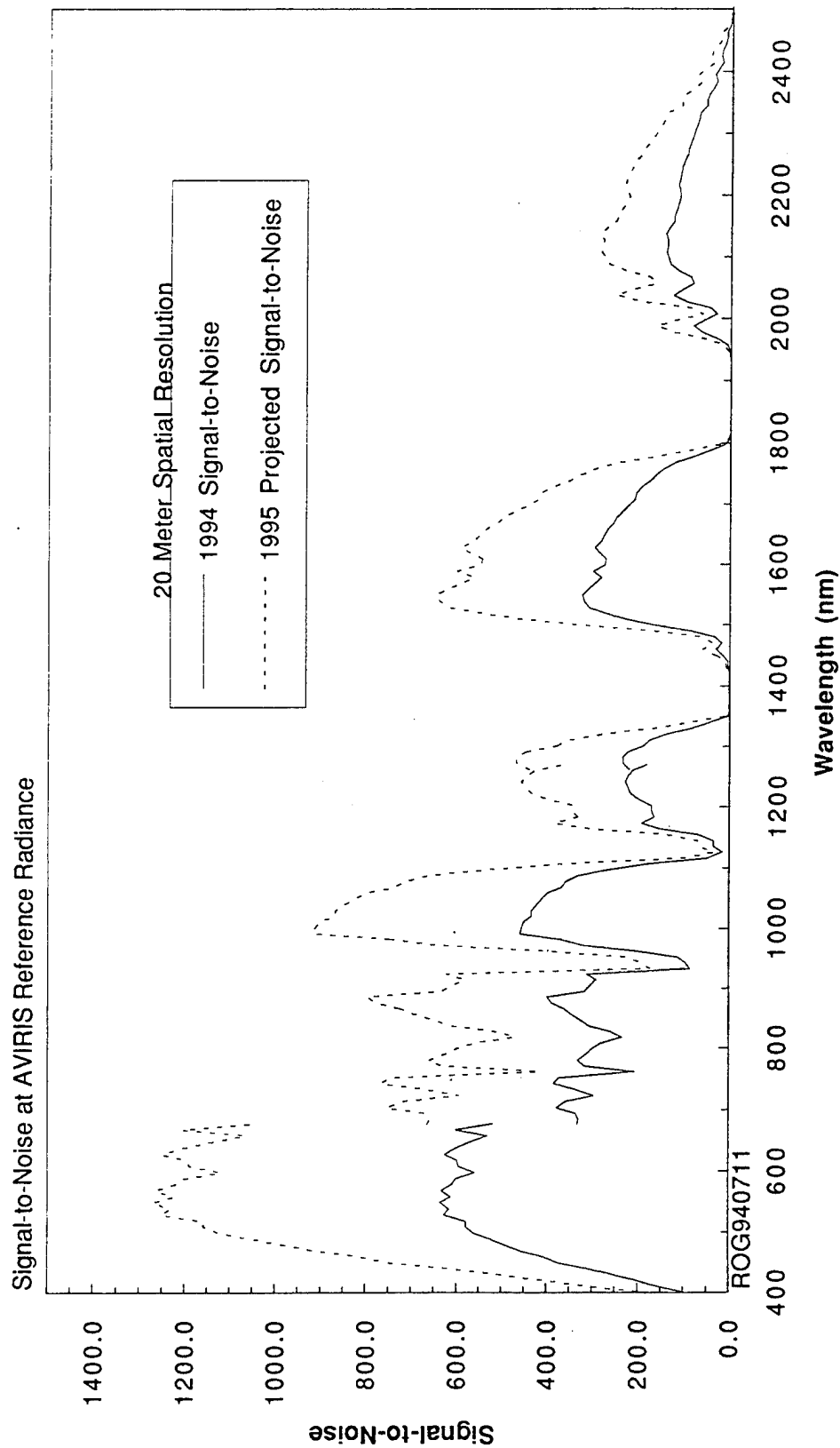
NASDA accepted a proposal to use AVIRIS to calibrate the AVNIR and OCTS sensors onboard the Japanese satellite ADEOS in 1996-8.

The USGS has initiated discussions and funding to use AVIRIS for environmental assessments in the National Parks.

AVIRIS will be used to support DOD-Civilian HYDICE experiment with AVIRIS' superior calibration and signal-to-noise

It is hoped that AVIRIS will support the NASA technology demonstration LEWIS sensor with AVIRIS' superior signal-to-noise and calibration. AVIRIS should provide precursor data sets, on orbit calibration, and on-orbit support to LEWIS.

AVIRIS Signal-to-Noise with 1995 Focal Planes



DISCUSSION

Why use imaging spectrometry?

The overarching terrestrial remote sensing objective is to derive accurate information about the surface and atmosphere from the measured electromagnetic spectrum

In the terrestrial environment 100s of compounds reflect, absorb, transmit and scatter energy in the spectral region 400 to 2500

For this reason, you can not unambiguously derive information for a single material from a single band, unless no other compounds affect the electromagnetic energy. (never true)

For this reason, with a spectrum you can derive information for numerous materials of interest directly and simultaneously as well as account for the other compounds present in the terrestrial environment

DISCUSSION

AVIRIS remains the most advanced sensor in the optical spectral region.

With the upgrades currently underway AVIRIS, with only 87 microseconds dwell time per spectrum, will exceed the performance of most laboratory spectrometers.

Only now with are we learning the quantitative molecular and scattering information contained in spectra acquired by AVIRIS.

This was learned in chemistry and physics a 100 years ago

Only now has technology advanced to allow development of actual imaging spectrometers

Given the thousands of compounds occurring in the environment, the approach taken by AVIRIS to spectrally measure the fundamental molecular absorptions of constituents of the terrestrial surface and atmosphere is unarguably sound.

Research with AVIRIS is leading to new quantitative algorithms spanning the disciplines of: Ecology, Geology, Coastal Oceanography and Limnology, the Atmosphere, Hydrology, Calibration, Hazards etc.

It should be noted that neither DOD-HYDICE or NASA-LEWIS will offer data of comparable to the 11 km swath, SNR and calibration characteristics of AVIRIS. AVIRIS does not compete, but complements these two future imaging spectrometers

AVIRIS DATA AVAILABILITY

ophelia.jpl.nasa.gov

To access:

Lists of all AVIRIS data acquired since 1992 by lat/lon and time
Single AVIRIS channel images of all data
Calibrated data ordering instructions

Type the following commands to a computer connected to the internet:

```
ftp ophelia.jpl.nasa.gov  
anonymous  
"your email address"  
cd pub  
ls  
get README
```

Follow the README file instructions or cd to qlook92 or qlook93, etc. and get the README, INDEX and quicklook-images.

ophelia.jpl.nasa.gov

INVERSION OF DOWNWELLING SPECTRAL RADIANCE FOR TROPOSPHERIC PROFILE RETRIEVALS: PRACTICAL ASPECTS

J.-M. Thériault and J.-L. Moncet*

DREV-Defence Research Establishment Valcartier
P.O. Box 8800, Québec, Canada, G0A 1R0

* AER-Atmospheric and Environmental Research, Inc.,
Cambridge, MA 02139 USA

ABSTRACT

Recent developments in remote sensing of atmospheric profiles with a ground-based FTIR spectrometer are presented. Several aspects of the inversion method for the retrieval of temperature and humidity profiles from IR emission spectra are reported. The main objective of the study is to report practical problems encountered in the inversion of experimental spectra. The development of the method is supported by current experiments performed with the DREV interferometer (DBIS - Double Beam Interferometer Sounder). In particular, the impacts of linearization errors, noise in measurements, spectral band selections and water vapor continuum on inversion results are discussed.

1. INTRODUCTION

In order to develop a method for the retrieval of temperature and water vapor profiles from IR emission spectra, the Defence Research Establishment Valcartier (DREV) has acquired a device referred to as the Double input Beam Interferometer Sounder (DBIS)². This sounder has been conceived to match the needs encountered in many remote sensing scenarios. It is a portable device composed of a Fourier spectrometer and one or optionally two telescopes that measures the atmospheric emission in the IR region from 3 to 20 μm at a spectral resolution of 1 cm^{-1} and at any prescribed viewing angles. Since summer 1992, the DBIS has been deployed in a series of field experiments, producing spectral data of good quality for a variety of sky conditions. These spectral data are now being utilized as a guide for the development of the inversion method. In this paper, a review of the remote sensing method is presented together with an analysis of recent experimental results.

2. SPECTRAL MEASUREMENTS AND CALCULATIONS

The DBIS consists of one or optionally two 10-in. diameter Cassegrain telescopes, optically coupled to a double-input port Fourier transform interferometer. The interferometer is a BOMEM model MB100 and has two detection units, one with an InSb detector and the other with a MCT detector. This configuration allows measurements of calibrated spectra according to the following specifications: 0-180° zenith angle, 5 mrad field of view, 3 to 20 μm spectral band at 1 cm^{-1} resolution. The pointing capability and small field of view of the instrument allow clear line-of-sight slant path measurements even in the presence of clouds and ensure good radiometric homogeneity of the probed scene at large zenith angle (Z. A.).

The radiometric calibration of DBIS spectra is based on the two-temperature method. Two temperatures are required because there are two unknowns: the gain and the offset (self emission) of the instrument. The implementation of this method is fully consistent with the solution given by

Revercomb et al.³. To obtain a calibrated emission spectrum, three measurements are required: the raw spectrum corresponding to the emission of the atmosphere and two raw spectra from the reference blackbodies. Each raw spectrum is obtained by coadding 40 individual scans taken at a resolution of 1 cm^{-1} . In these conditions of operation, the RMS noise has been measured to be smaller than 0.2 K (brightness temperature) almost everywhere in the usable portion of the 4-20 μm region.

In summer 1994, the DBIS has been run in a variety of clear sky conditions at Valcartier near Quebec City. This location and season may be characterized as midlatitude summer. The radiosonde launch site and the DBIS measurement site were situated at the Canadian Force Base Valcartier for this series of measurements. Typically, radiosondes were launched once a day (4 or 5 times a week) at 09:31 or 10:31 am local time. An example of an atmospheric emission spectrum expressed in brightness temperature appears in Fig. 1. The measurement was made on 20 June 94 in clear conditions at a zenith angle of 45° with 1 cm^{-1} resolution. The general shape of emission spectra is dominated by the temperature and the absorption properties of the constituents along the optical path. In spectral regions where the absorption is strong, the atmosphere radiates its energy like a blackbody at a temperature roughly equal to the temperature near the sounder. This is observed as strong absorption bands of CO_2 near $15 \mu\text{m}$ (660 cm^{-1}) and $4.3 \mu\text{m}$ (2450 cm^{-1}) and also in the $1350\text{-}1850 \text{ cm}^{-1}$ region where the absorption is mainly due to water vapor. If we exclude the important emission band of O_3 near $9.6 \mu\text{m}$ (1040 cm^{-1}), the atmospheric window regions from 800 to 1300 cm^{-1} and 2400 to 3000 cm^{-1} are dominated by the water vapor absorption lines and continuum. For comparison, the bottom curve of Fig. 1 represents the corresponding calculations performed with a recent version of the FASCOD3 model⁴.

3. REVIEW OF THE RETRIEVAL METHODOLOGY

The adopted approach is a minimum information type of inversion^{2,5}. The two main advantages of this approach are that no a priori information on the statistics of atmospheric profiles is required and it allows the simultaneous retrieval of temperature and water vapor profiles⁶. The formulation of this method can be summarized as follows. First, the forward problem of radiative transfer is linearized by considering that the measured radiance $R(v)$ is a first order perturbation of the radiance $R^0(v)$ computed with first guess profiles of temperature $T^0(z)$ and water vapor mixing ratio $\rho^0(z)$. In its matrix form, the linearized radiative transfer equation is written as

$$r = K x \quad (1)$$

In eq. 1, r is the perturbation vector of spectral measurements defined as $r = R(v) - R^0(v)$ and K is the matrix of partial derivatives where the rows of K are often defined as the weighting functions. The column vector x contains the perturbation profiles of temperature and mixing ratio. It is defined as $x = [T(z) - T^0(z); \rho^0(z) - \rho^0(z)]$. The minimum information solution of this overdetermined system of equations which contains about 1000 spectral elements for about 50 unknowns (30 levels for temperature and 20 levels for mixing ratio) is given by

$$x = [K^t S_e^{-1} K + S_b^{-1}]^{-1} K^t S_e^{-1} r \quad (2)$$

where S_e is a diagonal matrix having for elements the noise standard deviation associated with the spectral measurements and S_b is a diagonal matrix composed of damping parameters adjusted for each variable to be retrieved. These damping parameters are introduced to stabilize the solution which oscillates when improperly adjusted. Because of the linearization constraints in the problem, eq. 2

provides an approximate solution for the actual profiles. An improved solution might be obtained by iterations for which the K matrix is updated with the previous profile estimates.

There are two practical difficulties encountered in the implementation of this method. First, there is no systematic procedure to optimize the matrix of damping parameters (S_b). It has to be adjusted empirically based on retrieval simulations performed with typical atmospheres. Second, the method requires the evaluation of partial derivatives for each level and each parameter. For this, Moncet and colleagues⁷ have devised a scheme to greatly optimize calculations of the partial derivatives based on FASCOD. This scheme takes advantages of a radiative transfer formulation based on optical depths rather than transmittances. The partial derivatives are directly evaluated by an analytical expression involving perturbed and unperturbed layer optical depth matrices generated with a minimum number of FASCOD runs. For instance, only three runs are required: two runs to generate the optical depth matrices corresponding to temperature and water vapor perturbations respectively and one to generate the unperturbed atmosphere.

The current inversion algorithm used in the present work is based on the FASCOD3 model and includes the Moncet scheme for partial derivative calculations. In addition, we have developed a systematic procedure for the evaluation of first guess profiles required as input by the method (see Ref. 8). For water vapor, the first guess profile is given by an arithmetic average of midlatitude summer and US standard profile, scaled with the measured radiance in a narrow band of H_2O near 560 cm^{-1} . For temperature, the first guess profiles is given by an interpolation from profiles estimated near the surface ($< 0.5\text{ km}$) and above 8 km (assumed to be midlatitude summer). The near surface profile ($< 0.5\text{ km}$) is evaluated using an approximate expression proportional to the measured radiance in the strong absorption band of CO_2 near $15\text{ }\mu\text{m}$ ($630\text{-}700\text{ cm}^{-1}$).

4. RESULTS

The optimization of a retrieval method such as the minimum information type of inversion described above is a long term achievement mainly because of the large number of parameters involved in the inversion process. These parameters are: the quality of first guess profiles, the spectral resolution, the spectral coverage, the vertical leveling, the adjustment of the damping parameters at each level, the angle of observation (zenith angle), the precision of measurements and finally the accuracy of forward calculations.

In a previous study², good inversion results were obtained under certain conditions. First, it appeared essential to select a particular set of spectral channels for which the errors in forward calculations are reasonably small. Second, a further improvement in the forward calculations was achieved by modifying the foreign broadening coefficients of the water vapor continuum (at the edges of the $6.3\text{ }\mu\text{m}$ band) according to the results of a recent study⁹. This continuum is referred to as the CKD (Clough, Kneizys and Davies¹⁰) continuum first version. Inversions were achieved under the following conditions: uplooking measurements; spectral resolution of 2 cm^{-1} ; spectral selection of 3 bands $560\text{-}950\text{ cm}^{-1}$, $1280\text{-}1380\text{ cm}^{-1}$ and $1800\text{-}2000\text{ cm}^{-1}$; RMS noise of 2 K ; damping parameters for temperature equal to 100 K^2 and for water vapor equal to 4 (g/kg)^2 . These damping parameters may be seen as constraining the inversion process to temperature and mixing ratio excursions of the order of 10 K and 2 g/kg respectively.

In the present study, several new inversions have been made in the following conditions: zenith angle 30° or 45° ; spectral resolution of 1 cm^{-1} ; spectral selection of 3 bands $560\text{-}830\text{ cm}^{-1}$, $1275\text{-}1400\text{ cm}^{-1}$ and $1800\text{-}1990\text{ cm}^{-1}$; RMS noise of 2 K ; damping parameter were adjusted for each case. In addition, the water vapor continuum was further modified to include an increase of approximately 20% of the self broadening coefficients in the $560\text{-}830\text{ cm}^{-1}$ also consistent with ref. 9.

Figure 2a shows typical first guess profiles found by the estimation procedures compared to radiosonde profiles. Upper curves correspond to temperature and refer to the left scale. Figure 2b displays the corresponding radiance error introduced by the linear model (eq. 1) and the first guess profiles of Fig. 2a. It is expressed in brightness temperature units using a reference temperature of 290 K. As seen, the linearization error is maximum at approximately 780 cm^{-1} with an RMS value of 0.43 K. Fig. 3a represents a highly idealized case where the inversion has been performed on the linearized radiance (avoiding linearization error) with the first guess profiles of Fig. 2a. In this case, the best inversion was run with high values of damping parameters: approximately 1000 for temperature and 200 for mixing ratio. This idealized case is a good test to validate the inversion algorithm and coding. In Fig. 3b, the inversion has been performed on the exact calculated radiance. In this case the linearization error force the application of strong constraints on damping parameters: approximately 16 for temperature and 2 for mixing ratio. Figure 3c corresponds to inversions performed on a typical experimental spectrum for different versions of water vapor continuum included in the forward model. For these calculations, the first guesses were the radiosonde profiles (validation mode). As shown, the inversion done with the original version 1.0 of the CKD continuum (cor-1) disagrees with the radiosonde profiles (truth, thick lines)). A correction of foreign broadening coefficients, consistent with results of Ref. 9, improves the inversion (cor-2) especially for temperature. An additional correction for the self broadening component of the CKD continuum, consistent with results of Ref. 9, further improves the inversion (cor-3). Finally, Figs. 3d and 3e illustrate the effect of MCT detector non-linearity. This effect is easily observed in the measured brightness spectrum (Fig. 3e) where a frequency dependent offset of approximately 0.5 K exists between raw and corrected (FASCOD3) spectra. Figure 3d indicates the effect of the distortion on inversion results.

Figure 4 summarizes the results obtained with the actual inversion algorithm for three typical runs performed in August 1994. In the left column, radiosonde profiles of temperature and humidity are compared to profiles retrieved with radiosonde data as first guess inputs. Although the overall agreement is good there are slight differences that might be due to the fact that radiosonde and DBIS measurements are not perfectly coincident in time and direction. The right column of Fig. 4 represent the desired results where the whole inversion process has been applied to the experimental spectrum. In this case, the first guess profiles is derived using the systematic procedure which requires only data from the measured spectrum itself. The agreement between radiosonde and retrieved profiles is acceptable but limited by the resulting vertical resolution especially for water vapor mixing ratios. Finally, Figs. 4b, 4d, 4f represent the results that can be obtained with the minimum information type inversion in its present form. Potential improvements might be realized by a better selection of spectral bands, inclusion of missing species in the forward calculations and possibly a better evaluation of the reference blackbody emissivities.

5. CONCLUSION

The minimum information type inversion for the retrieval of temperature and humidity profiles from IR emission spectra has been tested on recent experimental measurements. The actual version of the method contains corrections for the self and foreign broadening coefficients of the CKD continuum, version 1.0. In addition, it includes a correction for the effects of non-linearity observed in experimental spectra recorded with the MCT detector. With these two corrections the inversion of measured spectral radiance is achievable and gives satisfactory results.

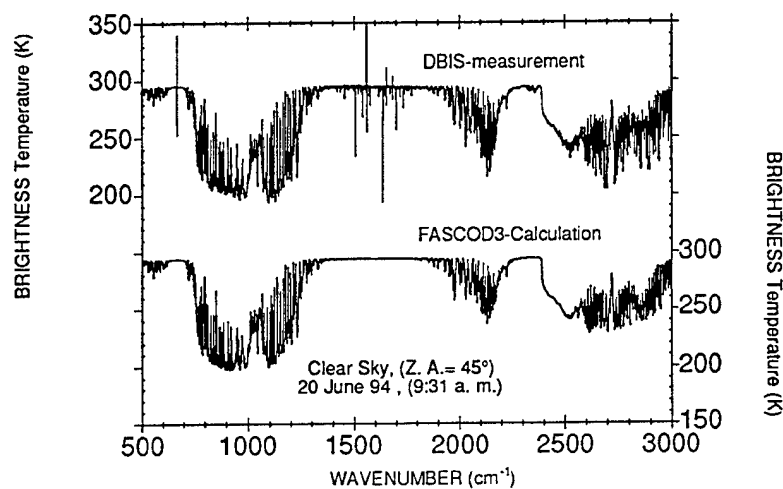


Fig. 1. Typical example of spectra measured with the DBIS and calculated with radiosonde inputs for a clear day corresponding to midlatitude summer conditions.

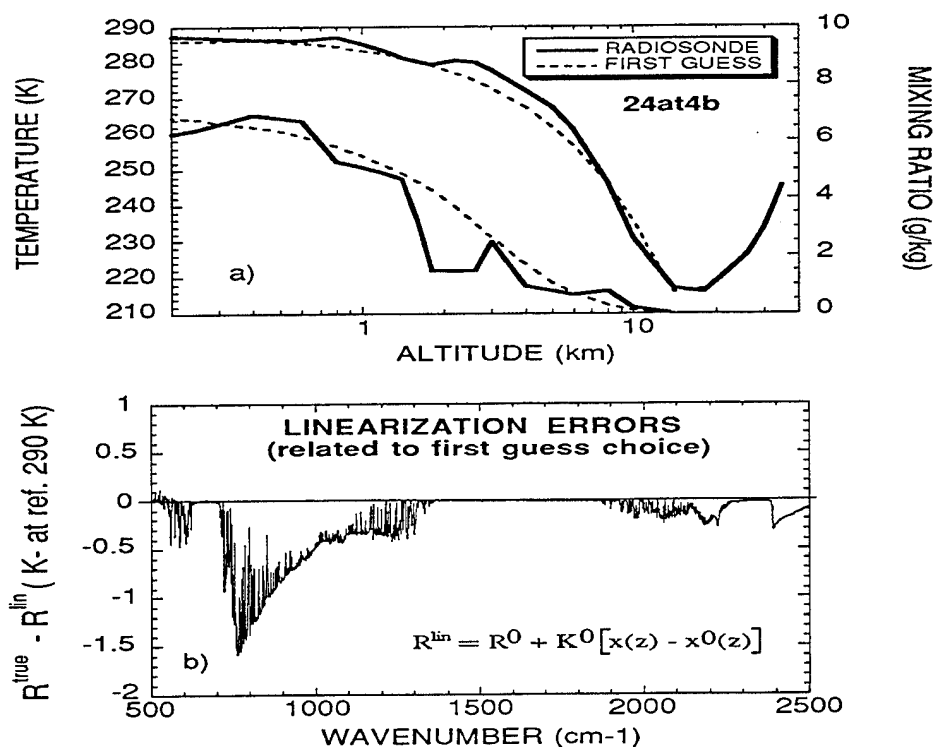


Fig. 2. Typical results (a) of the first guess estimation procedures for temperature and mixing ratio profiles evaluation and the resulting linearization errors (b).

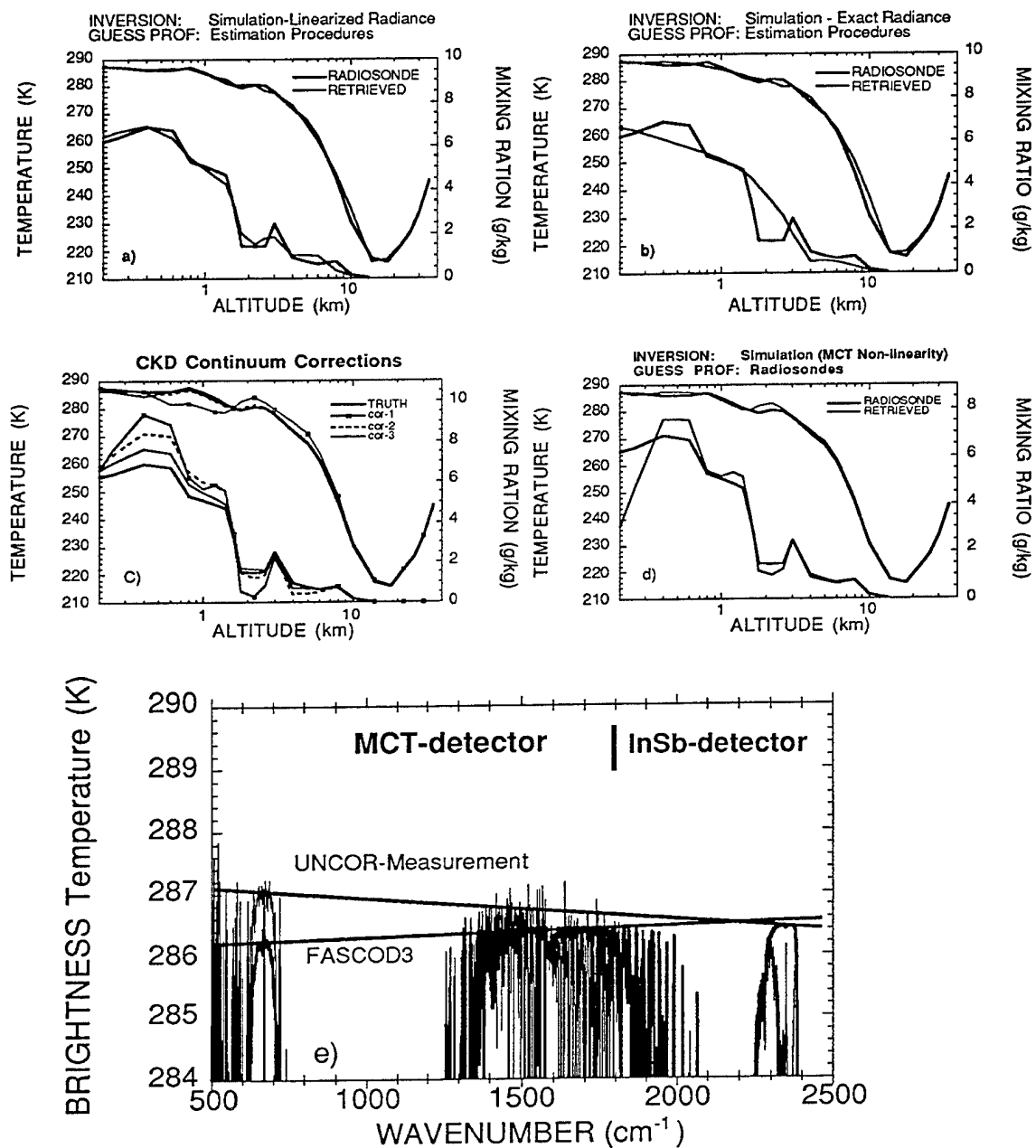


Fig. 3. Inversions showing the impact of linearization (a,b), CKD continuum corrections (c) and detector non-linearity (d) on retrieval accuracy. Graph (e) indicates the effect of non-linearity in the spectral domain.

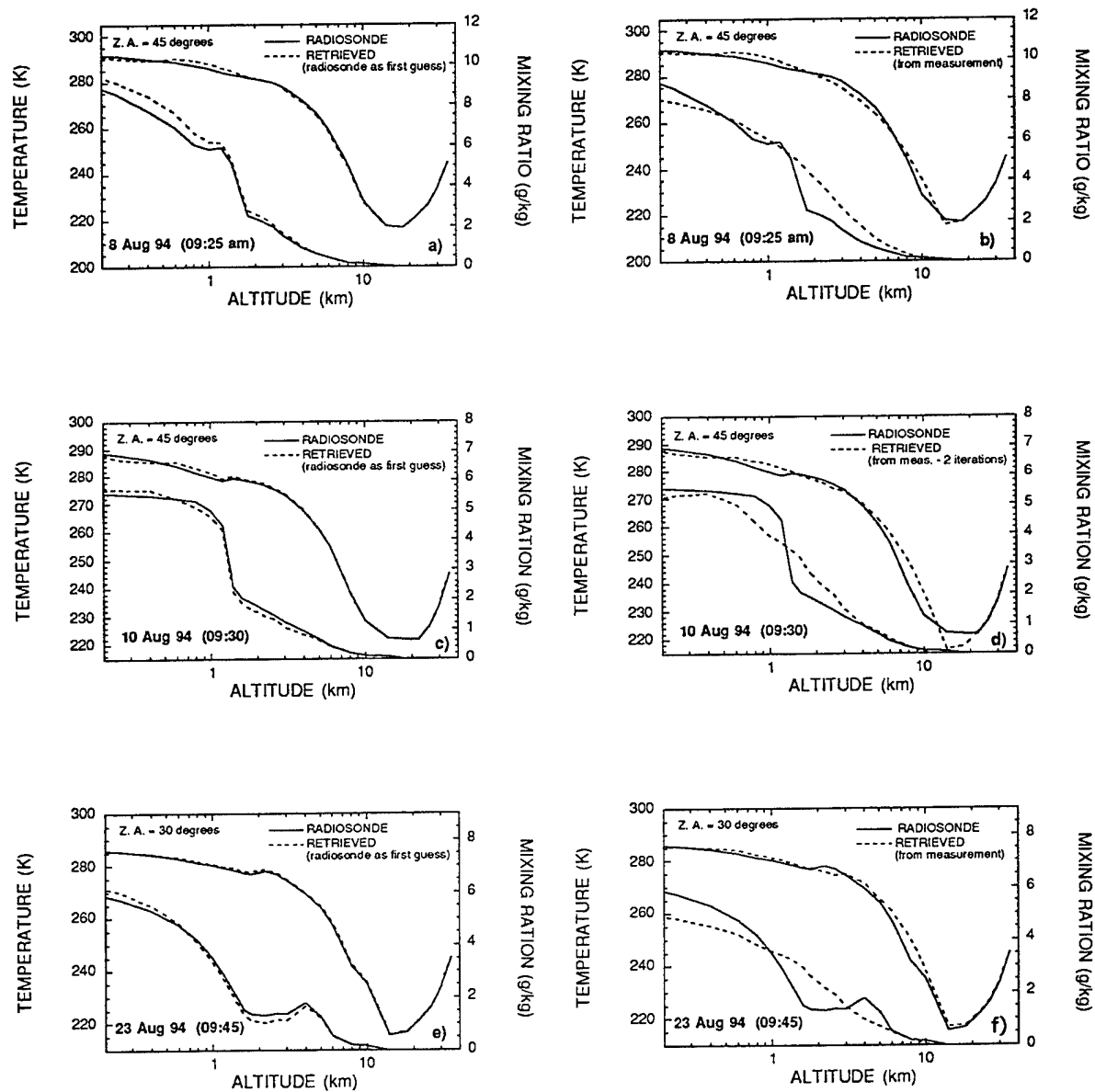


Fig. 4. Typical inversions for spectral measurements performed at DREV. Cases a, c and e correspond to the inversions of experimental spectra done with radiosonde data as first guess while for cases b, d and f the first guess is estimated by the evaluation procedures.

Temporal Phase Relationships Among Atmospheric Constituents

W. G. Egan, Natural Sciences Department, York College/City
University of New York Jamaica, NY 11451 and Physics Department,
Polytechnic University, Brooklyn, New York 11201

E-Mail: EGAN@YCVAX.YORK.CUNY.EDU

and

A. W. Hogan, U. S. Army Cold Regions Research and Engineering
Laboratory, Hanover, NH 03755-1290

ABSTRACT

A heretofore unrecognized temporal phase relationship between carbon dioxide, methane, ozone, aerosols, temperature, and water vapor has been found to exist at the South Pole. These temporal relationships appear to be worldwide, and have not been included in any modeling. The effects on atmospheric models will be significant.

INTRODUCTION

The Antarctic Continent is covered by a cold, dry air mass that is permanently resident over the South Polar Plateau; the air mass is unique in that it is never displaced, and is slowly modified by maritime polar air that encircles Antarctica. This is evidenced by the similarity of potential temperature at many stations in the air mass. This air mass overlays a snow and ice

surface which at most is a very weak source of carbon dioxide, water vapor, methane, ozone, water vapor, and aerosols. Some upper tropospheric air is mixed in by subsidence, especially in winter. At the South Pole, carbon dioxide, methane, and ozone are 180 degrees out of phase with water vapor and temperature, but aerosols are in phase with water vapor (Fig. 1). In Fig. 1, the concentrations are plotted along the vertical axis, and the monthly averages along the horizontal axis. The year 1986 is shown with the first half of the year appended to the latter half so that a complete cycle can be seen. The ozone and methane are in parts per billion (ppb), the partial pressure of water vapor in millibars (mb), the aerosol concentration per cubic centimeter (cm^3), and temperature in degrees Centigrade. The aerosols are shown as a 20-year average in order to minimize statistical fluctuations. The water vapor variations are approximately in phase with the aerosol variations, both of which lead the carbon dioxide variations, which are approximately in phase with the methane and ozone variations.

This time dependence can be more readily seen in the plots of Figs. 2, of variations of carbon dioxide and methane with water vapor; monthly averaged water vapor partial pressure is plotted on the horizontal axis and the carbon dioxide and methane monthly averaged concentrations on the vertical axis. The elliptical curve is a Lissajous Figure, analogous to electrical engineering terminology. The elliptical shape of the figure as it traces the months from January to December going clockwise is caused by the y-axis variation lagging the x-axis variation; in other words, both

the carbon dioxide, methane and ozone lag the water vapor variation and appears to be a function of, or be caused by the variations in water vapor. In contrast, the aerosols and temperature are in phase with the variations in water vapor. The solubility of the various gases appear to be related to the time sequence of appearance.

This functional variation of atmospheric gases appears to be worldwide, and can be seen on other scales such as daily, monthly, and annually, and is dependent on geological latitude.

The application of these results to LOWTRAN/MODTRAN is that the trace gases and aerosols cannot be considered independent, because of their relationship to water vapor. There could be a relationship to the foreign contribution of the water vapor continuum as suggested by the line structure shown in Fig. 3. The interrelationship of CO_2 , CH_4 , O_3 , aerosols, and H_2O vapor must be brought into any realistic atmospheric model by a functional dependence. As noted above, the primary variable appears to be water vapor (which is caused by temperature variations over a water vapor source). Even though we have shown these results at the South Pole where the air mass circulation is contained, the same relationships occur worldwide in association with circulation, exchange and mixing processes.

In terms of LOWTRAN and MODTRAN, assumed uniformly mixed gases of carbon dioxide and methane were found by bottle samples at the South Pole to be non-uniformly mixed; further the "uniformly" mixed gases CO_2 , CH_4 , N_2O , and CO , all of which are soluble in H_2O , cannot be considered independent in LOWTRAN or MODTRAN; this also includes O_3 ,

HNO₃, and aerosols. This input change can be accomplished for example in LOWTRAN 7 or MODTRAN3 in MODEL = 0 or 7 with user inserted values.

REFERENCES

1. W. G. Egan and A. W. Hogan, "Interpreting Air Chemistry Records at the South Pole", Transactions of the American Geophysical Union, 76, S171 (1995).
2. W. G. Egan, "Radiative Transfer Properties of the Sahara Region", Remote Sensing of the Environment, 50:182-193 (1994)

South Pole

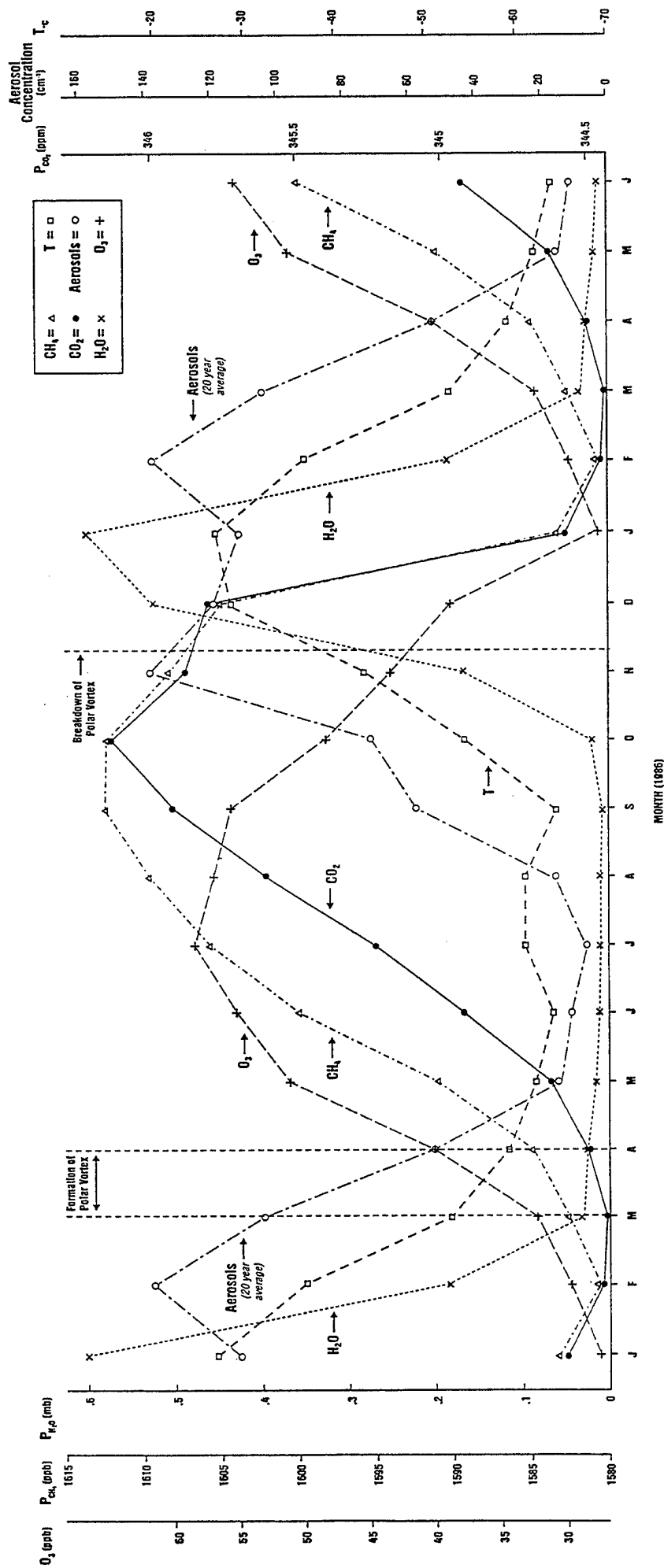


Figure 1. Chronology of variation in water vapor, carbon dioxide, ozone, aerosols, and temperature, at the South Pole.

South Pole

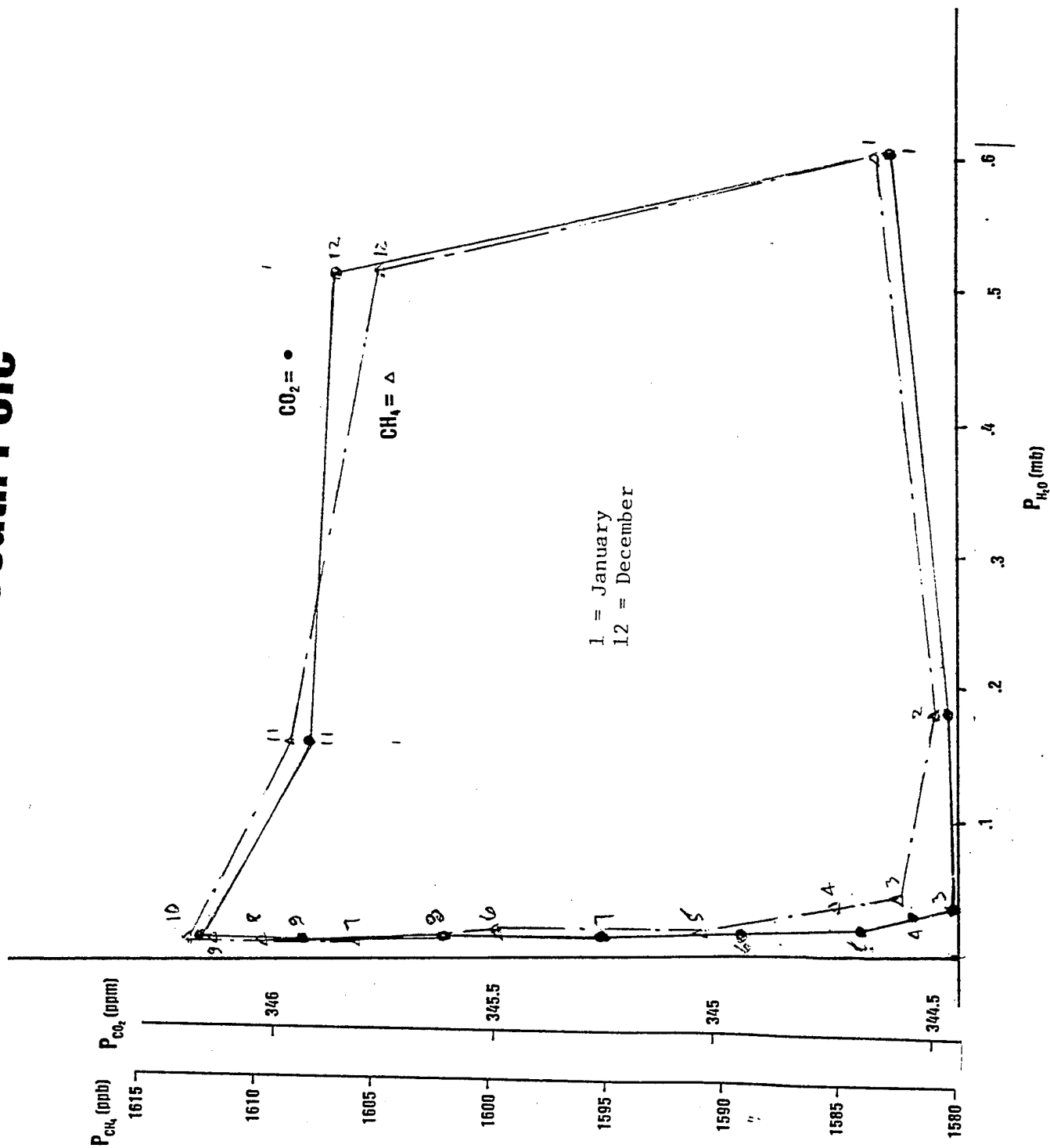


Figure 2. Lissajous Figure, showing relative variation in carbon dioxide and methane with respect to water vapor, at the South Pole

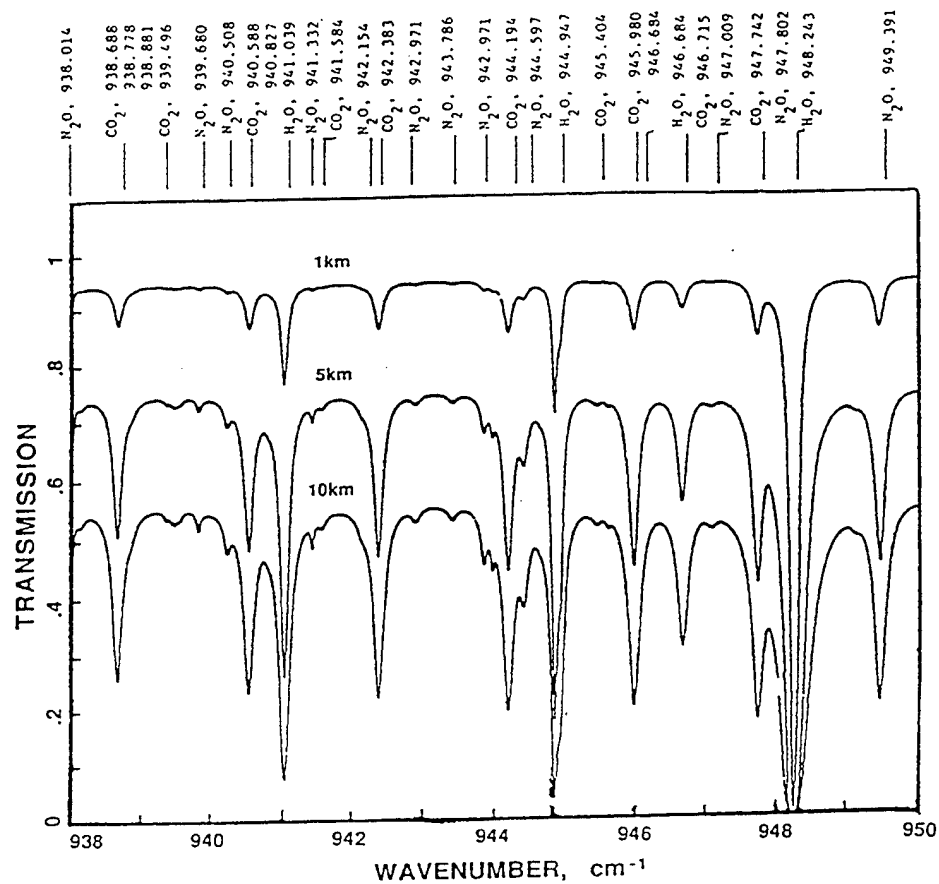


Figure 7. Typical boundary layer transmission of the Earth's atmosphere between wavelengths of $10.661 \mu\text{m}$ and $10.526 \mu\text{m}$ ($938\text{--}950 \text{ cm}^{-1}$ wave numbers) using rural aerosols and H_2O continuum of LOWTRAN 5 in a line-by-line model. The H_2O continuum is the main cause of the displacement of the maximum transmission below 1.0.

FASCOD3 Atmospheric Modeling of an SF₆ Plume Released from a Stationed Balloon

J. B. Koffend
Space and Environment Technology Center
THE AEROSPACE CORPORATION
El Segundo, CA 90245-4991

Assessing human exposure from and environmental impact of Titan IV launches requires the accurate prediction of the ground impact of toxic chemicals, both propellants and combustion products. Current numerical plume modeling techniques do not allow prediction of the cloud dispersion accurately enough to make reliable assessments of the impact on local population centers. As a prelude to validation experiments for these plume dispersion models, the FASCOD3 atmospheric radiance code is used in conjunction with IR camera characteristics to estimate the quality of experimental data from IR plume imaging studies of elevated tracer gas releases.

The narrow SF₆ feature near 950 cm⁻¹ lies in a spectral window that makes SF₆ an ideal IR imaging species for observation of plume transport in the atmosphere. Imaging of SF₆ in the infrared region is performed by using an IR camera and two interference filters, one (on-band) which contains the 950 cm⁻¹ SF₆ band while the other (off-band) filter excludes this spectral feature.

Whether the SF₆ plume can be detected depends upon the noise-equivalent-radiance (NER) of the cameras used. These calculations will help determine just how far the SF₆ can be tracked down wind from the blimp.

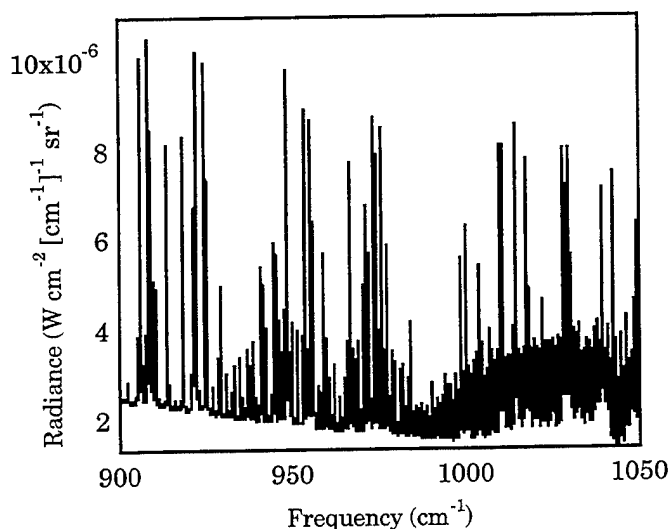


Fig. 1 FASCOD calculated spectrum for mid latitude summer looking straight up.

The column density (concentration path length product) of the SF₆ plume released from the blimp was calculated using a right circular cone model. The observer is a distance "d" downwind, looking up at a small cross section of the plume. The ratio of the diameter of the plume to the distance downwind is the aspect ratio. The gas is released from the blimp at a rate "RR" (release rate) in kg/hour. The concentration of the SF₆ in the small viewed portion of

the plume was calculated as follows. The volume of the SF₆ released in a segment of the plume is given by

$$V_{\text{SF}_6} = \text{RR} * t * \text{VM}_{\text{SF}_6} / M_{\text{SF}_6} \quad (1)$$

where RR is the SF₆ release rate, t is the time, VM_{SF₆} is the SF₆ molar volume, and M_{SF₆} is its molecular weight. For a very short segment of the plume (a few meters long), the plume is approximately cylindrical. The length of the cylinder is the product of the wind speed and the time. The diameter of the plume is the product of the distance down wind and the aspect ratio.

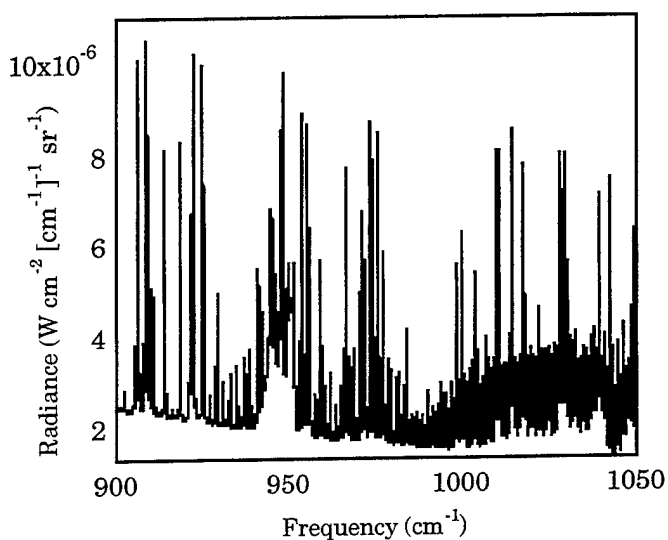


Fig. 2 FASCOD calculated spectrum for a mid latitude summer looking straight up. This spectrum includes the blimp releasing SF₆

The volume of the cylinder is given by

$$V = S_{\text{wind}} * t * \pi * (\text{ar} * d/2)^2 \quad (2)$$

where S_{wind} is the wind speed, t is the time, ar is the aspect ratio (plume diameter/distance down wind) and d is the down wind distance. The concentration of the SF₆ is the ratio of the SF₆ volume (Eq 1) to the plume segment volume (Eq 2), as shown in Eq 3.

$$[\text{SF}_6] = \frac{\text{RR} * \text{VM}_{\text{SF}_6}}{M_{\text{SF}_6} * \text{ar}^2 * d^2 * \pi * S_{\text{wind}}} \quad (3)$$

FASCOD3 radiance calculations were made for a ground based observer looking straight up. The observer's line of sight was taken to be perpendicular to the nominal plume line. A mid latitude summer atmosphere was used for the calculations. Shown in Fig. 1 and 2 are atmospheric radiance spectra for an observer looking straight up at a

mid latitude summer atmosphere. Figure 2 contains the spectrum with a blimp releasing 20 kg/hr SF_6 . The feature near 950 cm^{-1} , due to SF_6 , is the sole difference between the two spectra.

Transmission curves of the on-band and off-band SF_6 filters along with the SF_6 spectrum are displayed in Fig. 3. It is filters such as these that will be used to obtain IR imagery of the plume. The SF_6 plume images are

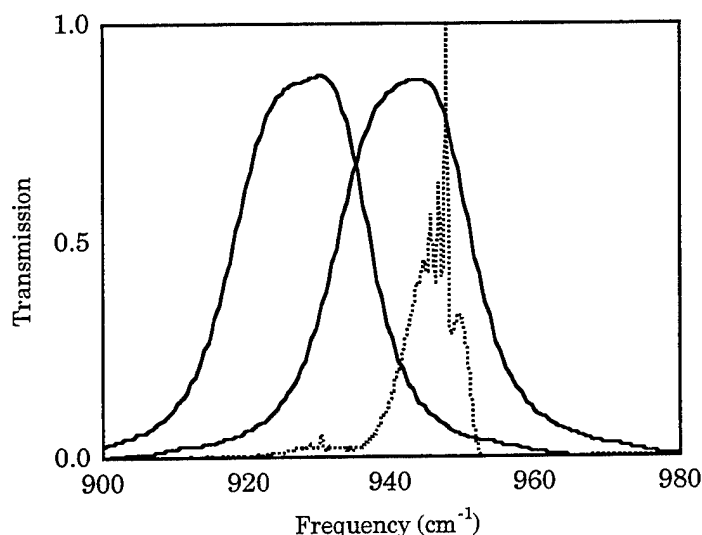


Fig. 3 Transmission curves for the on-band and off-band SF_6 filters. Shown as a dotted line is SF_6 spectrum.

obtained from the IR camera. On-band and off-band integrated radiance was determined for several down plume distances. Contained in Fig. 4 are the on-band/off-band radiance changes for a mid latitude summer SF_6 blimp release. We see that ΔL drops below $1 \mu\text{W cm}^{-2} \text{ sr}^{-1}$ for an observation point about 2 km down the plume from the release point. Noise-equivalent-radiance (NER) figures for an Inframetrics 522 infrared camera approach this figure for 3 second integration times. Hence for integration times of this magnitude we may track the SF_6 plume out to nearly 2 km. Since the NER function depends

upon $t^{-1/2}$, in principle, longer integration times would permit tracking of the

plume out to longer distances. We will use an Agema THV900 LW/ST camera, which exhibits least a factor of two smaller NER per frame for the same spatial resolution as the Inframetrics camera. Because of its fully digital nature and large dynamic range, NER improvement is effective to at least 30 seconds. Thus, longer tracking distances are possible using this camera.

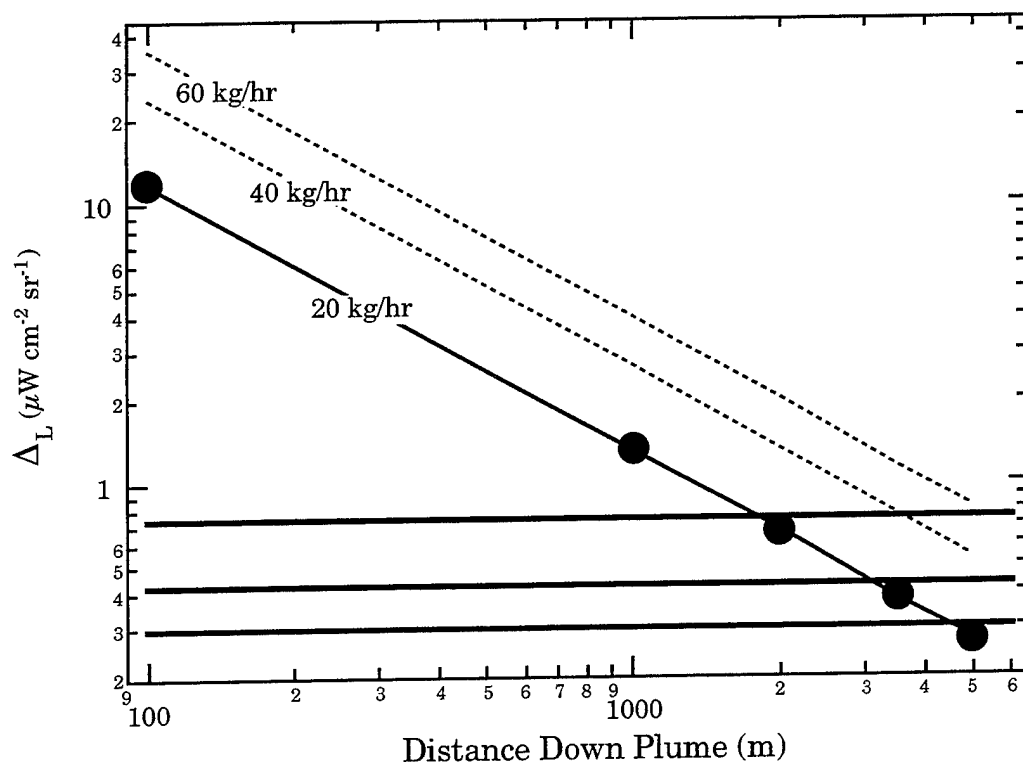


Fig. 4 On-band and off-band radiance plotted as a function of down wind distance. Three SF_6 release rates are shown. The three horizontal lines are the noise-equivalent-radiance for the Agema IR camera for 1, 5, and 10 sec integration times.

Trace Constituent Spectra from CIRRIS-1A Measurements and Concentration Profiles Retrieval

D. K. Zhou, G. E. Bingham, and A. J. Steed
Space Dynamics Laboratory, Utah State University
Logan, UT 84341

G. P. Anderson and R. M. Nadile
Geophysics Directorate, Phillips Laboratory
Hanscom Air Force Base, MA 01731

Abstract. During the STS-39 flight of April 28 - May 6, 1991, the Cryogenic Infrared Radiance Instrumentation for Shuttle (CIRRIS-1A) measured spectral and spatial ("Earthlimb scan") distributions of the atmospheric infrared (IR) emissions by using a Michelson interferometer. Trace constituent emissions were collected, and the spectra were analyzed to confirm the contributors of the infrared radiations. The computed spectra from AFGL FASCOD3 were used in comparison with observed spectra to identify the minor contributors to the emissions in this region. The preliminary vertical volume mixing ratio profiles of these trace gases (e.g., N_2O_5 , N_2O , $ClONO_2$, CH_4 , NO_2 , and H_2O) were retrieved by an onion-peeling routine using FASCOD3 as a forward model along with the NMC temperature and pressure profiles. The volume mixing ratio profiles were compared with other measurements.

1. Introduction

- i) CIRRIS-1A: The Cryogenic Infrared Radiance Instrumentation for Shuttle aboard STS-39 flown on April 28 - May 6, 1991. CIRRIS-1A payload includes a interferometer, a radiometer, photometers, low light video cameras, and a celestial aspect sensor.
- ii) CIRRIS-1A Earthlimb observations were successfully performed. A cryogenic Michelson interferometer in the CIRRIS-1A payload yielded high quality atmospheric IR spectra (moderate resolution 1.0 cm^{-1}) in the earthlimb observing mode. The measurements with stair-step attitude provide the "spatial" distributions of the atmospheric emissions, which made VMR retrieval possible (Tables 1 and 2).
- iii) Many atmospheric trace constituents have been identified by their infrared transitions (Figure 1). FASCOD3 has been used to compare the modelled and measured spectra, to analyze the overlapped spectra, and to identify their contributions in the spectral radiance.
- iv) An onion-peeling routine using FASCOD3 as a forward model has been setup to analyze

and retrieve greenhouse gaseous VMR by using an NLLS fitting algorithm. The HITRAN92 database is used. The VMR profiles are retrieved and compared with previous measurements.

2. Spectral Analysis

- i) The typical transitions of the species are verified through the retrieval tangent heights (scan by scan) using their cross sections from theoretically studied transitions and laboratory measurements.
- ii) The measured normalized spectra from different tangent heights are compared to identify the spectral radiance contribution removing one of the overlapped spectra (Figure 2).
- iii) FASCOD3 modelled spectra with and without a certain specie are used to identify the radiance contribution at a tangent height and verify the band overlapping region (Figures 3).
- iv) The spectral retrieval regions for atmospheric gases and their retrieval tangent heights are determined. The order of gaseous VMR retrievals is important to the VMRs uncertainties, which is decided through their overlapped spectra analysis (Figure 1).

3. Retrieval Algorithm

- i) FASCOD3 is used as a forward model with The HITRAN92 database (include: CFCs, N_2O_5 , ClONO_2 , etc.). The onion-peeling layer boundaries are setup according to measured spatial resolution.
- ii) Auxiliary data preparation: use CO_2 Q-branch at 791.5 cm^{-1} to analyze the altitude-temperature profiles and compare with NMC data. NMC altitude-pressure profiles are used. Aerosol extinctions are modified by using CO_2 laser band at 930 cm^{-1} and LOWTRAN "stratospheric background" model.
- iii) The climatological mid-latitude summer atmosphere profiles are used for initial setup for southern hemisphere measurements ($30^\circ\text{ S} \leq \text{Lat} \leq 42^\circ\text{ S}$). The gaseous VMRs retrieval order in the $800\text{--}1100\text{ cm}^{-1}$ region is O_3 , HNO_3 , CFC-11, and CFC-12; in the $1200\text{--}1400\text{ cm}^{-1}$ region it is CH_4 , N_2O_5 , N_2O , and ClONO_2 ; in the $1400\text{--}1700\text{ cm}^{-1}$ region it is H_2O , NO_2 . The VMRs retrievals are repeated to reduce the uncertainties.
- iv) The CIRRI-1A and FASCOD3 spectra are compared. The NLLS fitting algorithm is applied and a relatively broad wavenumber region is used for each atmospheric specie to minimize the VMR retrieval error for each data point.

4. Results and Comparison

- i) The spectra radiance-fit-comparison is made over a relatively large wavenumber region; the modelled spectra are calculated using the retrieved VMRs. The agreement between measured and model-fit spectra is remarkable in a large spectral region despite some discrepancies in small portions of the spectra (Figure 4).

- ii) The VMR profiles of O_3 , HNO_3 , CFC-11, and CFC-12 from IFR filter 7 ($770-1250\text{ cm}^{-1}$) were presented last year; the results from other IFR filters show the agreement.
- iii) The VMR profiles of CH_4 , N_2O_5 , N_2O , $ClONO_2$, H_2O , and NO_2 are preliminarily retrieved from the IFR filter 3 ($770-2400\text{ cm}^{-1}$) during the mid-night measurements (Figures 5).
- iv) All of these VMRs are compared with previous measurements which are indicated in their plots. These VMR distributions are in reasonable accord with other measurements considering the different measurement conditions (time, location, etc.).

5. Conclusions

- i) CIRRIS-1A low Earthlimb measurements ($TH < 60\text{ km}$) from the southern hemisphere are evaluated; the IFR spectra data have high quality in the broad IFR filter regions.
- ii) The spectral and spatial distributions of prominent greenhouse gases (CO_2 , CFC-11, HNO_3 , CFC-12, O_3 , N_2O_5 , N_2O , $ClONO_2$, CH_4 , NO_2 , H_2O) are successfully collected by the CIRRIS-1A interferometer.
- iii) FASCOD3 with HITRAN92 database has yielded high quality synthetic spectra to allow us to make spectral analysis and retrieve the VMRs in the onion-peeling routine.
- iv) The retrieved VMRs of these gases are compared with other measurements; the agreements of all of these gases yield the conclusion that modelled synthetic spectra are sufficiently accurate, and the measured data are sufficiently noise free to allow accurate retrieval of gases with weekly absorption spectra in the presence of other complex emitters.

6. Future Work

- i) In future work, the VMRs from northern hemispheric measurements will be retrieved and the comparisons between northern (daytime) and southern (nighttime) data sets are critical. Also, detailed comparisons with previous measurements and UARS data will be performed.
- ii) The retrieved VMRs may be input into an LLNL chemical-radiative-transport model; the CIRRIS-1A measurements and the 2-D model may be combined to produce the southern mid-latitude and northern polar region VMR distributions for these gases. The relationship between these gases will improve our understanding of atmospheric chemistry.

TABLE 1. CIRIS-1A Observations in the Stair-Step Attitude [THs < 60 km; σ < 2000 cm⁻¹]

Location #	IFR Filter # (region)	Latitude, Longitude	Local Time
1	5 (770-910 cm ⁻¹)	68 N, 115 E	8.9 hr (4/29/91)
2	5	67 N, 10 E	8.5 hr (4/29/91)
3	7 (770-1250 cm ⁻¹)	64 N, 179 E	13.2 hr (4/29/91)
4	3 (770-2400 cm ⁻¹)	64 N, 162 E	13.6 hr (4/29/91)
5	0 (open)	63 N, 70 E	7.3 hr (4/29/91)
6	3	62 N, 90 E	7.2 hr (4/29/91)
7	3	55 N, 162 W	14.5 hr (4/29/91)
8	0	54 N, 179 E	14.8 hr (4/29/91)
9	3	30 S, 12 W	1.4 hr (4/29/91)
10	7	30 S, 9 E	1.2 hr (4/29/91)
11	0	35 S, 6 W	0.1 hr (4/30/91)
12	5	40 S, 17 W	23.4 hr (4/29/91)
13	5	41 S, 137 E	22.8 hr (4/29/91)
14	3	42 S, 32 W	22.4 hr (4/29/91)
15	0	42 S, 48 W	22.8 hr (4/29/91)

TABLE 2. CIRIS-1A Stair-Step Attitude Measured Species in the Spectral and Spatial (Low Earthlimb) Region

Species	Spatial Region (km)	Spectral Regions (cm ⁻¹)	Measured Location #
CO ₂	10-60 ⁺	770-825, 930-970 [†]	1-15
CFC-11	10-25	830-860	1-15
HNO ₃	10-45	850-920	1-15
CFC-12	10-35	910-940, 1130-1170	3-11, 14, 15
O ₃	10-60 ⁺	970-1150	3-11, 14, 15
N ₂ O ₅	10-50	1220-1260	4, 6, 7, 9, 14
N ₂ O	10-50	1050-1150, 1250-1320 [*]	4, 6, 7, 9, 14
CLONO ₂	10-40	1280-1300	4, 6, 7, 9, 14
CH ₄	10-60 ⁺	1200-1400	4, 6, 7, 9, 14
H ₂ O	10-60 ⁺	1400-1750	4, 6, 7, 9, 14
NO ₂	10-60	1570-1650	4, 6, 7, 9, 14

⁺higher than 60 km.[†]not measured in filter 5.^{*}not measured in filter 7.

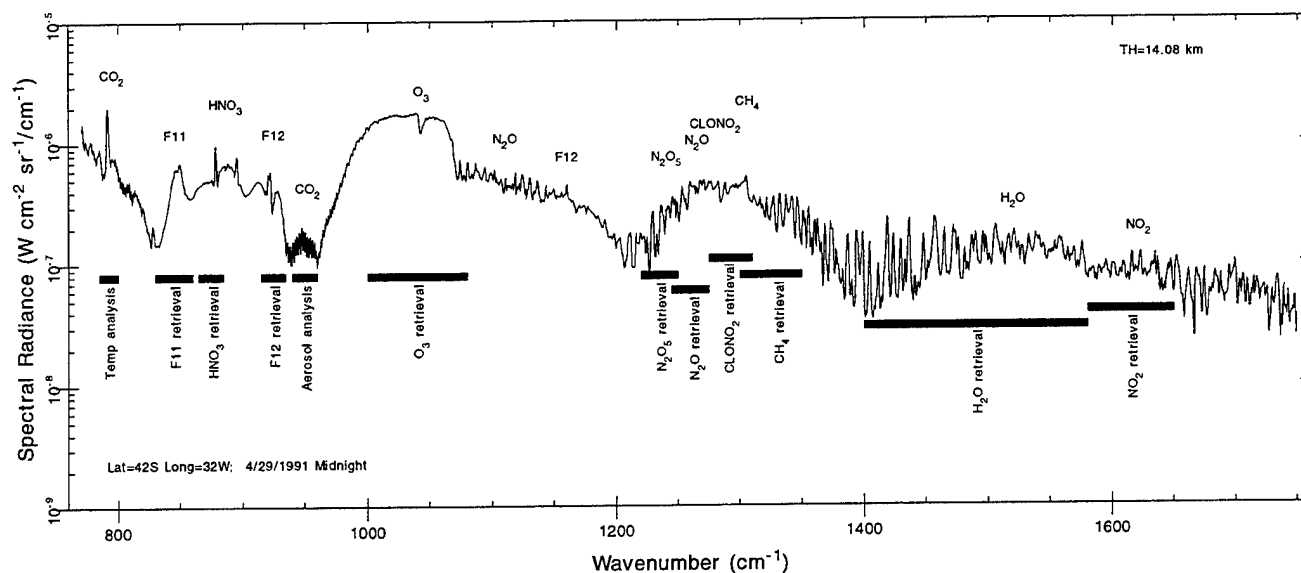


Figure 1. CIRRIIS-1A IFR filter 3 spectral data and retrieval regions.

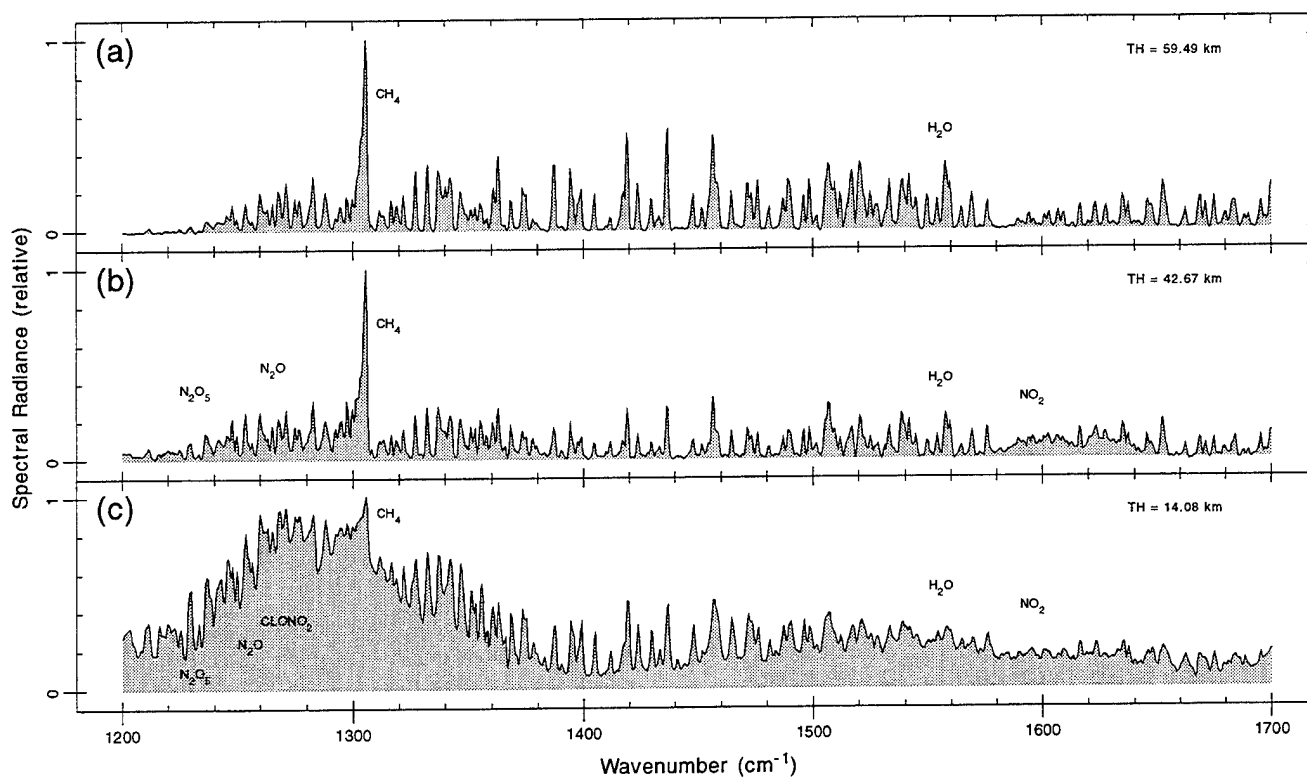


Figure 2. CIRRIIS-1A IFR spectral data at different THs.

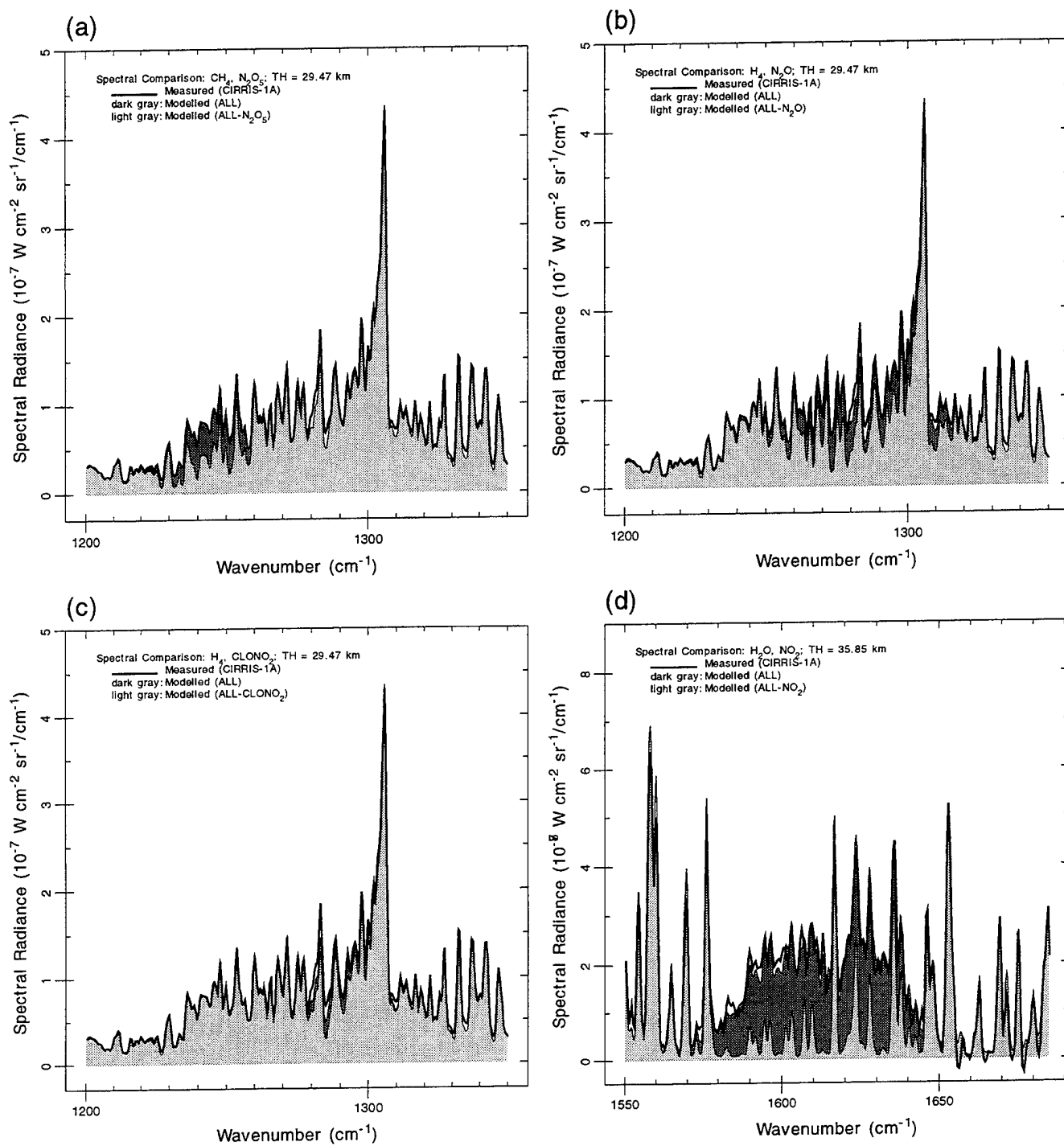


Figure 3. CIRRIS-FASCOD3 spectral comparisons.

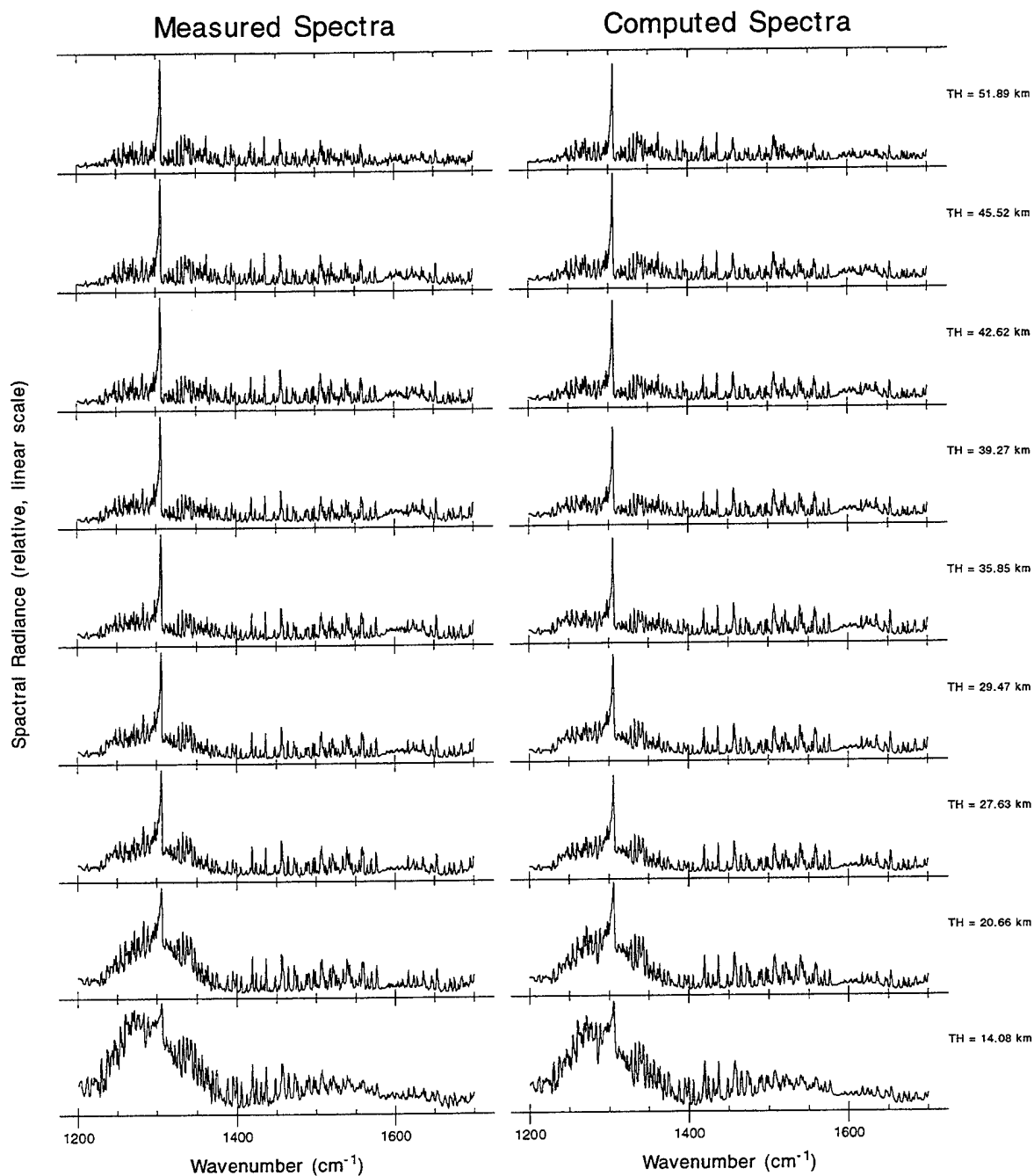


Figure 4. Comparisons for 42S 32W, 22.4HR 4/29/91 measurements.

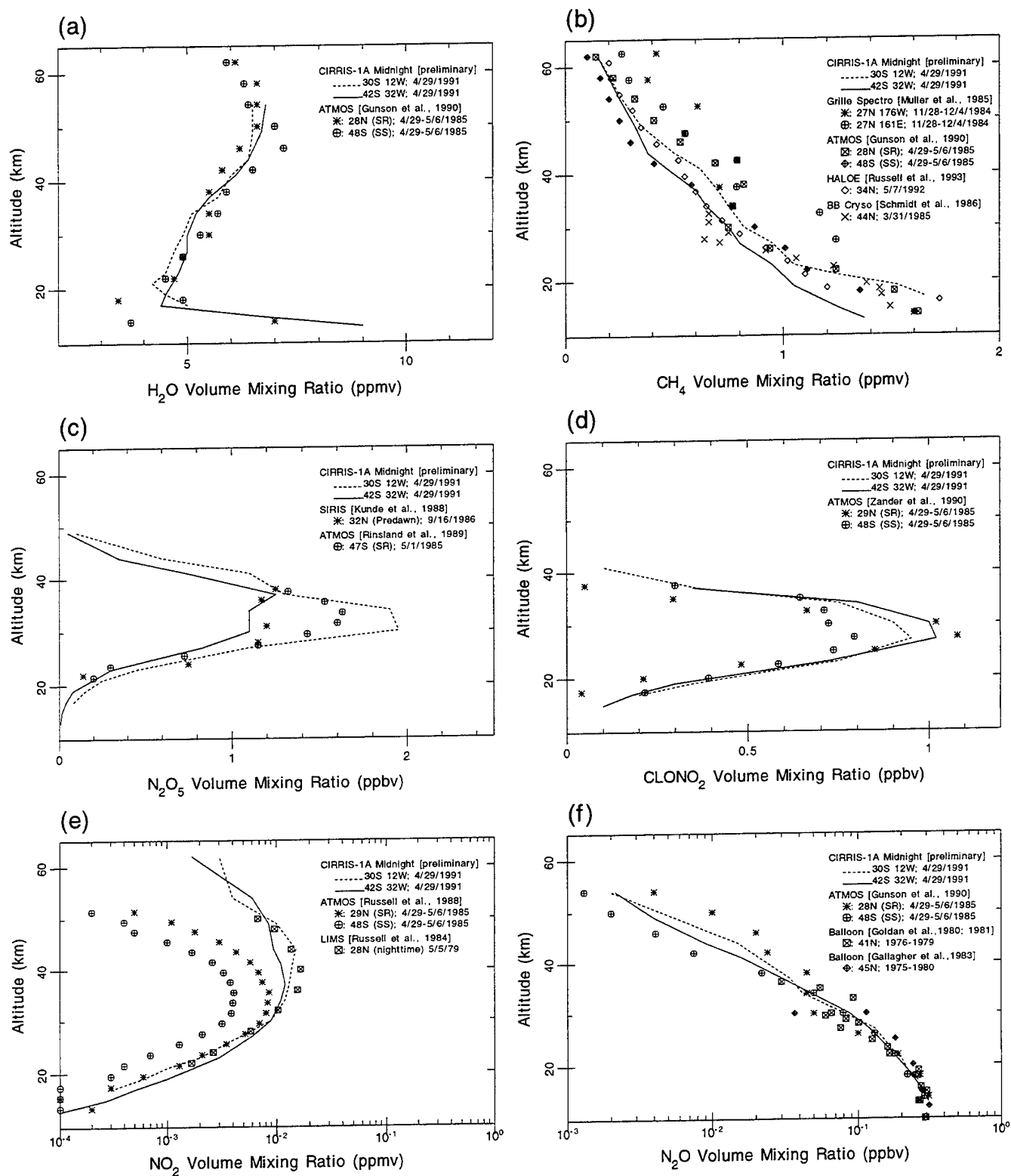


Figure 5. CIRRIS-1A vertical VMR profiles and comparisons.

CIRRIS-1A Earthlimb spectral measurements, calibration, and atmospheric O_3 , HNO_3 , CFC-12, CFC-11 profile retrieval

G. E. Bingham, D. K. Zhou, and A. J. Steed
Space Dynamics Laboratory, Utah State University, Logan, Utah

G. P. Anderson, D. R. Smith, J. H. Chetwynd, and R. M. Nadile
Geophysics Directorate, Phillips Laboratory, Hanscom Air Force Base, Massachusetts

1. Introduction

Concerns of stratospheric ozone depletion and the consequent increase in the amount of ultraviolet radiation reaching Earth's surface have resulted in extensive efforts to understand the use of the halogenated source gases such as chlorine (CFCs) and the odd nitrogen chemical family gases, etc. Scientists have postulated that three chemical families (NO_x , ClO_x , and HO_x) are important potential contributors to the ozone destruction through catalytic reactions [Farmer *et al.*, 1987; Rinsland *et al.*, 1991]. The infrared (IR) measurements of relevant atmospheric gases in the 7-13 μm spectral band provide information on the distribution of atmospheric trace gases which illuminate the mechanisms of chemically coupled trace concentrations and ozone depletion. Many experiments have been developed to measure IR emissions from atmospheric trace gases (e.g., LIMS [Gille *et al.*, 1984], ATMOS [Farmer *et al.*, 1987], UARS [Reber *et al.*, 1993; Roche *et al.*, 1993], etc.). The balloon-borne measurements, MIPAS (7-32 km) were reported by Von Clarmann *et al.* [1993a, 1993b]; they also presented an atmospheric gas retrieval algorithm using the Fast Atmospheric Signature Code-2 (FASCOD2) as a forward model.

Cryogenic Infrared Radiance Instrumentation for Shuttle (CIRRIS-1A) is a recent experiment measuring the atmospheric IR radiant emissions from the Discovery space shuttle (STS-39). The CIRRIS-1A experiment yielded high quality spectral and spatial atmospheric infrared measurements as part of the mission objective to collect trace gas IR emission spectra in the stratosphere and troposphere. These spectra show the lower Earthlimb radiance emitted from CO_2 , CFC-11, HNO_3 , CFC-12, O_3 , N_2O , NO_2 , N_2O_5 , CH_4 , $ClONO_2$, H_2O , etc. In this communication, the data processing method is reported along with calibration and CIRRIS-1A

interferometer spectral data ($\sim 1.0 \text{ cm}^{-1}$ resolution) in the 7-13 μm IR region. The lower Earthlimb spectra are analyzed to identify the transitions from trace gases. Vertical concentration profile retrievals of O_3 , HNO_3 , CFC-12, and CFC-11 are emphasized. Mixing ratio profiles of these gases in the 10-55 km altitude range are retrieved using an onion-peeling routine [Russell and Drayson, 1972; Niple *et al.*, 1980; Gordley and Russell, 1981] which uses FASCOD3 [Clough *et al.*, 1992; Clough *et al.*, 1989a; 1989b] with the HITRAN92 database [Rothman *et al.*, 1987; 1992] as a forward model. An example of the results of this retrieval are shown in the volume mixing ratio (VMR) profiles of O_3 , HNO_3 , CFC-12, and CFC-11 collected near 30° S latitude 9° E longitude during nighttime on April 29, 1991. Errors in the VMR profile measured by CIRRI-1A and this retrieval method are analyzed.

2. Sensor Description, Calibration, and Data Processing

2.1. Sensor Description

The CIRRI-1A experiment features a moderate spectral resolution ($\sim 1.0 \text{ cm}^{-1}$) Michelson interferometer and a high-spatial resolution radiometer which share the collection optics of a cryogenically cooled ($\sim 12 \text{ K}$) telescope complex. The CIRRI-1A instrument is designed to make spectral measurements in the 400-4000 cm^{-1} region and spatial measurements in 10-270 km altitude region of the atmosphere. A detailed description of the CIRRI-1A experiment has been reported by Bartschi *et al.* [1992] and Ahmadjian *et al.* [1990]. The observation and instrument parameters for the pertinent spectral data are listed in Table 1. Most of the CIRRI-1A data measurements were taken in a limb viewing geometry with the shuttle in a gravity gradient orientation traveling belly-to-ram. Figure 1 is a drawing of the CIRRI-1A in measurement

position with the shuttle in gravity gradient mode showing the scan capabilities of the gimbaled sensor; five interferometer detectors are also shown with relative footprint sizes.

The Michelson interferometer has a flex pivot design with three selectable scan lengths that provide spectral resolutions of 1, 4, and 8 cm^{-1} with moving mirror scan times of 9.7, 2.7, and 1.5 sec, respectively. The interferometer focal plane array is an impurity band conduction type arsenic-doped silicon (Si:As) array (FP3) with five various-sized detector elements to allow a wide range of measurement scenarios and resolutions. The focal plane optics are Ritchey-Chretien $f/1.6$. An 8-element filter wheel is used to reduce photon noise in selected bandpasses by minimizing out-of-band radiation. The CIRRIS-1A radiometer contains two focal plane arrays (FPA) whose images are overlapped by the use of a dichroic beamsplitter. The focal plane arrays include a 9-element arsenic-doped silicon (Si:As) array (FP1) and a 5-element bismuth-doped silicon (Si:Bi) array (FP2). These arrays are co-aligned with the interferometer focal plane. The 9-element FPA is located behind an 8-element filter wheel, and the 5-element FPA is housed behind a $2.95\text{ }\mu\text{m}$ fixed filter. The $2.95\text{ }\mu\text{m}$ fixed filter acts as a constant reference channel for comparison with the eight selectable bandpass filters. A combination of detector size, bias levels, and signal conditioning electronics makes the radiometer sensitive over a wide dynamic range; it is capable of measuring celestial star radiations, zodiacal light, Earthlimb emissions, hard-Earth emissions, etc.

The CIRRIS-1A sensor was mounted in a 2-axis gimbaled pointing system that allowed a wide range of Earthlimb measurements to be made. A celestial aspect sensor recorded the star field 45° above the IR line of sight (LOS) to provide high resolution pointing information while CIRRIS-1A collected Earthlimb data. The output of an analog horizon sensor which detected

a CO₂ layer emission source (~40 km) was used to provide real-time-pointing-input during the measurements, allowing the astronauts to maintain a constant pitch angle with respect to the horizon during scan sequences. All of the CIRRIS-1A sensors functioned well during the mission. Nearly 20 hours of prime data were collected and recorded on the flight tape recorders in many different measurement modes.

2.2. Calibration

The CIRRIS-1A sensor underwent an engineering evaluation before flight and a full calibration after the mission. The infrared calibration was conducted using a multifunction infrared calibration source (MIC2) designed by the Space Dynamics Laboratory of Utah State University. MIC2 contains extended, Jones, scatter, and point source functions within a single vacuum shell. Both radiometer and interferometer raw data were calibrated for separate radiometric parameters (e.g., absolute responsivity, spectral responsivity, spatial responsivity, and temporal responsivity, etc.). The calibration results for CIRRIS-1A sensors were reported [Space Dynamics Laboratory, 1995]. The measured spectra were calibrated to absolute radiance by using the following equation which includes the changes in sensitivity resulting in charges in the detector bias voltage, detector number, and filter position,

$$\phi_m = \frac{1}{R_a} \frac{1}{R_r} F[L(Resp)] \pm \sigma(n), \quad (1)$$

where:

ϕ_m = measured spectral radiance (W cm⁻² sr⁻¹ cm)

R_a = absolute responsivity (volts cm/W cm⁻² sr⁻¹ cm)

- R_r = relative spectral response as a function of wavenumber (unitless)
- F = Fourier transform operation results as a function of wavenumber (volt cm)
- L = linearity correction function (unitless)
- Resp = interferometer response as a function of interferometer slide position (volt)
- $\sigma(n)$ = measurement uncertainty.

The CIRIS-1A interferometer calibration equation (1) correlates the interferometers's response with incident spectral radiance. Specific calibration information can be found in the CIRIS-1A calibration report [*Space Dynamics Laboratory*, 1995]. The report includes information on the point source response function, which determined the effective field-of-view solid angle of each detector and its spatial line of sight. The report also detail the responses of the ancillary sensors that supported the main infrared instruments. Three terms (R_r , R_e and L) provide the relationship between the measured interferogram and the incident spectral flux. Each of these response terms in (1) were determined individually. The relative spectral response (R_r), adjusts each point in the transformed spectra for the variation in radiant sensitivity of the interferometer system as a function of wavelength. The R_r functions for each detector and filter were developed using the calibrator in the scatter and point source modes with external, and NIST (National Institute of Standards) traceable black body sources at 600° K and 1300° K. Since R_r is a series of coefficients that multiply each spectral radiance value, noise in the R_r curve adds directly to the noise in the spectrum, and R_r functions were determined by co-adding 60 to 70 interferograms. At high radiance levels, the interferometer detector bias voltages were reduced to provide additional dynamic range. While increasing the range by a factor of three, this also increased the nonlinearity of the system. A non-linearity correction was developed by

measuring the system AC-DC response of the interferometer which could be applied to the interferogram.

Application of R_r and L to the spectrum provides a peak normalized, relatively calibrated transform, which must then be adjusted to provide an absolutely calibrated spectral radiance. R_a is a single coefficient that is applied to the peak spectral response to provide the absolute calibration. R_a was measured using an extended area black body source located inside the calibrator. The temperature of this source, which covered the whole entrance aperture of the sensor, was measured using NIST traceable platinum resistance thermometers. To develop the R_a curve, the extended area source temperature was varied in about 5° K steps between 30° K and 300° K. Actual R_a values were linearly interpolated between the calibration values based on corrected interferogram DC values.

The spectral radiance uncertainty of each point in the spectral radiance curve [$\sigma(n)$] is a combination of dark and photon noise associated with the source being observed during the scan in question. Hence, $\sigma(n)$ varies with interferogram corrected DC level, filter, wavenumber, and scene. The signal to noise ratio (SNR) in the flight interferograms varies from less than 1 to about 1000. For CIRRIS-1A, $\sigma(n)$ is adequately described as a white function (applying to all frequencies within a transform band) which for detector 1 has a minimum in the region around 800 cm⁻¹ at a level of 1.3×10^{-12} (W cm⁻² sr⁻¹/cm⁻¹). Photon noise increases $\sigma(n)$ as the square root of the scene integrated spectral radiance.

One unusual feature of the CIRRIS-1A sensor is the presence of both a co-aligned precision radiometer and interferometer with detector sizes of similar magnitude. The radiometer and interferometer were calibrated separately, but using the same equipment. The

radiometer calibration was verified with measurements against two well known IR emitting stars. The output of these stars was not sufficient to allow high signal to noise measurements with the interferometer. The interferometer calibration can, however, be compared with the radiometer while the two instruments make vertical scans from the hard earth to the top of the atmosphere. A typical, vertical-profile comparing the radiometer determined radiance with the radiance calculated from integrating the interferometer spectral radiance curves is shown in Figure 2. This $855\text{--}1250\text{ cm}^{-1}$ region shows a near perfect correlation between the two instruments from the noise level down to about a 50 km tangent height, where the interferometer switched to the low bias mode. Below this level, the two profiles deviate by about 10%. The interferometer linearity correction brings these two profiles back together.

2.3. Data Processing

The CIRRIS-1A data presented in this paper were collected as vertical profiles which look like stair steps, with interferometer scans occurring in the horizontal portions of the stair step. Each long scan took 9.7 seconds, during which the gimbal system was held steady with respect to the atmospheric CO_2 radiance by the horizon sensor. Interferograms from each stair step were quality controlled and processed to spectral radiance using the interferometer processing routines of Optical Physics User System (OPUS) version 3.41XX, which contains the calibration coefficients described above. OPUS is a user friendly, workstation based software package which provides standard processing techniques for all of the CIRRIS-1A data. It was developed for the Optical Physics Branch of the Geophysical Directorate of the US Air Force Phillips Laboratory by the Space Data Analysis Laboratory of Boston College. Calibrated spectral radiance curves taken from OPUS were used as inputs to the retrieval process.

3. Measurements and Analysis

The wealth of greenhouse gas information available in a CIRRIS-1A typical spectrum is shown in the 780-1750 cm^{-1} region (Figure 3). This spectrum was measured at a tangent height of 14.08 km, a latitude of 41.98° S, a longitude of 31.93° W, and a local time of 22.34 hours on April 29, 1991. The infrared emissions from CFC-11, CFC-12, and HNO_3 are large enough to be identified in the window between the CO_2 15 μm band and the O_3 9.5 μm band. Other molecules, such as CH_4 , H_2O , N_2O , N_2O_5 , ClONO_2 , NO_2 , etc., are also identified by their IR transitions in the wavenumber region shown in Figure 3.

Figure 4 shows a three-dimensional spectral and spatial surface contour plot showing a vertical profile of CIRRIS-1A spectra, scan by scan, as measured from a tangent height of 10 km to 55 km. These spectral measurements were taken in a stair-step mode in the southern hemisphere near 30° S latitude, 9° E longitude during the nighttime of April 29, 1991. The emission bands of CFC-11, HNO_3 , and CFC-12 are readily identified and are clearly evident in the limb spectra corresponding to lower tangent heights but fade into the radiant emissions from other atmospheric molecules and sensor noise at higher altitudes. The difference in emission bands of optically thin CFC-11, HNO_3 , and CFC-12 when compared with the optically thick O_3 is apparent. Strong O_3 emission is still measurable above the stratosphere region, while HNO_3 is evident at tangent heights below ~45 km. CFC-12 appears below ~35 km and CFC-11 below ~25 km. The ozone profile in the region below 30 km shows some structure which is apparent where radiance briefly drops at a tangent height of about 23 km.

In the region between 830 and 940 cm^{-1} , the spectra of CFC-11, HNO_3 , and CFC-12 are overlapping. The quality of the data can be demonstrated by two scans from location 42° S, 32°

W at tangent heights of 14.08 km and 29.47 km which were subtracted to separate HNO_3 from the CFC bands as shown in Figure 5. Since the CIRRI-1A resolution is not high enough to identify the weak spectral emission lines, only strong emission features can be recognized. The HNO_3 ν_5 band Q branch at 879 cm^{-1} and the HNO_3 $2\nu_9$ band Q branch at 896 cm^{-1} are identified in the CIRRI-1A spectra. Figure 5 also shows that the ν_5 band Q branch is stronger and sharper than the Q branch of the $2\nu_9$ band. At the tangent height of 30 km, CFC-12 emissions are very small compared to HNO_3 emissions. The spectral peak at 885.5 cm^{-1} is recognized as the R branch sub-band of HNO_3 ν_5 as shown in Figure 5(b). This is in accordance with the laboratory spectra [Murcray and Goldman, 1981] and theoretical calculations of the HITRAN92 database [Rothman et al., 1987; 1992]. CFC-12 emissions become larger at lower tangent heights, and HNO_3 and CFC-12 overlap. In CIRRI-1A spectra, the CFC-11 ν_4 band appears at 847 cm^{-1} and the CFC-12 ν_6 band and ν_8 band Q branch appear at 922 cm^{-1} and 1161 cm^{-1} , respectively, as shown in Figure 3. The ability of CIRRI-1A spectra to clearly identify the CFC-12 ν_8 band in the 1161 cm^{-1} region is shown using two scans measured at tangent heights of 14.08 km and 20.66 km [see Figure 6(a) and Figure 6(b), respectively]. Differencing these two tangent heights removes the major effects of the large wavenumber wing of the ozone 1040 cm^{-1} band. The difference, shown in Figure 6(c), provides a clear CFC-12 ν_8 band spectrum in the 1161 cm^{-1} region. The principal overlapped molecules in this spectral region are O_3 , N_2O , CFC-12, and with other molecules, such as CFC-11, CFC-13, etc., making minor contributions at lower tangent heights [Murcray and Goldman, 1981]. The strong emission feature at 1161 cm^{-1} clearly belongs to the CFC-12 ν_8 Q branch. The N_2O emission spectrum is also identified in Figure 6(c) in the $1050\text{--}1150\text{ cm}^{-1}$ region.

4. Retrieval Algorithm

The onion-peeling algorithm runs layer by layer (from high to low) and compares a synthetic line-by-line spectrum (reduced to moderate resolution) with the CIRRIS-1A measured spectrum in order to find the fit radiance by the inversion scheme of nonlinear least squares fitting (NLLS) described by *Niple et al.* [1980]. This onion-peeling algorithm was set up using FASCOD3 to provide the synthetic comparison spectrum. In this application, FASCOD3 used the HITRAN92 database [*Rothman et al.*, 1987; 1992] to provide spectroscopic data including the trace gases such as the chlorofluorocarbons (CFCs), nitrogen pentoxide (N_2O_5), chlorine nitrate (ClONO_2), etc. This retrieval technique is similar to that used for the balloon-borne MIPAS limb emission measurements (high spectral resolution) using FASCOD2 [*Von Clarmann et al.*, 1993a; 1993b]. The trace gas vertical density distribution is strongly dependent on the temperature, pressure, and aerosol emission profile. Prior to concentration profile retrieval, the temperature and background continuum emission (e.g., aerosol) profiles are needed. In the routine used in these retrievals, the forward spectral calculations were reduced to a one-parameter problem by using selected spectral segments in order to analyze temperature, and retrieve aerosol and trace gases sequentially.

The CIRRIS-1A experiment did not carry ancillary sensors designed to provide the temperature, pressure and aerosol measurements necessary to retrieve the trace gas volume mixing ratios directly from the infrared data. An iterative process using the NMC stratospheric model data and the CO_2 emission regions of the IR were used in combination to derive these data [*Stiller et al.*, 1995]. The FASCOD3 was initially set up using the climatological mid-latitude

summer atmosphere profiles reported by *Anderson et al.* [1986]. At each measurement location, the NMC temperature and pressure data were used with a climatological aerosol profile to derive an initial O₃ profile. This trial O₃ profile was then used with climatological CFC-11, CFC-12, HNO₃, and other atmospheric gases VMRs to model the CO₂ emissions in the 785-800 cm⁻¹ and 940-960 cm⁻¹ spectral regions. Assuming the CO₂ VMR to be constant at 355 ppmv, the initial temperature and aerosol concentrations were adjusted to produce the best possible fit between the FASCOD3 and CIRRIS-1A data in the 790 and 950 cm⁻¹ regions respectively. An example of this fit in the 950 cm⁻¹ region is shown in Figure 7 for a measurement taken at 17.93 km. The NMC temperature and pressure profiles that were used in the retrieval of the VMR profiles in this paper are shown in Figures 8(a) and 8(b). Data points are shown at the onion-peeling layer boundaries. Pressure levels were not adjusted in the CIRRIS-1A retrievals, and observed variations in temperature did not exceed the NMC estimated error bars. Figure 8(c) shows the extracted aerosol extinction coefficient, using various subregions of the CO₂ band. The "stratospheric background" is used to select the profile type for the stratospheric aerosols in the model [*Berk et al.*, 1989]. The optical parameter databases for the model are Air Force Geophysics Laboratory (former Air Force Phillips Laboratory) supported and based on a current assessment of climatological study. Extinction is shown at 0.55 μm, because it was taken directly from the FASCOD3 model input. For comparison, a profile from the FASCOD3 climatology is also shown. The comparisons with OZAFS (50° S; September 1985) [*Elansky et al.*, 1991] and MIPAS (44° N; January/March 1991) [*Von Clarmann et al.*, 1993a] are shown in Figure 8(c) and it is noticed that the measurements were taken at different times and locations.

The greenhouse gas concentration profile retrievals were performed using the spectral

regions for individual gases shown in Figure 3, and using the corrected auxiliary data (temperature, pressure, aerosol extinction) plotted in Figure 8. First, the ozone profile was retrieved using several ν_3 sub-band spectral regions within the 1000-1100 cm^{-1} region. For HNO_3 , the ν_5 P and ν_5 Q branch regions (860-885 cm^{-1}) were used. CFC-11 and CFC-12 retrieval regions are 830-860 cm^{-1} and 915-935 cm^{-1} , respectively. Several segments of these regions were used instead of the complete region in order to reduce computation time. The impact of interfering gases was taken into account using modelled IR emissions for each gas density. Finally, the radiance-fit-comparison was made over a relatively large wavenumber region (shown in Figure 9) and the VMR of the layer was adjusted to minimize the calculated VMR error. Figure 9 shows examples of the fit between measured and modeled spectra data and the residual for these gases at the same spectral resolution. The spectral fit for O_3 , HNO_3 , and CFC-12 is congruous, but CFC-11 has a relatively poor fit as seen in Figure 9(d). A spectral comparison of the measured spectra and the modelled spectra used in retrieving the mixing ratios of O_3 , HNO_3 , CFC-12, and CFC-11 is shown in Figure 10. The agreement between measured and modelled spectra is remarkable in a relatively large spectral region despite some discrepancies in small portions of the spectra.

5. Error Analysis

The amount of error induced in the VMR by the calibration and retrieval process was estimated using a two step process. First, the expected error of all of the variables in the data reduction train of all of the CIRRIS-1A greenhouse gas measurement data set was examined. Second, the extremes of these data were then plugged into the FASCOD3 forward model and

the VMR adjusted upward or downward to provide the measured radiance level. The VMR errors for this data set have been roughly estimated using the FASCOD3 model to convert the different kinds of uncertainty sources into the VMR errors. The error estimates listed below, and those shown in Figure 8(c) and Figure 11 are these maximum error limits. Because these variables are inserted into the actual retrieval procedure, they include the effect of both measurement and retrieval error. VMR error is induced by measurement noise, calibration error, ancillary variable error, and retrieval error. The error level for VMRs, of course, depends on the molecule and the measured tangent height. This type of error analysis has been described in the MIPAS-B data evaluation and VMRs retrieval [Von Clarmann *et al.*, 1993a; 1993b]. The error analysis on ATMOS data for the same species presented here has been reported [Gunson *et al.*, 1990; Russell *et al.*, 1988; Zander *et al.*, 1987]. Error propagation in the onion-peeling technique can only be roughly estimated for evaluating earthlimb measurements.

Measurement noise and calibration errors have already been discussed. The SNR of the interferogram starts from a noise floor and increases with spectral radiance minus the square root of the total inband radiance. However, the SNR seldom exceeds 1000/1. Because a broad band technique is used, however, all of the spectral data used in the fitting band can be viewed as some what independent samples, reducing measurement noise term by some number approaching the square root of the number of samples. This is not entirely true through the whole chain, however, as uncertainty in the smoothed spectra increases with bandwidth.

The error in the interferometer radiance calibration in the filter and detector combinations used in this work is estimated to be $\pm 5\%$ to $\pm 10\%$. This exceptionally accurate calibration

estimate is based not only on the calibration technique, but on the ability to trace the calibration back to a stellar calibration via the radiometer.

6. Retrieval Results and Comparisons

The VMR profiles of O₃, HNO₃, CFC-12, and CFC-11 retrieved in the fashion described above are given in this section. These profiles were retrieved from the STS-39 Earthlimb measurements near 30° S latitude and 9° E longitude by the CIRRIS-1A interferometer filter 7 (770-1250 cm⁻¹). It is possible to analyze the full band spectrum for a number of interesting species using this interferometer filter at a given tangent height. Using a fit to the whole band reduces the uncertainty of the retrieved VMR. The CIRRIS-1A VMR profiles of the above species are compared with some of the previously measured VMR profiles in Figure 11(a) through Figure 11(d). The CIRRIS-1A results and uncertainties are calculated and tabulated in Table 2.

The profile of ozone plotted in Figure 11(a) shows a mixing ratio peak of 8.2 ppmv at 31 km. This profile is comparable with other measurements for ozone for the time of day, season, and location of the measurement. These differences must be considered when making comparisons to other measurements. The ROCOZ-A data in Figure 11(a) were taken from *Barnes et al.* [1986] results from September 26 and October 27, 1983 at Wallops Island, Virginia. The data of the 4-year (February 1988 - December 1991) LIDAR average for May were taken from 34.4° N, 117.7° W [McDermid, 1993]. The ATMOS data were taken near 28° N and 48° S (April 30 - May 6, 1985) [Gunson et al., 1990]. Since temperature and pressure information above 55 km was unavailable during CIRRIS-1A measurements, the ozone

mixing ratios of the upper layers (above 55 km) are derived using climatology data and have a larger uncertainty than lower altitude data. As a result, there was some difficulty in establishing a continuity in the ozone mixing ratio at 55 km, however, this retrieval uncertainty should not affect the ozone density calculation at tangent heights below 45 km.

The nitric acid profile shows that the mixing ratio increases to a maximum of ~ 5.6 ppbv at an altitude of 24 km, then decreases as the altitude increases. The HNO_3 VMR from CIRRIS-1A is plotted in Figure 11(b) along with the zonal mean LIMS and ATMOS HNO_3 profiles taken at same time of year during 1979 and 1985, respectively [Gille *et al.*, 1984; Russell *et al.*, 1988]. It should be noted that the CIRRIS-1A measurement (30° S, 9° E) was made at a different location than the LIMS and ATMOS data. LIMS measurements show that the HNO_3 vertical column amount (molecule/cm²) increases as the latitude increases [Gille *et al.*, 1984]. The HNO_3 peak altitude of CIRRIS-1A measurement is similar to both LIMS and ATMOS.

Chlorofluorocarbons are found in the troposphere and lower stratosphere region. Once in the stratosphere, they decrease rapidly as altitude increases. The maximum mixing ratio of CFC-11 is around 3.2×10^{-4} ppmv at the lowest measurement altitude (~ 12 km), while the mixing ratio of CFC-12 is around 5.7×10^{-4} ppmv. The mixing ratios for both gases decrease as the altitude increases. The error at lower tangent heights is relatively large since limb emission measurements from CFC-12 and CFC-11 are very sensitive to small tangent height and other auxiliary parameter errors. Measurements by other investigators are presented for comparison. These were taken by MIPAS-B-89 (France, 44° N; May 1989) [Von Clarmann *et al.*, 1993b], ATMOS (30° N, 47° S, 1985) [Zander *et al.*, 1987], and the data of in situ results (northern hemisphere, 1974-1982) [Fabian and Goerner, 1984]. The CFC VMRs are expected to be

increasing with time, which is indicated by those measurements. The CIRRIS-1A measurements in these profiles at ~ 10 km show an increase of about 9.5% per year compared with the ATMOS 1985 data and less than 2.3% per year compared with in situ 1974-1982 mean data. However, these comparisons and increasing rates are suggestive because of the lack of similar measurement conditions. The CIRRIS-1A data are in accordance with MIPAS-B-89 at lower altitudes. A relatively large error bar is associated to the CIRRIS-1A data point collected at 31 km for CFC-12 and 24 km for CFC-11 due to noise in the spectra and the weak CFC emissions found at higher tangent heights.

7. Conclusion

The infrared emissions from several prominent greenhouse gases were successfully measured as part of the STS-39 CIRRIS-1A mission. The use of the FASCOD3 and HITRAN92 spectral data provided a good combination with the calibrated spectra to obtain the vertical distribution of some of these gases. The CIRRIS-1A data set demonstrates the capability of a moderate resolution interferometer to monitor global distributions of the most prominent greenhouse gases in the 7-13 μm window. Since these gases are also active in the ozone reduction cycle, these data are doubly important. In this paper, vertical concentration profiles of O_3 , HNO_3 , CFC-12, CFC-11, and aerosols from one of the CIRRIS-1A measured spectral profiles collected in the southern hemisphere (30° S, 9° E) are shown.

This paper describes the data set, retrieval method and the accuracy of the CIRRIS-1A analysis. It has been shown that the use of the CO_2 laser band at 940 cm^{-1} provides an effective way to estimate aerosol emissions in the region where these emissions offset trace gas retrieval.

A major limitation of the CIRRIS-1A instrument complement, as it was flown, was the specific instrumentation with the lack of capability to measure gas temperature and pressure while simultaneously collecting spectral signatures. One of the larger error sources in the retrieval was associated with the use of temperature and pressure fields from the NMC model. However, fine tuning the NMC values using CO₂ emission at 790 cm⁻¹ greatly reduced this error. The accuracy of the tangent height determinations associated with this type of measurement was found to be extremely critical in the accuracy of the analysis, but was controlled in the CIRRIS-1A measurements, using star field images collected with the infrared data.

Scientifically, the CIRRIS-1A data set fills an important gap in the measurements between the ATMOS and UARS data sets. The CIRRIS-1A data set does not provide a comprehensive global sampling; but it is significant because it was collected only a few weeks before the Pinatubo eruption. The density profiles retrieved from other trace gases and other locations measured by CIRRIS-1A have also been performed and a detailed comparison between CIRRIS-1A profiles and comparisons with other measurements are in preparation.

Acknowledgments. We thank the many members of the CIRRIS-1A team who contributed to the collection, calibration, and preparation of the data presented in this study. This work was performed under contract F19628-81-C-0123 from the Geophysics Directorate of the US Air Force Phillips Laboratory. The CIRRIS-1A experiment was sponsored by the Strategic Defense Initiative Organization and Geophysics Directorate of the US Air Force Phillips Laboratory. The CIRRIS-1A was designed, built, tested, and calibrated by the Space Dynamics Laboratory of Utah State University.

References

- Ahmadjian, M., R. M. Nadile, J. O. Wise, and B. Bartschi, CIRRIS 1A Space Shuttle Experiment, *J. Spacecraft*, 27, 669-674, 1990.
- Anderson, G. P., S. A. Clough, F. X. Kneizys, J. H. Chetwynd, and E. P. Shettle, AFGL atmospheric constituent profiles (0-120 km), *GL-TR-86-0110*, Geophys. Lab., Hanscom AFB, Ma, 1986. ADA175173
- Barnes, R. A., A. C. Holland, and H. S. Lee, An improved rocket ozonesonde (ROCOZ-A) 2. Preparation of stratospheric ozone profiles, *J. Geophys. Res.*, 91, 14,521-14,531, 1986.
- Bartschi, B., A. Steed, J. Blakeley, M. Ahmadjian, J. Griffin, and R. Nadile, Cryogenic infrared radiance instrumentation for shuttle (CIRRIS 1A): Instrumentation and flight performance, *Proc. SPIE*, 1765, 64-74, 1992.
- Berk, A., L. S. Bernstein, and D. C. Robertson, MODTRAN: A moderate resolution model for LOWTRAN 7, *GL-TR-89-0122*, Geophys. Lab., Hanscom AFB, Ma, 1989. ADA214337
- Clough, S. A., F. X. Kneizys, G. P. Anderson, E. P. Shettle, J. H. Chetwynd, L. W. Abreu, L. A. Hall, and R. D. Worsham, FASCOD3: spectral simulation, *Proceedings of the 1988 International Radiation Symposium*, Ed. J. Lenoble and J-F. Geleyn, Deepak Publishing, Hampton, VA, 372-375, 1989a.
- Clough, S. A., R. D. Woreham, W. L. Smith, H. E. Revercomb, R. O. Knuteson, H. W. Woolf, G. P. Anderson, M. L. Hoke, and F. X. Kneizys, Validation of FASCODE calculations with HIS spectral radiance measurements, IRS '88: Current Problem in Atmospheric Radiation, *Proceedings of the 1988 International Radiation Symposium*, Ed. J. Lenoble and J-F. Geleyn, Deepak Publishing, Hampton, VA, 376-379, 1989b.

- Clough, S. A., M. J. Iacono, and J.-L. Moncet, Line-by-line calculations of atmospheric fluxes and cooling rate: application to water vapor, *J. Geophys. Res.*, 97, 15,761-15,785, 1992.
- Elansky, N. F., G. M. Grechko, M. E. Plotkin, and O. V. Postylykov, The ozone and aerosol fine structure experiment: observing the fine structure of ozone and aerosol distribution in the atmosphere from the Salyut 7 Orbiter3. Experimental results, *J. Geophys. Res.*, 96, 18,661-18,670, 1991.
- Fabian, P., and D. Gomer, The vertical distribution of halocarbons in the stratosphere, *Fresenius Z. Anal. Chem.*, 319, 890-897, 1984.
- Farmer, C. B., O. F. Raper, and F. G. O'Callaghan, Final report on the first flight of the ATMOS instrument during the Spacelab 3 mission, April 29 through May 6, 1985, *Jet Propul. Lab. Publ. 87-32*, 1987.
- Gille, J. C., J. M. Russell III, P. L. Bailey, E. E. Remsberg, L. L. Gordley, W. F. J. Evans, H. Fischer, B. W. Gandrud, A. Girard, J. E. Harries, and S. A. Beck, Accuracy and Precision of the Nitric Acid Concentrations Determined by the Limb Infrared Monitor of the Stratosphere Experiment on NIMBUS 7, *J. Geophys. Res.*, 89, 5,179-5,190, 1984.
- Gordley, L. L., and J. M. Russell III, Rapid inversion of limb radiance data using an emissivity growth approximation, *Applied Optics*, 20, 807-813, 1981.
- Gunson, M. R., C. B. Farmer, R. H. Norton, R. Zander, C. P. Rinsland, J. H. Shaw, and B. C. Gao, Measurements of CH₄, N₂O, CO, H₂O, and O₃ in the Middle Atmosphere by the Atmospheric Trace Molecule Spectroscopy Experiment on Spacelab 3, *J. Geophys. Res.*, 95, 13,867-13,882, 1990.
- McDermid, I. S., A 4-year climatology of stratospheric ozone from Lidar measurements at

- Table mountain, 34.4° N, *J. Geophys. Res.*, 98, 10,509-10,515, 1993.
- Murcray, D. G., and A. Goldman, Handbook of high resolution infrared laboratory spectra of atmospheric interest, *CRC Press*, 1981.
- Niple, E., W. G. Mankin, A. Goldman, D. G. Murcray, and F. J. Murcray, Stratospheric NO₂ and H₂O mixing ratio profiles from high resolution infrared solar spectra using nonlinear least squares, *Geophys. Res. Lett.*, 7, 489-492, 1980.
- Reber, C. A., C. E. Trevathan, R. J. McNeal, and M. R. Luther, The upper atmosphere research satellite (UARS) mission, *J. Geophys. Res.*, 98, 10,643-10,647, 1993.
- Rinsland, C. P., R. Zander, and P. Demoulin, Ground-based infrared measurements of HNO₃ total column abundances: long-term trend and variability, *J. Geophys. Res.*, 96, 9,379-9,389, 1991.
- Roche, A. E., J. B. Kumer, J. L. Mergenthaler, G. A. Ely, W. G. Uplinger, J. F. Potter, T. C. James, and L. W. Steritt, The Cryogenic Limb Array Etalon Spectrometer (CLAES) on UARS: experiment description and performance, *J. Geophys. Res.*, 98, 10,763-10,775, 1993.
- Rothman, L. S., et al., The HITRAN database: 1986 Edition, *Applied Optics*, 26, 4,058-4,097, 1987.
- Rothman, L. S., et al., The HITRAN molecular database: Editions of 1991 and 1992, *J. Quant. Spectrosc. Radiat. Transfer*, 48, 469-507, 1992.
- Russell, J. M., III and S. R. Drayson, The inference of atmospheric ozone using satellite horizon measurements in the 1024 cm⁻¹ band, *J. Atmospheric Sciences*, 29, 376-390, 1972.

- Russell, J. M., III, C. B. Farmer, C. P. Rinsland, R. Zander, L. Froidevaux, G. C. Toon, B. Gao, J. Shaw, and M. Gunson, Measurements of odd nitrogen compounds in the stratosphere by the ATMOS experiment on spacelab 3, *J. Geophys. Res.*, 93, 1,718-1,736, 1988.
- Space Dynamics Laboratory, CIRRI 1A post flight calibration final report, *SDL/92-091*, Space Dynamics Laboratory, Utah State University, Logan, Ut, 1995.
- Stiller, G. P., M. R. Gunson, L. L. Lowes, M. C. Abrams, O. F. Raper, C. B. Farmer, R. Zander, and C. P. Rinsland, Stratospheric and mesospheric pressure-temperature profiles from rotational analysis of CO₂ lines in atmospheric trace occultation spectra, *J. Geophys. Res.*, 100, 3,107-3,117, 1995.
- Von Clarmann, T., H. Fischer, F. Fried-Vallon, A. Linden, H. Oelhaf, C. Piesch, M. Seefeldner, and W. Volker, Retrieval of stratospheric O₃, HNO₃ and CLONO₂ profiles from 1992 MIPAS-B limb emission spectra: method, results, and error analysis, *J. Geophys. Res.*, 98, 20,495-20,506, 1993a.
- Von Clarmann, T., H. Fischer, and H. Oelhaf, Retrieval of atmospheric O₃, HNO₃, CFC-11 and CFC-12 profiles from MIPAS-B-89 limb emission spectra, *Appl. Opt.*, Vol. 32, No. 33, 6,808-6,817, 1993b.
- Zander, R., C. P. Rinsland, C. B. Farmer, and R. H. Norton, Infrared spectroscopic measurements of halogenated source gases in the stratosphere with the ATMOS instrument, *J. Geophys. Res.*, 92, 9,836-9,850, 1987.

G. P. Anderson, D. R. Smith, J. H. Chetwynd, and R. M. Nadile, Geophysics Directorate, Phillips Laboratory, Hanscom Air Force Base, Massachusetts 01731.

G. E. Bingham, D. K. Zhou, and A. J. Steed, Space Dynamics Laboratory, Utah State University, Logan, Utah 84321. (e-mail: gail.bingham@sdl.usu.edu; daniel.zhou@sdl.usu.edu; allan.steed@sdl.usu.edu)

Figure 1. A drawing of the shuttle Discovery in gravity gradient data collection attitude, indicating the CIRRIS-1A interferometer detectors and field of view (not to scale).

Figure 2. The vertical band radiance profiles from CIRRIS-1A radiometer denoted by dots and interferometer denoted by triangles measured under the same conditions near latitude 30° S and longitude 9° E, at local time 1.2 hours on April 29, 1991.

Figure 3. An example of greenhouse gas emission spectrum collected at 22.4 hours local time on April 29, 1991, and a tangent height of 14.08 km, latitude of 42° S longitude of 32° W, by interferometer detector 5 filter 3 ($770\text{--}2100\text{ cm}^{-1}$). The primary emitters are shown in this region, with indication of analysis and retrieval regions used in this paper.

Figure 4. The spectral distribution, collected in one stair-step mode in the wavenumber region of $800\text{--}1100\text{ cm}^{-1}$ and spatial region of 10–55 km. The data were taken near latitude 30° S and longitude 9° E, at local time 1.2 hours on April 29, 1991. This data set was used to present the VMR profiles.

Figure 5. CFC-11, CFC-12, and HNO_3 spectral overlapping are shown in the region of $830\text{--}960\text{ cm}^{-1}$; the HNO_3 spectral emission is taken off of CFC-11 and CFC-12 spectrum by using spectra of different tangent heights. The major radiance peaks are identified. The data were collected at 22.4 hours local time on April 29, 1991, latitude of 42° S longitude of 32° W.

Figure 6. CFC-12 ν_8 Q branch at 1161 cm^{-1} is obtained by subtracting two different tangent height scans; N_2O spectrum is also shown in the same manner. The data were collected at 22.4 hours local time on April 29, 1991, latitude of 42° S longitude of 32° W.

Figure 7. An example of comparison of CIRRIS-1A and modelled spectra in the CO_2 laser band region at a tangent height of 17.93 km which is used to retrieve the aerosol extinction.

Figure 8. The temperature and pressure data (from NMC) plotted in (a) and (b) at same time and location of the CIRRIS-1A data collection (30° S, 9° E). The temperature and pressure profiles show the vertical error bar of altitude, and horizontal error bar of temperature. The data points were the chosen boundaries of the onion-peeling layers. (c) the retrieved aerosol extinctions at $0.55\text{ }\mu\text{m}$ are plotted as open cycles with their error bars which are actual measured

points while the triangles are the chosen boundaries of the onion-peeling layers. The comparison profiles are also shown (see text).

Figure 9. Examples of comparison of CIRRIS-1A and modelled spectra in the (a) O_3 , (b) HNO_3 , (c) CFC-12, and (d) CFC-11 band regions which are used to retrieve their VMR profiles.

Figure 10. The comparison between measured and modelled spectra in the large spectral region of $800\text{--}1100\text{ cm}^{-1}$ by using retrieved VMR profiles of O_3 , HNO_3 , CFC-12, CFC-11, and aerosol.

Figure 11. The VMR profiles of (a) O_3 , (b) HNO_3 , (c) CFC-12, and (d) CFC-11 retrieved from 30° S and 9° E , Midnight April 29, 1991 data collection (plotted in Figures 4 and 10). The retrieved VMRs are plotted as open cycles with their error bars which are actual measured points while the triangles are the chosen boundaries of the onion-peeling layers. Some other measurements are reproduced for comparison (see text).

Table 1. STS-39 Observation and CIRRIS-1A Instrument Primary Parameters.

Parameter	Specification
Shuttle altitude	~260 km
Inclination	57°
Optical path difference	1.112 cm
Mirror speed	0.57 mm/sec
Long scan time	9.7 sec
Detectors	Si:As, five-element array
Spectral region (filter 7)	770-1250 cm ⁻¹
Spatial region	10-270 km

Table 2. Retrieved Results from CIRIS-1A Earthlimb Measurements Near 30° S Latitude 9° E Longitude at midnight April 29, 1991.

TH (km)	*Ext. (km ⁻¹)	O ₃ (ppmv)	HNO ₃ (ppbv)	CFC-12 (ppmv)	CFC-11 (ppmv)
11.84	$1.88 \pm 1.1 \times 10^3$	0.05 ± 0.03	0.12 ± 0.03	$5.57 \pm 1.1 \times 10^{-4}$	$3.20 \pm 0.6 \times 10^{-4}$
17.93	$1.71 \pm 0.9 \times 10^3$	0.50 ± 0.3	1.15 ± 0.2	$4.70 \pm 0.9 \times 10^{-4}$	$2.60 \pm 0.7 \times 10^{-4}$
24.40	$3.42 \pm 2.5 \times 10^4$	5.00 ± 1.0	5.60 ± 0.6	$3.10 \pm 1.0 \times 10^{-4}$	$7.50 \pm 4.0 \times 10^{-5}$
31.23	-----	8.20 ± 0.9	3.00 ± 0.7	$1.25 \pm 0.8 \times 10^{-4}$	-----
34.69	-----	7.30 ± 0.8	1.10 ± 0.3	-----	-----
40.96	-----	5.85 ± 0.6	0.35 ± 0.2	-----	-----
45.53	-----	4.60 ± 0.5	-----	-----	-----
47.53	-----	3.40 ± 0.4	-----	-----	-----
51.63	-----	1.80 ± 0.5	-----	-----	-----
58.06	-----	0.63 ± 0.3	-----	-----	-----

* The aerosol extinction coefficient at 0.55 μm .

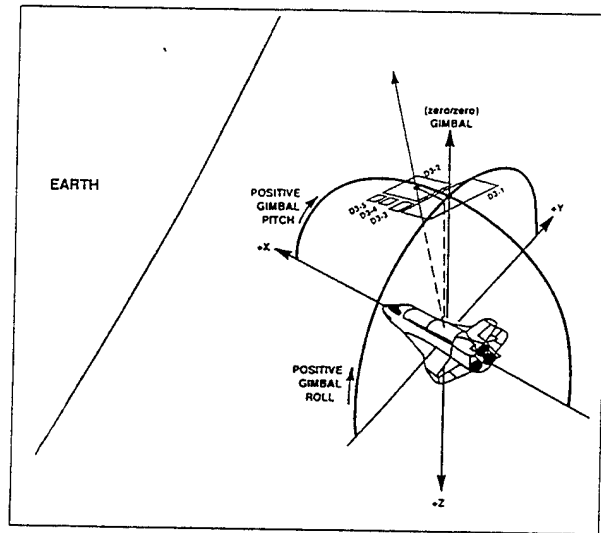


Figure 1

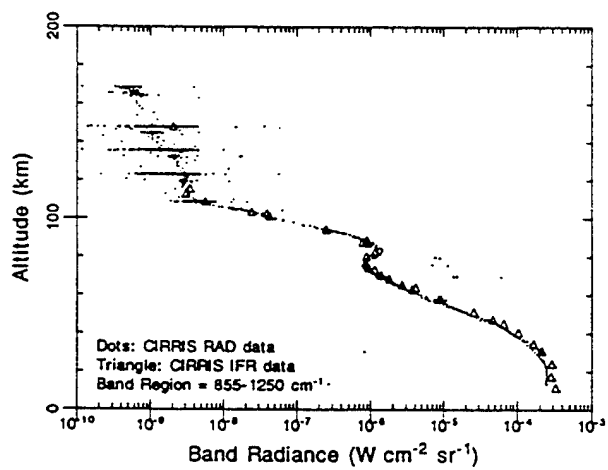


Figure 2

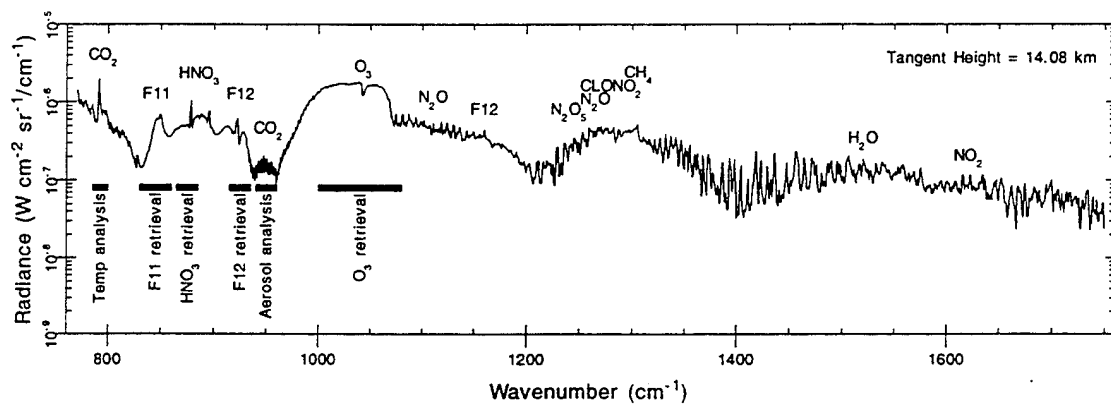


Figure 3

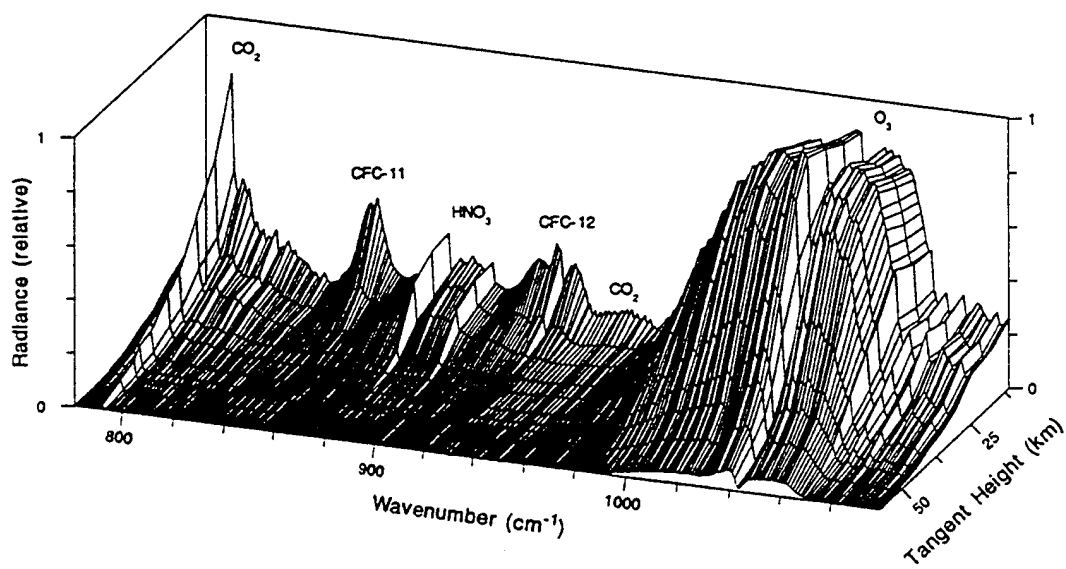


Figure 4

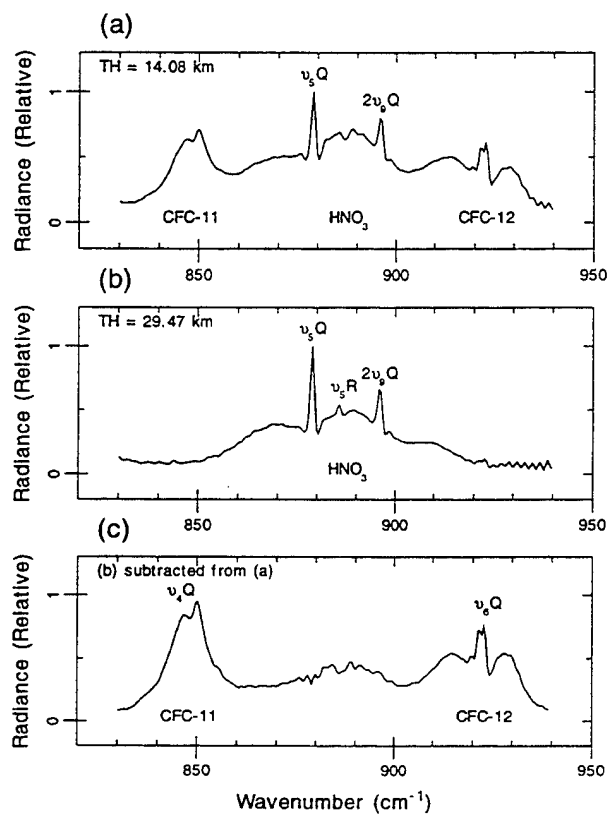


Figure 5

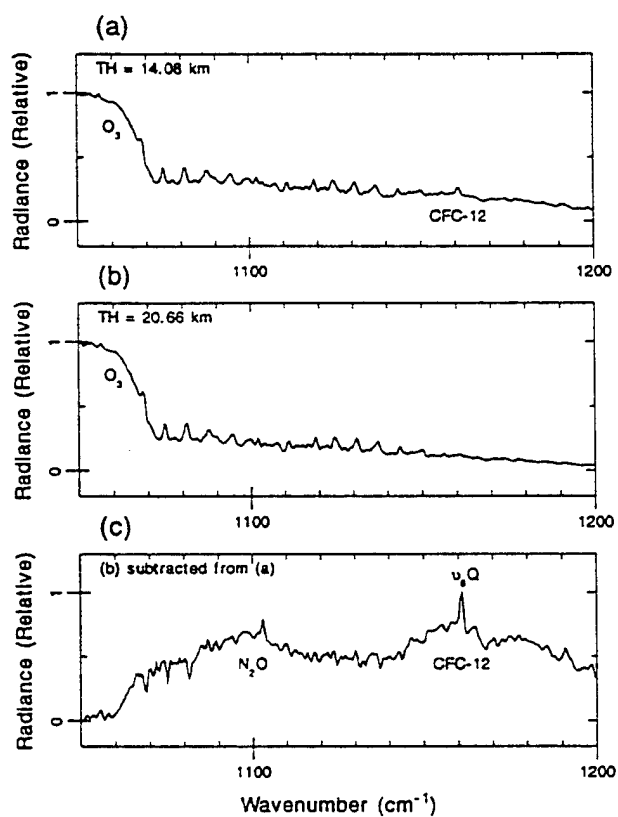


Figure 6

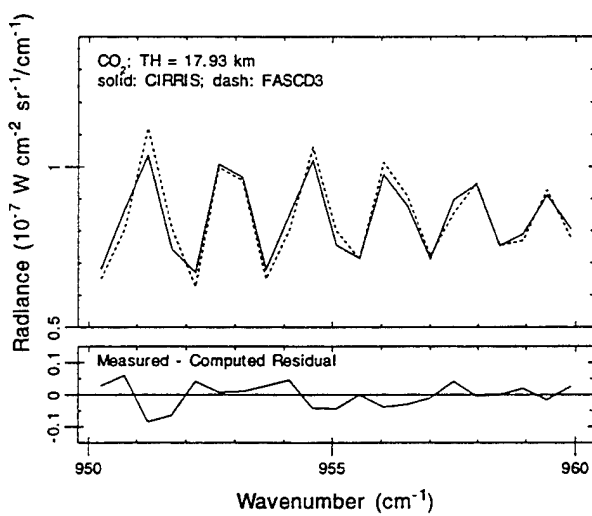


Figure 7

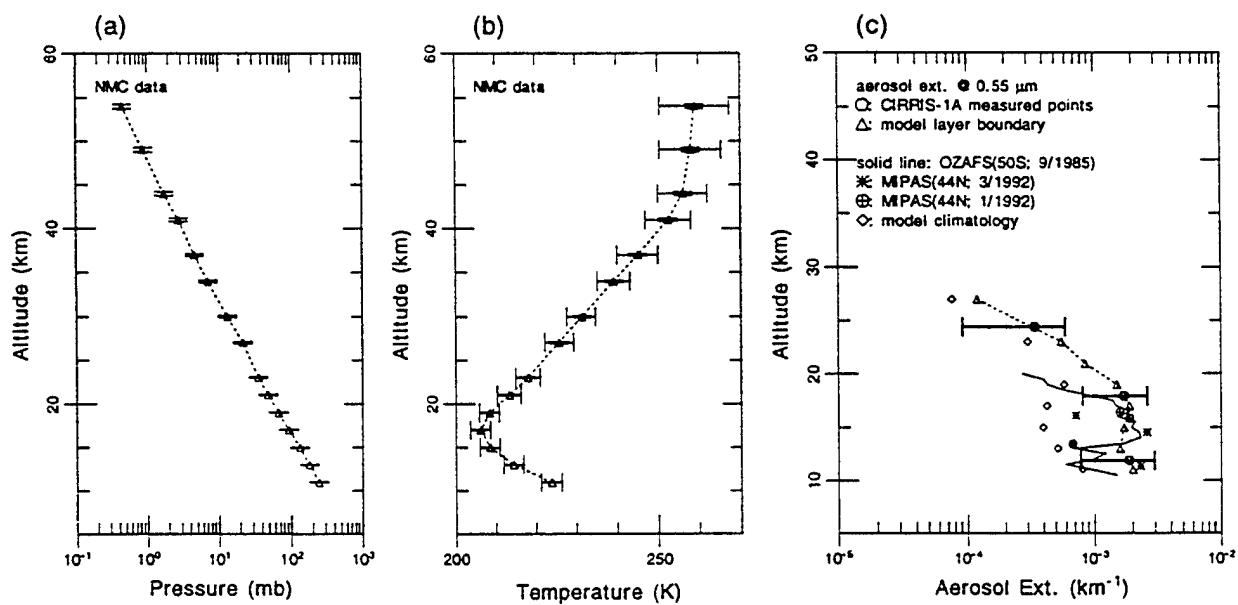


Figure 8

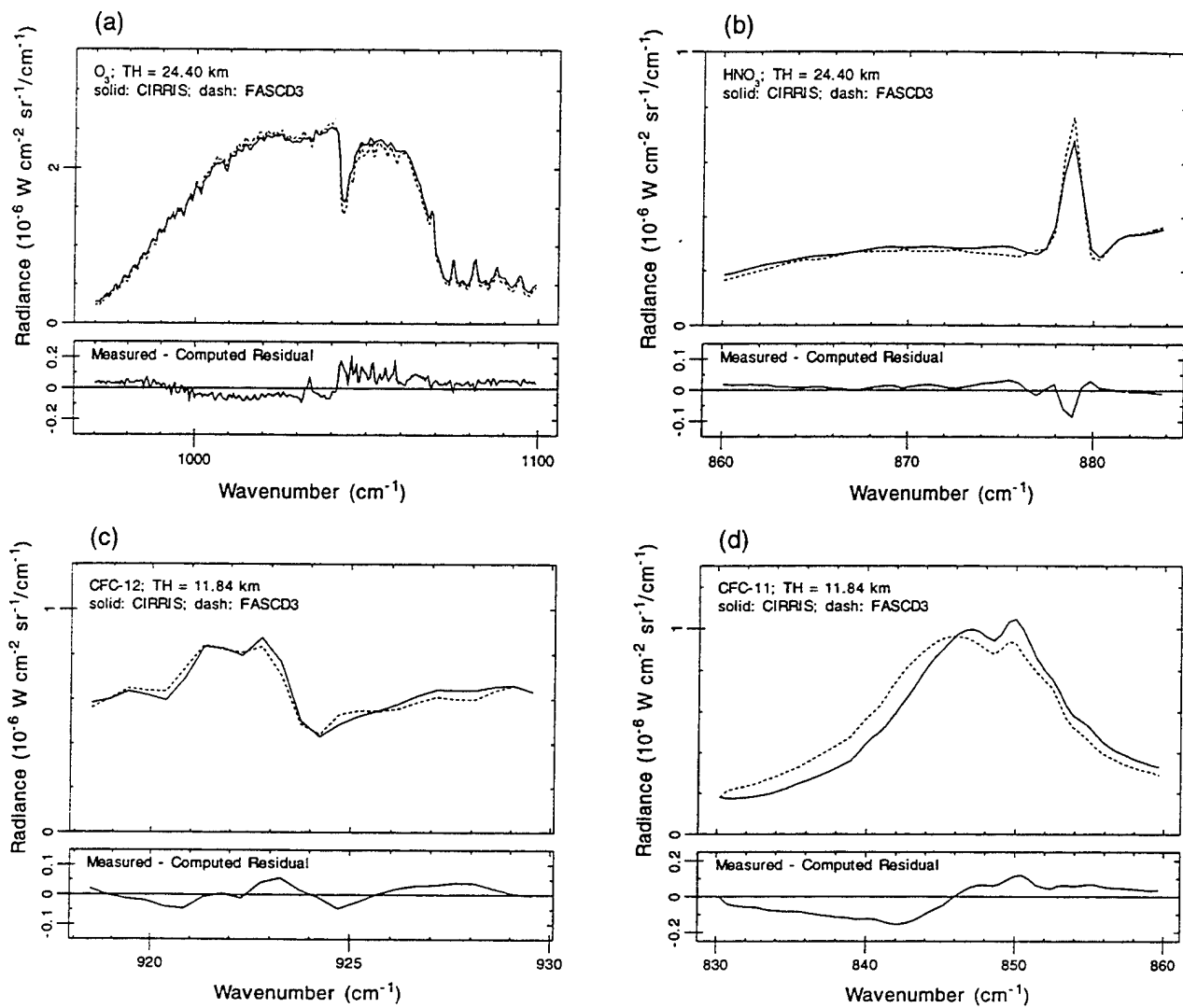


Figure 9

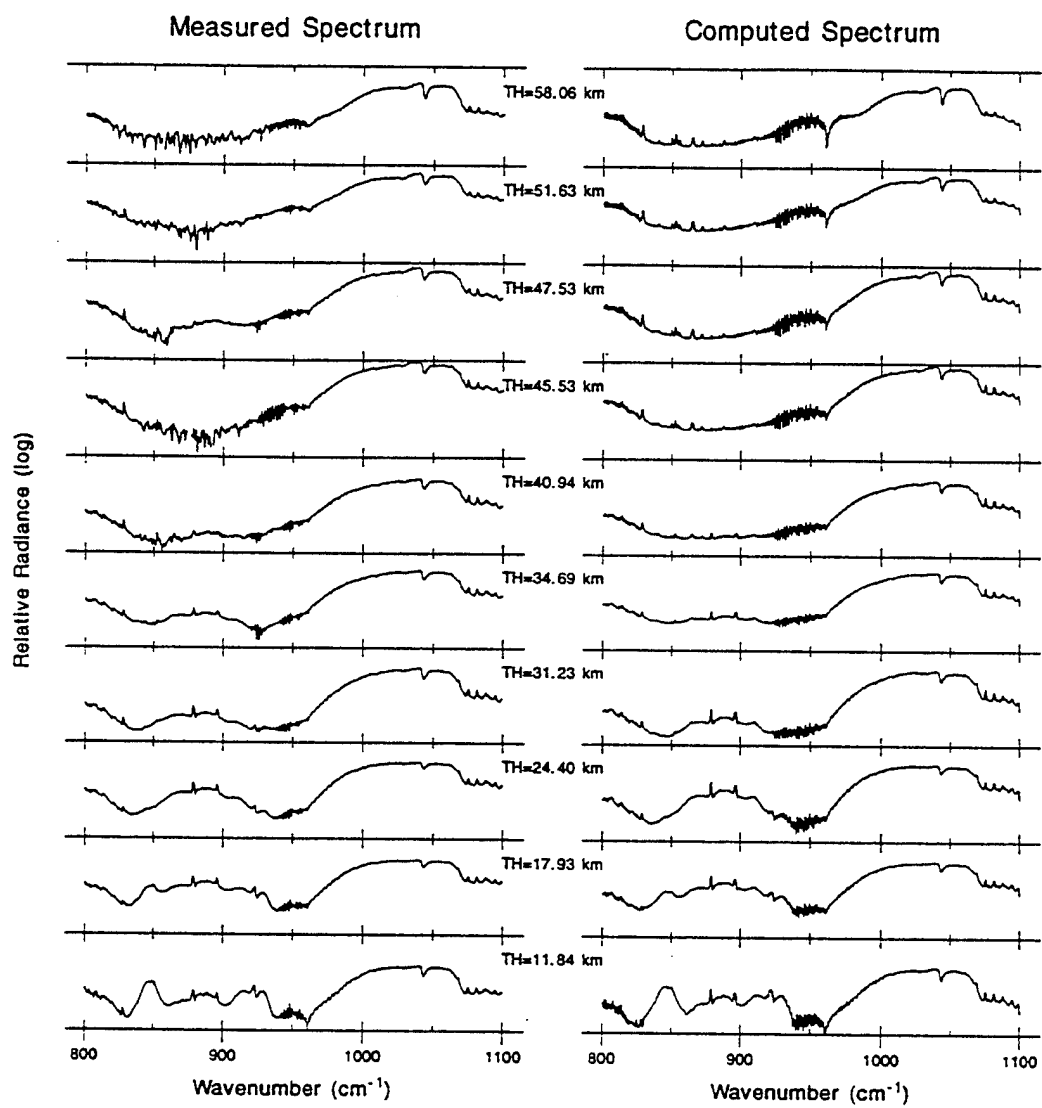


Figure 10

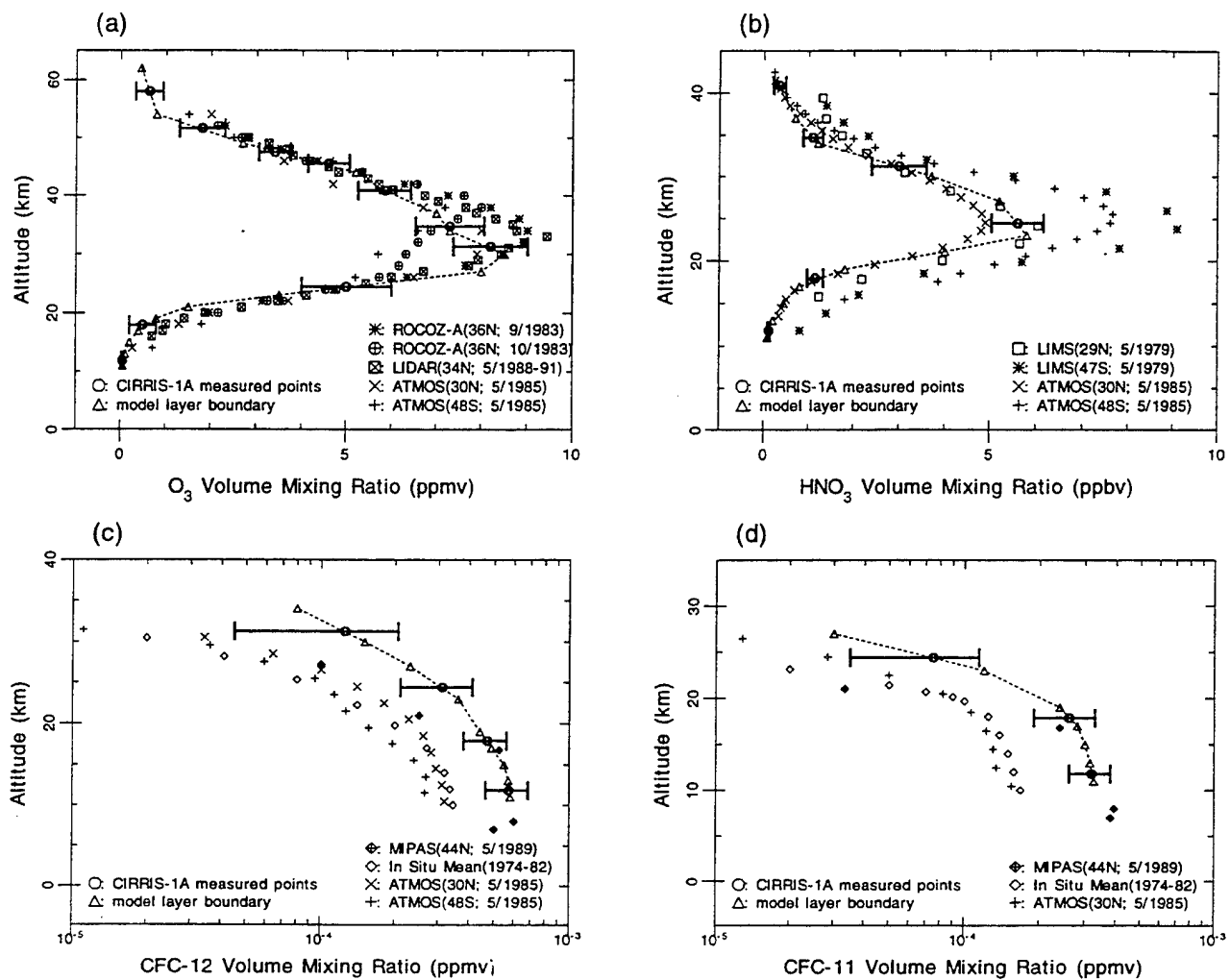


Figure 11

Non-LTE Effects on Nadir Viewing Temperature Sounding in the Stratosphere Using the CO₂ 4.3 μ m Band

Jeremy R. Winick, Optical Environment Division, Phillips Laboratory, Hanscom Air Force Base,
MA, 01731-3010

J.-L. Moncet, H.E. Snell, D.B. Hogan, Atmospheric and Environmental Research, Inc.,
Cambridge, MA 02139

P.P. Wintersteiner, ARCON Corporation, Waltham, MA

Jinxue Wang, Atmospheric Chemistry Division, NCAR, Boulder, CO

Abstract: Advanced high resolution infrared sensors provide the opportunity for remote sensing using optimized narrow wavelength regions. The 4.3 μ m band of CO₂ is a good candidate for retrieval of temperature because the lineshape of its nadir radiance is strongly dependent upon the stratospheric temperature profile. However, large non-LTE effects in the daytime mesosphere are known and have been measured in the limb emission. Using the Phillips Laboratory non-LTE ARC radiance code, FASCODE, and a generalized inversion routine based upon Rodgers' optimal estimation technique, we investigate retrieving stratospheric temperature from nadir radiances in the 2358-2365 cm⁻¹ region. In preliminary case studies we find that the enhanced non-LTE vibrational temperatures strongly effect the nadir spectra, but that non-LTE modeling and careful choice of instrumental bandwidth allow retrieval of stratospheric temperature to suitable accuracy.

I. Non-LTE Processes in the CO₂ 4.3 μ m Band

The nature of non-LTE radiance in the CO₂ 4.3 μ m band has been investigated by a number of groups since the 1970's (See for example, Kumer and James [1974], López-Puertas *et al.* [1986], Nebel *et al.* [1994].) The daytime vibrational temperatures of the 4.3 μ m emitting states are greatly enhanced above the lower mesosphere, predominantly due to solar excitation at 4.3, 2.7, and 2.0 μ m. Since the CO₂ fundamental ν_3 frequency is nearly resonant with the N₂(1-0) energy ($E_{CO_2} - E_{N_2} = 19 \text{ cm}^{-1}$), the vibrons are closely coupled. The radiative trapping of ν_3 fundamental photons magnifies the coupling. A comprehensive model must include many vibrational levels as shown in figure 1. It must also include the minor isotopes of the stronger bands since the great opacity of the fundamental transition of the major isotope, designated 626 (¹²C¹⁶O₂ = 626, ¹²C¹⁶O¹⁸O = 628, etc.), allows more effective layer-to-layer radiative transfer to occur in the minor isotopes.

The ARC model for the CO₂ 4.3 μ m states [Nebel *et al.*, 1994] calculates vibrational temperatures for the 626 isotope for the more than 20 states indicated in figure 1. In addition, vibrational temperatures for the minor isotopes (636, 628, and 627) are calculated for the fundamental (00011), the first hot band (01111), and the 01101 and 02201 levels as well as for the group 1 levels of the 636 isotope. The O(¹D) density needed as a direct source of N₂(v) is calculated off line for the appropriate conditions (time-of-day, solar zenith angle, SZA) using a 1-dimensional photochemical model (Winick *et al.*, 1985, Makhlof *et al.*, 1995).

Solar excitation is the predominant non-LTE excitation source in the daytime. The strong dependence of the vibrational temperature on the solar zenith angle is clearly shown in figure 2. With a higher sun, solar flux penetrates deeper into the atmosphere producing higher vibrational

temperatures (larger non-LTE enhancement) at lower altitudes. The SZA dependence above 100 km is due to the fact that the effective earthshine contribution from the 85-100 km region increases as the solar zenith angle decreases. Solar flux penetrates deeper into the atmosphere in the weaker bands (isotopes of the fundamental, hot bands excited at 4.3 μm , and bands excited at 2.0 and 2.7 μm), thus shifting peak excitation to lower altitudes.

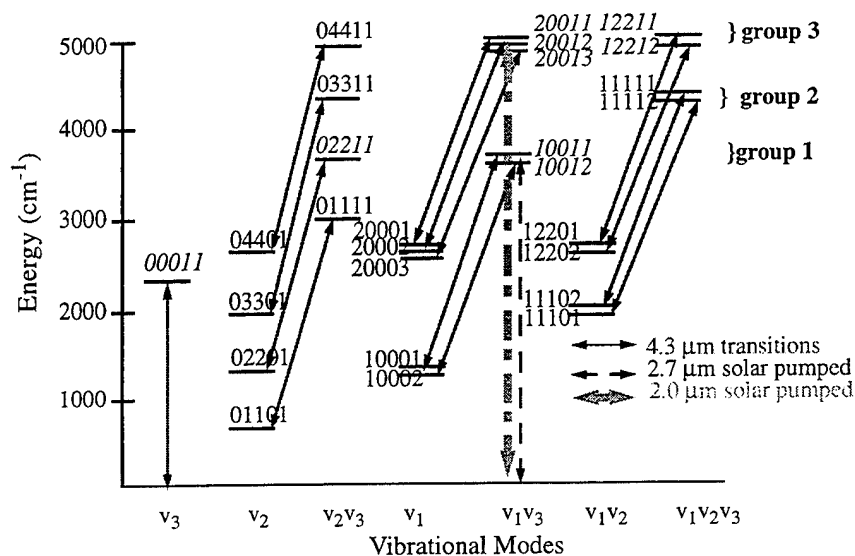


Figure 1. Energy diagram of CO_2 states included in ARC non-LTE model. The v_3 transitions at 4.3 μm and major solar excitation transitions at 2.7 and 2.0 μm are indicated.

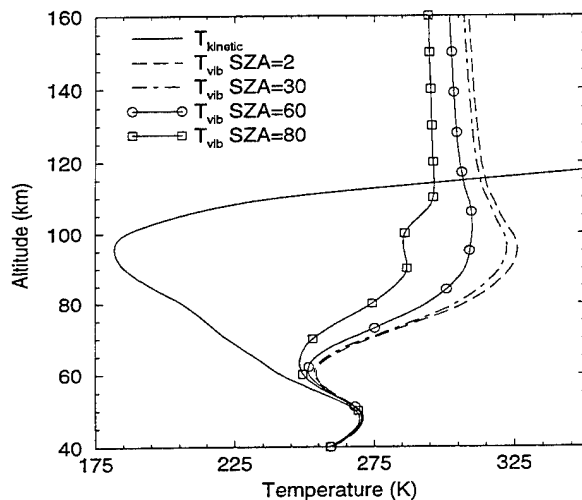


Figure 2. Solar zenith angle dependence of the 00011 626 vibrational temperature, for 10°N April model atmosphere.

In Figures 3(a) and (b) the vibrational temperature profiles for the 00011 and 01111 bands for 4 isotopic species are shown for $\text{SZA}=17^\circ$ and a smoothed US Standard Atmosphere profile [USSA 1976]. The first hot band lower state (01101) is the upper state of the 15 μm fundamental

which is very close to LTE below 90km [Wintersteiner et al., 1992].

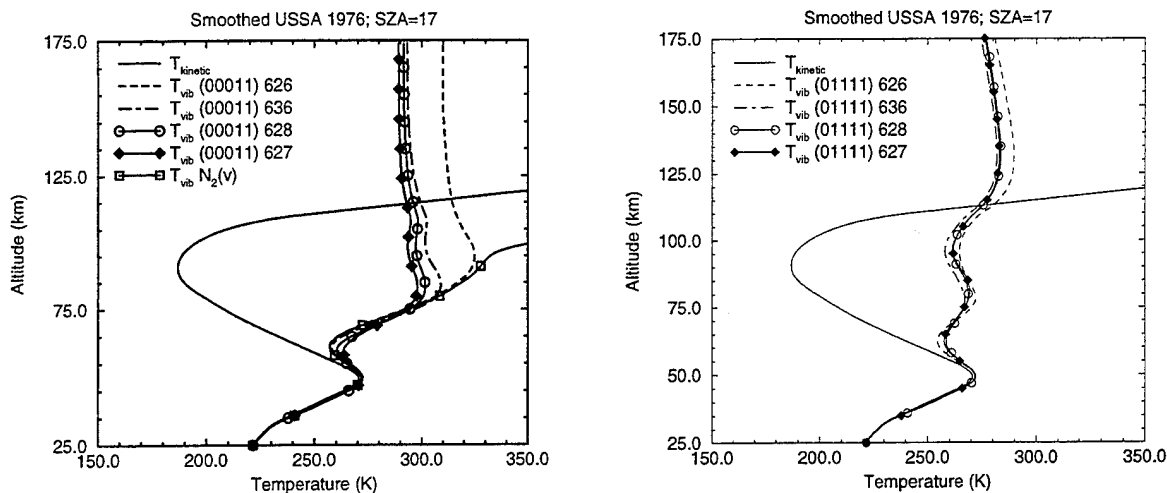


Figure 3. (a) Profiles of kinetic temperature and vibrational temperature for the fundamental states (00011) for 626, 636, 627 and 628 isotopes, for USSA 76 atmosphere, SZA=17°. (b) Profiles of vibrational temperature for the first hot band (01111).

2. Nadir Radiance

To effectively retrieve temperature, the nadir radiance must contain information about the temperature as a function of altitude. This information is contained in the Voigt lineshape if the lines are sufficiently optically thick. Then points on the line profile yield radiance corresponding to the emission temperatures of the atmosphere at the corresponding atmospheric level where $\tau \approx 1$; for LTE case they are representative of the Planck function. Thus we require lines that are optically thick throughout the stratospheric region in which we wish to retrieve. Avoiding as much of the non-LTE effect as possible will also be preferable since it will reduce the uncertainties stemming from the non-LTE forward calculation (discussed more in section 3).

An optimal frequency region to study is $2358\text{--}2365\text{ cm}^{-1}$, in which the strong CO_2 626 00011 P-branch lines dominate. These lines are optically thick, and their wide pressure-broadened profiles contain the required temperature information. Weaker lines of the 626 01111 and even weaker 627 and 628 lines also appear. The solar pumped group 1-3 bands which have greater non-LTE enhancements in the upper stratosphere are avoided by choosing this region. There is little or no interference from other radiating species, and the strong opacity even in the wings of the 626 (00011) precludes effects from the lower atmosphere (solar scattering off of clouds, water vapor etc.).

The vibrational temperatures obtained from the ARC model for SZA=17, and a smoothed US Standard Atmosphere 1976 are used as input in FASCODE in non-LTE mode to calculate the nadir viewing radiances. Nadir radiances in the 2364 cm^{-1} region (figure 4a) are dominated by the R20 line of (00011) 626 at 2364.105 cm^{-1} with weaker R37 627 at 2364.34 and R56 628 at 2364.42 and a moderately strong R42 line of the (01111) 626 at 2364.44 . In figure 4(b) the corresponding radiance obtained assuming LTE is shown. The non-LTE radiance exhibits a very

large enhancement in the line core emanating from the upper mesosphere, an enhancement that decreases further from line center, corresponding to emission from lower in the atmosphere.

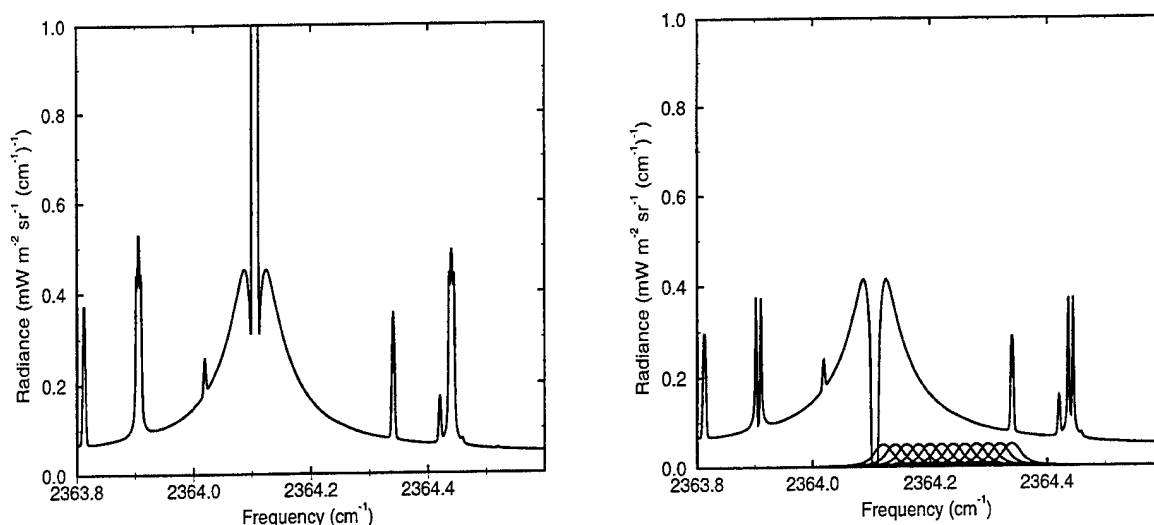


Figure 4. Nadir spectral radiance in the CO₂ 4.3-μm band. (a) Non-LTE has enhanced radiance in the core of strong lines (626 R20 at 2364.105 cm⁻¹) as opposed to absorption in the cold mesopause region in the LTE model in figure 4(b). Shape of prototype high resolution instrument channels also shown in 4(b).

3. Retrieval and Uncertainties

Since the nadir radiances shown in figure 4 exhibit large non-LTE enhancements, they cannot be ignored in any forward model used in the retrieval process. However, one can minimize the impact by using a high resolution instrument that is tuned to avoid most of the non-LTE core. A prototype instrument response is shown in figure 4(b) for which the strongest non-LTE portion is mostly outside the bandpass. The weak 627 line is included, but its non-LTE contribution even in the line center is quite small. The 01111 hot band which has a more significant non-LTE contribution is avoided. However, one must sample fairly near the core to obtain information on altitudes up to the 50 km region, and with the channel bandpass significant non-LTE is included as seen in figure 5. Most of the non-LTE component originates from above 50km; the uncertainty in this component can affect the retrieval.

To estimate the retrieval uncertainty caused by uncertainty in the non-LTE model, we calculated the non-LTE vibrational temperatures for a perturbed atmosphere. For the perturbed case we changed the temperature profile by adding 10K above 65km tapered to no change at 45 km. This approximates a possible variability in the unretrieved upper atmosphere temperature based upon the climatological mean. The temperature difference does not have a profound effect on the vibrational temperature in most of the mesosphere. (figure 6). The 00011 vibrational temperature above 75 km changes by less than 1K, with the maximum change of about 5K at 55 km. The vibrational temperature perturbation closely tracks temperature change up to 55 km then departs as the large non-LTE enhancement (figure 3) is dependent upon solar excitation. The 01111 band is more sensitive to the temperature perturbation throughout the mesosphere since the density of its lower state 01101 which is in LTE is dependent upon the temperature. For the 01111 band the vibrational temperature differences in the perturbed case stay at about 5K in the 70-100 km

region. We use the difference in the radiance of the perturbed and unperturbed radiance profiles as an estimate of the non-LTE induced uncertainty or a kind of “noise”.

In our test case we retrieve the temperature specified in the USSA model for SZA=17, starting with an initial guess temperature profile corresponding to the mid latitude summer profile. The temperature is retrieved using an optimal estimation least squares technique following Rodgers [1990]. We have performed retrievals using the radiance profile for the USSA under LTE conditions with “noise” specified above. The retrieval converges in just a few iterations to within $\pm 4\text{K}$ in the 25-55km region (figure 7). The error increases above and then becomes insensitive to the temperature. Similarly, below about 25 km altitude level it also becomes insensitive to temperature. Since the CO_2 mixing ratio is well known below 80-90 km, in the LTE region its radiance depends upon the temperature, which is the variable being retrieved. Above 60km there is little information on temperature. Fortunately, the large non-LTE enhancement is largely unaffected by the temperature profile, instead being determined by solar excitation and dependent largely on the SZA which in any measurement is well known.

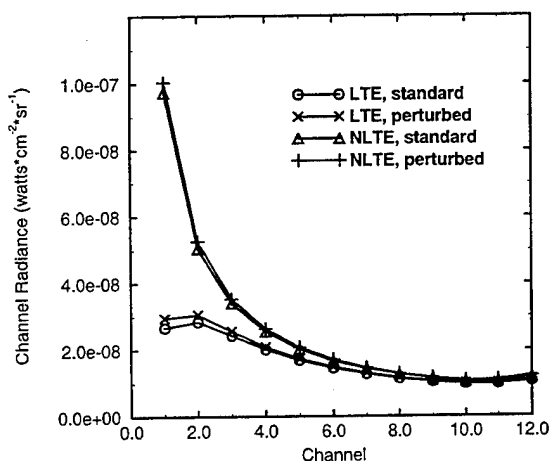


Fig. 5. Radiance for LTE and non-LTE for model and perturbed cases using instrument function in fig 4b.

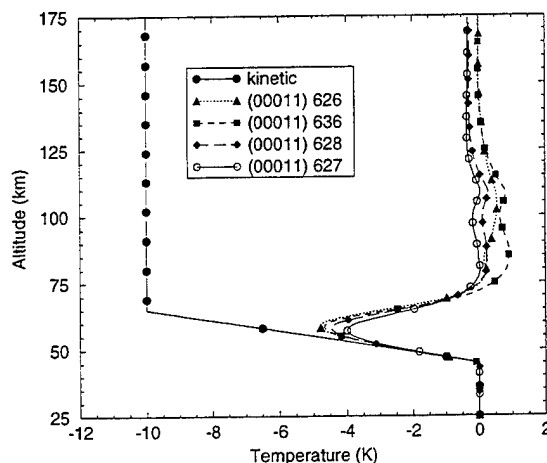


Fig. 6. Change in T_{vib} for the 00011 states when temperature profile is changed.

The retrievals done so far do not include possible systematic errors in the non-LTE model that could be caused by incorrect rate constants or mechanisms in the non-LTE model. These errors are difficult to assess without many comparisons to data for a wide variety of well documented atmospheric conditions. The CO_2 model has been validated with CIRIS limb viewing spectra. The agreement is quite good for daytime in the 55-75km tangent altitude region, but the atmospheric conditions were not well characterized. As long as solar excitation is dominant the non-LTE error should be quite small since the solar flux and linestrengths of the CO_2 are well known. The relative error in 45-60 km region is probably most uncertain since it is there that $\text{O}(^1\text{D})$, which is produced by ozone dissociation, is a major source of $\text{N}_2(\text{v})$. However, systematic non-LTE error will show up in any spectral measurements mostly confined to the line core region and should lead to a corrected non-LTE model. We are currently examining the sensitivity of the non-LTE “noise” for different temperature profiles and different SZA.

Summary

We have used the comprehensive Phillips Laboratory non-LTE ARC model to calculate non-LTE effects in the nadir viewing radiance in the 4.3- μm band. There are large enhancements in the radiance, especially in the core of the thick lines. A preliminary study of the indicates that stratospheric temperature can be retrieved in the 0.5 to 20 mb region using high resolution instruments and judicious choice of spectral region to sense. Further sensitivity studies involving different conditions are under way.

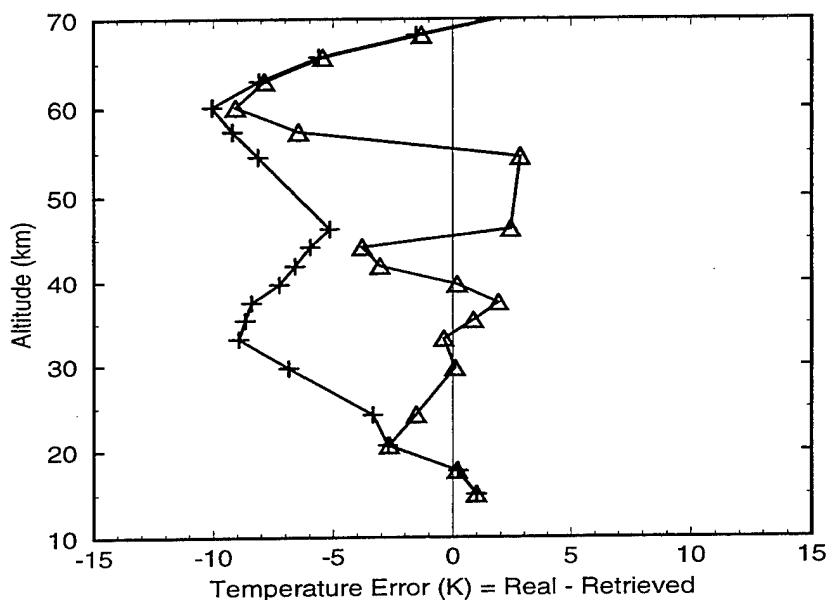


Fig. 7. Error in retrieval (temperature difference retrieved-true) which started with mid latitude summer profile (+) and converged (Δ) profile. Retrieval uses LTE radiance with non-LTE "noise".

Acknowledgments

J.R. Winick was partially funded by AFOSR under task PL92006. J.-L. Moncet, H.E. Snell, and D.B. Hogan were funded by ITT Aerospace, and P.P. Wintersteiner was funded by AFOSR through Phillips Laboratory contract F19628-90-C-0060.

References

- Kumer, J.B., and T.C. James, $\text{CO}_2(001)$ and N_2 vibrational temperatures in the $50 \leq z \leq \text{km}$ altitude range, *J. Geophys. Res.*, 79, 638-648, 1974.
- López-Puertas, M., M. R. Rodrigo, J. J. López-Moreno, and F. W. Taylor, A non-LTE radiative transfer model for infrared bands in the middle atmosphere. II CO_2 (2.7 and 4.3 μm) and water vapour (6.3 μm) bands and $\text{N}_2(1)$ and $\text{O}_2(1)$ vibrational levels. *J. Atmos. Terr. Phys.*, 48, 749-764, 1986.

- Makhlouf, U., R.H. Picard, J.R. Winick, Photochemical-dynamical modeling of the measured response of airglow to gravity waves: I. Basic model for OH airglow, *J. Geophys. Res.*, **100**, 11289-11311, 1995.
- Nebel, H., P. P. Wintersteiner, R.H. Picard, J. R. Winick, and R.D. Sharma, CO₂ non-local thermodynamic equilibrium radiative excitation and infrared dayglow at 4.3 μ m: Application to Spectral Infrared Rocket Experiment data, *J. Geophys. Res.*, **99**, 10409-10419, 1994.
- Rodgers, C.D., Characterization and error analysis of profiles retrieved from remote sounding measurements, *J. Geophys. Res.*, **95**, 5587-5595, 1990
- Wintersteiner, P.P., R.H. Picard, R.D. Sharma, J.R. Winick, and R.A. Joseph, Line-by-line radiative excitation model for the non-equilibrium atmosphere: Application to CO₂ 15- μ m emission, *J. Geophys. Res.*, **97**, 18083-18117, 1992.
- Winick, J.R., R.H. Picard, R.D. Sharma, and R.M. Nadile, Oxygen singlet delta 1.58-micrometer (0-1) limb radiance in the upper stratosphere and lower mesosphere, *J. Geophys. Res.*, **90**, 9804-9814, 1985.

THE USE OF MODTRAN TO ESTIMATE THE SO₂ CONTENT OF VOLCANIC PLUMES

Presentation to
18th Annual Conference on Atmospheric Transmission Models
Phillips Laboratory/Geophysics Directorate

Vincent J. Realmuto
Jet Propulsion Laboratory
California Institute of Technology
7 June 1995

Realmuto - Mapping SO₂ with MODTRAN

REMOTE SENSING OF VOLCANIC SO₂ (1)

Estimate the Volcanic Contribution to Global Atmospheric SO₂ Budget
Approximately 13×10^6 Mg per year
5 to 10 % of Anthropogenic Contributions

Monitor SO₂ Flux to Predict Eruptions
Change in Flux of Volatiles May Signal an Impending Eruption

Most Abundant Volatiles in Magma (mol %)

H ₂ O:	35 - 90
CO ₂ :	5 - 50
SO ₂ :	2 - 30

SO₂ is Most Amenable to Remote Sensing
Strong Absorption Bands in UV, TIR, and Microwave
Low Ambient Levels in Atmosphere

REMOTE SENSING OF VOLCANIC SO₂ (2)

Satellite-Based

Total Ozone Mapping Spectrometer (TOMS)

Measures UV Radiance

Global Maps Acquired Daily

Spatial Resolution at Nadir: 50 km

Detects Volcanic SO₂ Clouds in Stratosphere and Upper Troposphere

Ground-Based

Correlation Spectrometer (COSPEC)

Measures UV Radiance

SO₂ Loading Along Line-of-Sight (ppm-m)

Manual Set-Up and Operation

Portable System

Deployed in Automobiles, Boats, Light Aircraft

REMOTE SENSING OF VOLCANIC SO₂ (3)

Thermal Infrared (TIR) Imaging of SO₂ Plumes
Exploits Strong SO₂ Absorption Near 8.5 μm
Employs Multispectral TIR Image Data
Bridge Between TOMS and COSPEC

Existing Airborne Instruments
Thermal Infrared Multispectral Scanner (TIMS)
Multispectral Infrared and Visible Imaging
Spectrometer (MIVIS)
MODIS Airborne Simulator (MAS)

Future Spaceborne Instruments
Advanced Spaceborne Thermal Emission and
Reflection Radiometer (ASTER)
Moderate-Resolution Imaging Spectroradiometer
(MODIS)
Ocean Color and Temperature Scanner (OCTS)

Realnuto - Mapping SO₂ with MODTRAN

INPUT DATA

Image Data

Instrument-Perceived Radiance
Ground Emissivity
Color-Composite Index Image
Digital Elevation Model (DEM) - Optional

Non-Image Data

Altitude Profiles of Atmospheric Pressure, Temperature,
Water Vapor, and Constituents
Plume Altitude and Thickness
Spectral Response of Imaging Instrument

Realtime - Mapping SO₂ with MODTRAN

RETRIEVAL ALGORITHM (1)

Ground Temperature Retrieval

Requires 1 Run of MODTRAN

Spectral Range: 750 - 1300 cm^{-1} (7.7 - 13.3 μm)

Resolution: 1 cm^{-1} , 2 cm^{-1} FWHM

Ground Temperature: 0 K

Target Altitude: Ground Altitude + 0.5 m

Estimate $\tau(\lambda)$, $L_d(\lambda)$, and $L_u(\lambda)$ With No Contribution from Ground

Given $\varepsilon(\lambda)$, Find T_o That Fits Observed Radiance in Channels 4, 5, and 6

RETRIEVAL ALGORITHM (2)

SO₂ Concentration Retrieval

Requires 5 Runs of MODTRAN

Spectral Range: 980 - 1300 cm⁻¹ (7.7 - 10.2 μm)
Ground Temperature: T_o
Target Altitude: Ground Altitude
SO₂ Concentration Higher For Each Run

Define Piecewise Linear Function Describing the Reduction in Instrument-Perceived Radiance with Increasing SO₂

Fit Observed Radiance in Channels 1, 2, and 3 Using Iterative Least-Squares

Each Iteration Contains at Least 1 Call to Radiance vs. SO₂ Function

Realtime - Mapping SO₂ with MODTRAN

CONCLUSIONS

Retrieval Compares Favorably With COSPEC
Radiance vs. SO₂ Approximation Can Result in Overestimates $\leq 10\%$

Algorithm is Too Slow for Operational Status
9 - 15 sec/pixel on Sun 4/80 (SPARCstation 10)
Binning Algorithm Implemented to Limit Number of Runs of
MODTRAN Suite

Modifications to MODTRAN

"SO₂ - TRAN"

SO₂ Changes for Runs 2 - 6
Concentrations of 11 Other Gases Remain Unchanged
Each SO₂ Run Must Modify Results of Previous Run

Water Droplets

H₂SO₄ and Silicate Aerosols

Realauto - Mapping SO₂ with MODTRAN

Modeling local atmospheric effects by MODTRAN-3 code and vertical profiles in the area of Mt. Etna volcano, Sicily.

S.Teggi, S.Pugnaghi

Osservatorio Geofisico dell' Università di Modena, Modena, Italy

M.F.Buongiorno, M.P.Bogliolo

Istituto Nazionale di Geofisica, Roma, Italy

V.J.Realmuto

Jet Propulsion Laboratory, California Institute of Technology, CA, USA

Abstract Atmospheric modeling with a radiative transfer code is very important when ground or atmospheric physical properties are analysed by means of remote sensing data acquired by imaging spectrometers. In order to describe the local conditions in the low atmospheric layers, radiative transfer codes such as MODTRAN need to be adjusted with local information. In the present work several vertical profiles acquired on the Etna volcano (Sicily, Italy) were analysed and compared to understand the variations in the local atmospheric parameters caused by the high topographic relief, the proximity of the sea and by the gases and the water vapour clouds emitted by the volcano itself. In the studied cases it was found that the uncertainty on humidity profiles produces differences on surface temperature (T_s) estimate. Each variations of equivalent sea level water vapor amount of $1.g/cm^2$ produce a ΔT_s of about $5^\circ C$. The ground data used in this work were acquired in a joint effort of the Istituto Nazionale di Geofisica, the Università di Modena and the Jet Propulsion Laboratory, in the frame of the first MIVIS spectrometer deployment, organized by the Italian CNR, L.A.R.A. project in Southern Italy.

Introduction

Atmospheric modeling with a radiative transfer code is a crucial step when ground or atmospheric physical properties are analysed by means of remote sensing data acquired by imaging spectrometers. In order to obtain an accurate analysis, altitude atmospheric profiles, describing the local atmospheric characteristics, have to be given as input to the code. These profiles should be measured in the same place and at the same time of the images acquisition. Often local atmospheric measurements are not available and are replaced by profiles measured at the nearest meteorological station. These profiles are generally not representative of the local atmospheric conditions, because they are both non-local and non-simultaneous.

In this work we evaluate the importance of using local atmospheric profiles, acquired simultaneously with airborne imaging spectrometer data, and the influence of the topographic effect on the estimates of sur-

face temperature. The MODTRAN3 radiative transfer code was used to model the contribute of the atmosphere on the sensor measured radiances.

The image data used in this study were acquired in July 1994 during the "SICILIA 94" campaign, organized by the Italian CNR L.A.R.A. project for the first deployment of the MIVIS airborne imaging spectrometer [Bianchi *et al.*, 1994]. MIVIS acquired several images on the southern Italy volcanoes, in particular Etna, Vulcano and Stromboli. MIVIS most important characteristics are given in Tab.2. Contemporaneously with the images acquisition, a ground measurement campaign [Teggi *et al.*, 1994] of various parameters was performed by a joint effort of the Istituto Nazionale di Geofisica, the Università di Modena, the Jet Propulsion Laboratory and the Istituto Internazionale di Vulcanologia. The measurements carried out included radiosonde launches, COSPEC data acquisitions, ground temperature and surface reflectance

MIVIS - TIR Channels										
Channel	93	94	95	96	97	98	99	100	101	102
Lower Edge (μm)	8.21	8.61	9.05	9.41	9.86	10.21	10.74	11.24	11.74	12.24
Upper Edge (μm)	8.56	8.96	9.39	9.77	10.18	10.67	11.12	11.66	12.15	12.70

Table 1: Numbering and nominal spectral edges of the thermal IR channels of the MIVIS spectrometer.

measurements. The SO_2 volcanic plume investigation is one of the principal aims of the campaign.

Number of spectral channels	102
Total spectral coverage	0.43-12.70 μm
Inst. Field of View (IFOV)	2.0 mrad
Sample rate (angular step)	1.64 mrad
Total scan angle (FOV)	71.059°
Pixels per scan-line	755
Platform	CASA 212/200

Table 2: MIVIS most important technical characteristics.

Procedure for the estimate of surface temperature

The procedure is based on the MODTRAN3 radiative transfer code, which is used to model the radiance perceived by the sensor, in the TIR channels (Tab. 1), as it views the ground through the atmosphere. In the TIR spectral region, the general expression for this radiance, for a given optical path, is:

$$L_M(\lambda, T_s) = L_u(\lambda) + \{\epsilon(\lambda)B(\lambda, T_s) + [1 - \epsilon(\lambda)]L_d(\lambda)\}\tau(\lambda) \quad (1)$$

where T_s is the temperature of the ground; $L_u(\lambda)$ and $L_d(\lambda)$ represent the sky radiance at the instrument and at ground altitudes respectively; $\tau(\lambda)$ represents the spectral transmittance of the atmosphere; $\epsilon(\lambda)$ is the spectral emissivity of the ground. The optical path for each image pixel is defined by the IFOV of the sensor and the ground and sensor altitudes; these dependencies are omitted in eq. (1) to simplify the notation.

Eq. (1) requires the knowledge of the spectral emissivity. Since we are not interested in retrieving the exact values of surface temperature, but only in evaluating differences, we chose a mean emissivity, constant in all the MIVIS thermal channels. The value of ϵ for each pixel was estimated by assuming the mean value reported in the literature for the surface cover type corresponding to the pixel in esame [Salisbury et al., 1992].

On the basis of the above mentioned assumption, eq. (1) for each MIVIS thermal channel (i) becomes:

$$L_M^i(T_s) = L_u^i + \{\epsilon B^i(T_s) + (1 - \epsilon)L_d^i\}\tau^i \quad (2)$$

Since the studied volcanoes emit gas plumes bearing high concentration of SO_2 , the terms L_u^i , L_d^i and τ^i of eq. (2) were evaluated by means of the MODTRAN3 in the MIVIS channels (97-102) outside the SO_2 absorption band located between 8.7 and 9.4 microns [?].

Finally, we assumed that the ground temperature at each pixel is the value that yields the best weighted least square fit between the radiances calculated by using eq. (2) and the radiance values measured by MIVIS. We weighted the channel 102 less than the others because it is located near H_2O absorption band [Wolfe et al., 1988].

Application to the MIVIS data

In this work we used the MIVIS data acquired over Mt. Etna on July 23, 1994 and on July 24, 1994. Mt. Etna is an active volcano 3300 meters high, located on the east coast of Sicily (Italy). The summit craters are at about 20 Km from the sea.

Atmospheric profiles of temperature, pressure and relative humidity were measured in the area of Mt. Etna, by launching radiosondes from the sea level and from upper altitudes (Tab. 3). In addition to the profiles measured in situ, those measured at Trapani (the nearest TEMP station, 220 Km west of Mount Etna) were also collected [Boccolari et al., 1991, Pareschi

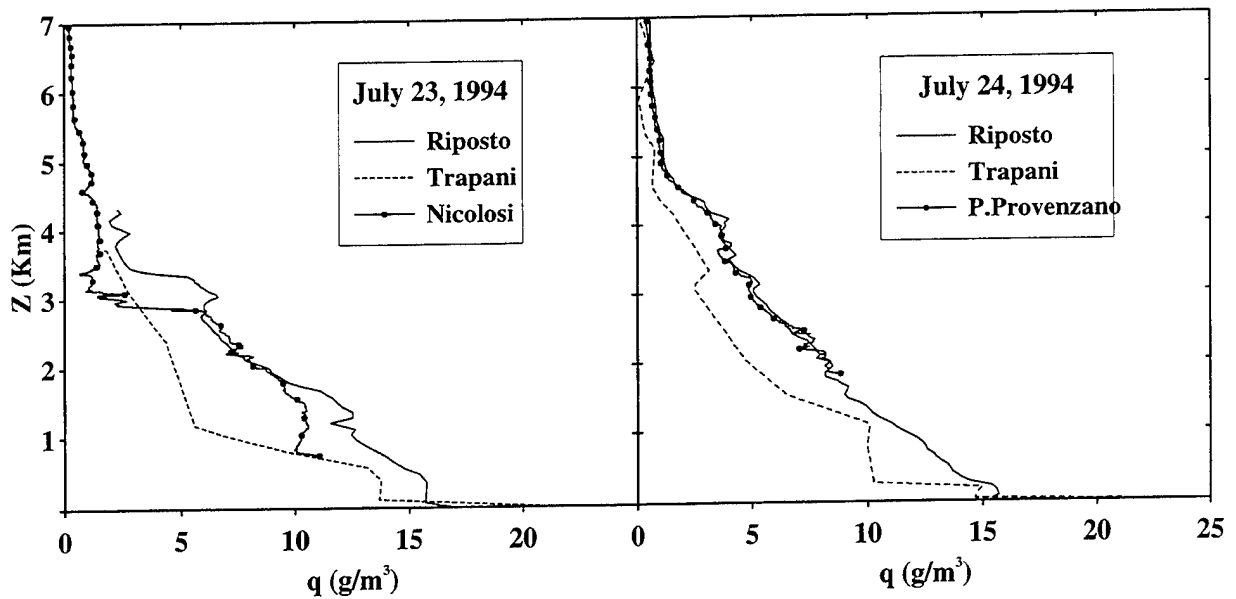


Figure 1: Altitude profiles of water vapor density (q) used for the two cases.

Day	Site	TMEC	Altitude
July 23	Riposto	09:45	Sea Level
July 23	Trapani	13:00	Sea Level
July 23	Nicolosi	09:25	730 m
July 24	Riposto	07:20	Sea Level
July 24	Trapani	13:00	Sea Level
July 24	P.Provenzano	07:50	1810 m

Table 3: Altitude profiles used for the three study cases.

p.c.]. Moreover, ground temperature measurements were carried out by using a thermal infrared thermometer (EVEREST); the measurements sites were located for July 23 at Torre del Filosofo (2910m) and for July 24 at Rifugio Sapienza (1850m).

The radiance values were retrieved from MIVIS pixel digital numbers (DNs) by means of the internal black body reference sources given for each scan-line in the thermal channels. The spectral response functions for each channel were not used since they were not available at the time of the data processing.

Several pixels (more than 30) were extracted from the calibrated images, in various sites located at differ-

ent altitudes: 3000 m, 2000 m, 1000 m and at the sea level. Other pixels were extracted in correspondence of the sites where surface temperature measurements were taken.

The surface temperature was then calculated for each pixel by using eq. (2) and the best fit procedure described in the previous section.

It was observed that the retrieved values of temperature are different depending on the atmospheric profile given in input to the MODTRAN3.

Discussion

The vertical absolute humidity profiles show relevant differences, particularly evident for those measured at Trapani (220 Km west of Etna) (Fig. 1).

Considering that water vapor is the most important absorber in the TIR spectral region, for each profile the equivalent sea level water vapor amount (w) was extracted by using the atmospheric column between each site (0,1000, 2000, 3000 m a.s.l.) and the MIVIS (5500 m a.s.l.).

In order to evaluate the influence of the water vapour content on the MIVIS retrieved T_s when using different profiles, we computed for each pixel the quantities:

$$\Delta T_s = T_{s,R} - T_{s,P} \quad ; \quad \Delta w = w_R - w_P \quad (3)$$

where the profile measured at Riposto (sea level) was

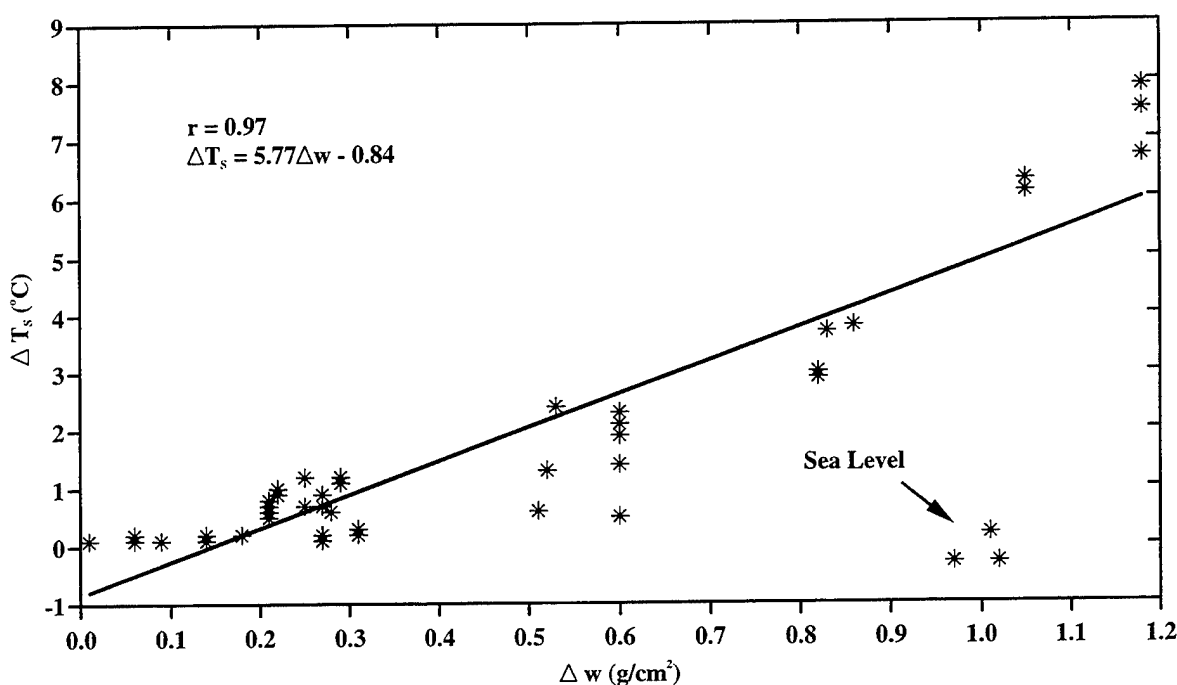


Figure 2: Differences in estimate temperatures vs Differences in water vapor amount (see text)

taken as a reference. In the equations w_R is the water vapour content of the reference profile; $T_{s,R}$ is the corresponding MIVIS retrieved surface temperature; $T_{s,P}$ and w_P are the values obtained using either the profiles of Trapani or those measured at upper altitudes.

Plotting the values of ΔT_s versus Δw (Fig. 2) it can be observed that, excluding a cluster of few points, there is a correlation between ΔT_s and Δw . The linear correlation coefficient is $r = 0.97$ (51 points) and the linear regression is $\Delta T_s = 5.77\Delta w - 0.84$.

Increasing values of Δw produce increasing values of ΔT_s ; therefore profiles that show high differences of water vapor content produce significant differences in the estimated T_s .

Due to the vertical distribution of water vapor, usually Δw is low for sites at upper altitudes and high for sites at lower altitudes.

For pixels at low altitudes, when the Trapani profile is used as input to MODTRAN3, the high values of Δw produce high differences in the T_s estimates, that in some cases are more than 7°C .

Viceversa, for pixels at higher altitudes, all the measured profiles generally show low values of Δw ; in these cases, the topographic effect does not have a significative influence on the T_s estimates, giving a ΔT_s less than 1°C .

Previous study [Realmuto et al., 1994] based on

TIMS data acquired over the same area highlights a small water vapour influence on T_s estimate and therefore on SO_2 abundance estimation. That case is in agreement with our work, in fact the test site was at about 3000m of altitude and the water vapor uncertainty can be neglected.

Fig. 2 show a cluster of points that do not follow the regression; the cluster is composed by sites at the sea level. We explain these cases as points that hold a very high water vapor content near the ground that damps the values of ΔT_s . This effect is under investigation.

It should be considered that ΔT_s is also function of the ground emissivity. Since during the "SICILIA 94" campaign no ground emissivity measurements were taken in the field. In this work were used mean values reported in literature [Salisbury et al., 1992]. New evaluations are foreseen using spectral emissivity [Campolieti et al., 1991, Pugnaghi et al., 1994] measured in laboratory on samples collected during the field activity.

Surface temperature readings using EVEREST IR thermometer and MIVIS estimate differ for some degrees. At this stage it can be considered a good result taking into account: the very few measurements; emissivity uncertainty; pixel heterogeneity; MIVIS exact spectral response functions lack. The surface temper-

atures taken in situ with the thermal infrared thermometer are probably very different from the real kinetic temperatures of the ground, because the instrument uses an emissivity set to 0.99, which is different from the real emissivity of the surface coverage. This means that the method used for the surface temperature measurement is not suitable as ground truth for the T_s estimates calculated by means of MIVIS data and MODTRAN3 atmospheric modeling.

Conclusions

Results show the importance of local, simultaneous atmospheric altitude profiles when surface temperature is estimated by remote sensing image data. This effect reflects on volcanic plume investigation (e.g. SO_2 estimate).

In the studied cases the measured water vapour profiles show similar trends above 3000 m; this means that the topographic effect is not very important for pixels located at high altitudes. Consequently, for these pixels, it is not necessary to use local profiles as input to the atmospheric modeling code. On the other hand, when ground physical properties are to be calculated from remote sensing images taken over mountainous regions, it is necessary to take into account the high variability of the lower part of the atmospheric profiles, generally due to different causes (topographic gradient, proximity of the sea). This effect can produce high uncertainty on water vapor content. The water vapor differences seen could be greater depending on time. In fact during the central hours of the day breeze and convective air motions, due to the ground heating, could occur [Stull, 1991, Oke, 1987].

In further applications with MIVIS data aimed to the characterization of the emitted volcanic plume, other parameter such as the surface spectral emissivity and the volcanic plume thickness and altitude will be analysed in detail by using both field data and atmospheric modeling.

References

Bianchi R., Marino C.M., "CNR LARA project, Italy: MIVIS/MIDAS environmental airborne hyperspectral remote sensing system", Proc. of the International Airborne remote Sensing Conference and Exhibition, Strasbourg, France, 12-15 September, 1994, III-613-619.

Boccolari M., Frontero P., Lombroso L., Morelli S., Pugnaghi S., Santangelo R.,

"Strutture dell'Osservatorio Geofisico di Modena a supporto di campagne di misura sul clima mediterraneo", Bollettino Geofisico, Anno XIV n.1., 1991.

Campolieti D., Pugnaghi S., Teggi S., "Temperatura superficiale da satellite e in laboratorio", Atti del Convegno Monitorare L'Ambiente Agrario E Forestale, Accademia dei Georgofili Ce.S.I.A., CNR di Sassari e Firenze, Porto Conte (SS) 4-6 Giugno 1991, pp. 619-633., 1991.

Oke T.R., "Boundary Layer Climates", Routledge, 1987.

Pugnaghi S., Teggi S., Bogliolo M.P., Buongiorno M.F., Geneselli F. "Misure di emissività di campioni rocciosi per validazioni nell'infrarosso termico", VI Convegno Nazionale A.I.T., Roma 1-4 Marzo, 1994.

Realmuto V.J., Abrams M.J., Buongiorno M.F., "The use of multispectral thermal infrared image data to estimate the sulfur dioxide flux from volcanoes: A case study from Mount Etna, Sicily, July 29, 1986, J. Geophys. Res., 99, 481-488, 1994.

Salisbury J.W., D'Aria D.M., "Emissivity of terrestrial materials in the 8-14 μ m atmospheric window", Rem. Sens. of Env., 42, 2, 83-106, 1992.

Stull R.B., "An Introduction to Boundary Layer Meteorology", Kluwer Academic Pub., 1991.

Teggi S., Pugnaghi S., Bogliolo M.P., Buongiorno M.F., Geneselli F., Salvi S., Caltabiano T., Abrams M.J., Pieri D.C., Realmuto V.J. "Misure radiometriche al suolo e profili verticali atmosferici per studi di aree vulcaniche: Dati acquisiti su Etna e Vulcano in concomitanza con la campagna di telerilevamento aereo "SICILIA 1994" del CNR (Progetto LARA)", 13mo Convegno Nazionale GNGTS, Roma 28-30, Nov. 1994.

Wolfe W.L., Zissis J. "The Infrared Handbook", Off. of Naval Research Dep. Navy, 1988.

Production of Vibrationally and Rotationally Excited NO in the Nighttime Terrestrial Thermosphere

R.D. Sharma¹, V.A. Kharchenko², Y. Sun²,
H. Dothe³, F. von Esse³ and A. Dalgarno²

- 1) Geophysics Directorate (GPOS), Phillips Laboratory, Hanscom AFB, MA 01731.
- 2) Harvard Smithsonian Center for Astrophysics, 60 Garden Street, Cambridge, MA 02138.
- 3) Mei Technology Corporation, 1050 Waltham Street, Lexington, MA 02173.

Abstract

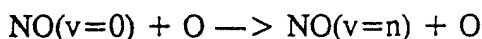
The rate of production of vibrationally and rotationally excited NO in the quiescent nighttime terrestrial thermosphere due to inelastic and reactive processes is calculated. The inelastic processes include the collisions of ambient NO with atomic O producing vibrationally excited, mostly $v=1$, rotationally thermalized NO. The reactive process is predominantly the reaction of ambient $N(^4S)$ with O_2 , producing vibrationally and highly rotationally excited NO. Both processes, chemical and inelastic, show a strong dependence on the geophysical parameters. The calculated emission is in good agreement with the rotationally thermal, as well as rotationally non-thermal, radiance in the fundamental vibration-rotation band of NO around $5.3 \mu m$ measured by the space shuttle experiment CIRRIS-1A. It is shown that chemically produced NO is a significant cooling mechanism at high altitudes even at night--a mechanism hitherto ignored in the calculations of the energy budget of the thermosphere.

NO Variability and Need to Construct Models

To understand the large spatial and temporal variability of NO, we need to model the processes which lead to production and loss of NO, with special emphasis on the population of vibrational, rotational, and spin-state levels. Because of the large value of the Einstein coefficient ($A_{1 \rightarrow 0} = 13.2 \text{ s}^{-1}$) for emitting $5.3 \mu m$ photons, these processes are expected to impact the heat budget of the thermosphere.

Mechanisms producing emission in the fundamental vibration-rotation band of NO near 5.3 μm

- (i) Inelastic collisions of NO with O



Produces rotationally thermalized NO mostly in vibrational level $v=1$.

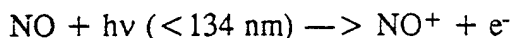
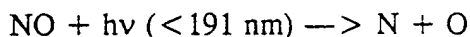
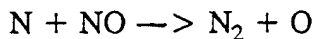
- (ii) $\text{N}(^2\text{D}) + \text{O}_2 \longrightarrow \text{NO}(v=n) + \text{O}$

Laboratory measurements at low temperature show that this reaction produces rotationally thermal NO with very high vibrational excitation, $v \leq 12$ levels have significant populations. High vibrational excitation sets it apart from process (i).

- (iii) $\text{N}_\text{f}(^4\text{S}) + \text{O}_2 \longrightarrow \text{NO}^*(v=n) + \text{O}$

Only fast N atoms ($E_\text{r} \geq 0.3\text{eV}$) can react, because of the barrier to the reaction. The reaction produces vibrationally excited and highly rotational excited NO. It has been identified as the source of bandheads in the observed fundamental V-R spectrum of NO. High rotational excitation sets this process apart from processes (i) and (ii).

Processes Leading to the Loss of NO



These processes have not been shown to depend strongly on the internal degrees of freedom.

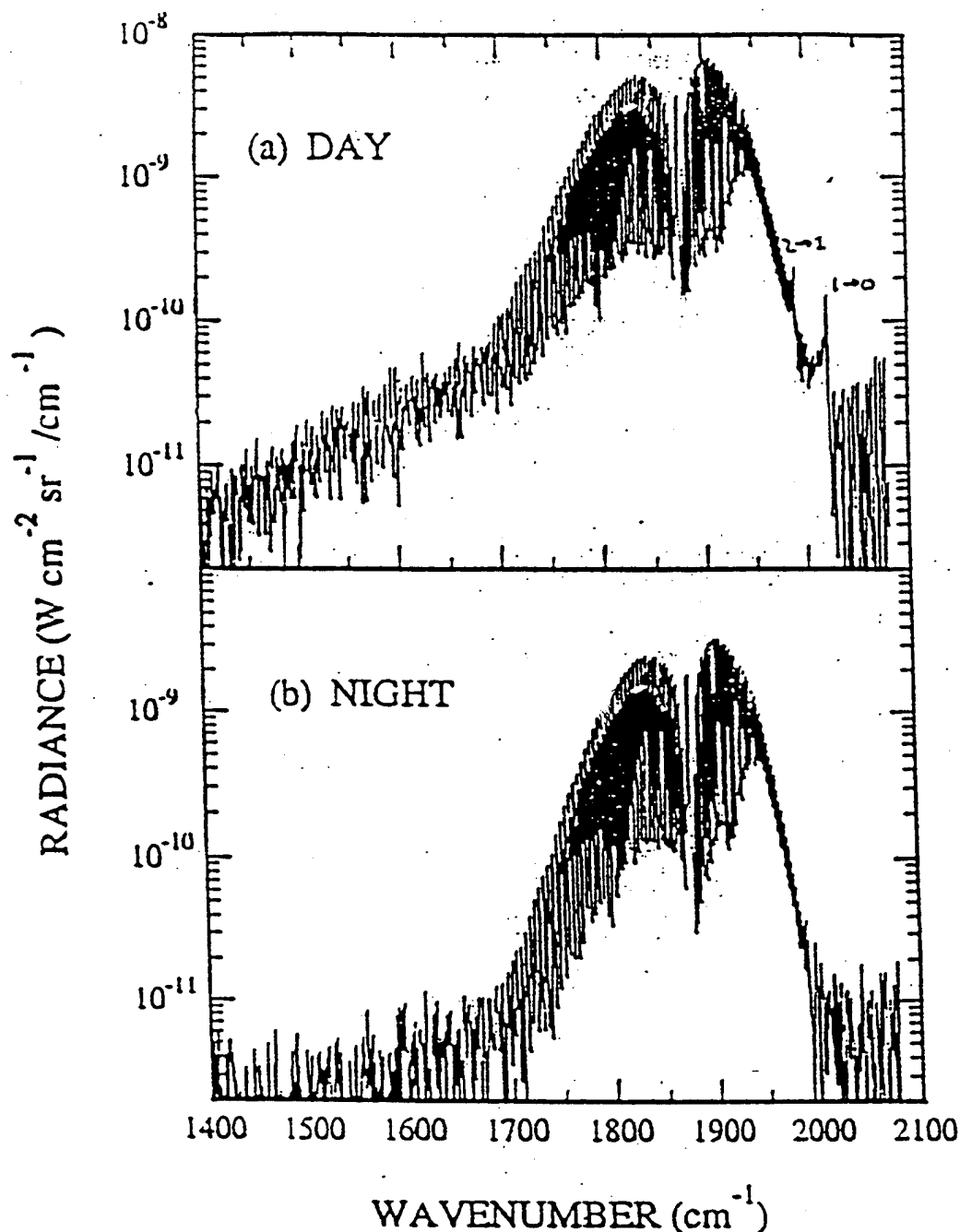
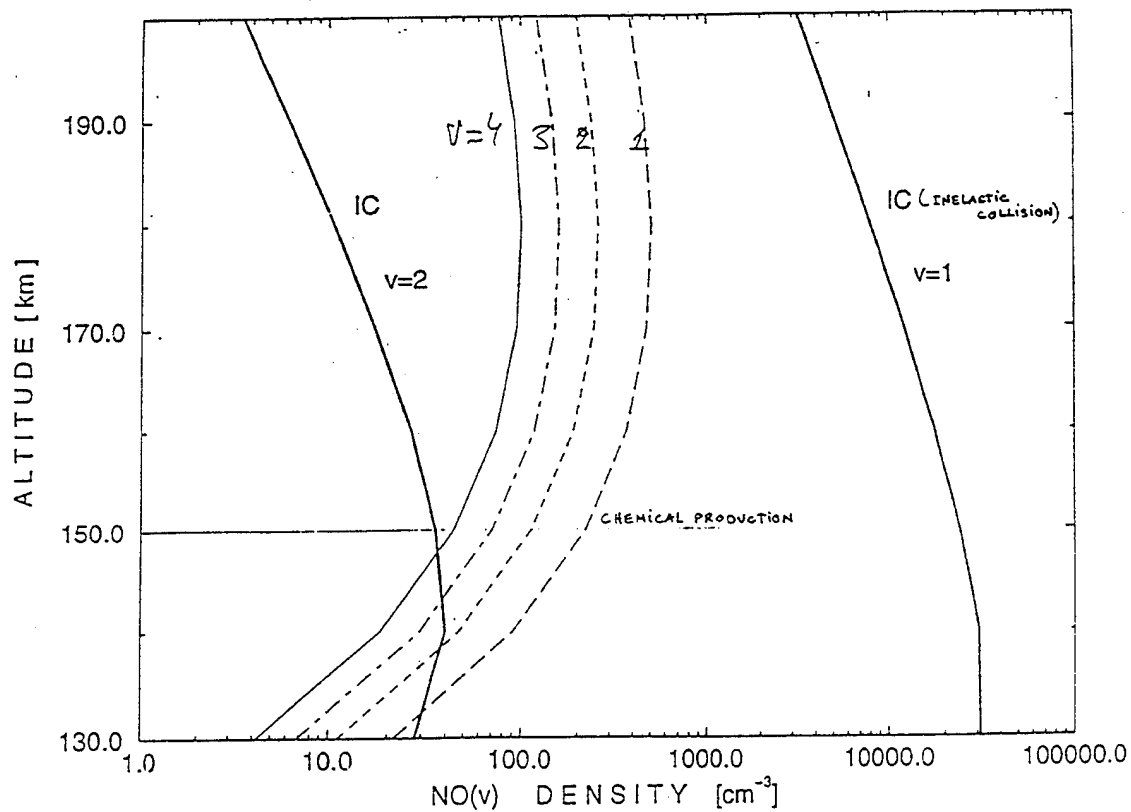
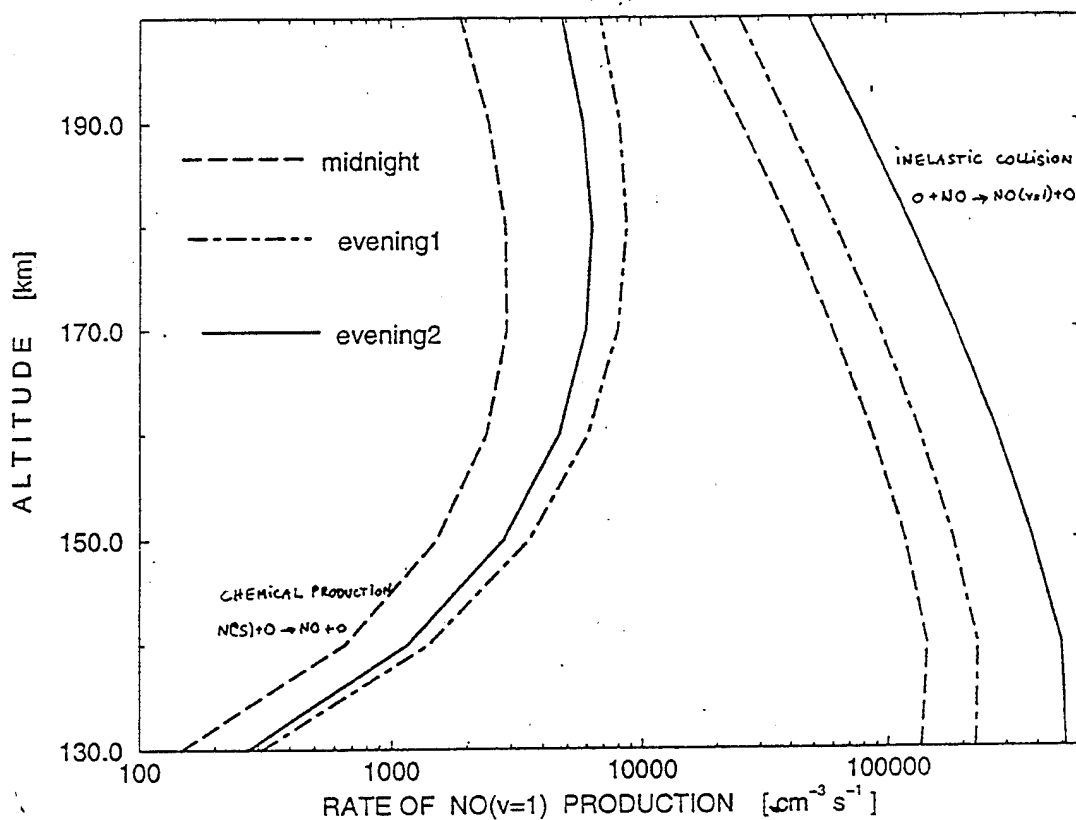
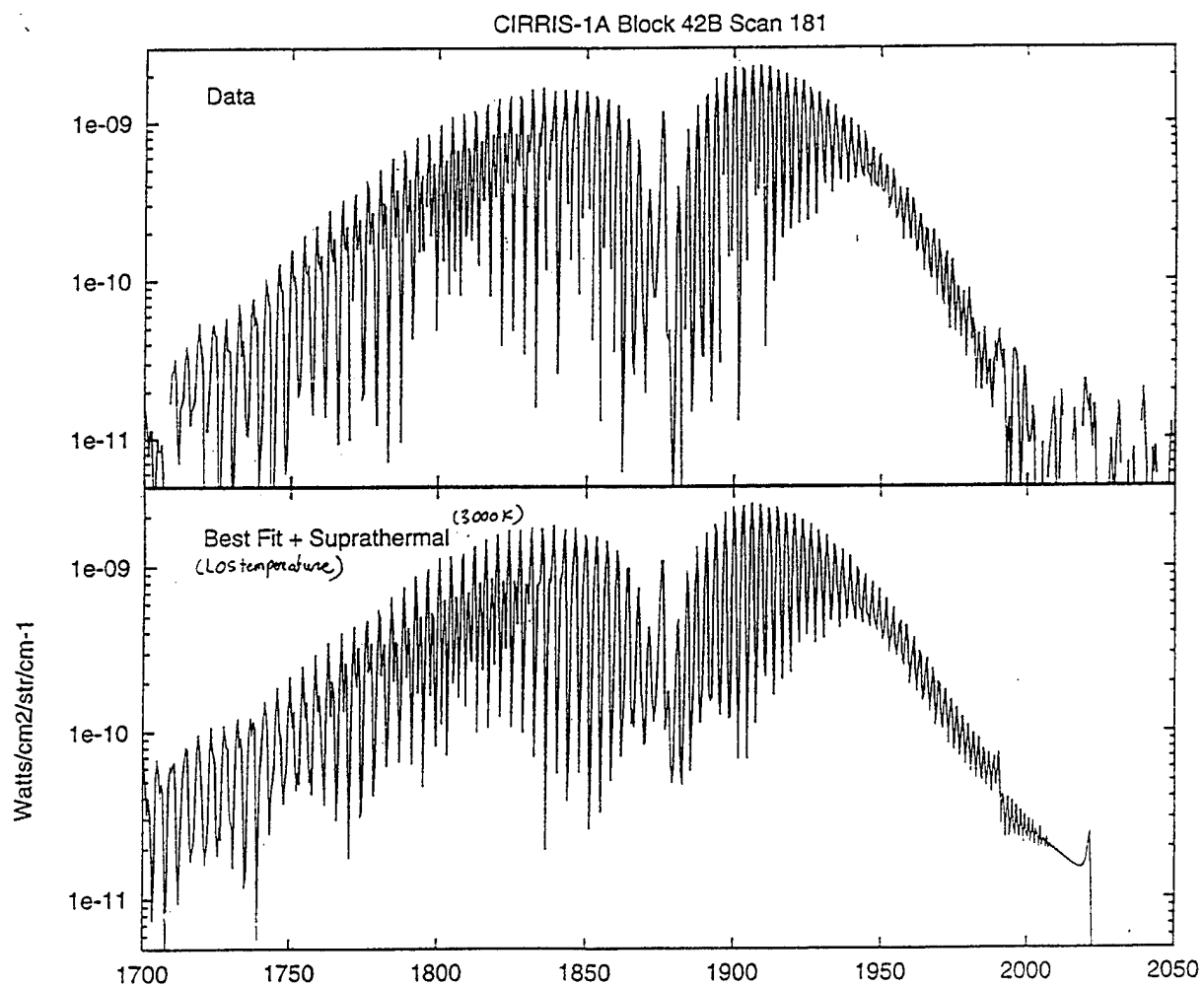
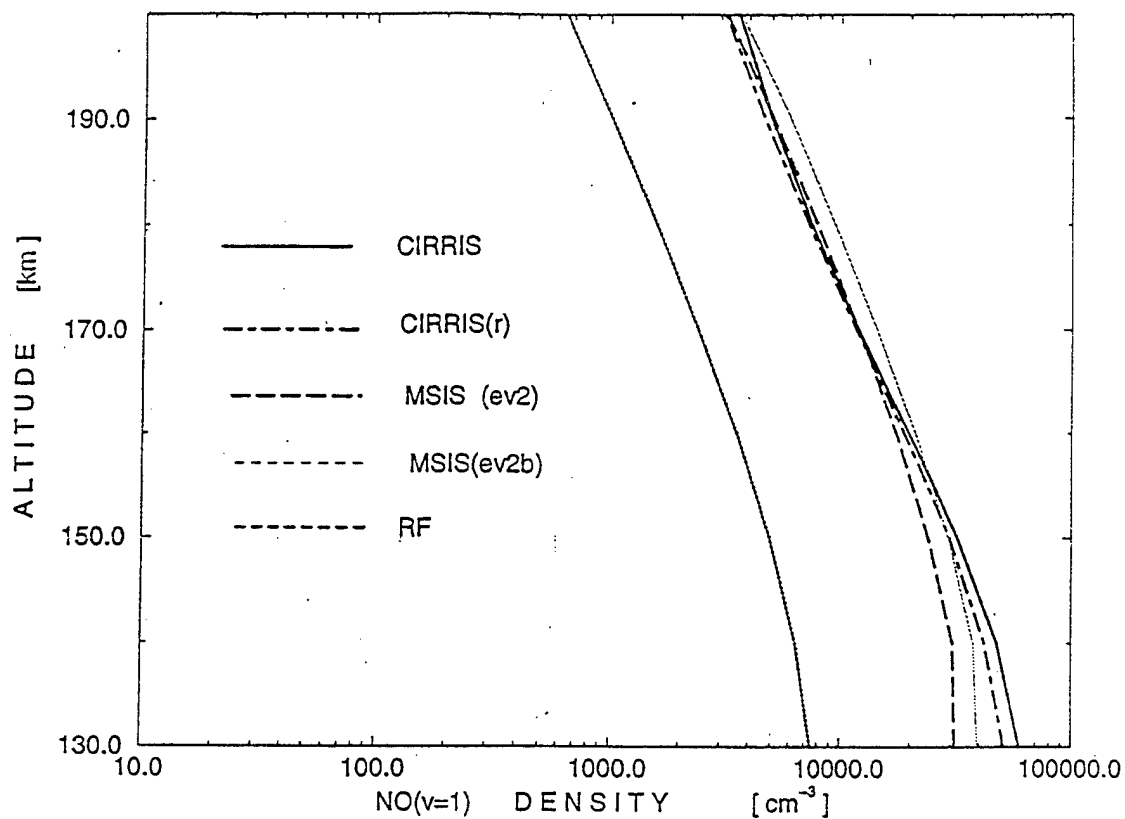


Figure 1. (a) Averaged daytime NO emission spectrum obtained using the 4.8-13 μm passband filter, plotted on a logarithmic vertical scale. Nine scans were averaged, with 127-128 km tangent height, 45° - 47° solar zenith angle, and 39° - 46° N latitude range. The NO R -branch band heads and high- J P -branch radiance are readily identifiable, as well as a series of lines due to CO emission in the 2000-2080 cm^{-1} region. (b) Averaged nighttime NO spectrum obtained using the open filter (2.5-25 μm). Eight scans were averaged, with 139-141 km tangent height, 111° - 118° solar zenith angle, and 36° - 41° S latitude range.





NO(v) Densities in the Lower Thermosphere

S.J. Lipson, W.A.M. Blumberg,
R.B. Lockwood, J.R. Lowell, and R.M. Nadile
Phillips Laboratory Geophysics Directorate
Hanscom AFB, MA

P.S. Armstrong and J.A. Dodd
Stewart Radiance Laboratory, Bedford, MA

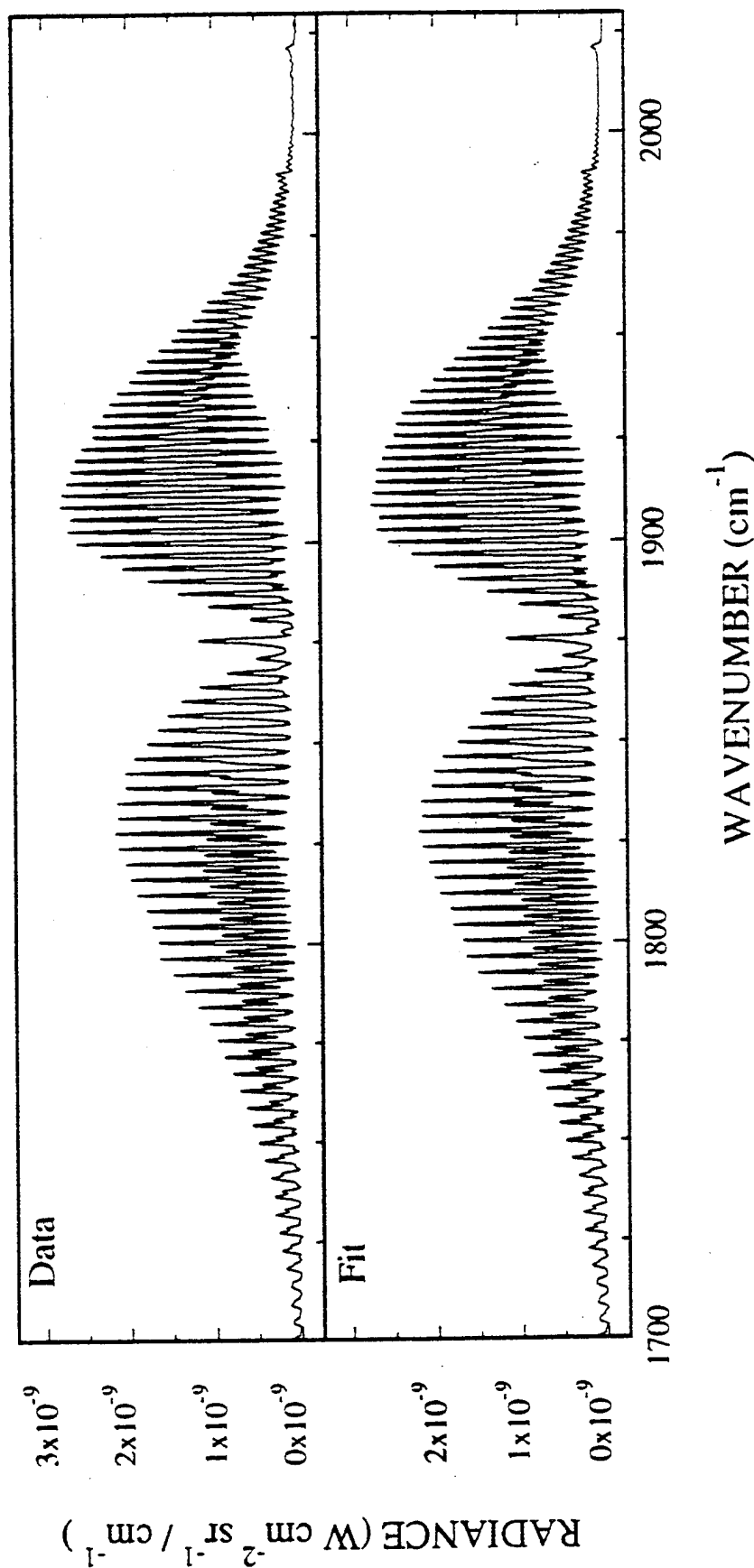
18th Annual Conference on Atmospheric Transmission Models
PL Geophysics Directorate, 8 June 1995
Supported by AFOSR and BMDO

Remote Sensing Using NO(v) IR Spectra

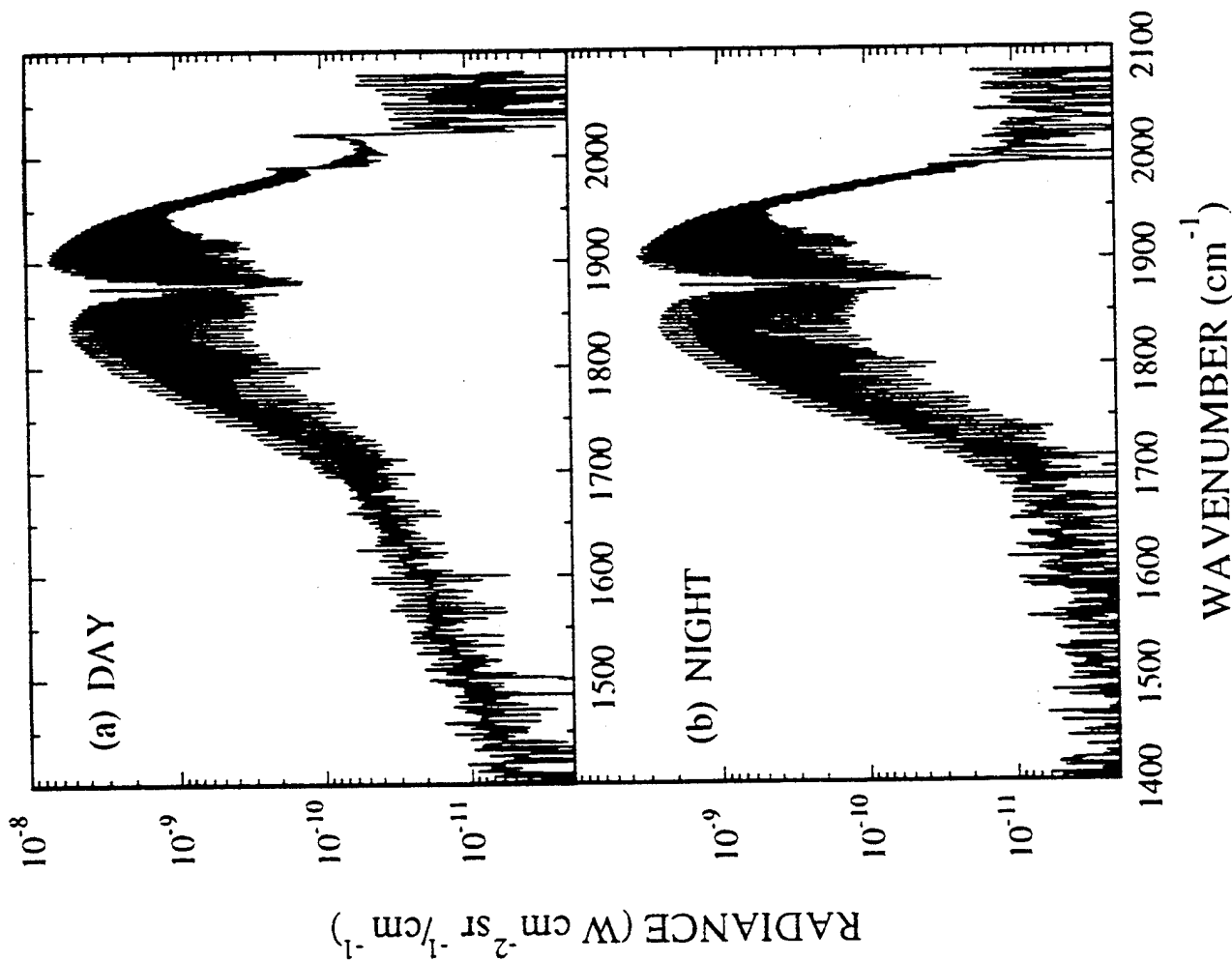
- Importance of NO in the thermosphere
 - Chemical/molecular energy conversion
 - Radiative cooling and temperature structure
 - Highly variable density stresses models
- Results obtained from CIRRIS 1A infrared data
 - NO(v) vibrational and spin-orbit populations
 - Dual-temperature rotational distributions
 - Nonequilibrium internal degrees of freedom
- Apply kinetic model to derived number densities
 - Determine dominant kinetic processes
 - Identify key unknowns to measure in lab
- Remote sensing of IR-inactive species
 - Obtain NO(v=0) without assuming O density
 - May then indirectly derive O density
 - Fast N atoms: precursor of hot NO

CIRIS 1A EXPERIMENT

- High S/N earthlimb spectra recorded by Shuttle-based Michelson interferometer (1 cm^{-1} resolution)
- Nitric oxide ($^2\Pi_{\Omega}$, $\Omega = 1/2, 3/2$) $\Delta v = 1$ emissions



Daytime and Nighttime Spectra

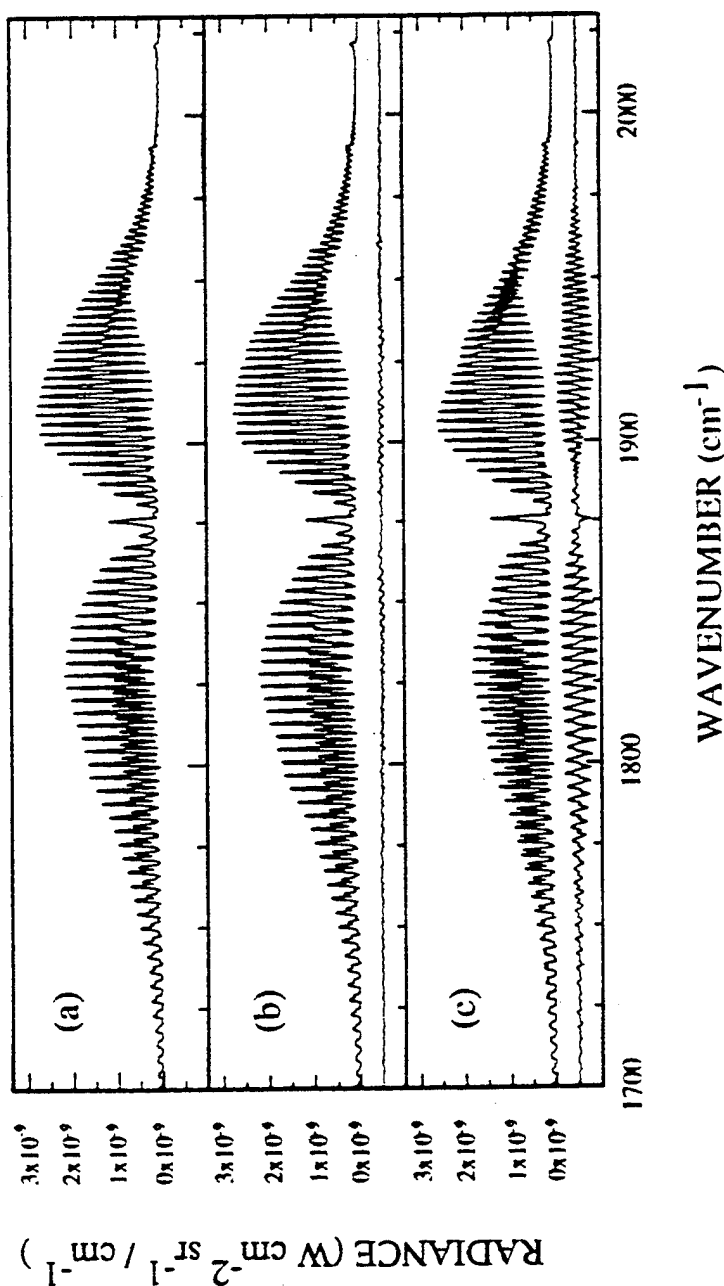


- Daytime
- 9 scan average
- 127-128 km
- SZA 45-47
- Lat 39-46 N
- High-J NO clearly present

- Nighttime
- 8 scan average
- 139-141 km
- SZA 111-118
- Lat 36-41 S

Synthetic Spectral Fitting

- Nonequilibrium population distributions
- Dual Boltzmann rotational approximation
- Subthermal spin-orbit populations
- Accuracy required for $\text{NO}(v>1)$

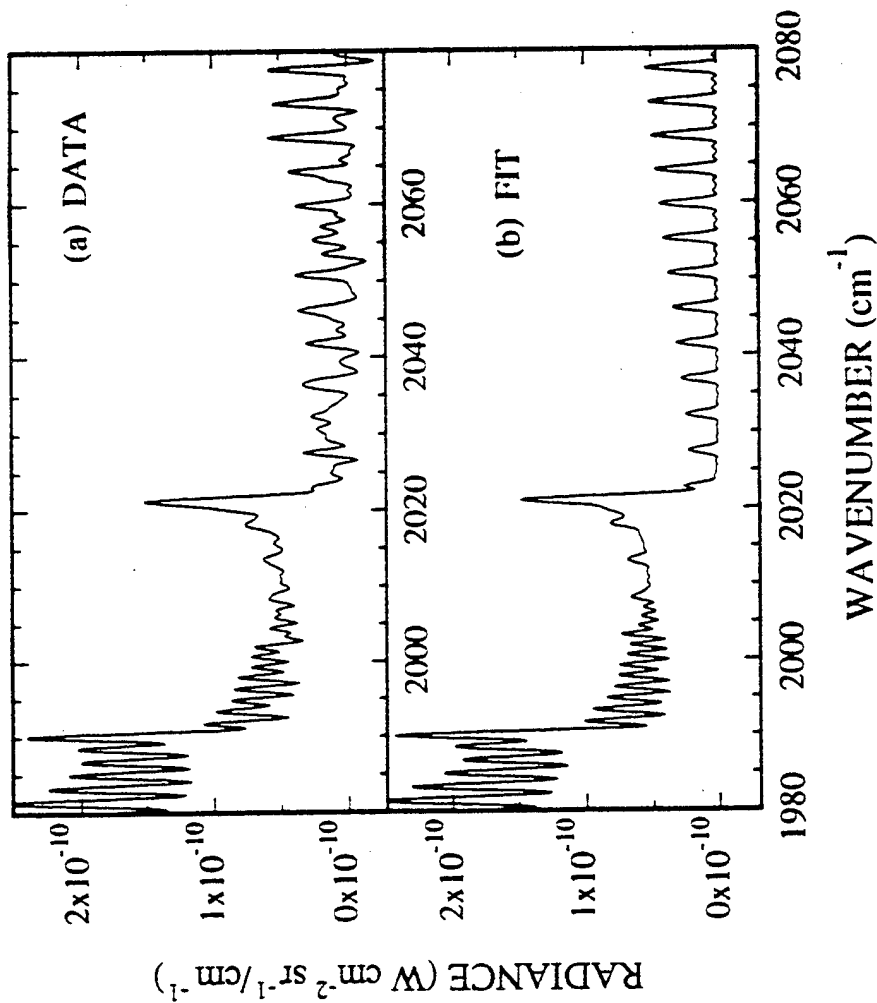


NLTE Rotation in NO and CO

- Band heads are clear in NO in dayglow and aurora
- Very high rotation in NO throughout dayglow data
- Reduced nonthermal rotation in NO in nighttime
- Window radiance from high-J P-branch is key result
- Vibrational distributions shown for dayglow and aurora
- Day and night rotational distributions and ratio shown
- Daytime effective rotational temperatures 600, 5000 K
- Nighttime effective rotational temperatures 600, 3000 K
- Elevated CO rotational temperature, both day and night
- Contributes underlying radiance to NO band head region
- CO radiance decreases at night less than NO does
- Collisional effects in CO proposed by Sharma

NO and CO Rotational Excitation

- Daytime spectrum showing NO($v=1,2$) band heads
- Elevated rotational temperature also seen in CO



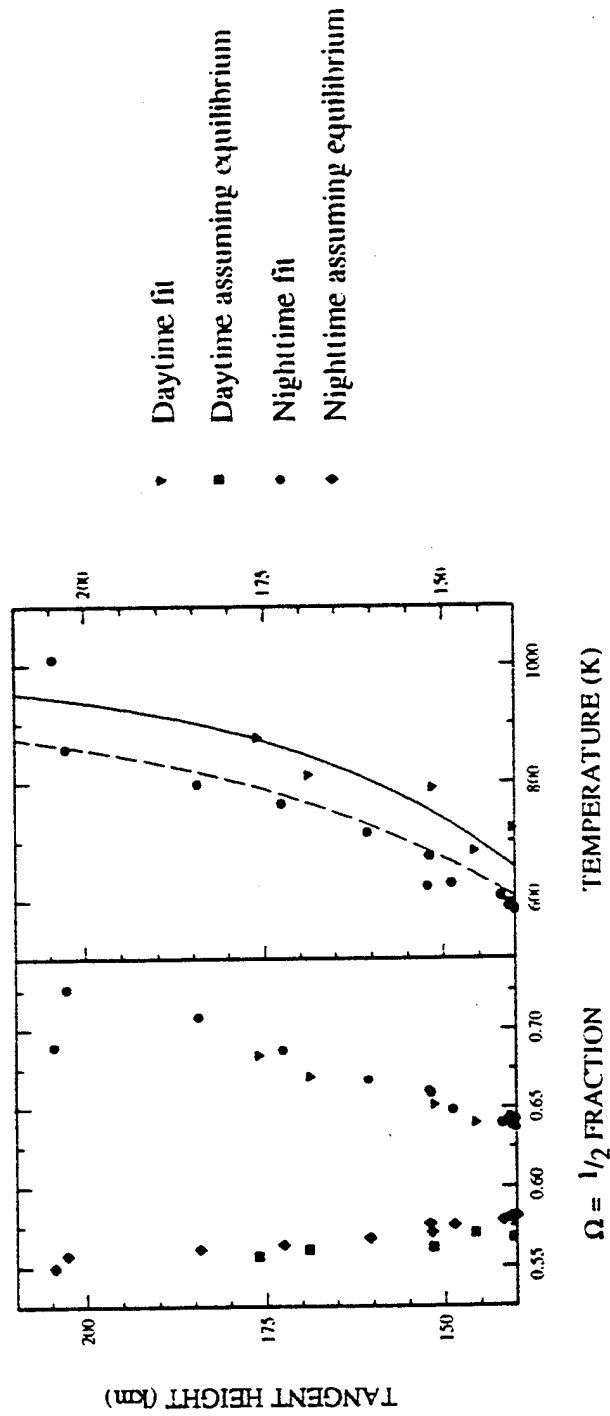
- Rotationally hot NO results from chemical formation
- Rotationally hot CO results from radiative transfer

Subthermal Spin-Orbit Distributions in NO

- Proposed spin-orbit preference in collisional upumping by O atoms, main source of NO($v=1$)
- Radiation, the primary loss mechanism for NO($v=1$), does not induce spin-orbit preference
- Collisional relaxation occurs at lower rate at high altitudes, explaining altitude dependence
- Chemical production has diurnal variation not observed in sublevel distributions
- Spin-orbit distributions depend only on altitude, not latitude or time of day

Thermal Temperature and Spin-Orbit Fractions

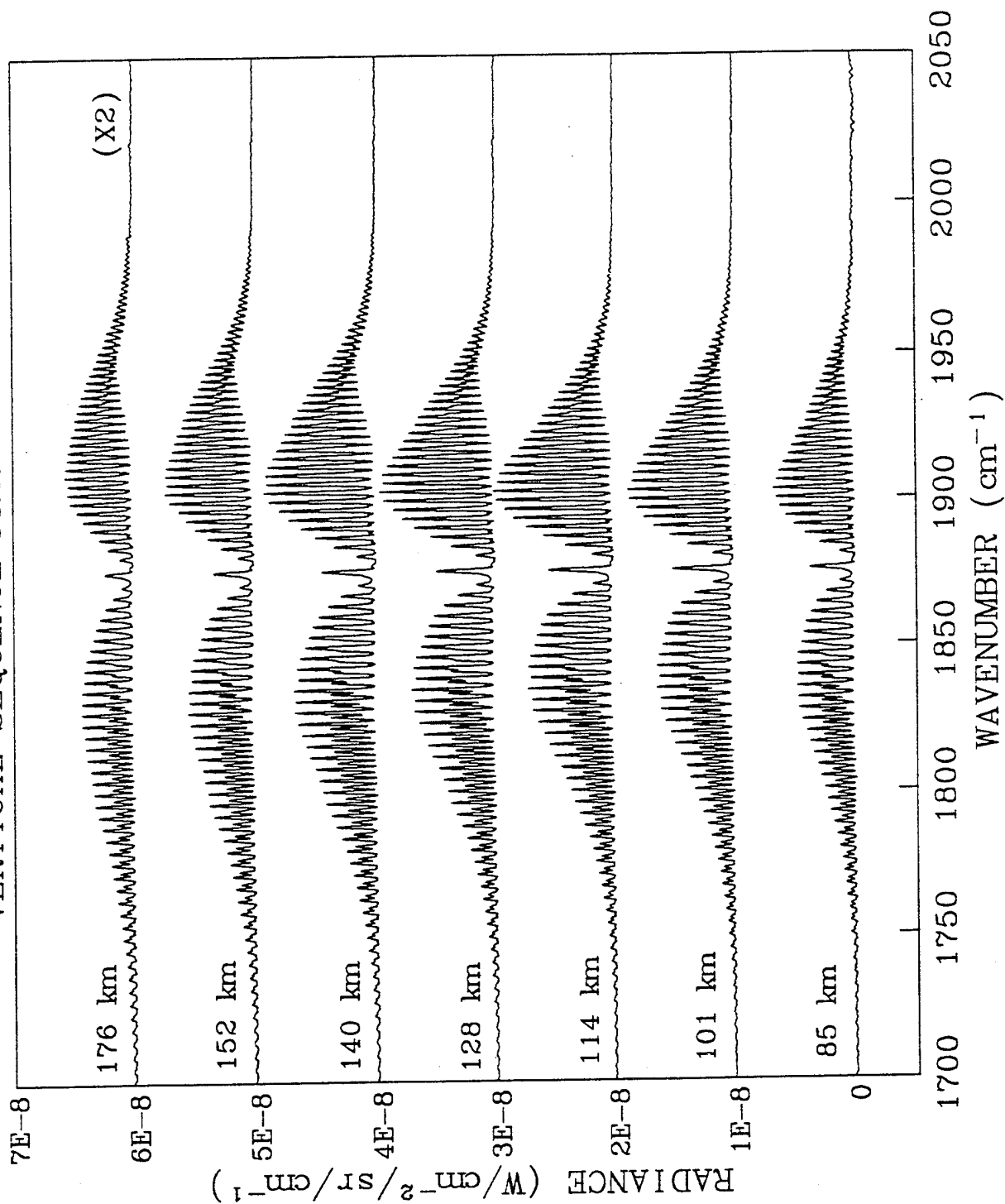
- Rotational temperature rises to 900 K with altitude
- Spin-orbit effective temperature falls to 200 K
- Diurnal temperature variation consistent with model
- Consistent with large set of low resolution data



Vertical Sequence of CIRRS 1A Spectra

- High resolution dayglow spectra required
 - Resolution needed for $\text{NO}(v>1)$ densities
 - Vibrational excitation evident in daytime
 - Spin-orbit sublevels accurately treated
- Near-consecutive sequence from Block 12a
 - Tangent height 85-176 km, about 15 km steps
 - Elapsed time about 100 s (10 s per scan)
 - Latitude 64° N, longitude 103° - 123° E
 - Solar zenith angle range 56 - 63°
- Qualitative features
 - Radiance falls at top and bottom of range
 - Highest altitude scan shown multiplied by 2
 - Rotational temperature increases with altitude

CIRRIS 1A NITRIC OXIDE DAYGLOW SPECTRA VERTICAL SEQUENCE FROM BLOCK 12A



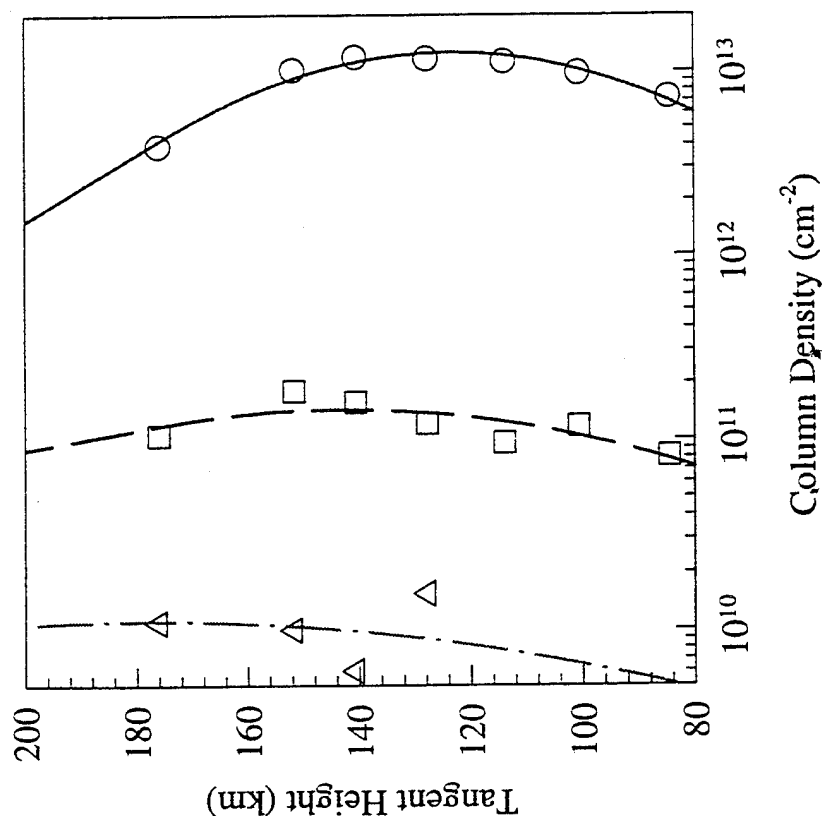
NO(v) Density Profiles

- Volumetric number densities determined
 - Derived from least-squares fits to spectra
 - Vertical profile smoothed by polynomial fit
 - Inverted using onion-peel algorithm
 - Sensitivity limit at about $v=3$
- Rotationally excited populations
 - High effective vibrational temperature
 - Formation and radiative cascade dominate
 - Near radiative equilibrium at high altitude
 - Less vibrational excitation at low altitude
- Rotationally thermalized populations
 - Low effective vibrational temperature
 - Collisional uppumping and radiation dominate
 - Thermal populations persist to lower altitude
 - Populations coupled to low v and $v=0$ levels

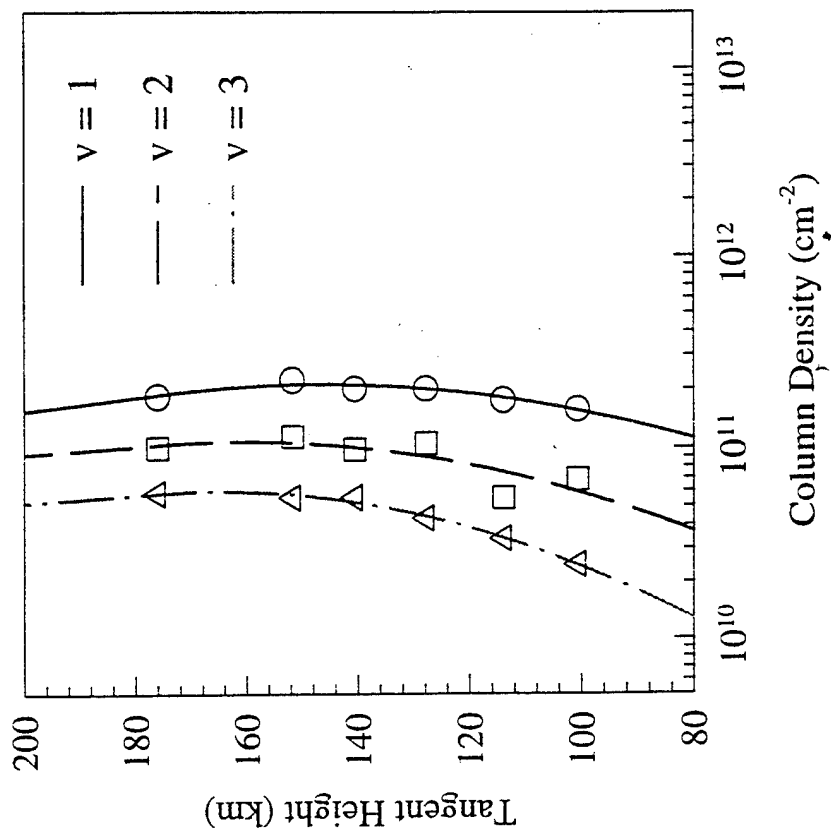
NO ($v=1-3$) Column Densities

- Points indicate spectral fits to CIRRIS 1A dayglow data
- Lines are polynomial fits through data points

Rotationally Thermal NO Column Densities



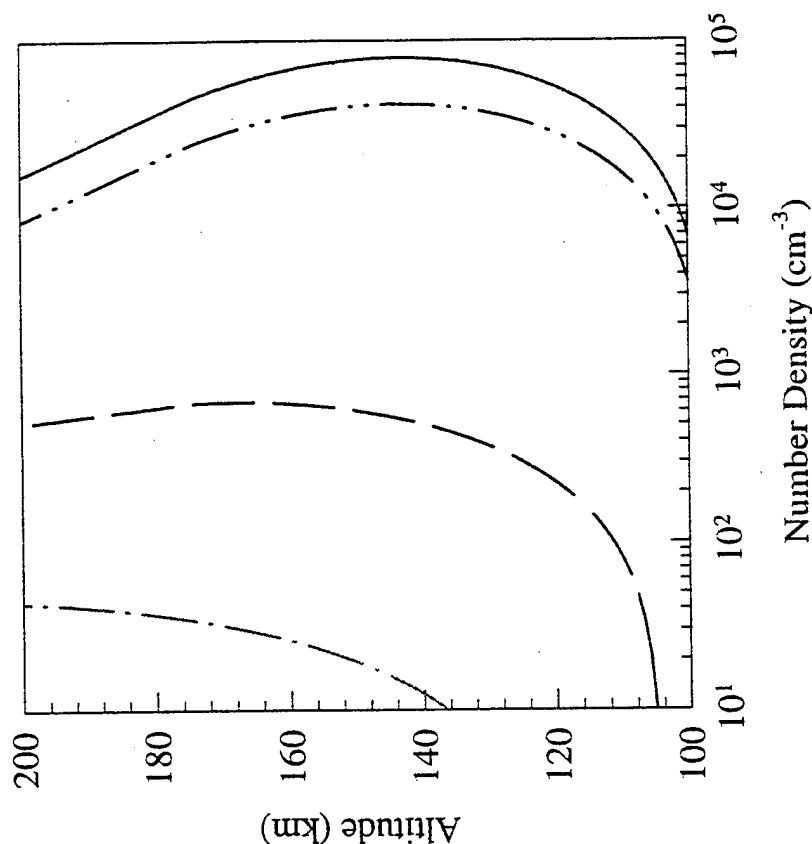
Rotationally Excited NO Column Densities



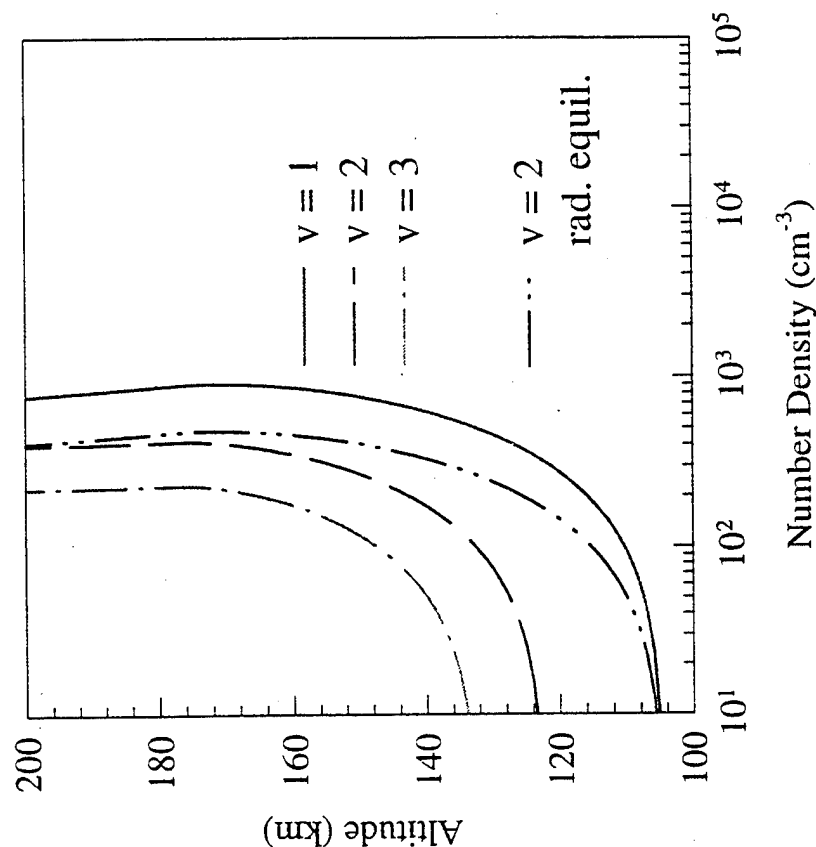
NO ($v=1-3$) Number Densities

- Based on vertical sequence of CIRRIS 1A dayglow data
- Obtained by numerically inverting column density curves

Rotationally Thermal NO Number Densities



Rotationally Excited NO Number Densities



NO(v) Density Model

- Determine nonequilibrium NO(v) populations
 - Invert to get volumetric NO(v) number densities
 - Both rotationally hot and thermal for each v
- Model important kinetic mechanisms
 - Vibrational uppumping and relaxation by O
 - Radiative and chemical production and loss
- Derive an estimate of NO(v=0) density
 - Important due to its emission and radiative cooling
 - New type of probe of highly variable NO density
- Identify key uncertainties
 - Uppumping/relaxation rates for NO(v>1) by O
 - Gives direction for future laboratory work
- Does not rely on assumed temperature or O density
 - Temperature obtained from rotational distribution
 - Can extract O density if certain rates are known

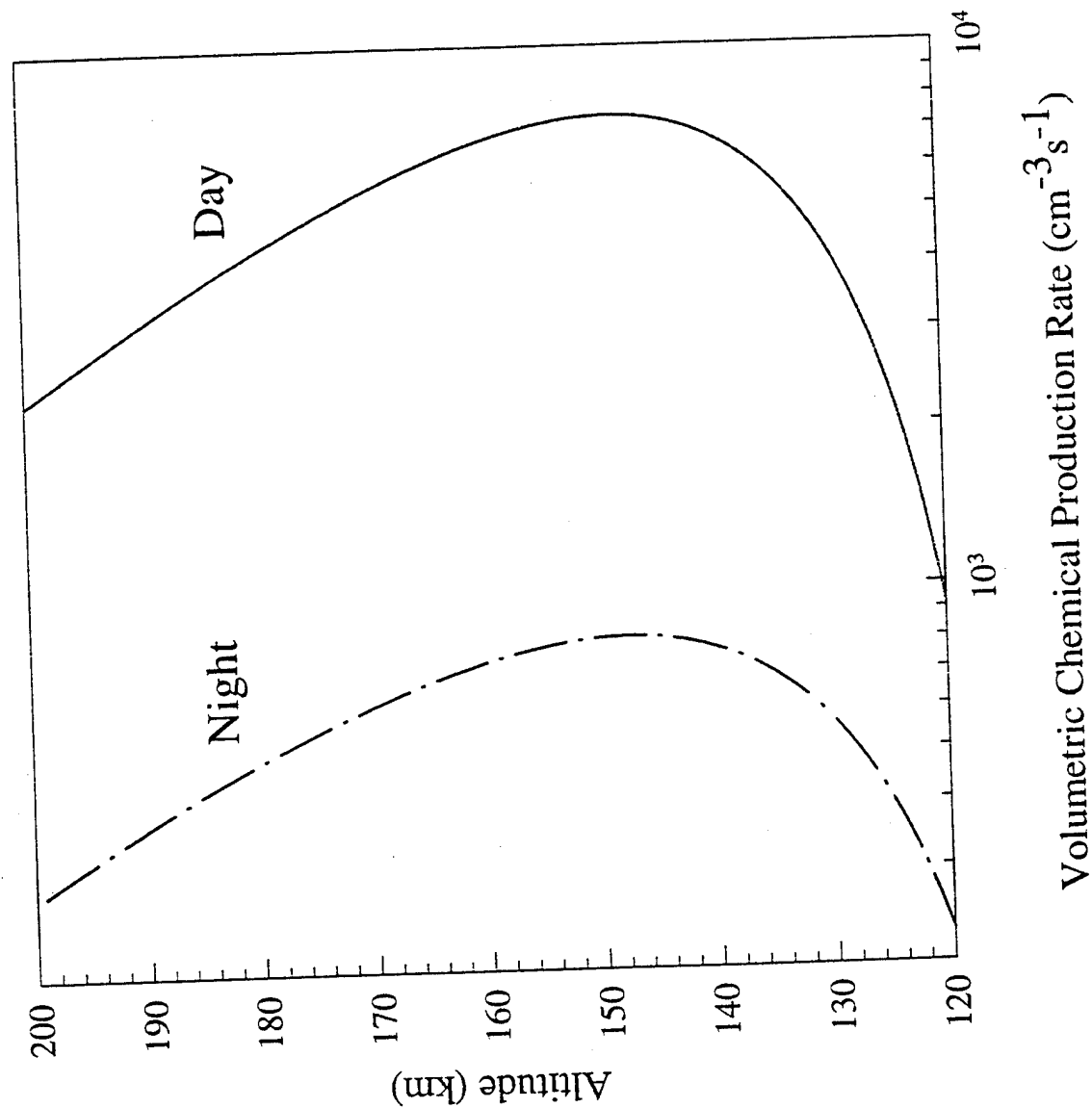
NO(v) Excitation/Production Terms

- Major contributions:
 - Collisional vibrational excitation (upumping)
 - Radiative cascade (especially for hot NO)
 - Cascade by collisional vibrational relaxation
 - Chemical formation via $\text{N} + \text{O}_2 \longrightarrow \text{NO} + \text{O}$
- Minor contributions:
 - Solar uv excitation, mainly from $v = 0$
 - Infrared excitation, mainly from $v - 1$
 - Rotational relaxation of hot NO to thermal
 - Transport (diffusion)

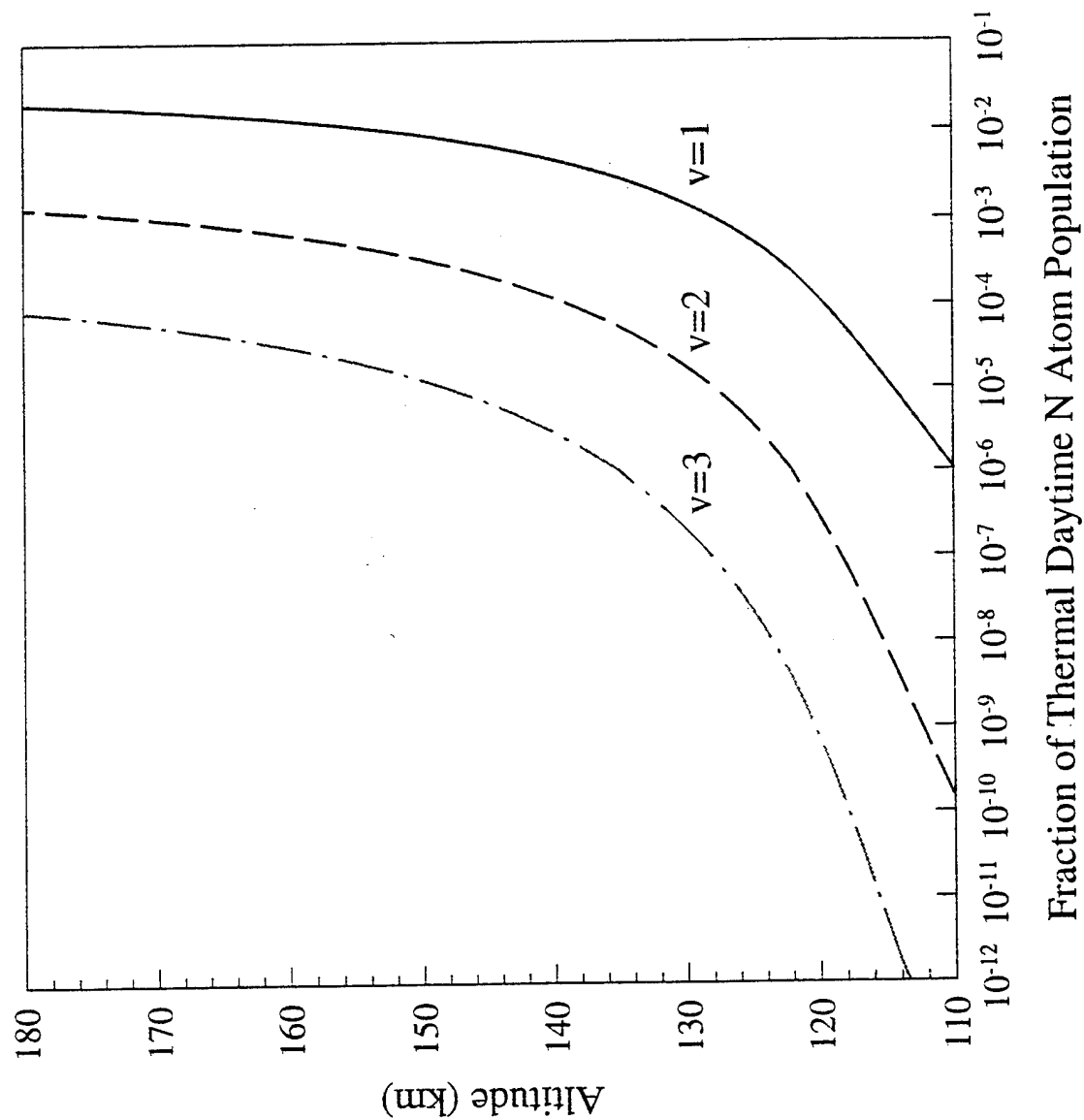
NO(v) Relaxation/Loss Terms

- Major contributions:
 - Infrared emission (mainly fundamental band)
 - Collisional vibrational relaxation (mainly by O)
 - Collisional vibrational excitation (upumping)
- Minor contributions:
 - Removal by ir or uv absorption
 - Chemical loss via $\text{NO} + \text{N} \rightarrow \text{N}_2 + \text{O}$
 - Rotational relaxation (applies to hot NO)
 - Transport (diffusion)

Nighttime and Daytime Production of NO From $N(^4S) + O_2$ Based on Maxwell-Boltzmann Distributions at MSIS Temperatures



N Atom Fractions With Energy Required to Produce NO* (1-3) in a Maxwell-Boltzmann Distribution at the MSIS Temperature



Steady-State Rate Equation Model of NO(v) Densities

- List source and sink terms for each v-level

$$\begin{aligned} d[\text{NO}(v)]/dt = 0 = & A_{v+1}[\text{NO}(v+1)] - A_v[\text{NO}(v)] \\ & + U_{v-1}[\text{NO}(v-1)][\text{O}] - U_v[\text{NO}(v)][\text{O}] \\ & + D_{v+1}[\text{NO}(v+1)][\text{O}] - D_v[\text{NO}(v)][\text{O}] \\ & + \text{Chem. Prod.} - \text{Chem. Loss} \dots \end{aligned}$$
- Write out coupled equations for NO(v=1-3)
- Collect terms in [O] and solve to remove them
- Solve for leading terms in [NO(v=0)]
- Determine main uncertainties

Estimating $[\text{NO}(0)]$ and $[\text{O}]$

Leading term in derivation of $\text{NO}(v=0)$ density from measured $\text{NO}(v=1)$ and $\text{NO}(v=2)$ densities:

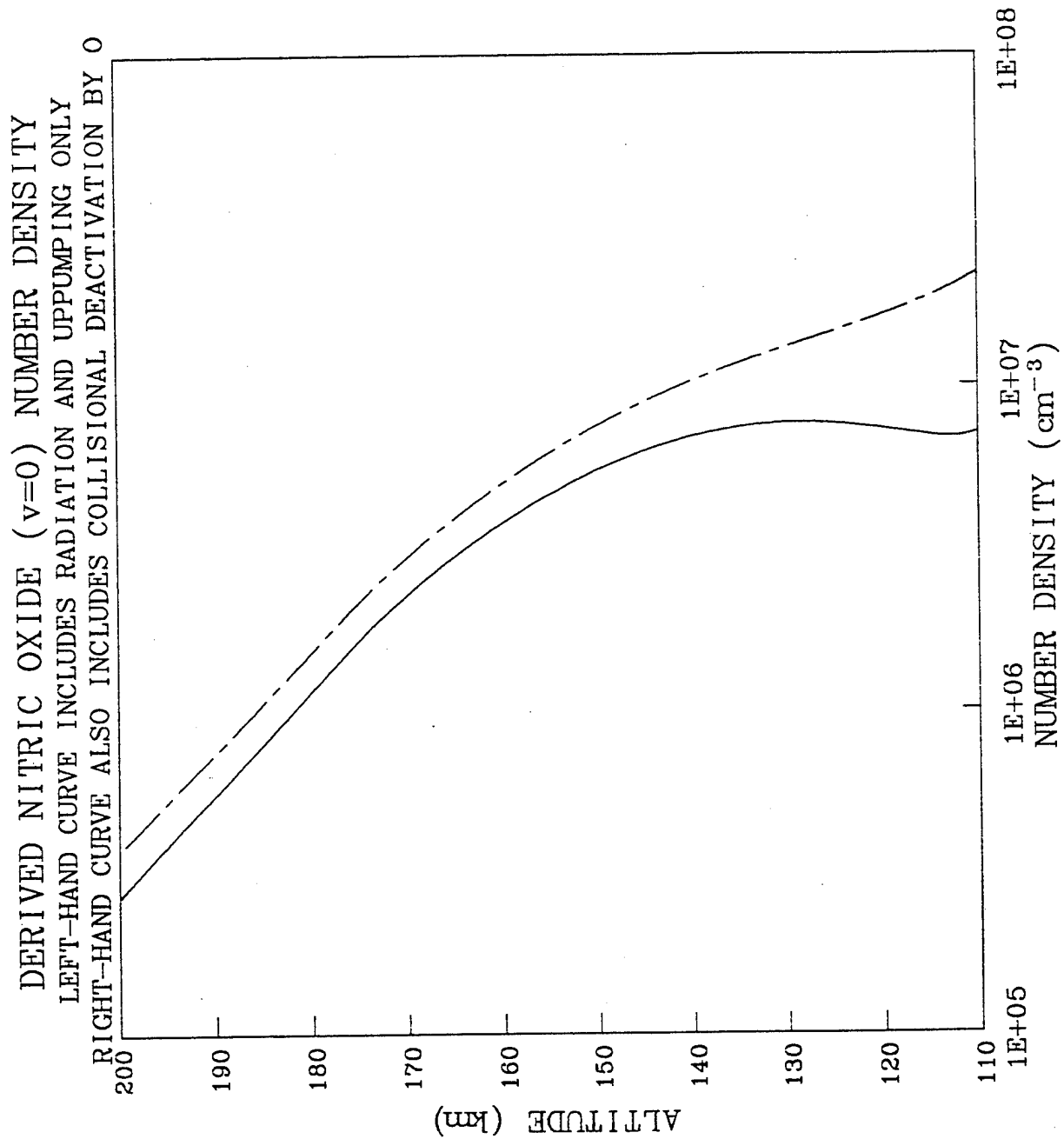
$$\frac{[\text{NO}(0)]}{[\text{NO}(1)]} = \frac{A(10) \quad k_U(12) \quad [\text{NO}(1)]}{A(21) \quad k_U(01) \quad [\text{NO}(2)]}$$

First-order independent of $[\text{O}]$ and T , but linearly dependent on vibrational scaling of k_U . Sensitivity to k_U is minimized by dependence on a ratio.

Future work: estimate of upumping rate from $\text{NO}(v)$ population ratios. Leading term is:

$$k_U(12) [\text{O}] = A(21) [\text{NO}(2)] / [\text{NO}(1)]$$

Uncertainty in k_U directly impacts calculated $[\text{O}]$.



Key Laboratory Measurement Identified: Relaxation of $\text{NO}(v=2)$ by O

- Requirements:
 - Temperature-dependent rate constant
 - Final state distribution ($v=0,1$)
- Applications:
 - Accurate modeling of $\text{NO}(v=2)$ relaxation
 - Upumping of $\text{NO}(v=0,1)$ to $v=2$
- Payoff:
 - Better estimate of $[\text{NO}(0)]$ from $[\text{NO}(v)]$
 - Allow estimate of $[\text{O}]$ from $[\text{NO}(v)]$

Results

- Analyzed high resolution CIRRIS 1A spectral data
 - Inverted to get volumetric NO number densities
 - Obtained vibrational/rotational distributions
- Determined nonequilibrium populations
 - High rotational excitation for several v levels
 - Subthermal NO spin-orbit populations
 - Elevated rotational temperature in CO
- Modeled important kinetic mechanisms
 - Vibrational upumping and relaxation by O
 - Radiative and chemical production and loss
 - Identified key uncertainties
- Remote sensing of additional species
 - Estimate of NO($v=0$) density derived
 - New type of probe of highly variable NO density
 - Technique for sensing O atom density proposed
 - New data on N-atom chemistry provided

Recent Advances in Gravity Wave Spectra and Implications for Radiance Structure Models

E.M. Dewan and R.H. Picard

Phillips Laboratory / Geophysics Directorate (GPOS)
Hanscom AFB, MA 01731-3010

Saturating gravity waves control the temporal and spatial fluctuation spectra of the middle atmosphere. These waves dominate the power spectra of physical parameters, such as temperature and density, as well as the those of the middle-atmospheric optical / infrared emission. Recent multi-pronged progress in gravity-wave spectra, in which PL/GP's SOAR and MAPSTAR programs have played a major role, is leading to increased understanding of middle-atmospheric structure, with resulting benefits for radiance structure models. (1) The several disparate theories of gravity-wave saturation, based on either linear instability (wave breaking) or nonlinearity, are converging, leading to the realization that both nonlinearity and instability are important in determining the form of the power spectrum and to some measure of agreement in testable predictions. (2) Multi-instrument databases, such as those from the ALOHA-93 Campaign, are becoming available which will allow critical tests of gravity-wave spectral models to be carried out. These databases include simultaneous lidar and multi-wavelength imager data to determine vertical and horizontal structure at the same time. The physics behind leading theories of gravity-wave power spectra will be reviewed, and ways to test the theories using the new data sets will be discussed. We also examine the role played by nonlinear wave-cascade effects in enabling the extension of previous theories of vertical-wavenumber spectra to horizontal-wavenumber and temporal-frequency spectra. Finally, the manner in which such spectral theories will lead to improved optical structure codes will be outlined.

Saturating atmospheric internal gravity waves (GW's) are known to dominate dynamical fluctuations in the atmosphere for all scales between the buoyancy scale ($\approx 5\text{-}50$ m) and the characteristic, or dominant, wavelength ($\approx 1\text{-}20$ km, depending on altitude). The irradiance fluctuations seen by exoatmospheric or endoatmospheric sensors will also be dominated by saturating IGW's in this range of scales. Hence, it is important to ask whether anything has been learned about saturating GW's which would enable improvements in atmospheric irradiance structure models. This question must be answered in the affirmative, for there has been significant recent progress along at least two fronts enabling us to understand better the power spectra of saturating gravity waves.

Firstly, there has been significant progress in the theory of gravity-wave spectra. Until recently, there were several competing theories which assumed either (1) that saturation occurred as a result of linear instability, that is the amplitude would grow until the wind profile became steep enough so that the shear was dynamically unstable (Richardson number $Ri < 1/4$) [Dewan and Good, 1986], or (2) that saturation happened when the wave amplitude was large enough that nonlinear

terms led to appreciable wave-wave interactions, draining the energy into other wave modes [Hines, 1991; Weinstock, 1990]. Lately there has been a convergence of power-spectral theories whereby the only two complete theories, capable of predicting all relevant power spectra, have been shown to lead to similar results. These are (1) the saturated-cascade theory of Dewan [1994], which takes both linear instability and nonlinear wave-wave cascade interactions seriously and assumes they are both happening at the same time, and (2) the diffusive filtering theory of Gardner [1994], which assumes that waves with small enough vertical wave numbers m are diffusively damped by wave-induced diffusion, a nonlinear wave-wave interaction process. We review a few highlights of gravity wave saturation theories, especially the saturated-cascade theory, below.

Secondly, multi-instrument data sets to test GW spectral theories are now becoming available. Such data sets may involve (1) combined optical and radar measurements, as obtained in several of the PL/GP MAPSTAR and SOAR program data sets (1983-present), especially the 1988 MAPSTAR Campaign data, or (2) combined lidar plus passive optical instruments, as in the NSF ALOHA-90 and ALOHA / ANLC-93 programs, in which SOAR and MAPSTAR team members played key roles. Radar in combination with optical / infrared instruments will give the analysis team access to the wind field in which observed wave structures propagate, as well as the eddy dissipation rate ϵ discussed below, while lidar in conjunction with optical imagers allows vertical structure to be observed at the same time as horizontal structure. At the same time, multi-instrument data sets will often contain redundant measurements through which internal checks on consistency of the data set can be implemented.

We now give a brief survey of the principal developments in GW saturation theory, as pertains especially to GW power spectra. Figure 1 [Dewan and Good, [1986] shows vertical-wavenumber (k_z) power spectra of the horizontal wind (v_x) in the stratosphere. These power spectra, or power spectral densities (PSD's), were obtained using smoke trails from two-stage Nike rockets launched under a great variety of conditions, yet they all fall on top of one another to a high degree of accuracy, falling as a function of k_z with a slope of -3. The spectra are, in every sense of the word, *universal*, at least up to the logarithmic error in the measurement ($\pm \log 2$). In Figure 2 a simple dimensional-analytic argument [Dewan and Good, [1986] for the form of the universal vertical-wavenumber spectrum of wind, $\Psi_{v_x}(k_z)$, is outlined. This argument, leading to the k_z^{-3} form for the spectrum, was based on a linear instability argument. This argument assumes that the wave becomes unstable and degenerates into turbulence when S , the vertical shear of v_x , is so large that the Richardson number, $Ri \equiv N^2 / S^2$, $< 1/4$ (dynamic or shear instability). It was based on a similar argument for instability of surface ocean waves, leading to formation of white caps, which predicted an ω^{-5} form for the temporal power spectra of wave heights. This form was experimentally confirmed [Phillips, 1966], as shown in the graph of Figure 2.

If we look at the horizontal-wavenumber PSD's of v_x , as obtained by *in situ* measurements from an instrumented aircraft (Figure 3), the spectrum is found to have a non-universal form with a slope of -5/3. The non-universality is made manifest by another dimensional argument based on wave-wave interaction, or *wave cascade*, as an amplitude-limiting mechanism which shows that the k_x spectrum depends on the turbulent-eddy energy dissipation rate ϵ , a quantity in which there are large variations. The temporal power spectra also exhibit non-universal behavior, as shown by the large variation in the curves of Figure 4. This figure shows temperature power spectra, $\Psi_T(\omega)$,

measured by the IRFWI (InfraRed FieldWidened Interferometer) looking at OH Meinel-band rotational temperatures from the mesopause region during the 1988 MAPSTAR Colorado Campaign. Dimensional arguments based on a nonlinear wave-cascade mechanism lead to an ω^{-2} slope with an ε -dependent coefficient, where ω is the intrinsic wave frequency. The slope is consistent with the experimental data, and values of ε inferred from the data are in the range measured by Hocking with radar.

We thus have a situation in which the vertical-wavenumber spectrum is universal and predicted by wave-limitation arguments based on linear instability, while the horizontal-wavenumber and temporal-frequency PSD's are non-universal and limited by nonlinear wave-wave interaction, or wave cascade. This situation is unsatisfactory unless linear-instability saturation and wave cascade are compatible. In Figure 5 we write the linear-instability saturation condition at the top and the wave-cascade condition at the bottom. In Figure 6 we require that they hold *simultaneously*, in other words, that an unstable, or saturated, cascade is occurring [Dewan, 1994]. This links up the k_z behavior with the k_x and ω behavior and leads immediately to the *saturated-cascade condition* at the bottom of Figure 6, which states that k_z^2 is proportional to ω . This relation can, alternately, be written as a proportionality between vertical wavelength λ_z and the square root of wave period τ , that is $\lambda_z \sim \tau^{1/2}$. The latter wavelength-period relation was previously found to hold in analyzing lidar data [Gardner and Voelz, 1987], as shown in Figure 7, while the corresponding relation between λ_x and τ ($\lambda_x \sim \tau^{3/2}$) has been seen in radar data.

Saturated-cascade theory is *complete*, in the sense that all dynamical power spectra are predicted (Figure 8), namely the spectra of v_x , v_z , T , and the fractional density perturbation $\Delta\rho/\rho$ as a function of k_x , k_z , and ω . All the spectra can be derived from the original "saturated spectrum" of Dewan & Good [1986] using the wavelength-period relation in conjunction with the usual wave dispersion and polarization relations. From Figure 8, all but three of the PSD's are seen to depend on ε , an indication of non-universality. Hence, ε is a controlling parameter. The range of values of ε in the troposphere, stratosphere, and mesosphere is shown in Figure 9. Radar measurements are designated by "R." It can be seen that, in the mesosphere for example, the overall range spans four orders of magnitude. Measurements of ε at the same time as measurements of power spectra are made would provide a powerful test of the influence of wave cascade processes in GW spectra and of the validity of our ideas on how GW saturation occurs, including the saturated-cascade hypothesis. One simple set of rough comparisons between saturated-cascade theory, augmented by representative values of ε for the stratosphere and mesosphere, and observation is shown in Figure 10.

So far we have dealt entirely with power spectra of dynamical variables responding to GW fluctuations. To obtain results of importance for radiance structure models, we require additional chemical-dynamical modeling of the radiative response to GW dynamical fluctuations. In the term "chemical" we mean to include any collisional and radiative production and loss processes as well, in fact any contributions to the continuity equation for the population of radiating states except the dynamical flux-divergence term. Such chemical-dynamical models, for example Makhlof *et al.* [1995], in conjunction with GW saturation models, will lead to improved first-principles radiance spectral models. An example of a chemical-dynamical model of radiative response to GW's is the realistic OH Meinel-band emission model of Makhlof *et al.* [1995].

Such modeling can be quite complex, for, in general, one needs to know all moments of the dynamical probability distribution functions in order to specify only the power spectra (second moments) of the radiance fluctuations. There are two cases, however, when the chemical-dynamical modeling of radiance power spectra is particularly simple. These cases are either (1) the dynamical fluctuations are Gaussian or (2) linear response of radiation to dynamical fluctuations is valid. In either of these cases, radiance PSD's depend *only* on dynamical PSD's.

We will consider in more detail the case where the GW dynamical fluctuations are small enough that linear response is valid. In Figure 11, we represent schematically the linear-response theory of optical / infrared radiance, or brightness, fluctuations. Column brightness B is related to a line integral of the volume emission rate $I(x,z,t)$ along the line-of-sight. The space-time frequency-response function $\eta(k_x, \omega)$ characterizes the linear filter relating temperature fluctuation to brightness fluctuation. Thus the power spectra of T and B are related by $|\eta|^2$, that is $\Psi_B(k_x, \omega) = |\eta(k_x, \omega)|^2 \Psi_T(k_x, \omega)$. If η can be calculated from a chemical-dynamical model or measured, one can construct a model of the brightness response to a GW.

If saturated-cascade theory holds, the wavelength-period relation allows one to eliminate the k_x dependence of η and write $\eta(k_x, \omega) = \eta(\omega)$ only. The response function so defined is, apart from a constant, the "Krassovsky eta" much used in describing OH airglow response to GW's. For the case of the OH Meinel (3,1) band, a specific model atmosphere, and (vertically, as well as horizontally) traveling GW's, the magnitude of the response function $\eta(\tau = 2\pi/\omega)$ is given by Figure 12. Figure 12 shows that, assuming the wavelength-period relation or saturated cascade to hold, there is a large and period- or frequency-dependent *amplification factor* which enhances the brightness fluctuations relative to the temperature fluctuations. Squaring $|\eta|$ and multiplying by the saturated-cascade temperature PSD, $\Psi_T(\omega)$, from Figure 8 yields the brightness PSD, $\Psi_B(\omega)$. Of course, the quantitative behavior of $|\eta(\omega)|$ will change if (1) the background atmospheric composition and temperature profiles are changed, (2) the background winds are changed, (3) the waves suffer ground reflection and have a vertical standing wave component, or (4) a different band or emitter is observed.

The above procedure for obtaining first-principles optical-structure codes which make use of modern saturated-GW power-spectral theory and of improved multi-instrument GW spectral databases can be extended from OH Meinel emission to other important radiators throughout the visible, ultraviolet, and infrared portions of the spectrum. At present, airglow response codes in the visible and near-infrared (OH Meinel bands, O_2 atmospheric bands, atomic-oxygen green line,) are the best developed. Codes for optically thin short-wave, mid-wave, and long-wave infrared bands involving no radiative excitation should also be near-term products, while codes for optically thick ultraviolet or infrared bands, such as CO_2 4.3 μm , using this fundamental approach will require further research advances in radiative transfer.

In conclusion, we have surveyed briefly recent work on GW saturation theory and chemical-dynamical models, along with related observational advances, to outline an approach to lead to much improved first-principles models and codes for optical structure. We have shown that the primary source of middle-atmospheric radiance fluctuations is atmospheric GW's and have indicated that a *complete* description of GW spectra comes from postulating that the conditions of linear-instability *saturation* and nonlinear wave *cascade* hold simultaneously [Dewan, 1994]. The

extensive ALOHA-93 Campaign database will add to existing MAPSTAR, SOAR, and CEDAR databases, taken in a "campaign" or an "observatory" mode, to provide important tests of saturated-cascade theory. The only fully developed alternative to saturated cascade at present (diffusive filtering theory [Gardner, 1994]), while requiring input of an empirical parameter, gives similar predictions from quite different physics. We have shown how GW fluctuation statistics plus chemical-dynamical modeling can predict radiance or brightness PSD's and, in the special, but very common, case of linear response, how radiance PSD's depend only on GW dynamical PSD's. As an example, we showed predictions for OH Meinel-band brightness PSD's based on the saturated-cascade hypothesis and the model of Makhlof *et al.* [1995]. Extending this approach will lead to needed and significant improvements in radiance structure codes.

We acknowledge technical contributions and helpful suggestions from Usama Makhlof.

REFERENCES

- Dewan, E.M., *Geophys. Res. Lett.*, **21**, 817, 1994.
Dewan, E.M., and R.E. Good, *J. Geophys. Res.*, **91**, 2742, 1986.
Gardner, C.S., *J. Geophys. Res.*, **99**, 20 601, 1994.
Gardner, C.S., and Voelz, *J. Geophys. Res.*, **92**, 4673, 1987.
Hines, C.O., *J. Atm. Sci.*, **48**, 1360, 1991.
Makhlof, U.B., R.H. Picard, and J.R. Winick, *J. Geophys. Res.*, **100**, 11 289, 1995.
Phillips, O.M., *The Dynamics of the Upper Ocean*, Cambridge University Press, New York, 1966.
Weinstock, J., *J. Atm. Sci.*, **47**, 2211, 1990.

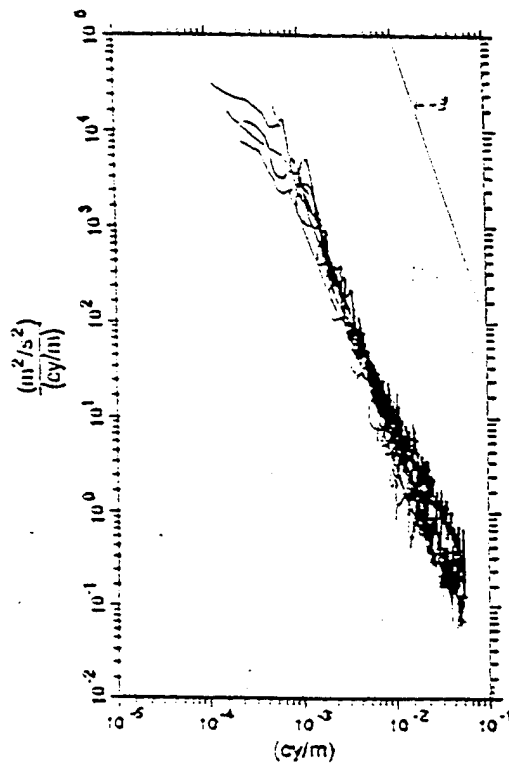


FIGURE 1

SATURATION OF WAVES

1. SURFACE OCEAN WAVES "WHITE CAPS"

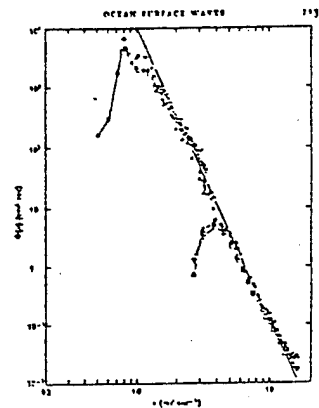
$$\text{PSD}_{\Delta z}(\omega) = \beta g^2 \omega^{-5} \quad [\text{DIMENSIONAL ARG.}]$$

2. EXPERIMENTAL CONFIRMATION

(PHILLIPS: (1966))

3. ANALOGY WITH INTERNAL WAVES: $RI < \frac{1}{4} \rightarrow \text{INSTAB.}$

$$N^2 < S^2 (.25)$$



$$\psi_{N_x}(k_3) \sim N^2 k_3^{-3}$$

FIGURE 2

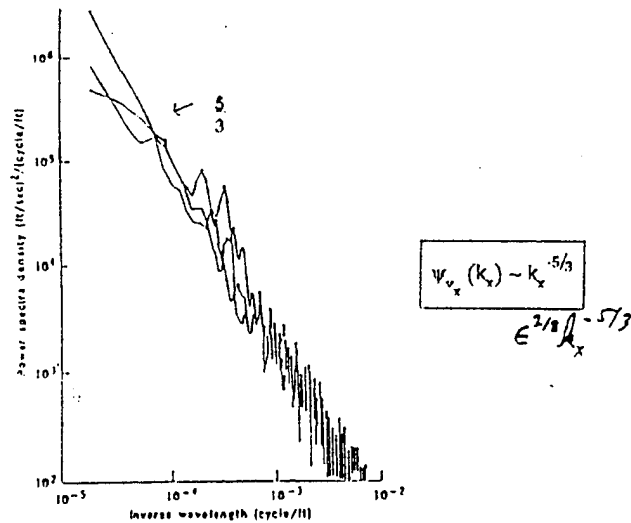


Fig. 1 (left). Power density spectrum of velocity fluctuations in the stratosphere measured in situ by Instrumented U-2 aircraft, test 280, run 7 (e). Maximum wavelength is about 12.2 km. Fig. 1 (right). Energy equations decomposed into mean wave and turbulence scales (derived from the Navier-Stokes equations).

DEWAN SCIENCE (1979), 204, 832
FIGURE 3

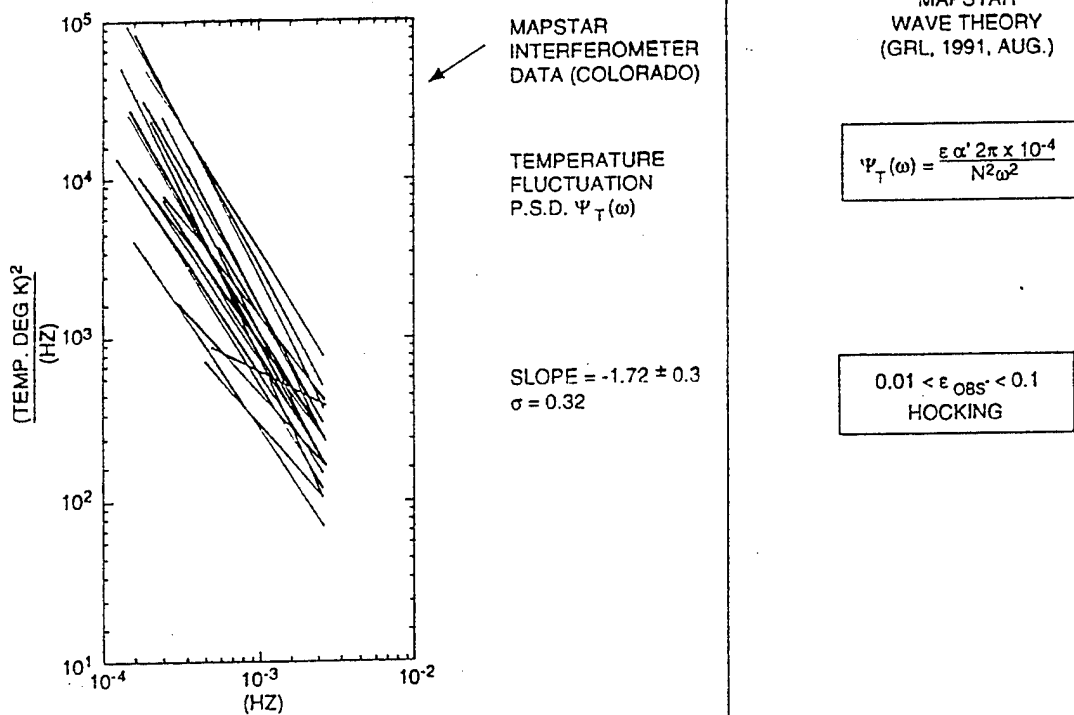


FIGURE 4

WHEN DO INTERNAL WAVES SATURATE?

$$Rl \equiv \frac{N^2}{S^2} - 1$$

$$\text{or } S^2 = N^2$$

$$S \equiv \left| \frac{\partial v_x}{\partial z} \right|$$

SINGLE COMPONENT

$$v_x^2 k_z^2 = a_1 N^2$$

$$v_x = v_0 e^{ik_z z}$$

$$\therefore \frac{\partial v_x(k_z)}{\partial z} = ik_z v_x$$

CASCADE CONDITION

$$\frac{v^2(\omega) 2\pi}{n\tau} = \text{const. } \varepsilon$$

$$\frac{v^2_{rms} f}{n} = \varepsilon$$

FIGURE 5

SATURATED - CASCADE CONDITION

SATURATION: $v_x^2(k_z) \cdot k_z^2 = a_1 N^2$	EQ 1
CASCADE: $v^2(\omega) \cdot \omega = a_2 (2\pi \varepsilon)$	EQ 2

- POLARIZATION REL. $v_z^2 = v_x^2 \frac{\omega^2}{N^2}$

- $(\omega < N) (\omega > f) \therefore v_x^2 \sim v^2$

- EQUATE $v_x^2 = v^2 + \text{ELIM. FROM EQ's 1 + 2}$

$k_z^2(\omega) = \frac{a_1}{a_2} \frac{N^2 \omega}{2\pi \varepsilon}$
SATURATED - CASCADE CONDITION

FIGURE 6

LIDAR OBSERVATIONS

GARDNER & VOELZ
JGR, 92, A5, 4673 (1987)

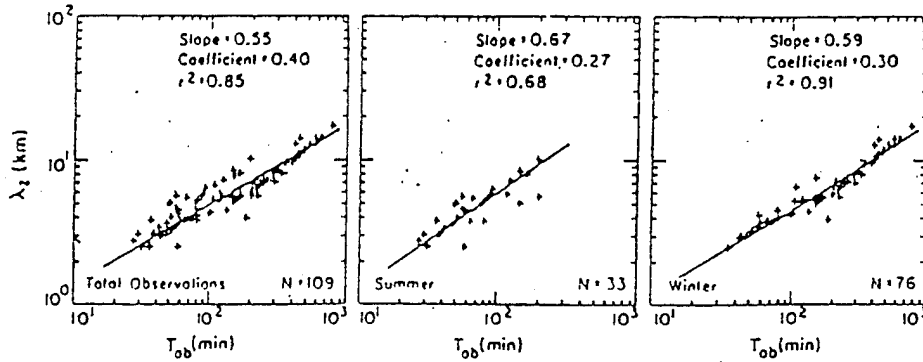


Fig. 15. Vertical wavelength versus observed period for total, summer and winter observations. The lines represent the power law fits of the form $\lambda_z = C(T_{obs})^p$, where C is the coefficient and p is the slope.

FIGURE 7

Table 1 Power Spectral Densities

Fluctuation	k_x	k_z	ω
Horizontal Velocity	$\psi_{v_x}^{(e)}(k_x) = \frac{\alpha(2\pi\epsilon)^{2\gamma} \left(\frac{a_2}{a_1}\right)^{2\gamma}}{3} k_x^{-3\gamma} \cdot (2\pi)$	$\psi_{v_x}^{(e)}(k_z) = \alpha N^2 k_z^{-3} \cdot (2\pi)$	$\psi_{v_x}^{(e)}(\omega) = \alpha(\epsilon\pi) \left(\frac{a_2}{a_1}\right) \omega^{-2} \cdot (2\pi)$
Vertical Velocity	$\psi_{v_z}^{(e)}(k_x) = \frac{\alpha(2\pi\epsilon)^{4\gamma}}{(3)N^2} \cdot \left(\frac{a_2}{a_1}\right)^{4\gamma} k_x^{-1\gamma} \cdot (2\pi)$	$\psi_{v_z}^{(e)}(k_z) = \frac{\alpha(2\pi\epsilon)^2 \left(\frac{a_2}{a_1}\right)^2}{N^4} k_z^{-1} \cdot (2\pi)$	$\psi_{v_z}^{(e)}(\omega) = \frac{\alpha(\epsilon\pi)}{N^2} \left(\frac{a_2}{a_1}\right) \cdot (2\pi)$
Temperature	$\psi_T^{(e)}(k_x) = \frac{\alpha}{N^2} \cdot \frac{(2\pi\epsilon)^{2\gamma}}{3} \left(\frac{a_2}{a_1}\right)^{2\gamma} \left[\frac{T(\gamma-1)}{H\gamma}\right]^2 k_x^{-3\gamma} \cdot (2\pi)$	$\psi_T^{(e)}(k_z) = \alpha \left[\frac{T(\gamma-1)}{H\gamma}\right]^2 k_z^{-3} \cdot (2\pi)$	$\psi_T^{(e)}(\omega) = \frac{\alpha(\epsilon\pi)}{N^2} \left(\frac{a_2}{a_1}\right) \left[\frac{T(\gamma-1)}{H\gamma}\right]^2 \omega^{-2} \cdot (2\pi)$
Fractional Density	$\psi_{\frac{\Delta\rho}{\rho}}^{(e)}(k_x) = \frac{\alpha(2\pi\epsilon)^{2\gamma}}{(3)N^2} \left(\frac{a_2}{a_1}\right)^{2\gamma} \left[\left(\frac{\gamma-1}{\gamma}\right)\frac{1}{H}\right]^2 k_x^{-3\gamma} \cdot (2\pi)$	$\psi_{\frac{\Delta\rho}{\rho}}^{(e)}(k_z) = \alpha \left[\left(\frac{\gamma-1}{\gamma}\right)\frac{1}{H}\right]^2 k_z^{-3} \cdot (2\pi)$	$\psi_{\frac{\Delta\rho}{\rho}}^{(e)}(\omega) = \frac{\alpha(\epsilon\pi)}{N^2} \left(\frac{a_2}{a_1}\right) \left[\left(\frac{\gamma-1}{\gamma}\right)\frac{1}{H}\right]^2 \omega^{-2} \cdot (2\pi)$
Saturated-Cascade Relations	$k_z^2 = \frac{\omega N^2}{2\pi\epsilon} \left(\frac{a_1}{a_2}\right), k_x^2 = \frac{\omega^3}{2\pi\epsilon} \left(\frac{a_1}{a_2}\right), k_z^3 = \frac{N^3}{2\pi\epsilon} \left(\frac{a_1}{a_2}\right) k_x$	Wavelength-Period Relations: $\lambda_z = \left[\tau_B \sqrt{\epsilon \left(\frac{a_2}{a_1}\right)}\right] \sqrt{\tau_{OBS}}$	
Characteristic Wave Numbers	$k_{z*} = \sqrt{\frac{N^2}{2\pi\epsilon} \left(\frac{a_1}{a_2}\right)}$	Maximum Wave Numbers	$k_{z_{max}} = k_{x_{max}} = \sqrt{\frac{N^3}{2\pi\epsilon} \left(\frac{a_1}{a_2}\right)}$

FIGURE 8

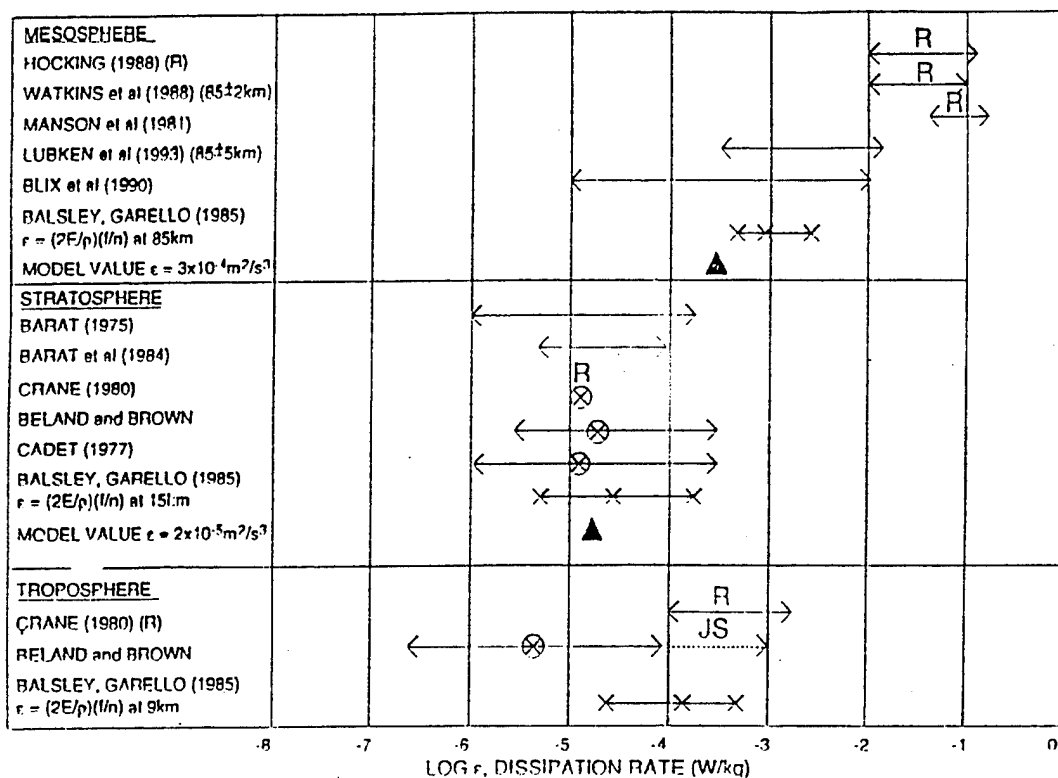


FIGURE 9

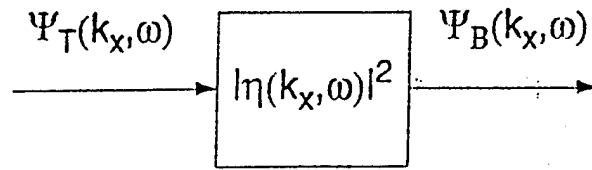
5 COMPARISONS BETWEEN THEORY AND "EXPERIMENT" [USING REPRESENTATIVE VALUES OF ϵ]

MESOSPHERE	$\epsilon = 3 \times 10^{-4} \text{ (m}^2/\text{s}^3)$
STRATOSPHERE	$\epsilon = 2 \times 10^{-5} \text{ (m}^2/\text{s}^3)$

QUANTITY	OBSERVATION	THEORY
MESOSPHERE		
$\lambda_z / (T^{1/2})$	50 (m/s ^{1/2})	77 (m/s ^{1/2})
$\omega^2 \psi_T(\omega)$	0.01 to 0.1 (°K) ² (Hz)	0.04 (°K) ² (Hz)
$\frac{\omega \Delta \rho}{\rho} (k_x = 2 \times 10^{-5} \text{ rad/s})$	6 to 10 ($\Delta \rho / \rho$) ² / (cy/m)	10 ($\Delta \rho / \rho$) ² / (cy/m)
STRATOSPHERE		
$\psi_{v_x} (k_x = 2 \times 10^{-3} \text{ rad/m})$	3 x 10 ³ (m/s) ² / (cy/m)	10 ³ (m/s) ³ / (cy/m)
$\psi_{v_x}(f)$	10 ⁵ to 2 x 10 ⁶ (m/s) ² / (cy/s)	1.4 x 10 ⁶ (m/s) ² / (cy/m)

FIGURE 10

Linear Response Radiance PSD's



$$B(x,t) = \int ds(z) I[x,z,t] = \text{brightness}$$

Ψ_B = brightness fluctuation PSD

- η = linear-response function resulting from data or photochemical-dynamical (PH/D) modeling
- Saturated-cascade theory (wavelength-period relation)
---> $\eta(k_x, \omega) = \eta(\omega)$ only
- Example - PH/D model for η : OH Meinel-band airglow (Makhlouf, Picard, & Winick, 1995)

FIGURE 11

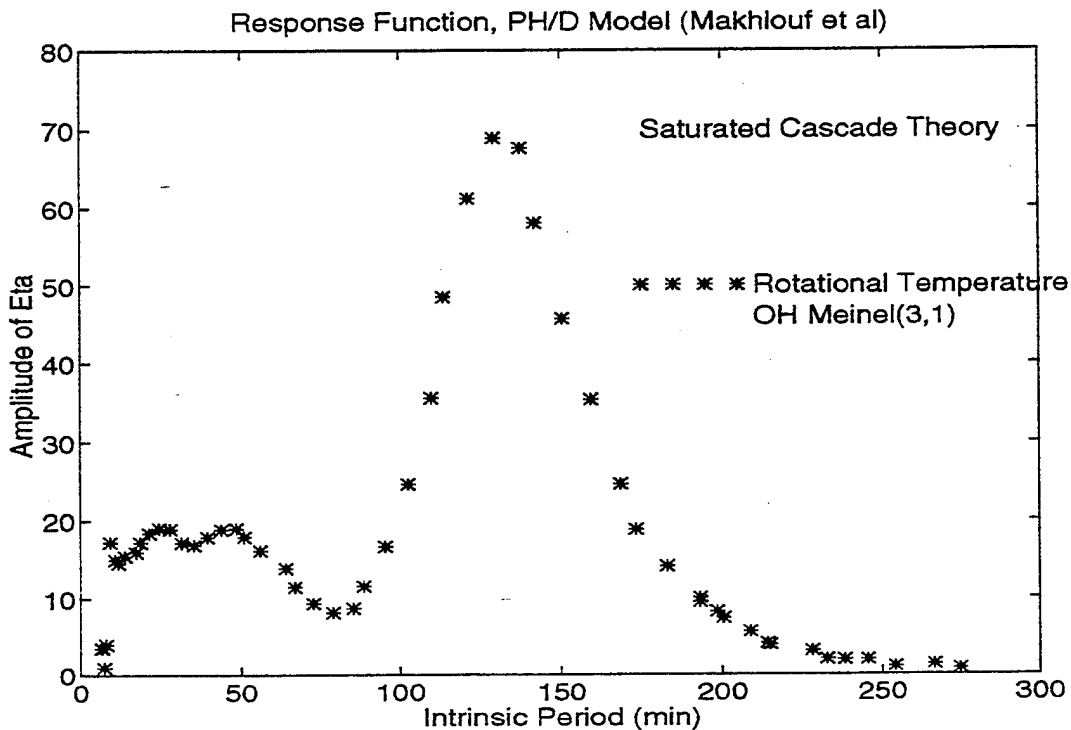


FIGURE 12

SHARC-4: MODEL FOR ATMOSPHERIC BACKGROUND RADIANCE STRUCTURES

June 1995

John Gruninger, James W. Duff, and Robert L. Sundberg
Spectral Sciences, Inc., 99 South Bedford St.,
Burlington, MA 01803

James H. Brown, Ramesh D. Sharma, and William A. M. Blumberg
Phillips Laboratory, Geophysics Directorate
Hanscom AFB, MA 01731

ABSTRACT

The SHARC-4 model of the NLTE infrared radiance fluctuations in the atmosphere due to fluctuations in the density of atmospheric species, individual molecular state populations, and kinetic temperatures and pressures along the sensor line of sight is described. The approach predicts the two dimensional radiance spatial covariance function and power spectral density, which are non-stationary and dependent on bandpass, sensor location, and field of view, from the underlying three dimensional temperature statistics. The SHARC algorithm is used to predict the non-equilibrium dependence of molecular state number density fluctuations on kinetic temperature and density fluctuations, and to calculate mean line of sight radiances and radiance derivatives.

1.0 INTRODUCTION

The calculation of infrared (IR) mean radiance, transmittance and their fluctuation statistics is important in many areas of atmospheric science, including the interpretation of satellite sensor measurements and for understanding the effects of turbulence structures on molecular excitation processes. The atmospheric infrared radiance fluctuations depend on fluctuations in atmospheric species number densities, vibrational state populations, and the kinetic temperatures along the sensor line-of-sight (LOS). The standard SHARC model¹ calculates mean LOS radiance and transmittance values. The SHARC structure model predicts the two-dimensional spatial covariance function of the radiance. The covariance function and its Fourier transform, the power spectral density (PSD), can be used directly in sensor models or in image synthesis models to create realizations of the predicted structure. The radiance statistics and images are non-stationary and are explicitly bandpass and sensor FOV dependent.

At lower altitudes (~50 km), collisional quenching of excited vibrational states is fast compared to radiative decay. Species tend to be in local thermodynamic equilibrium (LTE) and state populations can be determined from a Boltzmann distribution at the gas-kinetic temperature. At higher altitudes, there are an insufficient number of collisions to equilibrate vibrational energy before radiative decay occurs and the vibrational states can no longer be characterized by the kinetic temperature. Under these conditions, the vibrational states are in nonlocal thermodynamic equilibrium (NLTE). Models extending into the higher altitudes must describe these deviations from local thermodynamic equilibrium. SHARC assumes steady state kinetics for the atmospheric processes of collisional excitation, energy transfer, radiative decay,

1. R. L. Sundberg, J. W. Duff, J. H. Gruninger, L. S. Bernstein, M. W. Matthew, S. M. Alder-Golden, D. C. Robertson, R. D. Sharma, J. H. Brown, and R. J. Healey, "SHARC, A Model for Calculating Atmospheric Infrared Radiation Under Non-Equilibrium Conditions," in *The Upper Mesosphere and the Lower Thermosphere: A Review of Experiment and Theory*, Geophysical Monograph Series, 87, 287 - 295, 1995.

chemical production and illumination by the sun, earth and atmosphere. The model includes seven species which radiate in the 2-40 μm wavelength region. It includes NO, CO₂, O₃, H₂O, OH, CO, and CH₄. Isotopes of CO₂ and H₂O are also modeled. The number densities of the excited vibrational states are predicted and can be described in terms of a Boltzmann distribution with state dependent vibrational temperatures. Under LTE conditions, the responses to a kinetic temperature fluctuation can be described by a Boltzmann distribution corresponding to the new kinetic temperature. The emission from a small volume in the atmosphere depends only on the gas-kinetic temperature in that volume and is determined using the Planck blackbody emission source term at the new fluctuated temperature. Under NLTE conditions, the response of population changes to fluctuations in temperature and density are determined for each state by a perturbation model which uses the same steady state chemical-kinetics schemes that are used for the quiescent atmosphere. Fluctuations in the kinetic temperature can result in correlated or anti-correlated responses in vibrational state population. The magnitudes of the responses depend on the local chemical environment. NLTE emission depends on the vibrational temperatures of all species involved, as well as, the gas-kinetic temperature.

Fluctuations in atmospheric temperature and density have been measured directly using balloon, rocket, and satellite experiments. These experiments provide in-situ measurement of density, temperature and species concentrations. Ground based techniques used to determine atmospheric structure statistics include radar, lidar and airglow emission measurements. Taken together these measurements begin to provide the necessary structure statistics which characterize the atmosphere. Current estimates of these quantities have been summarized, in a 3-D non-stationary statistical model (NSS).² The NSS model provides a covariance function, PSD description of atmospheric temperature and density fluctuations. Horizontal altitude layers are assumed to be isotropic and stationary. The vertical variations are non-stationary. Model parameters (variance, vertical correlation length, and horizontal correlation length) are described as a function of altitude. The NSS model currently assumes a 1-D PSD spectral slope of -2 for all altitudes.

A simulation of the radiance fluctuations observed by a sensor array can be calculated by using a three-dimensional realization of the atmospheric temperature and density fluctuations and by intersecting a LOS for each pixel with the 3-D realization to determine the LOS radiance for each pixel in the sensor.³ Alternatively, the radiance statistics for the sensor FOV can be derived directly. The radiance statistical functions can be incorporated into sensor models, or image syntheses models, to create realizations of the radiance statistics. The model described here proceeds with the later approach although the former approach is being used to evaluate the algorithms. The radiance statistics predicted by SHARC explicitly include radiance fluctuation contributions along the entire LOS and not just the tangent point. The inputs to the calculation are altitude dependent temperature and density profiles, which can be obtained from the standard atmosphere generator code (SAG),⁴ the local temperature and density statistical quantities

2. L. A. Strugala, R. D. Sears, J. E. Newt, and B. J. Herman, "Production of Statistically Nonstationary Stochastic Structure Realizations for Infrared Background Scene Simulations," *Optical Engineering*, 32, 993 - 1000, 1993.

3. J. H. Brown, "Synthetic 3-D Atmospheric Temperature Structure: A Model for Known geophysical Power Spectra Using A Hybrid Autoregression and Fourier Technique," PL-TR-94-2150 Phillips Laboratory, 29 Randolph Road, Hanscom AFB, MA 01731-3010, May 1994. **ADA289058**

4. S. M. Alder-Golden, "Description of the SHARC Atmosphere Generator," PL-TR-93-2123, *Phillips Laboratory, 29 Randolph Road, Hanscom AFB, MA 01731-3010, May 1993.*

obtained from the NSS model and an atlas of molecular line parameters based on HITRAN-92.⁵ The SHARC model calculates the non-stationary LOS radiance covariance by performing LOS integrations over the products of radiance fluctuation amplitude functions,⁶ and the local kinetic temperature covariance. A key quantity derived by the model is a LOS radiance variance distribution function which determines the contribution to radiance variance of each portion of the LOS. The radiance variance distribution function act as a weighing function. It reveals contributions of temperature and density fluctuations to radiance variance along the LOS.

2.0 RADIANCE STRUCTURE STATISTICS AND IMAGES

The model has been applied to calculate the radiance structure for one of the MSX CO₂(v₃) bands (band B1) under day and night conditions. The predicted variance weighing functions for the day and night CO₂(v₃) are illustrated in Figures 1 and 2. They are given as a function of altitude from the upper atmosphere to the limb. Because of the opacity found in this bandpass, the emission from the later half of the LOS does not reach the observer and plays no role in the radiance statistics. There are strong diurnal effects with the day mean radiance being two orders of magnitude larger than the night radiance, above about 60 km. Solar pumping of the CO₂ hot bands is responsible for this difference below 90 km where the fundamental is essentially self absorbed. The magnitude of the variance distribution function determines the extent to which a particular portion of the atmosphere contributes to the radiance structure at the sensor. Strong absorption at approximately 40 km causes structure at this altitude to contribute to all tangent point altitudes below, for both day and night. Solar pumping effects the magnitudes of daytime mean radiance and the variance distribution function. There are knees in the nighttime and daytime weighing function at 120 km, 90 km and 45 km and a small daytime knee at 70 km. The effect of these knees is that the local atmospheric structure at the knee altitudes strongly affect the structure along the LOS with lower tangent point altitudes. For example, the 120 km knee causes the structure in LOS with tangent points between 90 and 120 to be dominated by the structure at 120 km. The nighttime knee is larger and therefore has a greater effect on the structure parameters. Likewise the strength of the daytime knee at 90 km and the existence of a small knee at 70 km significantly influence the LOS penetrating to lower altitudes, in fact all the way down to the next knee at 45 km.

The radiance statistics at the sensor can be compared to the temperature statistics at the tangent point altitude by projecting the radiance values to the tangent point range. This corresponds to converting a distance in the image plane to the corresponding distance at the tangent point (see Figure 3). The resulting radiance correlation lengths at the tangent point are shown in Figures 4 and 5. They track the temperature correlation lengths above 120 km (not shown), but below the knees in the radiance distribution function, the statistics are determined by the higher altitudes. This behavior results from dominance of the high altitude part of the LOS variance function for LOS paths which are below the knees in the variance distribution function, as shown in Figures 1 and 2. The magnitude of the knee determines the extent of the effect on the lower altitudes, thus leading to diurnal effects in the spatial structure. The calculated mean radiances and variances are illustrated in Figure 6. The relative variances, the absolute variances divided by the absolute mean radiance, as a function of altitude are illustrated in Figure 7. The relative variances are typically insensitive to small changes in the band edges and is typical for all CO₂(v₃) band

5. L. S. Rothman, R. R. Gamache, A. Goldman, L. R. Brown, R. A. Toth, H. M. Pickett, R. L. Pynter, J. -M. Flaud, C. Camy-Peyret, A. Barbe, N. Husson, C. P. Rinsland and M. A. H. Smith, "The HITRAN Molecular Database. Editions of 1991 and 1992," *J. Quant. Spectrosc. Radiat. Transfer*, 48, 469, 1992.

6. J. H. Gruninger, R. L. Sundberg, and P. De, "A Model For Atmospheric Radiance Clutter With Applications to Advanced BMD Interceptor Scenarios," *Proceedings of the IRIS Meeting on Targets, Backgrounds, and Discrimination*, February 1994.

passes. While the mean radiance during the day is two orders of magnitude larger during the day, the larger relative variances together with the shorter correlation lengths at the lower altitudes, would give the night radiance a larger relative gradient structure.

3.0 CONCLUSIONS

The radiance structure of atmospheric backgrounds is induced by local temperature and density fluctuations in the atmosphere. The model used here predicts the 2-D radiance covariance in the image plane of the sensor from a 3-D model of the temperature covariance. The mean radiances and radiance covariances are calculated using non-equilibrium vibrational state distributions. The model includes specific bandpass dependence, observer-target geometry effects, and diurnal effects. At high altitudes NLTE effects are important. These effects must be included in estimating the mean excited state number densities and the changes in number densities induced by temperature fluctuations. Perhaps the most important result of this work is the clear demonstration that the entire LOS path must be included to accurately determine the radiance statistics. The importance of various altitudes along the LOS can be assessed by examining the variance distribution function.

4.0 ACKNOWLEDGMENTS

This work sponsored by Ballistic Missile Defense Organization under Air Force Contract No. F19628-91-C-0083.

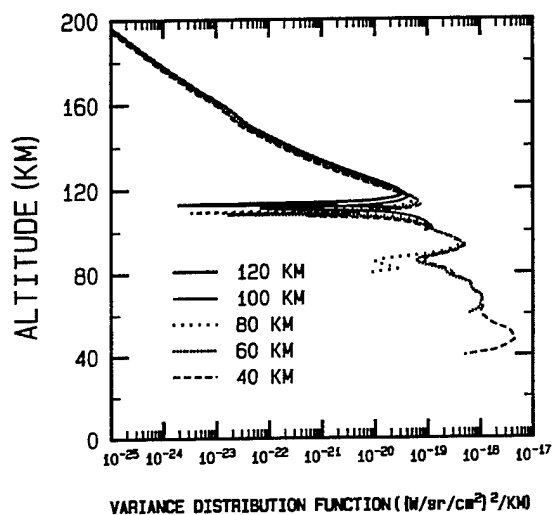


Figure 1. LOS Variance Distribution Functions for Daytime Limb in the $\text{CO}_2(\nu_3)$ Band Plotted as Functions of Altitude.

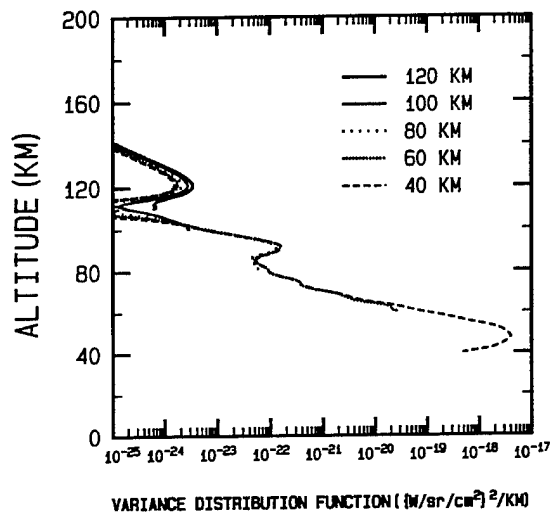


Figure 2. LOS Variance Distribution Functions for Nighttime Limb in the $\text{CO}_2(\nu_3)$ Band Plotted as Functions of Altitude.

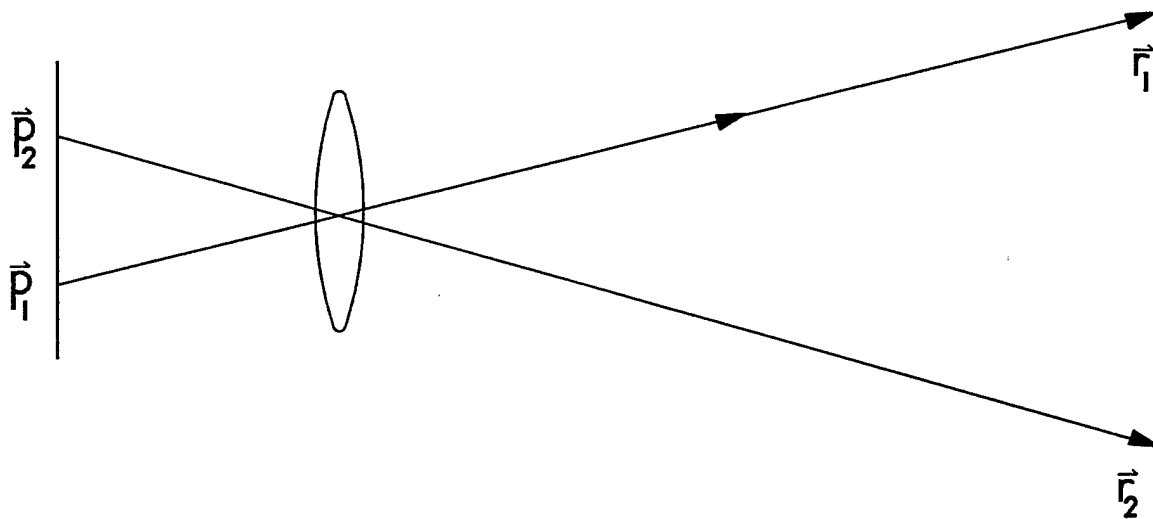


Figure 3. Cartoon of Sensor Image Plane, Optics, and Two LOS Extending into the Atmosphere.

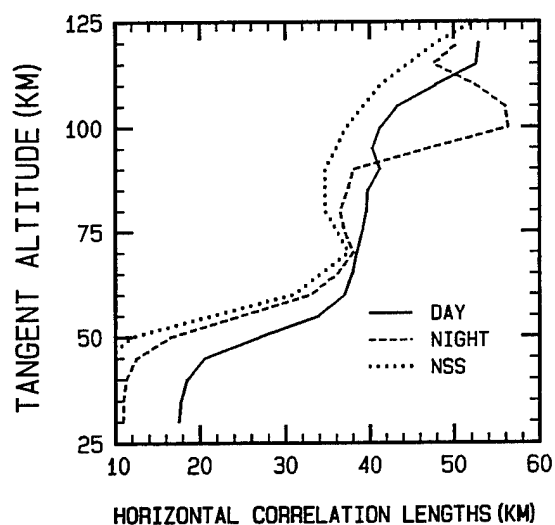


Figure 4. Horizontal Radiance Correlation Lengths Plotted as a Function of LOS Tangent Altitude for $\text{CO}_2(\nu_3)$ Band for Daytime and Nighttime Conditions and an Observer at 900 km Altitude. The Horizontal Atmospheric Temperature Correlation Lengths of the NSS Input Model Are Also Plotted for Comparison.

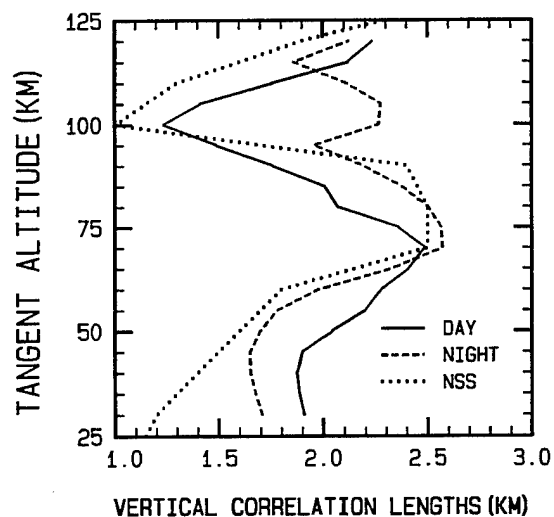


Figure 5. Vertical Radiance Correlation Lengths Plotted as a Function of LOS Tangent Altitude for $\text{CO}_2(\nu_3)$ Band for Daytime and Nighttime Conditions and an Observer at 900 km Altitude. The Vertical Atmospheric Temperature Correlation Lengths of the NSS Input Model Are Also Plotted for Comparison.

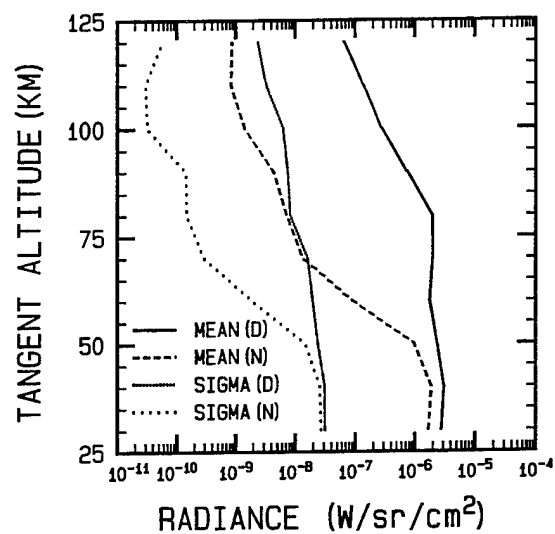


Figure 6. Mean Radiances and Variances, of the $\text{CO}_2(\nu_3)$ Band Radiance for Daytime and Nighttime Conditions as a Function of Tangent Point Altitude.

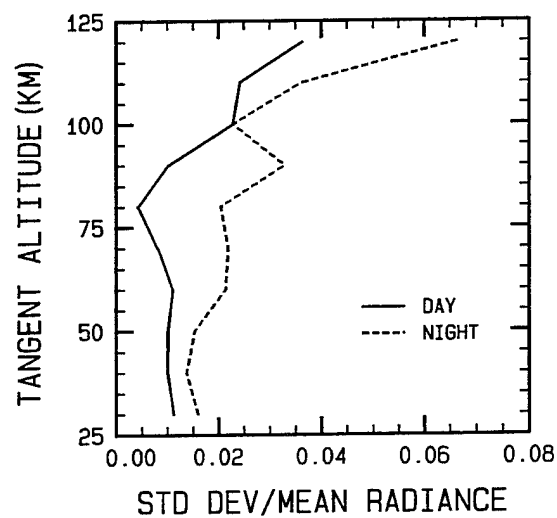
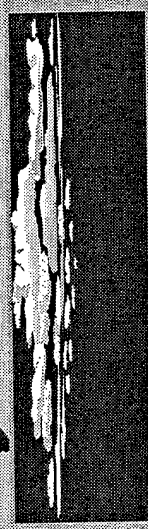


Figure 7. Relative Variances, of the $\text{CO}_2(\nu_3)$ Band Radiance for Daytime and Nighttime Conditions.

A fast "stretched-space" method for generating synthetic vertical sheets of non-stationary stochastic atmospheric structure for airflow simulation

James H. Brown
Neil Grossbard



A Stretched Space Transformation of a Non-Stationary PSD to a Stationary PSD

■ KEY

- Transform a Non-Stationary Auto-Covariance Function to a Stationary Auto-Covariance Function by Change of Lag and Space Variables
- Use the Resulting "Stretched Space" Stationary PSD to generate synthetic Stationary Structure in "Stretched Space"
- Transform Structure in "Stretched Space" Back to "Normal Space" to Obtain Non-Stationary Structure



A Stretched Space Transformation of a Non-Stationary PSD to a Stationary PSD

- Transformation Allows Use of a Single Application of an FFT or AR Algorithm to Generate Entire Structure.
- Method Allows Large (8192 x 1024) 2-D Synthetic Structure to be Generated in Small Amount of Time (~3 minutes). Much Faster Than Methods Now Being Used.



Known "Stationary" PSD & ACF

$$PSD(k) = \frac{\sigma^2 a^{2\nu} \Gamma\left(\nu + \frac{1}{2}\right)}{\sqrt{\pi} \Gamma(\nu) (a^2 + k^2)^{\nu + \frac{1}{2}}}$$

$$ACF(s) = B \left(C \frac{s}{L_c} \right)^\nu K_\nu \left(C \frac{s}{L_c} \right)$$

$$B = \frac{\sigma^2 2^{(1-\nu)}}{\Gamma(\nu)} \quad C = 2\pi \frac{2\sqrt{\pi} \Gamma(\nu)}{\Gamma\left(\nu + \frac{1}{2}\right)}^{-1}$$



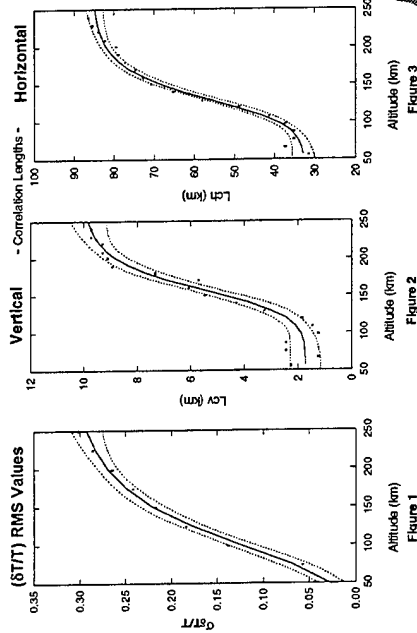
Coherence Length Parameter

$$L_c = \frac{\Gamma\left(v + \frac{1}{2}\right)}{2\sqrt{\pi}\Gamma(v)a}$$

Assume "measured" value of parameter "a" is an average over some altitude. Then L is a "geometric" average over altitude.

[Handwritten signature]

Model Parameter Specifications



$$Y = a + b/(1 + (x/c)^d) \text{ with 95\% confidence levels}$$

Figure 3

Figure 2

Figure 1

Stationary Vs. Non-Stationary ACF

Under stationary conditions the ACF is not a function of z

$$ACF(s) = E[f(z) * f(z+s)]$$

Under non-stationary conditions the ACF is a function of z. Such is the Case When Lc Depends on Altitude, z.

$$ACF(z,s) = E[f(z) * f(z+s)]$$

[Handwritten signature]

Change of Variables

Transform lag "s" to new lag variable "y" and transform altitude "z" to a space "t"

$$y = \gamma(z,s) \quad s(z,y) = \gamma^{-1}(z,s)$$

$$t = t(z)$$

So that,

$$ACF(y) = E[f(t) * f(t+y)]$$

Where ACF(y) is stationary

[Handwritten signature]

The Transformations

$$y = y(z, s) = \overline{L_c} \int_z^{z+s} \frac{dx}{L_c(x)}$$

$$t = t(z) = t_0 + \overline{L_c} \int_{z_0}^z \frac{dx}{L_c(x)}$$

We have arbitrarily set $t_0 = z_0 = 50$ km and $t = 300$ km when $z = 300$ km. So that,

$$\overline{L_c} = \frac{250}{\int_{50}^{300} \frac{1}{L_c(z)} dz}$$

"Stretched-space vs. altitude

$$t(z) = t_0 + \overline{L_c} \int_{z_0}^z \frac{dx}{L_c(x, 0)}$$

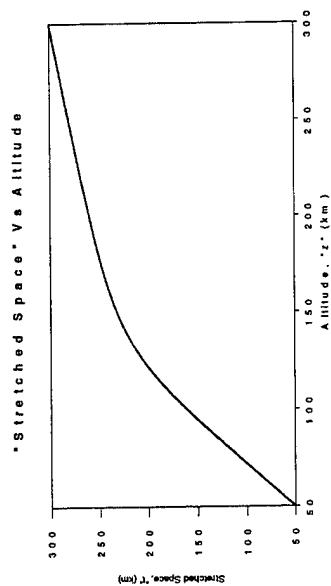


FIGURE 4.

Model & Synthetic PSD's

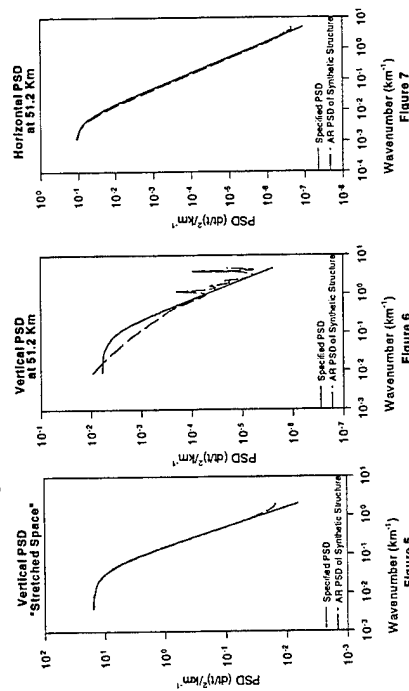


Figure 5

Figure 6

Figure 7

Variance Specification

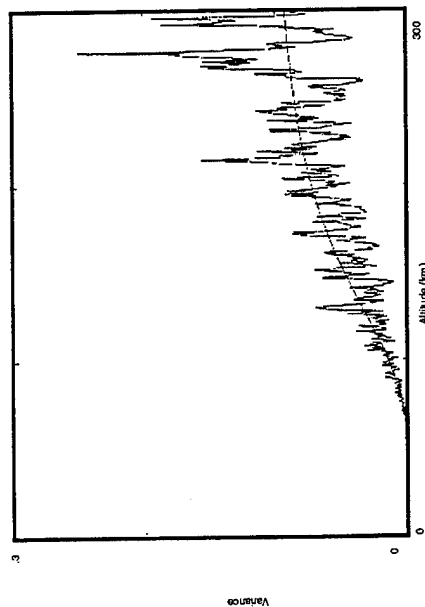
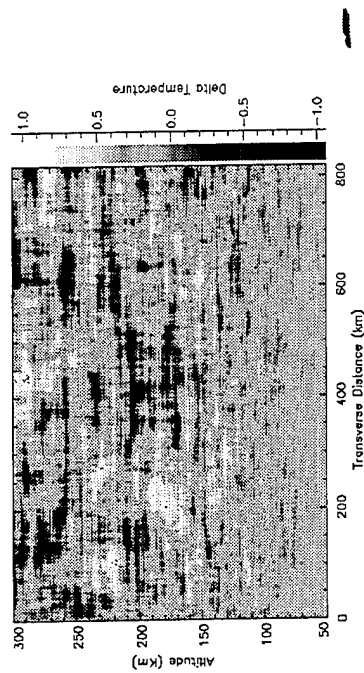


FIGURE 8

Image of Synthetic 2-D Non-Stationary Structure



Conclusion

- Real space altitude, "z" can be mapped into a *stretched space*, "t(z)" where the autocovariance function $ACF(y)$ is stationary. In practice, the increments in "t" were equally spaced.
- Fast - 3 minutes to create 8192 x 1024 vertical sheet on DEC Alpha computer.



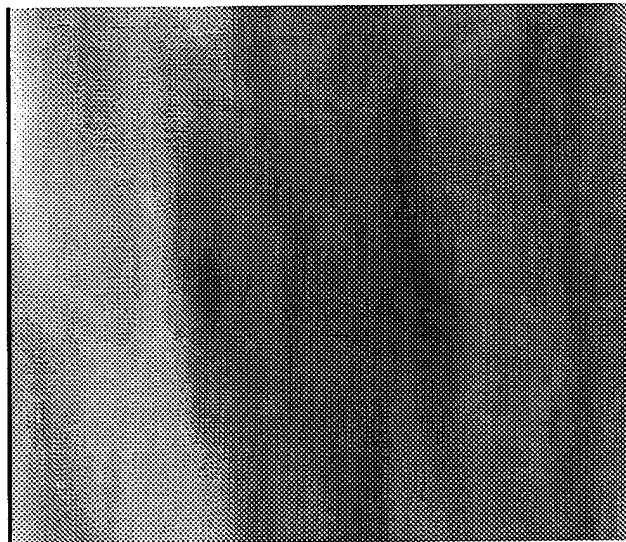
PLEXUS



Geophysics Atmosphere and Weather for Synthetic Environments

Dr. Frank O. Clark

**Geophysics Directorate
Department of the Air Force
Hanscom AFB, MA**



SASS

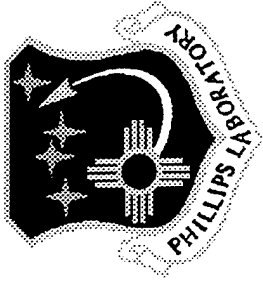
phone: 617-377-4139, fax: 617-377-8780, internet fclark@plh.af.mil



CBSD



Geophysics Directorate Purpose



- **Data and Models of Environment**
 - **Effects on fielded & proposed systems**
- **Fifty years of expertise**
 - **Field data of environmental phenomena**
 - **Conceptual models**
 - **Predictive codes (computer software models)**
 - **Disseminate data, models, & codes to DoD customers**
- **Role of PLEXUS**
 - **Single uniform accessible interface to codes**
 - **Applications knowledge supplied by expert system**



PLEXUS Customers



Pre-Phase Zero
conceptual design

IDA
Pentagon

Engineering
Optimization

SPO
contractors

Operational
Limits

Pentagon
contractors

Wargaming

STOW
WARBREAKER
JMASS, JSIMS
TBA, DEEM

Needs

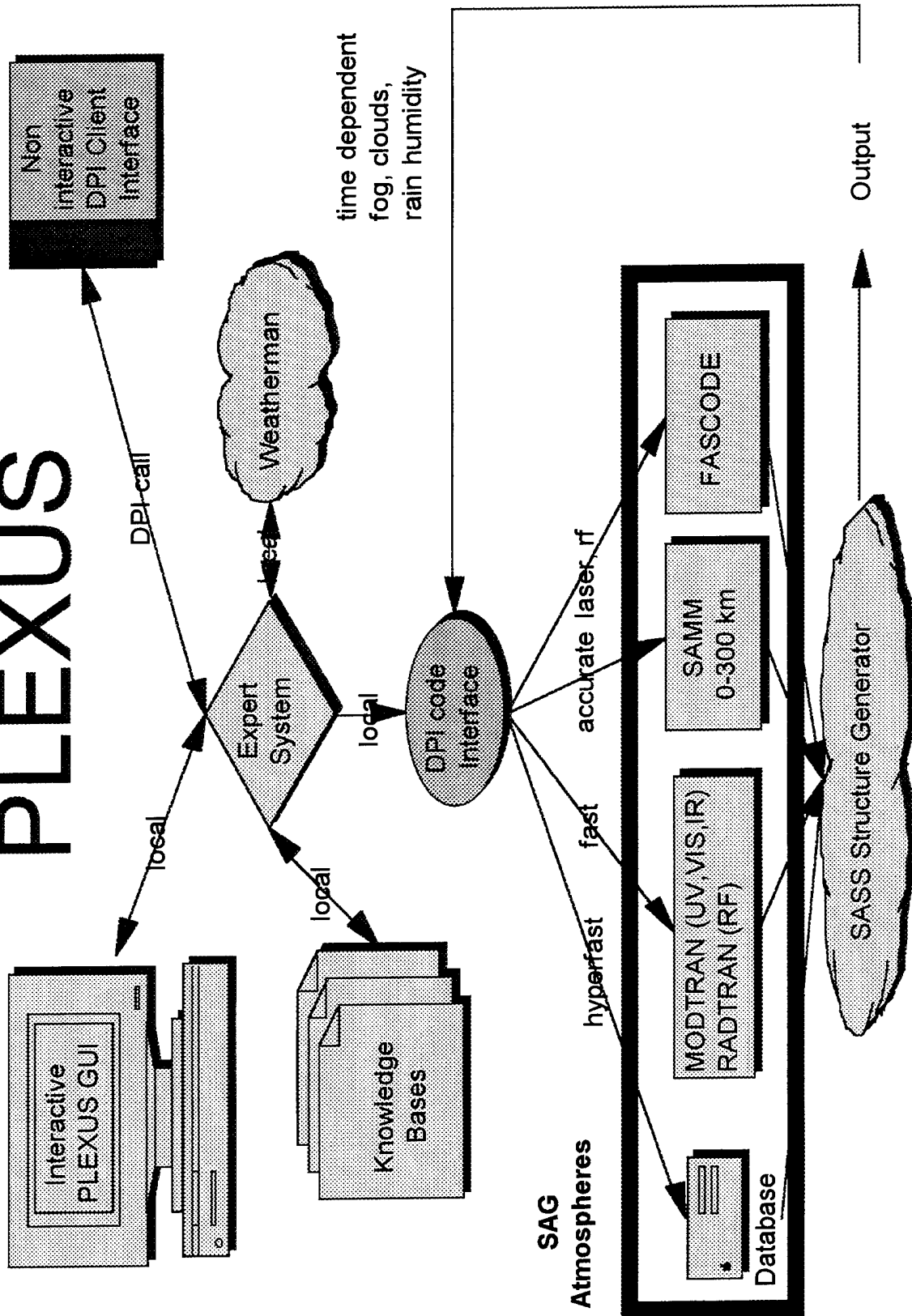
Atmosphere
UV to RF
laser weapons
ground to space

Weather
fog
clouds
rain



Architecture

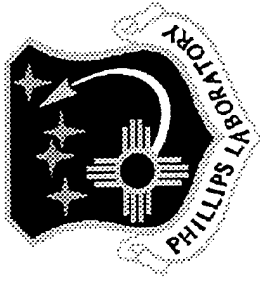
PLEXUS





Geophysics Directorate Codes

PLEXUS Expert System Environment



- **MODTRAN** (successor of LOWTRAN)

- Equilibrium lower atmosphere

- **FASCODE**

- high resolution (lasers, radar)

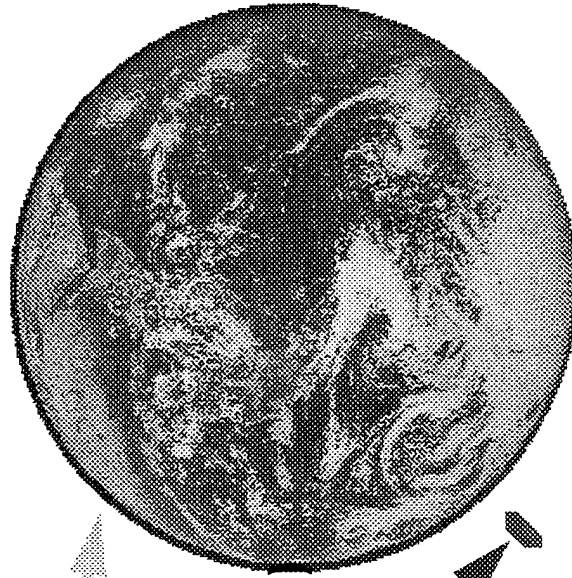
- **SAMM** (SHARC & MODTRAN MERGED)

- first principles combination

- ground to space (300 km)

- **RADTRAN**

- fast RF propagation



(We have you covered!)

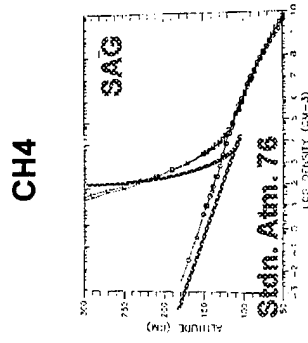
Dr. Frank O. Clark PL-GPOB, HAFB



Geophysics Directorate Codes

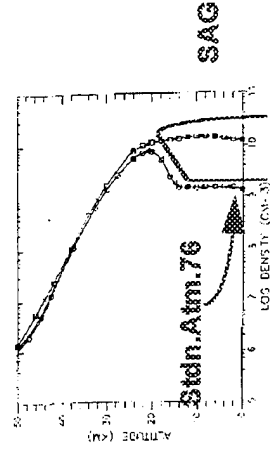
Standard Atmospheric Generator

- Based on Modern Data
 - Geographical variability
 - Seasonal variability
 - Time variability
- NASA MSIS 90E
 - satellite data base
- NRL climatology
 - data base (AWS)
- Contiguous ground-300 km
- Greatly improves code results
- Drives all codes in PLEXUS
 - default



ppm

HNO₃



ppm



Celestial Background Scene Descriptor CBSD



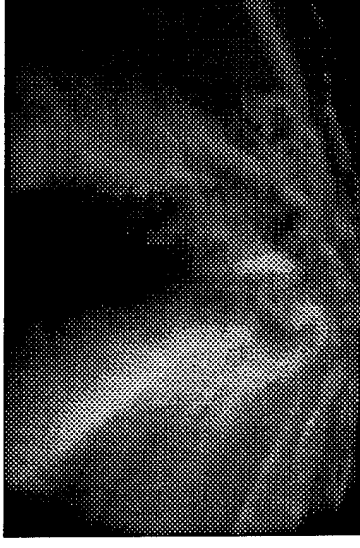
- Suite of Models
 - 2 to 30 microns
 - *visible to 30 microns (in progress)*
- Solar System:
 - Zodiacal Emission
 - Asteroids, Sun, Moon, Planets
- Galaxy:
 - IRAS PSC stars
 - Infrared Calibration Stars
 - Statistical stellar model (2-30 microns)
 - » *visible to 30 microns*
 - *visible to 30 microns bright star catalog (in progress)*
 - *H II regions (extended) (in progress)*



(denotes work in progress)



WEATHERMAN



A Geophysics Directorate Product
(Work in Progress)

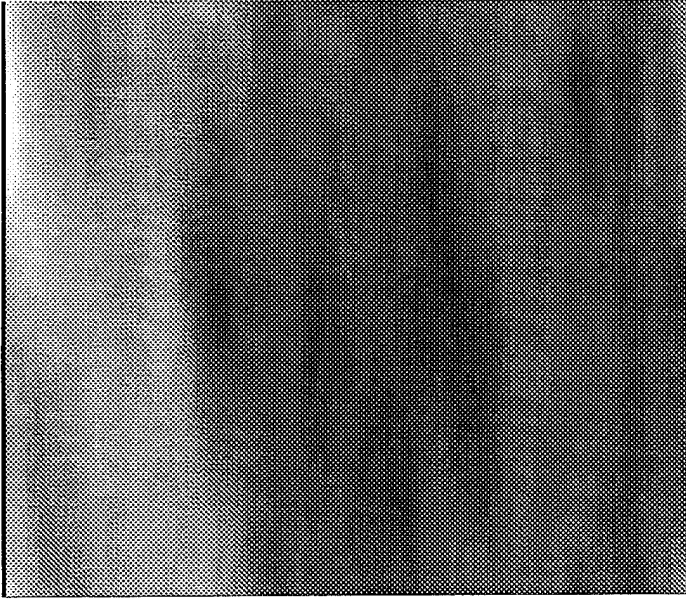
Concept!

- **Scenario Generator using existing validated codes**
 - **Self consistent multi-spectral weather (incl. lasers)**
 - across: MODTRAN, RADTRAN, SAMM, FASCODE
 - **small, fast, extensible, accurate**
 - **Multi-spectral: UV - microwave, ground - space, & lasers**
 - time dependent variability
 - formation & dispersal of fog, clouds, rain, humidity
- (collaboration with GPA)



SASS

Structured
Atmosphere
Scene
Simulator

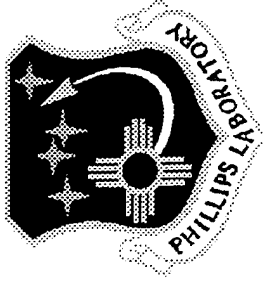


Work in Progress

- Altitude dependent structure
- Array of structure values
 - statistics of altitude dependence PSD
- Structure added upon radiance from any model
- FITS output (universal image format)
- FORTRAN
- Designed as a testbed
 - determine effective structure techniques



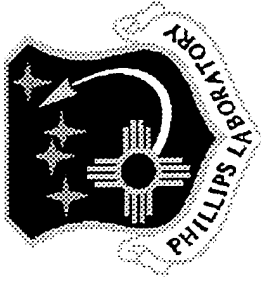
PLEXUS User Interface



- **Levels of Interface for Atmosphere:**
 - User experience
 - Wavelength or frequency regime
 - Set geometry
- **“Weather” input**



User Interface



- Let user work in “task” domain
- Let user work in their units
- Provide output in currently used format
- Let user have control over flow
- provide “convenient” output



Level of Expertise



Initial AIM Form - [c:\plexustaim\FOC.CPD]

File Help

Input Your Name (up to 8 Chars):

FOC

☐ First Time User

☒ Novice or Casual User

☐ Intermediate User

☐ Advanced User

For the Casual User, Many parameters are defaulted.

Continue

Use Tab and Shift-Tab or Mouse-Click to Navigate Between Controls



Wavelength

Specify Upper and Lower Spectral Limits - [c:\plexustaim\FOG.CPD]

File Wavelength Unit Interval Unit Help

Express
Keys



Select Type of Calculation:

☐ Moderate Resolution

Band Model for Integrated Band, Remote Sensing, etc.

☒ High Resolution

Line-By-Line Calculation for Laser, Microwave Applications

☐ Laser Line (129 Point Spectrum)

Set Spectral Limits:

Units: micron

Lower:

1.500000000e+00

Upper:

2.500000000e+00

OR

Band Center:

2

Band Width:

1

Set Spectral Output Interval:

Equivalent Spectral Interval:

micron

.01

at reference λ

1

Scanning Function:

Rectangular

Number of Frequency Points = 27

☐ Defaults Based On Limits

☒ User Defined

Go Back

Continue

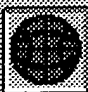


Since high resolution is required, FASCODE is recommended. Truncate spectrum to a 525 cm-1 width.

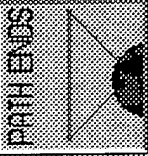
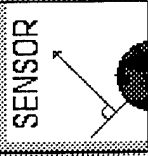
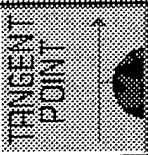


Geometry Feedback

Line-Of-Sight Specification

FileAngle UnitsLat UnitsLon UnitsAltitude UnitsUtilHelp



Set new path type:


Slant

Zenith

Nadir

Earth Graphic:

ZOOM

REDUCE

Ground Altitude above km0.000

Mean Sea Level:

Reference input altitudes to : ☒ Ground. ☐ Sea Level.

Initial (Observer) Location

Altitude KM0.000000e+00

Latitude Deg42.36

Longitude Deg +E-71.06

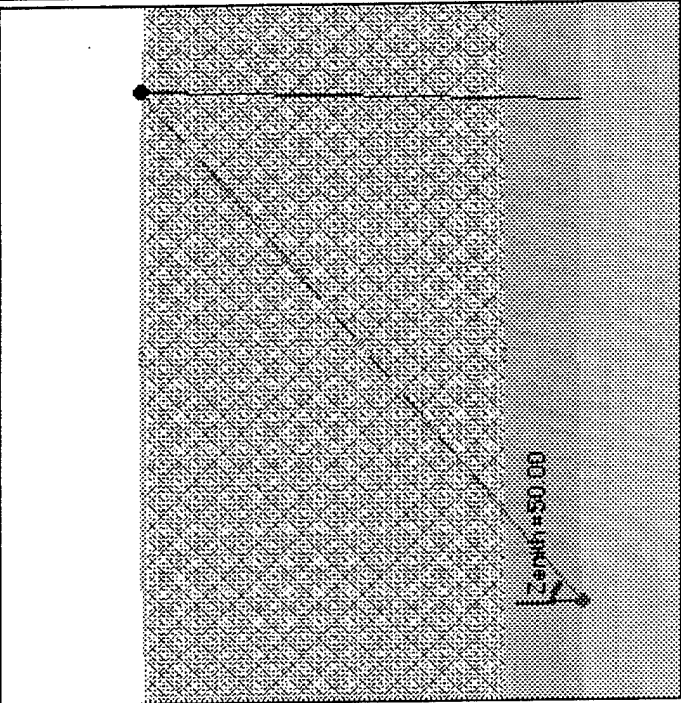
Sensor Geometry

Azimuth Deg89.9999999984

Zenith Deg50.00000000

Range to KM452.866580

Path End☒ Infinity

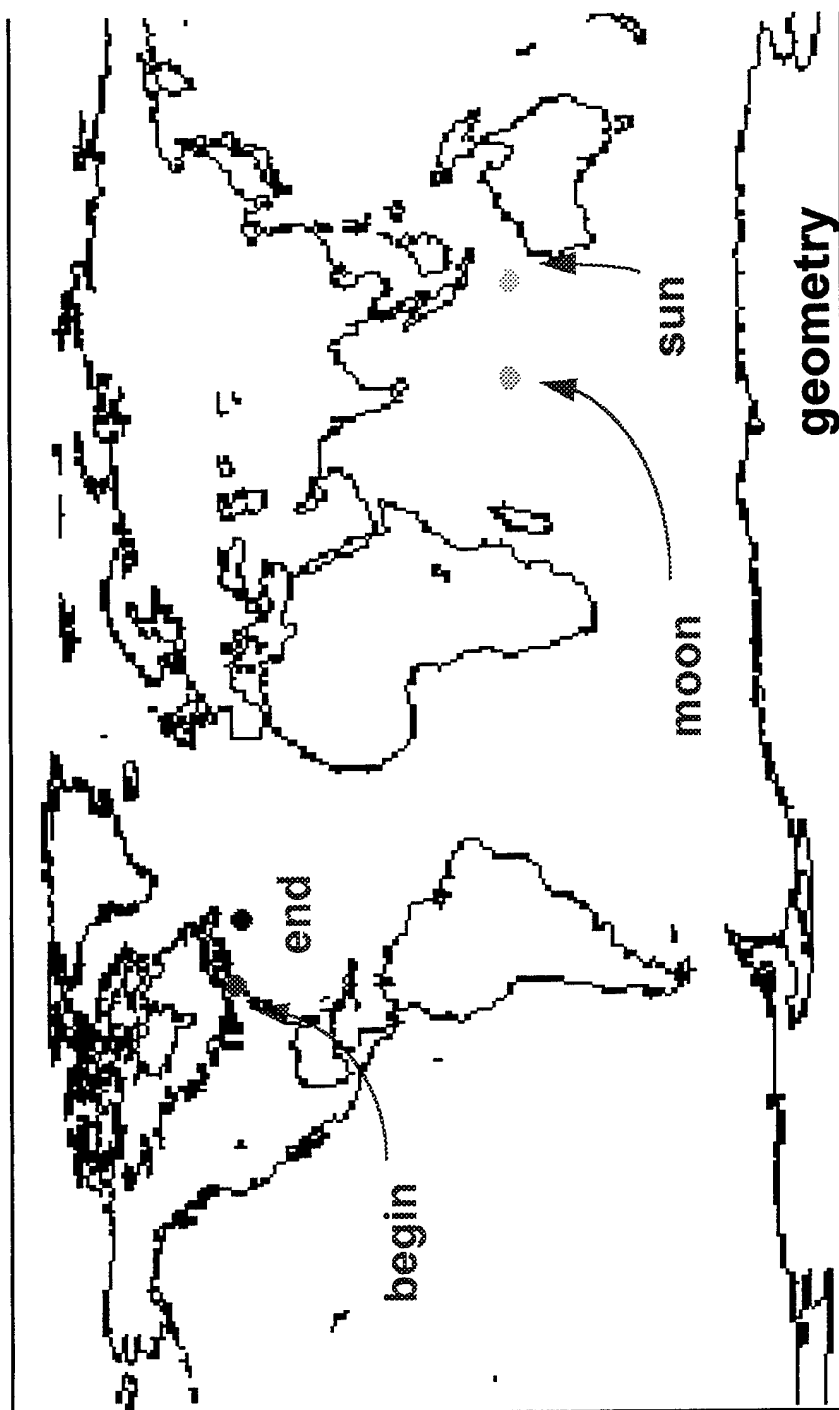


Go Back

Continue



Visual Feedback on Setup





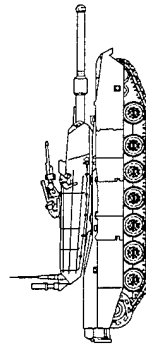
PLEXUS

Atmosphere & Weather Variables



Optimize:

design,
engineering,
operations,
war game.



Green zone

(all systems go)

Yellow zone

(ours work
theirs don't)

Red zone

(nothing works)

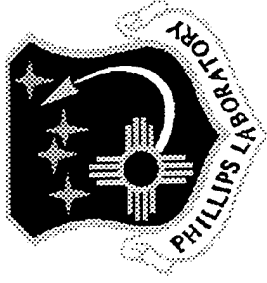


PLEXUS Non-interactive Inputs: Expert System Assisted

- **Location (path begin and end)**
- **Start Stop Wavelength**
- **Wavelength resolution**
- **Hyperfast, Fast, Accurate, or Laser**
- **Date, Time**



Non-interactive Inputs



- Hyperfast, Fast, Accurate or Laser
- Initial and final frequency & resolution
- Location, initial, and final
 - latitude, longitude, altitude
 - Observer to target distance
- Date, time



Code Input



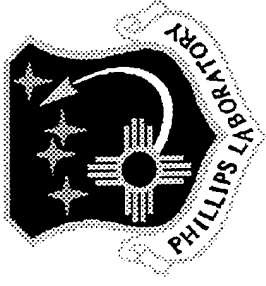
Date
Code
Logical_Flag_for_Modtran
Problem_Definition_File
X_Column_Pixels
Y_Row_Pixels
Pixel_Size
Image_Center_Longitude
Image_Center_Latitude
Image_Center_Longitude
Image_Center_Latitude
Image_Center_Right_Ascension
Image_Center_Declination
Image_Projection
Initial_Frequency
Final_Frequency
Spectral_Resolution
Start_Wavelength
End_Wavelength
Delta_Wavelength
Spectral_Filter_File
Execution_Mode
Flag_for_Multiple_Scattering
Printing_Step_Size
Flag_for_Laser_Options
Flag_for_Scanning_Function
Scanning_Function
Flag_for_Continuum
Flag_for_Line-by-Line_Functions
No_of_Points_per_Mean_1/2_Width
Printing_Mode
Control_to_Rerun_User-Atmosphere
Control_for_Multiple_Runs
Interactive/Batch
No_of_Radiators
Radiator_CO2_I1
Radiator_CO2_I2
Radiator_CO2_I3
Radiator_H2O
Radiator_O3
Radiator_CO
Radiator_NO
Radiator_OH
Radiator_NO+
S1_Model_Atmosphere_Output
S2_Selected_Transitions
S3_Molecular_Band_Information
S4_Not_Currently_Used
S5_Nemesis_Output
S6_Auroral_Output
S7_Final_Excited_State_Vib_Pop.

S8_Excited_State_Vib_Temp.
S9_LOS_Output
S10_Spectral_Radiance_Output
File_Line
File_Radiance
File_Transmittance
File_Output
Atmospheric_Path
CBSD_Observer_Altitude
Initial_Altitude
Initial_Latitude
Initial_Longitude
Final_Altitude
Final_Latitude
Final_Longitude
Initial_Zenith_Angle
Path_Azimuth_Angle_Earth
Observer_Target_Distance
Earth-Centered_Angle
Earth_Radius
Path_Long/Short_Index
Path_Case
Origin_Location
Spherical_Earth_Index
Tangent_Altitude
Tangent_Latitude
Tangent_Longitude
Tangent_Azimuth
Path_Azimuth_Case
Latitude_along_LOS_Vector
Longitude_along_LOS_Vector
Control_to_Read_Solar/Lunar_Geometry
Source_Sun/Moon
Sun_Altitude
Sun_Latitude
Sun_Longitude
Moon_Latitude
Moon_Longitude
Sun-Moon-Earth_Angle
Path_Azimuth_Angle_Sun
Solar_Zenith_Angle
Model_Atmosphere
Title_of_Model_Atmosphere
Modtran_Model_Atmosphere
Share_Model_Atmosphere
Fascode_Model_Atmosphere
User_defined_Model_Atmosphere
Sag_Altitudes
Temp_and_Press_Default
H2O_Default

O3_Default
CH4_Default
N2O_Default
CO_Default
CO2_Mixing_Ratio
Trace_Gases_Default
Geomagnetic_Activity_Index
Solar_Flux_Index
Solar_Flux_Index_Average
Day_of_Year
Greenwich_Time
Observation_Date
Observation_Time
Time_Stamp
Time_of_Day
Boundary_Temperature
Surface_Albedo_of_Earth
Boundary_Emissivity
Ground_Altitude
Boundary_Aer_Extinction+Vis.
Surface_Meteorological_Range
Tropo.+Strato_Aer_Season
Strato_Aer_Extinction+Profile
Air_Mass_Character
Cloud_or_Rain_Model
Rain_Rate
Vertical_Structure_Algorithm
Current_Wind_Speed
Average_Wind_Speed
Cirrus_Thickness
Cirrus_Base_Altitude
Cirrus_Ext_Coeff_@_0.55_um
Random_Number_Seed
Cloud_Ceiling_Height
Thickness_of_Cloud/Fog
Height_of_Inv./Boundary_Layer
Type_of_Aer_Phase_Function
Asymmetry_Factor_for_H-G_Phase_Function
Region_Total
R_Number
R_Type
R_Model
R_No_of_Photons
R_Max_Order_of_Scattering
R_Sunshine_Index
R_Earthshine_Index
Amb_Pop_FileName
Amb_Pop_Save_Index
Amb_No_of_Molecules
Amb_CO2_I1



PLEXUS



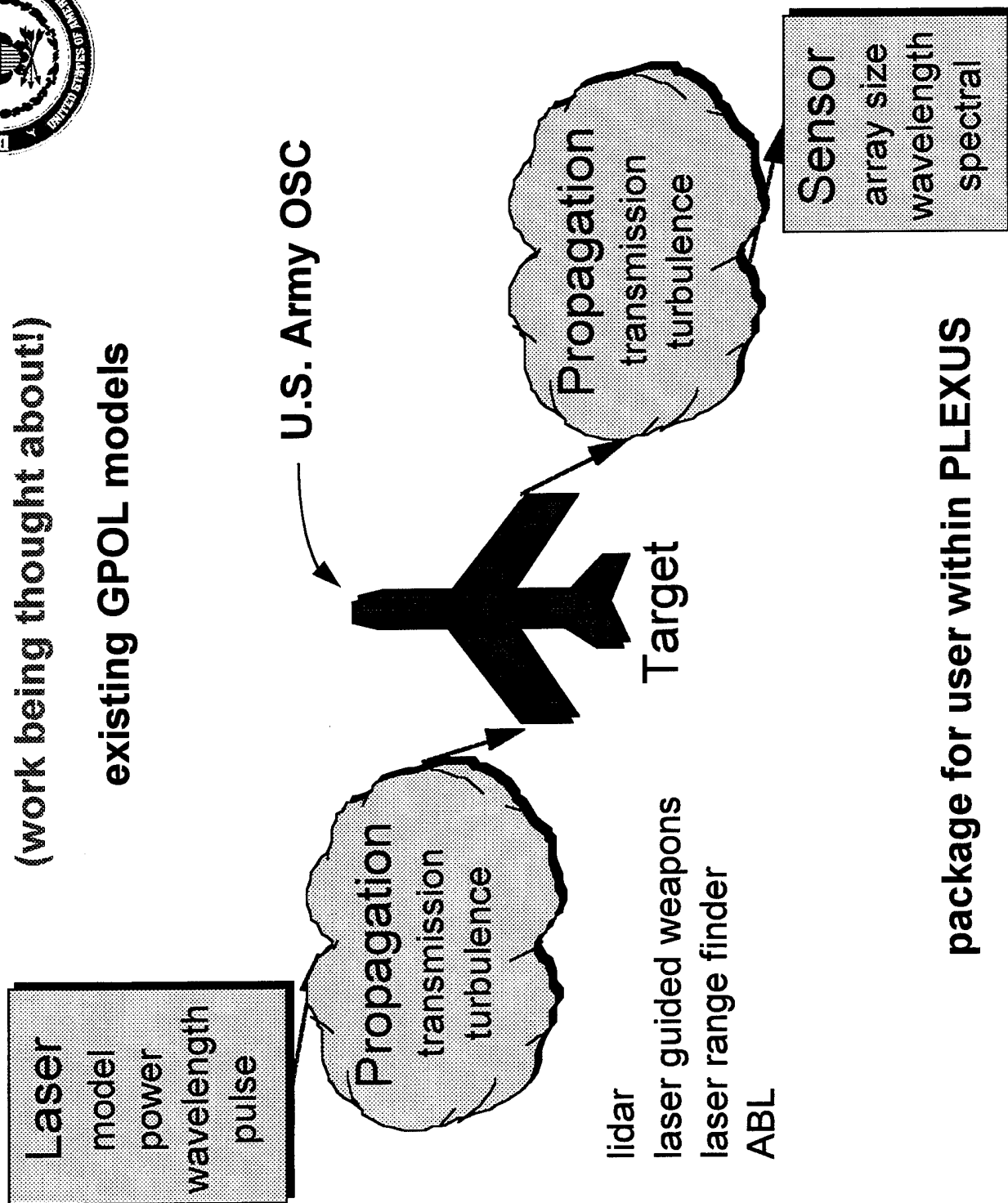
Where we will go next:

- **Architecture**
 - Distributed processing computing compliant
 - DMSO HLA, CORBA, OSF DCE, RPC
- **Cloud Structure (GPA models)**
- **Ionosphere (GPI models)**
- **Low resolution terrain model**
 - for existing codes
 - » use MOSART databases
- **Enhance SAG**

Laser Tools Suite

(work being thought about!)

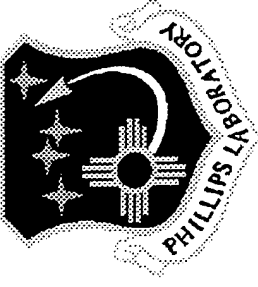
existing GPOL models



package for user within PLEXUS



PLEXUS



Why!

- **We offer value added expertise :**
 - **fundamental validated atmospheric physics,**
 - **codes, people, expertise, work in concert**
 - **solutions to DoD needs**
 - **entire atmosphere**
 - **ground to space**
 - **UV to microwave**
 - **self consistent weather effects**
 - **single focal point**
 - **straightforward inputs**



Geophysics Directorate

Hanscom Air Force Base



PLEXUS Summary

Multispectral Atmosphere including Weather

- task oriented, expert system based
- GUI + portable UNIX non-interactive
- ground to space
- validated multi-spectral: UV to microwave (RSN)
- weather object scenario player (*under construction*)
- architecture extensible / permits enhancements

validated state of the art atmosphere & weather

An Application of MODTRAN for Real-Time Infrared Scene Generation

Dr. David L. Quam
MTL Systems, Inc., Dayton, OH

ABSTRACT

Although MODTRAN is in wide use for calculating atmospheric transmittance and/or radiance in the infrared, visible and ultraviolet spectral regions, it is not suited for direct use in real-time simulation applications. This paper presents a table look-up method to make MODTRAN transmission and radiance data available to a real-time infrared (IR) scene generation simulator. A description of the method is presented with respect to the IR scene generator application. An error analysis of the table linear interpolation errors is presented, along with table parameters and breakpoints. In addition, test results are presented which show the method to give very good accuracy with rather few breakpoints.

1.0 INTRODUCTION

MODTRAN is the current program in wide use for calculating atmospheric transmittance and/or radiance in the infrared, visible and ultraviolet spectral regions. It was developed and is maintained by the Air Force Geophysics Laboratory to replace LOWTRAN7. The purpose of this paper is to describe the inclusion of MODTRAN atmospheric solar irradiance and path transmittance into EZ*IR by adding a preprocessor to set up irradiance and transmittance arrays calculated from MODTRAN. These arrays are then used in EZ*IR for irradiance calculations.

2.0 The MTL Infrared (IR) Scene Generator - EZ*IR

EZ*IR is a real-time, IR scene generator which functions in concert with an existing visual computer image generator. It is intended for use in three fundamental areas of infrared technology: *system effectiveness evaluation*, *system development/verification*, and *training simulation*. It provides realistic scene representation, including targets, backgrounds and clutter (including counter-measures), point sources, or extended targets, variable weather conditions, locations, time/date, static (fixed scene) and dynamic (moving scene) conditions, precision or accuracy commensurate with the system being driven or tested, outputs to drive scene generators (software) as well as scene projectors (hardware), and real-time execution (for real-time simulation aspects of testing, development, or training). EZ*IR complements the excellent existing capability of current visual simulations' three-dimensional spatial display characteristics.

EZ*IR's thermal model includes calculations of radiation, conduction, and convection, as well as material spectral

absorptivity, reflectivity, and emissivity. The system consists of a feature properties database, and functions to calculate solar irradiance, solar elevation angle, spectral reflectivity, atmospheric transmission, spectral absorptivity, sky irradiance, surface temperature, air temperature, and spectral radiant exitance. These functions are implemented in the simulation code as major subroutines. They are supported by other functional subroutines for the computation of numerical integrations, blackbody spectral emissions, and assorted other recurring mathematical and physical/optical calculations.

The simulation calculates the integrated radiant exitance (watts/square meter), for every feature in its feature list, which may be all the features in the DMA database plus a group of special features (hot, dynamic targets, for example) or some subset thereof, depending on the application. The total radiant exitance is the combined reflected and emitted components from a feature, integrated across the user-selected IR band of interest (usually 3-5 μ m or 8-14 μ m, or any sub-band thereof).

Information within EZ*IR may be accessed at different points, to support a variety of system output needs. Although the typical output of the model is a set of relative intensity values for the set of features in the band of interest, these data are derived from calculation of the reflected and emitted spectral radiant exitance components for each feature under consideration. Hence, for cases where absolute spectral radiant exitances are required, these may be obtained simply by accessing the outputs of the appropriate subroutines.

MODTRAN is used to calculate the solar irradiance on a target location at a given

altitude and solar incidence angle, and also to calculate the atmospheric transmittance from the target to the observer. These results are then incorporated into EZ*IR, using a table look-up interpolation method.

3.0 TECHNICAL APPROACH

A preprocessor was developed to call MODTRAN and generate arrays of solar irradiance and transmittance for two paths. The first path is from the sun to a target location. The target location can be either an aircraft or missile in flight, or a portion of the earth surface. The second path is from the target location to the observer location. The first path is based on the altitude of the target and the sun zenith angle, requiring two dimensions for the first array. The second path is based on the altitudes of both target and observer, and the slant range between them, requiring three dimensions for the second array. Several MODTRAN input parameters can be selected by the user, while the remaining parameters are fixed in the preprocessor. The user selectable parameters are identified in Table 1.

Table 1.
User Selectable MODTRAN Parameters

VARIABLE	NAME	DESCRIPTION
MODEL	Atmospheric Model	Selects the geographical seasonal model atmosphere
IHAZE	Haze	Controls lower atmosphere aerosol attenuation for haze and fog conditions
ICLD	Cloud	Controls both cloud and rain models
W1	Wavelength 1	Sets initial spectral wavelength
W2	Wavelength 2	Sets final spectral wavelength

The preprocessor contains a user query section, a MODTRAN preparation and run section, and a final section to put the MODTRAN output into the required arrays. The user query section allows the user to select certain parameters via an input screen. The user can select any of these parameters or use the default value. Selecting any parameter brings up a selection screen which describes the choices and allows easy selection.

The MODTRAN preparation and run section first prepares the MODTRAN input file, including the user selected parameters

and the fixed parameters required to run MODTRAN. While most parameters are set to the MODTRAN default value, some parameters are used to control the desired path parameters and spectral resolution. This input file also includes the variation of parameters for multiple MODTRAN runs necessary to generate all the elements in the two path arrays. The final preprocessor section extracts the transmittance information from the MODTRAN output file and loads it into the two arrays.

A run-time module was also developed to interpolate the data in the arrays for the actual run-time conditions. This module consists of a pair of interpolation sub-routines. The first subroutine is a two-dimensional interpolation routine, and the second is a three-dimensional interpolation routine. Both routines use a standard linear interpolation method to determine values between the breakpoints, and to limit results beyond the table boundaries to the boundary value.

3.1 Preprocessor Module: The atmospheric effects pre-processor module structure is shown in Figure 1. The module consists of a user query and MODTRAN input preparation program, ATMGEN1; a MODTRAN execution statement; a path array generation program, ATMGEN2; and two data files, one for MODTRAN input and one for MODTRAN output. Program ATMGEN1 provides the user with brief information describing each user choice and accepts user input for the five user selectable parameters. ATMGEN1 then writes TAPE5, which is the input file required by MODTRAN. After MODTRAN is run, ATMGEN2 reads MODTRAN's output file, TAPE6, and generates the solar irradiance path array and the transmittance path array.

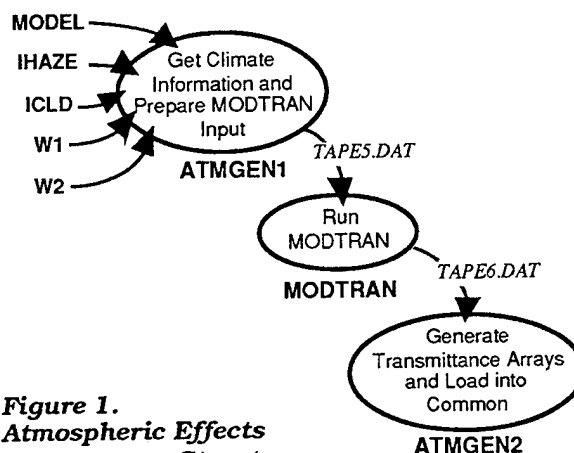


Figure 1.
Atmospheric Effects
Preprocessor Structure

An abbreviated example of the output arrays is shown here in Table 2.

Table 2.
Abridged File: ARYSREAD.DAT

Solar Irradiance		Altitude	=	.0 Km	&	Angle	=	0. degrees
.0000	.9340E-26	.1790E-02		.1836E-01		.4517E-01		.5361E-01 .5407E-01
.4896E-01	.3938E-01	.3793E-01		.2833E-01		.2996E-01		.2520E-01 .2351E-02
.1967E-01	.1885E-01	.1611E-01		.5475E-02		.2612E-03		.5843E-02 .7125E-02
.6251E-02	.5034E-02	.3491E-02		.9616E-03		.2153E-09		.4015E-17 .1122E-05
.2598E-03	.5660E-03	.4897E-03		.5537E-03		.5147E-03		.9081E-03 .1119E-02
.1032E-02	.9637E-03	.8969E-03		.7867E-03		.7470E-03		.5705E-03 .1342E-03
.2069E-13	.1280E-05	.6642E-04		.2662E-03		.2776E-03		.1878E-03 .1775E-03
.1085E-03								
Solar Irradiance		Altitude	=	.0 Km	&	Angle	=	15. degrees
.0000	.1443E-26	.1618E-02		.1710E-01		.4295E-01		.5143E-01 .5228E-01
.4754E-01	.3834E-01	.3709E-01		.2773E-01		.2944E-01		.2474E-01 .2243E-02
.1944E-01	.1868E-01	.1596E-01		.5391E-02		.2447E-03		.5749E-02 .7065E-02
.6211E-02	.4994E-02	.3445E-02		.9351E-03		.1383E-09		.1412E-17 .9635E-06
.2474E-03	.5481E-03	.4735E-03		.5402E-03		.5017E-03		.8960E-03 .1109E-02
.1025E-02	.9549E-03	.8904E-03		.7800E-03		.7407E-03		.5618E-03 .1316E-03
.1325E-13	.1139E-05	.6330E-04		.2613E-03		.2736E-03		.1838E-03 .1737E-03
.1053E-03								
Solar Irradiance		Altitude	=	.0 Km	&	Angle	=	90. degrees
.0000	.7749E-42	.2775E-03		.1898E-01		.5716E-01		.5064E-01 .8599E-01
.8689E-01	.7693E-01	.6644E-01		.5554E-01		.4699E-01		.3980E-01 .3132E-01
.2738E-01	.2358E-01	.2031E-01		.1571E-01		.1200E-01		.8530E-02 .8277E-02
.7239E-02	.5506E-02	.5121E-02		.4777E-02		.2821E-02		.6404E-03 .7077E-03
.2302E-02	.2299E-02	.2070E-02		.1546E-02		.1076E-02		.1266E-02 .1270E-02
.1134E-02	.1153E-02	.1040E-02		.8337E-03		.8060E-03		.6288E-03 .1768E-03
.1039E-11	.5222E-05	.1022E-03		.3440E-03		.2621E-03		.1370E-03 .2990E-03
.3540E-03								
Transmittance		T Alt	=	.0 Km, 0 Alt	=	.0 Km & Range	=	15.0 Km
3233E-01	1475	.6353E-01		.1410		.1197		.1105 .1363
.1130	.9490E-01	.1298		.1115		.1240		.1169 .1121
.9478E-01	.9018E-01	.1246		.1162		.1362		.1442 .1740
.1962	.1622	.1480		.1775		.1510		.1653 .1813
.1544	.1701	.1476		.1805		.1657		.1329 .1577
.1480	.1533	.1004		.1378		.1189		.1440
Transmittance		T Alt	=	.0 Km, 0 Alt	=	.0 Km & Range	=	12.2 Km
.5310E-01	.1960	.9491E-01		.1884		.1686		.1579 .1923
.1650	.1407	.1872		.1638		.1798		.1721 .1656
.1433	.1385	.1820		.1709		.1951		.2038 .2397
.2659	.2256	.2082		.2441		.2113		.2300 .2491
.2158	.2355	.2075		.2481		.2303		.1896 .2207
.2085	.2157	.1470		.1971		.1731		.2062
Transmittance		T Alt	=	15.0 Km, 0 Alt	=	.0 Km & Range	=	.0 Km
1.000	1.000	1.000		1.000		1.000		1.000
1.000	1.000	1.000		1.000		1.000		1.000
1.000	.9999	.9999		.9999		.9999		1.000
1.000	1.000	1.000		1.000		1.000		1.000
1.000	1.000	1.000		1.000		1.000		1.000
1.000	1.000	1.000		1.000		1.000		1.000

3.2 Run-Time Module: The atmospheric effects run-time module structure is shown in Figure 2.

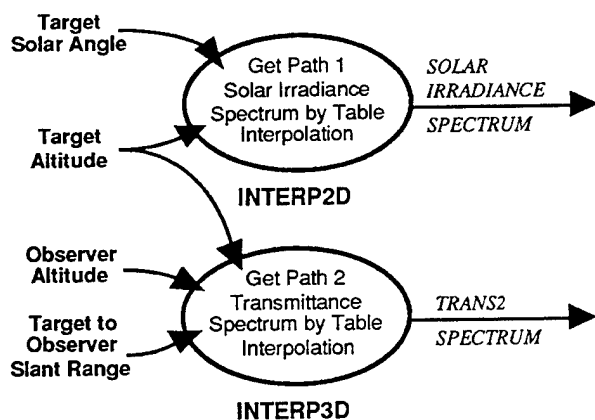


Figure 2. Atmospheric Effects Run-Time Structure

EZ*IR calls the two-dimensional interpolation subroutine, INTP2D, providing inputs of the current solar angle from the target and the current target altitude. INTP2D returns with the solar irradiance spectrum. The solar spectrum is provided in $0.1 \mu\text{m}$ increments from $0.1 \mu\text{m}$ to $5.0 \mu\text{m}$. EZ*IR then calls the three-dimensional interpolation subroutine, INTP3D, providing inputs of the current target altitude, current observer altitude, and the current slant range from the target to the observer. INTP3D returns with the target to observer path transmittance spectrum. The path transmittance spectrum is provided in $0.1 \mu\text{m}$ increments between the user selected spectral wavelengths.

4.0 PERFORMANCE

Performance factors include processing speed, accuracy, and validation. Processing speed and accuracy are both extremely important for real-time simulation of IR targets and scenes. Reasonable processor performance is necessary for affordable IR simulation and accuracy is necessary for most simulation purposes (system effectiveness evaluation, system development and verification, and training).

4.1 Processing Speed: Processing speed is enhanced by efficient programming and compilation. EZ*IR uses the approach of including only two interpolation subroutines in the run-time program, with most of the atmospheric calculations occurring in the preprocessor. This approach is extremely

efficient, requiring very little CPU effort during run-time. In conjunction with a modern optimizing compiler, this results in a very efficient run-time module. Actual run-time test results are presented in Section 5.

4.2 Accuracy: For 32-bit floating-point calculations, accuracy is primarily determined by the limitations of the interpolation scheme. The interpolation break points must be chosen such that the maximum error introduced by the interpolation remains below 2%. An error analysis was conducted along with verification testing to determine the actual level of accuracy.

The breakpoints in the transmittance arrays were chosen to minimize the number of array breakpoints while limiting the linear interpolation error. The MODTRAN accuracy is generally about 5%. The maximum linear interpolation error was chosen at 2%, as a compromise between reducing the number of array breakpoints and preserving the MODTRAN accuracy. Verification test results are presented in the next section.

5.0 TEST RESULTS

EZ*IR testing consisted of individual module testing and final benchmark testing of the complete run-time program. Test results for the atmospheric effects module are presented first, followed by the run-time benchmark test results.

The atmospheric effects module of EZ*IR consists of a preprocessor which generates two arrays from MODTRAN, and two run-time subroutines which interpolate results from these arrays. Because MODTRAN has undergone extensive verification and validation, these tests focus on (1) verifying the required resolution of the data points, and (2) verifying the software's ability to retrieve the appropriate data based on the given inputs. The former can be verified by comparing errors between the MODTRAN results for actual input conditions and interpolated results between array breakpoints. The latter can be verified by a three-step process of comparing (a) MODTRAN inputs with desired inputs, (b) generated array data with MODTRAN outputs, and (c) interpolated results with array values.

Consequently, the test plan for the atmospheric effects module of EZ*IR consists of four separate tests. The first test, M-1, identifies the errors resulting from linear interpolation of data from the solar

irradiance and atmospheric transmittance arrays. The second test, M-2, checks the capability of the preprocessor program, ATMGEN1, which generates the MODTRAN input file. The third test, M-3, checks the capability of the preprocessor program, ATMGEN2, which reads the MODTRAN output file and generates the solar irradiance and atmospheric transmittance arrays. The fourth test, M-4, checks the capability of the run-time interpolation subroutines.

Real-time performance testing of EZ*IR was conducted on a Silicon Graphics Indigo 2 with one R4400 200 MHz processor and 128 MB of RAM. The testing was accomplished with only the EZ*IR core calculations being conducted on the one processor, without any graphics presentation. Several benchmark cases were tested with the number of materials ranging from 13 to 1000, and the number of targets (vehicles) ranging from 0 to 30.

5.1 Summary of Test Results: The atmospheric effects preprocessor and run-time subroutines executable codes were run and functioned correctly. Except for a range value of 0.2 Km for the transmittance, all linear interpolation errors were within 2.1%. Although this exception resulted in errors approaching 6%, the likelihood of occurrence is small.

Actual EZ*IR run-time test results of material and target update rates are presented in Table 3 for several benchmark cases. A rather complicated case of 524 materials and 30 targets provides a target update rate of 20.9Hz and a material update rate of 0.5Hz on a single processor. This is more than adequate for real-time because maximum target temperature rates are typically well below 10Hz, and background (material) temperature rates are typically well below 0.1Hz.

Table 3. EZ*IR Real-Time Performance Test Results

NUMBER OF MATERIALS	NUMBER OF TARGETS	NUMBER OF HOTSPOTS/TARGET	AVERAGE NUMBER OF MATERIALS/FRAME	AVERAGE NUMBER OF TARGETS/FRAME	NUMBER OF FRAMES	MATERIAL RATE (Hz)	TARGET RATE (Hz)
13	0	0	13.0	0.0	9053	30.0	---
13	1	8	13.0	1.0	9069	30.0	30.1
13	7	8	13.0	7.0	9015	30.0	30.0
13	20	8	13.0	20.0	9016	29.9	30.0
13	30	8	3.8	22.9	9528	---	22.9
524	0	0	131.0	0.0	9097	7.5	---
524	1	8	130.6	1.0	9066	7.5	30.0
524	7	8	104.5	6.5	10269	6.0	27.8
524	20	8	27.2	19.0	9120	1.6	28.4
524	30	8	8.2	20.9	9055	0.5	20.9
1000	0	0	140.0	0.0	9058	4.2	---
1000	1	8	132.8	0.9	9102	4.0	28.1
1000	7	8	110.2	6.5	9078	3.3	27.7
1000	20	8	29.1	19.0	9131	0.9	28.4

5.2 Detailed Test Results: The details of the four individual atmospheric effects module tests are presented in the remaining pages of this section. The first test determines errors associated with the linear interpolation between array breakpoints. The other three tests verify proper generation and interpolation of the solar irradiance and atmospheric transmittance arrays.

Test M-1

Linear Interpolation Error Evaluation

1. Test Description — This test uses MODTRAN to generate solar irradiance and atmospheric transmittance for various target

and observer conditions. Three FORTRAN test programs were written to generate MODTRAN inputs, extract MODTRAN outputs, and conduct linear interpolation and calculate errors for this test.

2. Test Objective — The objective of this test was to determine the errors associated with linear interpolation between breakpoints in the solar irradiance and atmospheric transmittance arrays. The acceptance criteria for this error is 2% of the maximum value.

3. Test Configuration — The test configuration consists of the MODTRAN program, a FORTRAN test program (TEST1) to generate the MODTRAN input file, a

FORTTRAN test program (TEST2) to extract the integrated solar irradiance and integrated atmospheric transmittance from the MODTRAN output, and another FORTRAN test program (LINERR) to conduct linear interpolation and calculate errors and error percentages.

4. Test Procedure — The test procedure consisted of running TEST1 to generate the MODTRAN input, running MODTRAN, running TEST2, and finally running LINERR. This sequence of test runs were repeated to separately vary the solar angle, target altitude, observer altitude, and target to observer range. The final results were saved to a file by LINERR.

5. Test Results — The results of this test are a series of tables in a six column format. The first column is the parameter varied (solar angle, target altitude, observer altitude, or target to observer range). The second column is the MODTRAN output value for that parameter value, while the third column is the interpolated result. The fourth column is the error between the interpolated result and the actual MODTRAN result. The fifth column is the percentage error based on the current MODTRAN result, while the sixth column is the percentage error based on the maximum MODTRAN result in that table.

The first group of test results present errors in the transmitted solar irradiance. The errors in the solar irradiance for variations in solar angle at a target altitude of 2.0 Km are presented in Table 4.

Table 4.
Errors in Transmitted Solar Irradiance
Target Altitude = 2. Km

Sun Angle	Solar Irradiance	Table Irradiance	Error	% Error	% of Max
0.0	.102000	.102000	.000000	.000	.000
1.0	.102000	.101953	-.000047	-.046	-.046
2.0	.102000	.101907	-.000093	-.092	-.092
3.0	.102000	.101860	-.000140	-.137	-.137
4.0	.102000	.101813	-.000187	-.183	-.183
5.0	.101900	.101767	-.000133	-.131	-.131
6.0	.101900	.101720	-.000180	-.177	-.176
7.0	.101900	.101673	-.000227	-.222	-.222
8.0	.101800	.101627	-.000173	-.170	-.170
9.0	.101800	.101580	-.000220	-.216	-.216
10.0	.101700	.101533	-.000167	-.164	-.163
11.0	.101600	.101487	-.000113	-.112	-.111
12.0	.101600	.101440	-.000160	-.157	-.157
13.0	.101500	.101393	-.000107	-.105	-.105
14.0	.101400	.101347	-.000053	-.053	-.052
15.0	.101300	.101300	.000000	.000	.000
16.0	.101200	.101144	-.000056	-.055	-.055
17.0	.101100	.100988	-.000112	-.111	-.110
18.0	.101000	.100832	-.000168	-.166	-.165
19.0	.100800	.100676	-.000124	-.123	-.122
20.0	.100700	.100520	-.000180	-.179	-.176

70.0	.073640	.073640	.000000	.000	.000
71.0	.072070	.071594	-.000476	-.661	-.467
72.0	.070380	.069547	-.000833	-1.183	-.816
73.0	.068580	.067501	-.001079	-1.573	-1.058
74.0	.066650	.065455	-.001195	-1.793	-1.172
75.0	.064560	.063409	-.001151	-1.783	-1.129
76.0	.062320	.061363	-.000958	-1.536	-.939
77.0	.059890	.059316	-.000574	-.958	-.562
78.0	.057270	.057270	.000000	.000	.000
79.0	.054410	.054003	-.000407	-.749	-.400
80.0	.051310	.050735	-.000575	-1.121	-.564
81.0	.047910	.047467	-.000443	-.924	-.434
82.0	.044200	.044200	.000000	.000	.000
83.0	.040140	.039727	-.000413	-1.030	-.405
84.0	.035670	.035253	-.000417	-1.168	-.408
85.0	.030780	.030780	.000000	.000	.000
86.0	.025420	.024977	-.000443	-1.744	-.435
87.0	.019590	.019173	-.000417	-2.127	-.408
88.0	.013370	.013370	.000000	.000	.000
89.0	.007102	.007616	.000514	7.230	.503
90.0	.001861	.001861	.000000	.000	.000

Table 5 presents the transmitted solar irradiance errors for variations in target altitude at solar angle of 89°. Except for the 89° solar angle data, all percentage errors based on the maximum are below the 2% criteria. For the 89° solar angle data, the largest error is only 2.1%.

Table 5
Errors in Transmitted Solar Irradiance
Sun Angle = 89. degrees

Target Altitude	Solar Irradiance	Table Irradiance	Error	% Error	% of Max
0.0	.000002	.000002	.000000	.000	.000
0.2	.000005	.000011	.000007	142.403	.008
0.4	.000011	.000020	.000009	80.842	.010
0.6	.000030	.000030	.000000	.000	.000
0.8	.000087	.000164	.000077	89.117	.088
1.0	.000298	.000298	.000000	.000	.000
1.2	.000938	.001458	.000520	55.385	.595
1.4	.002129	.002619	.000490	22.995	.561
1.6	.003779	.003779	.000000	.000	.000
1.8	.005558	.005441	-.000117	-2.114	-.135
2.0	.007102	.007102	.000000	.000	.000
2.2	.008532	.008744	.000212	2.480	.242
2.4	.010120	.010385	.000265	2.621	.304
2.6	.011820	.012027	.000207	1.750	.237
2.8	.013580	.013668	.000088	.651	.101
3.0	.015310	.015310	.000000	.000	.000

7.0	.048640	.048640	.000000	.000	.000
7.2	.050490	.050073	-.000417	-.827	-.478
7.4	.052280	.051505	-.000775	-1.482	-.887
7.6	.054020	.052938	-.001082	-2.003	-1.240
7.8	.055710	.054371	-.001339	-2.404	-1.534
8.0	.057370	.055803	-.001567	-2.731	-1.795
8.2	.058980	.057236	-.001744	-2.957	-1.998
8.4	.060500	.058669	-.001831	-3.027	-2.098
8.6	.061940	.060101	-.001839	-2.968	-2.106
8.8	.063300	.061534	-.001766	-2.790	-2.023
9.0	.064590	.062967	-.001623	-2.513	-1.860
9.2	.065810	.064399	-.001411	-2.144	-1.616
9.4	.066970	.065832	-.001138	-1.699	-1.304
9.6	.068080	.067265	-.000815	-1.198	-.934
9.8	.069130	.068697	-.000433	-.626	-.496
10.0	.070130	.070130	.000000	.000	.000

14.0	.084680	.083858	-.000822	-.971	-.942
14.2	.085220	.084544	-.000676	-.793	-.774
14.4	.085750	.085231	-.000519	-.605	-.595
14.6	.086270	.085917	-.000353	-.409	-.404
14.8	.086790	.086604	-.000186	-.215	-.214
15.0	.087290	.087290	.000000	.000	.000

The second group of test results present errors in the atmospheric transmittance for the 8-12 μ m band. The transmittance errors for variations in target to observer range at target and observer altitudes of 0. Km for the 8-12 μ m band appear in Table 6.

Table 6. Errors in Atmospheric Transmittance — Target Altitude = 0. Km, Observer Altitude = 0. Km, 8-12 μ m

Range (Km)	Actual Transmittance	Table Trams	Error	% Error	% of Max
0.0	.999700	.999700	.000000	.000	.000
0.2	.956500	.960850	.004350	.455	.435
0.4	.922000	.922000	.000000	.000	.000
0.6	.891000	.894800	.003800	.426	.380
0.8	.862400	.867600	.005200	.603	.520
1.0	.835600	.840400	.004800	.574	.480
1.2	.810200	.813200	.003000	.370	.300
1.4	.786000	.786000	.000000	.000	.000
1.6	.762900	.765650	.002750	.360	.275
1.8	.740800	.745300	.004500	.607	.450
2.0	.719500	.724950	.005450	.757	.545
2.2	.700100	.704600	.004500	.643	.450
2.4	.679100	.684250	.005150	.758	.515
2.6	.659300	.663900	.004600	.698	.460
2.8	.641000	.643550	.002550	.398	.255
3.0	.623200	.623200	.000000	.000	.000

12.0	.192900	.193823	.000923	.479	.092
12.2	.188200	.188200	.000000	.000	.000
12.4	.183500	.184250	.000750	.409	.075
12.6	.179000	.180300	.001300	.726	.130
12.8	.174600	.176350	.001750	1.002	.175
13.0	.170300	.172400	.002100	1.233	.210
13.2	.166100	.168450	.002350	1.415	.235
13.4	.162000	.164500	.002500	1.543	.250
13.6	.158000	.160550	.002550	1.614	.255
13.8	.154100	.156600	.002500	1.622	.250
14.0	.150400	.152650	.002250	1.496	.225
14.2	.146700	.148700	.002000	1.363	.200
14.4	.143100	.144750	.001650	1.153	.165
14.6	.139600	.140800	.001200	.860	.120
14.8	.136200	.136850	.000650	.477	.065
15.0	.132900	.132900	.000000	.000	.000

Table 7 (on the next page) presents these same errors for variations in observer altitude at a target altitude of 2. Km and a range of 2. Km for the same 8-12 μ m band. This table is limited to observer altitudes of 4. Km and below because the altitude difference must be equal to or less than the range. All percentage errors based on the maximum are well below the 2% criteria for this group.

Table 7. Errors in Atmospheric Transmittance — Target Altitude = 2. Km, Range = 2. Km, 8-12 μ m

Observer Altitude	Actual Transmittance	Table Trans	Error	% Error	% of Max
0	.795200	.795200	.000000	.000	.000
.1	.799300	.801000	.001700	.213	.181
.2	.803700	.806800	.003100	.386	.330
.3	.808300	.812600	.004300	.532	.457
.4	.813100	.818400	.005300	.652	.564
.5	.818300	.824200	.005900	.721	.628
.6	.823800	.830000	.006200	.753	.660
.7	.829900	.835800	.005900	.711	.628
.8	.836700	.841600	.004900	.586	.521
.9	.844300	.847400	.003100	.367	.330
1.0	.853200	.853200	.000000	.000	.000
1.1	.862000	.858460	-.003540	-.411	-.377
1.2	.869700	.863720	-.005980	-.688	-.636
1.3	.876400	.868980	-.007420	-.847	-.789
1.4	.882200	.874240	-.007960	-.902	-.847
1.5	.887300	.879500	-.007800	-.879	-.830
1.6	.891900	.884760	-.007140	-.801	-.760
1.7	.895900	.890020	-.005880	-.656	-.626
1.8	.899600	.895280	-.004320	-.480	-.460
1.9	.902800	.900540	-.002260	-.250	-.240
2.0	.905800	.905800	.000000	.000	.000
2.1	.908200	.907510	-.000690	-.076	-.073
2.2	.910400	.909220	-.001180	-.130	-.126
2.3	.912600	.910930	-.001670	-.183	-.178
2.4	.914800	.912640	-.002160	-.236	-.230
2.5	.917000	.914350	-.002650	-.289	-.282
2.6	.919100	.916060	-.003040	-.331	-.323
2.7	.921300	.917770	-.003530	-.383	-.376
2.8	.923600	.919480	-.004120	-.446	-.438
2.9	.926000	.921190	-.004810	-.519	-.512
3.0	.926200	.922900	-.003300	-.356	-.351
3.1	.927900	.924610	-.003290	-.355	-.350
3.2	.929500	.926320	-.003180	-.342	-.338
3.3	.931000	.928030	-.002970	-.319	-.316
3.4	.932500	.929740	-.002760	-.296	-.294
3.5	.933900	.931450	-.002450	-.262	-.261
3.6	.935200	.933160	-.002040	-.218	-.217
3.7	.936400	.934870	-.001530	-.163	-.163
3.8	.937700	.936580	-.001120	-.119	-.119
3.9	.938800	.938290	-.000510	-.054	-.054
4.0	.940000	.940000	.000000	.000	.000

The final group of test results present errors in the atmospheric transmittance for the 3-5 μ m band. Table 8 presents transmittance errors for variations in target to observer range at target and observer altitudes of 0. Km for the 3-5 μ m band. Table 9 (on the next page) presents these errors for observer altitude variations at a target altitude of 6. Km and a range of 9.2 Km. Except for transmittance at a range of 0.2 Km, all percentage errors based on the maximum are well below the 2% criteria for this group. Although the error for this target to observer range value of 0.2 Km can approach 6%, it

was considered acceptable. This consideration was based on the small possibilities of occurrence, which do not warrant adding an additional breakpoint to the transmittance arrays.

Table 8. Errors in Atmospheric Transmittance — Target Altitude = 0. Km, Observer Altitude = 0. Km, 3-5 μ m

Range (Km)	Actual Transmittance	Table Trans	Error	% Error	% of Max
.0	.976100	.976100	.000000	.000	.000
.2	.795300	.852050	.056750	7.136	5.814
.4	.728000	.728000	.000000	.000	.000
.6	.678600	.692180	.013580	2.001	1.391
.8	.638700	.656360	.017660	2.765	1.809
1.0	.604800	.620540	.015740	2.603	1.613
1.2	.575200	.584720	.009520	1.655	.975
1.4	.548900	.548900	.000000	.000	.000
1.6	.525200	.530537	.005337	1.016	.547
1.8	.503600	.512175	.008575	1.703	.878
2.0	.483700	.493813	.010112	2.091	1.036
2.2	.466200	.475450	.009250	1.984	.948
2.4	.448000	.457088	.009088	2.028	.931
2.6	.431300	.438725	.007425	1.722	.761
2.8	.416200	.420363	.004162	1.000	.426
3.0	.402000	.402000	.000000	.000	.000
3.2	.388600	.391210	.002610	.672	.267
3.4	.375900	.380420	.004520	1.202	.463
3.6	.363800	.369630	.005830	1.603	.597
3.8	.352300	.358840	.006540	1.856	.670
4.0	.341400	.348050	.006650	1.948	.681

10.0	.151600	.152685	.001085	.715	.111
10.2	.147900	.149377	.001477	.999	.151
10.4	.144400	.146069	.001669	1.156	.171
10.6	.140900	.142762	.001862	1.321	.191
10.8	.137500	.139454	.001954	1.421	.200
11.0	.134200	.136146	.001946	1.450	.199
11.2	.131000	.132838	.001838	1.403	.188
11.4	.127900	.129531	.001631	1.275	.167
11.6	.124900	.126223	.001323	1.059	.136
11.8	.121900	.122915	.001015	.833	.104
12.0	.119100	.119608	.000508	.426	.052
12.2	.116300	.116300	.000000	.000	.000
12.4	.113600	.114000	.000400	.352	.041
12.6	.110900	.111700	.000800	.721	.082
12.8	.108400	.109400	.001000	.923	.102
13.0	.105800	.107100	.001300	.1229	.133
13.2	.103400	.104800	.001400	1.354	.143
13.4	.101000	.102500	.001500	1.485	.154
13.6	.098700	.100200	.001500	1.520	.154
13.8	.096400	.097900	.001500	1.556	.154
14.0	.094200	.095600	.001400	1.486	.143
14.2	.092100	.093300	.001200	1.303	.123
14.4	.090000	.091000	.001000	1.111	.102
14.6	.088000	.088700	.000700	.795	.072
14.8	.086000	.086400	.000400	.465	.041
15.0	.084100	.084100	.000000	.000	.000

Table 9. Errors in Atmospheric Transmittance — Target Altitude = 6. Km, Range = 9.2 Km, 3-5 μ m

Observer Altitude	Actual Transmittance	Table Trans	Error	% Error	% of Max
0	.406700	.406700	.000000	.000	.000
2	.421300	.421900	.000600	.142	.075
4	.437100	.437100	.000000	.000	.000
6	.454100	.454780	.000680	.150	.085
8	.472400	.472460	.000060	.013	.008
1.0	.492300	.490140	-.002160	-.439	-.271
1.2	.510800	.507820	-.002980	-.583	-.375
1.4	.525500	.525500	.000000	.000	.000
1.6	.538000	.535038	-.002962	-.551	-.372
1.8	.548800	.544575	-.004225	-.770	-.531
2.0	.558700	.554112	-.004588	-.821	-.577
2.2	.568100	.563650	-.004450	-.783	-.559
2.4	.577100	.573188	-.003912	-.678	-.492
2.6	.585800	.582725	-.003075	-.525	-.386
2.8	.594000	.592263	-.001737	-.293	-.218
3.0	.601800	.601800	.000000	.000	.000
3.2	.609200	.608320	-.000880	-.144	-.111
3.4	.616400	.614840	-.001560	-.253	-.196
3.6	.623400	.621360	-.002040	-.327	-.256
3.8	.630300	.627880	-.002420	-.384	-.304
4.0	.637100	.634400	-.002700	-.424	-.339
4.2	.643500	.640920	-.002580	-.401	-.324
4.4	.649700	.647440	-.002260	-.348	-.284
4.6	.655700	.653960	-.001740	-.265	-.219
4.8	.661500	.660480	-.001020	-.154	-.128
5.0	.667000	.667000	.000000	.000	.000
5.2	.672100	.671540	-.000560	-.083	-.070
5.4	.677100	.676080	-.001020	-.151	-.128
5.6	.681900	.680620	-.001280	-.188	-.161
5.8	.686500	.685160	-.001340	-.195	-.168
6.0	.690900	.689700	-.001200	-.174	-.151
6.2	.695600	.694240	-.001360	-.196	-.171
6.4	.700000	.698780	-.001220	-.174	-.153
6.6	.704300	.703320	-.000980	-.139	-.123
6.8	.708500	.707860	-.000640	-.090	-.080
7.0	.712400	.712400	.000000	.000	.000
7.2	.716100	.715469	-.000631	-.088	-.079
7.4	.719700	.718538	-.001162	-.161	-.146
7.6	.723100	.721608	-.001492	-.206	-.188
7.8	.726400	.724677	-.001723	-.237	-.217
8.0	.729600	.727746	-.001854	-.254	-.233
8.2	.732700	.730815	-.001885	-.257	-.237
8.4	.735700	.733885	-.001815	-.247	-.228
8.6	.738700	.736954	-.001746	-.236	-.219
8.8	.741600	.740023	-.001577	-.213	-.198
9.0	.744500	.743092	-.001408	-.189	-.177
9.2	.747200	.746162	-.001038	-.139	-.131
9.4	.749800	.749231	-.000569	-.076	-.072
9.6	.752300	.752300	.000000	.000	.000

9.8	.754700	.754238	-.000462	-.061	-.058
10.0	.757000	.756177	-.000823	-.109	-.103
10.2	.759200	.758115	-.001085	-.143	-.136
10.4	.761400	.760054	-.001346	-.177	-.169
10.6	.763400	.761992	-.001408	-.184	-.177
10.8	.765400	.763931	-.001469	-.192	-.185
11.0	.767300	.765869	-.001431	-.186	-.180
11.2	.769100	.767808	-.001292	-.168	-.162
11.4	.770900	.769746	-.001154	-.150	-.145
11.6	.772600	.771685	-.000915	-.118	-.115
11.8	.774300	.773623	-.000677	-.087	-.085
12.0	.775900	.775562	-.000338	-.044	-.043
12.2	.777500	.777500	.000000	.000	.000
12.4	.779000	.778800	-.000200	-.026	-.025
12.6	.780500	.780100	-.000400	-.051	-.050
12.8	.782000	.781400	-.000600	-.077	-.075
13.0	.783400	.782700	-.000700	-.089	-.088
13.2	.784800	.784000	-.000800	-.102	-.101
13.4	.786100	.785300	-.000800	-.102	-.101
13.6	.787400	.786600	-.000800	-.102	-.101
13.8	.788700	.787900	-.000800	-.101	-.101
14.0	.789900	.789200	-.000700	-.089	-.088
14.2	.791200	.790500	-.000700	-.088	-.088
14.4	.792300	.791800	-.000500	-.063	-.063
14.6	.793500	.793100	-.000400	-.050	-.050
14.8	.794600	.794400	-.000200	-.025	-.025
15.0	.795700	.795700	.000000	.000	.000

Test M-2

MODTRAN Input File Generation Evaluation

1. Test Description — This test checks the capability of the MODTRAN input generation program, ATMGEN1. The desired values of the MODTRAN input parameters were compared with the ATMGEN1 output file.

2. Test Objective — The objective of this test was to determine if the MODTRAN input file generation program functions correctly.

3. Test Configuration — The test configuration consists of the MODTRAN input generation program, ATMGEN1, and its output file, TAPE5.

4. Test Procedure — The test procedure consisted of running ATMGEN1 to generate the MODTRAN input file, TAPE5. This file was then compared with the desired values of the MODTRAN input parameters.

5. Test Results — The ATMGEN1 output file, TAPE5, agreed exactly with the desired MODTRAN input parameters for several runs with different operator answers to the ATMGEN1 queries.

Test M-3

MODTRAN Array Generation Evaluation

1. Test Description — This test checks the capability of the program, ATMGEN2, which reads the MODTRAN output file and generates the solar irradiance and atmospheric transmittance arrays. ATMGEN2 first reads the solar irradiance and transmittance data from the MODTRAN output file, then averages this data into the EZ*IR spectral bins, and finally generates the required arrays. The resulting arrays are then both written to two output files in two different forms. The output file ARRAYS.DAT contains the arrays in a FORTRAN readable form. The output file ARYSREAD.DAT contains the arrays in a form easily readable by humans, with headers identifying parameter values.

2. Test Objective — The objective of this test was to determine if the solar irradiance and atmospheric transmittance arrays are generated correctly.

3. Test Configuration — The test configuration consists of the MODTRAN output file, TAPE6, the array generation program, ATMGEN2, and its output file, ARRAYS.DAT.

4. Test Procedure — The test procedure consisted of running ATMGEN2 to read the MODTRAN output file, TAPE6, and generate the arrays. The file containing the arrays was then compared with the data in the MODTRAN output file, TAPE6, using spot check calculations. In addition, spot checks for consistency were made between the two output files, ARRAYS.DAT and ARYSREAD.DAT.

5. Test Results — The ATMGEN2 output file, ARYSREAD.DAT, agreed exactly with the spectral bin averaged data from the MODTRAN output file, TAPE6, for the spot checks calculated. In addition, the two output files, ARRAYS.DAT and ARYSREAD.DAT, agreed exactly for spot checks of equivalent locations. An abbreviated sample of ARYSREAD.DAT appears in Table 2.

Test M-4

Run-Time Interpolation Routine Evaluation

1. Test Description — This test checks the capability of the run-time interpolation subroutines, INTP2D and INTP3D, by calling the subroutines with various parameters. Some parameters are chosen at the breakpoints, some parameters are chosen

beyond the array limits, while others are chosen between breakpoints.

2. Test Objective — The objective of this test was to determine if the run-time interpolation subroutines functions correctly.

3. Test Configuration — The test configuration consists of a FORTRAN test program (CHKINT) to read the arrays data file, ARRAYS.DAT, and call the two interpolation subroutines, INTP2D and INTP3D, with various parameter values. Two output files were generated. CHKINT.DT1 contains results for parameters at array breakpoints and parameters beyond array limits. CHKINT.DT2 contains results for parameters between array breakpoints and parameters beyond array limits.

4. Test Procedure — The test procedure consisted of running CHKINT and comparing its output with direct values or interpolated values from the file ARYSREAD.DAT. At least four values in each output data file spectrum were compared with direct or interpolated array data.

5. Test Results — The CHKINT output data evaluated all agreed with the appropriate direct or interpolated array data.

6.0 CONCLUSIONS

The approach of using look-up tables to include MODTRAN results in a real-time IR simulation worked very well for the EZ*IR simulation. This method retains the accuracy of MODTRAN while meeting the real-time computation requirement. Although the look-up tables must be computed a priori, they are permanently stored for run-time use. This method is recommended for any simulation requiring MODTRAN results.

LAND DATA BASE REQUIREMENTS FOR ENVIRONMENTAL EFFECTS MODELS FOR USE IN DIS

by

Dr. William M. Cornette
Mr. David C. Anding
Mr. Frederick C. Mertz
Photon Research Associates, Inc.
10350 North Torrey Pines Road, Suite 300
La Jolla, California 92037-1020

1.0 INTRODUCTION

The Environmental Effects in Distributed Interactive Simulation (E^2 DIS) project is integrating into a Simulation Support Environment (SSE) software system a collection of government-developed environmental effects (E^2) models for use by simulator builders wanting to incorporate E^2 into their simulators (Ref. 4). Two of these models are the foundation of computer image generators (CIGs) and interface with the land data base. One model is required to calculate the diurnal variation in surface temperatures of natural and anthropic surfaces as affected by the natural environment. The second is required to calculate the emitted thermal and reflected solar/lunar and diffuse ambient radiation from these surfaces. These two models are the backbone of image rendering software in widespread use in the DIS community and are being actively developed for quantitative sensor simulations, such as Forward Looking Infrared (FLIR) systems. This paper presents the land data base specification requirements necessary to fully support quantitative image generation systems for visible "out-the-window" views and for sensors operating in any waveband from the ultraviolet to the millimeter wave, including data base content and level of detail. This paper also presents an overview of the two models' functions, their inputs and outputs which formed the basis for the requirements. Major issues include: (i) dealing with data base spatial resolutions ranging from submeter to kilometer; (ii) having material codes with sufficient breadth and detail to achieve continuous representations of real soils, vegetations, and other material types; and (iii) providing material properties which yield realistic and valid surface temperatures and radiances.

2.0 IMAGE GENERATION MODELS

CIGs are in widespread use in DIS. The most familiar ones generate visible "out-the-window" views of environments. These are red-green-blue (RGB) image renderings, typically derived from polygonal geometric representations of the environment overlaid with RGB texture maps (which provide the high spatial resolution detail within a polygon) derived from visible photographs. The images produced by these systems are not radiometrically quantitative (in the sense that brightness of a given image pixel has a unique radiance or luminance), but rather are qualitative color photographs, which can be realistic in appearance, but not radiometrically quantitative.

The more general CIGs being provided by the E^2 DIS project, and the ones needed to simulate sensors such as infrared FLIRs, are radiometrically quantitative. These systems also represent the environment geometrically, by either polygons or spatially uniform grids of altitudes referred to as "raster" data bases. In these systems, polygons may also be coupled to texture maps which provide high spatial resolution detail. However, for these quantitative CIGs, the vertex of every polygon (or every post position in a raster data base) and every pixel in a texture map (texel) is assigned a real material. In this material-based texture map, each texel has a spectrally varying reflectance and emittance and a temperature, allowing wavelength-selectable

simulations to be performed. Systems and data bases supporting these fundamental physical quantities are required to compute a quantitative thermally emitted and reflected radiance in support of E²DIS simulations.

2.1 General Radiance Equation

The basic CIG equation which must be evaluated to yield quantitative radiance at a pixel is:

$$H_{app} = [(H_{sol} * \cos(\phi) + H_{sky}) * \rho + H_{bb} * \epsilon] * T_{path} + H_{path}$$

where

H_{app}	=	Apparent radiance in W/cm ² /sr
H_{sol}	=	Solar radiance (at target) in W/cm ² /sr
ϕ	=	Angle between surface normal and direction to sun
H_{sky}	=	Skyshine radiance (at target) in W/cm ² /sr
H_{path}	=	Atmospheric path radiance in W/cm ² /sr
H_{bb}	=	Blackbody radiance in W/cm ² /sr
ρ	=	Surface material reflectance
ϵ	=	Surface material emittance
τ_{path}	=	Atmospheric path transmittance

The surface-related variables of this equation are θ , H_{bb} , and ρ , since for Lambertian surfaces $\epsilon = 1 - \rho$. The single geometric quantity is the angle between the surface normal and the direction to the sun, where sun direction depends upon latitude, longitude, date, and time of day. This angle is computed per vertex and interpolated per pixel. The blackbody radiance, H_{bb} , is controlled by the temperature of the surface and is multiplied by the surface emittance, ϵ . The surface material reflectance, ρ , depends upon the spectral response of the viewing sensor and the composition of the surface material. These surface quantities must be specified for every pixel in the scene. Because of this, the computation of image radiance from these quantities is a completely deterministic one.

This radiance equation sets the need for three categories of surface quantities which drive the land data base specification requirements. These are geometry, optical properties, and heat transfer properties.

2.1.1 Geometry

The geometry of land surfaces can conveniently be grouped into two categories: (1) those represented by a single-valued function of altitude (essentially all natural unvegetated surfaces); and (2) those requiring more than one altitude (such as low vegetation and tree canopies). The classic 100 meter scale Digital Terrain Elevation Data (DTED) from the Defense Mapping Agency (DMA) belongs to the first category; at each grid vertex the terrain elevation (altitude) is given. The scale of such data, in principle, can be any value, ranging from centimeters to kilometers. These data can be input to automatic processes which convert them to polygonal representations typically used in CIGs. When the spatial scales are larger than approximately 30 meters, most land surfaces can be represented by single-valued representations such as given by DTED. However, at smaller scales, say a few meters, fine features such as trees begin to be resolved and higher order functional representations are required. Such features are typically handled in CIGs by detailed polygonal representations of the fine feature object, much the same as an entity such as a tank, airplane, or building is represented. This works well, but it does impose the land data base specification requirement of providing the location of each fine feature plus enough further geometric information to develop its polygonal representation.

For the purposes of this paper, the term "geometry" is used to define the resolution cell or topology of a feature (e.g., a set of polygons). "Texture" is defined as the variability of a given material classification, both within a resolution cell (e.g., pixel or polygon) and between resolution cells with the same material assignment.

2.1.2 Optical Properties

The optical property of surfaces important to CIGs is the bidirectional reflectance distribution function (BRDF). In general, this quantity is a function of three angles; the elevation angle of the incident flux (ϕ_i), the elevation angle of the reflected flux (ϕ_r), and the relative azimuth between the incident and reflected fluxes ($\theta_i - \theta_r$). Corresponding to the BRDF is the directional emittance distribution function which is a function of the elevation angle (ϕ_r) of the emitted energy. The emittance can be obtained from the reflectance by applying conservation of energy, thereby reducing the amount of data required in the data base. Two special cases of the BRDF are Lambertian (which has no angular dependence) and specular (which only has non-zero reflectance when $\phi_i = \phi_r$ and $\theta_i - \theta_r = 180^\circ$). The most commonly used approximation is Lambertian, which is used here for simplicity and hereafter referred to as diffuse.

The basic CIG requirement is spectral diffuse reflectance spanning wavelengths from the visible through the infrared (0.4 to 14 μm) for a set of materials broad enough in scope to adequately sample the reflectance dimension for the environments of concern to DIS. The set will initially consist of a few hundred materials including water, soils, vegetation, anthropic surfaces, and paints, but will grow as needed.

The spectral resolution of the reflectance data (i.e., the ability to distinguish spectral features in the data) is a function of the material and the application. If a material's reflectance curve has little spectral variation, or if the sensor is fairly broadband (as is the case with most FLIRs), a spectrally coarse sampling of the reflectance data is appropriate. However, if the material has distinguishing spectral features and/or the sensor uses narrow spectral bands, a higher resolution data base is required.

2.1.3 Heat Transfer Properties

Any surface in a natural environment will experience changes in its surface temperature throughout the diurnal cycle as the radiative, convective, evaporative, and conductive fluxes change. The primary controller of these changes is the weather, particularly temperature, humidity, wind speed, and cloud cover (which greatly affects solar irradiation). Another major influencing factor in the surface temperature is the conductive heat exchange with the materials immediately below the surface. These heat transfer mechanisms are depicted in Figure 1. There are undoubtedly many implementations of solutions to this problem, but they all have one thing in common: the requirement for thermal and optical material properties of the surface and the substrate materials.

The heat transfer model being incorporated into the SSE for the E²DIS project has the following requirements for material properties for all surfaces except for large bodies of water, where the temperature can be defaulted to mean air temperature at the water surface or set by the user. Other algorithms will have similar requirements.

Thermal (Surface and Substrate Materials)

- Thickness (meters)
- Density (gm/m^3)
- Specific Heat ($\text{W}\cdot\text{sec}/\text{gm}\cdot\text{K}$)
- Conductance ($\text{W}/\text{m}\cdot\text{K}$)
- Characteristic Length (meters)

Optical Properties (Surface Material)

- Type of Surface (diffuse, directional, bidirectional)
- Diffuse Component Fraction
- Hemispherical Spectral Reflectance (throughout solar absorbing and thermal emitting regions)
- Surface Roughness Type, Standard Deviation, Correlation Length (bidirectional only)
- Fraction of Air and Type of Inclusion (snow only)

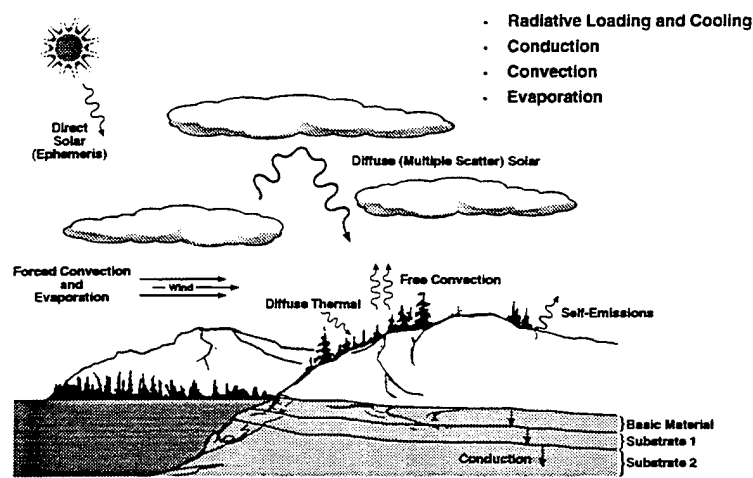


Figure 1. Terrain Surface Temperature Methodology.

3.0 LAND DATA BASE SPECIFICATION

The required land data base description for input to the CIG models is a point-by-point description of the material surface properties described in Section 2.0. There are basically two types of specifications which lead to the required data. One is an actual point-by-point specification of the needed data. The other is a statistical description from which the point-by-point specification can be derived. Recommendations regarding each of these specifications follow.

3.1 Geometry

Geometric specifications are given for the two categories of surfaces; single-valued and multi-valued. Each of these categories is discussed below.

3.1.1 Single-Valued Surfaces

Single-valued surfaces are those whose geometry is completely described by one variable, namely altitude. Within the context of DIS CIG applications this includes all non-vegetated natural surfaces. A common way of providing these data is specifying altitude on a regular spatial grid. This is adequate when the spatial scale is four or five times smaller than the highest viewing spatial resolution or when the surface geometry varies slowly with the horizontal dimension.

3.1.2 Multi-Valued Surfaces

Multi-valued surfaces become important when the viewing resolution is high enough to resolve fine features, such as trees, low vegetation, and anthropic structures. For these objects a single altitude specification is inadequate. What is needed is the type of object and its location within the regular grid, plus a description of its size.

3.1.3 Standardization

Currently, the definition of the geometry and texture of an object (e.g., building, railroad tracks, tree) are not provided by DMA. Each CIG developer has their own library of object geometries and texture maps. To insure consistency throughout DIS, it is crucial that the DMA provide both representative and site-specific geometries and textures for each object in the data base. These geometries and textures must span all resolutions. For example, a tree canopy could be a simple canopy height and texture at low resolution, a set of photographs of trees to be used as "billboards" at moderate resolution, and a detailed description of branch structure and leaf positions at high resolution.

3.2 Optical Properties

The optical properties of the surface materials, whether single-valued or multi-valued in their geometric representation, should be derived from a library of materials grouped by categories such as soils, vegetation, anthropic, and paints. Each material within this library would have the associated physical property descriptors (e.g., reflectance, density, conductance) given in Section 2.0.

The number of materials, the categories, and the descriptors would continually evolve and improve over time in regard to scope, detail, and accuracy of the values provided. The CIG input data problem is the spatial association of the library materials to the geometric descriptions. Typically this involves a linear combination of N materials at each location rather than assigning a single material to each spatial location, a daunting task complicated further by the fact that the material distributions change with season and precipitation history (e.g., rain, snow, deciduous vegetation). Since point-by-point classifications are needed (which could be provided deterministically or from statistical descriptors similar to the geometry), and since these classifications are changing with time, fixed material classifications registered to geometric data would not satisfy E²DIS CIG needs. What is needed is multispectral imagery at the desired spatial scale from which the needed classification can be derived through the use of standard multispectral (supervised or unsupervised) classification algorithms and techniques. This classification paradigm is identical to the use of visual RGB textures in visual "out-the-window" CIGs.

3.3 Thermal Properties

The Materials Library would contain the needed materials. Thermal properties data and the surface material classification would specify the thermal properties of the surface. However, for each geometric location an association of the substrate materials is required. The spatial resolution at which this is done is far less stringent than for surface material classification because it only influences the surface temperature and then only secondarily for most materials.

For the DIS CIG E²DIS project, the needed input data are 100 meter resolution specification of substrate materials affecting conductive heat transfer.

4.0 AVAILABLE RESOURCES FOR DATA

As mentioned above, an excellent source of the geometric data base is the DMA DTED data base. The corresponding Digital Feature Analysis Data (DFAD) (Ref. 1) data base contains a classification of surface types and features. However, in many cases these classifications are not adequate for a CIG application. Also, a material class in the DFAD does not presently exist with the necessary optical and thermal properties discussed above.

For the sake of brevity, this discussion will be limited to the "Landforms, Vegetation, and Miscellaneous Features" as an example. The other DFAD features are primarily anthropic, while these features are primarily natural, with a few exceptions:

- Metal fences
- Stone/brick walls, dams/weirs, water intake towers, tunnel entrances/exits
- Earthen work levees/embankments, cuttings, dams/weirs, ditches
- Concrete plaza/city square

The DFAD contains fourteen (14) Level 1 Surface Material Categories (SMC's) (Table 1), which at Level 2 are further broken down.

Table 1. DFAD Surface Material Categories.

Metal	Rock
Part Metal	Concrete
Stone/Brick	Soil
Composition	Wetland Vegetation/Marsh
Earthen Works	Trees
Water	Snow/Ice
Desert Sand	Asphalt

The DFAD Level 2 features for several of the SMC's are shown in Table 2. Furthermore, the DFAD provides clarification for some of the SMC's such as:

- Desert/sand is a combination of rock, gravel, and sand.
- Soil includes bare earth, cultivated ground, croplands, and grass.
- Trees (canopy) are defined as being greater than 8 meters above the surface.

Table 2. Sample DFAD Features.

WATER	DESERT/SAND	ROCK	SOIL	TREES
Dry Lake Salt Water Salt Pans Fresh Water Non-Perennial Stream Canal/Stream/Ditch	Sand Dunes Mud/Tidal Flats	Smooth Solid Rock Boulder Field/Lava Rocky Rough Surface	Ground Surface Soil (Forest Clearing) Tundra	Vegetation Orchards/Hedgerows Deciduous Trees Evergreen Trees Mixed Trees Vineyards

The E²DIS SSE Material Data Base consists of a number of material classifications, three of which are shown in Table 3. The elements of this data base were selected to be representative of a wide cross-section of materials that would be encountered in a DIS scenario. Categorization and groupings are based on physical properties and optical/thermal parameters.

Table 3. E²DIS SSE Terrain and Water Material Categories.

WATER	SOILS		VEGETATION
Water	Lump Coal	Loam Soil	Tundra
Ice	Road Gravel	Compact Soil	Scrub
Fresh Snow	Limestone Rock	Tilled Soil	Pine
Old Snow	Sandstone Rock	Wet Soil	Broadleaf
	Varnished Sandstone	Wet Lakebed	Lawn Grass
	Varnished Sand	Dry Lakebed	Dry Grass
	Black Sand	Wet Seabed	Scrub-Soil
	White Sand	Dry Seabed	Grass-Soil
	Lake Sand	Salt-Silt	Grass-Scrub
	Desert Sand	Silt-Sand	Pine-Scrub
	Beach Sand	Sand-Soil	Broadleaf-Scrub
	Loamy Sand	Sandstone-Soil	Broadleaf-Pine
	Sandy Loam	Limestone-Silt	Pine-Broadleaf
	Silty Loam	Limestone-Silt-Sand	Scrub-Grass-Soil
	Silty Clay	Limestone-Silt-Soil	
	Clay Soil		

The DFAD and SSE surface material classifications contain many similarities, indicating that a combining of the geometric (DFAD) and optical/thermal (SSE) classifications is a reasonable approach. However, certain elements of the DFAC SMC's create difficulties in a straightforward merger. For example, the inclusion of wet and dry features (e.g., fresh water versus dry lake; sand dunes versus mid/tidal flats) and the combining of disparate materials into a single category (e.g., croplands and grass as part of soil; rock, gravel, and sand as part of desert/sand), does not adequately represent the optical and thermal properties.

5.0 ISSUES AND RECOMMENDATIONS

This paper has clearly stated the land data base specifications required to support E²DIS CIG models. It has also demonstrated that there are certain deficiencies in the standard DMA products (e.g., DTED, DFAD; see Ref. 2) with regard to supporting CIG simulations in DIS in general. Obviously, these deficiencies must be addressed and eliminated. In achieving this, the possible approaches are many, but one important fact is pervasive, namely that the specific data base needs are dependent upon the application and can vary significantly from one application to the next.

The data base development problem is viewed as having four areas of concern. There are specificity, spatial resolution, spatial and temporal extent, and level of detail. A suggested data base structure is presented.

5.1 Specificity

Specificity is the degree to which a data base is site specific with regard to place and time. For those CIG applications that are site and time dependent (e.g., training for a specific mission), the terrain description (i.e., geometry, texture, optical properties, and thermal properties) must accurately represent the prevailing conditions. For example, it is not appropriate to classify a terrain element as "Clay" if it has been raining for the past week; rather, it should be classified as "Muddy Clay." A recommended way of doing this is to update the classification from site-specific visible and multispectral imagery consistent with the current conditions.

In contrast, many CIG applications only require representative data because they are using generic sites (e.g., the Fulda Gap, the Middle East, North Korea) and generic times (e.g., summer). For these applications, a library of representative or typical terrain descriptions is adequate. This library should contain sufficient

information to permit modelling of "representative conditions" at the location and time chosen, but would not require updates for the effects of prevailing conditions.

Both site-specific and representative data bases must contain the same type of information in regard to geometry, texture, optical properties, and thermal properties of the local surface cover, only the degree of specificity is different.

5.2 Spatial Resolution

The spatial resolution of the CIG application will dictate the type and scale of the terrain data base required.

For "coarse resolution" scenes (on the order of a kilometer), the geometry specifications in DTED is adequate, and DFAD SMC's, with some regrouping of categories and the possible addition of a few new categories (see Section 5.5), are adequate for material cover specification. However, they must be supplemented by texture, optical, and thermal specifications for each material classification.

For "medium resolution" scenes (on the order of 30-100 meters), DTED is generally adequate but must be supplemented by specific geometry representations for objects that can be resolved at this spatial scale. Also, the DFAD data base, as modified for Level I, must be supplemented by optical and thermal data bases, plus information on texture (e.g., photography) within a resolution cell.

For "fine resolution" scenes (on the order of a meter or less), both the DTED and DFAD SMC's are inadequate. Providing the needed data on this spatial scale on a global scale seems inappropriate from the perspective of the time and resources required to achieve it. Rather, providing stereo-photographic and multispectral imagery on demand for specific sites, coupled with libraries of optical and thermal data would appear to be a more appropriate solution.

5.3 Global and Seasonal Coverage

It is critical that the coverage of the DMA data base be global in extent, with full seasonal variability. For some applications, it may be acceptable to use a generic deciduous tree of a certain size, distributed with a given density, and with a generic soil underneath. However, in general, it is necessary to provide the CIG application with the type of tree (e.g., oak versus maple), its foliage state (e.g., bare, new growth, summer foliage, fall colors), the under-story vegetation (i.e., its foliage state and density), the type of soil (e.g., red clay versus black loam), and the climatic conditions (e.g., wet or dry).

One method for performing this is to make use of existing climatology, ecosystem, and geosystem data bases. For example, there exist excellent data bases for climate on a global scale for temperature, humidity, and other meteorological parameters on a 1 degree by 1 degree grid for each month of the year. Similarly, the Olson World Ecosystems data base (Ref. 3) provides a global ecosystem classification on a 10 minute grid, and the FAO Soil Map of the World (Ref. 3) provides soil information on a 2 minute grid.

5.4 Level of Detail

The level of detail at which the data base specification is provided must be expanded. It is recommended that a hierarchal data base would be most generic at the top level, and the specificity and detail would increase as one proceeds to lower levels. For example, an ordering might be soil, then sandy loam, followed by color and water content. The data base must be constructed in a self-consistent manner, so that as a CIG system goes from level to level within the data base, any changes observed are solely due to a better definition of the materials.

For geometry specifications, including anthropic objects, such as buildings, bridges, and railroads, it is not adequate to simply specify that an object exists at a location. Higher levels of detail must be given for the objects, including standard spatial renderings adequate to construct, for example, polygonal representations used by many CIG systems. These standard renderings could be either specific to an actual object or simply representative. In addition to the geometry, it is important that the texture, both within a resolution cell (e.g., a polygon) and between resolution cells of the same material category, be fully specified by DMA.

For optical properties, the data base must represent changes due to climate (e.g., wet versus dry soil), ecosystem (e.g., oak versus maple), and geosystem (e.g., red clay versus black loam). The data base must also provide optical properties at different spatial resolutions. For example, the reflectivity of a forest canopy at 100 meter resolution is different from the reflectivity of an individual leaf. In support of applications where a mixture of objects in a pixel is important, the data base should provide either specific or representative texture maps for various classes of material mixtures to insure that each CIG system renders the same scene in a consistent manner.

The level of detail for the thermal property representation must be consistent with the optical property level of detail. Therefore, a hierarchical representation, including such parameters as soil moisture, vegetation type and density, and sublayer composition and thickness, is required.

5.5 Data Base Structure

The current structure of the DMA data bases (e.g., DTED, DFAD) were initially designed to serve radar applications, and as such, perform very well for these applications. However, for the electro-optical/infrared (EO/IR) applications, the grouping of land SMC's creates problems and ambiguities. As indicated above, the inclusion of vegetation as part of the soil classification or mud/tidal flats with desert sand dunes is unacceptable in the EO/IR realm, due to vastly different optical and thermal properties, and even different thermal mechanisms, such as evaporation and evapotranspiration.

In order to correct this deficiency in the DMA data bases and to address the recommendations discussed above, a potential data base structure that would be analogous to the current structure is a hierarchical structure, consisting of several levels, each level being a further refinement of the level above. The DIS user could then chose the level appropriate to their own simulation, with assured consistency with other users operating at other levels and consistency when changing from far field to close range viewing, for example.

One potential set of levels are given below. These four levels are not meant to be definitive, but simply illustrative of the type of data base structure required for supporting DIS in the EO/IR environment.

- Level I: A slightly expanded set of DFAD Surface Material Categories, structured in a manner to avoid the incongruous groupings discussed above. This level would be appropriate for the coarse resolution simulations and those simulators capable of handling only a limited number of categories. For each category, a representative set of optical and thermal properties, together with necessary geometry and texture information, would be provided.
- Level II: For each category at Level I, a detailed break-out would be provided. Each category would consist of several hundred to perhaps a few thousand different Surface Material Types (SMT), together with geometry, texture, optical, and thermal properties appropriate for that generic SMT, independent of its global location. For example, a SMC of a Broadleaf Tree could be divided into different tree types (e.g., aspen, oak, maple, beech) and its various states (e.g., bare, new growth, full growth, and fall foliage). This level would be appropriate for a large number of applications that can handle the detail available at this level, but do not require SMT's specific to a given geographic location and time.

- Level III: This level would overlay the Level II Surface Material Types with global climatology, ecosystem, and geosystem data bases in order to provide a user with geometry, texture, optical, and thermal properties that are tailored for the particular global location (with a few kilometers) and average conditions at that time of year.
- Level IV: This level would be essentially identical to Level III, except that the geometry, texture, optical, and thermal properties would be defined for a particular site at a particular time. This level would be used for training for a specific upcoming mission, where recent data on the site is acquired, and the weather conditions (both measured and predicted) are used to generate the data.

5.6 Conclusion

The current DMA data bases, perhaps supplemented by existing climatology, ecosystem, and geosystem data bases, provide an excellent foundation upon which to build the global land data base for supporting DIS. An extensive effort to standardize the geometric representation, the optical properties, and the thermal properties of each object is still required in order for DMA to be fully responsive to the DIS community.

REFERENCES

1. Defense Mapping Agency. Digital Feature Analysis Data (DFAD) Level 1 and Level 2. Second Edition (1986). PS/ICE/200; PS/ICG/200.
2. Defense Mapping Agency. Digitizing the Future. 3rd Edition. DMA Stock No. DDIPDIGITALPAC.
3. National Oceanic and Atmospheric Administration/Environmental Protection Agency. Global Ecosystems Database. Version 1.0 (1992).
4. Naval Research Laboratory. Environmental Effects for Distributed Interactive Simulation System Design Document. Revision 1.0 (Draft Report) (1994).

AUTHORS

ABREU, L.W.	9,44,101
ACHARYA, P.K.	12,13,17,125,144,170
ADLER-GOLDEN, S.	8,96
AINSWORTH, T.L.	19,188
ANDERSON, G.P.	6,9,12,13,33,44,90,101,125,144,281,289
ANDING, D.C.	48,428
ARMSTRONG, P.S.	40,350
BERK, A.	12,125
BERNSTEIN, L.S.	12,125
BEVILACQUA, R.M.	19,188
BINGHAM, G.E.	33,281,289
BLUMBERG, W.A.M.	40,350,385
BOGLIOLO, M.P.	38,340
BROWN, J.	8,42,43,96,385,391
BROWN, P.D.	5,84
BUONGIORNO, M.F.	38,340
CAMY-PEYRET,	34,
CHETWYND, J.H.	6,9,12,44,90,101,125,289
CLARK, F.O.	45,46,395
CLOUGH, S.A.	5,9,14,84,101,150
CORNETTE, W.M.	13,17,48,144,170,428
COX, G.	2,55
CROW, K.M.	16,164
DALGARNO, A.	39,345
DEBRESTIAN, D.	19,188
DEWAN, E.M.	41,374
DODD, J.A.	40,350
DOTHE, H.	39,345
DOWNER, S.B.	45,
DUFF, J.	8,42,96,385
EGAN, W.G.	21,31,202,270
ESMOND, J.R.	2,55
von ESSE, F.	96,345
FROMM, M.	19,188
GALLERY, W.O.	9,101
GAMACHE, R.R.	1,49
GARNER, R.	22,210
GAUTIER, C.	10,28,120
GLACCUM, W.J.	19,188
GREEN, R.O.	28,248
GROSSBARD, N.J.	43,391
GRUNNINGER, J.	8,42,96,385
de HAAN, J.F.	29,
HAWAT, T.	34,
HOGAN, A.W.	31,270
HOGAN, D.B.	36,325
HOKE, M.L.	9,101
HOPPEL, K.W.	19,188
HORNSTEIN, J.S.	19,188

JEONG, L.S.	17,170
JESECK, P.	34,
JOSEPH, J.	21,202
KALIN, S.	23,218
KHARCHENKO, V.A.	39,345
KIMBALL, L.M.	101,
KNEIZYS, F.	9,101
KNUTESON, R.O.	5,84
KOFFEND, J.B.	32,277
KOKKE, J.M.M.	29,
KRIGMAN, S.	19,188
LEAN, J.	15,158
LEARNER, R.C.M.	2,55
LIPSON, S.J.	40,350
LOCKWOOD, R.D.	40,350
LOWELL, J.R.	40,350
LUCKE, R.L.	19,188
LUMPE, J.	19,188
MATSUMOTO, Y.	4,
McCANN, A.	1,49
McCLATCHEY, R.A.	101,
MERTZ, F.C.	48,428
MILLER, N.E.	5,84
MILLER, S.	6,90
MIMA, K.	18,182
MLAWER, E.J.	14,150
MONCET, J.-L.	6,35,36,90,263,325
MORIYAMA, M.	18,182
MURRAY, J.E.	2,55
NADILE, R.M.	33,40,281,289,350
NEER, M.E.	16,164
O'HIROK, W.	10,120
OHMURA, A.	23,218
PAIVA, C.A.	25,230
PARKINSON, W.H.	2,55
PAYAN, S.	34,
PHILBRICK, C.R.	26,27,242
PICARD, R.H.	7,41,72,374
PUGNAGHI, S.	38,340
QUAM, D.L.	47,418
REALMUTO, V.J.	37,38,322,340
REVERCOMB, H.E.	5,84
RICCHIAZZI, P.	10,120
ROBERT, D.A.	28,
ROBERTSON, D.C.	8,12,13,17,96,125,144,170
ROTHMAN, L.S.	1,9,49,101

SCHROEDER, J.	1,49
SELBY, J.E.A.	9,101
SHARMA, R.D.	8,39,42,96,345,385
SHETTLE, E.P.	9,19,101,188
SHIPPERT, T.R.	5,84
SMITH, D.R.	289
SMITH, W.L.	84
SNELL, H.E.	6,9,35,36,44,90,101,325
STEED, A.J.	33,281,289
STEVENS, T.D.	26,242
SUN, Y.	39,345
SUNDBERG, R.	96,385
TAUBMAN, S.J.	14,150
TEGGI, S.	38,340
THERIAULT, J.-M.	30,263
THOMAS, M.E.	3,61
THORNE, A.P.	2,55
TOFSTED, D.H.	24,224
TORGUET, R.	34,
TSUBAKI, H.	4,
TURNER, D.D.	84
VAIL, J.	44,
VERMOTE, E.F.	11,
VOLTZ, F.E.	20,200
WANG, J.	6,9,35,90,101,325
WATTSON, R.B.	1,49
WINNICK, J.R.	7,35,72,325
WINTERSTEINER, P.P.	7,35,72,325
YANG, S.	10,120
YOKOTA, T.	4,
YOSHINO, K.	2,55
ZHOU, D.K.	33,281,289
ZYNARSKI, A.	3,

ATMOSPHERIC TRANSMISSION MODELS MEETING

6-8 JUNE 1995

ATTENDANCE LIST

NAME	AFFILIATION	PHONE NUMBER
Abreu, Len	Abreu Consulting	(508) 256-5158
Acharya, Prabhat	SSI	(617) 273-4770
Adler-Golden, Steven	SSI	(617) 273-4770
Allen, Rodney J.	PL/GPAB	(617) 275-7581
Alley, Ron	JPL	(818) 354-0751
Bancroft, Barbara	MRC	(603) 891-0070 xt.239
Berk, Alexander	SSI	(617) 273-4770
Bernstein, Larry	Spectral Sciences	(617) 273-4770
Biral, Antonio Benato P.	UNICAMP-Brazil	
Blumberg, William	PL	(617) 377-3688
Brown, Patrick	AER	(617) 547-6209
Bunting, James T.	PL/GPAB	(617) 377-3493
Buongiorno, M. Fabrizia	Instituto Naz. Di Geofisica	(39) 6-51860939
Chance, Kelly	SAO	(617) 495-7389
Cheifetz, Mike	SPARTA	(617) 863-1060
Clough, Shepard A.	AER	(617) 349-2282
Conant, John	Aerodyne Research	(508) 663-9500
Cornette, William	PRA	(619) 455-9741
Crow, Katherine M.	SciTec, Inc	(609) 921-3892 xt. 248
Davidson, Gil	Photometrics	(617) 935-6500
Davis, Richard E.	NASA-LRC	(804) 864-1647
de Haan, Johan F.	Free Univ., Amsterdam	(+31) 20 4447958
Dothe, Hoang	Mei Tech	(617) 377-3654
Downer, Susan	MRC	(603) 891-0070 xt. 209
Egan, Walter	York College	(718) 441-6210
Gagnon, Grace	PL/GPOS	(617) 377-3687
Gallery, William	AER	(617) 349-2284
Gamache, Robert	U. Mass Lowell	(508) 459-7505
Garner, Richard	Photometrics, Inc	(617) 935-6500
Gillespie, Patti	ARL/BED	(505) 678-1817
Gouveia, Melanie J.	TASC	(617) 942-2000
Green, Robert O.	JPL	
Gruninger, John	SSI	(617) 273-4770
Hawat, Toufic Michel	IEMN/LPMA	(33) 27141370
Hestand, Dan	TASC	(617) 942-2000 xt. 2817
Higgins, Glenn	TASC	(703) 834-5000
Hogan, David	AER	(617) 547-6207
Hopke, Karen	Hughes Aircraft	(310) 616-6559
Humphrey, C.	VISIDYNE	(617) 272-2020
Ip, Precila	MRC	(603) 891-0070 xt.222

Kaelin, Simon	Swiss Fed. Inst., of Tech.	CH+ 1 257 5236
Koffend, Brooke	Aerospace Corp.	(310) 336-7412
Lean, Judith	NRL	(202) 767-5116
Linson, Paul	SAO/HCO	(617) 495-4865
Miller, Steven	PL/GPOS	(617) 377-2807
Mlawer, Eli	AER	(617) 349-2226
Moriyama, Masao	Nagasaki Univ.	481 958-47-1111 xt. 2640
Moylan, Bruce	Aero Thermo Tech.	(205) 922-1141
Noah, Meg	MRC	(603) 891-0070
Olga, Lado-Bordowsky	ENSSAT- Univ Rennes	96466613
Paboojian, Armand	ARCON	(617) 377-2262
Paiva, Clifford A.	Naval Surface Warfare Center	(703) 663-4781
Perlman, Sumner E.	KTAADV	(617) 527-0054
Philbrick, Russell	ARL/PSU	(814) 863-7682
Picard, Dick	PL/GPO	(617) 377-2222
Puckrin, Eldon	Trent University	(705) 748-1654
Putz, Erich	Inst. Meteorolgy and Geoph.	(063) 316-386-5258
Quam, David	MTL Systems	(513) 426-3111
Quiroga, Rafael	ITT/FSC	(805) 734-8232 xt. 5-7154
Raffensberger, Mark	TASC	(617) 942-2000
Ratkowski A.J.	PL/GPO	(617) 377-3655
Realmuto, Vince	JPL	(818) 354-1824
Ricchiazzi, Paul	UCSB/ICISS	(805) 893-4310
Robertson, David	SSI	(617) 273-4770
Rothman, Larry	PL/GPOS	(617) 377-2336
Schmidt, Eric	TASC	(617) 942-2000 xt. 3406
Schroeder, John	ONTAR	(617) 377-5314
Seliverstov, Dima	Mitre	(617) 353-8341
Shannon, Scott	Boston University	(617) 377-4198
Sharma, Ramesh	PL/GPOS	(617) 377-4198
Shettle, Eric P.	NRL	(202) 404-8152
Shirkey, Richard	ARL/BED	(505) 678-5470
Smarsh, David M. Major	WL/DOW	(513) 255-5496
Snell, Ned	AER	(617) 547-6207
Stevens, Tim	ARL/PSU	(814) 863-0851
Stokes, Jeff	PAR Government Sys. Corp.	(619) 551-9880
Stoner, William W.	SAIC	(617) 622-5603
Teggi, Sergio	Universita' Modena Italy	(39) 59370703
Theriault, Jean-Marc	DREV	(418) 844-4335
Tofsted, David	ARL/BED	(505) 678-3039
Tooth, Andy	Soverby Research Center	UK 117 9 363095
Vermote, Eric F.	NASA/GSFC	(301) 286-6232
Voltz, Fred	PL/GPOS	(617) 377-3666
Wan, Zhengming	UCSB	(805) 893-4541
Watt, David	UNH	(603) 802-2555
Wattson, Richard B.	SRL	(617) 275-8273
Weaver, Sandi	USAF, NAIC/TATW	(513) 257-7071
Wetmore, Alan	ARL/BED	(505) 678-5563

Winick, Jeremy
Wintersteiner, Peter
Wise, John
Woodford, Rich
Yokota, Tatsuya
Youmans, Doug
Zabela, Renee
Zachor A.S.
Zhan, Daniel
Zysnarski, Adam

PL/GPOS
ARCON
PL/GPO
USAFETAC/SYT
National Inst. Environ. Studies
W. J. Schafer
APL
Atmos. Rad.
SDL/USU
APL

(617) 377-3619
(617) 890-3330 xt.231
(617) 377-4442
(618) 256-5211
(+81)-298-50-2550
(508) 256 2070
(301) 953-6000 xt. 8632
(508) 263-1931
(301) 953-5470
(301) 953-5000